

Panayotis G. Kevrekidis
Dimitri J. Frantzeskakis
Ricardo Carretero-González
Editors

SPRINGER SERIES ON ATOMIC, OPTICAL AND PLASMA PHYSICS 45

Emergent Nonlinear Phenomena in Bose-Einstein Condensates

Theory and Experiment

Springer Series on

ATOMIC, OPTICAL, AND PLASMA PHYSICS 45

Springer Series on

ATOMIC, OPTICAL, AND PLASMA PHYSICS

The Springer Series on Atomic, Optical, and Plasma Physics covers in a comprehensive manner theory and experiment in the entire field of atoms and molecules and their interaction with electromagnetic radiation. Books in the series provide a rich source of new ideas and techniques with wide applications in fields such as chemistry, materials science, astrophysics, surface science, plasma technology, advanced optics, aeronomy, and engineering. Laser physics is a particular connecting theme that has provided much of the continuing impetus for new developments in the field. The purpose of the series is to cover the gap between standard undergraduate textbooks and the research literature with emphasis on the fundamental ideas, methods, techniques, and results in the field.

- 36 **Atom Tunneling Phenomena in Physics, Chemistry and Biology**

Editor: T. Miyazaki

- 37 **Charged Particle Traps**

Physics and Techniques of Charged Particle Field Confinement
By V.N. Gheorghe, F.G. Major, G. Werth

- 38 **Plasma Physics and Controlled Nuclear Fusion**

By K. Miyamoto

- 39 **Plasma-Material Interaction in Controlled Fusion**

By D. Naujoks

- 40 **Relativistic Quantum Theory of Atoms and Molecules**

Theory and Computation
By I.P. Grant

- 41 **Turbulent Particle-Laden Gas Flows**

By A.Y. Varaksin

- 42 **Phase Transitions of Simple Systems**

By B.M. Smirnov and S.R. Berry

- 43 **Collisions of Charged Particles with Molecules**

By Y. Itikawa

- 44 **Plasma Polarization Spectroscopy**

Editors: T. Fujimoto and A. Iwamae

- 45 **Emergent Nonlinear Phenomena in Bose-Einstein Condensates**

Theory and Experiment

Editors: P.G. Kevrekidis, D.J. Frantzeskakis, and R. Carretero-González

Panayotis G. Kevrekidis
Dimitri J. Frantzeskakis
Ricardo Carretero-González
(Editors)

Emergent Nonlinear Phenomena in Bose–Einstein Condensates

Theory and Experiment

With 108 Figures

Professor Panayotis G. Kevrekidis

University of Massachusetts, Amherst MA 01003-4515, USA

E-mail: kevrekid@math.umass.edu

Professor Dimitri J. Frantzeskakis

University of Athens, Athens 15784, Greece

E-mail: dfrantz@phys.uoa.gr

Professor Ricardo Carretero-González

San Diego State University, San Diego CA, 92182-7720, USA

E-mail: carreter@sciences.sdsu.edu

ISSN 1615-5653

ISBN 978-3-540-73590-8 Springer Berlin Heidelberg New York

Library of Congress Control Number: 2007932192

This work is subject to copyright. All rights are reserved, whether the whole or part of the material is concerned, specifically the rights of translation, reprinting, reuse of illustrations, recitation, broadcasting, reproduction on microfilm or in any other way, and storage in data banks. Duplication of this publication or parts thereof is permitted only under the provisions of the German Copyright Law of September 9, 1965, in its current version, and permission for use must always be obtained from Springer-Verlag. Violations are liable to prosecution under the German Copyright Law.

Springer is a part of Springer Science+Business Media.

springer.com

© Springer-Verlag Berlin Heidelberg 2008

The use of general descriptive names, registered names, trademarks, etc. in this publication does not imply, even in the absence of a specific statement, that such names are exempt from the relevant protective laws and regulations and therefore free for general use.

Typesetting and production: SPI Publisher Services

Cover design: eStudio Calmar Steinem

Printed on acid-free paper SPIN: 11801221 57/3180/SPI - 5 4 3 2 1 0

To:

Maria, Despina and Athena,
Eleni, Sofia and Apostolos-Ioannis,
Alexandra and Adrian.

For their support and the joy they bring to our lives.

Foreword

The field of Bose–Einstein condensation in atomic gases has been full of surprises. What happened after the first realization of Bose–Einstein condensates in 1995 has far exceeded the vision of their creators. Originally, I expected interesting studies of equilibrium properties and dynamics, but the Bose–Einstein condensate became a pristine platform for a host of scientific studies. The condensate turned out to be a well-controlled medium for nonlinear wave phenomena including four-wave mixing, dark and bright solitons, and dynamic instabilities. Rotating condensates gave access to the rich physics of vortices and vortex lattices. The availability of different hyperfine states led to multi-component or spinor condensates, and optical lattices opened up yet another major frontier which is still rapidly expanding. Feshbach resonances and condensation of fermion pairs will provide interesting phenomena to study for many more years to come.

This rapid development of the field has been fueled by a unique interplay between experiment and theory. Although experimentalists had the lead in realizing new systems, many phenomena were first predicted and then observed. The present book reflects this symbiosis by a balance of theoretical and experimental contributions. Twelve years after its beginning, the field has reached a degree of maturity which is much better represented by a comprehensive book than by a collection of original articles. I therefore expect this book not only to provide a valuable introduction to many young researchers who are joining this field, but also serve as a reference for further studies of nonlinear phenomena in this rich system.

Cambridge, MA, July 2007

Wolfgang Ketterle

Preface

The experimental realization of Bose–Einstein condensates (BECs) in 1995, in dilute atomic gases of ^{87}Rb and ^{23}Na , later honored with the Nobel Prize in Physics in 2001, was arguably one of the most important feats of the previous decade. The importance of this achievement is multi-faceted. Not only did it experimentally lead to the development and use of the newest and most sophisticated techniques for atomic cooling, trapping and imaging, but it also provided an excellent playground for comparison of theoretical predictions with experimental results. Not only did it pave the way for a deeper understanding of bosonic and fermionic behavior and of the crossover between the two, but it also led to fundamental advances in the study of coherent structures and patterns, including those of vortices and vortex lattices that were the theme of the Nobel Prize in Physics in 2003. Addressing and assessing this last impact aspect was one of the primary motivations of the present book.

A number of distinguished colleagues have succinctly described the “revolution” that was brought to the area of atomic physics by the realization of Bose–Einstein condensation. Nevertheless, one of the aspects that has perhaps been touched upon less is that of the cross-pollination that has emerged in the field of BECs with the fields of wave physics, nonlinear optics and nonlinear science more generally. The interface between these diverse areas of Physics has, perhaps primarily, been formulated by the presence of a very good mean-field model that can capture the experimental phenomenology not just qualitatively but also quantitatively in the appropriate limits. This model is the so-called Gross–Pitaevskii equation which is a form of the famous Nonlinear Schrödinger equation. The latter equation had been previously studied extensively in connection to nonlinear phenomena in optics, plasma physics and fluid dynamics. However, the BEC setting presented a number of novel particularities and flexibilities, including, but not limited to, the presence of external potentials and the possibilities for manipulation of these potentials or of the effective nonlinearity and dimensionality of the model. These features have naturally posed a wide array of exciting challenges that, in turn, have

spurred both experimental and theoretical developments at the cutting edge of nonlinear, atomic, and optical physics.

The idea for this book stemmed from the fact that in our own internal research excursions to this field, as well as in our interactions with our students and post-docs, we did not have a book to direct them to that addresses this interface: a book that covers this atomic physics theme, with a nonlinear wave dynamics bend and with references to other areas of physics where such notions arise. On the other hand, there are thousands of research papers and a tremendous amount of progress in this area, over the past 5–10 years. We felt that these would render such a book a valuable resource and a point of reference both for beginning, as well as for more seasoned researchers in this field. We decided that perhaps the best way to compile such a volume that would include a wide and diverse set of topics on nonlinear phenomena in BECs would be to invite a number of well-known experts to contribute a review each in their primary areas of focus within this wider theme. To make the relevant presentation more complete and to do justice to both the theoretical and the experimental aspects, we decided to partition each book part in two corresponding chapters. Our structuring of the table of contents of this volume was such as to try to touch upon the most important directions of this interface – admittedly, this is a selection that bears a personal flavor.

We were extremely lucky that our initial invitations and overall vision of this project were met with particular enthusiasm by a truly remarkable set of leading researchers in this field that kindly agreed to contribute. This book would simply not have materialized without their insightful, thorough and timely contributions, their professional and efficient coordination and their overall effort. We hope that the end result will be one that will be of value to a large number of researchers in this field, and will cover a significant gap in the literature of the subject. We also hope that it will serve as an educational resource for advanced students in Theoretical Physics, Experimental Physics and Applied Mathematics that are interested in this area.

Amherst, MA, USA,
Athens, Greece,
San Diego, CA, USA,
May 2007

*Panayotis Kevrekidis
Dimitri Frantzeskakis
Ricardo Carretero-González*

Contents

Part I Basic Mean-Field Theory for Bose–Einstein Condensates

1 Basic Mean-Field Theory for Bose–Einstein Condensates

<i>P.G. Kevrekidis, D.J. Frantzeskakis, and R. Carretero-González</i>	3
1.1 Introduction	3
1.2 The Gross–Pitaevskii (GP) Mean-Field Model	4
1.2.1 Origin and Basic Properties of the GP Equation	4
1.2.2 Repulsive and Attractive Interactions: Feshbach Resonance	5
1.2.3 The External Potential	6
1.3 Dimensionality Reduction	8
1.3.1 Length Scales	8
1.3.2 Derivation of Lower-Dimensional Models	9
1.3.3 The Discrete Nonlinear Schrödinger Equation	10
1.4 Ground State and Excitations	11
1.4.1 Ground State	11
1.4.2 Small-Amplitude Linear Excitations	12
1.4.3 Macroscopic Excitations: Solitons and Vortices	14
References	17

Part II Bright Solitons in Bose–Einstein Condensates

2 Bright Solitons in Bose–Einstein Condensates: Theory

<i>F.Kh. Abdullaev and J. Garnier</i>	25
2.1 Introduction	25
2.2 Bright Solitons in Quasi One-Dimensional BEC	27
2.2.1 The 1D Gross–Pitaevskii Equation	27
2.2.2 Adiabatic Soliton Compression	30
2.2.3 Transmission Through Nonlinear Barriers and Wells	32
2.2.4 Trapping by Dynamically Managed Linear Potentials	34

XII Contents

2.2.5	Controllable Soliton Emission by Spatial Variations of the Scattering Length	36
2.3	Bright Solitons in Nonlinear Optical Lattices	36
2.3.1	Propagation Through a Weak Nonlinear Periodic Potential	36
2.3.2	Propagation Through a Weak Random Nonlinear Potential	38
2.4	Multidimensional Bright Solitons in BECs	38
2.4.1	2D Bright Solitons in BECs with Time-Varying Scattering Length	38
2.4.2	2D Bright Solitons in BECs with Spatially-Varying Scattering Length	39
2.4.3	2D Bright Solitons in Dipolar BECs	40
2.4.4	3D Bright Solitons in Anisotropic Traps	40
2.5	Future Challenges	41
	References	41

3 Bright Solitons: Summary of Experimental Techniques

<i>L. Khaykovich</i>	45	
3.1	Introduction	45
3.2	Tunable Interatomic Interactions	46
3.2.1	Feshbach Resonance	46
3.2.2	Measure of the Interaction Strength	49
3.3	Optical Confinement of Bose–Einstein Condensates	50
3.3.1	BECs in Optical Traps	50
3.3.2	BECs in Low Dimensions	51
3.4	The Experiments	52
3.4.1	Formation of a Single Soliton	52
3.4.2	Soliton Trains	54
3.4.3	Formation of Solitons in Nearly 3D Traps	56
3.5	Origin of Higher Order Nonlinearity and its Impact on Soliton Dynamics	56
3.6	Conclusions	58
	References	59

Part III Dark Solitons in Bose–Einstein Condensates

4 Dark Solitons in Bose–Einstein Condensates: Theory

<i>V. V. Konotop</i>	65	
4.1	Condensate in an Elongated Trap	66
4.1.1	The Characteristic Scales	66
4.1.2	3D-to-1D Reduction of the Gross–Pitaevskii Equation	66
4.2	Dark Solitons in a Homogeneous Condensate	68
4.2.1	Dark Solitons of the Nonlinear Schrödinger Equation	68
4.2.2	On a Definition of a Dark Soliton	69

4.2.3	Dark Solitons and Sound Waves	71
4.2.4	Dark Solitons of the Quintic NLS Equation	72
4.3	Dark Solitons in a Trap	73
4.3.1	The Background Density Distribution	73
4.3.2	Landau Dynamics of a Soliton in an Inhomogeneous Condensate	74
4.3.3	Perturbation Theories and Long-Time Dynamics of a Dark Soliton	76
4.4	Nonconservative Dynamics of Dark Solitons	77
4.4.1	Effect of Dissipation on the Dark Soliton Evolution	77
4.4.2	Dark Solitons in Varying Traps	78
4.5	Theory of Generation of Dark Solitons	78
4.5.1	Phase Imprinting	79
4.5.2	Density Engineering	79
4.5.3	Generation of Trains of Dark Solitons	80
4.5.4	Feshbach-Resonance Management	80
	References	81

5 Dark Solitons in BECs: The First Experiments

<i>B.P. Anderson</i>	85	
5.1	Introduction	85
5.2	Overview of Experimental Approaches	86
5.2.1	Bose-Einstein Condensates as a Nonlinear Medium	86
5.2.2	Soliton Creation Techniques	87
5.2.3	Imaging	88
5.3	Observations with Dark Solitons	89
5.4	Conclusions	95
	References	96

Part IV Nonlinear Localization of BECs in Optical Lattices

6 Nonlinear Localization of BECs in Optical Lattices

<i>E.A. Ostrovskaya, M.K. Oberthaler, and Y.S. Kivshar</i>	99	
6.1	Introduction	99
6.2	Experimental Work Horse: Optical Potentials	100
6.3	BEC in a Periodic Potential: Theoretical Formalism	101
6.3.1	Mean-Field Model	101
6.3.2	Linear Bloch Waves	102
6.3.3	Nonlinear Bloch Waves	104
6.4	Dispersion/Diffraction Management: Experiment	106
6.5	Gap Solitons	109
6.5.1	Bright Solitons in Repulsive BEC	109
6.5.2	Soliton Trains and Anomalous Heating	113

XIV Contents

6.6	Self-Trapped States	117
6.6.1	Observation of the Macroscopic Self-Trapping	117
6.6.2	Truncated Bloch States	119
6.7	Gap Vortices	121
6.8	Multi-Component Gap States	124
6.9	Conclusions and Acknowledgments	128
	References	128

Part V Multi-Dimensional Solitons in Bose–Einstein Condensates

7 Multidimensional Solitons: Theory

<i>L.D. Carr and J. Brand</i>	133	
7.1	Introduction	133
7.2	Dark Solitons and Solitary Waves in Higher Dimensions	134
7.2.1	Dark Band and Planar Solitons	134
7.2.2	Ring Dark Solitons and Spherical Shell Solitons	137
7.2.3	Solitary Waves in Restricted Geometries	139
7.2.4	Vortex Rings and Rarefaction Pulses	141
7.2.5	Multi-Component Bose–Einstein Condensates	142
7.3	Bright Solitons in Higher Dimensions	143
7.3.1	Instability, Metastability, Stability	143
7.3.2	Bright Soliton Engineering: Pulsed Atom Lasers and Other Applications	146
7.3.3	Solitons in a Thermal Bath	148
7.3.4	Soliton–Soliton Interactions	148
7.3.5	Bright Ring Solitons and Quantum Vortices	149
7.4	Summary and Acknowledgments	152
	References	152

8 Experiments on Multidimensional Solitons

<i>J. Brand, L.D. Carr, and B.P. Anderson</i>	157	
8.1	Dimensional Aspects of Soliton Experiments in BECs	157
8.2	Preparation of Non-equilibrium BECs	158
8.2.1	Dark Soliton Quantum State Engineering	158
8.2.2	Density Engineering by Slow Light	159
8.3	Decay and Formation of Multidimensional Solitons	162
8.3.1	Quantum Shock Wave Dynamics and Soliton Shedding	162
8.3.2	Snake Instability and Vortex Ring Generation	163
8.4	Interacting Dark Solitons and Hybrid Structures	166
8.5	Conclusions	168
	References	168

Part VI Vortices in Bose–Einstein Condensates

9 Vortices in Bose–Einstein Condensates: Theory

<i>N.G. Parker, B. Jackson, A.M. Martin, and C.S. Adams</i>	173
9.1 Quantized Vortices	173
9.1.1 Theoretical Framework	173
9.1.2 Vortex Structures	175
9.2 Nucleation of Vortices	176
9.2.1 Rotation	176
9.2.2 Nucleation by a Moving Object	177
9.2.3 Other Mechanisms and Structures	178
9.3 Dynamics of Vortices	178
9.4 Stability of Vortices	180
9.4.1 Thermal Instabilities	180
9.4.2 Hydrodynamic Instabilities	180
9.5 Dipolar BECs	183
9.5.1 The Modified Gross–Pitaevskii Equation	183
9.5.2 Vortex Energy	184
9.6 Analogs of Gravitational Physics in BECs	184
9.6.1 Superradiance	185
References	186

10 Vortices in Bose–Einstein Condensates: Experiments

<i>F. Chevy</i>	191
10.1 Introduction: Vortices and Superfluidity	191
10.2 Nucleation of Vortices	192
10.2.1 Vortices in Liquid Helium	192
10.2.2 Phase Imprinting	192
10.2.3 Stirring	194
10.2.4 Rotationless nucleation	197
10.3 Experimental Characterization	198
10.3.1 Vortex Profile, Vortex Bending and Decay	198
10.3.2 Vortex Charge	198
10.3.3 Kelvin Modes of a Single Vortex Line	203
10.4 Conclusions	205
References	206

Part VII Vortex Lattices

11 Vortex Lattices in Bose–Einstein Condensates: Theory

<i>M. Ueda and H. Saito</i>	211
11.1 Hydrodynamic Theory of Vortices	211
11.2 Vortices in a Bose–Einstein Condensate	214

XVI Contents

11.3	Collective Modes of Vortices	218
11.3.1	Vortex Filament	218
11.3.2	Vortex Lattice	218
11.4	Dynamics of Vortex Nucleation	220
11.4.1	Scalar BEC	220
11.4.2	Spinor BEC	223
11.5	Fast Rotating BEC	225
	References	227

12 Vortex Lattices in Bose–Einstein Condensates: Experiments

<i>C. Raman</i>	229	
12.1	Overview	229
12.2	Experimental Observation	230
12.3	Spinning Condensates	232
12.4	Lattice Basics	233
12.5	Lattice Dynamics	235
12.6	Seeing the Phase	237
12.7	The Rotating Speed Limit	240
12.8	Summary and Outlook	241
	References	242

Part VIII Optical Lattices

13 Optical Lattices: Theory

<i>A. Smerzi and A. Trombettoni</i>	247	
13.1	Introduction	247
13.2	Discrete Equations for the Dynamics	249
13.2.1	Effects of Transverse Confinement	251
13.3	Excitation Spectra	253
13.3.1	Bloch Spectrum	254
13.3.2	Bogoliubov Spectrum	255
13.4	Landau and Dynamical Instabilities	256
13.5	Wave Packet Dynamics	258
	References	262

14 Bose–Einstein Condensates in Optical Lattices: Experiments

<i>O. Morsch</i>	267	
14.1	Introduction	267
14.1.1	Technical Considerations	268
14.1.2	Measurements, Observables and Calibration	269
14.2	Linear and Nonlinear Dynamics	271
14.2.1	Bloch Oscillations	271
14.2.2	Landau–Zener Tunneling	272

14.2.3 Josephson Effects	273
14.2.4 Instabilities	275
14.2.5 Dispersion Management and Solitons	276
14.3 Quantum Effects and the Mott Insulator Transition	277
14.4 Mixtures, Molecules and Fermions in Lattices	279
14.5 Perspectives	280
References	280

Part IX Multi-Component Bose–Einstein Condensates

15 Multi-Component Bose–Einstein Condensates: Theory

<i>B. Malomed</i>	287
15.1 Introduction	287
15.2 Basic Models: Coupled Gross–Pitaevskii Equations	288
15.3 Immiscible Species in One Dimension: Domain-walls and a Transition to Miscibility in Boson Gases	290
15.4 Degenerate Binary Fermion Gases	295
15.5 Symbiotic Solitons in Binary BECs	297
15.6 Domain-wall Crosses and “Propellers” in Two Dimensions	299
15.7 More Complex Models	301
15.8 Conclusions	302
References	303

16 Multi-Component Condensates: Experiment

<i>D.S. Hall</i>	307
16.1 Introduction	307
16.1.1 Imaging	308
16.1.2 Trapping	309
16.2 Pseudospinor Condensates	309
16.2.1 Component Separation and Domain Formation	311
16.2.2 Phase Coherence	314
16.2.3 Thermodynamics	315
16.2.4 Wavefunction Engineering	316
16.2.5 Spin Textures	317
16.3 Spinor Condensates	318
16.3.1 Basic Magnetic Properties	318
16.3.2 Spin Dynamics	320
16.3.3 Symmetry Breaking and Domain Formation	323
16.3.4 Thermodynamics	323
16.4 Future Prospects/Conclusions	324
References	324

Part X Manipulations of Coherent Matter-Waves

17 Manipulations of Coherent Matter-Waves

<i>P.G. Kevrekidis, D.J. Frantzeskakis, and R. Carretero-González</i>	331
17.1 Introduction	331
17.2 General Aspects of Guidance and Driving of Matter-Waves	332
17.2.1 Matter-Wave Solitons in the Mean-Field Picture	332
17.2.2 Time-Dependent External Potentials	333
17.3 Matter-Waves and Localized Impurities	335
17.3.1 Bright Matter-Wave Solitons	335
17.3.2 Dark Matter-Wave Solitons	336
17.3.3 Matter-Waves in Optical Lattices and Subject to Localized Impurities	337
17.4 Driving Matter-Waves by Optical Lattices	338
17.4.1 Bright Matter-Wave Solitons	338
17.4.2 Dark Matter-Wave Solitons	339
17.4.3 Matter-Wave Solitons in Optical Superlattices	340
17.5 Manipulations of Vortices	341
17.5.1 Manipulating Vortices by Localized Impurities	341
17.5.2 Vortices in Optical Lattices and Vortex Lattices	342
17.5.3 Vortex and Dark Soliton Nucleation Induced by Moving Impurities	343
17.6 Manipulations of the <i>s</i> -Wave Scattering Length	344
Conclusions	345
References	345

Part XI Beyond Gross–Pitaevskii Mean Field Theory

18 Beyond Gross–Pitaevskii Mean-Field Theory

<i>N.P. Proukakis</i>	353
18.1 Introduction	353
18.2 Microscopic Derivation of the Gross–Pitaevskii Equation	354
18.3 Generalized Mean-Fields: Static Thermal Cloud	357
18.4 Generalized Mean-Fields: Dynamic Thermal Cloud	359
18.4.1 Time-Dependent Hartree–Fock–Bogoliubov	359
18.4.2 Theory of Zaremba–Nikuni–Griffin	361
18.5 Kinetic Theories based on Probability Distribution Functions	363
18.5.1 Stoof’s Non-Equilibrium Theory	363
18.5.2 The Gardiner–Zoller Quantum Kinetic Master Equation ..	364
18.6 Stochastic Approaches to Condensate Dynamics	365
18.6.1 Classical Field Methods	365
18.6.2 The Stochastic Gross–Pitaevskii Equation	367

18.7 The Role of System Dimensionality	368
References	369

Part XII Asymptotic Reductions of the Gross–Pitaevskii Equation

19 Asymptotic Reductions of the Gross–Pitaevskii Equation	
<i>D.E. Pelinovsky</i>	377
19.1 Introduction	377
19.2 Class of Periodic Potentials	378
19.2.1 Small Strength: Coupled-Mode Equations	380
19.2.2 Moderate Strength: Continuous NLS Equations	382
19.2.3 Large Strength: Discrete NLS Equations	387
19.3 Class of Decaying Potentials	391
19.4 Class of Confining Potentials	394
Conclusions	396
References	397
Index	399

List of Contributors

Fatkhulla Kh. Abdullaev
Uzbek Academy of Sciences,
700084, Uzbekistan.
fatkh@uzsci.net

Charles S. Adams
Durham University,
Durham, DH1 3LE, UK.
c.s.adams@durham.ac.uk

Brian P. Anderson
University of Arizona,
Tucson, AZ 85721, USA.
bpa@optics.arizona.edu

Joachim Brand
Massey University
Auckland, New Zealand.
J.Brand@massey.ac.nz

Lincoln D. Carr
Colorado School of Mines,
Golden CO 80401, USA.
lcarr@mines.edu

Ricardo Carretero-González
San Diego State University,
San Diego CA, 92182-7720, USA.
carreter@sciences.sdsu.edu

Frédéric Chevy
Université Pierre et Marie-Curie,
75005 Paris, France.
chevy@lkb.ens.fr

Dimitri J. Frantzeskakis
University of Athens,
Athens 15784, Greece.
dfrantz@phys.uoa.gr

Josselin Garnier
Université Paris VII,
75251 Paris Cedex 5, France.
garnier@math.jussieu.fr

David S. Hall
Amherst College,
Amherst, MA 01002-5000, USA.
dshall@amherst.edu

Brian Jackson
Newcastle University,
Newcastle-upon-Tyne, NE1 7RU,
UK.
brian.jackson@newcastle.ac.uk

Panayotis G. Kevrekidis
University of Massachusetts,
Amherst MA 01003-4515, USA.
kevrekid@math.umass.edu

Lev Khaykovich

Bar Ilan University, Ramat-Gan,
52900 Israel.
hykovl@mail.biu.ac.il

Yuri S. Kivshar

Australian National University,
Canberra 0200, Australia.
ysk124@rsphysse.anu.edu.au

Vladimir V. Konotop

Universidade de Lisboa,
Lisboa 1649-003, Portugal.
konotop@ci.fc.ul.pt

Boris Malomed

Tel Aviv University,
Tel Aviv 69978, Israel.
malomed@eng.tau.ac.il

Andrew M. Martin

University of Melbourne,
Victoria 3010, Australia.
amm@ph.unimelb.edu.au

Oliver Morsch

Università degli Studi di Pisa,
56127 Pisa, Italy.
morsch@df.unipi.it

Markus K. Oberthaler

Universität Heidelberg,
69120 Heidelberg, Germany.
oberthaler@matterwave.de

Elena A. Ostrovskaya

Australian National University,
Canberra 0200, Australia.
ost124@rsphysse.anu.edu.au

Nicholas G. Parker

University of Melbourne,
Victoria 3010, Australia.
ngparker@ph.unimelb.edu.au

Dmitry E. Pelinovsky

McMaster University,
Hamilton, ON, L8S 4K1, Canada.
dmpeli@math.mcmaster.ca

Nikolaos P. Proukakis

Newcastle University,
Newcastle-upon-Tyne, NE1 7RU,
UK.
Nikolaos.Proukakis@ncl.ac.uk

Chandra Raman

Georgia Institute of Technology,
Atlanta, Georgia 30332-0430, USA.
craman@gatech.edu

Hiroki Saito

University of Electro-
Communications,
Tokyo 182-8585, Japan.
hsaito@hs.pc.uec.ac.jp

Augusto Smerzi

Universita' di Trento,
I-38050 Povo, Italy.
smerzi@science.unitn.it

Andrea Trombettoni

Int. School for Advanced Studies
I-34104, Trieste, Italy.
andreatr@sissa.it

Masahito Ueda

Tokyo Institute of Technology,
Tokyo 152-8551, Japan.
ueda@ap.titech.ac.jp

Part I

Basic Mean-Field Theory for Bose–Einstein Condensates

Basic Mean-Field Theory for Bose–Einstein Condensates

P.G. Kevrekidis, D.J. Frantzeskakis, and R. Carretero-González

1.1 Introduction

The phenomenon of Bose–Einstein condensation, initially predicted by Bose [1] and Einstein [2, 3] in 1924, refers to systems of particles obeying the Bose statistics. In particular, when a gas of bosonic particles is cooled below a critical transition temperature T_c , the particles merge into the Bose–Einstein condensate (BEC), in which a macroscopic number of particles (typically 10^3 to 10^6) share the same quantum state. Bose–Einstein condensation is in fact a quantum phase transition, which is connected to the manifestation of fundamental physical phenomena, such as superfluidity in liquid helium and superconductivity in metals (see, e.g., [4] for a relevant discussion and references). Dilute weakly-interacting BECs were first realized experimentally in 1995 in atomic gases, and specifically in vapors of rubidium [5] and sodium [6]. In the same year, first signatures of Bose–Einstein condensation in vapors of lithium were also reported [7] and were later more systematically confirmed [8]. The significance and importance of the emergence of BECs has been recognized through the 2001 Nobel prize in Physics [9, 10]. During the last years there has been an explosion of interest in the physics of BECs. Today, over fifty experimental groups around the world can routinely produce BECs, while an enormous amount of theoretical work has ensued.

From a theoretical standpoint, and for a wide range of experimentally relevant conditions, the dynamics of a BEC can be described by means of an effective mean-field theory. This approach is much simpler than treating the full many-body Schrödinger equation and can describe quite accurately the static and dynamical properties of BECs. The relevant model is a classical nonlinear evolution equation, the so-called Gross–Pitaevskii (GP) equation [11, 12]. In fact, this is a variant of the famous nonlinear Schrödinger (NLS) equation [13], which is a universal model describing the evolution of complex field envelopes in nonlinear dispersive media. The NLS is widely relevant to other areas of applications ranging from optics to fluid dynamics and plasma physics [14], while it is also interesting from a mathematical viewpoint [13–15]. In the case

of BECs, the nonlinearity in the GP model is introduced by the interatomic interactions, accounted for through an effective mean-field. Importantly, the study of the GP equation allows the prediction and description of important, and experimentally relevant, nonlinear effects and nonlinear states (such as solitons and vortices), which constitute the subject of this book.

This chapter is devoted to the mean-field description of BECs, the GP model and its properties. In particular, we present the derivation of the GP equation (see also Chap. 18) and some of its basic features. We discuss the different cases of repulsive and attractive interatomic interactions and how to control them via Feshbach resonances. We describe the external potentials that can be used to confine BECs, as well as how their form leads to specific types of simplified mean-field descriptions. Finally, we discuss the ground state properties of BECs and their small-amplitude excitations.

1.2 The Gross–Pitaevskii (GP) Mean-Field Model

1.2.1 Origin and Basic Properties of the GP Equation

The many-body Hamiltonian for N interacting bosons of mass m confined by an external potential $V_{\text{ext}}(\mathbf{r})$ is given in second quantization form by [16–18]

$$\hat{H} = \int d\mathbf{r} \hat{\Psi}^\dagger(\mathbf{r}) \left[-\frac{\hbar^2}{2m} \nabla^2 + V_{\text{ext}}(\mathbf{r}) \right] \hat{\Psi}(\mathbf{r}) + \frac{1}{2} \int d\mathbf{r} d\mathbf{r}' \hat{\Psi}^\dagger(\mathbf{r}) \hat{\Psi}^\dagger(\mathbf{r}') V(\mathbf{r} - \mathbf{r}') \hat{\Psi}(\mathbf{r}') \hat{\Psi}(\mathbf{r}), \quad (1.1)$$

where $\hat{\Psi}(\mathbf{r})$ and $\hat{\Psi}^\dagger(\mathbf{r})$ are the boson annihilation and creation field operators respectively, and $V(\mathbf{r} - \mathbf{r}')$ is the two-body interatomic potential. Adopting the well-established mean-field approximation [16–20], we use the decomposition $\hat{\Psi}(\mathbf{r}, t) = \Psi(\mathbf{r}, t) + \hat{\Psi}'(\mathbf{r}, t)$. In this expression, the complex function $\Psi(\mathbf{r}, t) \equiv \langle \hat{\Psi}(\mathbf{r}, t) \rangle$ (i.e., the expectation value of the field operator), has the meaning of an *order parameter* and is commonly known as the *macroscopic wavefunction of the condensate*. On the other hand, $\hat{\Psi}'(\mathbf{r}', t)$ describes the non-condensate part, which, at temperatures well below T_c , it is reasonable to assume that it is negligible (for a more formal and complete discussion please refer to Chap. 18). Then, the above prescription leads to a nontrivial zeroth-order theory for the BEC wavefunction as follows: First, from the Heisenberg equation $i\hbar(\partial\hat{\Psi}/\partial t) = [\hat{\Psi}, \hat{H}]$ for the field operator $\hat{\Psi}(\mathbf{r}, t)$, we obtain

$$i\hbar \frac{\partial}{\partial t} \hat{\Psi}(\mathbf{r}, t) = \left[-\frac{\hbar^2}{2m} \nabla^2 + V_{\text{ext}}(\mathbf{r}) + \int d\mathbf{r}' \hat{\Psi}^\dagger(\mathbf{r}', t) V(\mathbf{r}' - \mathbf{r}) \hat{\Psi}(\mathbf{r}', t) \right] \hat{\Psi}. \quad (1.2)$$

The next step is to simplify the interatomic interaction potential, $V(\mathbf{r}' - \mathbf{r})$. Consider the relevant case of a dilute ultracold gas with binary collisions at low energy, characterized by the *s*-wave scattering length a . In this limit, it can

be shown [16–18, 20] (see also Chap. 18) that the interatomic potential can be replaced by an effective interaction which is well described by a delta-function potential, $V(\mathbf{r}' - \mathbf{r}) = g\delta(\mathbf{r}' - \mathbf{r})$, where the coupling constant g is given by $g = 4\pi\hbar^2 a/m$. Employing this effective interaction potential and replacing the field operator $\hat{\Psi}$ with the classical field Ψ , (1.2) yields the GP equation,

$$i\hbar \frac{\partial}{\partial t} \Psi(\mathbf{r}, t) = \left[-\frac{\hbar^2}{2m} \nabla^2 + V_{\text{ext}}(\mathbf{r}) + g|\Psi(\mathbf{r}, t)|^2 \right] \Psi(\mathbf{r}, t). \quad (1.3)$$

The complex function Ψ in the GP (1.3) can be expressed in terms of the density $n(\mathbf{r}, t) \equiv |\Psi(\mathbf{r}, t)|^2$, and phase $S(\mathbf{r}, t)$ of the condensate as $\Psi(\mathbf{r}, t) = \sqrt{n(\mathbf{r}, t)} \exp[iS(\mathbf{r}, t)]$. Note that the phase $S(\mathbf{r}, t)$ fixes the atomic velocity as follows: The current density $\mathbf{j} = \frac{\hbar}{2mi} (\Psi^* \nabla \Psi - \Psi \nabla \Psi^*)$ (where star denotes complex conjugate), assumes a hydrodynamic form $\mathbf{j} = n\mathbf{v}$, with atomic velocity $\mathbf{v}(\mathbf{r}, t) = \frac{\hbar}{m} \nabla S(\mathbf{r}, t)$. This indicates that the atomic velocity is irrotational, i.e., $\nabla \times \mathbf{v} = 0$, which is a typical characteristic of *superfluids*. A detailed description on the hydrodynamics approach for the BEC superfluid can be found in Chap. 11.

The GP model conserves the total number of atoms, N , given by

$$N = \int d\mathbf{r} |\Psi(\mathbf{r}, t)|^2. \quad (1.4)$$

On the other hand, (1.3) can be written in canonical form, $i\hbar \frac{\partial}{\partial t} \Psi = \frac{\delta E}{\delta \Psi^*}$, where the dynamically conserved energy functional E is given by

$$E = \int d\mathbf{r} \left[\frac{\hbar^2}{2m} |\nabla \Psi|^2 + V_{\text{ext}} |\Psi|^2 + \frac{1}{2} g |\Psi|^4 \right] \quad (1.5)$$

with the three terms in the right-hand side representing, respectively, the kinetic energy, the potential energy and the interaction energy. Equations (1.4) and (1.5) indicate that the GP equation possesses two integrals of motion, the number of atoms N and the energy of the system E (provided, of course, that the external potential, V_{ext} , is time independent).

1.2.2 Repulsive and Attractive Interactions: Feshbach Resonance

The coefficient g which sets the nonlinearity strength in the GP (1.3), may take either positive or negative values; this is due to the fact that the scattering length may be $a > 0$ (e.g., for rubidium or sodium BEC) or $a < 0$ (e.g., for lithium BEC). The two cases correspond, respectively, to repulsive and attractive interactions between the atoms, or to defocusing and focusing Kerr-type nonlinearities in the language of nonlinear optics [13, 21].

Importantly, it is possible to control the interatomic interaction by changing the threshold collision dynamics, and consequently change the sign or the magnitude of the scattering length. This can be done upon applying an

external magnetic field, B , which controls the scattering length because of the rapid variation in collision properties associated with a threshold scattering resonance being a *Feshbach resonance* (see, e.g., [22] for the theoretical aspects, as well as [23, 24] and [25, 26] for relevant experimental results for sodium and rubidium condensates respectively). Specifically, the behavior of the scattering length near a Feshbach resonant magnetic field B_0 is typically of the form [27, 28],

$$a(B) = \tilde{a} \left(1 - \frac{\Delta}{B - B_0} \right), \quad (1.6)$$

where \tilde{a} is the value of the scattering length far from resonance and Δ represents the width of the resonance. On the other hand, a complementary way of tuning the scattering length can be achieved in low-dimensional setups (cf. Sect. 1.3). The extreme case of a very strong transversal confinement results in the so-called *confinement induced resonance*, at which the modified scattering length diverges [29, 30]. A third alternative approach uses the possibility of tuning the scattering length with an *optically induced Feshbach resonance* [31].

The possibility of the control over the interactions and collisional properties of the atoms was crucial for a variety of experimental discoveries such as the formation of bright matter-wave solitons [32–35], the formation of molecular BECs [36–38], and the revelation of the BEC–BCS (Bardeen–Cooper–Schrieffer) crossover [39, 40].

1.2.3 The External Potential

The external potential $V_{\text{ext}}(\mathbf{r})$ in the GP (1.3) can assume different forms, depending on the type of trapping, i.e., magnetic or optical. In particular, while in the first experiments BECs were confined by means of magnetic fields [9, 10, 16–18], later on the BEC confinement in purely optical fields became also possible. The first purely optical confinement of BECs was achieved in 1998 [41], where the condensate was first created in a magnetic trap and then was loaded into the optical dipole trap (see, e.g., relevant reviews in [42, 43]). However, from a 2001 experiment [44] it was demonstrated that it is possible to directly create and confine BECs in an optical dipole trap. The advantage of the optical dipole traps is that their shape is extremely flexible and controllable. An example of such control is a special case of optical potentials called optical lattices, in which the light field is a standing wave; in such a case, the resulting dipole potential is a crystal-like lattice of potential wells. Part VIII presents a detailed description on the theoretical and experimental aspects of optical lattices. In the first relevant experiments of [45, 46], cold atoms were trapped in optical lattices tuned close to resonance (i.e., the laser frequency was close to the atomic transition frequency); as a result, an effective dissipative behavior was observed due to the fact that spontaneous emission dominated the dipole trapping force. However, in

1996, non-dissipative far off-resonant optical lattices were first used to trap laser-cooled atoms [47]. Such far-detuned optical lattice potentials have been useful in elucidating novel physical phenomena in BECs (see, e.g., the recent review [48]).

In the case of the “standard” magnetic trap the external potential assumes the typical harmonic form:

$$V_{\text{MT}}(\mathbf{r}) = \frac{1}{2}m(\omega_x^2x^2 + \omega_y^2y^2 + \omega_z^2z^2), \quad (1.7)$$

where, in general, the trap frequencies $\omega_x, \omega_y, \omega_z$ along the three directions are different. As a result, the geometry of the trap and, hence, the shape of the condensate itself, may range from isotropic forms, to strongly anisotropic ones. In particular, if $\omega_x = \omega_y \equiv \omega_r \approx \omega_z$ the trap is isotropic and the BEC is almost spherical, while the cases $\omega_z < \omega_r$ or $\omega_r < \omega_z$ describe anisotropic traps in which the BEC is, respectively, elongated, “cigar shaped”, or flattened, “pancake-shaped”. The latter anisotropic cases, and especially the strongly anisotropic ones ($\omega_z \ll \omega_r$ or $\omega_r \ll \omega_z$), are particularly interesting as they are connected to effectively lower dimensional BECs, namely quasi one-dimensional (1D) and quasi two-dimensional (2D), respectively. At temperatures close to zero where phase fluctuations are negligible such *weakly-interacting* 1D and 2D condensates are possible (see a relevant discussion in Chap. 18), and have been realized experimentally in optical and magnetic traps [49], in optical lattice potentials [50–55], as well as surface microtraps [56, 57] (see also the recent review [58] for a relevant rigorous mathematical analysis). In this context, it is worth mentioning that even the limiting case of the purely 1D, *strongly-interacting*, so-called, Tonks–Girardeau gas [59, 60] (in which the interacting bosonic gas behaving like a system of free fermions) has recently been observed experimentally [61, 62].

On the other hand, as mentioned above, the optical lattice is imposed by a pair of laser beams forming a standing wave which generates a periodic potential. For example, a single periodic 1D standing wave of the form $E(z, t) = 2E_0 \cos(kz) \exp(-i\omega t)$ can be created by the superposition of the two identical beams, $E_{\pm}(z, t) = E_0 \exp[i(\pm kz - \omega t)]$, having the same polarization, amplitude E_0 , wavelength $\lambda = 2\pi/k$, and frequency ω . Since the dipole potential V_{dip} is proportional to the intensity $I \sim |E(z, t)|^2$ of the light field [43], this leads to a periodic potential, i.e., an optical lattice of the form $V_{\text{dip}} \equiv V_{\text{OL}} = V_0 \cos^2(kz)$. In such a case, the lattice periodicity is $\lambda/2$ and the lattice height is given by $V_0 \sim I_{\max}/\Delta\omega$, where I_{\max} is the maximum intensity of the light field and $\Delta\omega \equiv \omega - \omega_o$ is the detuning of the lasers from the atomic transition frequency ω_o . Note that atoms are trapped in the nodes (anti-nodes) of the optical lattice for blue- (red-) detuned laser beams, or $\Delta\omega > 0$ ($\Delta\omega < 0$). In a more general, three-dimensional (3D) setting, the optical lattice potential can take the following form:

$$V_{\text{OL}}(\mathbf{r}) = V_0 [\cos^2(k_x x + \phi_x) + \cos^2(k_y y + \phi_y) + \cos^2(k_z z + \phi_z)], \quad (1.8)$$

where $k_i = 2\pi/\lambda_i$ ($i \in \{x, y, z\}$), $\lambda_i = \lambda/[2 \sin(\theta_i/2)]$, θ_i are the (potentially variable) angles between the laser beams [48] (see also [63] and Part VIII) and ϕ_i are arbitrary phases.

It is also possible to realize experimentally an “optical superlattice”, characterized by two different periods. In particular, as demonstrated in [64], such an optical superlattice can be formed by the sequential creation of two lattice structures using four laser beams. A stationary 1D superlattice can be described as $V(z) = V_1 \cos(k_1 z) + V_2 \cos(k_2 z)$, where k_i , V_i denote, respectively, the wavenumbers and amplitudes of the sublattices. The experimental tunability of these parameters provides precise and flexible control over the shape and time-variation of the external potential.

It is worth mentioning that the magnetic or/and the optical dipole traps can be experimentally combined either together, or with other potentials; an example is far off-resonant laser beams, that can create effective repulsive potential barriers (for blue-detuned lasers) or attractive localized potentials (for red-detuned lasers). An important example of such a combination of a harmonic trap with a repulsive potential located at the center of the harmonic trap is the *double-well* potential. Such a potential has been used in the seminal interference experiment of [65], which demonstrated that BECs are in fact coherent matter-waves. Double-well potentials have also been created by a combination of a harmonic and a periodic optical potential [66]. Finally, other combinations, including, e.g., linear ramps of (gravitational) potential $V_{\text{ext}} = mgz$ have also been experimentally applied (see, e.g., [66, 67]). Additional recent possibilities include the design and implementation of external potentials, offered e.g., by the so-called *atom chips* [56, 57, 68, 69]. Generally, nowadays there exists a major flexibility for the creation of a wide variety of shapes and types (e.g., stationary, time-dependent, etc.) of external potentials.

1.3 Dimensionality Reduction

1.3.1 Length Scales

The confining frequencies ω_j ($j \in \{x, y, z\}$) of the magnetic trapping potential set characteristic length scales for the spatial size of the condensate through the characteristic harmonic oscillator lengths $a_{\text{ho},j} \equiv (\hbar/m\omega_j)^{1/2}$. Another important length scale, introduced by the effective mean-field nonlinearity, is the so-called “healing length” [16–18], which is the distance over which the kinetic energy and the interaction energy balance: if the BEC density grows from 0 to n over the distance ξ , the kinetic energy, $\sim \hbar^2/(2m\xi^2)$, and interaction energy, $\sim 4\pi\hbar^2 an/m$, become equal at the value of ξ given by

$$\xi = (8\pi na)^{-1/2}. \quad (1.9)$$

Note that the name of ξ is coined by the fact that it is actually the distance over which the BEC wavefunction Ψ “heals” over defects. Thus, the spatial widths of nonlinear excitations, such as dark solitons and vortices in BECs, are of $O(\xi)$.

1.3.2 Derivation of Lower-Dimensional Models

Let us assume that $\omega_x = \omega_y \equiv \omega_r$. Then, if the transverse harmonic oscillator length $a_{\text{ho},r} \equiv \sqrt{\hbar/m\omega_r} < \xi$, the transverse confinement of the condensate is so tight that the dynamics of such a cigar-shaped BEC can be considered to be effectively 1D. This allows for a reduction of the fully 3D GP equation to an effectively 1D GP model, which can be done for sufficiently small trapping frequency ratios ω_z/ω_r . It should be stressed, however, that such a reduction should be only considered as the 1D limit of a 3D mean-field theory and *not* as a genuine 1D theory (see, e.g., [58] for a relevant discussion). Similar considerations also hold for a pancake-shaped BEC, for which the condition $a_{\text{ho},z} < \xi$ along with the requirement of sufficiently small frequency ratios ω_r/ω_z , allows for a reduction to an effective 2D GP model. Such a reduction can be done following the same procedure as in the quasi-1D setting; thus, below we will confine ourselves to cigar-shaped BECs.

In the quasi-1D setting, assuming a highly anisotropic trap with $\omega_z \ll \omega_{\perp} \equiv \omega_x = \omega_y$, we may decompose the wavefunction Ψ in a longitudinal (along z) and a transverse [on the (x, y) plane] component, and seek for solutions of (1.3) in the form

$$\Psi(\mathbf{r}, t) = \psi(z, t) \Phi(r) \exp(-i\gamma t), \quad (1.10)$$

where $r^2 \equiv x^2 + y^2$, while the chemical potential γ and the transverse wavefunction $\Phi(r)$ are involved in the auxiliary problem for the transverse quantum harmonic oscillator,

$$\frac{\hbar^2}{2m} \nabla_{\perp}^2 \Phi - \frac{1}{2} m \omega_r^2 r^2 \Phi + \gamma \Phi = 0, \quad (1.11)$$

where $\nabla_{\perp}^2 \equiv \partial^2/\partial x^2 + \partial^2/\partial y^2$. Since the considered system is effectively 1D, it is natural to assume that the transverse component of the condensate wavefunction $\Phi(r)$ remains in the ground state; in such a case $\Phi(r)$ takes the form $\Phi(r) = \pi^{-1/2} a_r^{-1} \exp(-r^2/2a_r^2)$ [when considering the reduction from 3D to 2D the transverse wave function reduces to $\Phi(r) = \pi^{-1/4} a_r^{-1/2} \exp(-r^2/2a_r^2)$]. Then, substituting (1.10) into (1.3) and averaging the resulting equation in the r -direction (i.e., multiplying by $\Phi^* = \Phi$ and integrating with respect to r), we finally obtain the following 1D GP equation,

$$i\hbar \frac{\partial}{\partial t} \psi(z, t) = \left[-\frac{\hbar^2}{2m} \frac{\partial^2}{\partial z^2} + V(z) + \tilde{g} |\psi(z, t)|^2 \right] \psi(z, t), \quad (1.12)$$

where the new coupling constant \tilde{g} has an effective 1D form, namely $\tilde{g} = g/2\pi a_r^2 = 2a\hbar\omega_r$ and $V(z) = (1/2)m\omega_z^2 z^2$.

A similar reduction can be performed if, additionally, an optical lattice potential is present. In fact, it is possible (as, e.g., in the experiment in [70]) to tune ω_z so that it provides only a very weak trapping along the z -direction; in this way the shift in the potential trapping energies over the wells where the condensate is confined can be made practically negligible. In such a case, the potential in (1.12) is simply the 1D optical lattice $V(z) = V_0 \cos^2(kz)$. Similar considerations can be done e.g., in the quasi-2D case, introducing an “egg-carton potential” $V(x, y) = V_0 [\cos^2(k_x x) + \cos^2(k_y y)]$ for pancake-shaped condensates. We note in passing that dimensionality reduction techniques, such as the averaging method discussed above, are commonly used in other disciplines, e.g., in nonlinear fiber optics [21].

In the BEC context, apart from the above averaging method [71–73] (see also [74]), reduction of the 3D GP equation to 1D can be done self-consistently, using a multiscale expansion technique [75, 76], a variational approach [77] and other methods [78]. Importantly, many experimental results have been effectively described by lower dimensional GP models, also ones exhibiting *non-polynomial* nonlinearities [77] (see, e.g., the recent experiment [66]). It is relevant to note that lower-dimensional GP models with a *cubic-quintic* nonlinearity (that can also be obtained by Taylor expanding the non-polynomial nonlinearity of [77]) have been also been employed in various studies (see, e.g., [78–82]).

1.3.3 The Discrete Nonlinear Schrödinger Equation

Another useful reduction, which is relevant to deep optical lattice potentials, so that the chemical potential $\mu \ll V_0$ (see Sec. 1.4), is the one of the GP equation to a genuinely discrete model, the so-called *discrete NLS* (DNLS) equation [83]. Such a reduction has been introduced in the context of arrays of BEC droplets confined in the wells of an optical lattice in [84, 85] and further elaborated in [86]; we will follow the latter below. For convenience, we first use characteristic units, based on the lattice (and atomic) parameters, provided by the length k^{-1} (where $k = 2\pi/\lambda$ is the optical lattice wavenumber) and the recoil energy $E_{\text{rec}} = \hbar^2 k^2 / 2m$ (i.e., the kinetic energy gained by an atom when it absorbs a photon from the optical lattice), to express (1.12) in the following dimensionless form:

$$i \frac{\partial}{\partial t} \psi(z, t) = \left[-\frac{\partial^2}{\partial z^2} + V(z) + g|\psi(z, t)|^2 \right] \psi(z, t). \quad (1.13)$$

In (1.13), length is scaled in units of k^{-1} , time in units of \hbar/E_{rec} , the atomic density $|\psi|^2$ is rescaled in units of $(\pi^2/a)(a_r/\lambda)^2$, and energy is measured in units of the recoil energy. Finally, the coupling constant g in (1.13) is rescaled

to unity, i.e., $g = \pm 1$ for repulsive and attractive interatomic interactions respectively.

Next, assuming that $V(z)$ in (1.13) is a general periodic potential, i.e., $V(z + L) = V(z)$, we consider the eigenvalue problem associated to (1.13),

$$\frac{d^2\varphi_{k,\alpha}}{dz^2} + V(z)\varphi_{k,\alpha} = E_\alpha(k)\varphi_{k,\alpha}, \quad (1.14)$$

where $\varphi_{k,\alpha}$ has Bloch (Floquet) functions $\varphi_{k,\alpha} = \exp(ikx)\psi_{k,\alpha}(x)$, with $\psi_{k,\alpha}(x)$ being periodic with period L [α is an index labeling the energy bands $E_\alpha(k)$]. It is then useful to employ the (localized in each well of the optical lattice) Wannier functions [87], i.e., the Fourier transform of the Bloch functions. Due to the completeness of the Wannier basis, any solution of (1.13) can be expressed in the form $\psi(x, t) = \sum_{n,\alpha} c_{n,\alpha}(t)w_{n,\alpha}(x)$. Substituting the above expression into (1.13), and using the orthonormality of the Wannier basis, we obtain a set of differential equations for the coefficients [depending on the well (n) and band (α) index]. Upon suitable decay of the Fourier coefficients and the Wannier functions' prefactors (which can be systematically checked for given potential parameters), the model can then be reduced to

$$\begin{aligned} i\frac{dc_{n,\alpha}}{dt} = & \hat{\omega}_{0,\alpha}c_{n,\alpha} + \hat{\omega}_{1,\alpha}(c_{n-1,\alpha} + c_{n+1,\alpha}) \\ & + g \sum_{\alpha_1, \alpha_2, \alpha_3} W_{\alpha\alpha_1\alpha_2\alpha_3}^{nnnn} c_{n,\alpha_1}^* c_{n,\alpha_2} c_{n,\alpha_3}, \end{aligned} \quad (1.15)$$

where $W_{\alpha\alpha_1\alpha_2\alpha_3}^{nnnn} = \int_{-\infty}^{\infty} w_{n,\alpha} w_{n_1,\alpha_1} w_{n_2,\alpha_2} w_{n_3,\alpha_3} dx$. The latter equation degenerates into the tight-binding model [84, 85],

$$i\frac{dc_{n,\alpha}}{dt} = \hat{\omega}_{0,\alpha}c_{n,\alpha} + \hat{\omega}_{1,\alpha}(c_{n-1,\alpha} + c_{n+1,\alpha}) + gW_{1111}^{nnnn}|c_{n,\alpha}|^2c_{n,\alpha}, \quad (1.16)$$

if one restricts consideration only to the first band. Equation (1.16) is precisely the reduction of the NLS to its discrete counterpart: the discrete NLS (DNLS).

1.4 Ground State and Excitations

1.4.1 Ground State

The ground state of the GP model of (1.3) can readily be found upon expressing the condensate wave function as $\Psi(\mathbf{r}, t) = \Psi_0(\mathbf{r}) \exp(-i\mu t/\hbar)$, where Ψ_0 is a real function (normalized to the number of atoms, $\int d\mathbf{r} \Psi_0^2 = N$) and $\mu = \partial E / \partial N$ is the chemical potential. Substitution of the above expression into (1.3) yields the following steady-state equation for Ψ_0 :

$$\left[-\frac{\hbar^2}{2m} \nabla^2 + V_{\text{ext}}(\mathbf{r}) + g\Psi_0^2(\mathbf{r}) \right] \Psi_0(\mathbf{r}) = \mu \Psi_0(\mathbf{r}). \quad (1.17)$$

If $g = 0$, (1.17) reduces to the usual Schrödinger equation with potential V_{ext} . Then, for a harmonic external trapping potential [see (1.7)], the ground state of the system is obtained when letting all non-interacting bosons occupy the lowest single-particle state; there, Ψ_0 has the Gaussian profile

$$\Psi_0(\mathbf{r}) = \sqrt{N} \left(\frac{m\omega_{\text{ho}}}{\pi\hbar} \right)^{3/4} \exp \left[-\frac{m}{2\hbar} (\omega_x^2 x^2 + \omega_y^2 y^2 + \omega_z^2 z^2) \right], \quad (1.18)$$

where $\omega_{\text{ho}} = (\omega_x \omega_y \omega_z)^{1/3}$ is the geometric average of the confining frequencies.

For repulsive interatomic forces ($g > 0$, or scattering length $a > 0$), if the number of atoms of the condensate is sufficiently large so that $Na/a_{\text{ho}} \gg 1$, the atoms are pushed towards the rims of the condensate, resulting in slow spatial variations of the density. Then the kinetic energy (gradient) term is very small compared to the interaction and potential energies and becomes significant only close to the boundaries. Thus, the Laplacian kinetic energy term in (1.17) can safely be neglected. This results in the, so-called, Thomas–Fermi (TF) approximation [16–18] for the system’s ground state density profile:

$$n(\mathbf{r}) = |\Psi_0(\mathbf{r})|^2 = g^{-1} [\mu - V_{\text{ext}}(\mathbf{r})], \quad (1.19)$$

in the region where $\mu > V_{\text{ext}}(\mathbf{r})$, and $n = 0$ outside. In this approximation, for a spherically symmetric harmonic magnetic trap ($V_{\text{ext}} = V_{\text{MT}}$ with $\omega_{\text{ho}} = \omega_x = \omega_y = \omega_z$), the radius $R_{\text{TF}} = (2\mu/m)^{1/2}/\omega_{\text{ho}}$ for which $n(R_{\text{TF}}) = 0$, the so-called Thomas–Fermi radius, determines the size of the condensed cloud. Furthermore, the normalization condition connects μ and N through the equation $\mu = (\hbar\omega_{\text{ho}}/2)(15Na/a_{\text{ho}})^{2/5}$.

For attractive interatomic forces ($g < 0$, or $a < 0$), the density tends to increase at the trap center, while the kinetic energy tends to balance this increase. However, if the number of atoms N in the condensate exceeds a critical value, i.e., $N > N_{\text{cr}}$, the system is subject to *collapse* in a 2D or a 3D setting, respectively [13, 17, 18]. Collapse was observed experimentally in both cases of the attractive ${}^7\text{Li}$ [88] and ${}^{85}\text{Rb}$ condensate [89]. The critical number of atoms necessary for collapse in a spherical BEC is determined by the equation [90], $N_{\text{cr}}|a|/a_{\text{ho}} = 0.575$, where $|a|$ is the absolute value of the scattering length and $a_{\text{ho}} = (\hbar/m\omega_{\text{ho}})^{1/2}$. Importantly, collapse may not occur in a quasi-1D setting, which implies that cigar-shaped attractive BECs (confined in a trap with frequencies $\omega_z \ll \omega_r$) are not subject to collapse, provided that their number of atoms does not exceed the critical value given by the equation $N_{\text{cr}}|a|/a_{\text{ho},r} = 0.676$, with $a_{\text{ho},r}$ being the transverse harmonic oscillator length [71, 91, 92].

1.4.2 Small-Amplitude Linear Excitations

Let us now consider small-amplitude excitations of the condensate, which can be found in the framework of mean-field theory upon linearizing the

time-dependent GP equation around the ground state. Specifically, solutions of (1.3) can be sought in the form

$$\Psi(\mathbf{r}, t) = e^{-i\mu t/\hbar} \left[\Psi_0(\mathbf{r}) + \sum_j \left(u_j(\mathbf{r}) e^{-i\omega_j t} + v_j^*(\mathbf{r}) e^{i\omega_j^* t} \right) \right], \quad (1.20)$$

where u_j, v_j are small (generally complex) perturbations, describing the components of the condensate's (linear) response to the external perturbations that oscillate at frequencies $\pm\omega_j$ [the latter are (generally complex) eigenfrequencies]. Substituting (1.20) into (1.3), and keeping only the linear terms in u_j and v_j , the following set of equations is derived

$$\begin{aligned} \left[\hat{H}_0 - \mu + 2g\Psi_0^2(\mathbf{r}) \right] u_j(\mathbf{r}) + g\Psi_0^2(\mathbf{r})v_j(\mathbf{r}) &= \hbar\omega_j u_j(\mathbf{r}), \\ \left[\hat{H}_0 - \mu + 2g\Psi_0^2(\mathbf{r}) \right] v_j(\mathbf{r}) + g\Psi_0^{*2}(\mathbf{r})u_j(\mathbf{r}) &= -\hbar\omega_j v_j(\mathbf{r}), \end{aligned} \quad (1.21)$$

where $\hat{H}_0 \equiv -(\hbar^2/2m)\nabla^2 + V_{\text{ext}}(\mathbf{r})$. Equations (1.21) are known as the *Bogoliubov–de Gennes (BdG) equations*. These equations can also be derived using a purely quantum-mechanical approach [16–18, 20] and can be used, apart from the case of the ground state, for other states (such as solitons and vortices) with the function Ψ_0 being modified accordingly.

The BdG equations are intimately connected to the stability of the state Ψ_0 . Specifically, suitable combinations of (1.21) yield

$$(\omega_j - \omega_j^*) \int (|u_j|^2 - |v_j|^2) d\mathbf{r} = 0. \quad (1.22)$$

Equation (1.22) can be satisfied in two different ways: First, if $\omega_j - \omega_j^* = 0$, i.e., if the eigenfrequencies ω_j are real; in that case, the fact that $\text{Im}\{\omega_j\} = 0$ shows that the state Ψ_0 is *stable*. Note that, in this case, one can use the normalization condition for the eigenmodes u_j, v_j of the form $\int (|u_j|^2 + |v_j|^2) d\mathbf{r} = 1$. Alternatively, occurrence of complex eigenfrequencies ω_j (i.e., if $\omega_j - \omega_j^* \neq 0$ or $\text{Im}\{\omega_j\} \neq 0$), indicates *dynamical instability* of the state Ψ_0 ; in such a case, (1.22) is satisfied only if $\int |u_j|^2 d\mathbf{r} = \int |v_j|^2 d\mathbf{r}$.

The BdG equations provide interesting results even in the case of a uniform gas ($V_{\text{ext}}(\mathbf{r}) = 0$). In such a case, the amplitudes u and v are plane waves $\sim e^{i\mathbf{k}\cdot\mathbf{r}}$ (of wavevector \mathbf{k}) and (1.21) lead to a dispersion relation, known as the *Bogoliubov spectrum*:

$$(\hbar\omega)^2 = \left(\frac{\hbar^2 \mathbf{k}^2}{2m} \right) \left(\frac{\hbar^2 \mathbf{k}^2}{2m} + 2gn \right). \quad (1.23)$$

For small momenta $\hbar k$, (1.23) yields the phonon dispersion relation $\omega = cq$, where $c = \sqrt{gn/m}$ is the speed of sound. On the other hand, for large momenta, the spectrum provides the free particle energy $\hbar^2 k^2/(2m)$, with

the “crossover” between the two regimes occurring when the excitation wavelength is of the order of the healing length given by (1.9).

Finally, it should be noticed that in the case of attractive interatomic interactions $g < 0$, the speed of sound becomes imaginary, which indicates that long wavelength perturbations grow or decay exponentially in time. This effect is directly connected to the *modulational instability*, which leads to delocalization in momentum space and, in turn, to localization in position space and the formation of solitary-wave structures. The effect of modulational instability is responsible for the formation of bright matter-wave solitons [32–34], as was analyzed in detail by many theoretical works (see, e.g., [93–95], as well as [74, 96] and Chap. 2 for relevant reviews).

1.4.3 Macroscopic Excitations: Solitons and Vortices

Aside from the simpler states discussed above, strongly nonlinear and localized states have been observed experimentally in BECs by using various relevant techniques. These include phase engineering of the condensates in order to create vortices [97, 98] or dark matter-wave solitons in them [99–102] (see also Part III), the stirring (or rotation) of the condensates providing angular momentum and creating vortices [103, 104] (see also Part VI) and vortex-lattices [105–107] (see also Part VII), the change of scattering length (from repulsive to attractive via Feshbach resonances) to produce bright matter-wave solitons and soliton trains [32–34] in attractive condensates (see also Part II), or set into motion a repulsive BEC trapped in optical lattice to create gap matter-wave solitons [70] (see also Part IV). Both matter-wave solitons and vortices can be viewed as fundamental nonlinear excitations of the BECs, and as such have attracted considerable attention. As far as vortices and vortex lattices are concerned, it should be noted that their description and connection to phenomena as rich and profound as superconductivity and superfluidity, were one of the themes of the Nobel prize in Physics in 2003.

The main scope of the present book is to focus on such nonlinear phenomena and structures, emerging from the effective mean-field nonlinearity of BECs and to offer a review of the large volume of recent literature that has developed over the last decade in this forefront of research, interfacing between atomic, nonlinear and wave physics. Although the aforementioned nonlinear structures (i.e., the solitons and vortices) will thoroughly be discussed in the following chapters, it is worth closing this introductory chapter by briefly presenting the most fundamental ones, namely the bright and dark matter-wave solitons in 1D, as well as vortices in 2D. This way, we believe that it will be easier for the reader to follow the topical reviews that will be presented in the following chapters.

Let us again consider the dimensionless Gross–Pitaevskii (1.13). In the absence of the external potential, this equation becomes the “traditional” completely integrable NLS equation, which possesses different types of soliton solutions, depending on the parameter g . In particular, for *attractive* BECs

($g = -1$) the NLS equation possesses a *bright* soliton solution of the following form [108],

$$\psi(z, t) = \eta \operatorname{sech}[\eta(z - vt)] \exp[i(kz - \omega t)], \quad (1.24)$$

where η is the amplitude and inverse spatial width of the soliton, k is the soliton wavenumber, $\omega = \frac{1}{2}(k^2 - \eta^2)$ is the soliton frequency, and $v \equiv \partial\omega/\partial k = k$ is the soliton velocity. The bright soliton (1.24) is characterized by two independent parameters. Note that the “soliton dispersion relation” $\omega = \frac{1}{2}(k^2 - \eta^2)$ implies that $\omega < \frac{1}{2}k^2$, and, hence, the allowable region in the (k, ω) plane for bright solitons is located *below* the parabola $\omega = \frac{1}{2}k^2$, corresponding to the elementary excitations (linear waves) of the NLS equation. The bright soliton solution is shown in Fig. 1.1a for $\eta = 1$ and $v = 3$.

On the other hand, in the *repulsive* BEC case ($g = +1$), the NLS equation possesses a dark soliton solution [109], which can be considered as an excitation of the plane wave solution $\psi = \psi_0 \exp[i(kz - \omega t)]$. In particular, on a homogeneous background density ψ_0^2 , the dark soliton may be expressed (in the most general case of a moving background) as [109],

$$\psi(z, t) = \psi_0 (\cos \varphi \tanh \zeta + i \sin \varphi) \exp[i(kz - \omega t)], \quad (1.25)$$

where $\zeta \equiv \psi_0 \cos \varphi (z - vt)$, the parameter $\omega = (1/2)k^2 + \psi_0^2$ characterizes the dispersion relation of the background plane wave, while the remaining

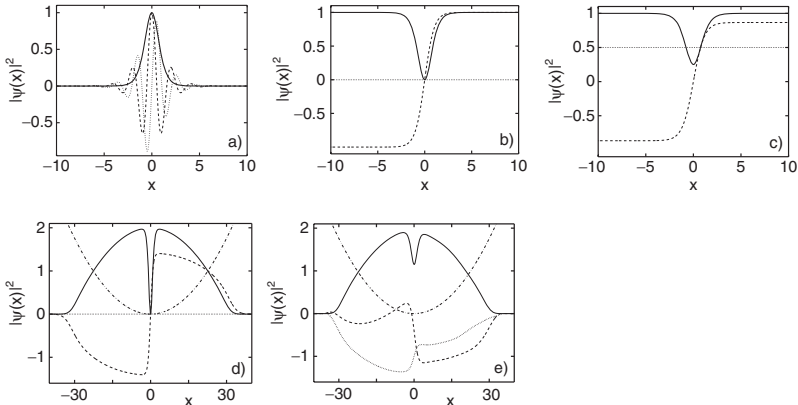


Fig. 1.1. One-dimensional excitations of the Gross–Pitaevskii equation. (a) Bright soliton in the absence of external potential with height $\eta = 1$ and velocity $v = 3$. (b) Stationary ($v = 0$) dark soliton in the absence of external potential with $k = 0$, $\mu = \psi_0^2 = 1$, $\varphi = 0$, and $\omega = 0$. (c) Moving gray soliton in the absence of external potential with $k = 0$, $\mu = \psi_0^2 = 1$, $v = 0.5$, $\varphi = \pi/6$, and $\omega = 1$. (d) Stationary ($v = 0$) dark soliton inside a magnetic trap with $\Omega = 1/16$ and $\mu = 2$. (e) Moving gray soliton inside a magnetic trap with $\Omega = 1/16$ and $\mu = 2$. In all panels the atomic density $|\psi(x)|^2$ is depicted by the *thick solid line* while the real and imaginary parts of the wavefunction are depicted with *thin dashed and dotted lines*, respectively. The magnetic external potential in (e) and (d) is depicted by the *thick dashed-dotted line*.

soliton and background parameters, v , φ and k , are connected through the relation $v = \psi_0 \sin \varphi + k$. Here, φ is the so-called *soliton phase angle*, or, simply, the phase shift of the dark soliton ($|\varphi| < \pi/2$), which describes the *darkness* of the soliton through the relation, $|\psi|^2 = 1 - \cos^2 \varphi \operatorname{sech}^2 \zeta$; this way, the limiting cases $\varphi = 0$ and $\cos \varphi \ll 1$ correspond to the so-called *black* and *gray* solitons, respectively. Note that the amplitude and velocity of the dark soliton are given by $\cos \varphi$ and $\sin \varphi$ respectively; thus, the black soliton, $\psi = \psi_0 \tanh(\psi_0 x) \exp(-i\mu t)$, is a stationary dark soliton ($v = 0$), while the gray soliton moves with a velocity close to the speed of sound ($v \sim \psi_0$). Apparently, the dark soliton solution (1.25) has three independent parameters, two for the background (ψ_0 and k) and one for the soliton (φ). Also, it should be noted that as in this case the dispersion relation implies that $\omega > k^2$, the allowable region in the (k, ω) plane for dark solitons is located *above* the parabola $\omega = \frac{1}{2}k^2$.

Usually, dark matter-wave solitons are considered in the simpler case where the background is at rest, i.e., $k = 0$; then, the frequency ω actually plays the role of a normalized one-dimensional chemical potential, namely $\mu \equiv \psi_0^2$, which is determined by the number of atoms of the condensate. Examples of such dark solitons, in the absence of external potential, are depicted in Fig 1.1b, c corresponding, respectively, to a quiescent, $v = 0$, dark soliton and a moving, $v = 0.5$, gray soliton. Moreover, it should be mentioned that in the case of an harmonically confined condensate, i.e., for $V(z) = \frac{1}{2}\Omega^2 z^2$ (Ω being the normalized trap strength) in (1.13), the background of the dark soliton can be approximated by the Thomas–Fermi cloud, $\psi_{\text{TF}}(z) = \sqrt{\mu - V(z)}$ [see (1.19)]; thus, the “composite” wavefunction (containing both the Thomas–Fermi background and the dark soliton) takes the approximate form $\psi = \psi_{\text{TF}}(z) \exp(-i\psi_0^2 t) \psi_{\text{DS}}(z, t)$, where $\psi_{\text{DS}}(z, t)$ is the dark soliton of (1.25). Examples of such a states are shown in Fig 1.1d, e corresponding, respectively, to a quiescent dark soliton and a moving gray soliton with $\Omega = 1/16$ and $\mu = 2$.

In the higher-dimensional setting, the NLS equation is no longer integrable. However, in the simplest 2D circularly symmetric setting, and for the repulsive BEC case ($g = +1$), stationary states with a phase singularity are possible. In the case of a homogeneous condensate ($\Omega = 0$), these states have the form $\psi(r, \theta, z) = \psi_0 U(r) \exp(im\theta - i\psi_0^2 t)$, where r and θ are the polar coordinates, ψ_0 is the background density, and the integer m is the so-called *winding number* or *vortex charge*. These vortex states are the higher-dimensional analogues of black solitons (with the circular symmetry), and satisfy the following boundary value problem (for $\psi_0 = 1$),

$$\frac{d^2 U}{dr^2} + \frac{1}{r} \frac{dU}{dr} - \frac{m^2}{r^2} U + (1 - U^2)U = 0 \quad (1.26)$$

(resulting from (1.13) with ∂_z^2 being substituted by the 2D Laplacian), for $r > 0$ and the boundary conditions $U(0) = 0$ and $U(+\infty) = 1$. The asymptotic behavior of the vortex profile $U(r)$ can be found from (1.26), i.e., $U(r) \sim r^{|m|}$

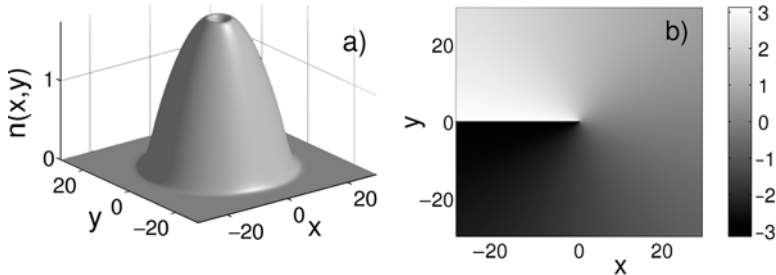


Fig. 1.2. Two-dimensional, singly charged ($m = 1$), vortex inside a magnetic trap with $\Omega = 0.1$. Depicted are (a) the density and (b) its phase profile for $\mu = 2$

as $r \rightarrow 0$, and $U(r) \sim 1 - \frac{m^2}{2r^2}$ as $r \rightarrow +\infty$. Similarly to the case of a dark soliton, a vortex in a condensate confined in the harmonic potential $V(r) = \frac{1}{2}\Omega^2 r^2$ is on top of the ground state profile which can be approximated by $\psi_{\text{TF}}(r) = \sqrt{\mu - V(r)}$; thus, in this case, the wavefunction can be approximated by $\psi = \psi_{\text{TF}}(r)U(r)\exp(im\theta - it)$. An example of such a vortex is shown in Fig. 1.2 for $\Omega = 0.1$, $m = 1$ and $\mu = 2$.

References

1. S.N. Bose, Z. Phys. **26**, 178 (1924)
2. A. Einstein, Sitzungsber. K. Preuss. Akad. Wiss., Phys. Math. Kl. **261** (1924)
3. A. Einstein, Sitzungsber. K. Preuss. Akad. Wiss., Phys. Math. Kl. **3** (1925)
4. A. Griffin, D.W. Snoke, S. Stringari (eds.), *Bose–Einstein Condensation* (Cambridge University Press, Cambridge, 1995)
5. M.H.J. Anderson, J.R. Ensher, M.R. Matthews, C.E. Wieman, Science **269**, 198 (1995)
6. K.B. Davis, M.-O. Mewes, M.R. Andrews, N.J. van Druten, D.S. Durfee, D.M. Kurn, W. Ketterle, Phys. Rev. Lett. **75**, 3969 (1995)
7. C.C. Bradley, C.A. Sackett, J.J. Tollett, R.G. Hulet, Phys. Rev. Lett. **75**, 1687 (1995)
8. See, e.g., C.C. Bradley, C.A. Sackett, J.J. Tollett, R.G. Hulet, Phys. Rev. Lett. **79**, 1170 (1997), and references therein
9. E.A. Cornell, C.E. Wieman, Rev. Mod. Phys. **74**, 875 (2002)
10. W. Ketterle, Rev. Mod. Phys. **74**, 1131 (2002)
11. E.P. Gross, J. Math. Phys. **4**, 195 (1963)
12. L.P. Pitaevskii, Sov. Phys. JETP **13**, 451 (1961)
13. C. Sulem, P.L. Sulem, *The Nonlinear Schrödinger Equation* (Springer, Berlin Heidelberg New York, 1999)
14. M.J. Ablowitz, B. Prinari, A.D. Trubatch, *Discrete and Continuous Nonlinear Schrödinger Systems* (Cambridge University Press, Cambridge, 2004)
15. J. Bourgain, *Global Solutions of Nonlinear Schrödinger Equations*, (American Mathematical Society, Providence, 1999)
16. F. Dalfovo, S. Giorgini, L.P. Pitaevskii, S. Stringari, Rev. Mod. Phys. **71**, 463 (1999)
17. L.P. Pitaevskii, S. Stringari, *Bose Einstein Condensation* (Clarendon Press Oxford, 2003)

18. C.J. Pethick, H. Smith, *Bose Einstein Condensation in Dilute Gases* (Cambridge University Press, Cambridge, 2004)
19. N.N. Bogoliubov, J. Phys. (Moscow) **11**, 23 (1947)
20. A.J. Leggett, Rev. Mod. Phys. **73**, 307 (2001)
21. Yu.S. Kivshar, G.P. Agrawal, *Optical Solitons: From Fibers to Photonic Crystals* (Academic, New York, 2003)
22. J. Weiner, *Cold and Ultracold Collisions in Quantum Microscopic and Mesoscopic Systems* (Cambridge University Press, Cambridge, 2003)
23. S. Inouye M.R. Andrews, J. Stenger, H.J. Miesner, D.M. Stamper-Kurn, W. Ketterle, Nature **392**, 151 (1998)
24. J. Stenger, S. Inouye, M.R. Andrews, H.-J. Miesner, D.M. Stamper-Kurn, W. Ketterle, Phys. Rev. Lett. **82**, 2422 (1999)
25. J.L. Roberts, N.R. Claussen, J.P. Burke, Jr., C.H. Greene, E.A. Cornell, C.E. Wieman , Phys. Rev. Lett. **81**, 5109 (1998)
26. S.L. Cornish, N.R. Claussen, J.L. Roberts, E.A. Cornell, C.E. Wieman, Phys. Rev. Lett. **85**, 1795 (2000)
27. A.J. Moerdijk, B.J. Verhaar, A. Axelsson, Phys. Rev. A **51**, 4852 (1995)
28. J.L. Roberts, N.R. Claussen, S.L. Cornish, C.E. Wieman, Phys. Rev. Lett. **85**, 728 (2000)
29. M. Olshanii, Phys. Rev. Lett. **81**, 938 (1998)
30. T. Bergeman, M.G. Moore, M. Olshanii, Phys. Rev. Lett. **91**, 163201 (2003)
31. M. Theis, G. Thalhammer, K. Winkler, M. Hellwig, G. Ruff, R. Grimm, J.H. Denschlag, Phys. Rev. Lett. **93**, 123001 (2004)
32. K.E. Strecker, G.B. Partridge, A.G. Truscott, R.G. Hulet, Nature **417** 150 (2002)
33. L. Khaykovich, F. Schreck, G. Ferrari, T. Bourdel, J. Cubizolles, L.D. Carr, Y. Castin, C. Salomon, Science, **296** 1290 (2002)
34. S.L. Cornish, S.T. Thompson, C.E. Wieman, Phys. Rev. Lett. **96**, 170401 (2006)
35. K.E. Strecker, G.B. Partridge, A.G. Truscott, R.G. Hulet, New J. Phys. **5**, 73 (2003)
36. J. Herbig, T. Kraemer, M. Mark, T. Weber, C. Chin, H.C. Nagerl, R. Grimm, Science **301**, 1510 (2003)
37. C.A. Regal, C. Ticknor, J.L. Bohn, D.S. Jin, Nature **424**, 47 (2003)
38. M. Greiner, C.A. Regal, D.S. Jin, Nature **426**, 537 (2003)
39. M. Bartenstein, A. Altmeyer, S. Riedl, S. Jochim, C. Chin, J.H. Denschlang, R. Grimm, Phys. Rev. Lett. **92**, 203201 (2004)
40. T. Bourdel, L. Khaykovich, J. Cubizolles, J. Zhang, F. Chevy, M. Teichmann, L. Tarruell, S.J.J.M.F. Kokkelmans, C. Salomon, Phys. Rev. Lett. **93**, 050401 (2004)
41. D.M. Stamper-Kurn, M.R. Andrews, A.P. Chikkatur, S. Inouye, H.J. Miesner, J. Stenger, W. Ketterle, Phys. Rev. Lett. **80**, 2027 (1998)
42. J. Weiner, V.S. Bagnato, S. Zilio, P.S. Julienne, Rev. Mod. Phys. **71**, 1 (1999)
43. R. Grimm, M. Weidmüller, Y.B. Ovchinnikov, Adv. At. Mol. Opt. Phys. **42**, 95 (2000)
44. M.D. Barrett, J.A. Sauer, M.S. Chapman, Phys. Rev. Lett. **87**, 010404 (2001)
45. P.S. Jessen, C. Gerz, P.D. Lett, W.D. Phillips, S.L. Rolston, R.J.C. Spreeuw, C.I. Westbrook, Phys. Rev. Lett. **69**, 49 (1992)
46. P. Verkerk, B. Lounis, C. Salomon, C. Cohen-Tanoudji, J.Y. Courtois, G. Grynberg, Phys. Rev. Lett. **68**, 3861 (1992)

47. B.P. Anderson, T.I. Gustavson, M.I. Kasevich, Phys. Rev. A **53**, R3727 (1996)
48. O. Morsch, M.K. Oberthaler, Rev. Mod. Phys. **78**, 179 (2006)
49. A. Görlitz, J.M. Vogels, A.E. Leanhardt, C. Raman, T.L. Gustavson, J.R. Abo-Shaeer, A.P. Chikkatur, S. Gupta, S. Inouye, T. Rosenband, W. Ketterle, Phys. Rev. Lett. **87**, 130402 (2001)
50. M. Greiner, I. Bloch, O. Mandel, T.W. Hänsch, T. Esslinger, Phys. Rev. Lett. **87**, 160405 (2001)
51. S. Burger, F.S. Cataliotti, C. Fort, P. Maddaloni, F. Minardi, M. Inguscio, Europhys. Lett. **57**, 1 (2002)
52. H. Moritz, T. Stöferle, M. Köhl, T. Esslinger, Phys. Rev. Lett. **91**, 250402 (2003)
53. F.S. Cataliotti, S. Burger, C. Fort, P. Maddaloni, F. Minardi, A. Trombettoni, A. Smerzi, M. Inguscio, Science **293**, 843 (2001)
54. S. Burger, F.S. Cataliotti, C. Fort, F. Minardi, M. Inguscio, M.L. Chiofalo, M.P. Tosi, Phys. Rev. Lett. **80**, 4447 (2001)
55. J.H. Denschlag, J.E. Simsarian, H. Haffner, C. McKenzie, A. Browaeys, D. Cho, K. Helmerson, S.L. Rolston, W.D. Phillips, J. Phys. B **35**, 3095 (2002)
56. W. Hänsel, P. Hommelhoff, T.W. Hänsch, J. Reichel, Nature (London) **413**, 501 (2001)
57. H. Ott, J. Fortagh, G. Schlotterbeck, A. Grossmann, C. Zimmermann, Phys. Rev. Lett. **87**, 230401 (2001)
58. E.H. Lieb, R. Seiringer, J.P. Solovej, J. Yngvason, *The Mathematics of the Bose Gas and its Condensation*. Oberwolfach Seminar Series, vol 34 (Birkhaeuser, Basel 2005) (arXiv:cond-mat/0610117)
59. L. Tonks, Phys. Rev. **50**, 955 (1936)
60. M. Girardeau, J. Math. Phys. (N.Y.) **1**, 516 (1960)
61. B. Paredes, A. Widera, V. Murg, O. Mandel, S. Fölling, I. Cirac, G.V. Shlyapnikov, T.W. Hänsch, I. Bloch, Nature **429**, 277 (2004)
62. T. Kinoshita, T. Wenger, D.S. Weiss, Science **305**, 1125 (2004)
63. O. Morsch, E. Arimondo, in ed. by T. Dauxois, S. Ruffo, E. Arimondo, M. Wilkens Dynamics and Thermodynamics of Systems with Long-Range Interactions, (Springer, Berlin, 2002), p. 312
64. S. Peil, J.V. Porto, B.L. Tolra, J.M. Obrecht, B.E. King, M. Subbotin, S.L. Rolston, W.D. Phillips, Phys. Rev. A **67**, 051603(R) (2003)
65. M.R. Andrews, C.G. Townsend, H.-J. Miesner, D.S. Durfee, D.M. Kurn, W. Ketterle, Science **275**, 637 (1999)
66. M. Albiez, R. Gati, J. Fölling, S. Hunsmann, M. Cristiani, M.K. Oberthaler, Phys. Rev. Lett. **95**, 010402 (2005)
67. B.P. Anderson, M.A. Kasevich, Science **282**, 1686 (1998)
68. R. Folman, J. Schmiedmayer, Nature **413**, 466 (2001)
69. R. Folman, P. Krueger, J. Schmiedmayer, J. Denschlag, C. Henkel, Adv. Atom. Mol. Opt. Phys. **48**, 263 (2002)
70. B. Eiermann, Th. Anker, M. Albiez, M. Taglieber, P. Treutlein, K.P. Marzlin, M.K. Oberthaler, Phys. Rev. Lett. **92**, 230401 (2004)
71. V.M. Pérez-García, H. Michinel, H. Herrero, Phys. Rev. A **57**, 3837 (1998)
72. A.D. Jackson, G.M. Kavoulakis, C.J. Pethick, Phys. Rev. A **58**, 2417 (1998)
73. Yu.S. Kivshar, T.J. Alexander, S.K. Turitsyn, Phys. Lett. A **278**, 225 (2001)
74. F.Kh. Abdullaev, A. Gammal, A.M. Kamchatnov, L. Tomio, Int. J. Mod. Phys. B **19**, 3415 (2005)

75. V.V. Konotop, M. Salerno, Phys. Rev. A **65**, 021602 (2002)
76. F.Kh. Abdullaev, A.M. Kamchatnov, V.V. Konotop, V.A. Brazhnyi, Phys. Rev. Lett. **90**, 230402 (2003)
77. L. Salasnich, A. Parola, L. Reatto, Phys. Rev. A **65**, 043614 (2002)
78. Y.B. Band, I. Towers, B.A. Malomed, Phys. Rev. A **67**, 023602 (2003)
79. Yu. Kagan, A.E. Muryshev, G.V. Shlyapnikov, Phys. Rev. Lett. **81**, 933 (1988)
80. F.Kh. Abdullaev, A. Gammal, L. Tomio, T. Frederico, Phys. Rev. A **63**, 043604 (2001)
81. A.E. Muryshev, G.V. Shlyapnikov, W. Ertmer, K. Sengstock, M. Lewenstein, Phys. Rev. Lett. **89**, 110401 (2002)
82. L. Khaykovich, B.A. Malomed, Phys. Rev. A **74**, 023607 (2006)
83. P.G. Kevrekidis, K.Ø. Rasmussen, A.R. Bishop, Int. J. Mod. Phys. B, **15**, 2833 (2001)
84. A. Trombettoni, A. Smerzi, Phys. Rev. Lett. **86**, 2353 (2001)
85. F.Kh. Abdullaev, B.B. Baizakov, S.A. Darmanyan, V.V. Konotop, M. Salerno, Phys. Rev. A **64**, 043606 (2001)
86. E.G. Alfimov, P.G. Kevrekidis, V.V. Konotop, M. Salerno, Phys. Rev. E **66**, 046608 (2002)
87. W. Kohn, Phys. Rev. **115**, 809 (1959)
88. J.M. Gerton, D. Strekalov, I. Prodan, R.G. Hulet, Nature **408**, 692 (2000)
89. E.A. Donley, N.R. Claussen, S.L. Cornish, J.L. Roberts, E.A. Cornell, C.E. Wieman, Nature, **412**, 295 (2001)
90. P.A. Ruprecht, M.J. Holland, K. Burnett, C.W. Clark, Phys. Rev. A **51**, 4704 (1995)
91. A. Gammal, T. Frederico, L. Tomio, Phys. Rev. A **64**, 055602 (2001)
92. A. Gammal, T. Frederico, L. Tomio, Phys. Rev. A **66**, 043619 (2002)
93. G. Theocharis, Z. Rapti, P.G. Kevrekidis, D.J. Frantzeskakis, V.V. Konotop, Phys. Rev. A **67**, 063610 (2003)
94. L. Salasnich, A. Parola, L. Reatto, Phys. Rev. Lett. **91**, 80405 (2003)
95. L.D. Carr, J. Brand, Phys. Rev. A **70**, 033607 (2004)
96. P.G. Kevrekidis, D.J. Frantzeskakis, Mod. Phys. Lett. B **18**, 173 (2004)
97. M.R. Matthews, B.P. Anderson, P.C. Haljan, D.S. Hall, C.E. Wieman, E.A. Cornell, Phys. Rev. Lett. **83**, 2498 (1999)
98. J.E. Williams, M.J. Holland, Nature **568**, 401 (1999)
99. J. Denschlag, J.E. Simsarian, D.L. Feder, C.W. Clark, L.A. Collins, J. Cubizolles, L. Deng, E.W. Hagley, K. Helmerson, W.P. Reinhardt, S.L. Rolston, B.I. Schneider, W.D. Phillips, Science, **287**, 97 (2000)
100. S. Burger, K. Bongs, S. Dettmer, W. Ertmer, K. Sengstock, A. Sanpera, G.V. Shlyapnikov, M. Lewenstein, Phys. Rev. Lett. **83**, 5198 (1999)
101. B.P. Anderson, P.C. Haljan, C.A. Regal, D.L. Feder, L.A. Collins, C.W. Clark, E.A. Cornell, Phys. Rev. Lett. **86**, 2926 (2001)
102. Z. Dutton, M. Budde, C. Slowe, L.V. Hau, Science **293**, 663 (2001)
103. K.W. Madison, F. Chevy, W. Wohlleben, J. Dalibard, Phys. Rev. Lett. **84**, 806 (1999)
104. S. Inouye, S. Gupta, T. Rosenband, A.P. Chikkatur, A. Görlitz, T.L. Gustavson, A.E. Leanhardt, D.E. Pritchard, W. Ketterle, Phys. Rev. Lett. **87**, 080402 (2001)
105. J.R. Abo-Shaeer, C. Raman, J.M. Vogels, W. Ketterle, Science **292**, 476 (2001)
106. J.R. Abo-Shaeer, C. Raman, W. Ketterle, Phys. Rev. Lett. **88**, 070409 (2002)

107. P. Engels, I. Coddington, P.C. Haljan, E.A. Cornell, Phys. Rev. Lett. **89**, 100403 (2002)
108. V.E. Zakharov, A.B. Shabat, Zh. Eksp. Teor. Fiz. **61**, 118 (1971) [Sov. Phys. JETP **34**, 62 (1971)]
109. V.E. Zakharov, A.B. Shabat, Zh. Eksp. Teor. Fiz. **64**, 1627 (1973) [Sov. Phys. JETP **37**, 823 (1973)]

Part II

Bright Solitons in Bose–Einstein Condensates

Bright Solitons in Bose–Einstein Condensates: Theory

F.Kh. Abdullaev and J. Garnier

2.1 Introduction

It is a well-known fact that the interplay of nonlinearity and dispersion leads to the appearance of localized wave packets moving without distortion. When the interaction between atoms is attractive (resp. repulsive), bright (resp. dark) solitons can be generated in BECs. Note that the term soliton is usually reserved to the localized solution of an integrable system [1]. Elastic scattering is a characteristic property of true solitons. However, many physical systems are described by nonintegrable systems which have stationary or moving localized solutions. Collisions between these solitary waves are usually inelastic, which is a clear indication that they are not true solitons. However, in this chapter, we will use the term soliton for these waves as well.

The typical system under consideration in this chapter is a Bose gas with attractive interaction between atoms in different types of trap potentials. Without a trap, a free 2D or 3D BEC with attractive interaction can collapse. Indeed, the Gross–Pitaevskii (GP) equation then takes the form of the cubic Nonlinear Schrödinger (NLS) equation. In the case of focusing nonlinearity (corresponding to negative scattering length) the solution can be singular or spreading [2]. In the 2D case, a necessary condition for collapse is that the number of atoms should exceed a critical one. In the 3D case collapse may, in principle, occur for any number of atoms. The simplest way to see this is to inspect the expressions for the energy E and the number of atoms N of the condensate in dimension D :

$$E = \int \left[\frac{\hbar^2}{2m} |\nabla \psi|^2 + V|\psi|^2 + \frac{g_D}{2} |\psi|^4 \right] d^D \mathbf{r}, \quad N = \int |\psi|^2 d^D \mathbf{r} \quad (2.1)$$

and to perform a dimensional analysis by assuming that L is the typical size of the BEC. From the expression of N , we find that $[\psi] \sim 1/L^{D/2}$. From the expression of E we find that the kinetic energy behaves like $1/L^2$, the potential energy (for $V \sim r^n$) like L^n , and the interaction energy like $1/L^D$. In the

following discussion, we assume that g_D is negative (attractive interaction) and that the potential V is a symmetric harmonic trap ($V \sim r^2$).

In the one-dimensional case ($D = 1$) the estimate for the energy E is

$$E \sim \frac{c_{\text{kin}}}{L^2} + c_{\text{pot}} L^2 - \frac{c_{\text{int}}}{L}, \quad (2.2)$$

where c_{kin} , c_{pot} and c_{int} are constants. The collapse is absent and a local minimum in L exists in the effective potential. This localized state is a bright matter-wave soliton. We will discuss its properties in the following sections.

For a two-dimensional ($D = 2$) condensate we obtain

$$E \sim \frac{c_{\text{kin}} - c_{\text{int}}}{L^2} + c_{\text{pot}} L^2 \sim \frac{N(N_c - N)}{L^2} \text{ for } L \ll 1.$$

Thus for $N > N_c$ collapse can occur. The value of the critical number is $N_c = 1.862 \times (\pi \hbar^2) / (|g_2|m)$ [3, 4].

For a three-dimensional ($D = 3$) condensate we have the estimate

$$E \sim \frac{c_{\text{kin}}}{L^2} + c_{\text{pot}} L^2 - \frac{c_{\text{int}}}{L^3}. \quad (2.3)$$

Here it is possible to generate a metastable state if the number of atoms N is small enough. The existence of such a state is due to the balance between the kinetic energy, the trap potential energy and the interaction energy. The criterion for parameters when this state disappears can be obtained from the requirement that the first and second derivatives of the energy $E(L)$ are equal to zero at the critical point. The energy can be calculated, for example, using the Gaussian ansatz for the wavefunction of the condensate. Then the variational approach gives the value $N_c = k_{\text{VA}} a_r / |a|$ for the critical number of atoms in the case of an attractive BEC in a spherical trap, with $a_r = \sqrt{\hbar / (m \omega_r)}$ and $k_{\text{VA}} \approx 0.67$. Numerical simulations show that the exact value of the dimensionless constant is $k \approx 0.574$. The experimental value for this parameter deviates from about 20% [5]: If the longitudinal frequency is equal to zero $\omega_z = 0$, then the variational approach with the Gaussian transverse profile and sech-type longitudinal profile gives $k_{\text{VA}} \approx 0.76$, while the numerical value is $k \approx 0.627$ [6]. In the case of the ${}^7\text{Li}$ condensate in the nearly symmetric trap with $a_r \approx 3 \mu\text{m}$ and $a \approx -1.45 \text{ nm}$ used in the experiments at Rice University, the critical number is approximately $N_c \sim 1400$ [7].

In this chapter we describe the main properties of bright solitons in BECs. We focus our attention on the dynamics of solitons in elongated BECs, when the quasi 1D GP equation is valid. The interaction of solitons with linear and nonlinear impurities, transmission of solitons through barriers, the dynamics of localized states in nonlinear periodic potentials will be considered. The dynamics of 2D bright solitons under the temporal and spatial Feshbach resonance management as well as stable 2D solitons in dipolar BECs are also analyzed.

2.2 Bright Solitons in Quasi One-Dimensional BEC

2.2.1 The 1D Gross–Pitaevskii Equation

The GP equation for an elongated BEC with varying in space and time trap potential $V(z, t)$ and atomic scattering length $a(z, t)$ is [8, 9]

$$i\hbar\psi_t + \frac{\hbar^2}{2m}\psi_{zz} - V(z, t)\psi - g(z, t)|\psi|^2\psi = 0, \quad (2.4)$$

with $g(z, t) = 2\hbar\omega_r a(z, t)$. In the case of a stationary harmonic trap we simply have $V(z, t) = (1/2)m\omega_z^2 z^2$. The validity of this equation is defined by the condition $(|a|N)/a_r \ll 1$ with $a_r = \sqrt{\hbar/(m\omega_r)}$. When $V = 0$ and the scattering length $a \equiv a_s$ is negative, this equation admits the well-known bright soliton solution

$$\psi(z, t) = \frac{a_r}{\sqrt{2|a_s|\kappa}} \operatorname{sech} \left(\frac{z - vt}{\kappa} \right) \exp \left[i \frac{mv}{\hbar} z - \frac{i}{\hbar} \left(\frac{mv^2}{2} - \frac{\hbar^2\kappa^2}{2m} \right) t \right], \quad (2.5)$$

where $\kappa = a_r^2/(|a_s|N)$ is the soliton width and v is the soliton velocity. Note that the condition $(|a_s|N)/a_r \ll 1$ for the validity of the 1D GP equation imposes $\kappa \gg a_r$. Bright solitons have been observed in experiments performed at Rice University [10] and at the Ecole Normale Supérieure in Paris [11]. The experiment at Rice University used ${}^7\text{Li}$, the scattering length was $a_s = -3a_0$ (where $a_0 \simeq 0.053$ nm is the Bohr radius), and the trap frequencies were $\omega_z = 2\pi \times 3.2$ Hz and $\omega_r = 2\pi \times 640$ Hz, which corresponds to $a_r \approx 1.5$ μm . The number of atoms in the soliton was $N \approx 6,000$, which corresponds to $\kappa \approx 2.5$ μm , in agreement with the number allowed by the theory.

In this chapter, we study the dynamics of bright solitons under different types of spatial and temporal modulations of the BEC and external potential parameters. The inhomogeneities of the potential $V(z, t)$ in (2.4) can be local (in the form of a well or a barrier) or extended (in the form of a periodic or random potential, generated, e.g., by an optical lattice or an optical speckle pattern). Temporal and spatial variations of the scattering length $a(z, t)$ can be produced by using the Feshbach resonance method (described in detail in the next chapter), namely by the variation of the external magnetic field $B(z, t)$ near the resonant value B_0 [12]. Small variations of the field near the resonant value can induce large variations of the scattering length according to the formula

$$a(z, t) = a_b \left(1 - \frac{\Delta}{B_0 - B(z, t)} \right),$$

where a_b is the background value of the atomic scattering length and Δ is the resonance width. Optical methods for manipulating the value of the scattering length are also possible [13]. This type of potential is produced by the optically

induced Feshbach resonance [14]. According to this technique, the periodic variation of the laser field intensity in the standing wave $I(z) = I_0 \cos^2(kz)$ produces the periodic variation of the atomic scattering length a of the form

$$a(z) = a_0 + \alpha \frac{I(z)}{\delta + \alpha I(z)}, \quad (2.6)$$

where δ is the detuning from the Feshbach resonance. When the detuning is large we have $a(z) = a_0 + a_1 \cos^2(kz)$. As a result, the mean-field nonlinear coefficient g (which is proportional to the scattering length a) in the GP equation has a spatial dependence [15, 16].

It should be noted that other forms of the 1D GP equation have been suggested:

1. *1D GP equation in the form of nonpolynomial NLS equation.* The exclusion of transverse degrees of freedom performed previously leads to the 1D GP equation. This derivation is valid only for a low density condensate. To obtain the equation for higher densities one can use the variational approach with the generalized ansatz for the wavefunction [17]

$$\Psi(x, y, z, t) = \frac{1}{\sqrt{\pi}\sigma(z, t)} \exp\left(-\frac{x^2 + y^2}{2\sigma^2(z, t)}\right) \psi(z, t).$$

The variational equation for the parameter σ has the form of a differential equation. With the hypothesis that the derivatives can be neglected, σ can be calculated from an algebraic equation, giving $\sigma^2 = \sigma^2(|\psi|^2) = a_r^2 \sqrt{1 + 2a|\psi|^2}$. The resulting 1D GP equation has the form of the non-polynomial NLS equation

$$i\hbar\psi_t = \left[-\frac{\hbar^2}{2m} \frac{\partial^2}{\partial z^2} + \frac{g_3|\psi|^2}{2\pi\sigma^2(|\psi|^2)} + \frac{\hbar\omega_r}{2} \left(\frac{\sigma^2(|\psi|^2)}{a_r^2} + \frac{a_r^2}{\sigma^2(|\psi|^2)} \right) + V(z) \right] \psi$$

with $g_3 = 4\pi\hbar^2 a/m$. In the weak interaction limit $|a|N|\psi|^2 \ll 1$, we have $\sigma^2 = a_r^2$ and this equation reduces to the 1D NLS equation with the effective nonlinearity parameter $g_1 = g_3/(2\pi a_r^2)$. If $|a|N/a_r > 2/3$, then there is no soliton solution due to the condensate collapse. The latter prediction as well as the parameters of the ground states are in good agreement with the numerical simulations of the full GP equation.

2. A 1D description that does not neglect the derivatives in the equation for σ has been suggested in [18]. The ansatz used for the variational approach is of the form

$$\Psi(x, y, z, t) = \frac{1}{\sqrt{\pi}\sigma(z, t)} \exp\left(-\frac{x^2 + y^2}{2\sigma^2(z, t)} + i\frac{b(z, t)}{2}(x^2 + y^2)\right) \psi(z, t).$$

In the dimensionless variables $\tilde{\psi} = \psi\sqrt{a_r}$, $\tilde{\sigma} = \sigma/a_r$, $\tilde{b} = a_r^2 b$, $\tilde{t} = \omega_r t$, $\tilde{z} = z/a_r$ the BEC evolution is described by (where we have dropped the tildes)

$$\mathrm{i}\psi_t + \frac{1}{2}\psi_{zz} - V(z)\psi - 3G\frac{|\psi|^2\psi}{\sigma^2} - \frac{1}{2}\left[\frac{2}{\sigma^2} + \frac{\sigma_{zz}}{\sigma} + \left(\frac{\sigma_z}{\sigma} - \frac{\mathrm{i}}{2}b_z\sigma^2\right)\frac{(|\psi|^2)_z}{|\psi|^2} - \frac{1}{2}b_z^2\sigma^4 - \frac{\mathrm{i}}{2}b_{zz}\sigma^2 - \mathrm{i}b_z\sigma\sigma_z\right] = 0, \quad (2.7)$$

$$(\sigma^2|\psi|^2)_t + \left[\frac{\mathrm{i}}{2}\sigma^2(\psi\psi_z^* - \psi^*\psi_z) + \sigma^4|\psi|^2b_z\right]_z = 2b\sigma^2|\psi|^2, \quad (2.8)$$

$$\begin{aligned} b_t &= \frac{\sigma_{zz}}{\sigma^3} + \frac{1 - \sigma_z^2}{\sigma^4} + \frac{\sigma_z}{\sigma^3}\frac{(|\psi|^2)_z}{|\psi|^2} - 1 - b^2 - b_z^2\sigma^2 \\ &\quad + \frac{\mathrm{i}(\psi_z\psi^* - \psi\psi_z^*)}{2|\psi|^2}b_z + 2G\frac{|\psi|^2}{\sigma^4} \end{aligned} \quad (2.9)$$

with $G = a/a_r$. Thus, the 3D GP equation has been transformed into a quasi-1D form for the case of the elongated cigar-shaped geometry when the radial distributions of the condensate density and its radial velocity can be approximated by simple Gaussian functions. The variables in (2.7)–(2.9) depend only on one spatial coordinate, which is very convenient in numerical simulations. Besides, the analysis of the system (2.7)–(2.9) predicts important phenomena such as the existence in the repulsive BEC case (if $G\rho_0 > 3.91$, where ρ_0 is the condensate density) of small-amplitude bright solitons propagating with the velocity close to the speed of sound.

We finally introduce the dimensionless form of the GP equation:

$$\mathrm{i}\psi_t + \psi_{zz} + 2|\psi|^2\psi = V_{\text{nl}}(z, t)|\psi|^2\psi + V_1(z, t)\psi. \quad (2.10)$$

This equation is obtained from (2.4) by the change of variables $\tilde{\psi} = \psi\sqrt{|a_s|}$, where $a_s < 0$ is the reference atomic scattering length, $\tilde{t} = \omega_r t$, $\tilde{z} = \sqrt{2}z/a_r$, and by dropping the tildes. Here $V_1(z, t)$ is the linear external potential and $V_{\text{nl}}(z, t) = 2 - 2a(z, t)/a_s$ is the nonlinear potential induced by the space–time variations of the scattering length a .

If $V_1 = V_{\text{nl}} = 0$, then this equation can be reduced to the integrable NLS equation. The bright soliton solution is:

$$\psi(z, t) = 2\nu_0 \operatorname{sech}[2\nu_0(z - \zeta(t))] \exp[2\mathrm{i}\mu_0(z - \zeta(t)) + \mathrm{i}\phi(t)], \quad (2.11)$$

its amplitude is $2\nu_0$, its width is $1/(2\nu_0)$, and its velocity is $4\mu_0$. In terms of the physical parameters that appear in the dimensional expression (2.5), they are given by

$$2\nu_0 = \frac{N|a_s|}{\sqrt{2}a_r} = \frac{\sqrt{2}a_r}{\kappa}, \quad 4\mu_0 = \frac{\sqrt{2}a_r mv}{\hbar}$$

The soliton center $\zeta(t)$ and phase $\phi(t)$ satisfy $\partial_t \zeta = 4\mu_0$ and $\partial_t \phi = 4(\nu_0^2 + \mu_0^2)$.

If V_1 and/or V_{nl} have spatial and/or time variations, then the matter-wave soliton experiences velocity and amplitude modulations and emits radiation.

2.2.2 Adiabatic Soliton Compression

Adiabatic spatial variations of the atomic scattering length can be used as an effective way for controlling the soliton parameters and for inducing changes in the solitons' shape, which could be useful for applications [15]. In contrast to abrupt variations, adiabatic changes make it possible to preserve the integrity of the soliton (no splitting occurs), thus leading to bright soliton compression with the increase of the matter density. The possibility to compress BEC solitons could be an experimental tool to investigate the range of validity of the 1D GP equation. Since the quasi 1D regime is valid for low densities, it would be indeed interesting to see how far one can compress a soliton in a real experiment by means of adiabatic changes of the scattering length.

To model the adiabatic variation of the atomic scattering length in 1D (cigar shaped) BECs we consider the normalized GP (2.10). We neglect the linear potential V_1 by assuming that the range of variation of the trap potential is very large in comparison with the size of the BEC. We assume that the scattering length a is a negative-valued, slowly varying function of space and time. As a consequence $2 - V_{\text{nl}} = 2a/a_s$ is a positive function since the reference length $a_s < 0$. Although the analysis can be performed for a general smooth function $V_{\text{nl}}(z, t)$, we only discuss here the spatially varying case $V_{\text{nl}} \equiv V_{\text{nl}}(z)$. By the transform of field $\check{\psi} = \sqrt{1 - V_{\text{nl}}(z)/2}\psi$, we get from (2.10):

$$i\check{\psi}_t + \check{\psi}_{zz} + 2|\check{\psi}|^2\check{\psi} = R(\check{\psi}), \quad R(\check{\psi}) = F(z)\check{\psi}_z, \quad F(z) = [\ln(1 - V_{\text{nl}}(z)/2)]_z.$$

The term $R(\check{\psi})$ can be considered as a small perturbation when the soliton width is much smaller than the scale of variation of the scattering length. The soliton solution of the GP equation under small perturbation can be assumed to be of the form

$$\check{\psi}(z, t) = 2\nu(t)\operatorname{sech}[2\nu(t)(z - \zeta(t))]\exp[i2\mu(t)(z - \zeta(t)) + i\phi(t)]. \quad (2.12)$$

Using the adiabatic perturbation theory for solitons [15], we find the equations for the soliton parameters

$$\frac{d\nu}{dt} = 4\nu\mu F(\zeta), \quad \frac{d\mu}{dt} = \frac{4}{3}\nu^2 F(\zeta), \quad \frac{d\zeta}{dt} = 4\mu, \quad (2.13)$$

whose solutions satisfy the relations

$$\nu(\zeta) = \nu_0 \left(1 - \frac{V_{\text{nl}}(\zeta)}{2}\right), \quad \mu^2(\zeta) = \mu_0^2 + \frac{\nu_0^2}{3} \left[\left(1 - \frac{V_{\text{nl}}(\zeta)}{2}\right)^2 - 1\right]. \quad (2.14)$$

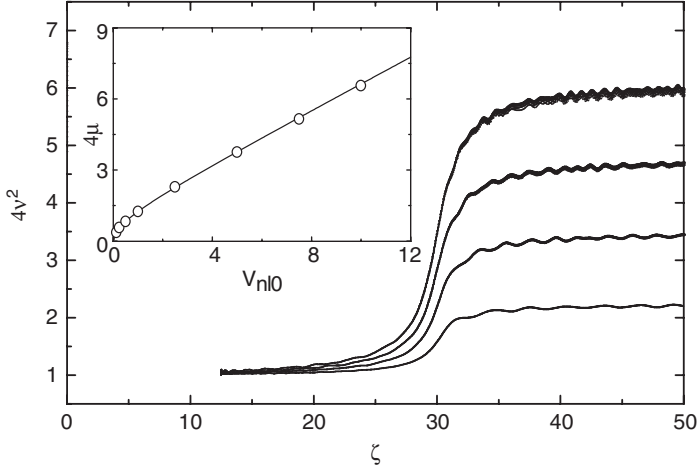


Fig. 2.1. The squared amplitude of a bright soliton vs. soliton center ζ for different values of the amplitude V_{nl0} of a kink-like spatial nonlinear inhomogeneity (2.15) centered at $z = L_f/2$. The curves, from bottom to top, refer to $V_{nl0} = 2.5, 5.0, 7.5, 10.0$, respectively. The other parameters are $s = 0.2$, $L_f = 60$, $\mu_0 = 0$, and $\nu_0 = 0.5$. The soliton is initially at rest, placed at position $\zeta_0 = 12.5$. In the inset we show the soliton final velocity 4μ as a function of V_{nl0} . The open dots are numerical values while the solid line is obtained from (2.14) [15]

These results can be compared to numerical simulations of (2.10) with the function $V_{nl}(z)$ given by

$$V_{nl}(z) = -V_{nl0} \left[\frac{1}{2} + \frac{1}{\pi} \arctan \left(s\pi(z - \frac{L_f}{2}) \right) \right] \quad (2.15)$$

This function models, for small s , an adiabatic change of the scattering length from $a(-\infty) = a_s$ to $a(+\infty) = (1 + V_{nl0}/2)a_s$. Figure 2.1 shows the amplitude of a bright soliton as a function of the soliton center. The soliton, initially at rest, is sucked into the higher scattering length region, and reaches a constant velocity after passing the inhomogeneity.

If the nonlinear potential $V_{nl}(z) = -V_{nl0}f(z)$ is not slowly varying, then internal degrees of freedom can be excited. To take such effects into consideration we assume that $|V_{nl0}| \ll 1$ and we consider that the solution has the form of a chirped sech-type profile

$$\psi(z, t) = A(t) \operatorname{sech}[2\nu(t)(z - \zeta(t))] \exp[iC(t)(z - \zeta(t)) + iB(t)(z - \zeta(t))^2 + i\phi(t)].$$

The variational equations for the parameters ν and ζ are [16]

$$\frac{d^2}{dt^2} \left(\frac{1}{\nu} \right) = \frac{256}{\pi^2} \nu^3 - \frac{16N}{\pi^2} \nu^2 - V_{nl0} \frac{24N}{\pi^2} \nu^2 \frac{\partial F}{\partial \nu}, \quad \frac{d^2 \zeta}{dt^2} = V_{nl0} N \frac{\partial F}{\partial \zeta}, \quad (2.16)$$

where $N = A^2/\nu$ is a conserved quantity and

$$F(\nu, \zeta) = \nu^2 \int_{-\infty}^{\infty} f(z) \operatorname{sech}^4[2\nu(z - \zeta)] dz.$$

If the inhomogeneity is Gaussian $f(z) = \exp(-z^2/l^2)$, with $\nu l \gg 1$, then we obtain $F(\nu, \zeta) = 2\nu f(\zeta)/3$. Thus, there exists a fixed point at $\zeta = 0$, given by $\nu_c = [N(1 + 2V_{nl0})]/16$. The soliton is trapped by the inhomogeneity for positive V_{nl0} . In the trapped regime, due to the nonzero chirp, the soliton width performs oscillations with the frequency $\omega_\nu = N^2(1 + 2V_{nl0})^2/(16\pi)$ and the soliton center also oscillates with the frequency $\omega_\zeta = N\sqrt{V_{nl0}(1 + 2V_{nl0})}/12/l$.

2.2.3 Transmission Through Nonlinear Barriers and Wells

When the matter-wave soliton moves in the linear and nonlinear potentials V_l and V_{nl} , the perturbation theory based on the Inverse Scattering Transform (IST) of the normalized GP (2.10) gives the evolutions of the localized soliton part of the matter-wave and the delocalized radiation [19,20]. A tractable perturbation analysis can be carried out by using series expansions with respect to the amplitudes V_{l0} and V_{nl0} of the linear and nonlinear potentials [21].

Quasi-Particle Approach

Applying the first-order perturbed IST theory [20] we obtain that the soliton center behaves like a quasi-particle moving in the effective potential W :

$$\frac{d^2\zeta}{dt^2} = -W'(\nu_0, \zeta(t)), \quad (2.17)$$

where the prime stands for a derivative with respect to ζ and $4\nu_0$ is the mass (number of atoms) of the soliton that is preserved. The effective potential has the form $W(\nu, \zeta) = W_l(\nu, \zeta) + W_{nl}(\nu, \zeta)$, with

$$W_l(\nu, \zeta) = K_{l,\nu} * V_l(\zeta), \quad K_{l,\nu}(\zeta) = 2\nu \operatorname{sech}^2(2\nu\zeta), \quad (2.18)$$

$$W_{nl}(\nu, \zeta) = K_{nl,\nu} * V_{nl}(\zeta), \quad K_{nl,\nu}(\zeta) = 4\nu^3 \operatorname{sech}^4(2\nu\zeta), \quad (2.19)$$

where $*$ stands for the convolution product: $K * V(\zeta) := \int_{-\infty}^{\infty} K(\zeta - z)V(z) dz$. In this first approximation terms of order V_{l0}^2 and V_{nl0}^2 are neglected. This approach gives the same result as the adiabatic perturbation theory for solitons that is a first-order method as well. This adiabatic perturbation theory was originally introduced for optical solitons [22] and it was recently applied to matter-wave solitons [23]. Here it is the first step of the analysis as we will include second-order and radiation effects in the next section. The predictions of the quasi-particle approach are qualitatively the same ones for linear and nonlinear potentials, so V denotes either V_l or V_{nl} in the following discussion [21].

Barrier potential. Let us first examine the case where the potential V is a barrier, meaning that $V \geq 0$ and $\lim_{|z| \rightarrow \infty} V(z) = 0$. When the soliton reaches the barrier, it slows down, and it eventually goes through the barrier if the input energy is above the maximal energy barrier, meaning $8\mu_0^2 > W_{\max}(\nu_0) := \max_z W(\nu_0, z)$. After passing through the barrier, the soliton recovers its initial mass and velocity. If, on the contrary, the velocity of the incoming soliton is such that $8\mu_0^2 < W_{\max}(\nu_0)$, then the soliton is reflected by the barrier. After the interaction with the barrier, the soliton mass and velocity take the values $4\nu_0$ and $-4\mu_0$, respectively. However, we shall see in the next section that the interaction with the barrier generates radiation which plays a significant role especially when $8\mu_0^2 \sim W_{\max}(\nu_0)$.

Potential well. We now examine the case where the potential is a well, meaning that $V \leq 0$ and $\lim_{|z| \rightarrow \infty} V(z) = 0$. When the soliton reaches the well, it speeds up, and it eventually goes through the well whatever its initial velocity is. However, we shall see in the next section that the interaction with the well generates radiation that reduces the soliton energy. As a result, the soliton cannot escape the well if its velocity is too small.

Radiation Effects

Applying the first-order perturbation IST theory for the radiation emission [20], we obtain that the radiated mass density is of order V_{l0}^2 and V_{nl0}^2 :

$$n(\lambda) = \frac{\pi[(\lambda - \mu)^2 + \nu^2]^2}{256\mu^6 \cosh^2\left(\frac{\pi}{4}\frac{\lambda^2 + \nu^2 - \mu^2}{\mu\nu}\right)} \times \left| \hat{V}_l(k(\lambda, \nu, \mu)) + \frac{[(\lambda + \mu)^2 + \nu^2][(\lambda - 3\mu)^2 + 8\mu^2 + \nu^2]}{12\mu^2} \hat{V}_{nl}(k(\lambda, \nu, \mu)) \right|^2, \quad (2.20)$$

where $k(\lambda, \nu, \mu) = [(\lambda - \mu)^2 + \nu^2]/\mu$ and $\hat{V}_{l,nl}(k) = \int V_{l,nl}(z) \exp(ikz) dz$. This formula is correct if the soliton goes through the potential and it allows us to capture the second-order evolution of the soliton parameters, as we show now. The mass (number of atoms) N and energy (Hamiltonian) E

$$N = \int_{-\infty}^{\infty} |\psi|^2 dz, \quad E = \int_{-\infty}^{\infty} [| \psi_z |^2 - |\psi|^4 + V_l(z)|\psi|^2 + \frac{1}{2}V_{nl}(z)|\psi|^4] dz$$

can be expressed in terms of radiation and soliton contributions:

$$N = 4\nu + \int_{-\infty}^{\infty} n(\lambda) d\lambda, \quad E = 2\nu \left[8\mu^2 - \frac{8\nu^2}{3} + W(\nu, \zeta) \right] + 4 \int_{-\infty}^{\infty} \lambda^2 n(\lambda) d\lambda.$$

The total mass and energy are preserved by the perturbed NLS (2.10), so that it is possible to determine the decay of the soliton mass and energy from the expressions of the radiated mass and energy. This in turn gives the decay

of the soliton parameters (ν, μ) which is proportional to V_{l0}^2 and V_{nl0}^2 . The coefficients (ν_T, μ_T) of the transmitted soliton are [21]

$$\nu_T = \nu_0 - \frac{1}{4} \int_{-\infty}^{\infty} n(\lambda) d\lambda, \quad \mu_T = \mu_0 - \frac{1}{8} \int_{-\infty}^{\infty} \frac{\lambda^2 + \nu_0^2 - \mu_0^2}{\mu_0 \nu_0} n(\lambda) d\lambda.$$

Nonlinear barrier. If $V_{l0} = 0$ and $V_{nl0} > 0$, then the quasi-particle approach predicts that the soliton is fully transmitted if its velocity is large enough so that $8\mu_0^2 > W_{\max}(\nu_0)$. Taking into account radiation yields that the transmission is not complete in the sense that the transmitted soliton mass is not equal to the incoming soliton mass.

Nonlinear well. If $V_{l0} = 0$ and $V_{nl0} < 0$ then the quasi-particle approach predicts full soliton transmission. The second-order analysis exhibits radiative mass and energy losses. As a result, if the initial velocity is not large enough, then the energy loss is too important and the soliton is trapped in the nonlinear potential.

Enhanced transmission by nonlinear modulation. A nonlinear positive potential V_{nl} can help a soliton going through a potential well V_l [23]. Indeed, the radiation emitted by the soliton due to the interaction with the linear well and with the nonlinear potential can cancel each other, resulting in an enhanced soliton transitivity [21]. Similarly a nonlinear negative modulation can help the soliton going through a linear barrier [24].

2.2.4 Trapping by Dynamically Managed Linear Potentials

The purpose of this section is to show how it is possible to dynamically manage a potential well by a rapid time modulation of a barrier. The BEC wavefunction ψ in a quasi 1D geometry with fast moving potential is described by the GP equation [25]

$$i\psi_t + \psi_{zz} + 2|\psi|^2\psi = V_l(z - f(t/\varepsilon), t)\psi, \quad (2.21)$$

where $f(\tau)$ is a periodic function with period 1. The small parameter ε describes the fast oscillation period in the dimensionless variables. A standard multi-scale expansion yields the averaged GP equation

$$i\psi_t + \psi_{zz} + 2|\psi|^2\psi = V_{\text{eff}}(z, t)\psi, \quad V_{\text{eff}}(z, t) = \int_0^1 V_l(z - f(\tau), t) d\tau. \quad (2.22)$$

If, for example, $f(\tau) = w \sin(2\pi\tau)$, then

$$V_{\text{eff}}(z, t) = K_{\text{eff}} * V_l(z, t), \quad K_{\text{eff}}(z) = \frac{1}{\pi} \frac{1}{\sqrt{w^2 - z^2}} \mathbf{1}_{(-w, w)}(z), \quad (2.23)$$

where $\mathbf{1}_{(-w, w)}(z) = 1$ if $z \in (-w, w)$ and 0 otherwise. Let us assume that the potential V_l is time-independent. Applying the first-order perturbed IST

the dynamics of the soliton center can be described as a quasi-particle (2.17) moving in the effective potential $W(\nu, \zeta) = K_{l,\nu} * V_{\text{eff}}(\zeta)$ where $K_{l,\nu}$ is given by (2.18). The quasi-particle potential is plotted in Fig. 2.2 for a Gaussian barrier potential V_l . The potential $W(\nu, \zeta)$ has a local minimum at $\zeta = 0$ between two global maxima that are close to $\zeta = \pm w$. The well amplitude is $\Delta W(\nu) = \max_z W(\nu, z) - W(\nu, 0)$.

Let us consider an input soliton centered at $\zeta = 0$ with parameters (ν_0, μ_0) . There is a critical value μ_c for the initial soliton velocity parameter μ_0 defined by $\mu_c^2 = \Delta W(\nu_0)/8$ that determines the type of motion:

- If $|\mu_0| < \mu_c$ then the soliton is trapped. Its motion is oscillatory between the positions $\pm\zeta_f$ defined by $W(\nu_0, \zeta_f) - W(\nu_0, 0) = 8\mu_0^2$.
- If $|\mu_0| > \mu_c$, then the soliton motion is unbounded. It escapes the well and its velocity parameter becomes μ_a given by $\mu_a^2 = \mu_0^2 + W(\nu_0, 0)/8$.

As can be seen in numerical simulations [25], if the initial soliton parameters are close to the critical case $|\mu_0| \sim \mu_c$, then radiation effects become non-negligible. The construction of an efficient trap requires to generate a barrier potential V_l that is high enough so that $\Delta W(\nu_0)$ is significantly larger than $8\mu_0^2$. Finally, if the potential V_l is not stationary but has an explicit time-dependence, then the equations derived in this section still hold true if the time-dependence is slow enough. If, for instance, $V_l(z, t)$ is a delta-like potential centered at the position $x_0(t)$, that moves slowly in time, then $V_{\text{eff}}(z, t) = K_{\text{eff}}(z - x_0(t))$ is a moving double-barrier potential that can be used to manage the soliton position (Fig. 2.2).

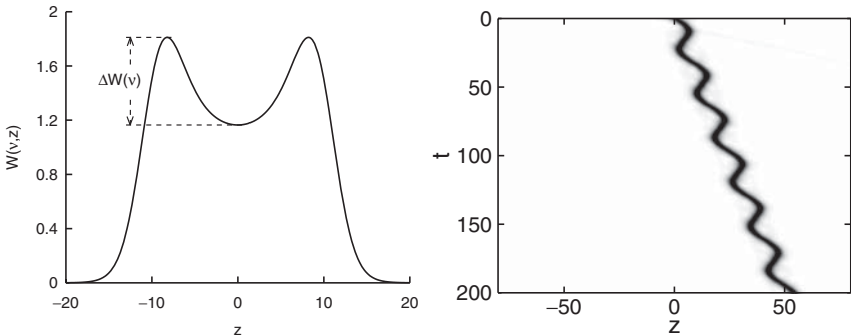


Fig. 2.2. *Left:* effective potential $W(\nu, z)$ for the quasi-particle motion (2.17). Here $\nu = 0.25$, $V_l(z) = 10 \exp(-z^2/4)$, and $f(\tau) = 10 \sin(2\pi\tau)$. *Right:* Evolution of a soliton with initial parameters $\nu_0 = \mu_0 = 0.25$ in the moving potential $V_l[z - 10 \sin(50t) - 0.25t]$.

2.2.5 Controllable Soliton Emission by Spatial Variations of the Scattering Length

An interesting application of spatial variations of the scattering length has been proposed and discussed in [26], which shows the possibility of controllable emission of bright solitons from a BEC by using a spatial variation of the scattering length along the trapping axis. The principle is the following one. A magnetic or optical Feshbach resonance technique is applied to a cigar-shaped BEC to induce a sharp variation of the scattering length along the axis, which is changed from positive (or zero) to negative. If the region of negative scattering length is located close to the edge of the trap, overlapping with the wing of the cloud, then the tail of the condensate is able to form a single soliton which, because of its higher internal energy, is outcoupled from the cloud and thus emitted outward. When the condensate refills the gap left out by the outgoing pulse a new soliton is emitted. This process continues as long as there is a large enough remnant of atoms in the trap and leads to a soliton burst escaping from the BEC.

The single soliton emission can be studied by a variational approach based on the 1D GP equation with a Gaussian ansatz for the wavefunction and a stepwise varying scattering length. This analysis shows that the single soliton emission is possible if the scattering length is negative enough in the tail of the cloud. This prediction is confirmed by numerical simulations of the 1D GP equation. These simulations also show that it is possible to generate a train of several hundreds of solitons with physical parameters corresponding to realistic configurations with rubidium or cesium.

2.3 Bright Solitons in Nonlinear Optical Lattices

New solitonic phenomena occur in BECs when the potentials are periodic in space, which can be produced by counter propagating laser beams. Such potentials can be used to control the soliton parameters or to generate gap bright solitons. A lot of work has been devoted to the case of linear periodic potentials [27]. Below we consider the propagation of nonlinear matter-wave packets and the wave emission by solitons in the presence of new types of inhomogeneities, namely under *nonlinear periodic or random potentials*, produced by periodic or random modulations of the atomic scattering length. The latter variations can be realized in a 1D BEC close to a magnetic wire with small fluctuations of current.

2.3.1 Propagation Through a Weak Nonlinear Periodic Potential

We consider an incoming soliton of the form (2.11) and we assume that the nonlinear potential is periodic $V_{nl}(z) = -V_{nl0} \cos(Kz)$. The soliton evolution can be analyzed using the first and the second-order perturbed IST theory

when $0 < V_{\text{nl}0} \ll 1$. The first-order perturbed IST theory predicts that the soliton mass is preserved and its center ζ obeys the quasi-particle equation (2.17) with the effective potential

$$W(\nu, \zeta) = -W_{\text{nl}0} \cos(K\zeta), \quad W_{\text{nl}0} = \frac{2\pi}{3} \frac{V_{\text{nl}0}\nu K}{\sinh(\frac{\pi K}{4\nu})} \left[1 + \frac{K^2}{16\nu^2} \right],$$

where 2ν is the soliton amplitude. The soliton can be trapped at $\zeta = 2\pi n/K, n = 0, \pm 1, \pm 2, \dots$, which correspond to the minima of the potential. The critical velocity for depinning the soliton starting from the minimum of the potential is $v_{\text{dp}} = 2\sqrt{W_{\text{nl}0}}$. From now on we assume that the initial soliton velocity $4\mu_0$ is larger than v_{dp} . The emission of matter-waves by the soliton can be investigated by taking into account second-order effects. Two possible regimes are found [28]:

1. If the modulation wavenumber K is smaller than ν_0^2/μ_0 , then radiation emission is negligible for times of order $V_{\text{nl}0}^{-2}$. The soliton parameters are almost constant in this regime.
2. If K is larger than ν_0^2/μ_0 , then the soliton emits a significant amount of radiation for times of order $V_{\text{nl}0}^{-2}$ (see Fig. 2.3). The soliton amplitude and velocity satisfy a system of ordinary differential equations (ODEs) given in [28]. The maximal radiative decay is obtained for K close to ν_0^2/μ_0 . If μ_0 is large enough, then the soliton mass 4ν decays to 0. If μ_0 is not very large, then the soliton mass 4ν decays, but the velocity 4μ decays faster, so that the condition $K\mu = \nu^2$ is reached at finite time. After this time, radiation emission is not noticeable anymore and this state persists for long propagation times. This shows that a meta-stable soliton exists even in the case $K > \mu_0/\nu_0^2$, at the expense of the emission of a small amount of radiation to allow the soliton to reach this state.

Bound states in the presence of nonlinear periodic potentials with moderate and strong modulations have been investigated by using an orbital stability analysis in [29] and the variational approach in [30]. It was shown that in the one-dimensional case with cubic nonlinearity the wave packets centered at a local maximum of the nonlinear optical lattice are stable, while wave packets centered at a local minimum of the lattice are stable against symmetric

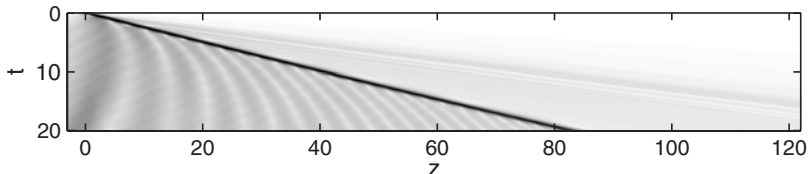


Fig. 2.3. Soliton profile $|\psi(z, t)|$. The initial soliton parameters are $\nu_0 = \mu_0 = 1$. Here $V_{\text{nl}0} = 0.4$ and $K = 2$, we can check that radiation emission is noticeable

perturbations only, while they are unstable against general perturbations. In the critical case (i.e. with quintic nonlinearity of the form $|\psi|^4\psi$) all localized solutions are practically unstable. Explicit solutions of the GP equation with spatially varying nonlinear potentials have been found in [31], in the particular case of periodic or localized nonlinear potentials. It was shown that localized nonlinearities can support an infinite number of multi-soliton bound states.

2.3.2 Propagation Through a Weak Random Nonlinear Potential

Here we assume that V_{nl} is a random zero-mean stationary process with auto-correlation function $B(z) = \langle V_{\text{nl}}(z)V_{\text{nl}}(0) \rangle$. For times of order $B(0)^{-1} \sim V_{\text{nl}0}^{-2}$ the soliton parameters satisfy a deterministic system of ODEs given in [28]. The analysis of this system gives the following results:

1. If $\mu_0 \gg \nu_0$, then the soliton velocity is almost constant, while the mass decays as a power law $\nu(t) \simeq \nu_0 (1 + t/T_c)^{-1/4}$. The decay time $T_c = [3\mu_0]/[32\hat{B}(4\mu_0)\nu_0^4]$ is inversely proportional to the forth power of the soliton amplitude, which shows that this type of disorder intensively destroys large-amplitude solitons.
2. If $\mu_0 \ll \nu_0$, then the soliton emits a very small amount of broadband radiation, its mass is almost constant, while the velocity decays very slowly, typically as a logarithm.
3. If $\mu_0 \sim \nu_0$, then the mass and velocity both decay during the early steps of the propagation (fully described by the system of ODEs). After this transitory regime, either the velocity becomes constant and the mass decays exponentially, or the mass becomes constant and the velocity decays logarithmically.

2.4 Multidimensional Bright Solitons in BECs

2.4.1 2D Bright Solitons in BECs with Time-Varying Scattering Length

In 2D or 3D BECs with attractive interactions bright solitons are unstable. Different schemes have been suggested for soliton stabilization. One of them is to vary rapidly in time the scattering length, which can be realized by using the Feshbach resonance management technique [8, 32]. Here we illustrate the main ideas on the example of the 2D GP equation with nonlinearity management. The mechanism for dynamical stabilization of 2D bright solitons by a rapid periodic variation in time of the scattering length has been suggested in [33, 34]. The dimensionless GP equation in this case has the form

$$i\psi_t + \nabla_\perp^2 \psi + [2 - V_{\text{nl}}(t)]|\psi|^2\psi = 0, \quad (2.24)$$

where $V_{\text{nl}}(t)$ is a periodic function and $\nabla_{\perp} = \partial_x^2 + \partial_y^2$. Using the variational approach or the moment method, the equation for the soliton width $w^2 = \int(x^2 + y^2)|\psi|^2 dx dy$ can be derived:

$$\frac{d^2w}{dt^2} = \frac{p(t)}{w^3}, \quad p(t) = Q_1 + Q_2 V_{\text{nl}}(t) \quad (2.25)$$

where Q_1 and Q_2 are invariants of the NLS equation and $p(t)$ is a periodic function that can be parameterized as $p(t) = \alpha + \beta \tilde{p}(t)$, with $\langle \tilde{p} \rangle = 0$ and $\max \tilde{p} = 1$. Using the theory of ODEs with periodic coefficients [35] it is found that a necessary condition for the existence of bound states is that the average value of p should be negative, which implies that $\alpha < 0$. Besides, the function p should change sign otherwise the solution would collapse, which implies $\alpha + |\beta| > 0$. The second condition is well satisfied in the strong nonlinearity management regime [36]. The parameter α is proportional to $N_c - N$, roughly speaking, where N_c is the critical mass equal to the mass of the Townes soliton. The numerical simulations performed in [35] for the 2D NLS equation show that it is possible to obtain a stable solution in the form of a Townes soliton with modulated parameters. When the initial data is taken in the form of the Gaussian function, the ODE (2.25) does not describe correctly the region of existence of the bound state. Numerical simulations show that the initial Gaussian pulse ejects a significant amount of radiation. The remaining part of the wave packet has the form of the Townes soliton with time-varying parameters. Results based on the averaging of the NLS equation with strong nonlinearity management and the analysis of the averaged equation have been obtained for the critical 1D NLS equation with quintic nonlinearity [37] and the NLS equation in the higher dimensional case [38, 39].

2.4.2 2D Bright Solitons in BECs with Spatially-Varying Scattering Length

Standing bright solitons in inhomogeneous condensed media have been studied in two dimensions in radial geometry. In the presence of a stepwise nonlinear inhomogeneity and harmonic trapping, solutions of the form $\psi(\rho, t) = \exp(i\lambda t)\phi(\rho)$, $\rho = \sqrt{x^2 + y^2}$, can be exhibited. Numerical simulations of the 2D GP equation have shown that the number of atoms of the standing bright soliton is strongly affected by the magnitude of the nonlinear inhomogeneity [40]. Radial nonlinear modulations $\gamma(\rho) = 2 - V_{\text{nl}}(\rho)$ in the form of a disk, annulus or narrow ring have been considered in [41], where it is shown that two-dimensional axisymmetric solitons are supported by such systems. In particular, the exact form of the solution can be found for an infinitely narrow ring.

If the nonlinearity coefficient is slowly varying, then the condition for the existence of 2D bright solitons can be obtained [42]. Let $f(\rho)$ be a smooth,

bounded, and positive function such that its first four derivatives do not grow faster than $C \exp(\rho)$ for some constant C , and

$$f(0)f^{(4)}(0) < C_2[f''(0)]^2, \quad C_2 \approx -1.6723.$$

If the nonlinearity coefficient is of the form $\gamma(\rho) = f(\epsilon\rho)$, then the ground state of the GP equation exists, is unique and stable for $\lambda > 0$ and for ϵ small enough. This means in particular that a necessary condition for the existence and stability of 2D bright solitons is that $\gamma^{(4)}(0)$ should be negative.

2.4.3 2D Bright Solitons in Dipolar BECs

As we mentioned before, in 2D BECs with short-range attractive potentials the solutions either become singular or spread out if the number of atoms exceeds the critical value. However, if the interatomic interactions have long-range characters, stable 2D bright solitons can exist. Recently a dipolar BEC of chromium atoms has been realized [43]. In distinction from the GP equation with local cubic nonlinear term, a dipolar condensate is described by the 3D GP equation with nonlocal nonlinearity

$$i\hbar \frac{\partial}{\partial t} \Psi = \left[-\frac{\hbar^2}{2m} \nabla^2 + V(\mathbf{r}) + g|\Psi|^2 + \int V_d(\mathbf{r} - \mathbf{r}') |\Psi(\mathbf{r}')|^2 d\mathbf{r}' \right] \Psi, \quad (2.26)$$

where $V_d(\mathbf{r}) = g_d(1 - 3\cos^2\theta)/r^3$ is the dipole-dipole potential, $g_d = \alpha d^2/(4\pi\epsilon_0)$ with ϵ_0 the vacuum permittivity and d the electric dipole, θ the angle formed by the vector joining the interacting particles and the dipole direction, and $-1/2 \leq \alpha \leq 1$ a tunable parameter by means of rotating orienting fields. Below we denote by $N = \int |\Psi|^2 d\mathbf{r}$ the number of atoms, we consider a trap potential $V(\mathbf{r}) = m\omega_z^2 z^2/2$ with no trapping in the xy plane, and we assume that the short-range interaction is repulsive $g = 4\pi\hbar^2 a/m > 0$. Applying the variational approach with a Gaussian ansatz [44], it is found that a stable solution can be obtained if

$$\frac{\tilde{g}_d}{3} < \sqrt{2\pi} + \frac{\tilde{g}}{4\pi} < -\frac{2\tilde{g}_d}{3}, \quad (2.27)$$

where $\tilde{g} = 8\pi Na/a_z$, $\tilde{g}_d = 2g_d N/(\hbar\omega_z a_z^3)$ and $a_z = \sqrt{\hbar/(m\omega_z)}$. This condition is valid if $\tilde{g}_d < 0$ and $|\tilde{g}_d|/\tilde{g} > 0.12$. Experimental realization of the chromium condensate, where $|\tilde{g}_d|/\tilde{g} \sim 0.03$, requires the additional reduction of short-range interactions via the Feshbach resonance. Numerical simulations show that the interactions between 2D bright solitons are inelastic.

2.4.4 3D Bright Solitons in Anisotropic Traps

As was pointed out at the beginning of this chapter, metastable states can exist in 3D BECs with trap potentials if the number of atoms is below a

critical value. In anisotropic traps long-living solitonic states can be formed. A recent experiment with ^{85}Rb condensate in a 3D magnetic trap confirms this prediction [45]. The bright matter-wave soliton has been observed during the collapse of ^{85}Rb condensate, occurring when the scattering length was switched from a positive value to a negative one. A system of highly robust solitons was generated. The observed interaction between solitons in the attractive condensate was repulsive. However, the solitons did not strongly overlap, so that they could survive for a few seconds and could be stable during around 40 collisions with each other. The observation of local spikes in the condensate density supports the idea of the formation of bright solitons train by a modulational instability of the condensate wavefunction [46–48]. Numerical simulations of the 3D GP equation predict the existence of a lower cut-off for the number of atoms below which no stable soliton can be found, in addition to the upper critical number [49].

2.5 Future Challenges

In conclusion we would like mention open problems that in our opinion could be of interest in the near future. First, one should study solitons in systems with long range interactions, such as cold dipolar gases, in different types of trap potentials, especially in optical lattices. Second, one should look for localized states in different types of linear-nonlinear periodic potentials, including ring-type configurations. Third, solitons and systems of solitons should be investigated in Fermi–Bose mixtures [50–53]. The manipulations of the relative ratio of bosons and fermions and the parameters of their interaction opens new possibilities for the existence of stable multidimensional bright solitons. Finally, properties of 3D solitons and soliton trains recently observed [45] require further consideration.

Authors are grateful for collaborations and/or useful discussions to A. Abdumalikov, B. Baizakov, J.G. Caputo, R.M. Galimzyanov, A. Gammal, L. Tomio, A.M. Kamchatnov, V.V. Konotop, R.A. Kraenkel, B.A. Malomed, and M. Salerno. F.Kh. Abdullaev is grateful to FAPESP for partial support.

References

1. V.E. Zakharov, A.B. Shabat, Soviet Phys. JETP **34**, 62 (1972)
2. L. Bergé, Phys. Rep. **303**, 259 (1998)
3. M. Weinstein, Commun. Math. Phys. **87**, 567 (1983)
4. A. Gammal, T. Frederico, L. Tomio, Phys. Rev. A **64**, 055602 (2001)
5. J.L. Roberts, N.R. Claussen, S.L. Cornish, E.A. Donley, E.A. Cornell, C.E. Wieman, Phys. Rev. Lett. **86**, 4211 (2001)
6. L.D. Carr, Y. Castin, Phys. Rev. A **66**, 063602 (2002)
7. C.C. Bradley, C.A. Sackett, R. Hulet, Phys. Rev. Lett. **78**, 985 (1997)

8. F.Kh. Abdullaev, A. Gammal, A.M. Kamchatnov, L. Tomio, Int. J. Mod. Phys. B **19**, 3415 (2005)
9. V.M. Pérez-García, H. Michinel, H. Herrero, Phys. Rev. A **57**, 3837 (1998)
10. K.E. Strecker, G.B. Partridge, A.G. Truscott, R.G. Hulet, Nature **417**, 150 (2002)
11. L. Khaykovich, F. Scherck, G. Ferrari, T. Bourdel, J. Cubizolles, L.D. Carr, Y. Castin, C. Salomon, Science **296**, 1290 (2002)
12. S. Inouye, M. R. Andrews, J. Stenger, H. J. Miesner, D. M. Stamper-Kurn, W. Ketterle, Nature **392**, 151 (1998)
13. P.O. Fedichev, Yu. Kagan, G.V. Shlyapnikov, and J.T.M. Walraven, Phys. Rev. Lett. **77**, 2913 (1996)
14. M. Theis, G. Thalhammaer, K. Winkler, M. Hellwig, G. Ruff, R. Grimm, J.H. Denschlag, Phys. Rev. Lett. **93**, 123001 (2004)
15. F.Kh. Abdullaev, M. Salerno, J. Phys. B **36**, 2851 (2003)
16. F.Kh. Abdullaev, A. Gammal, L. Tomio, J. Phys. B **37**, 635 (2004)
17. L. Salasnich, A. Parola, L. Reatto, Phys. Rev. A **65**, 043614 (2002)
18. A.M. Kamchatnov, V. Shchesnovich, Phys. Rev. A **70**, 023604 (2001)
19. S.V. Manakov, S. Novikov, J.P. Pitaevskii, V.E. Zakharov, *Theory of solitons* (Consultants Bureau, New York, 1984)
20. V.I. Karpman, Phys. Scr. **20**, 462 (1990)
21. J. Garnier, F.Kh. Abdullaev, Phys. Rev. A **74**, 013604 (2006)
22. Yu.S. Kivshar, B.A. Malomed, Rev. Mod. Phys. **61**, 763 (1989)
23. G. Theocharis, P. Schmelcher, P.G. Kevrekidis, D.J. Frantzeskakis, Phys. Rev. A **72**, 033614 (2005)
24. G. Theocharis, P. Schmelcher, P.G. Kevrekidis, D.J. Frantzeskakis, Phys. Rev. A **74**, 053614 (2006)
25. F.Kh. Abdullaev, J. Garnier, Phys. Rev. A **75**, 033603 (2007)
26. M.I. Rodas-Verde, H. Michinel, V.M. Pérez-García, Phys. Rev. Lett. **95**, 153903 (2005)
27. O. Morsch, M. Oberthaler, Rev. Mod. Phys. **78**, 179 (2006)
28. F.Kh. Abdullaev, J. Garnier, Phys. Rev. A **72**, 061605(R) (2005)
29. G. Fibich, Y. Sivan, M.I. Weinstein, Physica D **217**, 31 (2006)
30. H. Sakaguchi, B.A. Malomed, Phys. Rev. E **72**, 046610 (2005)
31. J. Belmonte-Beitia, V.M. Pérez-García, V. Vekslerchik, P.J. Torres, Phys. Rev. Lett. **98**, 064102 (2007)
32. B.A. Malomed, *Soliton management in periodic systems* (Springer, Berlin Heidelberg New York, 2006)
33. H. Saito, M. Ueda, Phy. Rev. Lett. **90**, 040403 (2003)
34. F.Kh. Abdullaev, J.G. Caputo, B.A. Malomed, R.A. Kraenkel, Phys. Rev. A **67**, 013605 (2003)
35. G.D. Montesinos, V.M. Pérez-García, P. Torres, Physica D **191**, 193 (2004)
36. D.E. Pelinovsky, P.G. Kevrekidis, D.J. Frantzeskakis, and V. Zharnitsky, Phys. Rev. E **70**, 047604 (2004)
37. F.Kh. Abdullaev, J. Garnier, Phys. Rev. E **72**, 035603(R) (2005)
38. V. Zharnitsky, D.E. Pelinovsky, Chaos **15** 037105 (2005)
39. P.G. Kevrekidis, D.E. Pelinovsky, A. Stefanov, J. Phys. A **39**, 479 (2006)
40. F.Kh. Abdullaev, V.S. Filho, A. Gammal, L. Tomio, Phys. Part. Nucl. **36**, S213 (2005)
41. H. Sakaguchi, B.A. Malomed, Phys. Rev. E **73**, 026601 (2006)

42. G. Fibich, X.P. Wang, Physica D **175**, 96 (2003)
43. A. Griesmaier, J. Werner, S. Hensler, J. Stuhler, T. Pfau, Phys. Rev. Lett. **94**, 160401 (2005)
44. P. Pedri, L. Santos, Phys. Rev. Lett. **95**, 200404 (2005)
45. S.L. Cornish, S. Thompson, C.E. Wieman, Phys. Rev. Lett. **96**, 170401 (2006)
46. A.M. Kamchatnov, A. Gammal, F.Kh. Abdullaev, R.A. Kraenkel, Phys. Lett. A **319**, 406 (2003)
47. L. Salasnich, A. Parola, L. Reatto, Phys. Rev. Lett. **91**, 080405 (2003)
48. L.D. Carr, J. Brand, Phys. Rev. Lett. **92**, 040401 (2004)
49. N.G. Parker, A.M. Martin, S.L. Cornish, C.S. Adams, arXiv:cond-mat/0603059
50. T. Karpiuk, M. Brewczyk, K. Rzazewski, Phys. Rev. A **73**, 053602 (2006)
51. J. Santhanam, V.M. Kenkre, V.V. Konotop, Phys. Rev. A **73**, 013612 (2006)
52. S.K. Adhikari, Phys. Rev. A **72**, 053608 (2005)
53. M. Salerno, Phys. Rev. A **72**, 063602 (2005)

Bright Solitons: Summary of Experimental Techniques

L. Khaykovich

3.1 Introduction

A uniform 3D BEC with attractive interactions is unstable because the gas tends to infinitely increase its density in order to decrease its interaction energy. This limitation is remarkably removed by an external trapping potential which stabilizes the system by introducing zero-point kinetic energy [1,2]. For an attractive BEC in a trap there is thus a critical number of atoms N_c below which the condensate is stable. Increasing number of atoms in the BEC leads to the collapse of the gas just as in the uniform case. First experiments with attractively interacting trapped Bose gases were carried out with lithium atoms in their doubly polarized state (in which the nuclear and electronic spin components have the largest possible values along the direction of the magnetic field) [3]. Later the experiments with ^{85}Rb (using tunable interactions) explored quantitatively the dependence of the critical number of atoms N_c on the strength of interatomic interactions [4]. The dynamics of growth and collapse of BECs with attractive interactions has been directly investigated in two notable experiments with ^7Li [5] and ^{85}Rb [6].

Remarkably, the 3D collapse can be readily avoided if a BEC is confined along two directions. Along the free direction, the condensate dispersion owing to its kinetic energy is balanced by the attractive interatomic interactions, resulting in the formation of bright solitons.¹ These solitons were demonstrated in two independent experiments with ^7Li atoms [7, 8]. The similar approaches used in both experiments, demonstrate the spectacular flexibility of recently developed experimental techniques for manipulating ultracold dilute atomic gases. In this chapter we shall discuss these techniques starting with tunable interatomic interactions achieved by means of Feshbach resonances. We then describe the optical trapping of atomic BECs and the

¹ Strictly speaking, they are solitary waves rather than solitons as their collisions are inelastic (see Sect. 3.5). However, we shall refer to them as solitons throughout this chapter.

reduction to low dimensional (1D and 2D) condensates. Next, we discuss the experimental demonstrations of solitons in Paris [7], Rice [8] and the more recent demonstration of solitons with ^{85}Rb atoms in a nearly 3D trap in Colorado [9]. Finally we discuss the prospects of bright soliton collisions experiments and the origin of higher order nonlinearity which is expected to appear in them.

3.2 Tunable Interatomic Interactions

3.2.1 Feshbach Resonance

Collisions in ultracold gases are extensively discussed in lectures [10] and books [1, 2]. Here, we shall only emphasize a few crucial points, while for full details we refer the reader to the literature.

Alkali atoms which are widely used in BEC experiments have a single electron outside closed shells. If we neglect for the following the magnetic dipole–dipole interactions (which introduce inelastic dipolar loss mechanism) the scattering potential of a pair of atoms is a central potential $V(r)$, where r is the atomic separation. The long-range part of the potential is due to van der Waals electric dipole–dipole attraction and its strongest contribution is of the form $-1/r^6$ while the short-range potential is dominated by strong repulsion due the overlap of electron clouds. Generally the interaction potential $V(r)$ can be decomposed to singlet $V_S(r)$ and triplet $V_T(r)$ terms depending on the spin state of the two electrons:

$$V(r) = V_S(r)P_S + V_T(r)P_T \quad (3.1)$$

where P_S and P_T are projection operators to singlet and triplet spin states. The singlet potential is in general much deeper than the triplet one because two electrons can occupy the same orbital (valence electron attraction).

The well established result of the scattering theory for the van der Waals type potential (decreasing sufficiently fast at infinity) is that the low energy scattering is isotropic (*s* – wave scattering) and characterized by a single parameter a called the scattering length [11]. Potentials for most alkali atoms are generally very well known thanks to their intensive study in cold atoms experiments. Scattering lengths for lithium isotopes have been measured by photo-associative spectroscopy and found to be (for bosonic ^7Li) $a_S = 1.7 \pm 0.1 \text{ nm}$ (singlet) and $a_T = -1.46 \pm 0.03 \text{ nm}$ (triplet) [12]. Scattering lengths of ^{85}Rb were determined to be $a_S = 127_{-18}^{+32} \text{ nm}$ and $a_T = -19.5 \pm 0.8 \text{ nm}$ in a Feshbach resonance study [13]. Scattering lengths for other alkali atoms are available in literature [1].

The scattering length defines all essential properties of the BEC and, most excitingly, it is variable and can be altered by either a shape resonance [10] or, now widely and successfully used in experiments, a Feshbach resonance.

This most powerful experimental technique allows tuning of strength and sign of interatomic interactions by simple change of an external magnetic field. Ever since their first experimental observation [14], Feshbach resonances revolutionized the field of cold atoms research, providing the experimentalists with unprecedented level of control. We shall therefore briefly discuss the origin of the resonance. For extensive discussion we refer the reader to review papers on the subject [15].

Two-atom scattering Hamiltonians can be represented most generally by two single atom Hamiltonians and the interaction potential $V(r)$. The single atom Hamiltonian includes hyperfine interaction term of the form $V_{\text{HF}} = \mathcal{E}_{\text{HF}} \mathbf{S}_i \mathbf{I}_i$ where \mathbf{S}_i is the electronic and \mathbf{I}_i is the nuclear spin. However the interatomic potential (3.1) depends on the *total* electronic spin $\mathbf{S}^2 = (\mathbf{S}_1 + \mathbf{S}_2)^2$ which does not commute with the hyperfine interaction term. In a collision process the hyperfine term can flip electronic spins and introduce coupling between the interaction potentials. Consider two atoms with their electronic spins $m_1 = m_2 = -1/2$ in a magnetic field B so that they are polarized and interact through a triplet potential. The continuum of the triplet potential lies below the continuum of the singlet potential because the latter one belongs to a different energy level which approaches a higher energy hyperfine state at low magnetic field. The resonance occurs when there is a bound state in the singlet potential which is close to the continuum of the triplet potential (see Fig. 3.1). Most significantly the resonance condition can be reached by simple change of the external magnetic field as only atoms interacting through a triplet potential are affected. Near the Feshbach resonance the scattering

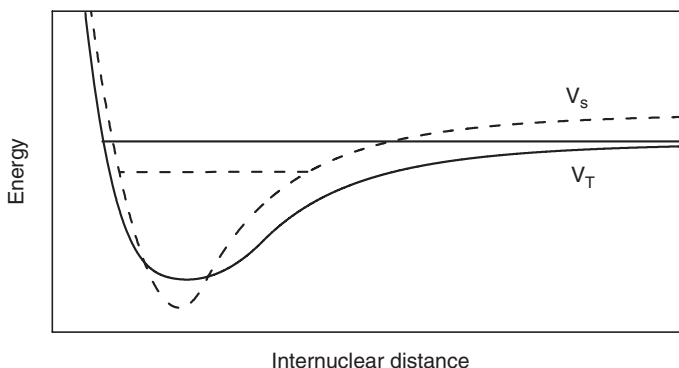


Fig. 3.1. Schematic representation of singlet and triplet interatomic potentials. Solid line shows the triplet interaction potential which is the entering channel of two colliding atoms. It can be shifted by means of a magnetic field offset to meet a bound state of the singlet potential (dashed line). The latter is the interaction potential of two atoms when the hyperfine interaction flips the spin of one of them. Feshbach resonance takes place when two energies (a triplet continuum and a singlet bound state) coincide

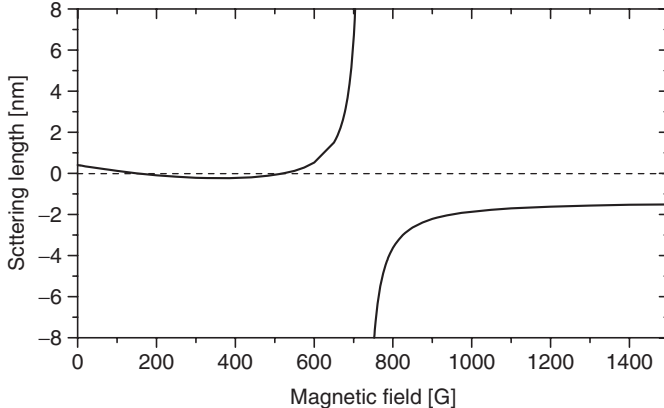


Fig. 3.2. Calculated magnetic field dependence of the scattering length for ${}^7\text{Li}$ in the absolute ground state [7]. The resonance position is at 725 G

length a is predicted to vary dispersively as a function of the magnetic field B [15]:

$$a(B) = \tilde{a} \left(1 - \frac{\Delta}{(B - B_0)} \right) \quad (3.2)$$

where \tilde{a} is the off-resonance background scattering length and Δ represents the width of the resonance.

In Fig. 3.2 the variation of effective scattering length with magnetic field around a Feshbach resonance, is shown for ${}^7\text{Li}$ atoms in their absolute ground state. Divergence around the magnetic field of 725 G is the signature of the resonance. Excluding the resonance there is an evolution of scattering potential from a combination of triplet and singlet potentials at zero magnetic field (with the scattering length $a = 0.4$ nm) to the purely triplet one (with the scattering length $a_T = -1.46$ nm) at high magnetic field. Combination of the two effects provides a very wide range of magnetic fields where the scattering length is negative and very small which suits perfectly the requirement for soliton production.

There is however, an inherent obstacle in the use of Feshbach resonances because they affect both elastic and *inelastic* collision rates. Consequently, severe limitations are set on the practical increase of the scattering length. This apparent drawback was put to good use in experiments, allowing for the accurate location of the resonance. Strong loss of atoms associated with different inelastic processes provides a simple and reliable experimental signature of the Feshbach resonance² [14]. In Fig. 3.3 inelastic scattering loss is shown for the theoretically predicted resonance of Fig. 3.2.

² Fermionic atoms constitute a remarkable exception to this rule, in that they are extremely stable against inelastic losses in the vicinity of a Feshbach resonance [16].

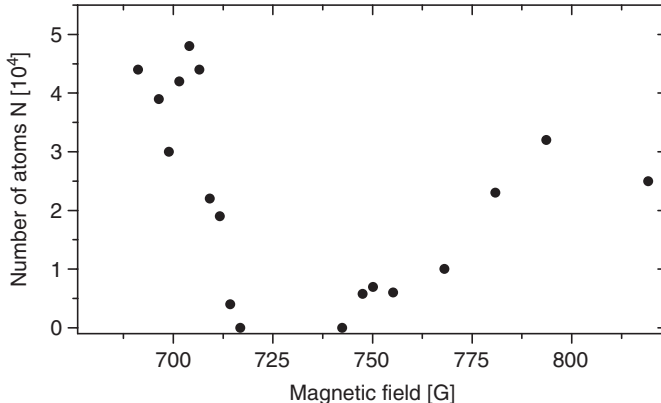


Fig. 3.3. Observation of a ${}^7\text{Li}$ Feshbach resonance through a rapid loss associated with the three-body recombination (two-body relaxation is impossible from the absolute ground state)

Applications of the Feshbach resonance are very diverse. Here we discuss only one of them which is the observation of matter-wave solitons. Other applications include the study of BCS transition, BEC-BCS crossover and molecular BEC in a two-spin-mixture Fermi gas [17], coherent atom–molecule oscillations with bosons [18] and many others that constantly emerge.

3.2.2 Measure of the Interaction Strength

An insight into the behavior of a BEC with attractive interactions can be obtained by means of a variational approach (see previous chapter and books [1, 2]). The collapse is predicted to occur when

$$k_c = \frac{N_c |a|}{a_{ho}} \approx 0.67 \quad (3.3)$$

where $a_{ho} = \sqrt{\hbar/m\omega_{ho}}$ is the mean harmonic oscillator length and N_c is the critical number of atoms. Experimentally somewhat lower value of $k_c = 0.46 \pm 0.06$ has been found [13].

The dimensionless parameter $k = N|a|/a_{ho}$ is very useful as a measure of interaction strength. For repulsive condensates ($a > 0$) in 3D traps the usual situation is $k \gg 1$. In this strongly interacting (Thomas–Fermi) limit, the kinetic energy of the condensate can be neglected and the Gross–Pitaevskii equation (GPE) is approximately solved by the familiar parabolic density profiles [1, 2]. For attractive condensates ($a < 0$) the k parameter should always be less than k_c according to (3.3). In a cylindrically symmetric trap which tightly confines atoms in two spatial dimensions, an accurate approximation of the 1D gas can be made when the interaction energy is small with respect

to the radial potential energy level spacing. The GPE then reduces to an effective 1D form:

$$i\hbar\psi_t = -\frac{\hbar^2}{2m}\psi_{xx} + g_{1D}|\psi|^2\psi + \hbar\omega_r\psi, \quad (3.4)$$

where $g_{1D} = 2a\hbar\omega_r$ is the renormalized quasi-1D interaction constant [19] and ω_r is the oscillation frequency in radial direction. The condensate wavefunction is well described by a Gaussian in the radial direction and a well known functional form of a bright soliton in the longitudinal (unbound) direction:

$$\psi(x, t) = e^{-i\mu t/\hbar} \frac{1}{\sqrt{2l}} \frac{1}{\cosh(x/l)}, \quad (3.5)$$

where l is the spatial extent of the soliton and $\mu = -\hbar^2/2ml^2$ is the chemical potential. Substituting (3.5) into (3.4) yields

$$l = \frac{2\hbar^2}{g_{1D}Nm} = a_r \frac{a_r}{N|a|} = \frac{a_r}{k_r}, \quad (3.6)$$

where $a_r = \sqrt{\hbar/m\omega_r}$ is the radial harmonic oscillator length and $k_r = N|a|/a_r$ is the ‘radial’ interaction strength.

In the 1D limit ($k_r \ll 1$) the longitudinal size of the soliton exceeds significantly its radial size. If however the interaction parameter k_r increases, the condensate wave packet shrinks in mainly longitudinal direction, approaches its 3D limit and, ultimately, collapses. $k_r \ll 1$ requires small atom number and/or weak interactions (small scattering length). Tuning of the scattering length to low values via the Feshbach resonance allows one to weaken interactions and thus to increase the number of atoms and to improve signal/noise ratios.

3.3 Optical Confinement of Bose–Einstein Condensates

3.3.1 BECs in Optical Traps

The possibility to tune interactions usually requires optical trapping as Feshbach resonance frequently occurs in states that cannot be magnetically trapped. Optical traps which rely on electric dipole interaction of an atom with far-detuned light offer the possibility to trap atoms in all internal states [20]. The optical potential imposed on an atom by a far-detuned laser is given by

$$U(\mathbf{r}) = \frac{\hbar\gamma^2}{8I_s} \frac{I(\mathbf{r})}{\delta}, \quad (3.7)$$

where δ is the laser detuning from the atomic resonance, I_s is the saturation intensity (which is usually of the order of a few $mW\text{ cm}^{-2}$) and γ is the natural linewidth of the excited state of atom. It is immediately seen from (3.7) that the red (blue) detuned laser provides attractive (repulsive) potential. The

attractive potential is most simply formed by focusing a single infrared laser beam into the center of the atomic cloud. This method is now widely used in many ultracold atom experiments [20].

Apart from the conservative potential $U(\mathbf{r})$, the laser light induces heating on atoms through spontaneous scattering of photons and power and position instabilities. To reduce heating by spontaneous emission very far detuned lasers are used (as the scattering rate scales as I/δ^2). In experiments [7, 8] infrared ($1.06\text{ }\mu\text{m}$) Nd:YAG lasers were used that provided almost 400 nm detuning from the atomic resonance (for Li atoms). Power and position jitters can be also, if necessary, controlled by the active feedback stabilization methods.

Initial pursuit of BECs by all-optical techniques was unsuccessful, though it stimulated development of numerous beautiful experimental techniques such as sub-recoil optical cooling [21], various optical dipole and lattice traps [20] and optical molasses [22], Raman sideband [23] and evaporative cooling [24] in such traps. The winning strategy for BECs, however, was proved to be the evaporative cooling in a magnetic trap. After being produced in the magnetic trap, the BEC was then transferred into an optical trap and various effects have been studied including the first experimental demonstration of a Feshbach resonance in sodium BEC [14].

Continued efforts toward ‘all-optical’ BECs were finally rewarded with ^{87}Rb [25] and ^{133}Cs [26] condensates obtained directly in optical traps. In the case of ^{87}Rb this method increased significantly the rate of BEC production as optical confinement can be easily made much stronger than that of a magnetic trap. The resulting condensates were $F = 1$ spinors [25]. However the main driving force beyond the search for all-optical ways to reach BEC threshold, was failed attempts to observe BEC of Cs atoms in a magnetic trap. Strongly enhanced two-body losses from the magnetically trappable states has blocked the ‘standard’ way to a Cs BEC [27].

Within the context of optical trapping, one should also mention the very intensive use of periodic optical potentials, having an immense impact on many cold-atom activities including solitons (see contribution to this volume on optical lattices and nonlinear localization of BECs in optical lattices).

3.3.2 BECs in Low Dimensions

Optical traps allow extreme control over trapping potentials and provide highly anisotropic configurations where the motion of atoms can be extinguished in one or two directions. This modifies significantly the behavior of the system for both attractive and repulsive condensates. In the attractive case highly anisotropic quasi-1D potential are essential to make 1D bright (and dark) solitons as was discussed in Sect. 3.2.2. For repulsive condensates consequences of the reduced dimensionality are very rich.

The 1D limit is obtained when the interaction energy becomes smaller than the energy level spacing of the external potential in tightly bound

radial direction. In this regime the size of the condensate wavefunction in the radial direction only slightly deviates from the Gaussian size of the ground state. This was experimentally observed by measuring the condensate released energy in both lithium [28] and sodium condensates [29]. Very elongated quasi-1D trapping geometries causes condensate fragmentation or, in other words, realization of quasi-condensates which locally behave like ordinary condensates but do not possess a globally uniform phase [30]. In these limits the collisional properties of atoms remain essentially 3D and the GPE stays relevant. At very low densities and very strong radial confinement a different limit of 1D systems, called Tonks–Girardeau gas of “impenetrable bosons”, has been recently experimentally observed [31]. This achievement provides now a new playground for the exciting subject of strongly correlated 1D quantum systems.

The 2D limit can be obtained in a pancake type trapping geometry with the tight confinement in only one direction. Experimentally it is achieved by either using cylindrical optics or retro-reflecting laser beam to build a standing wave which provides an array of pancake traps. The regime where interaction energy was smaller than the energy level spacing in the trap was experimentally shown in [29]. The most significant challenge for 2D systems however is the observation of different types of a phase transition associated with the emergence of a topological order providing binding of vortex–antivortex pairs. This Berezinskii–Kosterlitz–Thouless (BKT) phase transition occurs at finite temperature and was very recently observed in a stack of optical pancake traps [32].

3.4 The Experiments

3.4.1 Formation of a Single Soliton

An experiment in Paris which demonstrated formation of a single soliton, used lithium atoms in their absolute ground state trapped in a far detuned 1D optical dipole trap (a waveguide) [7]. We briefly discuss the apparatus and experimental procedure here while for full details we refer the reader to the original paper. Atoms from a thermal lithium beam are slowed in a Zeeman slower and loaded into a magneto-optical trap. These atoms are then transferred by means of a magnetic elevator into a Ioffe–Pritchard-type magnetic trap in a doubly polarized spin state $F = 2, m_F = 2$. In this state the scattering length is negative, relatively large ($a = -1.4$ nm) and insensitive to the external magnetic field. Evaporatively precooled to about $10 \mu\text{K}$, atoms are then loaded into a far detuned optical dipole trap formed by the intersection of two Nd:YAG laser beams oriented vertically and horizontally. Optically trapped atoms are then transferred to the lowest energy state ($F = 1, m_F = 1$) to take advantage of the magnetic tuning of the scattering length via a Feshbach resonance. The following evaporation step is performed at the magnetic field

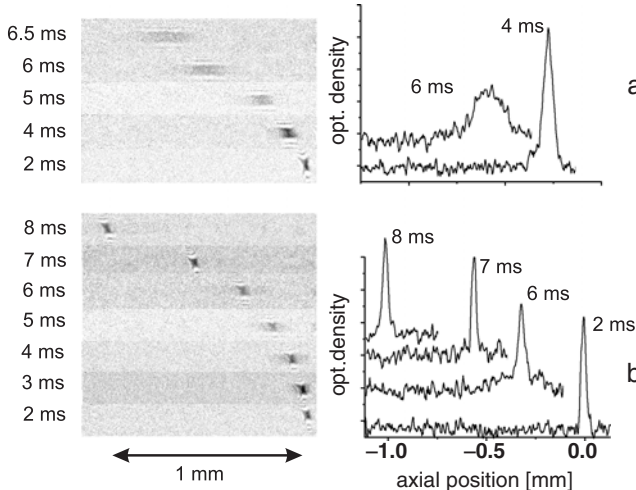


Fig. 3.4. Propagation of an ideal BEC (a) and of a soliton (b) in the horizontal 1D waveguide in the presence of an expulsive potential. Corresponding profiles in the propagation direction are integrated over the vertical direction (reprinted from [7])

of 665 G where $a = 2.1 \text{ nm}$ (see Fig. 3.2) by lowering the depth of the optical potential. A condensate with $N \approx 2 \times 10^4$ atoms is formed in a nearly isotropic trap. The scattering length is then tuned to zero to reduce three-body losses and the trap is adiabatically deformed into a cylindrically symmetric trap. The effective interaction is then tuned to the attractive regime by lowering the magnetic field strength to 425 G where $a = -0.21 \text{ nm}$ and the vertical laser beam is switched off completely by a mechanical shutter releasing the atomic cloud in an effective 1D optical waveguide (a horizontally oriented laser beam potential). At variable delays after switching off the vertical laser beam, the atomic cloud is measured by the absorption imaging technique.

The time evolution of an ideal gas ($a = 0$ at $B = 520$ G) in a waveguide is compared with a gas with attractive interactions ($a = -0.21 \text{ nm}$ at $B = 425$ G) in Fig. 3.4. In the propagation direction the current coils that are used to provide an offset magnetic field produce a slightly expulsive potential which overcomes the dipole trap. When the vertical laser beam is switched off, the atomic cloud is projected on the slope of this potential because of a small offset between the atomic initial position and the maximum of the potential. This causes a unidirectional drift toward the left (see Fig. 3.4). The width of the expanding cloud in the waveguide is considerably broader in the noninteracting case while for all observation times the soliton's width remains equal to the resolution limit of the imaging system.³ The soliton is observed to propagate over a macroscopic distance of 1.1 mm in 10 ms without decay.

³ More recently it was shown numerically that the soliton under the expulsive potential is not truly invariant in size [33].

Stability analysis which is done numerically by variational techniques shows a very narrow parameter region where the soliton could survive between the 3D collapse and the explosion imposed by the external explosive potential [7]. For the radial harmonic oscillator length $a_r = 1.4 \mu\text{m}$ and $a = -1.4 \text{ nm}$, the number of atoms that allows the soliton to be formed is $4.2 \times 10^3 \leq N \leq 5.2 \times 10^3$. Clearly, the explosive potential imposes severe limitation on soliton research and should be avoided. In a later theoretical paper however, an interesting phenomenon of soliton destabilization by quantum evaporation which can occur in a repulsive potential has been proposed [34].

3.4.2 Soliton Trains

In another experiment at Rice, formation and propagation of matter-wave soliton trains are observed rather than a single soliton [8]. Small differences in the experimental realization with that discussed in the previous section lead to different results. The stages until loading into an optical trap are essentially the same. The main difference, however, is in the realization of an optical trap. In the Rice experiment the optical trap consists of a focused infrared Nd:YAG laser for radial confinement and two cylindrically focused doubled Nd:YAG beams (blue-detuned repulsive optical potential) 250 μm apart, providing end-caps for longitudinal confinement. The evaporative cooling is then performed in this trap when the uniform magnetic field is ramped to a value of 700 G ($a = 10.6 \text{ nm}$) until the threshold to a BEC. Then the magnetic field is reduced to a value of 575 G where a is small and negative.

Soliton behavior is investigated by setting them in motion. This is achieved by displacing the infrared laser focus axially from the center of the magnetic trap and the end-caps. In this way the BEC is initially formed on the side of the weak longitudinal potential of the infrared laser beam and was held there by the green laser end-caps. On removing the end-caps, the atoms oscillate in the longitudinal potential for a varying duration before being imaged (Fig. 3.5). As can be seen in images, a solitons train was created rather than a single soliton. Moreover the solitons bunch at the turning points and spread out in the middle. The immediate conclusion is that there are repulsive interactions between neighboring solitons although the interatomic interactions are attractive.

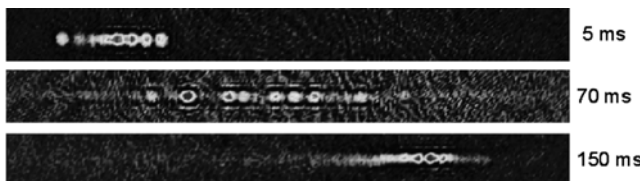


Fig. 3.5. Soliton train oscillation in the longitudinal potential. The solitons group at the turning points and spread out in the middle of the oscillation (reprinted by permission from Macmillan Publishers Ltd: [8], copyright (2002))

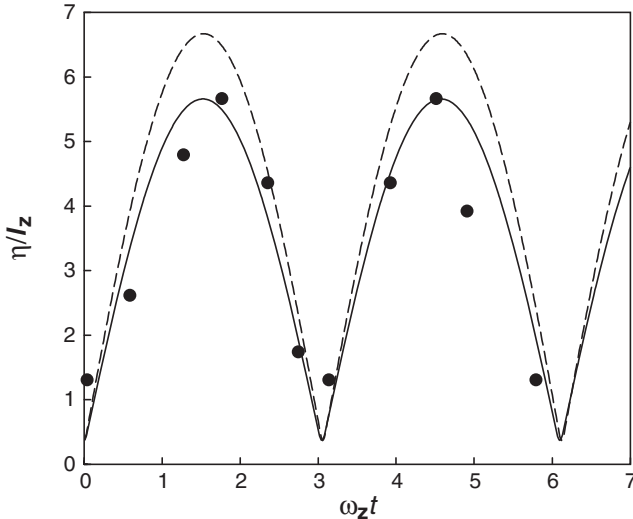


Fig. 3.6. Relative spacing between two neighboring solitons in the trap. The vertical axis is soliton separation in units of longitudinal harmonic oscillator length. The *solid curve* is a solution of the equation of motion of two solitons and the dashed curve neglects the interatomic attraction in the soliton interaction potential. The points are experimental data (reprinted with permission from [35], copyright (2002) by the American Physical Society)

It is very well known that two neighboring solitons with π phase difference interact repulsively. In Fig. 3.6 the relative spacing between solitons in the trap as a function of propagation time is shown. An explanation of the formation of soliton trains was suggested by the presence of the alternating phase structure. When the scattering length is changed from positive to negative the condensate becomes unstable to the growth of perturbations at a particular wavelength. The available length scale in a BEC is a healing length $\xi = 1/8\pi n|a|$ where n is the atomic density. In the repulsive condensate the phase is constant, but as the sign of the scattering length is switched, a mode with wavelength ξ becomes unstable so that initial quantum fluctuations imprint the condensate with an alternating phase structure [35]. Although simplified, the numerical simulations were able to produce up to seven solitons with alternating phases. The model suggested that the number of solitons produced should vary with the initial size of the condensate which was verified in the experiment.

The mechanism responsible for the formation of the soliton train and the long-term stability of solitons are as yet not completely understood. Another model suggests that self-interference fringes seed the perturbation modes and that the solitons within a train are actually created with arbitrary phases [36]. After a series of collapses induced by collisions between attracting solitons, a

final stable configuration is achieved in which only repelling solitons remain. It was experimentally observed that the total number of atoms in the train was about a fifth of the initial atom number in the repulsive condensate. Another model [37] also suggests that solitons are formed with arbitrary phases and the following time evolution shows missing peaks in soliton trains which can be identified in the experimental data of [8].

3.4.3 Formation of Solitons in Nearly 3D Traps

In a different experiment with ^{85}Rb atoms, a robust configuration of multiple solitons was created in a nearly symmetric magnetic trap during the collapse of an attractive condensate [9]. This experiment starts with the production of a stable condensate within the positive scattering length region of a broad Feshbach resonance which exists on a magnetically trappable state $|F = 2, m_F = -2\rangle$ at the field $B = 155\text{G}$ [38]. The radial (longitudinal) frequency of cylindrically symmetric trap was 17.3 Hz (6.8 Hz) where condensates of up to 1.5×10^4 atoms were formed. The collapse of the condensate was then induced by quickly switching the scattering length through zero to various negative scattering lengths. The number of atoms surviving the collapse was then investigated as a function of a final negative scattering length. Most remarkably, the number of atoms in the remnant attractive condensates was significantly greater than the critical number (for example at $a = -5.3\text{ nm}$ the remnant condensate contained about 10 times more atoms than the critical value). This curious discrepancy was interpreted as a formation of multiple solitons which were identified on absorption images as distinct clouds (see Fig. 3.7). The solitons oscillate for over three seconds colliding more than 40 times during this period. The remarkable stability of the soliton dynamics in the 3D trap was considered as a manifestation of π phase shift between the neighboring solitons. This conclusion was supported by numerical simulations of the experiment based on 3D GPE [39]. However, the origin of the alternating π phase shifts is still unresolved.

3.5 Origin of Higher Order Nonlinearity and its Impact on Soliton Dynamics

In Sect. 3.2.2 bright soliton is introduced as a special solution of 1D GPE (3.4) and it is therefore a 1D object. However, in all experiments discussed in Sect. 3.4 despite the differences in realizations of each specific trap where solitons were formed, the solitons themselves were similar in a sense of being almost 3D objects. In particular, in the Paris experiment [7], a stable soliton was only possible if its longitudinal size exceeded the transverse size by no more than 20%. In the experiment with Rb [9] the number of atoms per soliton was always close to N_c yielding solitons with almost complete spherical symmetry. It is an intuitive consequence of the soliton train formation process

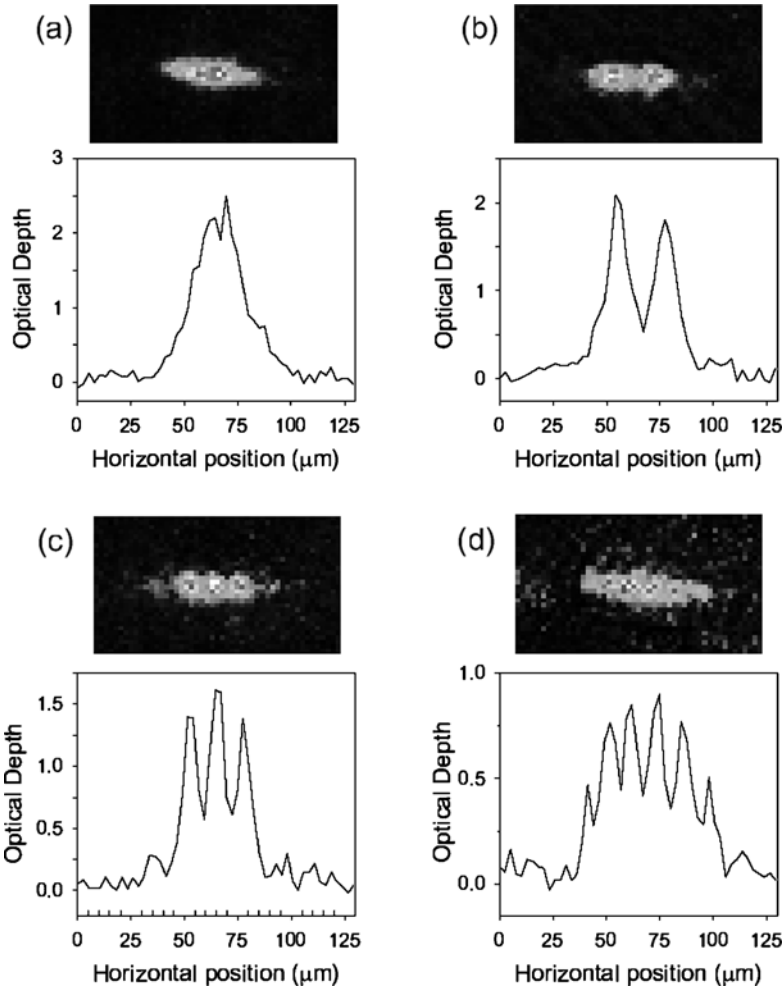


Fig. 3.7. Absorption images and cross sections of multiple solitons. When the negative scattering length a is small a single attractive condensate is formed with the number of atoms less than the critical number (a), for larger absolute value of the scattering length the condensate is split into a number of solitons (b)–(d) (reprinted with permission from [9], copyright (2006) by the American Physical Society)

that solitons were formed containing of about the critical number of atoms and thus close to a 3D geometry. In Sect. 3.4.2 the mechanism responsible for the soliton train formation was identified as a modulation instability (MI) caused by the unstable phase modes with a wavelength ξ (the condensate healing length) which is (in 1D form):

$$\xi = \frac{a_r}{\sqrt{8n_{1D}|a|}}, \quad (3.8)$$

where $n_{1D} = n\pi a_r^2$ is the linear density. If the negative scattering length is small such that $k_r \ll 1$ [see (3.6)], the denominator of (3.8) is very small yielding an effective 1D single soliton production (ξ is about the size of the initial condensate). However if $k_r > 1$, ξ becomes of the order of a_r very quickly. It can be seen by presenting the linear density as $n_{1D} = \lambda N/a_r$, where λ depends on the condensate longitudinal size before the scattering length is switched to a negative value. Assuming zero interactions for the initial conditions (as per [7, 8]), $\lambda = a_r/a_l = \sqrt{\omega_l/\omega_r}$ where $a_l = \sqrt{\hbar/m\omega_l}$ is the longitudinal harmonic oscillator length. In the Paris experiment [7] $\lambda \approx 0.27$ yielding $\xi < a_r$ which leads to a collapse where most of atoms are lost and to a single soliton formation with almost 3D geometry. In the Rice and the later ^{85}Rb experiments [8, 9] the situations were very similar, however, soliton trains of nearly 3D solitons were observed rather than a single soliton. These differences can be explained by a presence of trapping rather than anti-trapping longitudinal potential and significantly bigger initial number of atoms.

Recently, it was shown that the proximity of the soliton to being a 3D object strongly affects its properties, such as the character of its motion [40], interactions [41] and collisions [42]. In particular, it is demonstrated that a moving soliton immersed in a cloud of thermal atoms is subjected to a temperature-dependent friction force [40]. In a different proposal, thermal environment causes the soliton to split into two partially coherent solitonic structures which are analogous to optical random-phase solitons [43]. A collision between two solitons, which are by themselves stable, in a confined geometry may readily lead to collapse, if the total number of atoms in the soliton pair exceeds the critical value, and the phase difference between the solitons is (close to) zero [41]. A collision between two identical in-phase solitons can lead to a merger into a single pulse if their velocities are smaller than the critical velocity and symmetry breaking is readily obtained in collisions between two solitons with non-zero initial phase difference [42].

The way to avoid residual three-dimensionality in the experiments where multiple solitons are formed is to weaken the interaction strength after the formation process is completed. Experimental verification of different regimes and above theoretical proposals are still lacking.

3.6 Conclusions

Experimental observations of matter-wave solitons triggered vast theoretical research and many interesting questions have been raised. In this chapter we intended to show the state of the art experimental techniques that were recently developed in the field of ultracold atoms and allowed experimental demonstrations of different types of solitons. The power and flexibility of these techniques allow many intriguing tasks presented in theoretical proposals to

become an experimental reality. More experimental techniques will be soon available as the interest in this research field grows fast.

Acknowledgement. I thank R.G. Hulet, H.T.C. Stoof and S.L. Cornish for providing me with the material from their original work. I am grateful to Amichay Vardi for a careful reading of the manuscript and suggesting various improvements. This work was supported, in a part, by the Israel Science Foundation.

References

1. C.J. Pethick, H. Smith: *Bose-Einstein Condensation in Dilute Gases* (Cambridge University Press, Cambridge 2002)
2. L. Pitaevskii, S. Stringari: *Bose-Einstein Condensation* (Clarendon, Oxford 2003)
3. C.C. Bradley, C.A. Sackett, J.J. Tollet, R.G. Hulet, Phys. Rev. Lett. **75**, 1687 (1995); C.C. Bradley, C.A. Sackett, R.G. Hulet, Phys. Rev. Lett. **78**, 985 (1997)
4. J.L. Roberts, N.R. Claussen, S.L. Cornish, E.A. Donley, E.A. Cornell, C.E. Wieman, Phys. Rev. Lett. **86**, 4211 (2001)
5. G.M. Gerton, D. Strekalov, I. Prodan, R.G. Hulet, Nature **408**, 692 (2000)
6. E.A. Donley, N.R. Claussen, S.L. Cornish, J.L. Roberts, E.A. Cornell, C.E. Wieman, Nature **412**, 295 (2001)
7. L. Khaykovich, F. Schreck, G. Ferrari, T. Bourdel, J. Cubizolles, L.D. Carr, Y. Castin, C. Salomon, Science **256**, 1290 (2002)
8. K.E. Strecker, G.B. Partridge, A.G. Truscott, R.G. Hulet, Nature **417**, 150 (2002)
9. S.L. Cornish, S.T. Thompson, C.E. Wieman, Phys. Rev. Lett. **96**, 170401 (2006)
10. J. Dalibard: Collisional dynamics of ultra-cold atomic gases. In: *Bose-Einstein Condensation in Atomic Gases*, Proceedings of the Enrico Fermi International School of Physics, vol CXL, ed. by R. Inguscio, S. Stringari, C.E. Wieman (IOS Press, Amsterdam, 1999), pp. 321–349
11. L.D. Landau, E.M. Lifshitz: *Quantum Mechanics*, 3d edn. (Pergamon, Oxford, 1977), Sect. 131
12. E.R.I. Abraham, W.I. McAlexander, C.A. Sackett, R.G. Hulet, Phys. Rev. Lett. **74**, 1315 (1995); E.R.I. Abraham, C.A. Sackett, R.G. Hulet, Phys. Rev. A **55**, 3299 (1997)
13. J.L. Roberts, N.R. Claussen, J.P. Burke, C.H. Greene, E.A. Cornell, C.E. Wieman, Phys. Rev. Lett. **81**, 5109 (1998)
14. S. Inouye, K.B. Davis, M.R. Andrews, J. Stenger, H.-J. Miesner, D.M. Stamper-Kurn, W. Ketterle, Nature **392**, 151 (1998)
15. E. Timmermans, P. Tommasini, M. Hussein, A. Kerman, Phys. Rep. **315**, 199 (1999); R.A. Duine, H.T.C. Stoof, Phys. Rep. **396**, 115 (2004)
16. J. Cubizolles, T. Bourdel, S.J.J.M.F. Kokkelmans, G.V. Shlyapnikov, C. Salomon, Phys. Rev. Lett. **91**, 240401 (2003); S. Jochim, M. Bartenstein, A. Altmeyer, G. Hendl, S. Riedl, C. Chin, J. Hecker Denschlag, R. Grimm, Phys. Rev. Lett. **91**, 240402 (2003)
17. M. Greiner, C.A. Regal, D.S. Jin, Nature **426** 537 (2003); S. Jochim, M. Bartenstein, A. Altmeyer, G. Hendl, S. Riedl, C. Chin, J. Hecker Denschlag,

- R. Grimm, Science **302**, 2101 (2003); M.W. Zwierlein, C.A. Stan, C.H. Schunck, S.M.F. Raupach, S. Gupta, Z. Hadzibabic, W. Ketterle, Phys. Rev. Lett. **91**, 250401 (2003); T. Bourdel, L. Khaykovich, J. Cubizolles, J. Zhang, F. Chevy, M. Teichmann, L. Tarruell, S.J.J.M.F. Kokkelmans, C. Salomon, Phys. Rev. Lett. **91**, 250401 (2003)
18. E.A. Donley, N.R. Claussen, S.T. Thompson, C.E. Wieman, Nature, **417**, 529 (2002)
 19. Y. Castin: Bose-Einstein condensates in atomic gases: simple theoretical results, in *Coherent Atomic Matter Waves* ed. by R. Kaiser, C. Westbrook, F. David (Springer, Berlin Heidelberg New York, 2001), pp. 1–136
 20. R. Grimm, M. Weidemüller, Y.B. Ovchinnikov, Adv. At. Mol. Opt. Phys. **42**, 95 (2000); N. Friedman, A. Kaplan and N. Davidson, Adv. At. Mol. Opt. Phys. **48**, 99 (2002)
 21. F. Bardou, J.-P. Bouchaud, A. Aspect, C. Cohen-Tannoudji: *Lévy Statistics and Laser Cooling* (Cambridge University Press, Cambridge 2002)
 22. S.L. Winoto, M.T. DePue, N.E. Bramall, D.S. Weiss, Phys. Rev. A **59**, R19 (1999); M.T. DePue, C. McCormick, S.L. Winoto, S. Oliver, D.S. Weiss, Phys. Rev. Lett. **82**, 2262 (1999)
 23. S.E. Hamann, D.L. Haycock, G. Klose, P.H. Pax, I.H. Deutsch, P.S. Jessen, Phys. Rev. Lett. **80**, 4149 (1998); H. Perrin, A. Kuhn, I. Bouchoule, C. Salomon, Europhys. Lett. **42**, 395 (1998); V. Vuletić, C. Chin, A.J. Kerman, S. Chu, Phys. Rev. Lett. **81** 5768 (1998); A.J. Kerman, V. Vuletić, C. Chin, S. Chu, Phys. Rev. Lett. **84** 439 (2000)
 24. C.S. Adams, H.J. Lee, N. Davidson, M. Kasevich, S. Chu, Phys. Rev. Lett. **74**, 3577 (1995)
 25. M.D. Barrett, J.A. Sauer, M.S. Chapman, Phys. Rev. Lett. **87** 010404 (2001)
 26. T. Weber, J. Herbig, M. Mark, H.-C. Nägerl, R. Grimm, Science **299** 232 (2003)
 27. J. Söding, D. Guéry-Odelin, P. Desbiolles, G. Ferrari, J. Dalibard, Phys. Rev. Lett. **80** 1869 (1998)
 28. F. Schreck, L. Khaykovich, K.L. Corwin, G. Ferrari, T. Bourdel, J. Cubizolles, C. Salomon, Phys. Rev. Lett. **87** 080403 (2001)
 29. A. Görlitz, J.M. Vogels, A.E. Leanhardt, C. Raman, T.L. Gustavson, J.R. Abo-Shaeer, A.P. Chikkatur, S. Gupta, S. Inouye, T. Rosenband, W. Ketterle, Phys. Rev. Lett. **87** 130402 (2001)
 30. S. Dettmer, D. Hellweg, P. Rytyty, J.J. Arlt, W. Ertmer, K. Sengstock, D.S. Petrov, G.V. Shlyapnikov, H. Kreutzmann, L. Sanots, M. Lewenstein, Phys. Rev. Lett. **87**, 160406 (2001)
 31. B. Paredes, A. Widera, V. Murg, O. Mandel, S. Fölling, I. Cirac, G.V. Shlyapnikov, T.W. Hänsch, I. Bloch, Nature **429**, 277 (2004); T. Kinoshita, T. Wenger, D.S. Weiss, Science **305**, 1125 (2004)
 32. Z. Hadzibabic, P. Krüger, M. Cheneau, B. Battelier, J. Dalibard, Nature **441**, 1118 (2006)
 33. L. Salasnich, Phys. Rev. A **70**, 053617 (2004)
 34. L.D. Carr, Y. Castin, Phys. Rev. A **66**, 063602 (2002)
 35. U. Al Khawaja, H.T.C. Stoof, R.G. Hulet, K.E. Strecker, G.B. Partridge, Phys. Rev. Lett. **89**, 200404 (2002)
 36. L.D. Carr, J. Brand, Phys. Rev. Lett. **92**, 040401 (2004); L.D. Carr, J. Brand, Phys. Rev. A **70**, 033607 (2004)
 37. L. Salasnich, A. Parola, L. Reatto, Phys. Rev. Lett. **91**, 080405 (2003)

38. S.L. Cornish, N.R. Claussen, J.L. Roberts, E.A. Cornell, C.E. Wieman, Phys. Rev. Lett. **85**, 1795 (2000)
39. N.G. Parker, A.M. Martin, S.L. Cornish, C.S. Adams, cond-mat/0603059 (2006)
40. S. Sinha, A.Y. Cherny, D. Kovrizhin, J. Brand, Phys. Rev. Lett. **96**, 030406 (2006)
41. B.B. Baizakov, B.A. Malomed, M. Salerno, Phys. Rev. A **70**, 053613 (2004), and an article in *Nonlinear Waves: Classical and Quantum Aspects*, ed. by F.Kh. Abdullaev, V.V. Konotop (Kluwer, Dordrecht, 2004), pp. 61–80
42. L. Khaykovich, B.A. Malomed, Phys. Rev. A **74**, 023607 (2006)
43. H. Buljan, M. Segev, A. Vardi, Phys. Rev. Lett. **95**, 180401 (2005)

Part III

Dark Solitons in Bose–Einstein Condensates

Dark Solitons in Bose–Einstein Condensates: Theory

V.V. Konotop

The history of *dark solitons* starts with the pioneering paper by Tsuzuki [1], where exact soliton solutions of the Gross–Pitaevskii equation¹ (GPE) [2], also known as the nonlinear Schrödinger (NLS) equation, were obtained and their connection with Bogoliubov’s phonons [3] was revealed. The seminal paper by Zakharov and Shabat [4], devoted to Fraunhofer diffraction in a defocusing Kerr medium, was the next fundamental step in understanding the nature of dark solitons. The NLS equation was solved by means of the *inverse scattering transform* (see also [5, 6]), allowing one to obtain multisoliton solutions and, in particular, to recover Tsuzuki’s soliton. The work has opened new ways for systematic studies of dynamics of dark solitons in the presence of perturbations and of their generation. The *perturbation theory* for dark solitons was first proposed in [7] and later on in [8] in a different mathematical statement, while investigations of practical aspects of dark soliton generation were initiated by the works [9]. Earlier studies of dark solitons were focused on their optical applications and were stimulated by theoretical prediction [10], where the term “dark” was introduced, and experimental observation [11] of dark solitons in nonlinear optical fibers with normal dispersion.

First experimental generation of dark solitons [12] in a Bose–Einstein condensate (BEC) of ^{87}Rb atoms has stimulated new theoretical studies. Application of the theory to experiments already carried out and prediction of new effects in BECs, include consideration of such factors as multidimensionality of the system, trapping potentials, finite life-times of condensates, specific conditions of soliton generation, interaction of condensate with the thermal cloud, etc. In the present chapter we address only some of these issues, restricting ourselves to quasi-one-dimensional (1D) single-component atomic BECs in elongated traps at zero temperature. For detailed considerations of the topics mentioned above we refer to other chapters of this book, and in particular, Parts V, IX, and XI.

¹ In [1], the model was termed *Pitaevskii–Gross* equation.

4.1 Condensate in an Elongated Trap

4.1.1 The Characteristic Scales

Let us consider a condensate of atoms of mass m , and two-body interactions which are local and characterized by a positive s -wave scattering length $a_s > 0$. We assume that the BEC is confined by a cigar-shaped potential $V(\mathbf{r}) = (m\omega_0^2/2) (\mathbf{r}_\perp^2 + \nu^2 x^2)$ elongated in x -direction, i.e. with the aspect ratio $\nu = \omega_1/\omega_0 = a_0^2/a_1^2 \ll 1$, where $\mathbf{r}_\perp = (y, z)$, ω_0 and ω_1 are the transverse and longitudinal trap frequencies, and $a_{0,1} = \sqrt{\hbar/m\omega_{0,1}}$ are the respective linear oscillator lengths. Designating the maximal density of the condensate by n_0 , we also define the healing length $\xi = 1/\sqrt{8\pi a_s n_0}$.

The introduced spatial scales $\{a_s, a_0, a_1, \xi\}$ allow us to formulate the conditions of the theory to be developed. First, we require the scattering length a_s to be the smallest scale, i.e. $a_s \ll a_0, a_1, \xi$. This constraint is well satisfied in most experimental settings where a_s is of order of a few nanometers while all other scales are typically of order of (or bigger than) one micrometer. Then, at zero temperature one can employ the *mean-field approximation* and describe the condensate by the macroscopic wave function ψ solving the GPE [2, 13]:

$$i\hbar\psi_t = \left[-\frac{\hbar^2}{2m} \nabla^2 + g|\psi|^2 + V(\mathbf{r}) \right] \psi, \quad (4.1)$$

where $g = 4\pi\hbar^2 a_s / m$ and ψ is normalized to the total number of atoms N : $\int |\psi|^2 d\mathbf{r} = N$.

Next, we take into account that the characteristic scale of the *nonlinear* excitations, i.e. ones originated by two-body interactions, is of the healing length order. Then, for a system to display 1D behavior we have to impose two more conditions: (i) the size of the excitations must be much smaller than the longitudinal size of the condensate, and (ii) collisions among atoms must not result in transitions between transverse energy levels. Assuming that in the transverse direction only the ground state is occupied, these two constraints are equivalent to requirements for the densities of the longitudinal kinetic energy, $\mathcal{E}_{\text{kin}} = \hbar^2/(2m\xi^2)$, and of the energy of the two-body interactions, $\mathcal{E}_{\text{nl}} = gn_0$, to be much less than the density of the transverse kinetic energy, $\mathcal{E}_0 = \hbar^2/(2ma_0^2)$: $\mathcal{E}_{\text{kin}} \sim \mathcal{E}_{\text{nl}} \ll \mathcal{E}_0$. Combining these two requirements we obtain the constraints for the 1D dynamics of the condensate [14–16]:

$$a_0 \ll \xi \ll a_1. \quad (4.2)$$

4.1.2 3D-to-1D Reduction of the Gross–Pitaevskii Equation

In [17] it was realized that the elongated geometry of the trap allows one to reduce the 3D GPE (4.1) to an effectively 1D description. This can be done in a self-consistent and mathematically controllable manner by employing the *multiple-scale expansion* [18]. The method is based on a simple idea: when the

nonlinearity is weak, one can look for a solution of the GPE as a solution of the respective linear Schrödinger equation perturbed by the nonlinearity. To this end we introduce the small parameter $\epsilon = a_0/\xi \ll 1$ and rewrite (4.1) in a dimensionless form

$$i\Psi_T = -\nabla^2\Psi + (R_\perp^2 + \epsilon^4\Omega^2X^2/2)\Psi + 2\epsilon^2|\Psi|^2\Psi, \quad (4.3)$$

where $\Psi = \sqrt{4\pi a_s \xi^2} \psi$, $X = x/a_0$, $\mathbf{R}_\perp = \mathbf{r}_\perp/a_0$, $T = \omega_0 t/2$ and $\Omega^2 = 2\nu^2/\epsilon^4$. Combining the normalization condition $\int |\Psi|^2 d\mathbf{R} = N/(n_0 a_0^3)$ with the estimate $\int |\Psi|^2 d\mathbf{R} \sim \mathcal{O}(|\Psi|^2 a_1/a_0)$, we conclude that $|\Psi|^2 = \mathcal{O}(N/(n_0 a_0^2 a_1)) = \mathcal{O}(1)$, which is suitable for developing the expansion (see [16] for more details). Before that, however, we specify the magnitude of Ω , requiring $\Omega \ll 1$ (respectively, $\nu \ll \epsilon^2$).

Solutions of (4.3) are searched in the form $\Psi = \psi_0 + \epsilon\psi_1 + \dots$, where ψ_j are functions depending on the scaled variables $x_\alpha = \epsilon^\alpha X$ and $t_\alpha = \epsilon^\alpha T$, which are regarded as independent so that $\partial_T = \sum_{\alpha=0} \epsilon^\alpha \partial_{t_\alpha}$ and $\partial_X = \sum_{\alpha=0} \epsilon^\alpha \partial_{x_\alpha}$. Being interested in excitations localized on the scale ξ , we look for ψ_j independent on x_0 : $\psi_j = \psi_j(t_0; x_1; \mathbf{R}_\perp)$ (here in the argument only the most rapid variables are indicated). Substituting the introduced expansions in (4.3) and collecting terms of the same order of ϵ , we obtain the set of equations

$$i\partial_{t_0}\psi_j - \mathcal{L}\psi_j = F_j, \quad \mathcal{L} = -\nabla^2 + R_\perp^2. \quad (4.4)$$

For the three lowest orders we have $F_0 = 0$, $F_1 = -i\partial_{t_1}\psi_0$ and $F_2 = -i\partial_{t_1}\psi_1 - i\partial_{t_2}\psi_0 - \partial_{x_1}^2\psi_0 + (\Omega^2 x_1^2/2)\psi_0 + 2|\psi_0|^2\psi_0$.

Next we consider an auxiliary eigenvalue problem $\mathcal{L}\varphi_{\mathbf{n}}(\mathbf{R}_\perp) = \mu_{\mathbf{n}}\varphi_{\mathbf{n}}(\mathbf{R}_\perp)$, where \mathbf{n} stands for a pair of transverse quantum numbers. The eigenfunctions $\varphi_{\mathbf{n}}$ make up an orthonormal set: $\int \bar{\varphi}_{\mathbf{n}}\varphi_{\mathbf{n}'} d\mathbf{R}_\perp = \delta_{\mathbf{n}\mathbf{n}'}$ and (4.4) with $j = 0$ is satisfied by any superposition of the states $e^{-i\mu_{\mathbf{n}}t_0}\varphi_{\mathbf{n}}$. Choosing the ground state $\varphi_0 = \pi^{-1/2}e^{-R_\perp^2/2}$ which corresponds to $\mu_0 = 2$, we represent

$$\psi_1 = A(t_1; x_1)\varphi_0(\mathbf{R}_\perp)e^{-2it_0}, \quad (4.5)$$

where $A(t_1; x_1)$ is a slowly varying amplitude. Solutions of each of (4.4) grow with time, i.e. have *secular terms*, unless $\int \varphi_0 F_j d\mathbf{R}_\perp = 0$. This last condition, applied to the equation with $j = 1$, results in $\partial_{x_1}\psi_1 = 0$, i.e. in $\psi_1 \equiv 0$. Requiring absence of secular terms in (4.4) with $j = 2$ we arrive at the 1D GPE

$$i\tilde{\psi}_T = -\tilde{\psi}_{XX} + (\Omega^2 X^2/2)\tilde{\psi} + 2|\tilde{\psi}|^2\tilde{\psi} - \tilde{\mu}\tilde{\psi}, \quad (4.6)$$

where we have renamed $X = x_1$, $T = t_2$, and introduced the dimensionless chemical potential $\tilde{\mu}$: $\tilde{\psi}(T, X) = A(t_2, x_1)e^{i\tilde{\mu}t_2}$.

Below it will also be convenient to use (4.6) in the physical variables

$$i\hbar\psi_t = -\frac{\hbar^2}{2m}\psi_{xx} + \frac{1}{2}m\omega^2x^2\psi + g_1|\psi|^2\psi - \mu\psi, \quad (4.7)$$

where $g_1 = 2\hbar^2 a_s / ma_0^2$ [17,19]. The newly introduced function ψ (it is different from the order parameter in (4.1)) determines the linear density of the particles $n = |\psi|^2$ and is normalized to the total number of atoms: $\int |\psi|^2 dx = N$. We notice, that (4.7) can also be obtained by formal “averaging” of the GPE over the transverse direction, what is performed by multiplying (4.1) by φ_0 and integrating in the (y, z) -plane. The applicability of this procedure is given by the requirement (4.2) and is restricted to operators \mathcal{L} independent on x .

4.2 Dark Solitons in a Homogeneous Condensate

4.2.1 Dark Solitons of the Nonlinear Schrödinger Equation

Taking into account that Ω^2 in (4.6) is a small parameter, for the first step we set $\Omega = 0$ and consider the NLS equation

$$i\tilde{\psi}_T = -\tilde{\psi}_{XX} - 2(\rho^2 - |\tilde{\psi}|^2)\tilde{\psi} \quad (4.8)$$

where $\rho = \sqrt{\tilde{\mu}/2}$ determines the unperturbed condensate density ρ^2 (as it is clear $|\tilde{\psi}|^2 \equiv \rho^2$ is a solution of (4.8)). (4.8) is an *integrable* model, the initial value problem for which can be solved by means of the inverse scattering transform [4]. Now we recall some steps of the method, referring to [6] for the details.

First, we specify the problem by imposing *finite density* boundary conditions:

$$\tilde{\psi} \rightarrow \rho e^{\pm i\vartheta} \quad \text{at} \quad X \rightarrow \pm\infty, \quad (4.9)$$

where $\vartheta \in [-\pi/2, \pi/2]$ determines the condensate phases at the infinity. One readily ensures that conditions (4.9) are consistent with (4.8).

Next we consider the so-called *Zakharov-Shabat (ZS) spectral problem*

$$\frac{\partial \Phi}{\partial X} = \mathbf{U}\Phi; \quad \text{where} \quad \Phi = \begin{pmatrix} \Phi^{(11)} & \Phi^{(12)} \\ \Phi^{(21)} & \Phi^{(22)} \end{pmatrix} \quad \text{and} \quad \mathbf{U} = \begin{pmatrix} -i\lambda/2 & \bar{\psi} \\ \tilde{\psi} & i\lambda/2 \end{pmatrix} \quad (4.10)$$

(hereafter the overbar stands for complex conjugation). Its eigenfunctions Φ_{\pm} , satisfying boundary conditions $\Phi_{\pm} \rightarrow \exp(\pm i\vartheta \sigma_3/2)E(X)$ as $X \rightarrow \pm\infty$, with $E(X) = [I + (2\rho/z)\sigma_2]\exp(i k X \sigma_3/2)$, $I = \text{diag}(1,1)$, σ_j ($j = 1, 2, 3$) being the conventional Pauli matrices, and the parameters λ , k and z related by $2\lambda = z + 4\rho^2/z$ and $2k = z - 4\rho^2/z$, are called the *Jost functions*. The Jost functions are related by the monodromy matrix \mathbf{T} : $\Phi_- = \Phi_+ \mathbf{T}$. The elements of \mathbf{T} are considered as functions of λ on a double-sheet Riemann surface consisting of two complex planes λ cut along the real axis $(-\infty, -2\rho) \cup (2\rho, \infty)$, $\pm 2\rho$ being the branching points. The cuts constitute the continuous spectrum

of (4.10). The discrete spectrum of (4.10), which can be designated as λ_j ($j = 1, 2, \dots$), is real and belongs to the interval $(-2\rho, 2\rho)$. The elements of the monodromy matrix together with the discrete spectrum make up the so-called scattering data. Given the complex field $\tilde{\psi}$ the scattering data can be uniquely determined. The inverse statement is also valid: given the scattering data the “potential” $\tilde{\psi}$ can be restored.

It turns out that there exists a special class of the functions (the reflectionless potentials) $\tilde{\psi}$, for which the monodromy matrix \mathbf{T} is diagonal. An important fact, is that if $\tilde{\psi}$ is governed by the NLS equation (4.8), λ_j does not depend on time and dependence of the monodromy matrix on time is trivial: it is governed by the equation $\partial\mathbf{T}/\partial T = (i\lambda^2/2)[\sigma_3, \mathbf{T}]$. Thus, \mathbf{T} is diagonal at any T , provided it is diagonal at $T = 0$. The simplest reflectionless potential is called a *dark soliton* [4, 6]

$$\tilde{\psi}_s = \rho (\cos \vartheta + i \sin \vartheta \tanh [\eta (X - X(T))]) . \quad (4.11)$$

Here $X(T) = VT + X_0$, $V = -2\rho \cos \vartheta$, $\eta = \rho \sin \vartheta$ and X_0 is a real constant. This “potential” corresponds to a single eigenvalue $\lambda_1 = V$ of (4.10).

In the physical units introduced by (4.7), the dark soliton reads [1]

$$\psi_s(x, t) = \sqrt{n_0} \left(i \frac{v}{c} + \frac{\sqrt{c^2 - v^2}}{c} \tanh \left[\frac{x - X(t)}{\ell} \right] \right) . \quad (4.12)$$

Here $X(t) = vt + x_0$, v and x_0 are the velocity and the initial coordinate of the soliton, respectively, $c = \sqrt{gn_0/m}$ is the speed of sound, and $\ell = \hbar/(mv\sqrt{c^2 - v^2})$ is the width of the soliton.

The energy of the soliton can be defined as

$$E_s = \int \mathcal{E}_s dx = \int \left[\frac{\hbar^2}{2m} |\Psi_x|^2 + \frac{g_1}{2} (|\Psi|^2 - n_0)^2 \right] dx = \frac{4}{3} \hbar c n_0 \left(1 - \frac{v^2}{c^2} \right)^{3/2} . \quad (4.13)$$

Since $E_s > 0$, the dark soliton is thermodynamically unstable [20].

4.2.2 On a Definition of a Dark Soliton

In the theory of integrable systems solution (4.11) is called a *dark soliton*.² We will closely follow this definition, using the term “dark soliton” for a solution of the 1D GPE, possibly with external potential, which in the leading order of the theory is described by (4.8) subject to the boundary conditions (4.9). Respectively, the solitons we will refer to are *long living*, i.e. propagating

² Also the term *gray* soliton is used to underline moving solitons with nonzero density, contrary to the *black* soliton, which is static and has zero density in the center. Sometimes, the latter is also called *kink*.

without significant change of their shapes and have *energy localized in space*. Interactions of dark solitons are (almost) *elastic*, nonelastic effects appearing due to external potentials.

In the literature, the term “dark soliton” is also used to describe an effectively higher dimensional excitation, which along one of the spatial dimensions initially has a shape approximated by (4.11). Such objects, however, are unstable; in the BEC context this was discussed in [15, 21, 22] and observed experimentally in [23–25]. Transverse instabilities are developed at early stages of evolution provided the confining is not tight enough: $a_0 \gtrsim \xi$.

Another usage of the term “dark soliton” is a designation of a localized hole in the atomic density in a toroidal trap [26]. In the 1D limit, the problem is described by the NLS equation with periodic boundary conditions. This is an integrable model [6] possessing periodic solutions different from a dark soliton (4.11). The respective solutions in the small amplitude limit (see Sect. 4.2.3) were found in [1], where using the representation $\tilde{\psi} = \rho(X, T) \exp(i \int w(X, T) dX)$ (4.8) was rewritten in the hydrodynamical form (here $\tilde{n}(X, T) = \rho^2(X, T)$)

$$\frac{\partial \tilde{n}}{\partial T} + 2 \frac{\partial \tilde{n} w}{\partial X} = 0, \quad \frac{\partial w}{\partial T} + \frac{\partial}{\partial X} \left[w^2 + 2\tilde{n} + \frac{1}{4\tilde{n}^2} \left(\frac{\partial \tilde{n}}{\partial X} \right)^2 - \frac{1}{2\tilde{n}} \frac{\partial^2 \tilde{n}}{\partial X^2} \right] = 0. \quad (4.14)$$

Considering large amplitudes and imposing the periodic boundary conditions $n(X) = n(X+L)$, where L is the length of the ring trap, one finds the simplest solution: $\rho = (4K(k)/L)sn(4K(k)x/L, k)$ where $2\sqrt{2(1+k^2)}K(k)/\rho_0 = L$, $sn(\cdot, \cdot)$ is the Jacobi elliptic function with the elliptic modulus k , $K(k)$ is the complete elliptic integral of the first kind. When $k \rightarrow 1$ it can be viewed as two coupled dark solitons. Other solutions, including a single dark-soliton, can be found in [27]. They represent a suitable model for testing the fundamental relation between the many-body theory and the mean-field approximation [28].

The term “dark soliton” is attributed also to an anti-symmetric distribution in a 1D parabolic trap either in the case of weak nonlinearity or in the case of a narrow trap ($\epsilon \sim 1$ in our notations) and large number of particles [29, 30]. This interpretation is based on the fact, that the zero velocity soliton in a parabolic trap can be viewed as a one node eigenfunction of the nonlinear problem

$$-\frac{d^2 u_n}{dX^2} + \sigma u_n^3 + \frac{1}{2} \Omega^2 X^2 u_n = \mu_n u_n \quad (4.15)$$

with $\sigma = 2$. In (4.15) we have taken into account that the eigenvalues are real and introduced σ parameterizing the problem which is considered subject to the fixed number of particles. The respective entity does not possess dynamical properties of a soliton; in particular, it cannot be made moving, but represents a mode of a nonlinear oscillator [31], satisfying zero boundary

conditions (cf. (4.9)). The correspondence between the black soliton and the first nonlinear mode can be exploited for generation of a dark soliton [32] (see also Sect. 4.5.4).

4.2.3 Dark Solitons and Sound Waves

The amplitude of a dark soliton, i.e. depth of the density hole $n_0(1 - v^2/c^2)$, decreases as the velocity approaches the speed of sound. This raises a question about relation between dark solitons and phonons. The problem was solved in [1], where it was obtained that in the limit $v \rightarrow c$ dark solitons are described by the Korteweg–de Vries (KdV) equation. Later on, in [33], the deep link between NLS and KdV equations was established on the level of the inverse scattering transform. In [34] it was shown that small amplitude solitons of an NLS-like equation with arbitrary density-dependent nonlinearity are described by the KdV equation. In the context of BEC applications this approach was explored in [35, 36].

Let us look for a soliton of (4.8) in the form $\tilde{\psi} = q(\zeta, \tau)e^{-i\varphi(\zeta, \tau)}$ where $q = \rho(1 + \varepsilon^2 q_1 + \varepsilon^4 q_2 + \dots)$ and $\varphi = \varepsilon\varphi_1 + \varepsilon^3\varphi_2 + \dots$, and the new independent variables are given by $\zeta = \varepsilon(X - \tilde{V}T)$ and $\tau = \varepsilon^3 t$ (the formal small parameter ε is different from ϵ introduced on Sec. 4.1.1 and will be determined below). The boundary conditions for the new dependent variables follow from (4.9): $\lim_{|\zeta| \rightarrow \infty} q = 0$ and $\lim_{\zeta \rightarrow \pm\infty} \varphi = \pm\vartheta$. Substituting these expansions in (4.8) and gathering terms of the same order in ϵ one readily ensures that the first two orders are satisfied identically. In the orders, ε^2 and ε^3 , one obtains equations $4\rho^2 q_1 = \tilde{V}\varphi_{1\zeta}$ and $\tilde{V}q_1 = \varphi_{1\zeta}$ which are consistent only if $\tilde{V} = 2\rho = \tilde{c}$, where \tilde{c} is the sound velocity in the dimensionless units. The requirement of consistency of the equations of ε^4 and ε^5 orders leads to the KdV equation for the amplitude of a dark soliton:

$$4\rho q_{1\tau} + 24\rho^2 q_1 q_{1\zeta} + q_{1\zeta\zeta\zeta} = 0. \quad (4.16)$$

Recalling the one-soliton solution of the KdV equation (see e.g. [5]) and restoring the original variables we obtain $\varepsilon^2 q_1 = -\vartheta^2/2 \cosh^2[\rho\vartheta(X - VT)]$ and $\varepsilon\varphi_1 = \vartheta \tanh[\rho\vartheta(X - VT)]$, where $V = \tilde{c} - \rho\vartheta^2$ is the soliton velocity and the small parameter is given by $\varepsilon = \vartheta$, i.e. ϑ must be small enough.

The question about the relation between dark solitons and sound waves can be put in a different context. One can consider linear phonons in a BEC in “the dark soliton state” [20, 21], which are described by a solution of (4.8) in a form $\tilde{\psi} = \tilde{\psi}_s + u$, where u is a small ($|u| \ll \rho$) complex field describing phonons. In the absence of a trap, this problem can be solved exactly for an arbitrary moving dark soliton. Indeed, defining $|u\rangle = \text{col}(\bar{u}, u)$, substituting $\tilde{\psi}_s$ in (4.8), and linearizing with respect to u one obtains the system

$$i\frac{\partial}{\partial T}|u\rangle + \mathbf{L}|u\rangle = 0, \quad \mathbf{L} = -\left(\frac{\partial^2}{\partial X^2} + 2\rho^2 - 4|\psi_s|^2\right)\sigma_3 + 2\begin{pmatrix} 0 & \bar{\psi}_s^2 \\ -\psi_s^2 & 0 \end{pmatrix}. \quad (4.17)$$

Next we define the squared Jost functions ($j = 1, 2$): $|F_{\pm}^{(j)}\rangle = \text{col}([F_{\pm}^{(1j)}]^2, [F_{\pm}^{(2j)}]^2)$. One can ensure that for the one soliton case they are eigenfunctions of the operator \mathbf{L} : $\mathbf{L}|F_{\pm}^{(j)}\rangle = [(-1)^{1+j}\sqrt{\lambda^2 - 4\rho^2}\lambda]/4|F_{\pm}^{(j)}\rangle$. The squared Jost functions, either $|F_+^{(1,2)}\rangle$ or $|F_-^{(1,2)}\rangle$, make up a complete set [8], thus allowing one to express any vector $|u\rangle$ through their superposition. The one-soliton Jost functions, and thus $|F_{\pm}^{(j)}\rangle$, are known in an explicit form (see e.g. [8, 37]), which provides the general solution of the problem of a sound wave against the dark soliton background.

The complete (i.e. including all orders of perturbations) solution of the nonlinear problem (4.8) with the initial condition $\tilde{\psi} = \tilde{\psi}_s + u$ can also be found by means of the inverse scattering transform. Quasi-linear modes u result in (and are described by) nonzero nondiagonal elements of the monodromy matrix \mathbf{T} . For an integrable system there exists an asymptotic superposition principle [5], establishing that at $T \rightarrow \infty$ a solution can be represented as a superposition of solitons (defined by the time independent discrete spectrum) and phonons. This means that within the framework of the NLS equation there occurs no energy loss/gain of a kink due to scattering of phonons.

4.2.4 Dark Solitons of the Quintic NLS Equation

Dark solitons exist in more generic polynomial models. As an example we consider higher approximations to the Bogoliubov theory expanding the chemical potential with respect to the density n [13]: $\mu = a_s n [b_1 + b_2(na_s^3)^{1/2} - b_3(na_s^3)\ln(na_s^3)] + g_2 n^2$. Here $b_1 = 4\pi\hbar^2/m$ and $b_{2,3}$ can be calculated. The coefficient g_2 depends on three-body interactions and cannot be obtained explicitly. Let us assume that $g_2 > 0$ and that by means of Feshbach resonance it is achieved that $a_s = 0$. Then the mean-field equation for the macroscopic wavefunction acquires the form of the *quintic* NLS equation:

$$i\hbar\psi_t = -\frac{\hbar^2}{2m}\psi_{xx} + \tilde{g}_2|\psi|^4\psi - \mu\psi \quad (4.18)$$

with $\tilde{g}_2 = g_2/(3\pi^2 a_{\perp}^4)$. In the absence of the trap, $\omega = 0$, the dark soliton solution of (4.18) is given by [38, 42]: $\Psi_s(x, t) = \sqrt{n_s(x, t)} \exp[i\theta_s(x, t)]$ where

$$n_s(x, t) = n_0 - \frac{12n_0(c^2 - v^2)e^{(x-X(t))/\ell}}{c^2(4 + e^{(x-X(t))/\ell})^2 - 12(c^2 - v^2)}, \quad (4.19)$$

$$\theta_s(x, t) = -\arctan\left(\frac{c^2e^{(x-X(t))/\ell} - 2c^2 + 6v^2}{6v\sqrt{c^2 - v^2}}\right), \quad (4.20)$$

and $\ell = \hbar/(2m\sqrt{c^2 - v^2})$.

Another form of the quintic NLS equation (4.18), with $\tilde{g}_2 = \hbar^2\pi^2/(2m)$, was suggested in [38] for description of 1D gas of impenetrable bosons –

the Tonks–Girardeau (TG) gas [39]. The stationary version of (4.18), where $\psi_T \equiv 0$, was rigorously derived in [40] for the ground state of the TG gas, as minimizing the energy functional with the density $\mathcal{E} = (\hbar^2/2m)[(\sqrt{n})_x]^2 + gn^3/3$. It was, however, established [41] that the quintic NLS equation fails to produce a satisfactory description of the mean-field dynamics of the TG gas.

4.3 Dark Solitons in a Trap

4.3.1 The Background Density Distribution

From the mathematical point of view the impact of a trap on soliton dynamics is dramatic, because it changes the boundary conditions for the wavefunction: a solution of (4.6) satisfies zero boundary conditions $\tilde{\psi} \rightarrow 0$ at $x \rightarrow \pm\infty$, while the dark soliton of (4.8) is subject to the finite density boundary conditions (4.9). From the physical point of view the trap imposes strong constraints on the solitary wave solution, in particular, forbidding small amplitude dark solitons. Indeed, as we established in Sect. 4.2.3, existence of a soliton in a parabolic trap implies smallness of the soliton width ℓ compared to the trap width a_l , i.e. the constraint [42] $\hbar\omega/m \ll c^2 - v^2$, which does not allow the small amplitude limit corresponding to $v \rightarrow c$. Moreover, at ω small enough a small amplitude soliton can reach a domain where the density is so small that the dynamics is linear and thus dispersion dominating the nonlinearity can result in decay of a solitary wave in phonons [16]. In the opposite case of a large amplitude the dark soliton can be reflected from the potential what will lead to oscillatory motion. For the first time this scenario was observed in numerical experiments reported in [43].

That is why we focus on slow solitons and following [16, 44, 45], define a real-valued function $F(x)$ such that $n_0(x) = n_0 F^2(x)$, with $n_0 = n_0(0)$ and $F(0) = 1$, is the background density. $F(x)$ solves the nonlinear eigenvalue problem

$$-\frac{\hbar^2}{2m}F_{xx} + g_1 n_0 F^3 + [U(x) - \mu]F = 0, \quad F_x(0) = 0, \quad \lim_{x \rightarrow \infty} F(x) = 0. \quad (4.21)$$

The function $F(x)$ has two well known limits. In the quasi-linear limit ($gn_0 \ll \hbar^2/(2ma_l^2)$) and for the parabolic trap $U_\omega(x) = m\omega^2 x^2/2$ the respective distribution, normalized to the total number of atoms N , is well approximated by the Gaussian: $n_0(x) \approx n_G(x) \equiv \sqrt{N} \exp(-x^2/2a_l^2)/(\pi a_l^2)^{1/4}$. In the “nonlinear” limit $n_0(x)$ is given by the Thomas–Fermi (TF) distribution: $n_{\text{TF}}(x) \equiv [\mu - U(x)]/g$, valid for $|x| < x_{\text{TF}}$ where x_{TF} is the TF radius determined from the relation $U(x_{\text{TF}}) = \mu$. The chemical potential is now expressed through the maximal intensity by means of the asymptotic formula [16] (see [46] for more details): $\mu = g_1 n_0 + \hbar^2 \omega_l^2 / (4g_1 n_0 m) + \mathcal{O}(\omega_l^4)$.

Next, we look for a solution of (4.7) in the form $\psi = F(x)\phi(x, t)$. The equation for ϕ follows directly from (4.7) and (4.21):

$$i\hbar\phi_t + \frac{\hbar^2}{2m}\phi_{xx} - g_1(|\phi|^2 - n_0)\phi = R[\phi, F]. \quad (4.22)$$

Here $R[\phi, F] \equiv -(\hbar^2/m)(F_x\phi_x)/F + g_1n_0(F^2 - 1)(|\phi|^2 - n_0)\phi$. (4.22) becomes useful if R is small enough, so that it can be considered as a perturbation. Then, even in the presence of a parabolic trap the concept of a dark soliton is meaningful in terms of ϕ , the latter solves (4.22) subject to boundary conditions $\phi \rightarrow \sqrt{n_0}e^{\pm i\vartheta}$ [see (4.9)], which are consistent with (4.22) since $\lim_{|x| \rightarrow \infty} R = 0$. Recalling (4.2), one ensures that smallness of $R[\phi, F]$ is determined by $\Omega^2 \ll 1$.

4.3.2 Landau Dynamics of a Soliton in an Inhomogeneous Condensate

Like solitons in general, dark solitons in BECs display particle-like behavior. Therefore, they can be treated as quasi-particles, different from linear phonons. To highlight particle like behavior of a dark soliton, we describe the soliton dynamics in a parabolic trap within the framework of the *local density approximation* [42, 47], which relies on the use of the local speed of the sound, $c(x)$ against an inhomogeneous background $n_0(x)$: $c(x) \equiv \sqrt{g_1n_0(x)/m}$ [3].

Physical justification of this approximation is based on the following representation for the dark soliton energy [42, 47] (4.13)

$$E_s \approx \int_{|x-X|<\delta} \left\{ \frac{\hbar^2}{2m} |\Psi_x|^2 + \frac{g_1}{2} [| \Psi |^4 - n_0^2(X)] - g_1 n_0(X)[| \Psi |^2 - n_0(X)] \right\} dx. \quad (4.23)$$

Here δ is a parameter such that $\ell \ll \delta \ll a_l$ and X is the coordinate of the soliton center. In the leading order the integral in (4.23) depends neither on particular choice of δ , nor on the explicit form of the trap potential.

In the local density approximation the energy conservation law (4.13) can be rewritten as $c^2(X) - v^2 = (\mathcal{G}E)^{2/3}$ where $\mathcal{G} = 3g_1/(4\hbar m)$. For the TF background distribution one has $c^2(X) = g_1n_{\text{TF}}(X)/m = c_0^2 - \omega^2 X^2/2$ with $c_0 = \sqrt{\mu/m}$. Taking into account that $v = dX/dt$ is the velocity of a soliton this leads to the relation [14, 20, 47]

$$\frac{m_*}{2} \left(\frac{dX}{dt} \right)^2 + \frac{m_*\omega_s^2}{2} X^2 = E_* . \quad (4.24)$$

Here we introduced $m_* = 2m$, $\omega_s = \omega/\sqrt{2}$ and the effective energy $E_* = m_*c_*^2/2$ with $c_*^2 = c_0^2 - (\mathcal{G}E_*)^{2/3}$. The amplitude of oscillations governed by (4.24) is $X_* = \sqrt{2E_*/m_*\omega_s^2}$.

The frequency of oscillation of the soliton, $\omega/\sqrt{2}$, was obtained in [14] and reproduced by means of different approaches in [16, 20, 45, 46].

For models with higher nonlinearity, like for instance the quintic NLS equation, computing of a frequency and amplitude of oscillations is a more complex task [36, 42]. The problem, however, can be solved in the limit of small velocities: $v \ll c$ corresponding to small X_* , by taking into account that a black soliton has zero density in its center [42]. To this end, expanding the conservation law $E_s(c(X), v) = E_0$, written in the local density approximation, i.e. with the use of the functional form (4.12), and thus considered as a function of the position X and velocity v of the soliton, in the Taylor series we obtain $E_s = (\partial E_0 / \partial v^2)v^2 + (\partial E_0 / \partial X^2)X^2$, where the subindex “0” stands for the quantities computed at $X = 0$ and $v = 0$ (for a detailed explanation of this approach see [42]). For a Newtonian particle one has to require $E_s = (v^2 + \omega_s^2 x^2) m_s / 2$. Comparison of these two expressions for E_s gives $m_s = 2\partial E_0 / \partial v^2$ and $\omega_s = \sqrt{(\partial E_0 / \partial X^2) / (\partial E_0 / \partial v^2)}$. Next, we recall that $-dE/d\mu = \mathcal{N}$, where \mathcal{N} is a number of particles “expelled” from the center of the soliton and that is why it is negative. Thus [42] $m_s = \mathcal{N}m_*$ is a (negative) mass of a dark soliton. For the dark soliton of the GPE considered above one computes $|\mathcal{N}| = 2\sqrt{2}\hbar n_0/(mc_0)$ and $\omega/\sqrt{2}$ (for the results for the quintic NLS equation with a parabolic trap see Table I of [42]).

Reflection of the dark soliton from the potential can be understood by considering a turning point as a point where due to decreasing density of the background the dark soliton becomes black, i.e. its amplitude becomes equal to the depth of the potential. That is why, the amplitude of the soliton oscillations X_* must grow as the soliton amplitude decreases, which was numerically observed in [16]. From these arguments it also follows that the amplitude of oscillations must increase with the number of particles or with the scattering length. This last effect was obtained in [48], where it was also suggested that the phenomenon can be exploited for enhancement of phase sensitivity of atomic interferometers.

A negative mass of a dark soliton, m_s , can be observed directly in the process of interaction of a dark soliton with a delta-impurity [49]. When the background is initially homogeneous, a “repulsive” impurity (i.e. very narrow potential barrier) can attract a dark soliton, the latter providing the minimum of the density at the maximum of the barrier. In the same problem, but with different initial conditions, where the background is deformed by the defect, the repulsive impurity repels sufficiently slow solitons [45, 50], which can be understood as reflection from a turning point where a dark soliton becomes black, because of the decrease of the background density induced by the impurity.

4.3.3 Perturbation Theories and Long-Time Dynamics of a Dark Soliton

If the right-hand side of (4.22) is small enough, say $R[\tilde{\psi}, F] \sim \tilde{\epsilon} \ll 1$, it can be taken into account within the framework of a perturbation theory. This means that one can look for a solution of (4.22) in a form $\tilde{\psi} = \psi_0 + \tilde{\epsilon}\psi_1 + \mathcal{O}(\tilde{\epsilon}^2)$, where ψ_j are considered to be dependent on X, T , and on slow time $\tau = \tilde{\epsilon}T$ (or more generally on slow times [46, 50] $\tau_\alpha = \tilde{\epsilon}^\alpha T$, $\alpha = 1, 2, \dots$) regarded as independent variables. The term ψ_0 is called adiabatic approximation and in the leading order it solves the NLS equation. Then the first-order term ψ_1 is governed by the linear equation $(i\partial_T + \mathbf{L})|\psi_1\rangle = \sigma_3|R\rangle - i\partial_\tau|\psi_0\rangle$ where we have defined $|\psi_{0,1}\rangle = \text{col}(\tilde{\psi}_{0,1}, \psi_{0,1})$ and $|R\rangle = \text{col}(R, R)$. Dependence of the adiabatic approximation on slow time is determined from the condition of absence of the secular terms of this equation.

The perturbation theory suggested in [7] and used in later studies (see e.g. [45, 46, 50]), relies on the adiabatic approximation in a form (4.11) with time dependent phase $\vartheta(\tau)$ and $X(T, \tau)$ to be determined from the condition of absence of secular terms. Such a form of the adiabatic approximation, however, does not satisfy the finite density boundary conditions (4.9) because $\psi_{0\tau}$ does not vanish at infinity, and also does not allow elimination of all secular terms (see discussions in [8, 46]). This makes it necessary calculation of the first order correction, which for a dark soliton in a parabolic trap was done in [46]³. In this way, the following dynamical equation was obtained for the soliton center:

$$X_{TT} + \Omega^2 X = \frac{\Omega^2 X_T}{2\sqrt{(1 - \Omega^2 X^2/4)^3(1 - (X_T^2 + \Omega^2 X^2)/4)}} + \mathcal{O}(\Omega^4). \quad (4.25)$$

In the case of a slow dark soliton, $X_T = \mathcal{O}(\Omega^2)$, one recovers (4.24) (with implicit terms of Ω^4 order). In the limit $\Omega^2 X^2 + X_T^2 \rightarrow 4$, corresponding to a small amplitude soliton, (4.25) is not applicable. Thus the most interesting region of the application of (4.25) is the case of intermediate velocities $1 \ll |X_T| \ll 1/\Omega^2$. In this region (4.25) describes dissipative dynamics. Similar results were also obtained numerically: energy losses of a soliton due to emission of sound waves were observed in a system with energy pump [51] and for a “dimple” potential [52].

An alternative perturbation theory for a dark soliton [8, 16, 49] is based on the adiabatic ansatz. $\tilde{\psi}_0 = \rho e^{i\tilde{\epsilon}\varphi(X, T)} [\cos \vartheta + i \sin \vartheta \tanh \eta(\tau) (X - X(T, \tau))]$, where $\varphi \rightarrow 0$ at $|X| \rightarrow \infty$. The phase φ describes linear currents induced by the perturbation and propagating away from the soliton. This ansatz satisfies the finite density boundary conditions and allows one to eliminate secular terms for a rather general form of perturbation (for exceptions see [8]) by proper choice of the functions $\varphi(X, T)$, $\eta(\tau)$, and $X(T, \tau)$. Based on the expansion over the complete set of the squared Jost functions (see Sect. 4.2.3), the

³ More precisely in [46] an operator obtained from \mathbf{L} by changing to a moving frame was considered.

theory allows for computing in quadratures the Green function of the operator \mathbf{L} and thus the first order correction $|\psi_1\rangle$. In [16] this approach was exploited for obtaining corrections to (4.24) for a slow dark soliton, $V \sim \tilde{\epsilon} = \Omega^2$. In particular, there was obtained a small ($\sim \Omega^2$) shift of the frequency of oscillation: $\omega_s = (1 + v^2/9n_0)\omega/\sqrt{2}$ (the physical units). Frequency blue shift was also observed in numerical simulations [16, 53].

Another outcome of the approach of [16] is the presence of higher harmonics in the oscillatory motion of a dark soliton. To understand this phenomenon we observe, that although approximate dynamics of a soliton is characterized by the frequency $\omega/\sqrt{2}$, the center of mass of the condensate $x_c = \int x|\psi|^2 dx / \int |\psi|^2 dx$ in a parabolic trap satisfies the Ehrenfest theorem: $d^2x_c/dt^2 + \omega^2 x_c = 0$, and therefore oscillates with the frequency ω : $x_c = x_{c0} \sin(\omega t + \varphi_0)$ (see also numerical simulations in [54]). Thus, there exists frequency mismatch between oscillations of the soliton and the background and one can expect that in the long-time dynamics a soliton undergoes weak beatings, i.e., amplitude oscillations with the frequency corresponding to $(1 - 1/\sqrt{2})\omega \approx 0.29\omega$. This phenomenon was observed in numerical simulations reported in [16, 51].

4.4 Nonconservative Dynamics of Dark Solitons

4.4.1 Effect of Dissipation on the Dark Soliton Evolution

The effect of dissipation on a dark soliton was highlighted in the experiments reported in [12], where there was observed decay of the soliton contrast that was about 50% during 10 ms. Recalling the main steps of the derivation of (4.7) we conclude that within the framework of the mean-field approximation there exist at least two “internal” reasons for dissipation of the soliton energy even at zero temperature.

First, dissipative losses of a soliton occur due to emission and scattering of sound waves in inhomogeneous condensate. In the perturbation theories, discussed in Sect. 4.3.3, emission of sound is described by the first two terms of the expansion: ψ_0 and ψ_1 (notice that in the dark soliton case ψ_0 contributes to the change of the background). Radiative losses of a soliton is a relatively weak process: in a parabolic trap it is of order Ω^2 . In its turn, interaction of phonons reflected by the potential with the soliton is of the same order of Ω^2 . Since delay between emission and interaction is of order of $\Omega^{-1/2}$ (or a_1/c in the physical units), the effect of interaction of a soliton with phonons becomes appreciable only in long-time dynamics. For different confining potentials soliton-phonon interactions were numerically studied in [51–53].

Second, while deriving (4.7) (see Sect. 4.1.2) we neglected transverse degrees of freedom which are coupled with the ground state by the nonlinearity originated by two-body interactions. Population of higher transverse

levels can be accounted within the framework of the multiple-scale expansion by including the respective modes in the ansatz (4.5). This leads to a system of coupled NLS equations. Then invoking nonintegrability [15] one again arrives at nonelastic interactions of a soliton with sound (in [15] it was suggested to use the quintic NLS equation).

4.4.2 Dark Solitons in Varying Traps

One can test particle-like properties of a dark soliton, applying the laws of the Hamiltonian mechanics to a dark soliton in a slowly varying parabolic trap. The respective motion is characterized by conservation of the adiabatic invariant $I(E_s) = (2\pi)^{-1} \oint p dX$, where the canonical momentum, $p = \int_0^v (\partial E_s / \partial v) dv / v$, for the dark soliton can be computed explicitly: $p = -2n\hbar [v\sqrt{c^2 - v^2} + c^2 \arcsin(v/c)] / c^2$. In its turn, I defines the frequency $1/\omega_s = dI/dE_s = (1/2\pi) \oint dX/v$.

Taking into account that the frequency of a dark soliton in a parabolic trap, $\omega_s = \omega/\sqrt{2}$, does not depend on the energy E_s and using the obvious condition $I = 0$ at $v \rightarrow 0$, one computes $I = (E_s - 4\hbar m c_0^3 / 3g_1) \sqrt{2}/\omega$. In the TF approximation [13] $c_0^2 \propto \omega^{2/3}$ and thus preserving the adiabatic integral implies constancy of E_s/ω , i.e. $E_s \propto \omega$. From the link $c_0 \propto \omega^{1/3}$, one also concludes that $E_* \propto \omega^{2/3}$, with E_* defined in (4.24). Hence the amplitude of the soliton oscillations is given by $X_* \propto \omega^{-2/3}$.

The scaling law $X_* \sim \omega^{-\gamma}$, was observed in direct numerical simulations [42], for relatively large densities, where γ was close to the predicted value $2/3$. However, as the condensate density was decreasing, the exponent γ was also decreasing approaching $1/2$ in the limit of small n_0 . To explain this phenomenon we recall that the above consideration was based on the TF approximation, where $n_0 \approx n_{\text{TF}} \propto \omega^{2/3}$, which fails at $n_0 \rightarrow 0$, and must be substituted by the Gaussian approximation. Repeating the above arguments for $n_0 \approx n_G \propto \omega^{1/2}$ one arrives at the linear oscillator scaling law $X_* \propto \omega^{-1/2}$.

Another usage of a varying trap – energy pumping compensating radiative losses of a soliton was suggested in [51]. More specifically, it was shown that by means of two periodically varying out-of-phase Gaussian paddles, affecting the soliton at the turning points one can stabilize its energy at a fixed value. This process is accompanied by enhancement of interaction between soliton and radiation, as well as by significant enhancement of the beatings.

4.5 Theory of Generation of Dark Solitons

Now we consider controllable generation of dark solitons, i.e., producing solitons with a priori given parameters. Neglecting the finite dimensional size of the condensate, i.e. putting $\Omega = 0$, it is natural to employ the inverse scattering transform outlined in Sect. 4.2.1, allowing one to reduce the consideration to analysis of ZS spectral problem [9].

4.5.1 Phase Imprinting

Since characteristics of a dark soliton (4.11) are determined by the phase ϑ , a natural way to generate it is to impose proper initial phase distribution. Such idea was suggested in [55] and experimentally implemented in [12, 23]. In practice the method consists in applying a short duration (shorter than \hbar/μ) laser pulse to a part of a cigar-shaped condensate, what imprints an additional phase without changing the density. In the absence of the longitudinal trap, a number and characteristics of generated dark solitons can be obtained by solving ZS problem (4.10) with the “potential” $\tilde{\psi} = \rho \exp[i\varphi(X)]$ where $\lim_{x \rightarrow \pm\infty} \varphi(X) = \pm\vartheta$ [9, 56, 58, 61]. To this end, following [56], we observe that the eigenvector of a discrete eigenvalue λ_1 allows the representation $\Phi^{(j1)} = r(X) \exp[-i(-1)^j (S(X) - \varphi(X))/2]$, where $j = 1, 2$ and $r(X) \rightarrow 0$ as $|x| \rightarrow \infty$. Next, one ensures that S solves the equation of the forced pendulum: $S_X = (\varphi_x - \lambda) - 2 \sin S$, while r is determined by the phase: $r = r_0 \exp\left(\rho \int_0^X \cos S(x) dx\right)$ (r_0 is a constant). The obtained equation has particularly simple solution for the case of the “phase step” $\varphi = \Delta\theta(x)$ where Δ is a constant and $\theta(x)$ is the Heaviside step function, resulting in the only eigenvalue [9]: $\lambda_1 = 2\rho \cos(\Delta/2)$ for which a soliton exists at an arbitrary phase difference Δ , which reflects the fact that the generation of dark solitons is a thresholdless process [6, 9].

In experiment [12] it was observed, that the “main” soliton is accompanied by creation of a wave packet having velocity close to the speed of sound and moving away from the soliton. In this context we notice the fact known in theory [37]: even small initial perturbation of a soliton can result in generation of a small amplitude, i.e. moving with the sound velocity, satellite dark soliton.

4.5.2 Density Engineering

Now we consider the generation of dark solitons by means of initial change of the density [9, 25, 58, 61] and illustrate the problem using a simplified model of a boxlike initial pulse [9]: $\tilde{\psi} = \rho_0$ for $|X| > x_0$ and $\tilde{\psi} = \rho_1$ for $|X| < x_0$ (it is assumed that $0 < \rho_1 < \rho_0$). In this case the ZS spectral problem admits explicit solution, as it can be solved exactly on each of the intervals $|X| < x_0$ and $|X| > x_0$. The respective discrete eigenvalues satisfy the transcendental equation: $(\lambda^2 - 4\rho_0\rho_1) \tanh(x_0(\lambda - 4\rho_1^2)^{1/2}) = [(\lambda^2 - 4\rho_1^2)(4\rho_0^2 - \lambda^2)]^{1/2}$, which can be solved in the limit $\rho_0 - \rho_1 \ll \rho_0$: $\lambda_{1,2} = \pm 2\rho_0[1 - 2x_0^2(\rho_0 - \rho_1)^2]$. We notice that there appear two eigenvalues and they are located in the vicinity of the edges of the continuum spectrum $\pm 2\rho$. Since now the condensate phases at infinities are equal, two small amplitude dark solitons are created.

Finally, one can combine the two approaches, phase imprinting and density engineering. Such possibilities were studied numerically in [57, 58]. Here we also mention a suggestion [59] to use a parabolic trap combined with a localized impurity in order to generate local density perturbation leading to creation of a dark soliton.

4.5.3 Generation of Trains of Dark Solitons

So far we considered examples of creation of either a single soliton or a pair of dark solitons. Similarly, one can generate multi-solitonic pulses, the number of which is defined by the initial conditions [6]. As two examples we mention here the estimate [9] $N_s \sim 4\rho_0 x_0/\pi$ for a number of dark solitons produced by the density engineering, as described in Sect. 4.5.2 provided $\rho_0 \gg \rho_1, x_0^{-1}$; and the estimate $N_s = [\sqrt{\gamma^2 + 4x_0\gamma}/2\pi] + [\sqrt{\gamma^2 - 4x_0\gamma}/2\pi] + 1$ (here the rectangular brackets stand for the integer part) for a number of solitons created from the linear phase step: $\varphi = \gamma X/x_0$ for $|X| < x_0$ [56].

For generation of solitonic trains in a more general case of large but smooth initial data, one can use the representation introduced by (4.14) and look for the eigenfunctions in the form $\Phi_{1,2} = \chi_{1,2}(X) \exp(-(\mathrm{i}/2) \int w(X, t) dX)$. Then, neglecting terms with ρ_X and w_X one can apply WKB approximation [5, 60] to ZS problem, and formulate the respective Bohr–Sommerfeld quantization rule in the form [61]: $\int_{x_n^{(-)}}^{x_n^{(+)}} \sqrt{(\lambda_n - w(x))^2 - 4\rho(x)} dx = \pi(2n + 1)$, where n is a positive integer, $x_n^{(\pm)}$ are the classical turning points.

4.5.4 Feshbach-Resonance Management

A different method of soliton generation was proposed in [32, 62]. It is based on the possibility of temporal change of the scattering length, we write it as $a_s(t) = a_0 \sigma(t)$ where $\sigma(t)$ is a slow function of time, by means of Feshbach resonance. Since the “black” soliton can be viewed as an eigenfunction of the nonlinear eigenvalue problem (4.15), one can consider the branch of solutions, parametrized by σ , which at $\sigma = 0$ represents the first eigenfunction of the linear oscillator, $u_1 = (\sqrt{2}\Omega^3/\pi)^{1/4} X \exp(-\Omega^2 X^2/2\sqrt{2})$ corresponding to $\mu_1 = 3\Omega/\sqrt{2}$, and for $\sigma \gg 1$ becomes the black soliton against the TF background, $u_1 \approx \sqrt{(2\mu_1 - \Omega^2 X^2)/2\sigma} \tanh(\sqrt{\mu_1} X)$, with the chemical potential $\mu_1 = (3\sigma\Omega)^{3/2}/\pi^{5/2}$ (the eigenfunctions are considered to have the unity norm).

Thus by changing the scattering length one can transform the Gauss–Hermite distribution of the first energetic level of the linear oscillator into a dark soliton against an inhomogeneous background. It has been verified numerically [32] that, if this process is adiabatic, generation of sound waves is not significant and the final black soliton is stable.

In a similar way, i.e. by increasing adiabatically $a_s(t)$ from zero (or negligibly small value) until a given value a_0 , but starting with linear periodic density distributions (which can be created, for example, with help of an optical lattice) one can generate a train of dark solitons, each one appearing in the minimum of the original periodic solution of the GPE [62].

Acknowledgement. The author is grateful to V.A. Brazhnyi, V.E. Vekslerchik, L.D. Carr, and N. Pavloff for useful comments. The work was supported by Ministerio de Educación y Ciencia (MEC, Spain) under the grant SAB2005-0195 and by the grant POCI/FIS/56237/2004 (FCT, Portugal and European program FEDER).

References

1. T. Tsuzuki, J. Low Temp. Phys. **4**, 441 (1971)
2. L.P. Pitaevskii, Zh. Eksp. Teor. Fiz. **40**, 646 (1961) [Sov. Phys. JETP **13**, 451 (1961)]; E.P. Gross, Nuovo Cimento **20**, 454 (1961)
3. N. Bogoliubov, J. Phys. **11**, 23 (1947)
4. V.E. Zakharov, A.B. Sabat, Zh. Eksp. Teor. Fiz. **64**, 1627 (1973) [Sov. Phys. JETP **37**, 823 (1972)]
5. S.P. Novikov, S.V. Manakov, L.P. Pitaevskii, V.E. Zakharov, *Theory of solitons: Inverse Scattering Method* (Consultants Bureau, New York, 1980)
6. L.D. Faddeev, L.A. Takhtajan *Hamiltonian Methods in the Theory of Solitons* (Springer, Berlin Heidelberg New York, 1987)
7. I.M. Uzunov, V.S. Gerdjikov, Phys. Rev. A **47**, 1582 (1993)
8. V.V. Konotop, V.E. Vekslerchik, Phys. Rev. E **49**, 2397 (1994)
9. S.A. Gredeskul, Yu.S. Kivshar, Phys. Rev. Lett. **62**, 977 (1989); S.A. Gredeskul, Yu. S. Kivshar, M. Yanovskaya, Phys. Rev. A **41**, 3994 (1990)
10. A. Hasegawa, F. Tappert, Appl. Phys. Lett., **23**, 171 (1973)
11. D. Krökel, N.J. Halas, G. Giuliani, D. Grischkowsky, Phys. Rev. Lett. **60**, 29 (1988)
12. S. Burger, K. Bongs, S. Dettmer, W. Ertmer, K. Sengstock, A. Sanpera, G.V. Shlyapnikov, and M. Lewenstein, Phys. Rev. Lett. **83**, 5198 (1999)
13. L.P. Pitaevskii, and S. Stringari, *Bose–Einstein Condensation* (Oxford University Press, Oxford, 2003)
14. Th. Busch and J. R. Anglin, cond-mat/9809408; Phys. Rev. Lett. **84**, 2298 (2000)
15. A. Muryshev, G.V. Shlyapnikov, W. Ertmer, K. Sengstock, M. Lewenstein, Phys. Rev. Lett. **89**, 110401 (2002)
16. V.A. Brazhnyi, V.V. Konotop, Phys. Rev. A **68**, 043613 (2003)
17. V.M. Pérez-García, H. Michinel, H. Herrero, Phys. Rev. A **57**, 3837 (1998)
18. See, e.g., J. Kevorkian, J.D. Cole, *Multiple Scale and Singular Perturbation Methods* (Springer, Berlin Heidelberg New York, 1996)
19. D.S. Petrov, G.V. Shlyapnikov, J.T.M. Walraven, Phys. Rev. Lett. **85**, 3745 (2000)
20. P.O. Fedichev, A.E. Muryshev, and G.V. Shlyapnikov, Phys. Rev. A, **60** 3220 (1999)
21. A.E. Muryshev, H.B. van Linden van den Heuvell, G.V. Shlyapnikov, **60**, R2665 (1999)
22. D.L. Feder, M.S. Pindzola, L.A. Collins, B.I. Schneider, C.W. Clark, Phys. Rev. A **62**, 053606 (2000); P.G. Kevrekidis, G. Theocharis, D.J. Frantzeskakis, A. Trombettoni, Phys. Rev. A **70**, 023602 (2004)
23. J. Denschlag, J.E. Simsarian, D.L. Feder, C.W. Clark, L.A. Collins, J. Cubizolles, L. Deng, E.W. Hagley, K. Helmerson, W.P. Reinhardt, S.L. Rolston, B.I. Schneider, W.D. Phillips, Science **287**, 97 (2000)

24. B.P. Anderson, P.C. Haljan, C.A. Regal, D.L. Feder, L.A. Collins, C.W. Clark, E.A. Cornell, Phys. Rev. Lett. **86**, 2926 (2001)
25. Z. Dutton, M. Budde, C. Slowe, L.V. Hau, Science, **293**, 663 (2001)
26. P.D. Drummond, A. Eleftheriou, K. Huang, K.V. Kheruntsyan, Phys. Rev. A **63**, 053602 (2001); J. Brand, W.P. Reinhardt, J. Phys. B **34**, L113 (2001)
27. L.D. Carr, M.A. Leung, W.P. Reinhardt, J. Phys. B, **33**, 3983 (2000); R. Kanamoto, L.D. Carr, M. Ueda, arXiv:0704.3114
28. M. Girardeau Phys. Rev. Lett. **84**, 5691 (2000)
29. J. Dziarmaga, Z.P. Karkuszewski, K. Sacha, Phys. Rev. A **66**, 043615 (2002); J. Dziarmaga, K. Sacha, Phys. Rev. A **66**, 043620 (2002)
30. S.K. Adhikari, J. Low Temp. Phys. **143**, 267 (2006)
31. Yu.S. Kivshar, T.J. Alexander, S.K. Turitsyn, Phys. Lett. A **278**, 225 (2001)
32. P.G. Kevrekidis, V.V. Konotop, A. Rodriguez, D.J. Frantzeskakis, J. Phys. B **38**, 1173 (2005)
33. V.E. Zakharov, E.A. Kuznetsov, Physica D **18**, 455 (1986)
34. F.G. Bass, V.V. Konotop, S.A. Puzenko, Phys. Rev. A **46**, 4185 (1992)
35. G. Huang, M.G. Velarde, V. Makarov, Phys. Rev. A **64**, 013617 (2001); G.X. Huang, J. Szeftel, and S.H. Zhu Phys. Rev. A **65**, 053605 (2002)
36. D.J. Frantzeskakis, N.P. Proukakis, P.G. Kevrekidis, Phys. Rev. A **70**, 015601 (2004)
37. V.V. Konotop, V.E. Vekslerchick, J. Phys. A **25**, 40372 (1992)
38. E.B. Kolomeisky, T.J. Newman, J.P. Straley, X. Qi, Phys. Rev. Lett. **85**, 1146 (2000)
39. L. Tonks, Phys. Rev. **50**, 955 (1936); M. Girardeau, J. Math. Phys. **1**, 516 (1960)
40. E.H. Lieb, R. Seiringer, J. Yngvason. Phys. Rev. Lett. **91**, 150401 (2003)
41. M.D. Girardeau, E.M. Wright, Phys. Rev. Lett. **84**, 5239 (2000)
42. V.A. Brazhnyi, V.V. Konotop, L.P. Pitaevskii, Phys. Rev. A **73**, 053601 (2006)
43. W.P. Reinhardt, W. Clark, J. Phys. B, **30**, L785 (1997)
44. T. Hong, Y.Z. Wang, Y.S. Huo, Phys. Rev. A **58**, 3128 (1998)
45. D.J. Frantzeskakis, G. Theocharis, F.K. Diakonos, P. Schmelcher, Yu.S. Kivshar, Phys. Rev. A **66**, 053608 (2002)
46. D.E. Pelinovsky, D.J. Frantzeskakis, P.G. Kevrekidis, Phys. Rev. E **72**, 016615 (2005)
47. V.V. Konotop, L. Pitaevskii, Phys. Rev. Lett. **93**, 240403 (2004)
48. A. Negretti, C. Henkel, J. Phys. B **37**, L385 (2004)
49. V.V. Konotop, V.M. Pérez-García, Yi-Fa Tang, L. Vázquez, Phys. Lett. A **236**, 314 (1997)
50. N. Bilas, N. Pavloff, Phys. Rev. A **72**, 033618 (2005)
51. N.P. Proukakis, N.G. Parker, C.F. Barenghi, C.S. Adams, Phys. Rev. Lett. **93**, 130408 (2004)
52. N.G. Parker, N.P. Proukakis, M. Leadbeater, C.S. Adams, Phys. Rev. Lett. **90**, 220401 (2003)
53. N.G. Parker, N.P. Proukakis, M. Leadbeater, C.S. Adams, J. Phys. B **36**, 2891 (2003)
54. C. Hernandez Tenorio, E. Villagran Vargas, V.N. Serkin, M. Agüero Granados, T.L. Belyaeva, R. Peña Moreno, L. Morales Lara, Quant. Electron. **35**, 929 (2005)
55. L. Dobrek, M. Gajda, M. Lewenstein, K. Sengstock, G. Birkl, W. Ertmer, Phys. Rev. A **60**, R3381 (1999)

56. B. Wu, J. Liu, Q. Niu, Phys. Rev. Lett. **88**, 034101 (2002)
57. L.D. Carr, J. Brand, S. Burger, A. Sanpera Phys. Rev. A **63**, 051601(R) (2001)
58. S. Burger, L.D. Carr, P. Öhberg, K. Sengstock, A. Sanpera, Phys. Rev. A **65**, 043611 (2002)
59. G. Theocharis, D.G. Kevrekidis, H.E. Nistazakis, D.J. Frantzeskakis, A.R. Bishop, Phys. Lett. A **337**, 441 (2005)
60. Z.W. Lewis, Phys. Lett. A **112**, 99 (1985)
61. V.A. Brazhnyi, A.M. Kamchatnov, Phys. Rev. A **68**, 043614 (2003)
62. F.Kh. Abdullaev, A.M. Kamchatnov, V.V. Konotop, V.A. Brazhnyi, Phys. Rev. Lett. **90**, 230402 (2003); V.A. Brazhnyi, V.V. Konotop, Phys. Rev. A **72**, 033615 (2005)

Dark Solitons in BECs: The First Experiments

B.P. Anderson

5.1 Introduction

This chapter is oriented towards a review of the first two experimental studies of planar dark solitons in Bose–Einstein condensates (BECs). These experiments were direct and convincing demonstrations of the nonlinear dynamics of coherent matter-waves, and of the uses of laser light in BEC quantum-state manipulation. The experimental results were also successfully described with quantitative theoretical predictions and numerical simulations, some of which are discussed in the first portions of this chapter and Part V. The two experiments reviewed here, simultaneously and independently pursued at the University of Hannover [1] and at NIST in Gaithersburg [2], were the first to create and study planar dark solitons in BECs. Subsequent BEC dark soliton experiments at JILA [3] and Harvard University [4, 5] also demonstrated new methods for creating dark solitons in BECs. These later experiments, however, which will be mentioned briefly in this chapter, were more focused towards studies of the dynamical instabilities and decay products of planar dark solitons; a review of the JILA and Harvard experiments is given in Part V.

As a general note, the distinction between *solitons* and *solitary waves* has often been debated among mathematicians, engineers, and physicists. In this review, however, as is the case in much of the BEC literature, such a distinction will *not* be made. A discussion of these terms can be found in [6]. Furthermore, as the subject of this chapter, all references to solitons imply *planar dark solitons*, as already discussed in depth in the previous chapter. Other chapters in this volume contain in-depth reviews of other types of solitons in BECs, such as bright solitons in BECs with attractive interatomic interactions, and vortex rings and vortex lines, which are often referred to as vortex solitons. As a working phenomenological definition for this chapter, a dark soliton in a BEC is characterized by a planar density notch that spans the BEC, at which there is a localized decrease in atom number density. The density notch is correlated with a sudden change in the condensate’s quantum phase across

the notch, and the propagation velocity of the soliton through the atom cloud and the depth of the density notch are intimately related to the phase jump. These concepts will be further described below.

This chapter is intended as a general overview and review for both researchers within the BEC community, and for a wider range of scientists and mathematicians interested in nonlinear dynamics in BEC experiments. Some experimental and technical details are thus necessarily omitted in favor of an overall conceptual description of the first experimental studies of dark solitons in BECs.

5.2 Overview of Experimental Approaches

In this section, we give a general overview of ideas, experimental techniques, and typical experimental parameters that are common to many or most of the BEC dark soliton experiments to-date. This discussion will serve as both a preview of the experiments to be described in detail within this chapter, and as a broader overview that relates these first experiments to the experimental results discussed in Chap. 8.

5.2.1 Bose–Einstein Condensates as a Nonlinear Medium

Currently, all reported experimental results regarding studies of planar dark soliton creation and dynamics in BECs have exclusively involved magnetically trapped BECs, as opposed to optically trapped condensates, although there is no reason in principle why optical traps can not be used in dark soliton experiments. The confining potentials of magnetic traps have geometries that create either (1) cylindrically symmetric oblate BECs, in traps with one axis of tight confinement, and weaker radial confinement (the so-called pancake-shaped trap geometries); (2) cylindrically symmetric prolate BECs, in traps with one axis of weak confinement, and tighter radial confinement (the so-called cigar-shaped traps); or (3) spheroidal BECs in traps with no symmetry axis. Although dark soliton experiments so far have used either ^{87}Rb or ^{23}Na atoms as the condensate atomic species, any condensate with repulsive interatomic interactions (s -wave scattering length $a_s > 0$) may in-principle support dark solitons.

In BEC experiments, the *healing length* of the condensate is a length scale that characterizes the maximum sharpness of density features within a BEC. Because a steep atomic density gradient in a BEC is associated with more kinetic energy than a smoother gradient, the BEC can not support density features that are sharper than limits imposed by the total energy, or chemical potential, of the BEC. A steep density gradient thus tends to spatially broaden and become smoother, thereby lowering its associated kinetic energy. However, in the case of an ideal dark soliton with a sharp density notch and a π phase jump across the notch, repulsive atomic interactions in the bulk of atoms on

either side of the soliton notch push on the dark notch from either side. This then minimizes the spatial width of the density notch, while the π phase jump across the notch prevents the two BEC halves from merging together. For dark solitons, the healing length ξ is the characteristic length scale that emerges in the balance between these opposite tendencies, and is often defined by the expression

$$\xi = \frac{1}{\sqrt{8\pi n_0 a_s}},$$

where n_0 is the peak atomic density of the condensed atoms, typically on the order of 10^{13} to 10^{14} atoms per cm^3 . The healing length is typically just under $1 \mu\text{m}$. Any condensate features with a size scale approaching the healing length will therefore usually not be optically resolvable if the condensate remains trapped. This is indeed the case for dark soliton notches in single-component condensates, and for other features as well, such as vortex cores. Condensates must then be spatially expanded in order to optically resolve solitons, as discussed below.

The speed of sound c_s in a condensate also depends on the healing length through the relation $c_s = \frac{\hbar}{m\xi\sqrt{2}}$, where m is the mass of an atom in the BEC [7, 8]. Typical values for c_s are on the order of a few millimeters per second. The propagation speed v_{sol} of a dark soliton, however, depends on the phase step δ across the notch, or equivalently on the depth n_d of the soliton notch, defined as the difference between the local bulk condensate density n and the minimum density of the atoms within the soliton notch:

$$v_{\text{sol}} = c_s \cos(\delta/2) = c_s[1 - (n_d/n)]^{1/2}.$$

Soliton propagation speed is thus below c_s [9].

5.2.2 Soliton Creation Techniques

The methods used to create dark solitons in BECs can be grouped into three categories: (1) phase engineering techniques, which involve a primary direct manipulation of BEC phase; (2) density engineering techniques, which involve a primary direct manipulation of BEC density, and (3) quantum state engineering techniques that involve a combination of density and phase engineering. A similar categorization of soliton creation methods is described in reference [10]. Note that to create a dark soliton in a uniform-phase BEC, both phase and density must somehow be manipulated, so all soliton creation techniques involve some amount of phase and density manipulation; creation of a perfect dark soliton state would ideally involve both types of methods. However, with the exception of the quantum state engineering work at JILA [3], BEC dark soliton experiments have used either density or phase manipulation techniques as the primary means of creating dark solitons.

Phase engineering methods generally make use of phase imprinting by a laser beam, in which an off-resonance laser beam is used to write phase steps

or gradients into the BEC phase profile. It is thus worth briefly reviewing the induced dipole interaction between an atom and off-resonance laser light. With a laser beam of intensity I , and having an optical angular frequency detuned Δ from an optical transition of linewidth Γ of the atom, the induced dipole-interaction energy shift of the atom is given by the expression

$$U_{\text{dip}} = \frac{\hbar\Gamma}{8} \cdot \frac{I/I_{\text{sat}}}{\Delta/\Gamma},$$

where I_{sat} is the saturation intensity for the transition. Thus red-detuned light, with $\Delta < 0$, lowers the potential energy of an atom (relative to regions where light is not present) and can be used in creating an attractive potential well for the atom. Blue-detuned light ($\Delta > 0$) raises the atomic energy. With either red- or blue-detuned laser light incident on only a portion of a BEC for a short time τ , that portion of the condensate acquires a phase shift of magnitude $U_{\text{dip}}\tau/\hbar$ relative to the remainder of the BEC. Additional discussion of these concepts can be found in reference [11].

The induced dipole interaction can in principle also be used to manipulate the density profile of a BEC. Such techniques are indeed widespread, as in BEC optical lattice work [12, 13]. However, the two reported dark soliton experiments that have primarily relied on density manipulation, both from the Harvard University group [4, 5], used laser light and quantum interference in a very different way to create a planar density notch in a BEC. These two experiments, along with the JILA dark soliton experiment, are reviewed in Part V.

5.2.3 Imaging

As mentioned above, a planar dark soliton in a BEC has a spatial extent that bisects the entire BEC, and a notch width that is on the order of the sub-micron healing length. Thus, in order to optically resolve a density notch in a BEC, the entire condensate is suddenly released from its confining potential and allowed to ballistically expand for times on the order of a few milliseconds. Expansion of the BEC is accompanied by spatial expansion of the soliton density notch residing within the cloud, which can then be optically resolved with a standard imaging system. Observation techniques for expanded BECs typically involve illuminating the cloud with near-resonant laser light, and imaging the absorptive “shadow” of the BEC onto a CCD camera. The image produced is related to the spatial profile of the cloud’s optical depth integrated along the imaging direction; information about the BEC atomic density profile can then be extracted from the absorption image. Solitons and their dynamics can be detected with an imaging beam that propagates parallel to the soliton nodal plane.

This common expansion imaging technique unfortunately destroys the condensate, and multiple similar images must be carefully correlated with each

other in order to produce a meaningful data set. Such was the case for the experiments reviewed in this chapter, where soliton propagation velocities across a BEC were measured using condensates that were allowed to expand after controlled changes were made to the pre-expansion conditions. Other imaging and data collection techniques important for individual experiments, particularly BEC interferometry, will be described below in the relevant experimental sections below.

5.3 Observations with Dark Solitons

Along with demonstrations of the ability to create dark solitons, measurements of soliton propagation through a trapped BEC were major new achievements of the NIST and Hannover experiments. Both experiments used phase engineering with a masked laser beam to imprint a phase step across a planar region through the BEC, and general principles of this method that are common to both experiments will now be discussed.

As described above, an off-resonant laser beam can induce a shift in the energy of a trapped atom relative to an atom in a region that does not feel the force of the laser beam. Shining a laser beam onto a portion of a BEC for a short time τ induces a phase shift relative to the portion of the BEC that is not illuminated. The magnitude of the induced phase step, δ , is proportional to τ and the laser intensity, and inversely proportional to the detuning of the laser beam from an atomic resonance. Additional general details of using laser light for BEC phase imprinting can be found in reference [14], for example.

In the experiments at Hannover and NIST that incorporated phase imprinting for creating dark solitons, τ was kept much shorter than the correlation time t_c of the BEC, where $t_c = \hbar/\mu$ and μ is the chemical potential of the BEC. In this sense, the phase imprint can be thought of as an impulse that shifts the relative phase between portions of the BEC, but is so short that neither correlations across the atom cloud nor significant atomic motion can occur during the impulse. Changes in the BEC density during the imprinting can then be neglected. At longer times after the imprint, however, the condensate density distribution does indeed react to the phase imprint impulse; such effects have been observed and are a significant consequence of the phase imprinting method. To implement phase imprinting, both the NIST and Hannover groups used a procedure in which a partially masked off-resonant beam of laser light illuminated half the condensate, as illustrated in Fig. 5.1. The beam was then removed after a short time τ , and the resulting dynamics of the BEC and the soliton created within were studied.

The Hannover Experiment

The dark soliton experiment at the University of Hannover [1] involved cigar-shaped BECs of ^{87}Rb trapped in the $|F = 2, m_F = 2\rangle$ atomic state. Typical

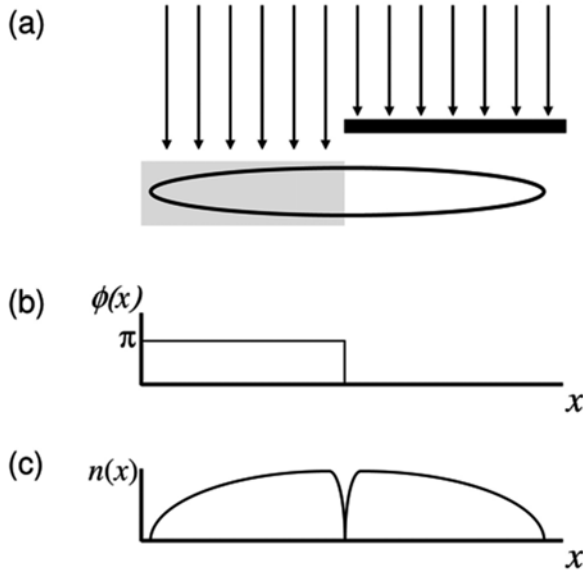


Fig. 5.1. (a) An illustration of the phase imprinting technique, with the arrows representing different portions of the phase imprinting laser beam. Part of the light is blocked by a mask (the dark bar), while the remainder of the beam illuminates half of the BEC (the oval). The illuminated portion is shown here as a gray region. For an ideal dark soliton, the condensate phase $\phi(x)$ jumps by $\delta = \pi$ at the location of the soliton, as illustrated in (b), and a completely dark density notch develops at the plane of the phase jump, as shown in (c) with a conceptual illustration of the BEC density profile $n(x)$. In these figures, it is assumed that the dark soliton density notch is in a plane perpendicular to the x direction. In the phase imprinting methods reviewed, the density notch is formed as a secondary result of the primary phase imprinting method

BECs contained 1.5×10^5 atoms, with reported condensate fractions of at least 90% in a static magnetic trapping potential. The trapping frequencies used were $\omega_x = 2\pi \times 14$ Hz along the axial direction, and $\omega_{\perp} = 2\pi \times 425$ Hz radially, giving a geometric mean oscillator frequency of $\bar{\omega} = 2\pi \times 136$ Hz. For these conditions, the BEC chemical potential was $\mu \approx \hbar \cdot 2\pi \times 3,000$ Hz, with a corresponding speed of sound of $c_s \approx 3.7 \text{ mm s}^{-1}$ and a BEC correlation time t_c of approximately 50 μs .

The phase imprint used to make a soliton was such that the soliton nodal plane divided the BEC along its long axis (the x direction) into two halves, since only one half of the BEC was illuminated by the phase imprinting light. To achieve short-enough phase imprinting times τ at laser detunings and intensities such that photon scattering was negligible, the Hannover group used a blue-detuned beam with a wavelength of 532 nm (far from the ^{87}Rb resonance at 780 nm) and intensity $I \sim 20 \text{ W mm}^{-2}$. A phase imprint time of $\tau = 20 \mu\text{s}$ then resulted in a phase step between the two halves of the BEC

of $\delta = \pi$, appropriate for the creation of a dark soliton. For these imprinting conditions, the expected atom–photon scattering time was ~ 500 s, and photon scattering was thus indeed negligible during the $20\text{ }\mu\text{s}$ imprinting pulse.

This phase imprint method, without a corresponding BEC density manipulation step, necessarily involves writing a steep phase *gradient* into a small section of the BEC that connects the two soliton halves. The width of this region corresponds to the sharpness of the imprint mask edge. Because the edge sharpness of the imprinting laser field is limited by optical diffraction in an imaging system, the sharpness of the field edge l_e is of the order of a few microns, and was under $3\text{ }\mu\text{m}$ in the Hannover experiment. The phase gradient is then estimated as a phase increase of 0 to π across a section of the BEC that is l_e in width. A phase gradient $\frac{\partial\phi(x)}{\partial x}$ in the x direction across a portion of the BEC also implies a velocity imprint to that portion of the BEC through the relation $v_x = \frac{\hbar}{m} \frac{\partial\phi(x)}{\partial x}$, where m is the atomic mass. Momentum is transferred to a slice of atoms across the middle of the BEC, and those atoms then propagate as a density wave out of the imprint edge region. Roughly, the initial velocity of these atoms can be approximated by

$$v_x = \frac{\hbar}{m} \frac{\partial\phi(x)}{\partial x} = \frac{\hbar}{m} \frac{\pi}{l_e}.$$

This value was on the order of mm s^{-1} for the Hannover values of $l_e \sim 3\text{ }\mu\text{m}$ and phase jumps of $\delta \sim \pi$. Left behind, in the space originally occupied by the now-propagating atoms, was a density notch with a π phase step across it.

After the phase imprint, the BEC was held in the magnetic trap for a variable evolution time t_{ev} before the magnetic trapping field was extinguished, at which time the atom cloud expanded for 4 ms and was observed with standard absorption imaging techniques. A series of images taken at different values of t_{ev} is shown in Fig. 5.2. For short evolution times, a density notch in the cloud was clearly observed. By varying t_{ev} , the propagation of this density notch was measured via the expansion images, and the notch was reported to travel through the cloud with a velocity v_{sol} between 2.0 and 3.0 mm s^{-1} , depending on the experimentally adjustable parameters of l_e and the imprinted phase step δ (see [1] for further discussion of these dependencies). As expected, the observed velocities were less than the calculated value of c_s . A plot showing soliton position along x vs. evolution time t_{ev} is given in Fig. 5.3.

The phase imprinting step created a positive density wave, or localized increase in atom number density, in addition to the dark soliton density notch. This density wave traveled near the speed of sound, in the direction opposite to that of the dark soliton, and was partially responsible for the creation of a *second* density notch that also traveled in the direction opposite to that of the original dark soliton but at roughly the same speed as that of the original dark soliton. It is believed that this second notch was a second dark soliton, created through a coherent evolution of local BEC phase due to the presence of the positive density wave. The experimental observations also revealed a decrease in the soliton contrast (depth) by 50% over a time scale of 10 ms, which the

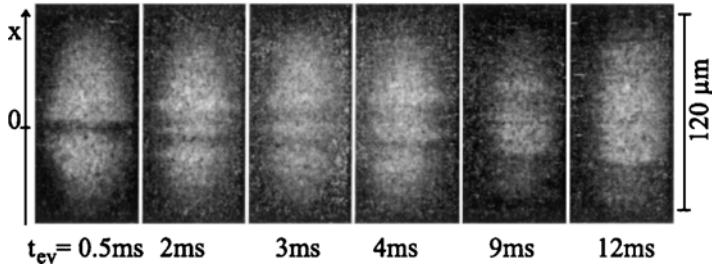


Fig. 5.2. Absorption images of expanded BECs show the x position of a primary dark soliton as it propagates through the magnetically trapped BEC for different evolution times t_{ev} . The soliton is the dark horizontal stripe in the first image, and is seen to propagate downward in later images. A secondary dark soliton can also be seen to propagate upwards (see text). For these images, $\delta = \pi$ and the ballistic expansion time was 4 ms. Figure reprinted with permission from [1]. Copyright 1999 by the American Physical Society

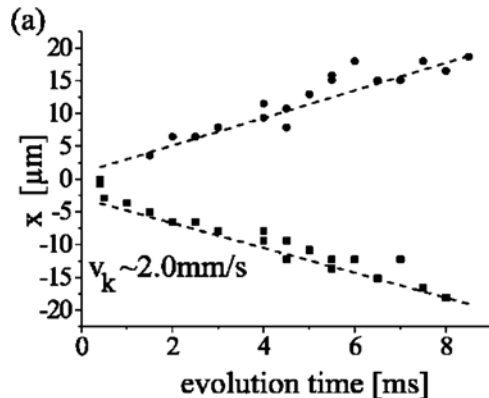


Fig. 5.3. The positions of the experimentally observed density minima of the principal and secondary dark solitons are shown vs. evolution time in the magnetic trap for $\delta \sim 0.5\pi$. The dashed lines show results from a 3D simulation for 5×10^4 atoms, $l_e = 3 \mu\text{m}$, and $\delta = 2\pi/3$. The soliton velocity is indicated by the variable v_k . Figure reprinted with permission from [1]. Copyright 1999 by the American Physical Society

Hannover group interpreted as a sign of dissipation due to the thermal cloud decreasing the energy of the soliton.

The group further compared experimental observations with numerical simulations of the 3D GPE that assumed 5×10^4 atoms at zero temperature. The following results were noted in the simulations: (1) the simulated phase imprinting step showed the creation of a density wave with a density maximum that travels near the speed of sound, in accordance with experimental observations; (2) for a fixed value of l_e and increasing values of

δ from π to 2π , 3π , etc., multiple solitons were created. This trend was also seen in the experiment. (3) The soliton velocity decreased as l_e decreased, as seen in the experiment; and (4) the simulation showed the creation of a second density notch, interpreted as a soliton. Additional theoretical analysis related to this experiment can be found in [15].

The NIST Experiment

In parallel with the Hannover group, the NIST BEC group at Gaithersburg was independently creating and studying dark solitons in BECs [2]. Their phase imprinting approach to soliton creation was similar to the approach described above, but the NIST group used BECs of ^{23}Na containing $\sim 1.7 \times 10^6$ atoms in the $|F = 1, m_F = -1\rangle$ state. The BEC was held in a magnetic trap with trapping frequencies of $\omega_x = \sqrt{2}\omega_y = 2\omega_z = 2\pi \times 28$ Hz, a much more spheroidal trap than the Hannover group. In this trap, the geometric mean trapping frequency was $\bar{\omega} \sim 2\pi \times 20$ Hz. These numbers give a BEC chemical potential of $\mu/\hbar \sim 2\pi \times 470$ Hz, a speed of sound of $c_s \sim 2.8 \text{ mm s}^{-1}$, and a correlation time of $t_c \sim 340 \mu\text{s}$.

The NIST group used phase-imprinting light pulses with τ on the order of $1 \mu\text{s}$ to create solitons of varying notch depths. A matter-wave interferometer based on Bragg scattering [16] was then used to evaluate the actual phase jump δ imparted to the portion of the condensate illuminated by the imprinting light. This interferometer worked as follows. First, a pair of counter-propagating laser beams was pulsed on, and placed the atoms of the BEC into a superposition of two momentum states $|A\rangle$ and $|B\rangle$. Within 1 ms, the two states separated in space due to the difference in their momenta. A phase-imprinting step as previously described was then applied to state $|A\rangle$ only, using another laser beam. Since the state- $|B\rangle$ atoms did not receive a phase imprint, they could serve as an unperturbed phase reference for the phase imprinted onto the state- $|A\rangle$ atoms. Finally, two further Bragg pulses allowed the two spatially separated portions of the superposition to recombine and interfere.

In this interference stage, the phase difference between the atoms in the two states $|A\rangle$ and $|B\rangle$ regulated the location in space where the atoms were observed (the interferometer port). For example, if the state- $|A\rangle$ phase imprinting step were removed from the experiment, the final interference between $|A\rangle$ and $|B\rangle$ resulted in all atoms exiting the interferometer in Port 1, as labeled in Fig. 5.4. But if instead a masked laser beam were used to imprint a phase step of π onto *half* of the state- $|A\rangle$ atoms (as represented by the darkened half of the $|A\rangle$ atoms in Fig. 5.4), that same half of the final recombined BEC would appear in Port 2 (shown in Fig. 5.4) after the recombination step. With this technique, the NIST group verified that an appropriate phase imprinting step could be characterized and controlled such that the phase jump appropriate for a dark soliton could be imprinted onto a BEC.

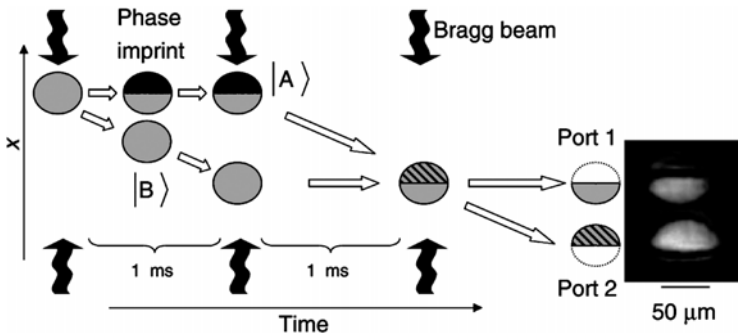


Fig. 5.4. A space–time diagram of the matter-wave interferometer used to measure the spatial phase step imprinted across a BEC. The Bragg laser pulses are shown as wavy arrows. The image shows the output of the two ports when a π phase step was imprinted. See reference [2] for more details on the timing and frequencies of the laser beams. Figure reprinted with permission from [2]. Copyright 2000 AAAS

In studies of the dynamics of BEC dark solitons, the interferometric method was not used. With the Bragg pulses omitted, a single BEC was created. Half of the BEC then received a phase imprint with the masked laser beam, and the atom cloud was observed using the standard technique of imaging the BEC after expansion from the magnetic trap. For technical reasons, a phase imprint corresponding to 1.5π was found to lead to the optimal formation of solitons, and the resulting BEC was held in the magnetic trap for a variable time t_{ev} before release, expansion, and imaging. The soliton propagation speed was thus measured by varying t_{ev} , using a methodology similar to the Hannover group, with the result that the mean soliton speed was found to be $v_{sol} = 1.8 \pm 0.4 \text{ mm s}^{-1}$, less than the speed of sound c_s . In corresponding numerical simulations using the 3D GPE, a 1.5π phase step, and a value of $2 \mu\text{m}$ for l_e , a mean soliton speed of 1.6 mm s^{-1} was obtained, in agreement with the experimental results. Images from the NIST experiment are shown in Fig. 5.5, with visual comparisons of corresponding simulations.

After the phase imprint, density waves and secondary dark solitons were also observed, similar to the Hannover experiment. However, the NIST dark soliton density notches were also observed to bend as they propagated towards the edge of the BEC, both in the experiments and in the simulations. This curvature was attributed to the soliton velocity in the center of the BEC being greatest since the atomic density there was highest. Such a change in the shape of the soliton was pronounced in the NIST experiment due to the spheroidal nature of the NIST trap. Furthermore, as the soliton propagated away from the BEC center, it appeared to slow down. Due to the relationship between soliton depth, speed, and phase jump, this slowing was correlated with the soliton depth becoming a larger fraction of the decreasing local atomic density.

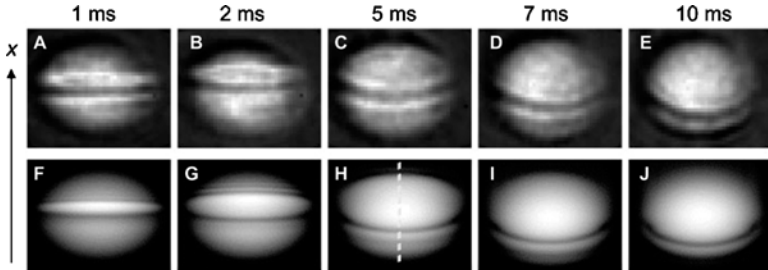


Fig. 5.5. Experimental (**A–E**) and corresponding theoretical (**F–J**) images of the integrated BEC density are shown for various times after a phase step of $\delta \sim 1.5\pi$ was imprinted to the top half of the BEC. The width of each frame is $70\text{ }\mu\text{m}$. Figure reprinted with permission from [2]. Copyright 2000 AAAS

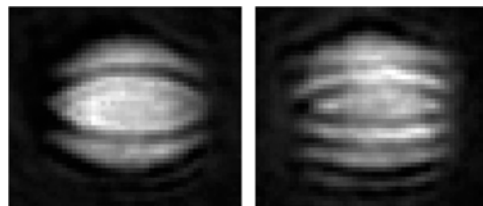


Fig. 5.6. A stripe-shaped imprint across the center of the BEC leads to the generation of multiple dark solitons. These images were acquired with 6 ms expansion after a phase jump of 1.5π (left image) and 2π (right image). Images reprinted with permission from [2]. Copyright 2000 AAAS

For phase steps of $\delta \sim 0.5\pi$, the soliton speed was observed to approach c_s . For phase steps larger than 1.5π , multiple solitons were generated and observed. Additional changes to the phase imprinting step included using a stripe of light across the center of the BEC, which imprinted two dark solitons that propagated in opposite directions. Example images of BECs with multiple dark solitons are shown in Fig. 5.6.

5.4 Conclusions

The first two experiments with dark solitons in Bose–Einstein condensates demonstrated a number of important fundamental concepts. First, these experiments showed that phase imprinting can be effectively used for quantum phase engineering, at least for the specific case of planar dark soliton creation. Second, they verified that BECs comprised of atoms with repulsive interactions can indeed support dark solitons, as expected. Third, these experiments confirmed that dark solitons in BECs can approximately maintain their shape as they propagate through the BEC at speeds below that of sound in the BEC.

Finally, the comparisons between data, theory, and numerical simulations were convincing demonstrations that the concepts of dark solitons as first studied in other areas of nonlinear dynamics were being appropriately applied to the new nonlinear medium of atomic gas BECs. Overall, these two experiments were the first of a larger group of dark soliton experiments in BECs. Further closely related experimental work in this area was also performed by the Hannover group [17]. Altogether different experiments with planar dark solitons were pursued in other groups, in particular with experimental work at JILA [3] and Harvard University [4]. The results from these last two groups are reviewed in Part V of this volume.

BPA acknowledges support from the National Science Foundation and the Army Research Office in the preparation of this review.

References

1. S. Burger, K. Bongs, S. Dettmer, W. Ertmer, K. Sengstock, A. Sanpera, G.V. Shlyapnikov, M. Lewenstein, Phys. Rev. Lett. **83**, 5198 (1999)
2. J. Denschlag, J.E. Simsarian, D.L. Feder, C.W. Clark, L.A. Collins, J. Cubizolles, L. Deng, E.W. Hagley, K. Helmerson, W.P. Reinhardt, S.W. Rolston, B.I. Schneider, W.D. Phillips, Science **287**, 97 (2000)
3. B.P. Anderson, P.C. Haljan, C.A. Regal, D.L. Feder, L.A. Collins, C.W. Clark, E.A. Cornell, Phys. Rev. Lett. **86**, 2926 (2001)
4. Z. Dutton, M. Budde, C. Slowe, L.V. Hau, Science **293**, 663 (2001)
5. N.S. Ginsberg, J. Brand, L.V. Hau, Phys. Rev. Lett. **94**, 40403 (2005)
6. A.C. Scott, F.Y.F. Chu, D.W. McLaughlin, Proc. IEEE **61**, 1443 (1973)
7. M.R. Andrews, D.M. Kurn, H.-J. Miesner, D.S. Durfee, C.G. Townsend, S. Inouye, W. Ketterle, Phys. Rev. Lett. **79**, 553 (1997)
8. F. Dalfovo, S. Giorgini, L.P. Pitaevskii, S. Stringari, Rev. Mod. Phys. **71**, 463 (1999)
9. W.P. Reinhardt, C.W. Clark, J. Phys. B **30**, L785 (1997); A.D. Jackson, G.M. Kavoulakis, C.J. Pethick, Phys. Rev. A **58**, 2417 (1998); P.O. Fedichev, A.E. Muryshev, G.V. Shlyapnikov, Phys. Rev. A **60**, 3220 (1999)
10. S. Burger, L.D. Carr, P. Öhberg, K. Sengstock, A. Sanpera, Phys. Rev. A **65**, 043611 (2002)
11. H.J. Metcalf, P. Van der Straten, *Laser Cooling and Trapping* (Springer, Berlin Heidelberg New York, 1999)
12. B.P. Anderson, M.A. Kasevich, Science **282**, 1686 (1998)
13. M. Greiner, O. Mandel, T. Esslinger, T.W. Hänsch, I. Bloch, Nature **415**, 39 (2002)
14. L. Dobrek, M. Gajda, M. Lewenstein, K. Sengstock, G. Birk, W. Ertmer, Phys. Rev. A **60**, 3381 (1999)
15. A. Muryshev, G. V. Shlyapnikov, W. Ertmer, K. Sengstock, M. Lewenstein, Phys. Rev. Lett. **89**, 110401 (2002)
16. M. Kozuma, L. Deng, E.W. Hagley, J. Wen, R. Lutwak, K. Helmerson, S.L. Rolston, W. D. Phillips, Phys. Rev. Lett. **82**, 871 (1999)
17. K. Bongs, S. Burger, D. Hellweg, M. Kottke, S. Dettmer, T. Rinkleff, L. Cacciapuoti, J. Arlt, K. Sengstock, W. Ertmer, J. Opt. B **5**, S124 (2003)

Part IV

Nonlinear Localization of BECs in Optical Lattices

Nonlinear Localization of BECs in Optical Lattices

E.A. Ostrovskaya, M.K. Oberthaler, and Y.S. Kivshar

6.1 Introduction

In this chapter we review the effects of spatial localization of a Bose–Einstein condensate (BEC) that arise due to the combination of the intrinsic nonlinearity of a condensate due to *repulsive* atomic interactions and Bragg scattering of a matter-wave on a periodic potential of an optical lattice (OL). It goes without saying that we will not discuss the trivial case of very deep periodic potentials which leads to trapping of the atoms within single sites. Instead, we will address the situation where the *single* particle tunneling rate is still much faster than the observation time. Under such conditions, a nontrivial localization becomes possible due to the fact that, at the edges of a Brillouin zone (BZ) of the lattice, the condensate experiences anomalous diffraction (dispersion), the magnitude of which can be controlled by tuning the depth of the OL potential. Keeping a wave packet from spreading can therefore be either achieved by actively controlling the dispersion or by utilizing the interaction between atoms. The first approach is known as dispersion/diffraction management and the second one leads to nonlinearly localized states.

The anomalous diffraction (dispersion) gives rise to the effects that are normally absent in a repulsive condensate. One of this effects is the modulational (dynamical) instability of the extended nonlinear Bloch waves that underpins the condensate localization, as well as leading to enhanced growth of the thermal fraction. The other effect is the spatial localization of a repulsive condensates inside the linear band gaps. The localized states take the form of gap solitons, for low atom numbers, and self-trapped states, for high atom numbers. Here we describe both the experimental observations and theoretical studies of the dispersion management, as well as formation and properties of nonlinear localized states of the BECs in 1D OLs. Although the recent progress in the studies of nonlinear localization is driven by the experiments with 1D OLs, we also summarize theoretical predictions of novel localized states with a nontrivial phase that may exist in 2D and 3D lattices.

6.2 Experimental Work Horse: Optical Potentials

The details concerning the experimental realization and detection of ultracold gases can be found in literature [1] and will not be addressed here. In this Section we will briefly recapitulate how OLs, i.e. periodic potentials, are realized and what parameters are under experimental control.

The success of atomic gases as an experimental system for the investigation of many different aspects of physics follows from the fact that atoms resonantly interact with light [2]. For example, the spontaneous emission is the prerequisite for the implementation of laser cooling since it allows us to dissipate kinetic energy of the atoms. In contrast to this incoherent process, the coherent redistribution of photons between different light modes via stimulated emission leads to the conservative potentials known as light shift or dipole potentials for atoms. In a classical picture these potentials are a consequence of the interaction of the dipole induced by the light with the light field itself. As the main result one finds that the ensuing potential is proportional to the *light intensity* and inversely proportional to the frequency difference between the laser light and the atomic transition. Since the decoherence, or incoherent spontaneous emission process, scales inversely with the *square* of the frequency difference, it is always possible to realize a situation such that the incoherent processes are negligible.

The optical dipole potentials are thus as variable as the light intensity $I(\mathbf{r})$ distributions. Using L light beams impinging on the atoms from different directions \mathbf{k}_j , and with different amplitudes \mathbf{E}_j , potentials $V(\mathbf{r})$ of the form:

$$V(\mathbf{r}) \propto I(\mathbf{r}) = \frac{c\epsilon_0}{2} \sum_{j,l=1}^L \mathbf{E}_j \mathbf{E}_l^* e^{i(\mathbf{k}_j - \mathbf{k}_l) \cdot \mathbf{r}}, \quad \mathbf{E}(\mathbf{r}) = \sum_{j=1}^L \mathbf{E}_j e^{i\mathbf{k}_j \cdot \mathbf{r}}, \quad (6.1)$$

can be realized. Some examples of the resulting light distributions, i.e. potentials for the atoms, are shown in Fig. 6.1. It is important to understand that each pattern results from many beam interferences (see (6.1)), and thus it is obvious that the pattern depends on the relative phase between the beams. In the case of two and three beam interference this only leads to a shift of the pattern while the ‘light crystal’ symmetry is invariant under the phase change. For more beams, the phase change, as indicated on the right-hand side in Fig. 6.1, leads to different pattern shapes. In the real experiment, controlling the phase implies a mechanical stability of the light path lengths much better than a wavelength. However, this sensitivity is easily suppressed by using the fact that the atoms have inertia and hence can only react to potential changes at a finite time. The desired pattern is usually built up with standing light waves (two beam interference), i.e., periodic potentials, but the frequencies of the standing light waves are chosen differently. Therefore, the cross interference terms are not stationary but lead to moving patterns. As we will see below, the resulting velocity is directly proportional to the frequency difference. Using MHz frequency differences, straightforwardly realized by acousto

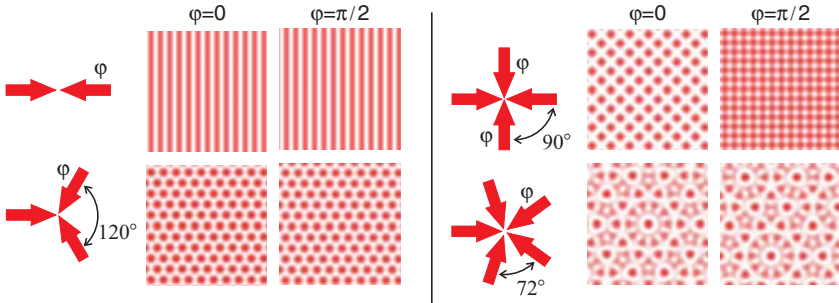


Fig. 6.1. A selection of OLs. The light intensities are a result of the many beam interferences, as indicated. In the special case of two and three beam interference, a change of the relative phase does not affect the symmetry of the intensity distribution but only leads to a translation. In the case of four and more beam interference the pattern symmetry becomes dependent on the relative phase

optical modulators, the many beam interferences are perfectly averaged out on the typical timescale of the motion of the atoms.

In the special case of two counter propagating interfering light beams with wavelength λ , a potential of the form $V(x) = \frac{V_0}{2} \cos(4\pi x/\lambda)$ is realized. Introducing a small (kHz range) frequency difference $\Delta\nu$, a moving periodic potential with velocity $v = \nu\lambda/2$ is realized. Since the frequency difference is easily controlled experimentally, OLs can be accelerated and moved with constant velocity arbitrarily on the time scale of the motion of the atoms. Combined with the ability to control the light intensity, i.e. potential height, the optical potentials constitute the work horse for coherent manipulation of ultra cold gases and BECs.

6.3 BEC in a Periodic Potential: Theoretical Formalism

6.3.1 Mean-Field Model

In the theoretical modeling of the nonlinear dynamics of matter-waves in OLs, we rely on the mean-field Gross–Pitaevskii equation (GPE):

$$i\hbar\psi_t = \left[-\frac{\hbar^2}{2m} \nabla^2 + g_{3D} |\psi|^2 + V(r) \right] \psi, \quad (6.2)$$

where ψ is wavefunction, m is atomic mass, $g_{3D} = 4\pi\hbar^2 a/m$, a is the s -wave scattering length. The trapping potential, $V(r)$, in general consists of an anisotropic magnetic or optical trapping component and a periodic OL:

$$V(x, r) = \frac{m}{2} (\omega_x x^2 + \omega_y y^2 + \omega_z z^2) + V_{OL}(x, y), \quad (6.3)$$

where, $\omega_{x,y,z}$ are the harmonic trap frequencies.

In this chapter we will primarily focus our attention on the cases of a one-dimensional (1D) OL potential:

$$V_{\text{OL}}(x) = V_0 \sin^2(kx), \quad (6.4)$$

and the simplest “square” two-dimensional (2D) OL:

$$V_{\text{OL}}(x, y) = V_0 [\sin^2(kx) + \sin^2(ky)], \quad (6.5)$$

created by a pair (two pairs) of interfering laser beams with the same wavelength λ (see Sec. 6.2). The periodicity of the OL is defined by $d = \pi/k = (\lambda/2) \sin(\varphi/2)$, where φ is the angle between the laser beams.

Equation (6.2) can be made dimensionless using the characteristic length $a_L = d/\pi$, energy $E_L = 2E_r = \hbar^2/m a_L^2$, and time $\omega_L^{-1} = \hbar/E_L$ scales of the lattice. In these units, the two-body interaction coefficient is given by $g_{3D} = 4\pi(a_s/a_L)$, and the lattice depth is measured in units of the lattice recoil energy, E_r .

6.3.2 Linear Bloch Waves

For the case of a condensate trapped in an effectively 1D atomic waveguide with the trapping frequencies ω_x and $\omega_{y,z} \equiv \omega_\perp$, co-aligned with a 1D OL along the x -axis, our mean-field model can be reduced to a 1D GPE with a periodic potential. This reduction is possible as long as the excitations in the transverse directions can be assumed to be “frozen” (see discussion in Sect. 6.5.1). In this case, the transverse wavefunction can be described by the ground state of a 2D radially symmetric quantum harmonic oscillator, with the normalization condition: $\int_{-\infty}^{\infty} |\Phi|^2 dr = 1$. The 3D wavefunction then separates as $\Psi(x, r, t) = \Phi(r)\psi(x, t)$, and the transverse dimensions can be integrated out in (6.2) [3], yielding the 1D GPE:

$$i \frac{\partial \psi}{\partial t} = \left\{ -\frac{1}{2} \frac{\partial^2}{\partial x^2} + V_{\text{OL}}(x) + \sigma |\psi(x, t)|^2 \right\} \psi \quad (6.6)$$

where the wavefunction is rescaled as $\psi \rightarrow \psi \sqrt{g_{1D}}$, $g_{1D} = 2(a_s/a_L)(\omega_\perp/\omega_L)$, $\sigma = \text{sign}(g_{1D})$, and the external potential is approximated by (6.4), by neglecting the contribution of the harmonic confinement in the direction of the lattice.

The stationary states of a condensate in a 1D OL are described by solutions of (6.6) of the form: $\psi(x, t) = \phi(x) \exp(-i\mu t)$, where μ is the corresponding chemical potential. In the case of a noninteracting condensate ($g_{1D} = 0$), the condensate wavefunction can be presented as a superposition of Bloch waves, $\phi(x) = b_1 \phi_1(x) e^{iqx} + b_2 \phi_2(x) e^{-iqx}$, where $\phi_{1,2}(x)$ have periodicity of the lattice potential, $b_{1,2}$ are constants, and q is the quasimomentum. The linear matter-wave spectrum consists of bands of eigenvalues $\mu_{n,q}$ in which $q(\mu)$ is a (real) wavenumber of Bloch waves [4]. The bands are separated by gaps in which $\text{Im}(q) \neq 0$. The solutions at the band edges are stationary matter-wave Bloch states shown in Fig. 6.2.

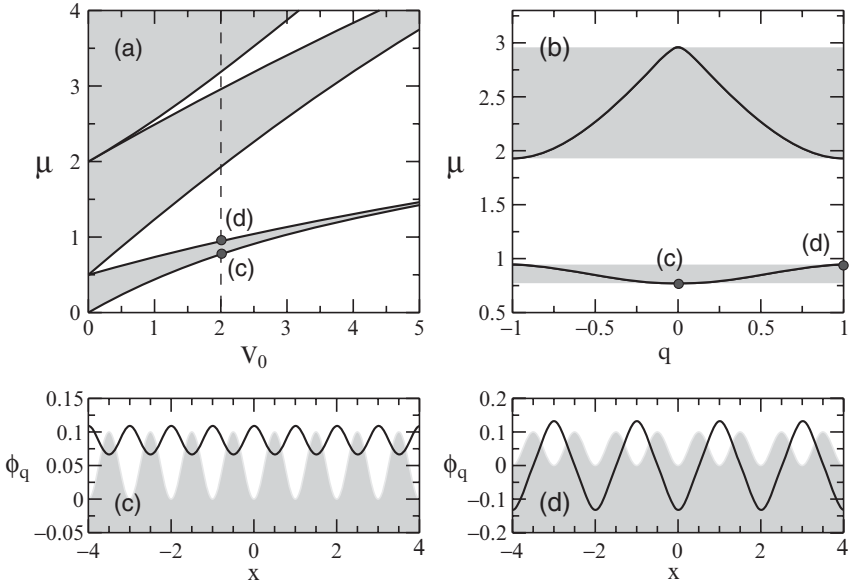


Fig. 6.2. (a,b) Band-gap structure and (c,d) Bloch matter-waves corresponding to (c) the middle and (d) the edge of the ground band in a 1D OL for $V_0 = 2.0$

Similar reduction of dimensionality in the model (6.2) can be performed in the case of a “pancake” condensate cloud trapped in a 2D OL (6.5). In this case we assume that the weak confinement characterized by trap frequencies $\omega_{x,y}$ has little effect on the stationary states of the condensate in the 2D lattice formed in the (x,y) plane of the condensate cloud. Under this assumption, the trap component of the confining potential in the lattice plane can be neglected, and the model can be reduced to a 2D GPE:

$$i\frac{\partial\psi}{\partial t} = \left\{ -\frac{1}{2}\nabla_{\perp}^2 + V_{\text{OL}}(x, y) + \sigma|\psi|^2 \right\} \psi. \quad (6.7)$$

where $\nabla_{\perp} = \partial^2/\partial x^2 + \partial^2/\partial y^2$, $V_{\text{OL}}(x, y)$ is the periodic potential of the OL, $\sigma = \text{sign}(g_{2D})$, and the wavefunction is rescaled as $\psi \rightarrow \psi\sqrt{g_{2D}}$, with $g_{2D} = g_{3D}/\sqrt{2}$.

Stationary (time-independent) states of the condensate in an infinite periodic potential of a 2D OL are described by solutions of (6.7) of the form: $\psi(\mathbf{r}, t) = \phi(\mathbf{r}) \exp(-i\mu t)$, where μ is the chemical potential, corresponding to the energy level of the stationary state in the lattice potential. In the case of a noninteracting condensate, the stationary wavefunction can be sought in the form $\phi(\mathbf{r}) = u_{\mathbf{q}}(\mathbf{r}) \exp(i\mathbf{q}\mathbf{r})$, where the wavevector \mathbf{q} belongs to a BZ of the OL, and $u_{\mathbf{q}}(\mathbf{r}) = u_{\mathbf{q}}(\mathbf{r} + \mathbf{d})$ is a periodic (Bloch) function with the periodicity of the lattice. The band-gap structure of the spectrum $\mu(\mathbf{q})$ of the atomic

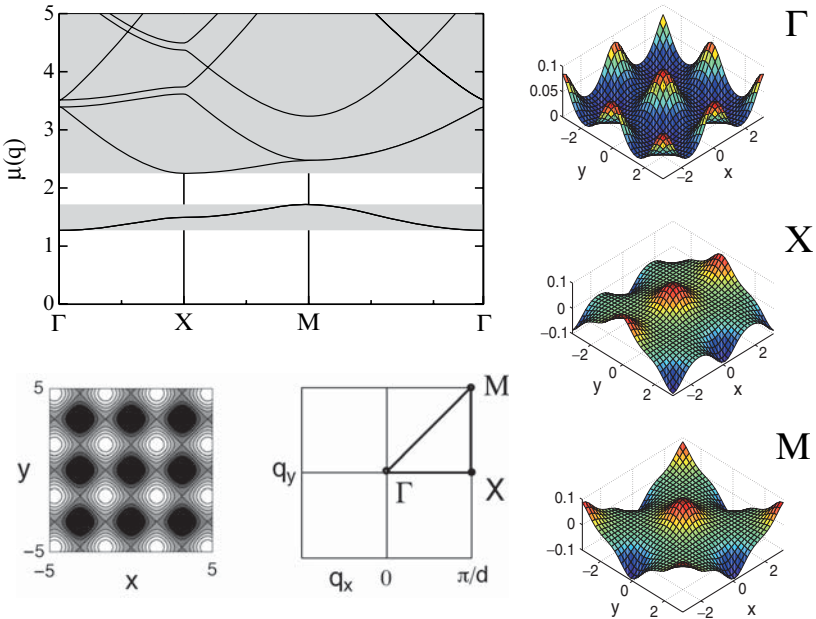


Fig. 6.3. Band gap structure and corresponding Bloch matter-waves at the three high symmetry points, Γ , X , and M of the first irreducible BZ in a square 2D OL ($V_0 = 1.5$) [5]

Bloch waves in the square 2D lattice (6.5) is shown in Fig. 6.3, in the reduced zone representation.

In the presence of nonlinearity, three basic classes of nonlinear stationary states are supported by an OL. These are spatially extended nonlinear Bloch waves, truncated Bloch waves or self-trapped states with an arbitrary localization length, and strongly localized matter-wave gap solitons. The knowledge of the structure of the band-gap spectrum of the linear Bloch waves is essential for our understanding of the phenomenon of nonlinear localization that occurs due to the interplay of the lattice periodicity and the intrinsic nonlinearity of matter-waves.

6.3.3 Nonlinear Bloch Waves

Although Bloch waves are a concept originally applied to the linear systems, spatially extended nonlinear Bloch waves with the periodicity of the lattice potential exist also in the presence of atomic interaction (see Fig. 6.4). When the nonlinearity is weak, the nonlinear Bloch states are qualitatively similar to the linear ones. As the local condensate density (and hence the nonlinearity) grows, the chemical potential associated with the Bloch state at the edges of the linear band “shifts” into the gap of the linear spectrum. The magnitude of

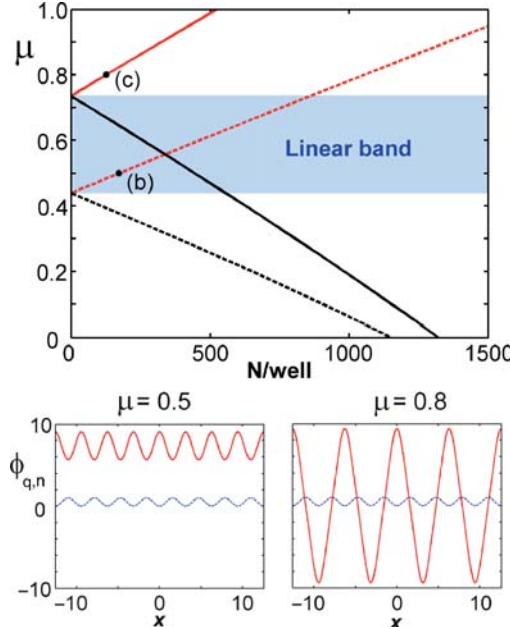


Fig. 6.4. *Top:* Nonlinear shift of the band edges corresponding to the Bloch states at quasimomenta $q = 0$ (dashed) and $q = 1$ (solid) for a repulsive [lines marked with points (b) and (c)], $g_{1D} = 0.001$, and attractive (unmarked lines), $g_{1D} = -0.001$, condensate in a shallow 1D OL ($V_0 = 1.0$), shown as a dependence of chemical potential on the number of atoms per lattice site. *Bottom:* Spatial structure of the nonlinear Bloch waves for a repulsive BEC corresponding to marked points in the top panel, low-amplitude curves depict the lattice potential. (figure courtesy of P.J.Y. Louis [7])

the shift is proportional to the nonlinearity, while its direction is determined by the sign of the scattering length. In the experiments, the condensate can be loaded into the ground or excited Bloch state with a high degree of control [6]. Such loading is usually performed in the density regimes when the condensate behavior is linear or only weakly nonlinear.

The nonlinear Bloch waves at different values of quasimomenta have different stability properties. In a repulsive BEC ($g = 1$), Bloch states corresponding to the bottom of the ground band ($q = 0$) are stable. On the contrary, the nonlinear Bloch states corresponding to the edge of the BZ ($q = 1$), or the top of the linear ground band exhibit the so-called modulational (or dynamical) instability [8], which arises in response to inevitable small fluctuations of the condensate density and results in the exponential growth of Bogoliubov excitations. The dynamical instability has been detected experimentally, when the condensates with large numbers of atoms were adiabatically driven to the edge of the BZ, or nonadiabatically loaded into the $q = 1$ state [9–11]. It leads

to spatial fragmentation of the BEC density and enhanced loss of condensate atoms to the thermal (uncondensed) fraction. However, as will be discussed in Sect. 6.5.2, the nonlinear instability of the Bloch states also underpins the effect of nonlinear localization of repulsive condensates, and it is linked to the formation of atomic gap solitons.

6.4 Dispersion/Diffraction Management: Experiment

Quantum mechanically, any wave packet with a finite spatial width in free space will undergo dispersion, i.e. will expand with a velocity that is inversely proportional to its original size. In the presence of a periodic potential, dispersion still takes place, but now the effect of the periodicity of the potential has to be taken into account. Very often it is sufficient to approximate the true dispersion relation, i.e. energy momentum relation $E(q)$, with a parabola [see Fig. 6.5e]. Here, in the linear case, the energy, E , is equivalent to the chemical potential, μ (in general the chemical potential also includes mean-field interaction energy). Since in free space the dispersion relation is also quadratic in momentum, the curvature of the parabola can be directly associated with an effective mass. As depicted in Fig. 6.5, this mass can be positive or negative resulting in either normal or anomalous dispersion. In both cases the dispersion will lead to a spreading of the wave packet, but in the negative mass regime the effective time evolution is running backwards (due to the symmetry of the Schrödinger equation in free space: $m < 0, t > 0 \rightarrow m > 0, t < 0$). This control has been demonstrated experimentally [12–14], where both regimes were experimentally explored. It was shown that an OL can be used to effectively control the dispersion of a BEC. This dispersion management is analogous to similar schemes used in fiber optics [15].

In the following, we will discuss how weak OLs can be used to modify the dispersion of matter-wave packets, focusing on the control of the spreading of the wave packets. The experimental protocol is depicted in Fig. 6.5. The ^{87}Rb BEC with repulsive atomic interaction is realized in a crossed beam dipole trap (Fig. 6.5a). After one of the light beams is switched off, two additional light beams are slowly switched on, forming a periodic potential along the waveguide (Fig. 6.5b,c). With that procedure the atoms are adiabatically prepared at the quasimomentum $q = 0$. If the periodic potential is not accelerated the expansion of a wave packet centered at the quasimomentum $q = 0$, corresponding to the positive effective mass (i.e. normal dispersion), can be studied. In contrast, if the potential is slowly accelerated to the velocity $v = \hbar k/m$, the atomic cloud is prepared at the BZ edge i.e. expansion is governed by the anomalous dispersion (situation depicted in Fig. 6.5d). In both cases the wave packet expands as shown in the right panels of Fig. 6.5. Since in the linear regime the realization of negative mass corresponds to a time reversal, the initial expansion in the normal mass regime can be compensated by

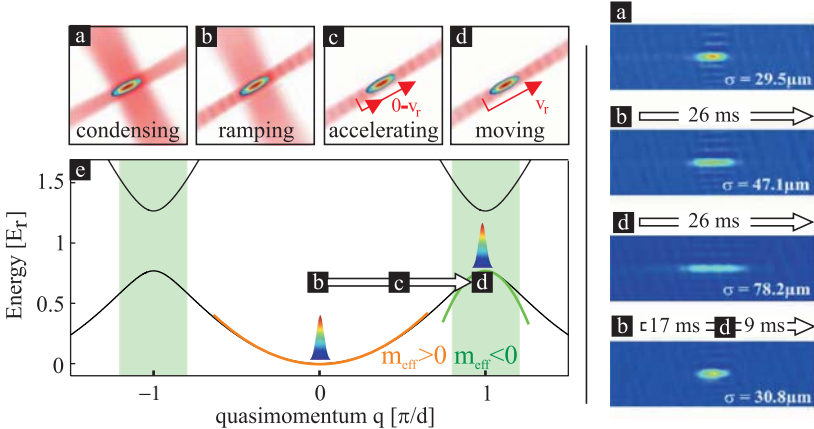


Fig. 6.5. (a) Preparation of atoms in a crossed beam dipole trap leading to a small initial wave packet. (b) Slow ramping up of the periodic potential prepares the atom at the positive mass regime – normal dispersion. (c,d) Accelerating the OL to a constant velocity prepares the atoms in the negative mass regime. In both cases the expected broadening of the wave packet is observed. If the dispersion is switched from one regime to the other during the propagation by changing the velocity of the periodic potential, the effects of normal and anomalous dispersion cancel. The wave packet, which has initially broadened under the influence of normal dispersion, reverses its expansion and compresses until it regains its initial shape

propagation in the negative mass regime. The experimental demonstration of this effect can be seen in Fig. 6.5.

It is important to note that up to now we have neglected the interaction between the atoms present in a BEC. Especially in the negative mass regime the initial propagation is significantly affected by the interaction. The negative mass implies that the repulsive atom-atom interaction leads to a contraction of the atomic cloud and thus to an increase in atomic density, implying an increase of the interaction energy leading to faster compression. This is very similar to the implosion/collapse exhibited by attractive condensates in a 3D trapping geometry. However, in the case discussed here the compression only happens along the direction of the 1D periodic potential. This collapse will continue until the interaction energy becomes comparable to the transverse trapping frequency and thus will lead to the excitation of transverse motion. This manifests itself in a heating of the gas and has actually been observed experimentally [13]. For the wave packet dynamics discussed here this fact massively simplifies the theoretical description, since the reduced density allows us to use the linear theory. With that in mind, the observed rectangular shape of the wave packets (see Fig. 6.6) can be understood as a direct consequence of the anharmonicity of the dispersion relation which implies a maximum expansion velocity corresponding to an infinite effective mass. The direct comparison with theory in Fig. 6.6 shows the quantitative

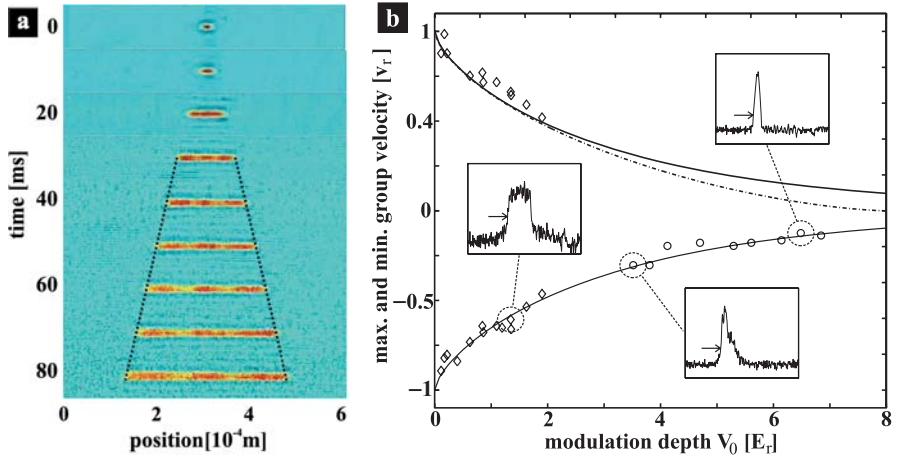


Fig. 6.6. Linear propagation with higher order dispersion. (a) Absorption images for the expansion time in the waveguide as indicated. The wave packets become square shaped, clearly revealing the effect of the high order dispersion. The *dotted lines* indicate the maximum allowed velocity in the lowest band for the chosen potential height of $0.44E_r$. (b) Quantitative agreement between measured and predicted maximum velocity as a function of potential height

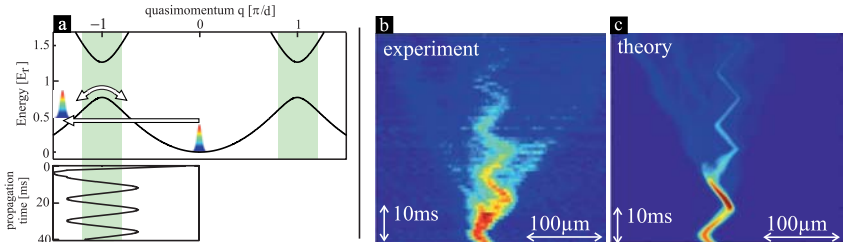


Fig. 6.7. Dynamical dispersion management for matter-waves. (a) The quasimomentum is periodically changed by exciting transverse dipole oscillations of the condensate. (b) The experimental observation of suppression of dispersion. (c) In the theoretical description the interaction between the atoms is taken into account and explains the observed dynamics, as well as the radiation, quite well

agreement of the linear description and experimental observations in the long time limit.

Continuous dispersion management can be implemented by applying a periodic force on the atoms leading to a temporal change of the quasimomentum following from Newton's law: $\hbar\dot{q}_c = F$. In Fig. 6.7 the experimental results are shown and compared with theory [14]. Clearly, continuous dispersion management allows to inhibit dispersion, but due to the residual atom–atom interaction (also taken into account in the theoretical description), the spreading cannot be totally suppressed and thus the wave packet eventually splits up.

6.5 Gap Solitons

6.5.1 Bright Solitons in Repulsive BEC

Theory

The concept of the effective mass, used to elucidate the mechanism for the diffraction/dispersion management of a BEC wave packet in a linear regime, can also be employed in the situation when the nonlinearity plays an important role in the condensate dynamics. Here we will consider this regime in more detail. The nonlinear dynamics of a BEC wave packet prepared in a spectral band with the index n can be described by using the Bloch-wave envelope approximation [16, 17]. In the 1D case, the approximation yields: $\phi = f(x, t)\phi_{q,n}(x) \exp(-i\mu t)$, where μ is the chemical potential, $\phi_{q,n}$ is the linear Bloch wave corresponding to the quasimomentum q , and $f(x, t)$ is a slowly varying envelope. The behavior of the envelope, $f(x, t)$ is then governed by the reduced Gross–Pitaevskii model:

$$i\frac{\partial f}{\partial t} = \left(-\frac{D}{2}\frac{\partial^2}{\partial x^2} + \tilde{g}_{1D}|f(x, t)|^2 \right) f(x, t), \quad (6.8)$$

where $D = \partial^2\mu/\partial q^2 = \partial v_g/\partial q$ is the effective group velocity dispersion, and $\tilde{g}_{1D} = g_{1D} \int |\phi_{q,n}|^4 dx / \int |\phi_{q,n}|^2 dx$. It can be seen that, depending on the curvature of the spectral band, the effective dispersion of a wave packet can be positive or negative. The effective dispersion (or the inverse effective mass $D = m_{\text{eff}}^{-1}$) of the matter-wave packet becomes negative near the top edge of the ground band ($n = 0, q = 1$). This anomalous dispersion can effectively lead to focusing of the matter-wave packet, as described in the previous section.

Moreover, the balance of the repulsive mean-field interaction ($g_{1D} > 0$) and negative dispersion near the top of every spectral band (see Fig. 6.2), can lead to formation of spatially localized nonspreadng wave packets – *matter-wave solitons* with zero group velocity. The chemical potentials corresponding to such localized waves lie in the gaps of the linear Bloch-wave spectrum.

By employing the multi-scale perturbation series expansion for the chemical potential and the gap soliton envelope, it is possible to show that, in general, two types of gap solitons bifurcate from each band edge [18]. These are the bright solitons centered on the maximum (off-site) and minimum (on-site) of the lattice potential, respectively. Families of the on- and off-site gap solitons are presented in Fig. 6.8, for the case of a repulsive condensate. The families are characterized by the number of atoms, N , in a localized state. Such localized states exist within all gaps [4, 19].

The spatial structure of gap solitons (see Fig. 6.8) [4, 20] illustrates one of the key issues in their experimental observation [21]. In the experiment, the condensate is driven to the top edge of the ground band in a moving 1D OL in order to reach the regime of $D < 0$. This procedure ensures that the gap soliton forms close to the bifurcation point, near the bottom edge of the

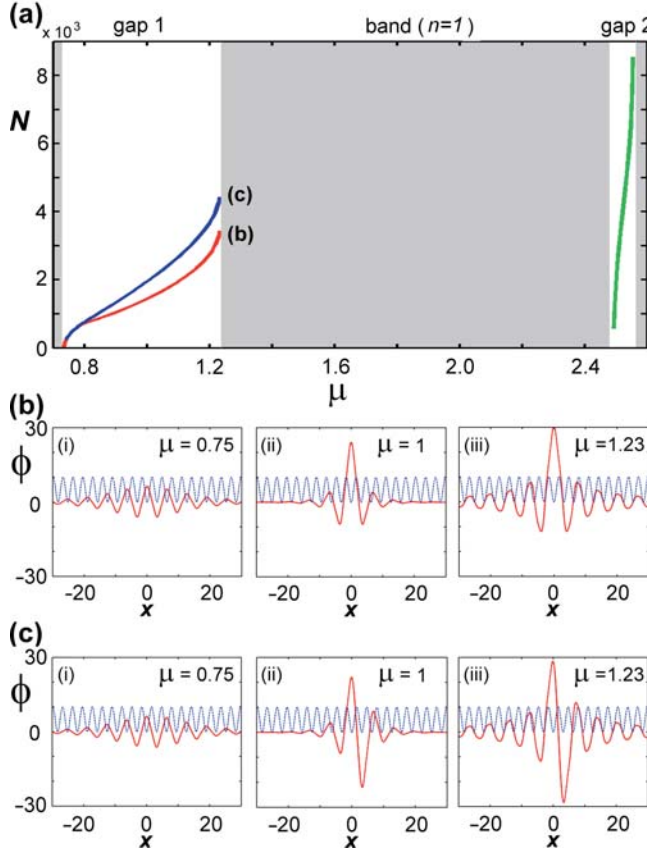


Fig. 6.8. (a) Bifurcations of matter-wave gap solitons off the linear band edges in a 1D OL ($g_{1D} = 0.001$, $V_0 = 1.0$). Panels (b,c) show the spatial structure of the on-site [row (b)] and off-site [row (c)] states (figure courtesy of P.J.Y. Louis [7])

spectral gap (Fig. 6.8i). At this point a gap soliton is well approximated by a broad, low-amplitude sech-like envelope $f(x)$ of the corresponding Bloch wave, centered either on- or off-site. The soliton is relatively weakly localized and has low density (number of particles). This one of the reasons why preparation of a very small condensate was required to observe a 1D gap soliton in an experiment, another reason being the need to avoid transverse excitations, as explained in the following Section. The distinction between the on-site and off-site states does not play significant role in their dynamical formation because the off-site state undergoes symmetry-breaking instability and transforms into a stable on-site state.

The envelope theory can also be successfully applied to condensates in 2D and 3D OLS [22]. In higher dimensions, the effective dispersion (mass) of the matter-wave packet becomes a tensor quantity. In order to achieve the

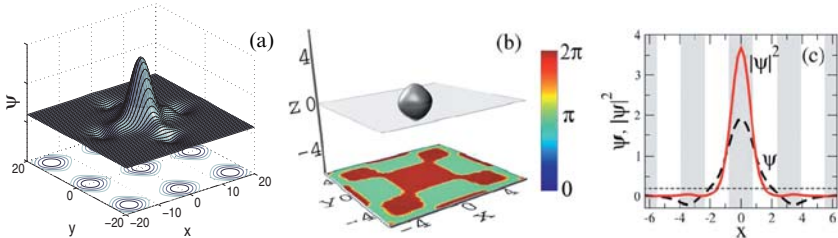


Fig. 6.9. (a) Atomic gap soliton in a 2D OL ($g_{1D} = 1$, $V_0 = 1.5$, $\mu = 0.9$). (b) Density and (c) cross-cuts of the condensate wavefunction (dashed) and density (solid) for a gap soliton in a 3D lattice ($\mu = 7.9$, $V_0 = 6.0$)

anomalous dispersion regime and formation of bright gap solitons in a repulsive condensate, all components of the dispersion tensor must be negative. This condition is realized only at the edges of complete spectral gaps. Theory predicts that both 2D and 3D gap solitons exist in the complete spectral gaps [23, 24]. Their typical spatial structure is shown in Fig. 6.9 for chemical potentials corresponding to the middle of the first complete gap. The “staggered” phase structure of the gap soliton tails, resulting from the underlying Bloch state is clearly visible in Fig. 6.9.

Experiment

In the following we will focus on the experimentally observed case of the 1D propagation of interacting matter-waves in a weak periodic potential. Furthermore, we will restrict our discussion to the case of the condensate prepared at the BZ edge, as discussed above.

The first experimental requirement is a 1D waveguide for a condensate. Such a waveguide can be realized with a slightly focused laser beam utilizing the discussed dipole force (see Sect. 6.2). One-dimensional dynamics is expected as long as no transverse excitations occur. In the noninteracting situation, the transverse degrees decouple perfectly but, in the interacting case, care has to be taken. Naively one would thus expect that higher transverse frequencies are favorable to realize a 1D situation, but the opposite is the case. The interaction energy is proportional to the density of the atoms and thus also increases with increasing transverse trapping frequency. As a matter of fact, it turns out that the criterion for reaching the 1D situation is given *only* by the condition that the linear density has to be smaller than the critical density $n_{1D} < 1/2a$ where a is the s -wave scattering length. For ^{87}Rb this corresponds to $n_{1D} < 100 \text{ atoms } \mu\text{m}^{-1}$. Clearly, even in this regime, there will be a residual coupling of the different transverse states leading for example to a finite life time of solitons, but ideally this coupling is negligible for the time scales of interest (for detailed discussion see [25]). Thus, for 1D experiments with BECs one would choose the counter intuitive approach, namely a weak

transverse confinement, in order to increase the total number of particles but keeping the density smaller than the critical one.

Given that the physical situation is described as 1D, and the momentum distribution is small enough, such that the effective mass approximation can be applied, the total number of atoms in a gap soliton is given by $N = \hbar/a\alpha_{nl}\omega_{\perp}x_0m_{\text{eff}}$ where a represents the s -wave scattering length, with the numerical factor α_{nl} taking into account the increase in peak density due to the periodic potential (in the limit of weak periodic potentials ($\alpha_{nl} = 1.5$ for $q = \pi/d$ [17]), ω_{\perp} represents the transverse trapping frequency, x_0 is the soliton width and m_{eff} is the effective mass at the band edge. The inverse scaling of the total number of particles with the transverse trapping frequency is compatible with the statement about the one-dimensionality made above. Also, the inverse mass and wave packet size scaling is qualitatively obvious since a stronger dispersion has to be compensated by a stronger interaction. For experimentally achievable parameters for Rb atoms the total number of atoms is of the order of few hundred particles.

Historically, it turned out, that the main difficulty in the experiment is that the number of atoms in the initial condensate has to be below 1,000 atoms, otherwise transverse excitations due to the initial collapse are unavoidable. After many unsuccessful attempts to directly produce small atom number condensates the solution was to coherently remove atoms utilizing Bragg scattering just before the preparation to the band edge. The consequent acceleration of the periodic potential leads to the preparation of the resting atoms at the BZ edge while the moving atoms perform Landau-Zener tunneling to the upper bands and thus just stay behind, i.e. they are not accelerated. The experimental observation of the formation of the soliton is shown in Fig. 6.10. As expected, a spatially localized soliton is formed while the excessive atoms are ‘radiated’. They form a square shaped pedestal which expands as a linear wave, with the maximal group velocity of the lowest band (see Sect. 6.4).

The atomic system in an OL enables a very direct control of the effective mass. The dynamics for different signs of the mass can be easily checked by comparing the evolution in a accelerated and moving (negative mass) and a resting (positive mass) periodic potential. Analysis of the width of the observed wave packet makes it obvious that the repulsive interaction can only compensate for the spreading due to dispersion if the mass is negative. As can be seen in Fig. 6.11a, the wave packet explodes in the positive mass regime while a nonspreadng packet is formed in the negative mass regime. Since the width of the gap monotonically increases with the height of the periodic potential (see Fig. 6.2a), the absolute value of the effective mass at the band edge can be tuned by changing the intensity of the standing light wave forming the periodic potential. Thus the scaling of the product of atom number in the soliton and its width, $Nx_0 \propto 1/m_{\text{eff}}$, can be directly confirmed as depicted in Fig. 6.11b. Further details can be found in [21].

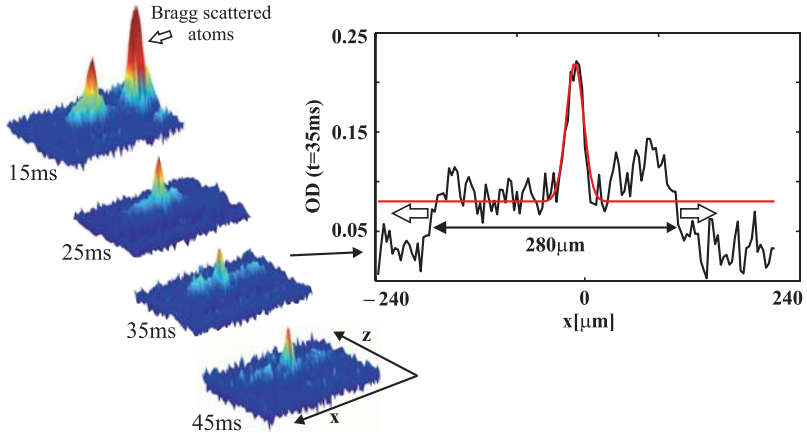


Fig. 6.10. Single absorption images revealing the preparation of atomic gap-solitons. The images are shown in the co-moving frame of the OL. Thus only at the early times of preparation 15 ms the removed (Bragg scattered) atoms are visible. The inset shows that the soliton is formed on top of radiated atoms forming a square shaped wave packet expanding with the maximal velocity allowed the lowest band

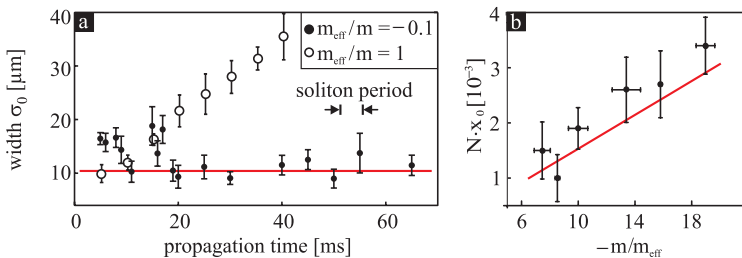


Fig. 6.11. Systematics on gap solitons. (a) Comparison of propagation in the positive and negative mass regime. Clearly in the repulsive atom–atom interaction regime nonspread ing wave packets are only formed in the negative mass regime (*filled circles*). In the positive mass regime the atomic cloud explodes (*empty circles*). (b) The product of atom number and width of the soliton scales inversely with the effective mass. The solid lines represent the prediction of the simple 1D effective mass theory without free parameters since the potential height and trapping frequencies can be measured independently

6.5.2 Soliton Trains and Anomalous Heating

As pointed out in Sect. 6.5.1, the experimental observation of a 1D gap soliton [21] required initial preparation of the condensate with a small number of atoms in the ground state of the 1D lattice, i.e. in the middle of the BZ. The BEC was then driven to the edge of the BZ by adiabatically accelerating the OL, followed by evolution at the band edge in the lattice moving with a constant velocity. A similar loading procedure, but with condensates containing

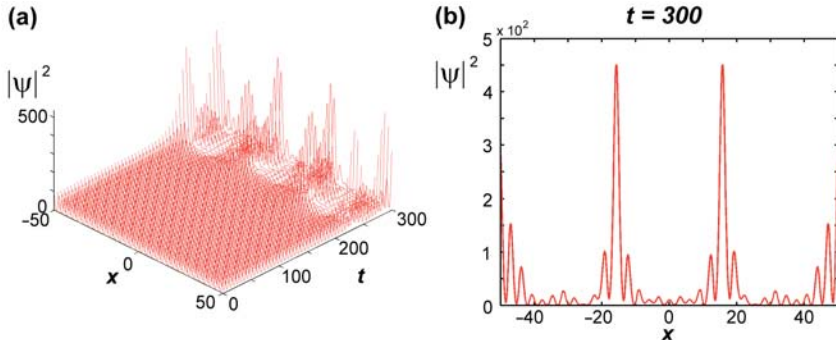


Fig. 6.12. Formation of gap soliton trains during evolution of the unstable homogeneous Bloch state. Shown are (a) temporal evolution of the condensate density, and (b) final “train” state at $t = 300$ ($g_{1D} = 10^{-3}$, $\mu = 0.8$, $V_0 = 1.0$) (figure courtesy of P.J.Y. Louis [7])

a large number of atoms [9, 11] enabled observation of another intrinsic non-linear effect – the dynamical (modulational) instability of the Bloch wave at the BZ edge and associated anomalous heating of the condensate.

On the other hand, theoretical predictions based on the 1D mean-field model [8], have indicated that the dynamics of a Bloch wave beyond the onset of the dynamical instability can lead to the formation of gap soliton trains, as shown in Fig. 6.12, for the case of an infinite (homogeneous) Bloch wave. More realistic dynamical simulations of the experimental loading procedure performed with the initial wave packet of a finite width, containing a large number of atoms [26], have confirmed that the inhomogeneous unstable Bloch states also decay into trains of localized gap solitons.

Although the dynamics beyond the onset of the modulational instability in a moving lattice has been linked to both, formation of gap solitons [26, 27] and anomalous heating [9], the result of the competition between these two effects cannot be captured by the mean-field model. Instead, the truncated Wigner method, which incorporates both thermal atoms and quantum fluctuations, can be employed in the analysis of the condensate dynamics [28].

In the framework of truncated Wigner approach (TWA), the atomic field of a BEC in a 1D OL is described by a stochastic wavefunction $\alpha(x)$ that obeys the dynamical equation [29, 30] formally identical to the 1D GPE (6.6). The difference from the Gross–Pitaevskii theory arises in the stochastic initial conditions, where quantum or thermal fluctuations enter the description of the initial physical state. In order to obtain quantum correlations of the atomic field $\hat{\Psi}$, the stochastic GPE equation has to be solved for a large number of trajectories, whose initial states $\alpha(x, t = 0)$ are assigned according to the Wigner distribution of the assumed quantum state of the BEC. The mean-field of the condensate and its density are then found as: $\psi_0(x) \equiv \langle \hat{\Psi}(x) \rangle = \alpha(x)$, and $n_0(x) = |\psi_0(x)|^2$, where angle brackets denote quantum ensemble

average, and overline denotes stochastic average over many trajectories. The total density, including that of the thermal cloud, is given by $n_{\text{tot}}(x) \equiv n_0(x) + n_{\text{therm}}(x) = \alpha^*(x)\alpha(x) - \frac{1}{2}\delta(x,x)$, where the form of $\delta(x,x)$ depends on the chosen basis [28].

The initial state of the Bose gas is modeled as a ground state coherent condensate with Bogoliubov excitations. This is realized by using the initial state [31]:

$$\alpha(x, t=0) = \psi_0(x) + \sum_q \left(u_q(x)\eta_q\sqrt{p_q} - v_q(x)\eta_q^*\sqrt{p_q} \right), \quad (6.9)$$

where $\psi_0(x)$ denotes the ground state of the condensate and η_q is a complex Gaussian noise that has correlations: $\overline{\eta_q\eta_{q'}} = 0$ and $\overline{\eta_q^*\eta_{q'}} = \delta_{q,q'}$. The population of modes accounts for both Bose distributed thermal atoms and vacuum fluctuations with half a virtual particle per mode [32]:

$$p_q = \left[\exp \left(\frac{\epsilon_q - \mu}{k_B T} \right) - 1 \right]^{-1} + \frac{1}{2}. \quad (6.10)$$

Here T is the temperature of the Bose gas and k_B is the Boltzmann constant.

The single-trajectory TWA simulations provide the signatures of the nonlinear localization that may be seen in a “single-shot” experiment [28]. However, in order to determine populations of condensed and uncondensed atomic fractions, averaging over many trajectories is required. This is similar to the averaging over many experimental realizations. Typical results of the single-trajectory simulation are shown in Fig. 6.13a,b, for evolution of a repulsive BEC prepared at the edge of the first BZ of a 1D lattice by nonadiabatic loading technique [33]. The solitons are clearly visible in the condensate

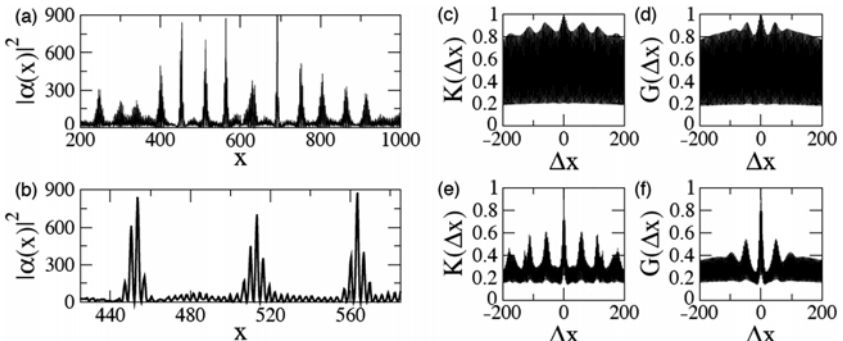


Fig. 6.13. Signatures of nonlinear localization in the single-trajectory TWA simulation of the evolution of the condensate nonadiabatically loaded into the quasimomentum $q = 1$ state. Shown are (a,b) snapshots of the condensate density showing the gap soliton train, (c,e) single-trajectory density correlation function before and after the train formation, and (d,f) integrated correlation function of the averaged over 1000 trajectories ($g_{1D} = 10^{-4}$, $V_0 = 2.0$)

density, with the single soliton containing approximately 3×10^3 atoms and displaying the characteristic “staggered” phase structure of a gap state [34]. The exact position of the solitons in every “single-shot” realization of the atom field is uncertain due to the quantum fluctuations triggering the modulational instability, and hence the signature of localization in the density does not survive averaging over many realizations (trajectories). Instead, the decay of the second order (density) correlation function of the atomic field, $K(\Delta x) = \int_{-\infty}^{\infty} dx |\alpha(x + \Delta x)|^2 |\alpha(x)|^2$, can provide clear, experimentally detectable signature of localization in both single-shot and multiple experiments (see Fig. 6.13c–f). The density correlation function captures both the average size of the localized structures and spacing between them [28].

If the dynamical instability is seeded only by the quantum noise of the initial state, like in Fig. 6.13, the solitons form at random positions in each realization of the experiment. If one would like to generate the solitons in a controlled fashion, the formation of solitons at fixed locations can be achieved by the imprinting of a periodic phase onto the initial BEC cloud before the condensate is loaded into a moving lattice. Furthermore, the phase-imprinting leads to periodic density modulations of the condensate, which facilitates the development of modulational (dynamical) instability and significantly reduces the time scale of the soliton train formation [28]. As a result, the soliton train

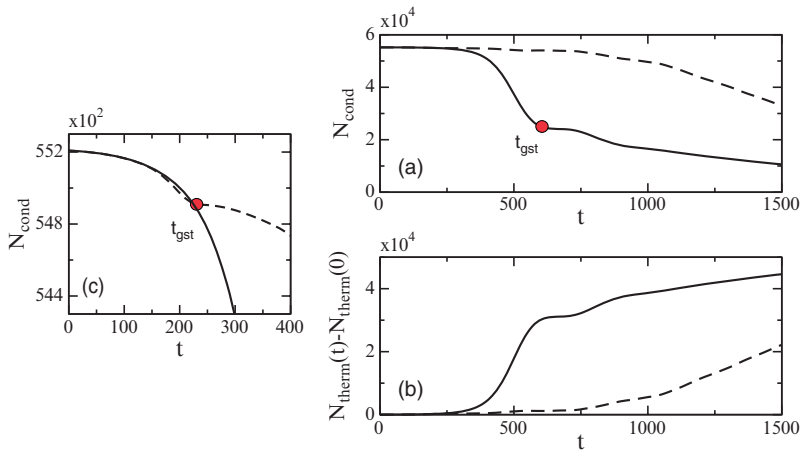


Fig. 6.14. (a) Loss of BEC atoms and (b) growth of the thermal fraction during approximately 2.5 ms of nonadiabatic loading followed by approximately 2.4 s of the evolution at the BZ edge. Shown are numbers of condensed and uncondensed atoms during the evolution without (*solid lines*) and with (*dashed lines*) the initial phase imprinting. The dot marks the approximate time of the gap soliton train formation in the scenario without initial phase imprinting. *Left panel:* A close-up on the atom loss curves in (a) with the dot marking the time of gap soliton train formation with initial phase imprinting ($g_{1D} = 1.0$, $V_0 = 2.0$)

forms at the time when only a small fraction of BEC atoms is lost to the thermal cloud due to the anomalous heating, as seen in Fig. 6.14.

6.6 Self-Trapped States

6.6.1 Observation of the Macroscopic Self-Trapping

The experiments discussed so far have been performed in the regime of weak periodic potentials and weak interaction, i.e. the dispersion is only given by linear properties of the system. Entering the regime where this assumption is no longer justified is experimentally extremely simple, and can be achieved by increasing the light intensity of the standing light wave. With this, one reaches the regime of deep periodic potentials, where intuitive insight can be gained by assuming that the single particle wavefunction of the ground state of the individual site (Wannier state) is macroscopically occupied. Thus the resulting dynamics is governed by interaction between the atoms on each site as well as the tunneling between adjacent sites [35]. With this in mind, the global dynamics, i.e. that of the matter-wave packet envelope, can be understood qualitatively.

In the case when the atoms are prepared at the quasimomentum $q = 0$, it is expected that the initially localized atomic cloud would expand according to the high effective mass, much slower than in the absence of a periodic potential. Since we are dealing with interacting atoms, the cloud does not only expand in real space, but “explodes”, i.e. its momentum distribution also expands. In the limit of few atoms, the interaction energy will not lead to significant broadening of the momentum distribution, and thus the atomic cloud should expand according to the assumption of the constant effective mass. If the initial interaction energy is high enough to accelerate the atoms to quasi-momenta of the order of half the BZ, the assumption of a constant mass across the atomic cloud is no longer fulfilled, and thus a quantitative description within this approximation will fail. Furthermore, the interaction will lead to a new localization effect known as macroscopic self-trapping [36], connected to the formation of truncated nonlinear Bloch states [37] (see Sect. 6.6.2). From the discussion of dispersion management (Sect. 6.4), a formation of a wave packet with steep edges is expected due to the presence of infinite mass at $q = \pi/2d$ (deep potential limit). But in contrast to the experimental observations in the linear regime, the steep edges do not move. This can be understood on the microscopic level, i.e. site-to-site dynamics. The spreading of the wave packet on the single site scale results from Josephson-like tunneling from one site to another. This happens as long as the interaction energy difference between the two sites is smaller than the energy associated with the single particle tunneling, i.e. the width of the band. As soon as the interaction energy overcomes the linear tunneling energy splitting, the tunneling stops and the population imbalance is locked to its initial value [38, 39]. From this simple

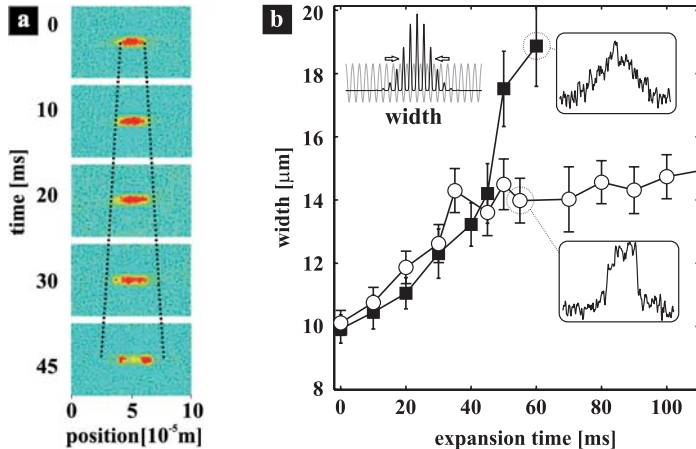


Fig. 6.15. Demonstration of nonspreadng wave packets in the deep periodic potential limit. (a) Absorption images of the atomic cloud for different expansion times in a deep periodic potential. The *dotted line* indicates the expected expansion in the linear regime. (b) Direct comparison of diffusive and self-trapped propagation. Above a critical atom number [5,000(600) atoms] the wave packet stops spreading after a short initial expansion (*open circles*). Normal spreading is observed for approximately 2,000(200) atoms (*squares*)

consideration it is expected that there exists a critical atom number (more precisely density) above which the wave packet will initially expand, then develop steep edges, and finally stop spreading.

The experimental observation of this effect can be seen in Fig. 6.15 [40]. Absorption images of the atomic gas after the indicated propagation time are depicted in Fig. 6.15a. The dotted line in the graph represents the expected expansion in the linear regime, i.e. with the maximum velocity of the lowest band. Clearly, the expansion velocity is reduced. As expected from the reasoning above, the wave packet should expand if the initial atom number is reduced. This comparison is shown in Fig. 6.15b.

Our understanding that the basic mechanism for self-trapping is the expansion of the momentum distribution, such that the quasimomenta associated with the infinite mass are populated, suggests that there is an interplay between the initial interaction energy (atomic density) and the potential height. Although the local (site-to-site) dynamics is very complex, the evolution of the root mean square width of the wave packet, i.e. the global dynamics, can be predicted analytically within a very simple model. In [36] a Gaussian profile wave packet parameterized by the width $\gamma(t)$ and the quadratic spatial phase $\delta(t)$, is used as an ansatz for quasimomentum $q = 0$ to solve the discrete nonlinear Schrödinger equation (DNLS). The time evolution of the width $\gamma(t)$ is obtained analytically, by applying a variational principle. The result of this simple model is that the dynamics of the wave packet width is solely determined by the two global parameters – the density

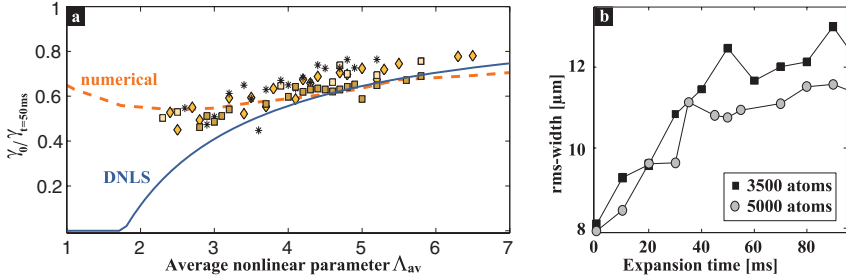


Fig. 6.16. (a) Experimental investigation of the scaling behavior. Experimentally the parameter $\Lambda_{av} \equiv \Lambda/\Lambda_c$ was varied by using three different periodic potential depths: $s = 10.6(3)$ (stars), $11.1(3)$ (squares) and $11.5(3)$ (diamonds). For each potential depth wave packets with different atom numbers and initial widths are prepared and the width for $t = 50$ ms is determined. The experimental data show qualitatively the scaling behavior predicted by the analytical scaling law (*solid line*) and are in quantitative agreement with the results of the numerical integration of the DNLS (*dashed line*). (b) The nature of the scaling: increasing Λ/Λ_c (by e.g. increasing the atom number) leads to a faster trapping (BZ edge is reached earlier due to fast momentum spread), and thus to a smaller final width

of the atoms and the depth of the periodic potential. Also a critical parameter, $\Lambda_{av} \equiv \Lambda/\Lambda_c \propto \mu_{av}^{\text{loc}}/K$, can be deduced, which governs the transition from the diffusive to the self-trapping regime (here μ_{av}^{loc} is the average local chemical potential, and K is the single particle tunneling splitting). A surprising result of this model is the prediction of a scaling behavior for the ratio of the initial to final wave packet width $\gamma_0/\gamma_\infty = 1 - \Lambda_c/\Lambda$ for $\Lambda/\Lambda_c > 1$. For $\Lambda/\Lambda_c < 1$ the width is not bound and thus the system is in the diffusive regime. Since $\Lambda/\Lambda_c \propto \mu_{av}^{\text{loc}}/K$, the self-trapping regime is reached by either reducing the initial width, increasing the height of the periodic potential or, as shown in Fig. 6.15, by increasing the number of atoms.

Scaling means that all data points, i.e. different experimental settings with the same Λ/Λ_c , collapse onto a single universal curve. The experimental results shown in Fig. 6.16 confirm the universal scaling dependence on Λ/Λ_c and follow qualitatively the prediction of the simple model. The dashed line in Fig. 6.16 is the result of the numerical integration of the DNLS equation evaluated at a chosen expansion time. It shows quantitative agreement with the experiment. The difference between the numerical (dashed line) and analytical calculation (solid line) is due to the initial non-Gaussian shape (numerically obtained ground state) and the strong deviation from the Gaussian shape for long propagation times.

6.6.2 Truncated Bloch States

Experimental observation of a single gap soliton [21] required preparation of a weakly nonlinear BEC with a small number of atoms. Macroscopic

self-trapped states discussed above represent a seemingly different localized state with steep edges and a large number of atoms [40], where the increasing nonlinearity of the BEC wave packet enables the transition from the diffusive regime of condensate expansion in a deep 1D OL to the regime where the initial expansion stops and the width remains finite. As described above, this effect can indeed be attributed to the self-trapping mechanism of energy localization described by discrete tight-binding nonlinear models [36].

However, the experimental observations [40] can also be explained by the excitation of a new type of gap state, which serves as a link between the two fundamental types of nonlinear lattice states described above – the spatially extended nonlinear Bloch waves (Sec. 6.3.2) and the spatially localized gap solitons (Sect. 6.5.1). These self-trapped states may be viewed as “truncated” nonlinear Bloch waves [37] localized in the gaps of the linear Bloch-wave spectrum (see Fig. 6.17C,D), with the “truncation” due to the macroscopic self-trapping in a Bose–Josephson junction at the edge of the localized state. Because the nonlinear Bloch states extend into the linear gaps (see Sect. 6.3.3, Fig. 6.4), the self-trapped states can be associated with a nonlinear Bloch state

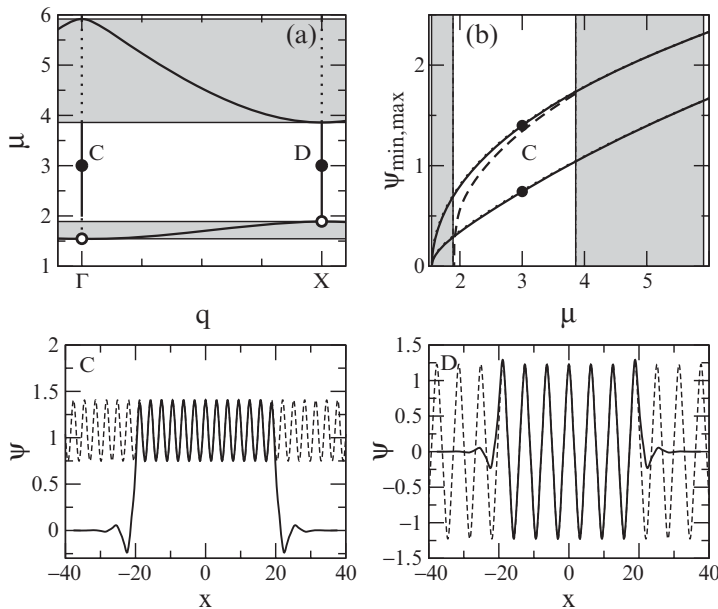


Fig. 6.17. (a) Band-gap diagram of the 1D OL ($V_0 = 4.0$) showing bifurcation of nonlinear Bloch waves (*dotted lines*) from the band edges (*open circles*) and the domain of existence of self-trapped states (*solid lines*). Bands are shaded. *Solid circles* correspond to the self-trapped in panels C and D. *Dashed lines* in C and D are the corresponding nonlinear Bloch waves. (b) Maximum (*upper solid line*) and minimum (*lower solid line*) amplitudes of the ground state nonlinear Bloch wave vs. chemical potential compared to the peak amplitude of a gap soliton (*dashed line*)

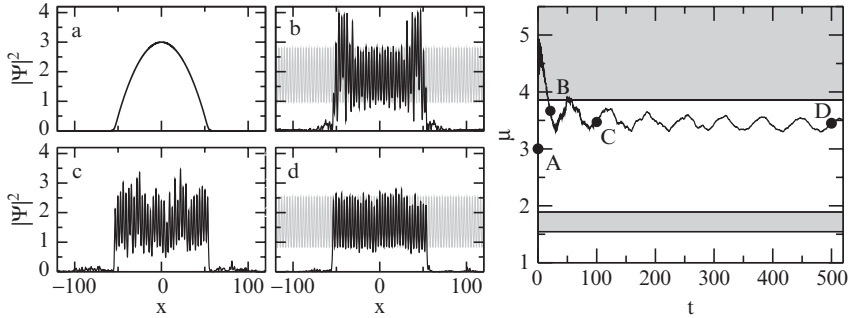


Fig. 6.18. (a–d) Time sequence of the nonadiabatic excitation of a 1D self-trapped state (d) in a 1D lattice from a Thomas–Fermi initial state (a). The external trap is switched off and the lattice ($V_0 = 4$) turned on at $t = 0$. Right panel shows the evolution of the chemical potential of the condensate relative to the band-gap structure, with the marked stages of evolution illustrated in (a–d)

corresponding to any band edge (see Fig. 6.17a). In this, the self-trapped states differ dramatically from gap solitons. The self-trapped states of the repulsive BEC existing within the first spectral gap and associated with the ground state nonlinear Bloch wave (Fig. 6.17C) are dynamically robust, whereas the truncated state corresponding to the excited nonlinear Bloch wave (Fig. 6.17D) inherits the modulational instability of the associated Bloch state. This picture reveals that, although the self-trapped gap states can be excited only above a certain density threshold [37], they exist well beyond the tight-binding regime.

Remarkably, the dynamical GPE simulations for 1D, 2D, and 3D OLs predict that the self-trapped gap states can be generated experimentally in any dimension, and for arbitrarily large initial atom numbers, by nonadiabatic loading of the BEC initially confined, e.g., in a magnetic trap into a stationary OL [37] (see Fig. 6.18). An example of resulting dynamical localization within the gap is shown in Fig. 6.18 for a 1D case. The initial number of atoms in the condensate and the width of the atomic cloud will determine the width of the self-trapped state. Its peak density, however, is bound from above by that of a gap soliton.

In 2D and 3D OLs a self-trapped state can, in principle, be used as a broad background that supports nontrivial phase states formed by phase imprinting [37], and hence provides a means for obtaining dynamically stable stationary gap vortices.

6.7 Gap Vortices

In 2D and 3D OLs nonlinear gap states of a repulsive BEC can possess a nontrivial phase [24, 42, 43]. Such states are spatially localized “gap vortices”. The existence of vortices in a lattice is not obvious due to the lack of rotationalal

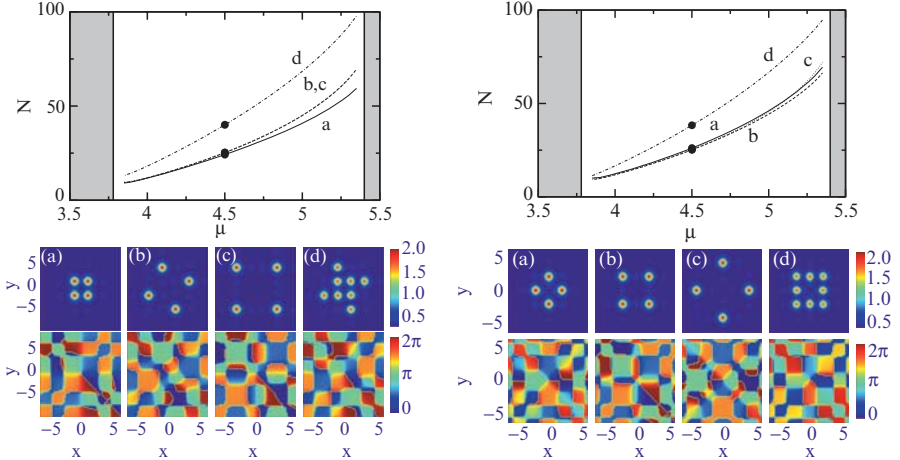


Fig. 6.19. Families of (left) off-site and (right) on-site narrow gap vortices shown as dependence of peak density on chemical potential within the first complete gap of a 2D lattice ($V_0 = 4.0$). Bottom panels show characteristic density and phase distributions for the marked families of the gap solitons [41]

symmetry and nonconservation of angular momentum. However, a vortex can exist in a lattice as a structure with the atomic density strongly modulated by the lattice, indicating a persisting circular particle flow, and a phase singularity at the core, which is a telltale of a vortex structure [43, 44]. The density and phase structure of the two basic types (on-site and off-site) of gap vortices with the narrowest localization area are shown in Fig. 6.19. The phase distribution shows characteristic $0 \rightarrow 2\pi$ winding of a vortex phase in the central area and π phase modulation of the vortex “tails”.

Examination of the particle flow around the core of gap vortices shows that vortices of different symmetry types have different physical origin. Indeed, the complicated flow structure associated with on-site vortices (Fig. 6.20b) and wide-radius off-site vortices shown in (Fig. 6.19, left, b–d) reveals their link to the M -point Bloch state at the edge of the complete gap (see Fig. 6.3). For instance, the narrowest four-site on-site vortex can be interpreted as a $0 \rightarrow 2\pi$ phase ramp imprinted onto a cluster of four gap vortices, with the structure of the “far-field” wavefunction identical to that of the M -point Bloch state. In contrary, the simplest off-site vortex (Fig. 6.19, left, a) displays a simple particle flow (Fig. 6.20a) that connects it to broad vortices imprinted onto truncated Γ -point Bloch states (Fig. 6.20c,d). These broad vortices can be found with an arbitrary area of localization and for an arbitrary large particle number in a localized state [41]. They can be interpreted as a $0 \rightarrow 2\pi$ phase ramp imprinted onto a 2D self-trapped gap state.

The mean-field simulations of the BEC dynamics suggest that a single vortex prepared in a magnetic trap can be nonadiabatically loaded into a

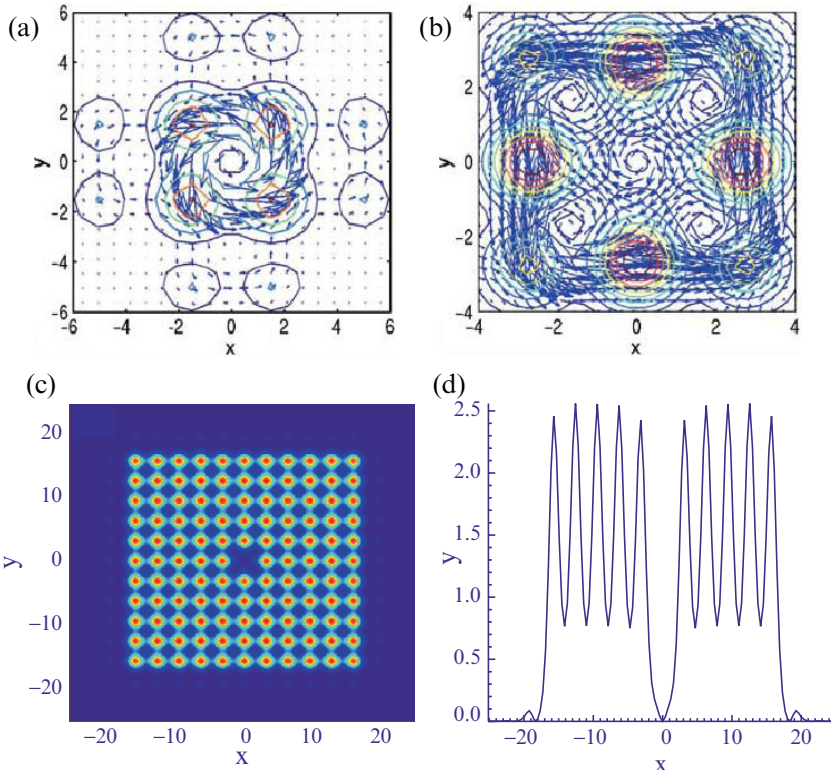


Fig. 6.20. Particle flow structure, $\text{Im}(\phi^* \nabla \phi)$, for the narrow (a) off-site and (b) on-site vortices shown in Fig. 6.19, left (a) and right (a), respectively, plotted together with contours of the atomic density. (c) The simple particle flow of a broad off-site vortex, and (d) its radial density structure displaying a typical structure of a truncated nonlinear Bloch wave, i.e. a self-trapped state

lattice and retain its characteristic features [41]. Figure 6.21 shows typical results of the simulations of the evolution of a condensate prepared in a quasi-2D magnetic trap with a charge one vortex imprinted onto a Thomas–Fermi profile, which is simultaneously released from the trap and loaded into a 2D OL at $t = 0$. The final state preserves the phase winding structure of the vortex while developing the complex structure of singularity characteristic of the gap state. This nonadiabatic generation process is quite robust, provided the density and spatial extent of the initial state are of the order characteristic of the gap vortex. Both narrow and broad (self-trapped) gap vortices can be generated this way [41].

Moreover, the nonadiabatic vortex generation can be employed for loading vortex lines created in a 3D BEC cloud into a 3D OL [24]. In the case of a strongly anisotropic (cigar-shaped) condensate, the condensate in a lattice

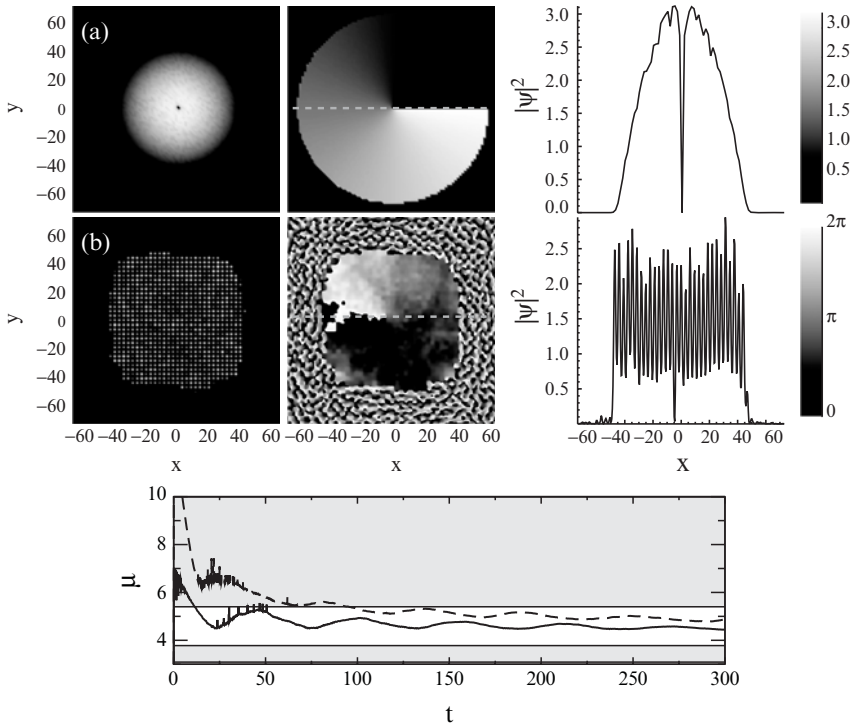


Fig. 6.21. Nonadiabatic generation of a 2D broad gap vortex. (a) Initial state: a vortex imprinted onto a 2D Thomas–Fermi cloud, shown with the phase distribution and cross-section of the density. (b) Final state of the evolution: self-trapped broad gap vortex. (c) Evolution of the chemical potential, relative to the band-gap structure, from the initial (a) to the final (b) state. Bands are *shaded*. *Dashed line* shows evolution towards a gap vortex from an initial vortex state with larger number of atoms (not shown)

evolves into a “vortex stack”, while preserving the singular line. The isotropic initial density leads to the formation of a 3D broad self-trapped vortex.

6.8 Multi-Component Gap States

The development of optical trapping techniques for BECs has enabled the confinement of atoms independently of their spin orientation in so-called spinor condensates [45, 46] (see also Part IX). Since an OL is one of the most frequently used optical traps for ultra-cold matter, understanding of the effect of the spin degree of freedom on the nonlinear properties of BECs in periodic potentials is of great importance.

In the framework of mean-field theory, the wavefunctions, $\Psi_{\pm 1,0}$, of the three hyperfine components ($m_F = \pm 1, 0$) of a spinor condensate obey the

following set of coupled GPEs [47] in the dimensionless form (see Sect. 6.3.1):

$$\begin{aligned} i\partial\Psi_{\pm 1}/\partial t &= \mathcal{L}\Psi_{\pm 1} + \lambda_a (|\Psi_{\pm 1}|^2 + |\Psi_0|^2 - |\Psi_{\mp 1}|^2) \Psi_{\pm 1} + \lambda_a \Psi_0^2 \Psi_{\mp 1}^*, \\ i\partial\Psi_0/\partial t &= \mathcal{L}\Psi_0 + \lambda_a (|\Psi_{-1}|^2 + |\Psi_{+1}|^2) \Psi_0 + 2\lambda_a \Psi_{+1} \Psi_{-1} \Psi_0^*, \end{aligned} \quad (6.11)$$

where $\mathcal{L} = -\frac{1}{2}\nabla^2 + V(\mathbf{r}) + \lambda_s (|\Psi_{-1}|^2 + |\Psi_0|^2 + |\Psi_{+1}|^2)$. Here, as in Sect. 6.3.1, the confining potential is a combination of a 1D OL V_{OL} and a transverse harmonic potential with the frequency ω_\perp . Similarly to the case of a single-component condensate, (6.11) can be reduced to a 1D system for a strongly anisotropic BEC cloud, and this is the case that we consider in this section.

Spinor condensates exhibit both spin-independent and spin-dependent nonlinear inter-atomic interactions, characterized by the coefficients λ_s , and λ_a , respectively. Although $|\lambda_a| \ll |\lambda_s|$, the sign of λ_a determines the properties of the ground and excited states. A BEC of bosonic spin-1 ($F = 1$) atoms can be either *ferromagnetic* (e.g. ^{87}Rb , $\lambda_a < 0$) or *polar* (e.g. ^{23}Na , $\lambda_a > 0$) in nature [48], with the two types of BECs having different average values of the total spin and different symmetry properties.

Any state of the three component system can be characterized by its normalized local spin vector [48]: $\mathbf{s} \equiv (\mathcal{S}_x, \mathcal{S}_y, \mathcal{S}_z)^T = \mathbf{s}/n_{\text{Tot}}$, where $n_{\text{Tot}} \equiv \sum n_j(x, t) = \sum |\psi_j(x, t)|^2$ is the total BEC density, and:

$$\mathbf{s}(x) \equiv \begin{pmatrix} \sqrt{2} \operatorname{Re}\{\psi_0^* \psi_{+1} + \psi_{-1}^* \psi_0\} \\ -\sqrt{2} \operatorname{Im}\{\psi_0^* \psi_{+1} + \psi_{-1}^* \psi_0\} \\ n_{-1} - n_{+1} \end{pmatrix}. \quad (6.12)$$

The averaged (total) spin is defined as: $\langle \mathbf{s} \rangle \equiv \int dx \mathbf{s}(x)/\int dx n_{\text{Tot}}$, and has the maximal value of 1. In the absence of a magnetic field, due to the rotational symmetry both the total angular momentum of the system $\langle \mathbf{s} \rangle$, and its magnetization $\langle \mathcal{S}_z \rangle = \int_{-\infty}^{+\infty} (n_{-1} - n_{+1}) dx$ are conserved.

A stationary state of a spinor system, $\psi_j(x, t) = \phi_j(x) \exp(-i\mu_j t) \exp(i\theta_j)$, where $\phi_j(x)$ are real wavefunctions, μ_j are chemical potentials, and θ_j are phases of the three hyperfine components, has to satisfy the phase matching condition for the chemical potentials, $2\mu_0 = \mu_{+1} + \mu_{-1}$. In addition, the relative phase between the components, $\Delta\theta = 2\theta_0 - (\theta_{+1} + \theta_{-1})$, can only take values 0 or π . Both the stationary states with all three components in-phase with one another ($\Delta\theta = 0$) and the states in which one of the components ($m_F = +1$ or $m_F = -1$) is *out-of-phase* with the others ($\Delta\theta = \pi$) always exist in the system, regardless of the sign of λ_a . However, the *in-phase* stationary states minimize the spin-dependent part of the total energy (Hamiltonian) for $\lambda_a < 0$, while the *out-of-phase* states minimize the spin-dependent energy for $\lambda_a > 0$ [48]. The spin-dependent part of the Hamiltonian thus determines the *ground state* of the condensate: *ferromagnetic* for $\lambda_a < 0$, and *polar* for $\lambda_a > 0$ [48–50]. In the presence of repulsive spin-independent interactions, the OL supports the existence of all three nonlinear stationary states of spinor

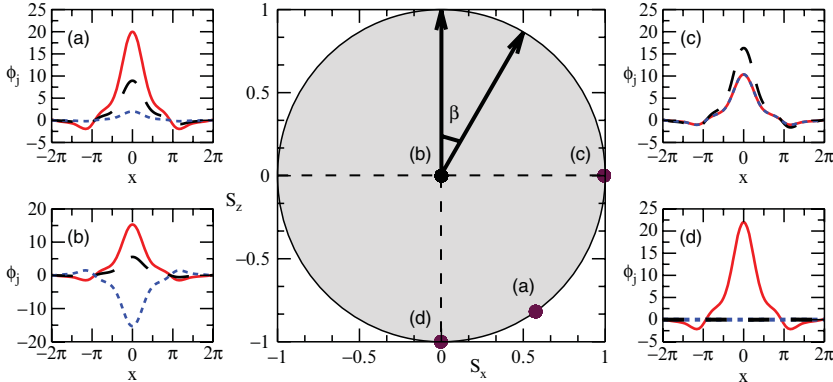


Fig. 6.22. Examples of spatial structure of the (a,c,d) ferromagnetic-type (*in-phase*) and (b) polar-type, (*out-of-phase*) gap solitons of a *polar*²³Na condensate in an OL ($V_0 = 4.0$, $\mu = 2.8$). Solid, dotted, and dashed lines show the ϕ_{-1} , ϕ_{+1} , and ϕ_0 components, respectively. The corresponding values of the local spin vector \mathbf{S} are plotted in the plane $S_y = 0$ of the 3D spin sphere (shaded). Due to the validity of the SMA, relative populations of the different hyperfine states can be determined by simple rotation by the angle β in the spin space

condensate: multi-component nonlinear Bloch waves, vector gap solitons, and self-trapped gap states.

Examples of both in-phase and out-of phase multi-component spinor gap solitons are shown in Fig. 6.22. These are well described by the so-called single-mode approximation (SMA) [49–51], which is valid when the size of a condensate is smaller than the spin healing length $\xi_{\text{spin}} = 2\pi/\sqrt{2|\lambda_a|n}$. SMA assumes that all three components of the condensate can be treated as if trapped in the *same* effective potential created by an OL and the combined mean-field densities of the spinor components. All the components therefore share a common density profile: $\phi_j(x) = \phi(x)\zeta_j$, that obeys the single GPE obtained from the model (6.11) under the assumption $\mu \equiv \mu_0 = \mu_{+1} = \mu_{-1}$. As a consequence of a shared density, the distribution of the local spin $\mathbf{S}(x)$ is reduced to a single point in the 3D spin space.

Apart from the “fundamental” gap states, an OL can support the “excited” spinor gap states with more complex spatial structure containing a larger number of atoms (see Fig. 6.23). Due to the dramatic differences between the spatial density distributions in the three hyperfine states, such states do not obey the SMA. The existence of the non-SMA states is counter-intuitive as the size of gap solitons is an order of magnitude smaller than a typical spin domain [52]. These states may be thought of as a composite of the self-trapped states with a phase “twist” *and* gap solitons, in which a gap soliton is localized in the combined effective potential of the self-trapped state and the lattice. The spin degeneracy is removed due to the difference in chemical potentials, i.e. $\mu_{-1} \neq \mu_{+1}$, so the populations in each hyperfine component are no longer

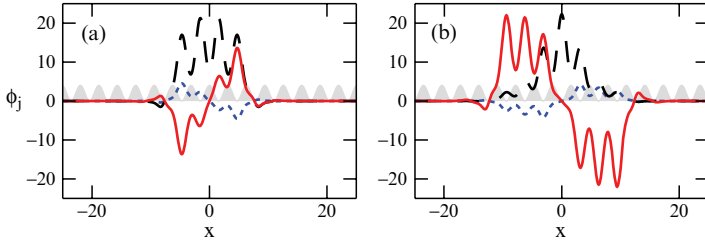


Fig. 6.23. Non-SMA stationary states for a ^{23}Na condensate: (a) centered on the potential maximum (i.e. *off-site*) and (b) centered on the potential minimum (i.e. *on-site*). Both stationary states are found for the values of the chemical potentials: $\mu_{+1} = 2.8$, $\mu_{-1} = 2.7$ and $\mu_0 = \frac{1}{2}(\mu_{+1} + \mu_{-1}) = 2.75$. *Solid*, *dotted*, and *dashed* lines mark ϕ_{+1} , ϕ_{-1} , and ϕ_0 components, respectively. *Shaded* is the corresponding OL potential ($V_0 = 4.0$)

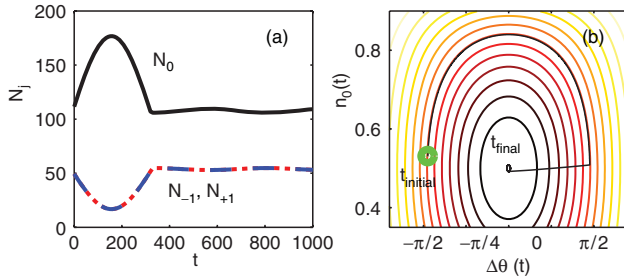


Fig. 6.24. Dynamics of nonequilibrium states in ^{87}Rb ($\mu = 2.8$, $V_0 = 4$). (a) Spin mixing oscillations of the populations (fractional atom numbers) between $m_F = -1$ (dotted), $m_F = +1$ (dashed) and $m_F = 0$ (solid) hyperfine components, arrested due to application of the magnetic field of magnitude $B = 1$ Gauss over the period of $t_B = \simeq 2$ (1.4 ms). (b) The dynamical trajectories in the $n_0(\Delta\theta)$ phase space for the scenario presented in panel (a)

governed by simple rotation through spin space. The values of the local spin tend to cover the whole range $0 < |\mathcal{S}| < 1$ and gap solitons acquire complex spin structure across the localization region [47].

If a spinor BEC is initially prepared in a nonstationary spin configuration (e.g., due to population imbalance within the stationary state), a general spin-mixing dynamics occurs [46, 49, 51]. In contrast to large spinor clouds in magnetic traps, the nonequilibrium evolution of gap solitons can be very accurately described by the SMA and generally consists of periodic exchange of populations between different hyperfine components [51]. Controlled manipulation of the coherent spinor dynamics can be achieved by application of a pulsed magnetic field [46]. The resulting management of the relative phase of the hyperfine components due to the quadratic Zeeman effect can lead to the arrest of the spin-mixing oscillations in the spatially localized state of the spinor condensate described by the SMA, as demonstrated in Fig. 6.24. As this

effect is reversible, it allows flexible manipulations of the multi-component gap solitons, which opens up possibilities for controlled manipulation of the spinor condensate in a lattice as a means of quantum state engineering, which is an essential element of quantum computing schemes.

6.9 Conclusions and Acknowledgments

In this chapter, we have attempted to summarize our recent experimental and theoretical studies of the nonlinear localization effects that Bose–Einstein condensates exhibit in optical lattices. In particular, we have outlined the theory and experimental prerequisites for the dispersion management of matter-waves, observation of atomic gap solitons and self-trapped states. We have also presented the investigation of the competition between the nonlinear localization and heating of the condensate due to dynamical instabilities, and discussed properties of the nontrivial localized lattice states: gap vortices and spinor gap solitons, their excitation, and manipulation.

We are tremendously indebted to our numerous colleagues and PhD students at the University of Konstanz, Kirchhoff Institut für Physik at University of Heidelberg, and the Nonlinear Physics Centre at the Australian National University, who have contributed greatly to the work presented in this Chapter. In particular, we would like to thank Bernd Eiermann, Thomas Anker, Michael Albiez, Pearl Louis, Tristram Alexander, and Beata Dąbrowska-Wüster. The work of E.A.O. and Yu.S.K. was supported by the Australian Research Council (ARC).

References

1. W. Ketterle, D.S. Durfee, D.M. Stamper-Kurn, *Making, probing and understanding Bose–Einstein condensates*, Bose–Einstein condensation in atomic gases, Proceedings of the International School of Physics ‘Enrico Fermi’, Course CXL, ed. by M. Inguscio, S. Stringari, C.E. Wieman (IOS Press, Amsterdam, 1999) pp. 67–176
2. H.J. Metcalf, P. van der Straten, *Laser cooling and trapping* (Springer, New York, 1999)
3. V.M. Pérez-García, H. Michinel, H. Herrero, Phys. Rev. A **57**, 3837 (1998)
4. P.J. Louis, E.A. Ostrovskaya, C.M. Savage, Yu.S. Kivshar, Phys. Rev. A **67**, 013602 (2003)
5. E.A. Ostrovskaya, Yu.S. Kivshar, Opt. Express **12**, 19 (2004)
6. J.H. Denschlag, J.E. Simsarian, H. Haffner, C. McKenzie, A. Browaeys, D. Cho, K. Helmerson, S.L. Rolston, W.D. Phillips, J. Phys. B **35**, 3095 (2002)
7. P.J.Y. Louis, *Matter-wave solitons in optical lattices and superlattices*, PhD Thesis, The Australian National University, 2005
8. V.V. Konotop, M. Salerno, Phys. Rev. A, **65**, 021602(R) (2002)
9. L. Fallani, L. De Sarlo, J.E. Lye, M. Modugno, R. Saers, C. Fort, M. Inguscio, Phys. Rev. Lett. **93**, 140406 (2004)

10. M. Cristiani, O. Morsch, N. Malossi, M. Jona-Lasinio, M. Anderlini, E. Courtade, E. Arimondo, Opt. Express **12**, 4 (2004)
11. L. De Sarlo, L. Fallani, J.E. Lye, M. Modugno, R. Saers, C. Fort, M. Inguscio, Phys. Rev. A **72**, 013603 (2005)
12. B. Eiermann, P. Treutlein, T. Anker, M. Albiez, M. Taglieber, K.-P. Marzlin, M.K. Oberthaler, Phys. Rev. Lett. **91**, 060402 (2003)
13. L. Fallani, F.S. Cataliotti, J. Catani, C. Fort, M. Modugno, M. Zawada, M. Inguscio, Phys. Rev. Lett. **91**, 240405 (2003)
14. Th. Anker, M. Albiez, B. Eiermann, M. Taglieber, M.K. Oberthaler, Opt. Express, **12**, 11 (2004)
15. Y.S. Kivshar, G.P. Agrawal, *Optical Solitons, From fibers to photonic crystals* (Elsevier Science, Amsterdam, 2003)
16. C.M. de Sterke, J.E. Sipe, Phys. Rev. A **38**, 5149 (1988)
17. M. Steel, W. Zhang, *Bloch function description of a Bose-Einstein condensate in a finite optical lattice*, cond-mat/9810284 (1998)
18. D.E. Pelinovsky, A.A. Sukhorukov, Yu.S. Kivshar, Phys. Rev. E **70**, 036618 (2004)
19. N.K. Efremidis, D.N. Christodoulides, Phys. Rev. A **67** 063608 (2003)
20. V. Ahufinger, A. Sanpera, P. Pedri, L. Santos, M. Lewenstein, Phys. Rev. A, **69**, 053604 (2004)
21. B. Eiermann, Th. Anker, M. Albiez, M. Taglieber, P. Treutlein, K.-P. Marzlin, M.K. Oberthaler, Phys. Rev. Lett. **92**, 230401 (2004)
22. H. Pu, L.O. Baksmaty, W. Zhang, N.P. Bigelow, P. Meystre, Phys. Rev. A **67**, 43605 (2003)
23. E.A. Ostrovskaya, Yu.S. Kivshar, Phys. Rev. Lett. **90**, 160407 (2003)
24. T.J. Alexander, E.A. Ostrovskaya, A.A. Sukhorukov, Yu.S. Kivshar, Phys. Rev. A **72**, 043603 (2005)
25. K.M. Hilligsoe, M.K. Oberthaler, K.-P. Marzlin, Phys. Rev. A **66**, 063605 (2002)
26. B.J. Dąbrowska, E.A. Ostrovskaya, Y.S. Kivshar, Phys. Rev. A **73**, 033603 (2006)
27. I. Carusotto, D. Embriaco, G.C. La Rocca, Phys. Rev. A **65**, 053611 (2002)
28. B.J. Dąbrowska-Wüster, S. Wüster, A.S. Bradley, M.J. Davis, E.A. Ostrovskaya, *Quantum effects in the dynamical localization of Bose-Einstein condensates in optical lattices*, cond-mat/0607332 (2006)
29. P.D. Drummond, S.J. Carter, J. Opt. Soc. Am. B **4**, 1565 (1987)
30. M.J. Steel, M.K. Olsen, L.I. Plimak, P.D. Drummond, S.M. Tan, M.J. Collett, D.F. Walls, R. Graham, Phys. Rev. A **58**, 4824 (1998)
31. J. Ruostekoski, L. Isella, Phys. Rev. Lett. **95**, 110403 (2005)
32. A. Sinatra, C. Lobo, Y. Castin, J. Phys. B **35**, 3599 (2002)
33. A. S. Mellish, G. Duffy, C. McKenzie, R. Geursen, A.C. Wilson, Phys. Rev. A **68**, 051601(R) (2003)
34. V. Ahufinger, A. Sanpera, Phys. Rev. Lett. **94**, 130403 (2005)
35. G.L. Alfimov, P.G. Kevrekidis, V.V. Konotop and M. Salerno, Phys. Rev. E **66**, 046608 (2002)
36. A. Trombettoni, A. Smerzi, Phys. Rev. Lett. **86**, 2353 (2001)
37. T.J. Alexander, E.A. Ostrovskaya, Yu.S. Kivshar, Phys. Rev. Lett. **96**, 040401 (2006)
38. For a summary of the dynamics see e.g. S. Raghavan, A. Smerzi, S. Fantoni, S.R. Shenoy Phys. Rev. A **59**, 620 (1999)

39. M. Albiez, R. Gati, J. Fölling, S. Hunsmann, M. Cristiani, M.K. Oberthaler, Phys. Rev. Lett. **95**, 010402 (2005)
40. Th. Anker, M. Albiez, R. Gati, S. Hunsmann, B. Eiermann, A. Trombettoni, M.K. Oberthaler Phys. Rev. Lett. **94**, 020403 (2005)
41. E.A. Ostrovskaya, T.J. Alexander, Yu.S. Kivshar, Phys. Rev. A **74**, 023605 (2006)
42. E.A. Ostrovskaya, Yu.S. Kivshar, Phys. Rev. Lett. **93**, 160405 (2004)
43. T.J. Alexander, A.A. Sukhorukov, Yu.S. Kivshar, Phys. Rev. Lett. **93**, 063901 (2004)
44. R. Carretero-González, P.G. Kevrekidis, B.A. Malomed, D.J. Frantzeskakis, Phys. Rev. Lett. **94**, 203901 (2005)
45. D.M. Stamper-Kurn, M.R. Andrews, A.P. Chikkatur, S. Inouye, H.-J. Miesner, J. Stenger, W. Ketterle, Phys. Rev. Lett. **80**, 2027 (1998)
46. M.-S. Cahng, C.D. Hamley, M.D. Barrett, J.A. Sauer, K.M. Fortier, W. Zhang, L. You, M.S. Chapman, Phys. Rev. Lett. **92**, 140403 (2004)
47. B.J. Dąbrowska-Wüster, E.A. Ostrovskaya, T.J. Alexander, Yu.S. Kivshar, Phys. Rev. A **75**, 023617 (2007)
48. T.-L. Ho, Phys. Rev. Lett. **81**, 742 (1998)
49. H. Pu, C.K. Law, S. Raghavan, J.H. Eberly, N.P. Bigelow, Phys. Rev. A **60**, 1463 (1999)
50. S. Yi, Ö.E. Müstecaplıoglu, C.P. Sun, L. You, Phys. Rev. A **66**, 011601(R) (2002)
51. W. Zhang, D.L. Zhou, M.-S. Chang, M.S. Chapman, L. You, Phys. Rev. A **72**, 013602 (2005)
52. H.-J. Miesner, D.M. Stamper-Kurn, J. Stenger, S. Inouye, A.P. Chikkatur, W. Ketterle, Phys. Rev. Lett. **82**, 2228 (1999)

Part V

Multi-Dimensional Solitons in Bose–Einstein Condensates

Multidimensional Solitons: Theory

L.D. Carr and J. Brand

7.1 Introduction

The one-dimensional solitons described in Parts II and III of this book can be extended into two and three dimensions. Such extensions are generally unstable [1]. However, in the tightly confined geometries associated with trapped Bose–Einstein condensates (BECs) both bright and dark solitons extended into two and three dimensions can be stabilized for times longer than the lifetime of experiments [2–4]. BECs offer the opportunity to tune a matter-wave gradually from one to two and to three dimensions [5, 6]. In the crossover regimes, new nonlinear objects can appear, such as the *svortex*, a solitary wave which is a soliton-vortex hybrid [7, 8]. The general question of crossover dimensions is an intriguing one in physics.

We will consider both the stable and unstable regimes of higher dimensional solitons, treating such objects theoretically but with an eye towards BEC experiments. BECs are typically contained in harmonic traps, and have a profile ranging from Gaussian to inverse parabolic (cf. the Thomas–Fermi limit in Sect. 4.3 of Chap. 1), depending on the interaction strength [5]. They span tens to hundreds of microns. Their lifetime is on the order of one to a hundred seconds. Both thermal and quantum fluctuations can play a significant role in their dynamics [5]. We must take into account all of these factors when discussing solitons. Moreover, the finite non-uniform nature of trapped BECs leads to significantly different nonlinear dynamics than that found in the GPE for uniform media. To cite a simple example, even in one dimension with periodic boundary conditions the finite domain of the condensate leads to spontaneous symmetry breaking and quantum phase transitions [9, 10].

There are also solitons which do not have a 1D analog. For instance, a vortex–anti-vortex pair in 2D is a solitary wave as it represents a localized excitation which moves coherently [11]. An example in 3D is a vortex ring [12–14]. More complicated topological solitons, such as skyrmions, are possible in multi-component condensates [15]. We will discuss such solitons as

well. It is worth noting that some of these scenarios have also been addressed in the context of nonlinear optics [16].

In keeping with the theme of this book, we will deal mathematically only with the mean-field theory of BECs, described by the Gross–Pitaevskii Equation (GPE), and linear perturbations of the mean field, described by the Bogoliubov–de-Gennes equations (BDGE), see Sect. 4 of Chap. 1. The GPE and BDGE can be derived rigorously from first principles from a second quantized quantum field theory for binary interactions between atoms in a dilute weakly interacting Bose gas well below the critical temperature for Bose–Einstein condensation, as discussed in Chap. 1 and the references therein. We note that there are significant subtleties in interpretation of BDGE solutions; see the appendix of [17] for a discussion of these issues. The GPE plus BDGE picture has an excellent interpretation in terms of quantum fluid dynamics, as discussed by Fetter and Svidzinsky [18].

Lastly, we note that the majority of higher-dimensional results, particularly for non-uniform trapped BECs, are achieved numerically. Many excellent references in computational science describe rigorous numerical methods for the GPE and BDGE (e.g. [19] and references therein). Due to the paucity of exact analytical results, we focus primarily on a coherent summary of numerical studies.

We introduce a small set of notation before proceeding. The effective non-linearity is given by $g_{\text{eff}} = gN$, which can be obtained by a simple rescaling of the wavefunction amplitude. Then the wavefunction $\Psi(\mathbf{r}, t)$ is normalized to unity. An axisymmetric harmonic trap can be characterized by its asymmetry parameter $\lambda \equiv \omega_z/\omega_r$, where ω_r is the radial trapping frequency and ω_z the axial trapping frequency. The harmonic oscillator lengths are given by $\ell_z \equiv \sqrt{\hbar/m\omega_z}$ and $\ell_r \equiv \sqrt{\hbar/m\omega_r}$.

7.2 Dark Solitons and Solitary Waves in Higher Dimensions

7.2.1 Dark Band and Planar Solitons

In a three dimensional system a standing dark soliton takes the form of a planar node; in two dimensions the node is a line, sometimes called a band. When such a soliton moves with respect to the background condensate, the notch fills in, so that the density in the region of the soliton is reduced but does not form a node; a detailed description is provided in Part III. We term these *planar solitons* and *band solitons*, respectively. In uniform media it is well known that both planar and band solitons decay via the snake instability. A sinusoidal mode transverse to the plane/band grows exponentially. The arcs of this “snake” break off into vortex–anti-vortex pairs. In the context of Bose–Einstein condensates, this has actually been suggested as a way to produce

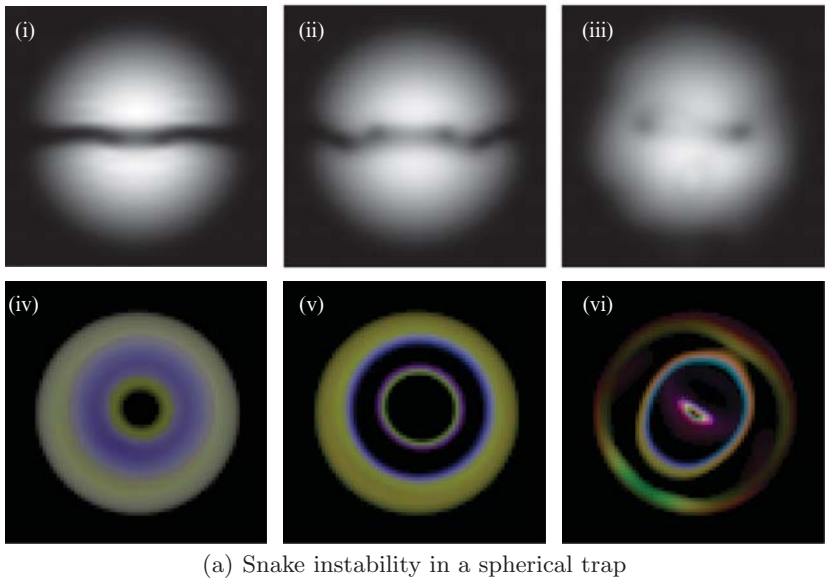
both vortices and anti-vortices in the same condensate, which is not otherwise possible with the usual stirring techniques.

The decay time for band solitons has been calculated with the BDGE, i.e., by considering linear perturbations to band/planar dark soliton stationary state of the GPE [20, 21]. *Nonlinear* instability times can be significantly shorter, and are determined from the numerical integration of the GPE. A band soliton then decays into an infinite chain of vortex anti-vortex pairs. Depending on the initial condition, these pairs can join to form solitary waves or annihilate in vortex–anti-vortex collisions.

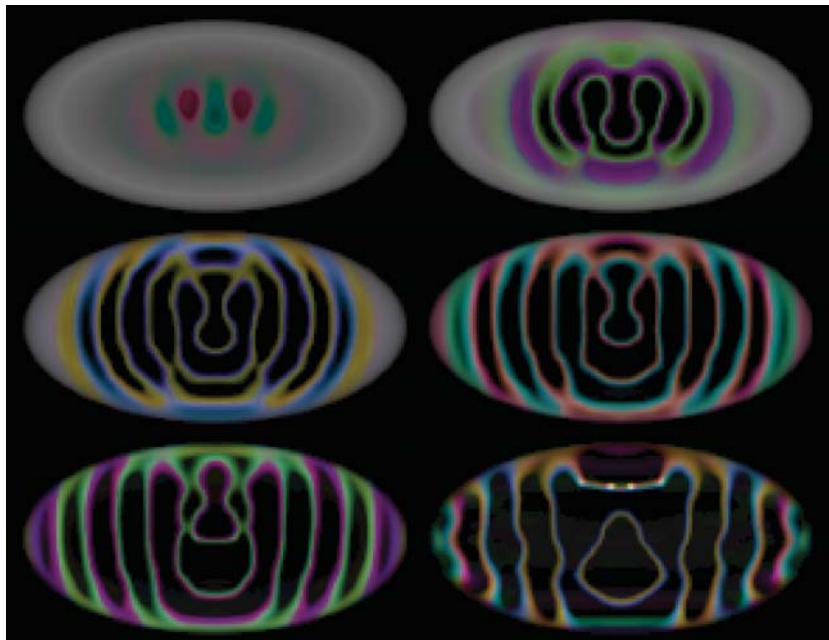
The nonlinear dynamics following decay of a planar soliton can be significantly more complex, as linear excitations leading to the snake instability can occur in two dimensions. The vortices produced are vortex lines which can rotate and/or combine to form vortex rings [22]. Keeping in mind that a velocity field can equally well be characterized by a vorticity field under certain simple assumptions [13], the decay of large arrays of planar vortices can lead to turbulence, characterized by densely tangled vortex lines [23, 24].

In trapped BECs the situation is quite different. In the three-dimensional harmonic trap the condensate, for sufficiently large nonlinearity, has a central parabolic profile and Gaussian tails. In this regime, called the *Thomas–Fermi regime*, as defined in Sect. 4 of Chap. 1, there is an additional mechanism for instability. Since a planar soliton moves at a fraction of the sound velocity which depends on its depth, and the sound velocity is proportional to the square root of density [5], the non-uniform density profile causes the soliton to travel more slowly at the edges of the condensate than the center. An initially uniform planar soliton formed in the center of the trap deforms into a U-shaped propagation front. When this wavefront reaches the edge of the trap it is deflected, and the trailing edges curl up to form vortices [25]. Thus there are two competing instability mechanisms for planar dark solitons in BECs. In initial experiments on planar solitons, it was in fact the non-uniformity-induced instability which dominated, as discussed in Chap. 8. Here, we emphasize the snake instability.

Shown in Fig. 7.1 (reproduced with permission of the authors [4]) are the precise dynamics of the snake instability in a harmonic trap for an initially stationary planar soliton with realistic experimental parameters. In Fig. 1(a) the condensate contains 10^5 atoms and is in a spherical trap with $\omega_r = \omega_z = 2\pi \times 50$ rad/s. The initial single planar soliton state is obtained with imaginary time relaxation. Shown in the panels are snapshots after real time propagation of 47, 50, and 77 ms for Fig. 1(a)(i)–(iii) and (iv)–(vi). In (i)–(iii), the brightness is proportional to the condensate density, and the images correspond to densities integrated down the line of sight. In (iv)–(vi), the brightness is *inversely* proportional to the condensate density, and regions outside the Thomas–Fermi sphere are rendered transparent in order to visualize nodes in the condensate interior; the color corresponds to the phase: $\phi = 0$ through 2π is represented by the sequence red–green–blue–red. The view is perpendicular



(a) Snake instability in a spherical trap



(b) Snake instability in a non-axisymmetric trap

Fig. 7.1. Dynamical instability of a single planar soliton in a trapped Bose–Einstein condensates. See text for full description

to the original nodal plane of the soliton; prior to the snake instability the dark soliton would appear as a featureless disk.

In Fig. 1(b) the breakup of an initial planar soliton is shown as a function of time for $N = 10^6$ atoms, $\omega_x = 2\pi \times 14$ rad/s, $\omega_y/\omega_x = \sqrt{2}$, and $\omega_z/\omega_x = 2$, the precise geometry of [25]. From the top left to the bottom right in raster order are shown times $t = 15\text{--}20$ ms in 1 ms increments after the initial state is formed. The view is along \hat{y} , and the Hamiltonian was constrained to even parity along \hat{x} and \hat{z} for ease of computation. The rendering is identical to that of Figs. 1(a)(iv)–(vi). The filamentation is almost entirely constrained to the original nodal (x, z) -plane.

These figures describe only the mean-field picture. Recent studies have shown that finite temperature can cause significant dissipative effects even in one dimension [26, 27], while coupling to transverse modes can lead to dissipation within the GPE/BDGE picture [28]. Moreover, even in one dimension quantum fluctuations determined by the BDGE “blur” a dark soliton, due to uncertainty in the position of the density minimum [29]. A full theory of dark band and planar soliton dynamics with even lowest order finite temperature and quantum effects remains a significant challenge to the computational and theoretical scientific communities, although general theoretical prescriptions in this direction exist [30–32].

7.2.2 Ring Dark Solitons and Spherical Shell Solitons

Another way to create a higher dimensional soliton is to wrap a band or planar soliton back around on itself. In two dimensions this takes the form of a nodal ring, termed a *ring dark soliton*. In three dimensions such an object is a nodal spherical shell, termed a *spherical shell soliton*. These objects are always unstable in harmonic traps, but can have lifetimes longer than that of BEC experiments. Multiple ring solitons can be nested within each other. It is mathematically intriguing that such solutions are *nonlinear Bessel functions*, by which we mean solutions to the equation

$$\eta_q'' + \frac{1}{\chi} \eta_q' - \frac{q^2}{\chi^2} \eta_q - \eta_q^3 + \eta_q = 0, \quad (7.1)$$

where the wavefunction has been rescaled as

$$\psi(\mathbf{r}, t) = \sqrt{\frac{\mu}{g}} \eta_q(\chi) \exp(iq\phi) \exp(-i\mu t/\hbar) \exp(i\theta_0). \quad (7.2)$$

Here μ is the chemical potential, q is the winding number of a central vortex, θ_0 is an arbitrary phase, and the coordinate system is cylindrical with coordinates χ, ϕ , with $\chi \equiv (\sqrt{2m\mu/\hbar})r$. Equation (7.1) is clearly the generating equation of a Bessel function, modified by the nonlinear term η_q^3 .

In infinitely extended repulsive condensates, the solutions to (7.2) include the uniform ground state, singly and multiply-quantized vortices, and ring

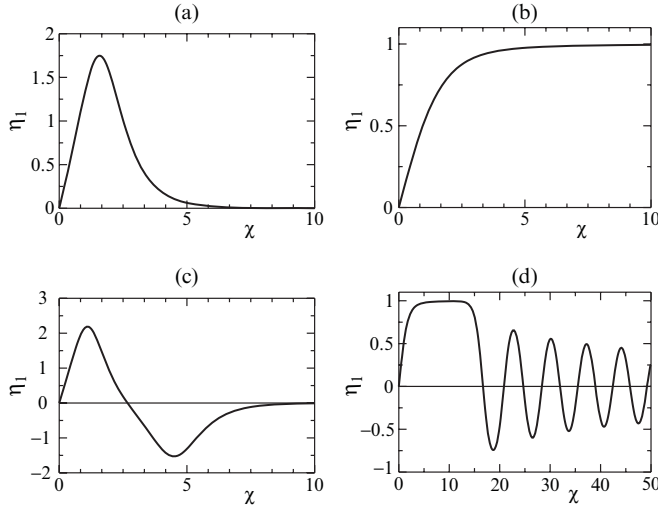


Fig. 7.2. A quantum vortex of winding number $q = 1$ in free space: (a) attractive case; (b) repulsive case. It is evident in (a) that a bright vortex is also a bright ring soliton. A radially excited state: (c) the first excited state in the attractive case; (d) in the repulsive case, a radially excited state requires an infinite number of nodes and asymptotically resembles the Coulomb function [33]. The radial dependence of the order parameter of an infinitely extended condensate is depicted. Note that all axes are dimensionless: η_1 is a rescaled radial density while χ is a rescaled radial coordinate

soliton solutions, as illustrated in Fig. 7.2b,d. The latter require a countably infinite number of nested dark ring solitons, where each soliton is a radial node corresponding to a node of the nonlinear Bessel function. The asymptotic form of these solutions has been studied in [33].

In contrast, in harmonically trapped condensates, ring solitons can be added to a solution one by one, so that there is a denumerably infinite set of ring soliton solutions for fixed nonlinearity. The linear stability analysis of these solutions and subsequent nonlinear dynamics of their breakup has been studied via the BDGE and GPE in the context of both BECs [33–35] and optics [36–41]. The dominant decay modes of single ring solitons in harmonically trapped BECs with and without a central vortex of winding number unity are the quadrupole and octupole, respectively [33]. In general, instabilities in higher dimensions can lead to new nonlinear structures; in Refs. [34] it is shown that ring solitons decay into vortex necklaces, as was later observed in optics experiments [42]. References [34, 35] also provide an analytical description of ring dark soliton dynamics in BECs. It has been suggested that, by use of an optical phase-shifting technique such as that employed in creating planar solitons [25, 26, 43], one might be able to generate ring solitons in experiments on BECs and observe their subsequent dynamics.

We note that structures similar to those of the stationary spherical shell solitons have been observed as transients in an experiment by Ginsberg et al. [44] and in simulated collisions of vortex rings [45] as will be discussed in Sect. 7.2.3 and Chap. 8.

7.2.3 Solitary Waves in Restricted Geometries

When a condensate is confined to a strongly prolate harmonic trap such that its transverse dimensions are not so small as to approach the healing length but not so large as to be effectively three-dimensional, new families of solitary waves arise. It suffices to consider the case $\omega_z = 0$, $\omega_r \neq 0$, so that the condensate forms an infinitely long cylinder. Physically, one can loosely interpret this as a multi-mode waveguide, where a uniform condensate forms the “vacuum” and solitary waves can propagate in the z direction. In this picture, one maintains a finite linear particle density $n_1 = N/L$, counting the number of particles per unit length along the symmetry axis z .

A mathematical representation of this geometry is realized by the GPE in the following dimensionless form:

$$i \frac{\partial \Psi}{\partial t} = -\frac{1}{2} \nabla^2 \Psi + \frac{1}{2} r^2 \Psi + 4\pi\gamma |\Psi|^2 \Psi, \quad (7.3)$$

where $r = \sqrt{x^2 + y^2}$ is the radial coordinate and $\nabla^2 = \partial^2/\partial x^2 + \partial^2/\partial y^2 + \partial^2/\partial z^2$ is the Laplacian operator [46]. The dimensionless coupling constant $\gamma \equiv n_1 a$ is the only parameter entering the equation, where a is the scattering length. Length is measured in units of the transverse oscillator length ℓ_r and the unit of time is $1/\omega_r$. At $z \rightarrow \pm\infty$ the wave function approaches the ground state in the transverse plane with $\partial\Psi/\partial z = 0$ and a transverse normalization of $2\pi \int dr r |\Psi|^2 = 1$.

The parameter γ characterizes the dimensionality of the problem (see Sect. 3 in Chap. 1 for more details on this reduction). In fact, γ is closely related to the number of healing lengths that fit into the transverse diameter of the cylindrical BEC cloud. Consequently, $\gamma \ll 1$ corresponds to the one-dimensional regime, where the transverse profile of the density is Gaussian and the waveguide is single-mode. In this regime, the only solitary waves known are the familiar family of dark solitons from the one-dimensional NLS. Three-dimensional aspects only become relevant when we consider effects that are sensitive to the breaking of integrability in the system as it has been found, e.g., in the interactions of phonons with solitons [47]. For $\gamma \gg 1$, the condensate enters the Thomas–Fermi regime for which the transverse density profile is approximated by an inverted parabola (cf. Sect. 4 in Chap. 1). In this regime various families of solitary waves with different structures co-exist. Figure 7.3 shows a schematic of possible configurations.

Families of cylindrically symmetric solitary waves have been numerically characterized by Komineas and Papanicolaou [22, 46, 49] and consist

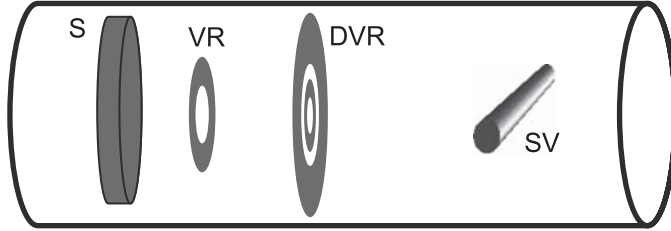


Fig. 7.3. Schematic of solitary wave configurations in a cylindrical BEC. The band soliton (S) has a nodal plane perpendicular to the trap axis and shows axial and inversion symmetry. The vortex ring (VR) is axisymmetric and has a vortex line (line singularity in the phase) in the configuration of a closed ring around the trap axis. The double vortex ring (DVR) has the same symmetries as the VR but features two concentric loops of vortex lines. The solitonic vortex (SV) has no symmetry. A vortex line is configured perpendicular to the trap axis and does not close in itself but terminates at the condensate boundaries

of dark solitons, vortex rings and double rings (see Fig. 7.3). The only non-axisymmetric solitary wave discovered so far is the solitonic vortex, or svortext [7], which consists of a vortex line perpendicular to the cylinder axis. This nonlinear excitation has solitonic properties in that it is a stable solitary wave which propagates coherently, and can be generated by stirring in toroidal traps or by spontaneous decay from an unstable band soliton [7, 8]. The dispersion relation of the svortext was calculated for a cylindrical geometry in [48], as shown in Fig. 7.4 (reproduced with permission of the authors [48]).

The picture that emerges from the numerical calculations is the following. For $\gamma < 1.5$ the situation is quasi-one-dimensional and only one solitary wave with the essential properties and structure of the 1D dark soliton exists. For $\gamma > 1.5$ there is a bifurcation and the non-axisymmetric svortext excitation coexists with axisymmetric solitary waves, i.e., band solitons. For $\gamma > 4$, there is another bifurcation and vortex rings coexist with band solitons and svortices. For even larger γ more bifurcations can be expected leading to a “zoo” of solitary waves. Numerical calculations up to $\gamma = 20$ have been performed in [48, 49]. The stability properties of these families of solitary waves have not been studied in detail, although svortices and vortex rings are believed to be dynamically stable.

The stability of vortex rings in particular has been tested numerically by simulating head-on collisions [45], as shown in Fig. 7.5. It was found that vortex rings collide elastically at large and small velocities while dramatically violent collisions occur at intermediate velocities. While these results could be explained in terms of the known dispersion diagrams like Fig. 7.4, a peculiar observation from the simulations was that inelastic collisions can generate shell structures of nearly spherical symmetry reminiscent of the spherical shell solitons discussed in Sect. 7.2.2. Similar structures were also observed in the experiment of [44], which will be discussed in more detail in Chap. 8.

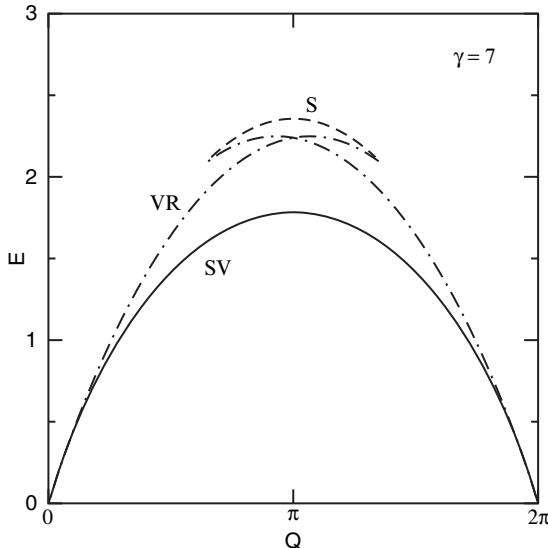


Fig. 7.4. The energy E versus impulse Q dispersion relation of the known solitary waves in the cylindrical BEC at $\gamma = 7$ from [48]. Shown are the branches of the svortex (SV), vortex rings (VR), and the band soliton (S). The slope dE/dQ of the dispersion relation gives the velocity of the solitary wave. The density structure of vortex rings and the time-dynamics of their head-on collision is shown in Fig. 7.5

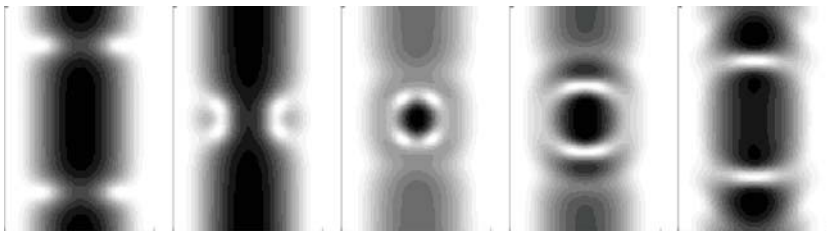


Fig. 7.5. Inelastic collision of vortex rings produces a transient shell structure of near spherical symmetry, from [45]. Plotted is the density $|\Psi|^2$ on the $y = 0$ plane at different time frames showing the head-on collision of a pair of vortex rings at $\gamma = 7$ with $v \equiv dE/dQ = 0.34v_s$, where $v_s = 1.61$ is the speed of sound in the units of (7.3)

7.2.4 Vortex Rings and Rarefaction Pulses

We now turn to the discussion of solitary waves that are localized on a significantly smaller scale than the condensate dimensions. In this case the idealization to a homogeneous condensate is appropriate, and the local density approximation can be applied to obtain non-uniform results. In fact, most of the work done in this direction assumes an infinite and homogeneous

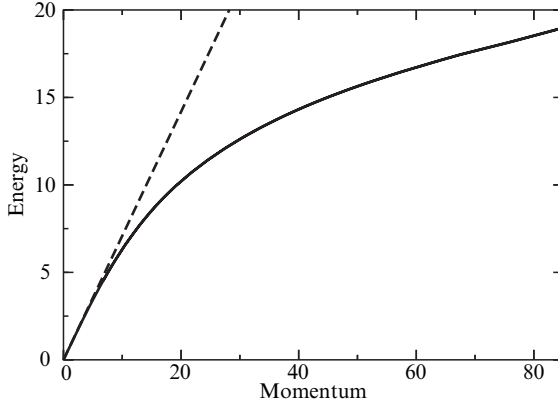


Fig. 7.6. Dispersion relation [11, 51] for 2D (x, z) solitary waves (solid line). The dashed line shows the dispersion relation of sound for comparison

background density. The ground-breaking work in this area was done in the 1980s by Jones and Roberts, who computed the dispersion relation of 2D and 3D solitary waves [11], as reproduced in Fig. 7.6 [51]. In three dimensions, the solitary waves they found are a family of vortex rings with varying diameter, which is related to the energy, the impulse, and the velocity. As the diameter is decreased to the order of the healing length, the phase singularity disappears; nevertheless, a branch of solitary waves can be found. As these waves have reduced particle density in the region where they are localized, they are also called *rarefaction pulses*. Analytical formulas in the form of Padé approximants for 3D solitary waves are given in [52].

The stability of the Jones–Roberts solitons was first discussed in [53], but rigorous results were only obtained recently [50, 54]. It is interesting to note that simulations showed that head-on collisions of vortex rings are always highly inelastic [55], in contrast to the situation in cylindrical traps discussed above. There has also been some work on the interactions between 3D solitons, vortex lines, and phonon radiation in the context of superfluid turbulence [50, 56]. Recent work in a hydrodynamic framework hints that the properties of vortex rings can be dramatically modified by Kelvin-wave excitations to the extent that the vortex rings may change their direction of propagation [57].

Another specific sort of multidimensional soliton is a solitary wave moving along a vortex line that extends through a homogeneous condensate. Such excitations were discussed recently in [58].

7.2.5 Multi-Component Bose–Einstein Condensates

Multi-component condensates offer rich opportunities for the study of solitonic and solitary waves in higher dimensions. A great deal of work has been done in this area. We touch very briefly on this subject. The main idea

behind topological solitons in multi-component BECs is as follows. Repulsive inter-species and intra-species interactions in a multi-component BEC will tend to make the total particle density uniform by filling up low-density regions of vortex cores with particles from another component. Under the assumption of a uniform total density, the vectorial order parameter has a prescribed constant length and becomes a mapping of three-dimensional real space to a sphere. Topological solitons are found as solutions with nontrivial topology resulting from this mapping. Examples of topological solitons are skyrmions in three dimensions and baby-skyrmions in two dimensions. A very large number of different vortex textures are possible in multi-component BECs [15, 59–61]. Various suggestions have been made to observe skyrmions and other such objects in BECs, but none have been achieved so far in experiments [62–69]. There is an ongoing discussion about the potential stability and experimental observability of such solutions [70]. In the case of dipolar BECs where long-range interactions play a role in addition to the contact interaction considered so far, spin textures may form spontaneously and the stability conditions change [71].

We would also like to mention that a generalization of the Jones–Roberts solitons to two-component condensates with a variety of different solitary wave families is described in [72]. Nonlinear phenomena in multi-component BECs are discussed in more detail in Part IX.

7.3 Bright Solitons in Higher Dimensions

While dark solitons are excitations of a condensate that take the form of density notches, bright solitons are ground or metastable states of a condensate, even in higher dimensions. Thus an attractive BEC is *itself* a soliton. Most experiments have focused on the unstable regimes of bright solitons [73–75]; we will also discuss the many theoretical proposals based on stable regimes, which are only just beginning to be explored in experiments [76–78].

7.3.1 Instability, Metastability, Stability

Bright soliton solutions to the GPE with a constant external potential $V(\mathbf{r}) = V_0$ are unstable to collapse in three dimensions. In one dimension bright solitons are stable. In two dimensions they either collapse or expand indefinitely, depending on the initial conditions and the strength of the effective nonlinear coefficient. The precise balance between expansion and collapse is known as the Townes soliton, or Townes profile [80, 81]. These now standard results for a constant potential in one, two, and three dimensions are presented rigorously in Sulem and Sulem [1]. However, with the addition of an external harmonic trapping potential, metastability can be achieved in three dimensions. This is easy to see by considering the scaling of the three energy terms in the GPE. The kinetic energy scales as $1/R^2$, where R is the

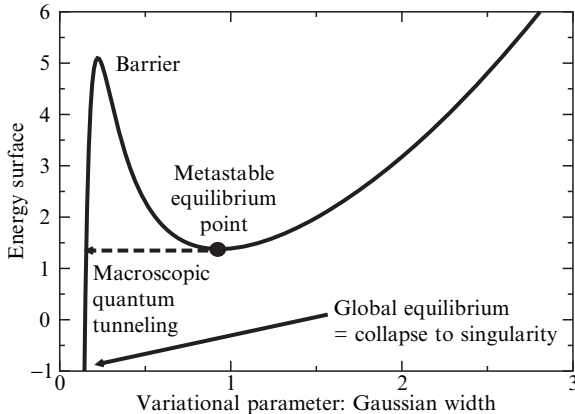


Fig. 7.7. Metastability and macroscopic quantum tunneling: Shown is a representative energy surface for a variational Gaussian ansatz in an isotropic 3D harmonic trap for attractive interactions $g_{\text{eff}} < 0$, as a function of the single variational parameter, the width of the Gaussian. One observes that non-singular solutions (non-zero width) are always metastable. The height of the collapse barrier decreases as $N \rightarrow N_c$; N_c is the critical number of atoms for which the barrier disappears and collapse is driven classically. Macroscopic quantum tunneling towards collapse can also occur through the barrier, as sketched on the plot [79]

radius of a single bright soliton. The mean-field energy scales as $-1/R^3$, since the wavefunction is proportional to $R^{-3/2}$. The potential energy scales as R^2 . Thus the additional contribution of the potential leads to a metastable region.

In Fig. 7.7 is shown a simple variational study for the energy surface in the isotropic case, with R taken as a variational parameter for a Gaussian variational ansatz [82–88]. Since the state shown in Fig. 7.7 is metastable, quantum tunneling can cause the solution to tunnel through the barrier towards $R = 0$, i.e., collapse. Ueda and Leggett [79] derived an expression for the tunneling exponent based on a Gaussian variational ansatz:

$$\frac{S^B}{\hbar} \simeq 4.58N \left(1 - \frac{N}{N_c}\right)^{5/4} \quad (7.4)$$

where the tunneling rate is given by $\Gamma = A \exp(-S^B/\hbar)$ and N_c is the critical number of atoms past which the condensate loses metastability and becomes unstable to collapse. This is one of many instances in which macroscopic quantum tunneling manifests in BECs, even within the mean-field description [87, 89–91]. One must also make careful estimates of thermal fluctuations, which can push the condensate up over the variational barrier. A simple estimate can be made by requiring that the thermal energy $k_B T$ be much less than the difference between the energy of the metastable state and that of the barrier peak, as sketched in Fig 7.7.

The tunneling barrier becomes large for condensates in prolate traps with $\lambda \ll 1$. The soliton then deforms from a spherical shape to an elongated shape. This is a simple experimental signature of the effective dimensionality of the soliton. For oblate traps, i.e., $\lambda \gg 1$, the soliton becomes two dimensional. Then the condensate is either stable or unstable [86] within the radial degrees of freedom. For sufficiently large $|g_{\text{eff}}|$ the condensate collapses; for smaller $|g_{\text{eff}}|$ its expansion is prevented by the external harmonic potential. The effect of the asymmetry λ has been studied both variationally and via numerical solution of the GPE [86, 87, 92].

However, condensates in trapped BECs are always mathematically metastable to three-dimensional collapse, whether the effective dimensionality be one-, two-, or three-dimensional, due to quantum tunneling. It is simply that the tunneling time associated with three-dimensional collapse becomes exponentially long; indeed, it is so much longer than experimental lifetimes of 1–100 s that it can be ignored. BEC experiments are rife with such metastabilities; for instance, the ground state of the kinds of alkali metal gases used to make BECs is in fact a crystalline solid, and the atomic gas is only in a metastable state, albeit long-lived. In practice, we ignore all metastabilities not relevant to the time scale of measurements, and assign an effective dimensionality to the GPE to describe bright soliton properties.

Ignoring macroscopic quantum tunneling, the threshold for bright soliton collapse can be determined by variational ansatz from the mean-field theory. This has an analytical expression in two special cases, both of interest for BECs. For an isotropic or nearly isotropic condensate [5, 82, 83, 86], the critical number of atoms is

$$N_c = 0.6501 \frac{\bar{\ell}}{|a|}, \quad (7.5)$$

where $\bar{\ell} \equiv (\ell_r^2 \ell_z)^{1/3}$ is the geometric mean of the harmonic oscillator lengths. For a condensate which is confined only in the radial direction, $N_c = 0.7598 \ell_r / |a|$ [87]. This case is especially interesting as it corresponds to the propagation of a bright soliton in a waveguide. Since bright solitons are themselves BECs which self-cool to zero temperature [87], they have been suggested as carriers of information in atom circuits on a chip. We note that numerical studies of the GPE show that the actual critical number is shifted by 10–20% as compared to the variational result; this can be incorporated by simply shifting the constant prefactor.

Lastly, although we have focused on the mean-field and its linear perturbations as described by the GPE and BDGE, this picture is inadequate for describing the dynamics of attractive BECs past the collapse threshold. The essential reason is that the density becomes so large that $\sqrt{n|a|^3} \sim 1$, where n is the number density and a the scattering length. The mean-field theory, which relies on a diluteness approximation [5, 6], necessarily breaks down at this point. Nevertheless, a number of attempts have been made to describe collapse dynamics with mean field theories. For instance, some

authors have modified the GPE by adding an effective loss rate due to three-body recombination [84, 93, 94]. Other authors have considered a generalized time-dependent Hartree–Fock–Bogoliubov (HFB) theory which couples the mean atomic field to a mean molecular field as well as normal and anomalous atomic quantum fluctuations [95, 96]. A recent extensive study of Wüster et al. [97] has focused on reproducing the time of onset of collapse found in the experiment of [75] comparing simulations using the GPE, HFB, and the stochastic truncated Wigner approximation method for including the effects of quantum fluctuations. The conclusion of this study was that the effect of quantum fluctuations, as compared to GPE simulations, was small and could not explain the discrepancies between the time scales found in the simulations and the significantly faster collapse times seen in the experiment.

7.3.2 Bright Soliton Engineering: Pulsed Atom Lasers and Other Applications

An area that has only begun to be explored experimentally is the many regimes in which bright solitons are stable. As pointed out in Sect. 7.3.1, bright solitons are always metastable in Bose–Einstein condensates, due to the geometries in which they are made. However, the instability times due to quantum tunneling can be much longer than the lifetime of experiments. All of the “stable” applications of BECs which are discussed in Sections 7.3.2–7.3.5 are therefore technically unstable; however, we use the term *experimental stability* to emphasize that from the point of view of measurement they are stable.

In one of the first experimental demonstrations of a bright soliton, a train of nearly 3D bright solitons was created from an elongated BEC via modulational instability [77], as described in Chap. 2. On the other hand, another experiment published simultaneously [87] produced a single bright soliton with a weakly *expulsive* harmonic potential in the z direction, i.e., a harmonic trap turned upside down; the radial harmonic trap was kept quite strong, so that the soliton propagated down a waveguide. The expulsive potential was then used to push the soliton along and accelerate its dynamics. A combination of these two experimental techniques leads to a *pulsed atom soliton laser* as follows [98]. The large repulsive scattering length of an initially highly elongated BEC is suddenly tuned small and negative with a Feshbach resonance. At the same time, the trap is flipped over in the z direction, i.e., $\omega_z \rightarrow i\omega_z$. The subsequent nonlinear evolution of the wavefunction creates a series of pulses via modulational instability seeded by linear interference fringes according to the Feynman propagator [99]. These self-cooling “mini-BECs” each contain on the order of 10^3 to 10^4 atoms. They are prevented from overlapping, and thereby collapsing, by the expulsive potential, and maintain their phase coherence over 500 ms. This sequence of events is illustrated in Fig. 7.8.

Improvements on this design have since been suggested in which many more laser pulses can be produced from a better controlled reservoir. In [100],

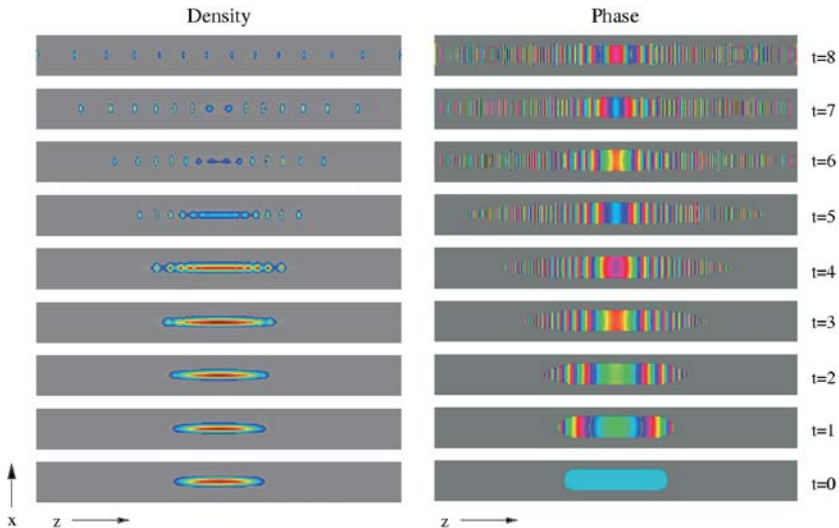


Fig. 7.8. *Pulsed atom soliton laser:* An initial state created by changing the scattering length of a condensate from large and positive to small and negative and then projecting the condensate on to an explosive harmonic potential results in spontaneous modulational instability and a series of phase-coherent pulses, or “mini-BECs.” Shown are the evolution of the density and phase along a two dimensional cut at $y = 0$. A set of well-defined solitonic pulses is evident in the latest (*top*) panel. The strong variations in the phase at late times is due to the high momentum of the solitons caused by the explosive harmonic potential. Note that the phase is shown on the color circle, i.e., modulo 2π , while the density is in arbitrary relative units rescaled for each plot. For $N = 10^4$ atoms, $a = -3a_0$, and a trap geometry of $\omega_\rho = 2\pi \times 2.44$ kHz, $\omega_z = 2\pi i \times 2.26$ Hz, the time units are scaled to 22 ms and the spatial units to $10\mu\text{m}$. Note that the aspect ratio of the plots showing a region of 0.822 by 153 length units was changed for visualization

a dual-core approach is used to produce a matter-wave soliton laser from attractive BECs. Two elongated quasi-one-dimensional condensates, or “cores” are laid side by side. The first condensate serves as a reservoir for the second via macroscopic quantum tunneling. The scattering length is small and positive in the first condensate, and small and negative in the second. Bright solitons form in the second condensate, and are emitted through a semi-transparent barrier at one end.

Carpentier and Michinel [101] investigate this idea in much greater detail by considering many possible spatial variations of the scattering length to maximize output and control over pulse size and velocity. In a second paper, they use a similar idea to create a bright soliton accelerator in a ring-shaped trap, similar to the “nevatron” already realized experimentally with repulsive BECs [102], but with many advantages over the first demonstration [103]. A *temporal* variation of the scattering length has also been used to engineer

bright solitons. For instance, a bright soliton in free three-dimensional space can be stabilized by rapidly oscillating the scattering length from positive to negative [104–107].

We would like to point out that even though the “engineering” examples we have cited in this section do not take advantage of the principles of quantum mechanical superposition or entanglement, nevertheless the nonlinear effects which are key to their operation result from averaging over a quantum many body wavefunction. Moreover, quantum fluctuations must be considered in any serious attempt at designing a pulsed atom laser and other such devices. Therefore, they can be considered as examples of quantum engineering.

7.3.3 Solitons in a Thermal Bath

The study of thermal effects on bright matter-wave solitons is highly relevant in light of potential applications of solitons, and has just begun to be explored. The multidimensional aspects of bright solitons in a BEC are very important in this context. The microscopic interactions between solitons and independent thermal particles are described by the BDGE to lowest order in $1/N$, where N is the number of particles in the soliton. In one dimension the scattering problem of a single-particle with a soliton can be solved exactly in the BDGE [108] and the full quantum field theory [109]. It is found that the scattering of thermal particles on the soliton is *reflectionless*, i.e., the transmission coefficient is unity, which is a consequence of the integrable nature of the nonlinear Schrödinger (NLS) equation. This is a very useful property for possible applications of bright solitons in high-precision interferometry.

However, the extent into transverse dimensions that solitons have in a waveguide geometry breaks the integrability of the NLS equation and allows for a finite reflection probability of scattering thermal particles. During such reflection events, momentum is transferred from the thermal particle to the soliton, which affects the soliton’s center-of-mass motion. Therefore, a soliton immersed in a thermal cloud can experience diffusive motion or be subject to a frictional force when it is moving with a relative velocity to the background. In [108], the friction and diffusion coefficients were determined based on a calculation of the reflection probability of thermal particles scattering off a soliton. Other approaches to describing the interaction based on the Hartree–Fock–Bogoliubov formalism can potentially treat the nonlinear coupled dynamics of the thermal cloud and the BEC. Studies in this direction are reported in [110, 111].

7.3.4 Soliton–Soliton Interactions

Soliton–soliton interactions in one dimension have been described completely and analytically by Gordon [112]. They are perfectly elastic. However, new features arise in trapped BECs. The imposition of a trapping potential can lead to chaotic dynamics for three or more solitons, even in one dimension [113].

Higher-dimensional effects can lead to inelastic collisions [98, 114, 115]. The subject of collisions of bright solitons in trapped BECs is only just beginning to be studied.

The essential effects of higher dimensionality are as follows. When two identical bright solitons overlap they double their number of atoms N . Thus it is possible for N to be temporarily greater than N_c , as defined in (7.5). The time for collapse to occur can be estimated from g_{eff} . Elasticity is then a question of whether or not the two solitons spend enough time overlapping to undergo collapse or partial collapse, at least within the mean-field picture of the GPE. This is determined by their relative velocity [114]. An additional factor is their relative phase and amplitude. In one dimension, a relative amplitude difference is equivalent to a phase difference [112]. If the phase difference $\Delta\phi$ satisfies $\pi/2 \leq \Delta\phi \leq 3\pi/2$ then the solitons can never overlap. On the other hand, if their phase difference satisfies $-\pi/2 < \Delta\phi < \pi/2$, then partial overlap occurs, with full overlap for $\Delta\phi = 0$ [116]. Initial studies indicate that the situation is vastly more complex in higher dimensions. For example, bright solitons can collide so inelastically that they “stick,” releasing excess energy and relative momentum by emitting a few particles, similar to the way that a soliton in one dimension adjusts to its preferred shape and thereby self-cools [87, 117].

It has been suggested, based on initial experiments on bright soliton trains, that bright soliton collisions can in fact lead to annihilation [77]. Beyond the mean-field theory, it is known experimentally that there is a bounce from collapse, as described in Sect. 7.3.1. Consider two solitons in a soliton train, each with a number of atoms near the critical number and therefore nearly three dimensional. The harmonic trap and/or initial conditions can drive them to overlap. If they do so for a sufficient period of time partial collapse occurs, leaving one soliton behind. The loss of atoms is not properly described by the mean-field theory. Even if the solitons are initially arranged with nodes between them, drift of relative phase due to quantum fluctuations can eventually lead to their being able to overlap. This is one explanation of the occasional disappearance of a member of the soliton trains of [77].

Therefore, in addition to the exploration of bright soliton collisions within the three-dimensional mean-field theory of the GPE, the effects of finite temperature [27] and higher order quantum theories [95] need to be considered as well in order to model experimental dynamics. The mean-field theory can only provide, at best, the threshold for collapse-related effects. This remains an important open problem for theorists to address.

7.3.5 Bright Ring Solitons and Quantum Vortices

The attractive analog of a vortex in a repulsive BEC in free space is in fact a bright ring soliton [118]. This point is illustrated in Fig. 7.2, where it can be seen that the wavefunction approaches zero as $r \rightarrow \infty$, in contradistinction to vortices in repulsive BECs where the wavefunction approaches a non-zero

constant. The stability of vortices in attractive BECs has been investigated theoretically [82, 83, 119, 120] since shortly after the experimental observation of a BEC. However, no experiment to date has tested theoretical predictions of bright ring solitons.

Static studies, which consider stationary solutions of the GPE and their linear perturbations as described by the BDGE, have found that all bright ring solitons and their radial excitations are unstable [118, 120]. Initial studies predicted an enhanced critical number over a bright soliton, and therefore *enhanced* stability. However, these studies considered only radial collapse. In fact, bright ring solitons are azimuthally unstable, as later analysis with the BDGE showed [120]. Although we have avoided significant analytical description thus far in this review, it is useful to state the form of the BDGE for a centrally located axisymmetric vortex [121] in an effectively two-dimensional condensate. We first transform the Bogoliubov amplitudes u and v according to

$$\begin{pmatrix} u(\mathbf{r}) \\ v(\mathbf{r}) \end{pmatrix} = \frac{e^{im\phi}}{\ell_r} \begin{pmatrix} e^{iq\phi} \tilde{u}_m(\tilde{r}) \\ e^{-iq\phi} \tilde{v}_m(\tilde{r}) \end{pmatrix}, \quad (7.6)$$

where $\tilde{r} = \sqrt{x^2 + y^2}/\ell_r$ and we neglect perturbations in the z direction, considering only a strongly oblate trap for simplicity. Equation 7.6) represents a partial wave of angular momentum m relative to a condensate with a vortex of winding number q . Then in harmonic oscillator units the BDGE become

$$\mathcal{L}_+ \tilde{u}_m - \tilde{g}_{\text{eff}} |\tilde{f}_q|^2 \tilde{v}_m = \frac{\Omega_m}{\omega} \tilde{u}_m, \quad (7.7)$$

$$\mathcal{L}_- \tilde{v}_m - \tilde{g}_{\text{eff}} |\tilde{f}_q|^2 \tilde{u}_m = -\frac{\Omega_m}{\omega} \tilde{v}_m, \quad (7.8)$$

where

$$\mathcal{L}_\pm \equiv -\frac{1}{2} \left(\frac{\partial^2}{\partial \tilde{r}^2} + \frac{1}{\tilde{r}} \frac{\partial}{\partial \tilde{r}} - \frac{(q \pm m)^2}{\tilde{r}^2} - \tilde{r}^2 \right) + 2\tilde{g}_{\text{eff}} |\tilde{f}_m|^2 - \tilde{\mu} \quad (7.9)$$

Here Ω_m are the eigenvalues for Bogoliubov modes with angular momentum m and \tilde{f}_q is the radial portion of condensate wavefunction with winding number q ; the tildes throughout these rescaled BDGE indicate harmonic oscillator units. The different centrifugal barriers inherent in \mathcal{L}_\pm show that the two amplitudes behave differently near the origin, with $\tilde{u}_m \propto \tilde{r}^{|m+q|}$ and $\tilde{v}_m \propto \tilde{r}^{|m-q|}$ as $\tilde{r} \rightarrow 0$. Note that \tilde{f}_q is normalized to unity.

We briefly highlight the results of studies of (7.7)–(7.8) for $\tilde{g}_{\text{eff}} < 0$. The dominant instability mode is quadrupolar for $m = 1$, a single bright soliton, and small \tilde{g}_{eff} . The linear instability time is given by $T_m = 2\pi/\text{Im}(\Omega_m)$. This time can be much longer than experiments, so that bright ring solitons do indeed have the possibility of being observed.

While multiple dark ring solitons consist of nested nodal rings, separated by regions of nonzero density and constant phase, multiple bright ring solitons consist of multiple rings of non-zero density and constant phase separated by

nodes. These multiple bright ring soliton solutions are in fact radial excitations of a vortex in an attractive BEC. In free space, there is a denumerably infinite number of such states, which form an excited state spectrum of bright ring solitons in two dimensions for fixed winding number under the constraint that the wavefunction approach zero as the radial coordinate approaches infinity. This result has been formally proved for winding number zero for the Townes soliton [1] and numerically demonstrated for non-zero winding number [118]. The first excited state for winding number $m = 1$ is shown in Fig. 7.2c. This is in contrast to dark ring solitons, which only appear in an infinite number of concentric rings in free space, as shown in Fig. 7.2d.

It has been shown that a similar sequence of radially excited states of attractive vortices occurs in a harmonic trap, and that, for sufficiently small \tilde{g}_{eff} , their instability times can be long compared to experiments [118].

Nonlinear dynamical studies of trapped bright ring solitons have found cyclical behavior in their azimuthal break-up, among other intriguing behaviors [122, 123]. Figure 7.9 shows one example of this cyclical behavior. The initial state is a bright ring soliton plus a small symmetry-breaking azimuthal perturbation. The ring splits via the quadrupole instability into two density peaks, i.e., two bright solitons. The soliton pair rotates around the origin, then recombines to reform the original ring. Panels g and h suggest the possibility of observation by sudden switching of the scattering length and expansion

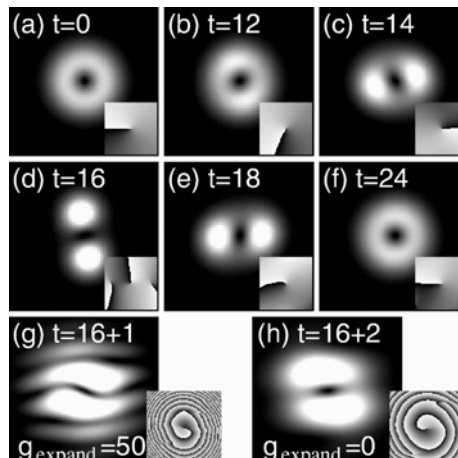


Fig. 7.9. Nonlinear dynamical split-merge cycle of bright ring soliton. (a)–(f) Shown is the time evolution of the density profile in two dimensions. The insets present gray-scale plots of the phase modulo 2π . Panels (g) and (h) show what occurs when the trap is switched off and the condensate is allowed to expand with (g) large positive scattering length and (h) zero scattering length. This is a common experimental technique to magnify condensate features too small to otherwise resolve. Reproduced with permission of the authors [122]

of the condensate, a common experimental technique. We note that parallels have been suggested in multi-component BECs as well [124].

Finally, it is worth mentioning that the stabilization of higher dimensional solitons by means of optical lattices (cf. Parts IV and VIII) has also been proposed in [125–128].

7.4 Summary and Acknowledgments

We have described a few of the many manifestations of soliton-like phenomena in Bose–Einstein condensates in two and three dimensions. A brief list for repulsive nonlinearity includes dark band solitons, dark planar solitons, dark ring solitons, spherical shell solitons, families of solitary waves, and skyrmions and vortex textures; while for attractive nonlinearity one finds metastable bright solitons, quantum tunneling and quantum evaporation of bright solitons, pulsed atom soliton lasers, bright ring solitons, and the split-merge cycle. We think some of the most exciting outstanding problems in this field are the higher order quantum and thermal effects on solitonic phenomena, as we have indicated sporadically throughout our discussion.

There is great deal both in and beyond our over one hundred references that we have been unable to cover in the space allotted; we sincerely hope we have not offended the many investigators whose work we have not been able to include.

The authors would like to thank the editors of this book, who have done a wonderful job facilitating a much-needed review of nonlinear phenomena in BECs. We thank our mentor William Reinhardt, who many years ago led us both in the direction of solitons and BECs as a graduate student and post-doctoral fellow, respectively. LDC thanks Charles Clark for many useful discussions and scientific collaborations which led to writing this chapter. LDC gratefully acknowledges the National Science Foundation for continuing support.

References

1. C. Sulem, P.L. Sulem, *Nonlinear Schrödinger Equations: Self-focusing Instability and Wave Collapse* (Springer, New York, 1999)
2. A.E. Muryshhev, H.B. van Linden van den Heuvell, G.V. Shlyapnikov, Phys. Rev. A **60**, R2665 (1999)
3. L.D. Carr, M.A. Leung, W.P. Reinhardt, J. Phys. B **33**, 3983 (2000)
4. D.L. Feder, M.S. Pindzola, L.A. Collins, B.L. Schneider, C.W. Clark, Phys. Rev. A **62**, 053606 (2000)
5. F. Dalfovo, S. Giorgini, L.P. Pitaevskii, S. Stringari, Rev. Mod. Phys. **71**, 463 (1999)
6. A.J. Leggett, Rev. Mod. Phys. **73**, 307 (2001)
7. J. Brand, W.P. Reinhardt, J. Phys. B **34**, L113 (2001)

8. J. Brand, W.P. Reinhardt, Phys. Rev. A **65**, 043612 (2002)
9. L.D. Carr, C.W. Clark, W.P. Reinhardt, Phys. Rev. A **62**, 063611 (2000)
10. R. Kanamoto, H. Saito, M. Ueda, Phys. Rev. Lett. **94**, 090404 (2005)
11. C.A. Jones, P.H. Roberts, J. Phys. A **15**, 2599 (1982)
12. R.J. Donnelly, *Quantized Vortices in Helium II* (Cambridge University Press, New York, 1991)
13. P.G. Saffman, *Vortex Dynamics* (Cambridge University Press, New York, 1992)
14. B.P. Anderson, P.C. Haljan, C.A. Regal, D.L. Feder, L.A. Collins, C.W. Clark, E.A. Cornell, Phys. Rev. Lett. **86**, 2926 (2001)
15. E.J. Mueller, Phys. Rev. A **69**, 033606 (2004)
16. B.A. Malomed, D. Mihalache, F. Wise, L. Torner, J. Opt. B **7**, R53 (2005)
17. L.J. Garay, J.R. Anglin, J.I. Cirac, P. Zoller, Phys. Rev. A **63**, 023611 (2001)
18. A.L. Fetter, A.A. Svidzinsky, J. Phys. **13**, R135 (2001)
19. V.M. Pérez-García, X.Y. Liu, App. Math. Comp. **144**, 215 (2003)
20. C.T. Law, G.A. Swartzlander, Opt. Lett. **18**, 586 (1993)
21. G.S. McDonald, K.S. Syed, W.J. Firth, Opt. Commun. **95**, 281 (1993)
22. S. Komineas, in *Nonlinear Waves in Complex Systems*, ed. by J.G. Caputo, M.P. Soerensen, Eur. Phys. J. Special Topics **147**, 133–152 (2007)
23. K.W. Schwarz, Phys. Rev. B **31**, 5782 (1985)
24. K.W. Schwarz, Phys. Rev. B **38**, 2398 (1988)
25. J. Denschlag, J.E. Simsarian, D.L. Feder, C.W. Clark, L.A. Collins, J. Cubizolles, L. Deng, E.W. Hagley, K. Helmerson, W.P. Reinhardt, S.L. Rolston, B.I. Schneider, W.D. Phillips, Science **287**, 97 (2000)
26. S. Burger, K. Bongs, S. Dettmer, W. Ertmer, K. Sengstock, A. Sanpera, G.V. Shlyapnikov, M. Lewenstein, Phys. Rev. Lett. **83**, 5198 (1999)
27. B. Jackson, C.F. Barenghi, N.P. Proukakis, e-print cond-mat/0610082 (2006)
28. P.O. Fedichev, A.E. Muryshev, G.V. Shlyapnikov, Phys. Rev. A **60**, 3220 (1999)
29. J. Dziarmaga, Z.P. Karkuszewski, K. Sacha, J. Phys. B **36**, 1217 (2003)
30. E. Zaremba, T. Nikuni, A. Griffin, J. Low Temp. Phys. **116**, 277 (1999)
31. S.A. Morgan, Ph.D. thesis, St. John's College, University of Oxford, 1999
32. M.J. Davis, S.A. Morgan, K. Burnett, Phys. Rev. A **66**, 053618 (2002)
33. L.D. Carr, C.W. Clark, Phys. Rev. A **74**, 043613 (2006)
34. G. Theocharis, D.J. Frantzeskakis, P.G. Kevrekidis, B.A. Malomed, Y.S. Kivshar, Phys. Rev. Lett. **90**, 120403 (2003)
35. G. Theocharis, P. Schmelcher, M.K. Oberthaler, P.G. Kevrekidis, D.J. Frantzeskakis, Phys. Rev. A **72**, 023609 (2005)
36. Y.S. Kivshar, X. Yang, Phys. Rev. E **49**, 1657 (1994)
37. W. Dreischuh, A. Fliesser, I. Velchev, S. Dinev, L. Windholz, App. Phys. B **62**, 139 (1996)
38. D. Neshev, A. Dreischuh, V. Kamenov, I. Stefanov, S. Dinev, W. Fließer, L. Windholz, Appl. Phys. B **64**, 429 (1997)
39. D.J. Frantzeskakis, B.A. Malomed, Phys. Lett. A **264**, 179 (2000)
40. H.E. Nistazakis, D.J. Frantzeskakis, B.A. Malomed, P.G. Kevrekidis, Phys. Lett. A **285**, 157 (2001)
41. A. Dreischuh, D. Neshev, G.G. Paulus, F. Grasbon, H. Walther, Phys. Rev. E **66**, 066611 (2002)
42. J. Yang, I. Makasyuk, P.G. Kevrekidis, H. Martin, B.A. Malomed, D.J. Frantzeskakis, Z. Chen, Phys. Rev. Lett. **94**, 113902 (2005)

43. L.D. Carr, J. Brand, S. Burger, A. Sanpera, Phys. Rev. A **63**, 051601 (2001)
44. N.J. Ginsberg, J. Brand, L.V. Hau, Phys. Rev. Lett. **94**, 040403 (2005)
45. S. Komineas, J. Brand, Phys. Rev. Lett. **95**, 110401 (2005)
46. S. Komineas, N. Papanicolaou, Phys. Rev. Lett. **89**, 070402 (2002)
47. A.E. Muryshev, G. Shlyapnikov, W. Ertmer, K. Sengstock, M. Lewenstein, Phys. Rev. Lett. **89**, 110401 (2002)
48. S. Komineas, N. Papanicolaou, Phys. Rev. A **68**, 043617 (2003)
49. S. Komineas, N. Papanicolaou, Phys. Rev. A **67**, 023615 (2003)
50. N.G. Berloff, J. Phys. A **37**, 1617 (2004)
51. Natalia Berloff provided us with the numerical data used in this figure.
52. N.G. Berloff, J. Phys. A **37**, 1617 (2004)
53. C.A. Jones, S.J. Puttermann, P.H. Roberts, J. Phys. A **19**, 2991 (1986)
54. S. Tsuchiya, F. Dalfovo, C. Tozzo, L. Pitaevskii, e-print cond-mat/0607160, (2006)
55. J. Koplik, H. Levine, Phys. Rev. Lett. **76**, 4745 (1996)
56. M. Leadbeater, D.C. Samuels, C.F. Barenghi, C.S. Adams, Phys. Rev. A **67**, 015601 (2003)
57. C.F. Barenghi, R. Hanninen, M. Tsubota, Phys. Rev. E **74**, 046303 (2006)
58. N.G. Berloff, Phys. Rev. A **94**, 010403 (2005)
59. J. Ruostekoski, Phys. Rev. A **70**, 041601 (2004)
60. K. Kasamatsu, M. Tsubota, M. Ueda, Phys. Rev. A **71**, 043611 (2005)
61. W.V. Pogosov, R. Kawate, T. Mizushima, K. Machida, Phys. Rev. A **72**, 063605 (2005)
62. T. Busch, J.R. Anglin, Phys. Rev. A **60**, R2669 (1999)
63. U.A. Khawaja, H. Stoof, Nature **411**, 918 (2001)
64. U.A. Khawaja, H.T.C. Stoof, Phys. Rev. A **64**, 043612 (2001)
65. C.M. Savage, J. Ruostekoski, Phys. Rev. Lett. **91**, 010403 (2003)
66. R.A. Battye, N.R. Cooper, P.M. Sutcliffe, Phys. Rev. Lett. **88**, 080401 (2002)
67. I.F. Herbut, M. Oshikawa, Phys. Rev. Lett. **97**, 080403 (2006)
68. J. Ruostekoski, J.R. Anglin, Phys. Rev. Lett. **86**, 3934 (2001)
69. T. Mizushima, K. Machida, T. Kita, Phys. Rev. Lett. **89**, 030401 (2002)
70. H. Zhai, W.Q. Chen, Z. Xu, L. Chang, Phys. Rev. A **68**, 043602 (2003)
71. S. Yi, H. Pu, Phys. Rev. Lett. **97**, 020401 (2006)
72. N.G. Berloff, Phys. Rev. Lett. **94**, 120401 (2005)
73. C.A. Sackett, H.T.C. Stoof, R.G. Hulet, Phys. Rev. Lett. **80**, 2031 (1998)
74. C.A. Sackett, J.M. Gerton, M. Welling, R.G. Hulet, Phys. Rev. Lett. **82**, 876 (1999)
75. E.A. Donley, N.R. Claussen, S.L. Cornish, J.L. Roberts, E.A. Cornell, C.E. Wieman, Nature **412**, 295 (2001)
76. L. Khaykovich, F. Schreck, F. Ferrari, T. Bourdel, J. Cubizolles, L.D. Carr, Y. Castin, C. Salomon, Science **296**, 1290 (2002)
77. K.E. Strecker, G.B. Partridge, A.G. Truscott, R.G. Hulet, Nature **417**, 150 (2002)
78. S.L. Cornish, S.T. Thompson, C.E. Wieman, Phys. Rev. Lett. **96**, 170401 (2006)
79. M. Ueda, A.J. Leggett, Phys. Rev. Lett. **80**, 1576 (1998)
80. R.Y. Chiao, E. Garmire, C.H. Townes, Phys. Rev. Lett. **13**, 479 (1964)
81. K.D. Moll, A.L. Gaeta, G. Fibich, Phys. Rev. Lett. **90**, 203902 (2003)
82. R.J. Dodd, M. Edwards, C.J. Williams, C.W. Clark, M.J. Holland, P.A. Ruprecht, K. Burnett, Phys. Rev. A **54**, 661 (1996)

83. R.J. Dodd, J. Res. NIST **101**, 545 (1996)
84. Y. Kagan, E.L. Surkov, G.V. Shlyapnikov, Phys. Rev. Lett. **79**, 2604 (1997)
85. Y. Kagan, E.L. Surkov, G.V. Shlyapnikov, Phys. Rev. A **55**, R18 (1997)
86. V.M. Pérez-García, H. Michinel, J.I. Cirac, M. Lewenstein, P. Zoller, Phys. Rev. A **56**, 1424 (1997)
87. L.D. Carr, Y. Castin, Phys. Rev. A **66**, 063602 (2002)
88. B.A. Malomed, Progr. Optics **43**, 71 (2002)
89. N. Moiseyev, L.D. Carr, B.A. Malomed, Y.B. Band, J. Phys. B **37**, L1 (2004)
90. L.D. Carr, M.J. Holland, B.A. Malomed, J. Phys. B **38**, 3217 (2005)
91. N. Moiseyev, L.S. Cederbaum, Phys. Rev. A **72**, 033605 (2005)
92. A. Gammal, T. Frederico, L. Tomio, Phys. Rev. A **64**, 055602 (2001)
93. H. Saito, M. Ueda, Phys. Rev. A **65**, 033624 (2002)
94. K. Gawryluk, M. Brewczyk, M. Gajda, J. Mostowski, Phys. Rev. B **39**, L1 (2006)
95. J.N. Milstein, C. Menotti, M.J. Holland, New J. Phys. **5**, 52 (2003)
96. S. Wuster, J.J. Hope, C.M. Savage, Phys. Rev. A **71**, 033604 (2005)
97. S. Wüster, B.J. Dabrowska-Wüster, A.S. Bradley, M.J. Davis, P.B. Blakie, J.J. Hope, C.M. Savage, Phys. Rev. A **75**, 043611 (2007)
98. L.D. Carr, J. Brand, Phys. Rev. A **70**, 033607 (2004)
99. L.D. Carr, J. Brand, Phys. Rev. Lett. **92**, 040401 (2004)
100. P.Y. Chen, B.A. Malomed, J. Phys. B **38**, 4221 (2005)
101. A.V. Carpentier, H. Michinel, Europhys. Lett. **78**, 10002 (2007)
102. J.A. Sauer, M.D. Barrett, M.S. Chapman, Phys. Rev. Lett. **87**, 270401 (2001)
103. A.V. Carpentier, H. Michinel, M.I. Rodas-Verde, V.M. Pérez-García, Phys. Rev. A **74**, 013619 (2006)
104. H. Saito, M. Ueda, Phys. Rev. Lett. **90**, 040403 (2003)
105. H. Saito, M. Ueda, Phys. Rev. A **70**, 053610 (2004)
106. S.K. Adhikari, Phys. Rev. A **69**, 063613 (2004)
107. F.K. Abdullaev, J.G. Caputo, R.A. Kraenkel, B.A. Malomed, Phys. Rev. A **67**, 013605 (2003)
108. S. Sinha, A.Y. Cherny, D. Kovrizhin, J. Brand, Phys. Rev. Lett. **96**, 030406 (2006)
109. J.B. McGuire, J. Math. Phys. **5**, 622 (1964)
110. H. Buljan, M. Segev, A. Vardi, Phys. Rev. Lett. **95**, 180401 (2005)
111. I.M. Merhasin, B.A. Malomed, Y.B. Band, Phys. Rev. A **74**, 033614 (2006)
112. J.P. Gordon, Opt. Lett. **8**, 596 (1983)
113. A.D. Martin, C.S. Adams, S.A. Gardiner, Phys. Rev. Lett. **98**, 020402 (2007)
114. N.G. Parker, A.M. Martin, S.L. Cornish, C.S. Adams, e-print cond-mat/0603059 (2006)
115. L. Khaykovich, B.A. Malomed, Phys. Rev. A **74**, 023607 (2006)
116. L.D. Carr, J.N. Kutz, W.P. Reinhardt, Phys. Rev. E **63**, 066604 (2001)
117. J. Satsuma, N. Yajima, Prog. Theor. Phys. (Suppl.) **55**, 284 (1974)
118. L.D. Carr, C.W. Clark, Phys. Rev. Lett. **97**, 010403 (2006)
119. P.A. Ruprecht, M.J. Holland, K. Burnett, M. Edwards, Phys. Rev. A **51**, 4704 (1995)
120. H. Pu, C.K. Law, J.H. Eberly, N.P. Bigelow, Phys. Rev. A **59**, 1533 (1999)
121. A.A. Svidzinsky, A.L. Fetter, Phys. Rev. A **58**, 3168 (1998)
122. H. Saito, M. Ueda, Phys. Rev. Lett. **89**, 190402 (2002)
123. H. Saito, M. Ueda, Phys. Rev. A **69**, 013604 (2004)

124. J.J. García-Ripoll, V.M. Pérez-García, Phys. Rev. Lett. **84**, 4264 (2000)
125. B.B. Baizakov, B.A. Malomed, M. Salerno, Europhys. Lett. **63** 642 (2003)
126. J. Yang, Z.H. Musslimani, Opt. Lett. **28** 2094 (2003)
127. B.B. Baizakov, B.A. Malomed, M. Salerno, Phys. Rev. A **70** 053613 (2004)
128. D. Mihalache, Mazilu, F. Lederer, Y.V. Kartashov, L.-C. Crasovan, L. Torner, Phys. Rev. E **70** 055603(R) (2004)

Experiments on Multidimensional Solitons

J. Brand, L.D. Carr, and B.P. Anderson

8.1 Dimensional Aspects of Soliton Experiments in BECs

The experimental work on solitons in BECs during the past decade has been extremely important in two respects. First, experiments have shown unambiguously that solitons and related nonlinear waves do exist in BECs. This was disputed at the time when the first experiments were performed in 1999 [1, 2] and may still be found surprising given that we are dealing with a quantum many-body system driven towards strongly non-equilibrium dynamics. Second, the experiments have inspired theoretical work in many directions. A particular example is the work on solitary waves in dimensional crossovers induced by trapping potentials that restrict the geometry, as discussed in Chap. 7.

A ubiquitous feature in all of the experimental realizations of solitons so far is the three-dimensional nature of experimental set-ups, which can never be completely neglected in the interpretation of the results obtained. In this respect almost all of the experimental work discussed in this book falls into the wider area of “multidimensional solitons.” In order to avoid the duplication of discussions led in other chapters, we chose to narrow the scope of this chapter to discuss mainly solitary waves with a genuinely multidimensional structure. We therefore restrict the discussion to experimental studies of the creation and dynamics of vortex rings in experiments at JILA [3] and Harvard [4, 5]. In particular, we completely omit the vast body of experimental work on line vortices and the related baby-skyrmions, i.e., vortices with filled cores [6, 7]), as these will be covered in Part VI.

We also completely omit the experiments on bright solitons, and the first planar dark soliton experiments [1, 2] that were primarily concerned with soliton observation and propagation in BECs rather than dynamical instabilities and soliton decay. Detailed reviews of these experiments can be found in Parts II and III, respectively.

8.2 Preparation of Non-equilibrium BECs

None of the solitons and nonlinear waves discussed in this chapter are ground states. Rather, they are defects in the background density of the BEC. In order to facilitate the generation of such defects, the condensate is brought into an unstable or genuinely time-dependent dynamical state, such as a planar dark soliton in a single-component condensate. More stable multi-dimensional solitons can then form spontaneously as the decay product of an unstable initial state. In particular, vortex rings have been created by decay of moving or stationary planar dark solitons. The planar solitons themselves have been created by density engineering, which will be discussed below, by phase engineering, as discussed in Part III, or by a combination of both, which may be called *quantum state engineering*. Two different realizations of quantum state engineering have been proposed in Refs. [8, 9].

8.2.1 Dark Soliton Quantum State Engineering

The method used at JILA to create planar dark solitons [10] in BECs is an example of quantum state engineering that manipulates both the BEC density and phase [3]. The technique relies on the ability to place a BEC into a superposition of two spatially overlapped components, where both the relative quantum phase and the amplitudes of the superposition components can be engineered to have a desired variation across the BEC [8]. For the JILA experiments with ^{87}Rb , a BEC has phase-coherent components created from the internal hyperfine atomic states $|1\rangle \equiv |F = 1, m_F = -1\rangle$ and $|2\rangle \equiv |F = 2, m_F = 1\rangle$. The two components are coupled with a precisely engineered two-photon microwave field, enabling the overall superposition to be manipulated. To visualize this, let $|\psi\rangle$ be a state vector which represents the spatial and temporal variations of the two-component BEC. Then, the superposition takes the form $|\psi\rangle = c_1 e^{i\phi_1} \cdot |1\rangle + c_2 e^{i\phi_2} \cdot |2\rangle$, where c_1 , c_2 , ϕ_1 , and ϕ_2 are real scalars which depend on time and space. Then $|c_j|^2$ is the number density of the j^{th} component and $\phi_1 - \phi_2$ is the relative phase. Two-component phase and density manipulation requires control of c_1 , c_2 , and $\phi_1 - \phi_2$ in order to produce a final engineered superposition. Once the desired superposition is created, the microwave coupling drive is removed.

In the JILA experiment, the two atomic states effectively shared a potential well in all spatial coordinates. The two components also have nearly identical intra- and inter-component scattering lengths. Thus the sum $|c_1|^2 + |c_2|^2$ remained approximately constant in space and time during microwave-induced internal state conversion, i.e., the *total* atomic density of the BEC did not significantly change, regardless of the spatial structure of the superposition. For example, if ϕ_2 is constant across the BEC, and $\phi_1 - \phi_2 = 0$ for $z < 0$ and π for $z > 0$, where z labels the vertical spatial direction, there will be a π phase jump across the $z = 0$ plane of the part of the BEC made up of $|1\rangle$

atoms. This phase jump corresponds to the phase jump across a horizontal dark soliton nodal plane.

With these general concepts, planar dark solitons were created in a nearly spherical potential with a mean trapping frequency of ~ 7.7 Hz and at temperatures of $T \approx 23$ nK, or $T/T_c \approx 0.8$. With an initial BEC made entirely of $\sim 10^6$ atoms in state $|2\rangle$, a two-photon microwave field coupled the two atomic states inducing transitions $|2\rangle \rightarrow |1\rangle$ while a laser-induced AC Stark shift altered the detuning of the microwave field from the atomic resonance. The beam was modulated across the BEC such that the coherent atomic transitions on opposite sides of the BEC were driven out of phase, resulting in a relative phase of π between the two halves of the component- $|1\rangle$ BEC. Additionally, transfer of atoms from $|2\rangle$ to $|1\rangle$ at the center of the BEC atom cloud was suppressed. Engineered superpositions of a dark soliton state in component $|1\rangle$ and uniform-phase states of component $|2\rangle$ were thus created. More precisely, a *filled* dark soliton was created in component $|1\rangle$, with atoms in component $|2\rangle$ occupying the dark soliton nodal plane in $|1\rangle$, since the total BEC atomic density $|c_1|^2 + |c_2|^2$ remained approximately constant in time and space. The dark soliton remained dynamically stable as long as the component- $|2\rangle$ “filling” remained intact. To study planar dark soliton dynamical instabilities, including observations of soliton decay into vortex rings, the $|2\rangle$ atoms were first removed with a short blast of a laser tuned to an electronic transition of the $|2\rangle$ atoms. The subsequent observations will be described in Sect. 8.3.

The JILA state-engineering technique represents a general method for creating topological states, as described by Williams and Holland [8]. For example, the two-component engineering technique was also used to create vortices in BECs [6], and prior experimental results may be interpreted in terms of the creation of a vertical stack of filled horizontal dark solitons in a single BEC [11]. Additional details and references regarding this technique, and results of other experiments may be found in the experimental portion of Part IX.

8.2.2 Density Engineering by Slow Light

The method used in the lab of Lene Hau at Harvard to create nonlinear waves [4, 5] may be described as density engineering of the BEC. There are two stages in the process. First, a density depletion of the size scale of a couple of micrometers, or several healing lengths, is created on a microsecond timescale. In the next stage, the condensate reacts on the millisecond time scale by developing shock waves which shed soliton wave fronts. Here we describe the creation of the initial density depletions.

The scheme for creating density depletions is based on the method of ultra-slow light pulse propagation by *electromagnetically induced transparency* (EIT) [12, 13] and an extension thereof termed *roadblock* for light [14, 15]. The experiments work with a rather large BEC of 1.5 to a few million ^{23}Na atoms. The effect of EIT makes use of the level structure of ^{23}Na and involves mainly

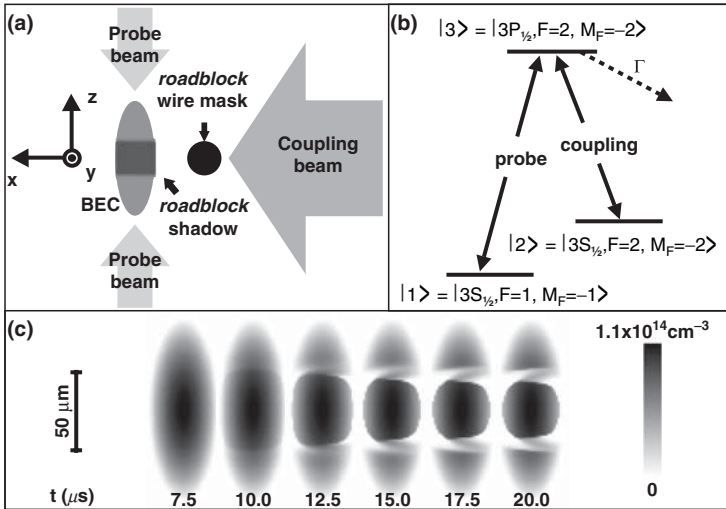


Fig. 8.1. Creation of defects by density engineering, from [5]. (a) Schematic of experimental set up for slow-light propagation via EIT and double light roadblock. (b) Energy level diagram of Na for EIT and slow-light. (c) Two-dimensional simulation of slow-light propagation on the double road block showing the density of atoms in state $|1\rangle$

the three states labeled $|1\rangle$, $|2\rangle$, and $|3\rangle$, in Fig. 8.1b, where $|1\rangle$ is the ground state. A laser pulse tuned exactly on the $|1\rangle - |3\rangle$ transition (labeled “probe”) would not be able to propagate in a BEC of atoms in the $|1\rangle$ state. The medium would absorb all the photons and appear opaque. If, however, the levels $|2\rangle$ and $|3\rangle$ are coupled by another laser field, the $|1\rangle - |3\rangle$ transition line splits into two lines and photons cannot be absorbed at the original transition frequency due to interference of the transition amplitudes. This effect is called EIT because the medium becomes transparent at the original transition frequency. Another consequence of this scenario is that the index of refraction n varies strongly around the EIT frequency. This, in turn, leads to a greatly reduced group velocity which is indirectly proportional to the frequency gradient of n . In this way the speed of light was reduced to a group velocity of 17 m/s [14, 16].

The reduction of the group velocity of light leads to a compression of light pulses in space by the same factor. In this way, a few microsecond long laser pulse of a kilometer length in vacuum is compressed to about $50 \mu\text{m}$, at which point it is completely contained in the BEC. When the coupling beam is turned off abruptly at this point, light propagation stops completely and the energy and phase of the probe beam are stored in the condensate in the form of atoms in the $|2\rangle$ state. By turning the coupling beam back on after a time window of the order of microseconds, the light pulse can be re-released coherently [15].

The idea behind the “light roadblock” is to transfer the above described technique of stopping light from the temporal to the spatial domain. The coupling beam does not illuminate the entire BEC cloud because part of it is

shaded by means of a razor blade [4] or a wire mask [5]. Figure 8.1a shows a schematic of the experimental set-up of a double roadblock with a wire mask and two slow-light probe beams from [5].

As the slow light pulse reaches the edge of the shadowed region of the BEC, the group velocity is reduced further, which in turn compresses the pulse further. At the size scale of a few microns, the stopped light transfers atoms from state $|1\rangle$ into state $|2\rangle$. Since the atoms in state $|2\rangle$ carry a photon-induced recoil momentum, they are ejected out of the condensate and leave within 1 ms without contributing much to the dynamics of the BEC of atoms in state $|1\rangle$. Figure 8.2 illustrates this point clearly in simulations of

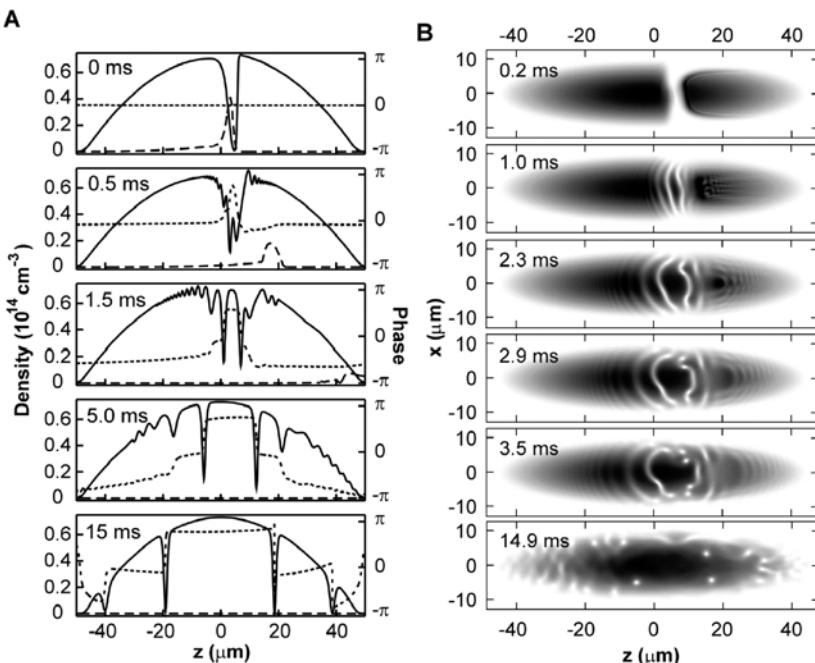


Fig. 8.2. Simulations of slow-light and BEC dynamics. **(A)** One-dimensional simulation of the coupled dynamics of light and matter-wave fields showing dynamics after the stopping of a light pulse on a single roadblock. The *solid* and *dashed* lines show the densities of $|1\rangle$ atoms and $|2\rangle$ atoms, respectively. The phase of the condensate in $|1\rangle$ is shown by the *dotted line*. Atoms in state $|2\rangle$ are clearly seen to leave the condensate without affecting the ensuing dynamics of the state $|1\rangle$ BEC. The evolution from density defects into dark solitons is clearly seen from the phase profile of the BEC. **(B)** Two-dimensional simulation of the state $|1\rangle$ BEC dynamics after creation of a defect. Shown are *gray-scale* plots of the condensate density. The cigar-like shape of the BEC induced by the trapping potential and the development and propagation of dark soliton fronts (*white lines*) and vortices (*white dots*) are clearly visible. Reproduced from [4] with permission from AAAS

the dynamics in a coupled GPE model. The evolution of the density of state $|1\rangle$ atoms during the slow-light propagation in the case of a double road block is shown in Fig. 8.1c.

8.3 Decay and Formation of Multidimensional Solitons

8.3.1 Quantum Shock Wave Dynamics and Soliton Shedding

Density engineering as performed in the Harvard experiments [4, 5] and described in Sect. 8.2.2 primarily creates localized density voids of the shape of a narrow disk in a slowly-varying background that is determined by the external trapping potential. Simulations of the ensuing dynamics are shown in Fig. 8.2. The condensate reacts to the creation of the defect and to the missing mean-field repulsion from the removed atoms by rushing in to fill the void. This way, a wave of density depletion emanates from the void at roughly the local speed of sound. However, due to the variation of the speed of sound over the density profile, the wave form steepens at the back to form a shock front. The variation of the speed of sound over the density profile is a general nonlinear sound wave effect, that will become important whenever the density variation is comparable to the density itself. Due to quantum pressure in the superfluid hydrodynamics of the BEC, shock fronts of a size scale smaller than the condensate healing length are not permitted. Instead, dark solitons in the form of planar and modulated wave fronts are shed, as seen in the simulations of Fig. 8.2 and the schematic of Fig. 8.3.

During the propagation of the shock wave, a train of solitons is generated in its wake. The solitons shed first are the deepest and equal in amplitude to the original density wave; then shallower solitons follow. Due to the inverse relationship between the depth of the soliton and its speed, the deep solitons which were created earlier move more slowly than the ones created at later times. The deeper solitons also carry a larger amount of excitation energy, which is taken away from the shock wave. During its propagation the shock wave will therefore lose depth and energy and eventually disperse into fast-moving shallow solitons and sound waves. This superfluid version of a shock wave is also called a *quantum shock wave*.

For theoretical investigations of shock waves in BECs see Refs. [17–20]. The dynamics of shock-wave formation and soliton shedding as described above could not be observed *in situ* due to limits in the optical resolution for in-trap imaging. However, the resulting trains of dark soliton fronts are clearly seen in the experimental data shown in Fig. 8.3.

Detailed theoretical studies and experimental observations of shock wave formation and dynamics have been reported recently by Hoefer et al. [21]. The decay dynamics of the shock front was described theoretically in terms of a *dispersive shock wave*. The shock waves studied in this work form from

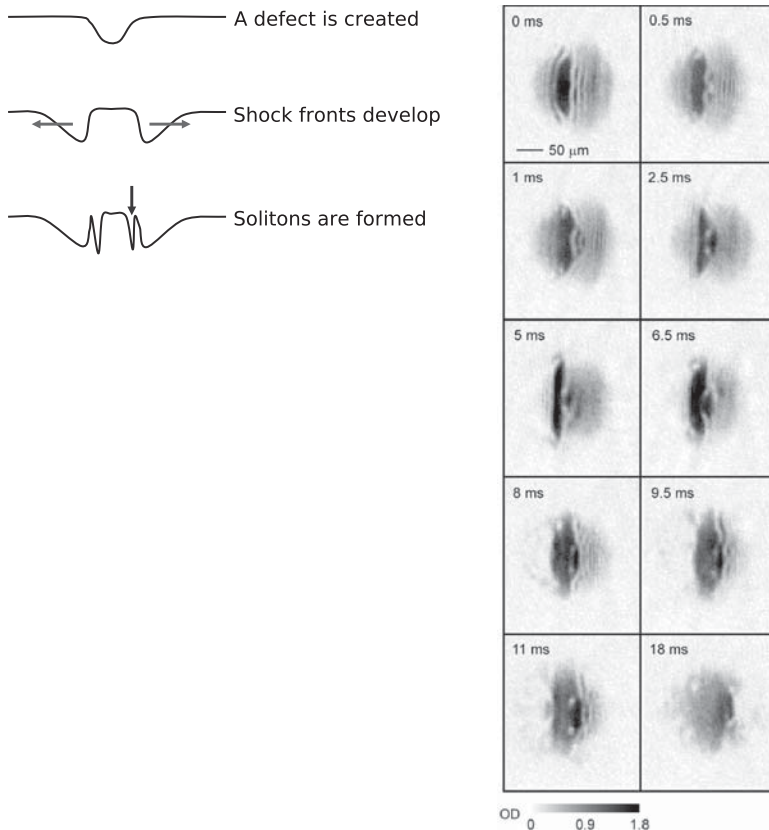


Fig. 8.3. *Left:* Schematic of shock-wave formation and soliton shedding after creation of a density void. *Right:* Experimental data after expansion showing wave front dynamics following the creation of a single density defect. The slice images clearly show planar band soliton fronts at initial stages that undergo a snake instability and decay into vortex rings. The times cited refer to in-trap evolution before the expansion phase. From [4]. Reproduced with permission from AAAS

positive density deformations (bright density waves) after the pulsed application of a strongly repulsive, focused laser beam to a BEC rather than from a collapsing cavity as in the Harvard experiments. Thus the details of the formation and subsequent dynamics of the shock wave are different from the situation described above.

8.3.2 Snake Instability and Vortex Ring Generation

The decay of planar dark soliton fronts and the subsequent formation of vortex rings were seen in two quite different experiments done in the labs of JILA and Harvard and both published in 2001. The mechanism of decay is a dynamical

instability of planar dark solitons, a three-dimensional BEC equivalent of the snake instability of optical dark solitons [22, 23]. In the following we discuss the observations from both experiments.

8.3.2.1 Harvard Experiments

We discussed above how shock waves caused by collapsing voids have lead to the creation of dark soliton wavefronts in the Harvard experiments [4, 5]. The dynamics of these wave fronts and their decay into vortex rings has been probed experimentally. The size scale of solitons and vortex cores is of the order of the healing length, in this case about $1 \mu\text{m}$. In order to increase the size of the density features to be more easily imaged, the condensate is suddenly released from the trap and expands due to mean-field pressure while it falls in the gravitational field of the earth. After a typical delay time of about 15 to 20 ms, a single slice of the cloud is selectively imaged by near-resonant absorption after illumination by a pump laser through a slit mask.

The initial expansion image of Fig. 8.3 clearly shows a train of soliton wave fronts to the right of the dark density feature. During the subsequent time evolution the deepest of the soliton wave fronts undergoes the snake instability while the shallower solitons to the right appear to be more stable. The snaking of the deep soliton front eventually leads to the creation of a vortex ring. The signature of a vortex ring in the experimental images are pairs of white dots. The dots show the depleted core region of the vortex ring intersecting the plane of imaging twice. The slice imaging technique was used to tomographically scan the expanded cloud and explore the three-dimensional structure of the observed defects. The experimental data was found consistent with the assumption that the snake dynamics and vortex generation obey cylindrical symmetry for most of the process, except for late stages of the time evolution as seen in the bottom panels of Fig. 8.3. This observation suggests that the snake dynamics are seeded by geometrical preconditioning, i.e., bending of soliton fronts due to the geometry of the created defects, trapping potential, etc., rather than being seeded by thermal or quantum fluctuations.

Extensive simulations of the dynamics of the BEC both in the trap and during the expansion phase have revealed that nonlinear wave dynamics still take place during the latter [5]. Therefore, theoretical modeling is essential for the understanding and interpretation of the experimental results.

8.3.2.2 JILA Experiments

Using two-component state engineering to create dark solitons in BECs, the JILA group also observed dark solitons decay into vortex rings [3]. The underlying mechanism of decay is presumed to be again the snake instability, although in the JILA experiment the actual “snaking” was not resolved, as was the case in the Harvard experiment.

As described in Sect. 2.1, planar dark solitons at JILA were formed in two-component condensates, with atoms of component $|2\rangle$ filling the nodal plane of a planar dark soliton in component $|1\rangle$. The soliton state and the filling could be separately distinguished with in-trap state-selective phase-contrast imaging, i.e., *without* releasing the BEC from the trap. This confirmed that the soliton's density notch bisected the BEC. In an orthogonal coordinate system with axes labeled by x , y and z , with z along the vertical, the soliton was always created with a normal vector in the (y,z) plane. Although the soliton orientation was not further controlled, images of filled solitons along the x -direction revealed the orientation of each soliton created. Simultaneous images taken along the y direction also showed the soliton plane on the occasions when it was horizontal. This non-destructive two-axis imaging technique was used to identify the initial orientation of the soliton nodal planes of the BECs for correlation with subsequent images of soliton decay.

To investigate and study dynamical instabilities of *single*-component dark solitons, the component- $|2\rangle$ filling was removed with a 100 ms blast of laser light resonant with an electronic transition of the $|2\rangle$ atoms, which left behind a dark soliton in component $|1\rangle$. The trapped BEC was then held for a variable time, typically less than 100 ms, before release from the confining potential and absorption imaging after 56 ms of expansion. Dark solitons were not observed in expansion images, even though the corresponding in-trap images showed that filled dark solitons were indeed created. Instead, pairs of density dips in the expanded images were observed. For x -axis images, two density dips were often seen to lie along a line that approximately matched the orientation of the corresponding filled dark soliton image for that same BEC, taken just before the soliton filling was removed. For example, if an in-trap image along x showed that the dark soliton was aligned in a horizontal plane, the two density dips would be seen in the expansion image along an imaginary horizontal line. If a soliton did happen to lie in such a horizontal plane, the soliton nodal plane was then also seen with in-trap images acquired along the y direction. The corresponding y -direction expansion images in these cases also showed two density dips. Example images are shown in Fig. 8.4.

The pairs of density dips in the expansion images indicate the presence of vortex rings in the BECs, the predicted decay products of dynamical instabilities of dark solitons in three-dimensional BECs [24]. Similar to a line vortex (see Part VI of this volume), and described earlier in this chapter, a vortex ring in a BEC is characterized by the absence of atoms in a toroidal region within the BEC, with quantized superfluid flow around the fluid-free toroid. An x -direction column density profile of a BEC with a vortex ring then appears as a smooth atom cloud with two “holes” separated by the vortex ring diameter, with a faint line connecting the holes. However, if the faint line cannot be seen then single-directional imaging does not easily distinguish between single vortex rings and a pair of vortex lines. Therefore, two-directional imaging was used to identify the presence of ring-like structures, as two density-dips were seen in the expansion images from two orthogonal directions for the

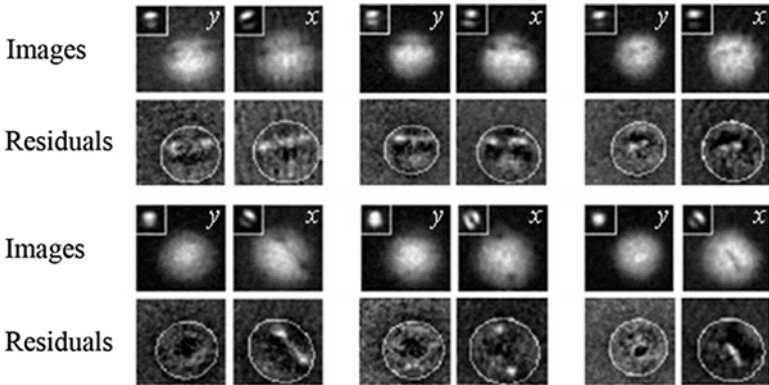


Fig. 8.4. Images of filled dark solitons (insets) and subsequent expansion images with density dips that correspond to atomic fluid displaced by vortex rings. Each image set consists of two expansion images simultaneously acquired along the x and y directions, and residuals obtained after subtracting a Thomas–Fermi (TF) fit of each image. The TF outline is shown as white ellipses in the residuals; the lighter regions within correspond to fluid depletion in the BEC. Note that in these images of condensates, the light–dark areas are reversed from the images of the Harvard condensates. Each full-size image represents an area of $220\ \mu\text{m} \times 220\ \mu\text{m}$. The figure is similar to Fig. 4 of [3]

cases where the in-trap images showed the initial dark soliton nodes to be horizontal.

The experimental results indicated that solitons decayed to vortex rings by the end of the 100 ms removal of the $|2\rangle$ atoms. The observations were consistent with numerical simulations, also described in [3]. However, while numerical results predicted the presence of up to three vortex rings, the experimental results revealed no more than a single vortex ring per image. Nevertheless, the experimental results confirmed the theoretical expectations of soliton decay, and demonstrated that multi-dimensional vortex rings were stable topological soliton structures that could be created and observed in BECs.

8.4 Interacting Dark Solitons and Hybrid Structures

In the Harvard experiment reported in [5], collisions of soliton fronts and vortex rings were probed. In order to facilitate the interaction between nonlinear waves, density engineering was used to generate density voids in two different locations within the same BEC simultaneously. A schematic of the experimental set up is shown in Fig. 8.1a and a simulation of the defect creation stage is shown in Fig. 8.1c. The mechanism of soliton shedding from shock waves as described in Sect. 8.3.1 leads to dark soliton fronts emanating from

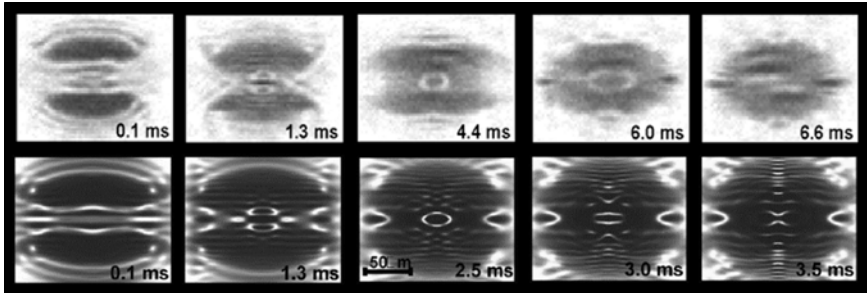


Fig. 8.5. Experiment (*top*) and simulation (*bottom*) of nonlinear-wave collisions from [5]. The apparent agreement is a strong indicator for the validity of the Gross–Pitaevskii approach to describe the non-equilibrium dynamics of BECs

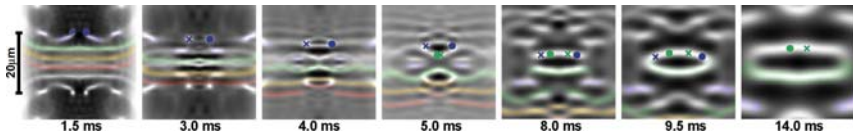


Fig. 8.6. Simulation of nonlinear-wave evolution during free expansion phase, from [5]. Phase singularities from vortex rings in the cylindrically symmetric BEC are marked in the upper halves of the frames by crosses or dots. The sequence shows the intricate dynamics that eventually leads to the formation of hybrid low-density shell structures composed of vortex rings and dark soliton fronts

two centers. In the central part of the BEC this leads to the head-on collision of trains of dark soliton fronts.

Figure 8.5 shows the experimental images of the condensate density (top row) and the results of a corresponding Gross–Pitaevskii simulation (bottom row). The images show unexpected intermediate structures in the form of low-density shells around a high-density core of oblate to spherical geometry. These structures are reminiscent of nonlinear Bessel-function-type stationary solutions of the nonlinear Schrödinger equation [5, 25–27] as discussed in Chap. 7. In the experiment, the shell structures are of transient nature and may be closely related to the transient shell structures seen in simulations of head-on collisions of vortex rings [28].

Further insight into the structure of the observed shell structures and their formation can be extracted from the GPE simulations of the experiment as shown in Figs. 8.5 and 8.6. These simulations revealed that the shell structures are not present while the BEC is in the trap but rather are formed during the expansion phase. The intricate dynamics that leads to the formation of shell structures involves decay of planar dark soliton fronts via the snake instability into vortex rings, repeated collisions of vortex rings with soliton fronts, the propelling and bending of soliton fronts by the inhomogeneous velocity fields associated with vortex rings, and finally the reconnection processes between

soliton wave fronts and annihilation of vortex ring pairs. The simulated evolution during the expansion phase is shown in Fig. 8.6.

8.5 Conclusions

Clearly the experimental investigation of multidimensional solitons has just begun. In particular, as three-dimensional waveguide structures on atom chips or in the form of toroidal traps become available, it will become possible and indeed, quite important to study the propagation modes of solitary waves in these geometries. Furthermore, as the theoretical work reviewed in Chap. 7 suggests, there is much to be expected from the experimental investigation of topological solitons and other nonlinear waves in spinor condensates. We note that the spontaneous formation of topological defects such as spin vortices has been observed very recently in an experiment at Berkeley [29] by quenching a spinor BEC through a ferromagnetic phase transition.

The authors are indebted to Zac Dutton for a careful reading of the manuscript. JB thanks Lene Hau, Naomi Ginsberg, and Sean Garner for many useful discussions and hospitality during his visits at Harvard University. LDC gratefully acknowledges the support of the National Science Foundation. BPA acknowledges support from the National Science Foundation and the Army Research Office.

References

1. S. Burger, K. Bongs, S. Dettmer, W. Ertmer, K. Sengstock, A. Sanpera, G.V. Shlyapnikov, M. Lewenstein, Phys. Rev. Lett. **83**, 5198 (1999)
2. J. Denschlag, J.E. Simsarian, D.L. Feder, C.W. Clark, L.A. Collins, J. Cubizolles, L. Deng, E.W. Hagley, K. Helmerson, W.P. Reinhardt, S.L. Rolston, B.I. Schneider, W.D. Phillips, Science **287**, 97 (2000)
3. B.P. Anderson, P.C. Haljan, C.A. Regal, D.L. Feder, L.A. Collins, C.W. Clark, E.A. Cornell, Phys. Rev. Lett. **86**, 2926 (2001)
4. Z. Dutton, M. Budde, C. Slowe, L.V. Hau, Science **293**, 663 (2001)
5. N.S. Ginsberg, J. Brand, L.V. Hau, Phys. Rev. Lett. **94**, 040403 (2005)
6. M.R. Matthews, B.P. Anderson, P.C. Haljan, D.S. Hall, C.E. Wieman, E.A. Cornell, Phys. Rev. Lett. **83**, 2498 (1999)
7. B.P. Anderson, et al. Phys. Rev. Lett. **85**, 2857 (2000)
8. J.E. Williams, M.J. Holland, Nature **401**, 568 (1999)
9. L.D. Carr, J. Brand, S. Burger, A. Sanpera, Phys. Rev. A **63**, 051601(R) (2001)
10. See Part III of this volume for theoretical and experimental reviews of dark solitons in BECs
11. M.R. Matthews, B.P. Anderson, P.C. Haljan, D.S. Hall, M.J. Holland, J.E. Williams, C.E. Wieman, E.A. Cornell, Phys. Rev. Lett. **83**, 3358 (1999)
12. K.-J. Boller, A. Imamolu, S.E. Harris, Phys. Rev. Lett. **66**, 2593–2596 (1991)
13. J.E. Field, K.H. Hahn, S.E. Harris, Phys. Rev. Lett. **67**, 3062–3065 (1991)
14. L.V. Hau, S.E. Harris, Z. Dutton, C.H. Behroozi, Nature **397**, 594 (1999)

15. C. Liu, Z. Dutton, C.H. Behroozi, L.V. Hau, *Nature* **409**, 490 (2001)
16. Z. Dutton, N.S. Ginsberg, C. Slowe, L.V. Hau, *Europhys. News* **35** (2004)
17. M. Zak, I. Kulikov, *Phys. Lett. A* **307**, 99–106 (2003)
18. V.M. Pérez-García, V.V. Konotop, V.A. Brazhnyi, *Phys. Rev. Lett.* **92**, 220403 (2004)
19. A.M. Kamchatnov, A. Gammal, R.A. Kraenkel, *Phys. Rev. A* **69**, 063605 (2004)
20. B. Damski, *Phys. Rev. A* **69**, 043610 (2004)
21. M.A. Hoefer, et al. *Phys. Rev. A* **74**, 023623 (2006)
22. A.V. Mamaev, M. Saffman, A.A. Zozulya, *Phys. Rev. Lett.* **76**, 226ca2 (1996); A.V. Mamaev et al., *Phys. Rev. A* **54**, 870 (1996)
23. V. Tikhonenko, J. Christou, B. Luther-Davies, Y.S. Kivshar, *Opt. Lett.* **21**, 1129–1131 (1996)
24. D.L. Feder, M.S. Pindzola, L.A. Collins, B.I. Schneider, C.W. Clark, *Phys. Rev. A* **62**, 053606 (2000)
25. G. Theocharis, D.J. Frantzeskakis, P.G. Kevrekidis, B.A. Malomed, Y.S. Kivshar, *Phys. Rev. Lett.* **90**, 120403 (2003)
26. G. Theocharis, P. Schmelcher, M.K. Oberthaler, P.G. Kevrekidis, D.J. Frantzeskakis, *Phys. Rev. A* **72**, 023609 (2005)
27. L.D. Carr, C.W. Clark, *Phys. Rev. A* **74**, 043613 (2006)
28. S. Komineas, J. Brand, *Phys. Rev. Lett.* **95**, 110401 (2005)
29. L.E. Sadler, J.M. Higbie, S.R. Leslie, M. Vengalattore, D.M. Stamper-Kurn, *Nature* **443**, 312–315 (2006)

Part VI

Vortices in Bose–Einstein Condensates

Vortices in Bose–Einstein Condensates: Theory

N.G. Parker, B. Jackson, A.M. Martin, and C.S. Adams

9.1 Quantized Vortices

Vortices are pervasive in nature, representing the breakdown of laminar fluid flow and hence playing a key role in turbulence. The fluid rotation associated with a vortex can be parameterized by the circulation $\Gamma = \oint d\mathbf{r} \cdot \mathbf{v}(\mathbf{r})$ about the vortex, where $\mathbf{v}(\mathbf{r})$ is the fluid velocity field. While classical vortices can take any value of circulation, superfluids are irrotational, and any rotation or angular momentum is constrained to occur through vortices with quantized circulation. Quantized vortices also play a key role in the dissipation of transport in superfluids. In BECs quantized vortices have been observed in several forms, including single vortices [1,2], vortex lattices [3–6] (see also Part VII), and vortex pairs and rings [7–9]. The recent observation of quantized vortices in a fermionic gas was taken as a clear signature of the underlying condensation and superfluidity of fermion pairs [10]. In addition to BECs, quantized vortices also occur in superfluid helium [11,12], nonlinear optics, and type-II superconductors [13].

9.1.1 Theoretical Framework

9.1.1.1 Quantization of Circulation

Quantized vortices represent phase defects in the superfluid topology of the system. Under the Madelung transformation, the macroscopic condensate ‘wavefunction’ $\psi(\mathbf{r}, t)$ can be expressed in terms of a fluid density $n(\mathbf{r}, t)$ and a macroscopic phase $S(\mathbf{r}, t)$ via $\psi(\mathbf{r}) = \sqrt{n(\mathbf{r}, t)} \exp[iS(\mathbf{r}, t)]$. In order that the wavefunction remains single-valued, the change in phase around any closed contour C must be an integer multiple of 2π ,

$$\int_C \nabla S \cdot d\mathbf{l} = 2\pi q, \quad (9.1)$$

where q is an integer. The gradient of the phase S defines the superfluid velocity via $\mathbf{v}(\mathbf{r}, t) = (\hbar/m)\nabla S(\mathbf{r}, t)$. This implies that the circulation about the contour C is given by,

$$\Gamma = \int_C \mathbf{v} \cdot d\mathbf{l} = q \left(\frac{\hbar}{m} \right). \quad (9.2)$$

In other words, the circulation of fluid is quantized in units of (\hbar/m) . The circulating fluid velocity about a vortex is given by $\mathbf{v}(r, \theta) = q\hbar/(mr)\hat{\theta}$, where r is the radius from the core and $\hat{\theta}$ is the azimuthal unit vector.

9.1.1.2 Theoretical Model

The Gross–Pitaevskii equation (GPE) provides an excellent description of BECs at the mean-field level in the limit of ultra-cold temperatures [14]. It supports quantized vortices, and has been shown to give a good description of the static properties and dynamics of vortices [14, 15]. Dilute BECs require a confining potential, formed by magnetic or optical fields, which typically varies quadratically with position. We will assume an axially-symmetric harmonic trap of the form $V = \frac{1}{2}m(\omega_r^2 r^2 + \omega_z^2 z^2)$, where ω_r and ω_z are the radial and axial trap frequencies respectively. Excitation spectra of BEC states can be obtained using the Bogoliubov equations, and specify the stability of stationary solutions of the GPE. For example, the presence of the so-called anomalous modes of a vortex in a trapped BEC are indicative of their thermodynamic instability. The GPE can also give a qualitative, and sometimes quantitative, understanding of vortices in superfluid helium [11, 12].

Although this chapter deals primarily with vortices in repulsively-interacting BECs, vortices in attractively-interacting BECs have also received theoretical interest. The presence of a vortex in a trapped BEC with attractive interactions is less energetically favorable than for repulsive interactions [16]. Indeed, a harmonically-confined attractive BEC with angular momentum is expected to exhibit a center-of-mass motion rather than a vortex [17]. The use of anharmonic confinement can, however, support metastable vortices, as well as regimes of center-of-mass motion and instability [18–20].

Various approximations have been made to incorporate thermal effects into the GPE to describe vortices at finite temperature (see also Part XI). The Popov approximation self-consistently couples the condensate to a normal gas component using the Bogoliubov–de-Gennes formalism [21] (cf. Chap. 1 Sect. 4.2). Other approaches involve the addition of thermal/quantum noise to the system, such as the stochastic GPE method [22–24] and the classical field/truncated Wigner methods [25–28]. Thermal effects can also be simulated by adding a phenomenological dissipation term to the GPE [29].

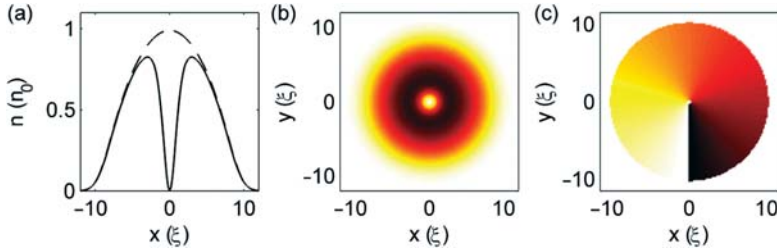


Fig. 9.1. Profile of a singly-quantized ($q = 1$) vortex at the center of a harmonically-confined BEC: (a) condensate density along the $y = 0$ axis (solid line) and the corresponding density profile in the absence of the vortex (dashed line). (b) 2D density and (c) phase profile of the vortex state. These profiles are calculated numerically by propagating the 2D GPE in imaginary time subject to an azimuthal 2π phase variation around the trap center

9.1.1.3 Basic Properties of Vortices

In a homogeneous system, a quantized vortex has the 2D form,

$$\psi(r, \theta) = \sqrt{n_v(r)} \exp(iq\theta). \quad (9.3)$$

The vortex density profile $n_v(r)$ has no analytic solution, although approximate solutions exist [30]. Vortex solutions can be obtained numerically by propagating the GPE in imaginary time ($t \rightarrow -it$) [31], whereby the GPE converges to the lowest energy state of the system (providing it is stable). By enforcing the phase distribution of (9.3), a vortex solution is generated. Figure 9.1 shows the solution for a $q = 1$ vortex at the center of a harmonically-confined BEC. The vortex consists of a node of zero density with a width characterized by the condensate healing length $\xi = \hbar/\sqrt{mn_0g}$, where $g = 4\pi\hbar^2a/m$ (with a the s-wave scattering length and m the atomic mass) and n_0 is the peak density in the absence of the vortex. For typical BEC parameters [3], $\xi \sim 0.2 \mu m$. For a $q = 1$ vortex at the center of an axially-symmetric potential, each particle carries \hbar of angular momentum. However, if the vortex is off-center, the angular momentum per particle becomes a function of position [15].

9.1.2 Vortex Structures

Increasing the vortex charge widens the core due to centrifugal effects. In harmonically-confined condensates a multiply-quantized vortex with $q > 1$ is energetically unfavorable compared to a configuration of singly-charged vortices [32, 33]. Hence, a rotating BEC generally contains an array of singly-charged vortices in the form of a triangular Abrikosov lattice [3–6, 34] (see also Part VII), similar to those found in rotating superfluid helium [11]. A $q > 1$

vortex can decay by splitting into singly-quantized vortices via a dynamical instability [35, 36], but is stable for some interaction strengths [37]. Multiply-charged vortices are also predicted to be stabilized by a suitable localized pinning potential [38] or the addition of quartic confinement [33].

Two-dimensional vortex–antivortex pairs (i.e. two vortices with equal but opposite circulation) and 3D vortex rings arise in the dissipation of superflow, and represent solutions to the homogeneous GPE in the moving frame [39, 40], with their motion being self-induced by the velocity field of the vortex lines. When the vortex lines are so close that they begin to overlap, these states are no longer stable and evolves into a rarefaction pulse [39].

Having more than one spin component in the BECs (cf. Part IX) provides an additional topology to vortex structures. Coreless vortices and vortex ‘molecules’ in coupled two-component BECs have been probed experimentally [41] and theoretically [42]. More exotic vortex structures such as skyrmion excitations [43] and half-quantum vortex rings [44] have also been proposed.

9.2 Nucleation of Vortices

Vortices can be generated by rotation, a moving obstacle, or phase imprinting methods. Below we discuss each method in turn.

9.2.1 Rotation

As discussed in the previous section, a BEC can only rotate through the existence of quantized vortex lines. Vortex nucleation occurs only when the rotation frequency Ω of the container exceeds a critical value Ω_c [15, 32, 46]. Consider a condensate in an axially-symmetric trap which is rotating about the z -axis at frequency Ω . In the Thomas–Fermi limit, the presence of a vortex becomes energetically favorable when Ω exceeds a critical value given by [47],

$$\Omega_c = \frac{5}{2} \frac{\hbar}{mR^2} \ln \frac{0.67R}{\xi}. \quad (9.4)$$

This is derived by integrating the kinetic energy density $mn(r)v(r)^2/2$ of the vortex velocity field in the radial plane. The lower and upper limits of the integration are set by the healing length ξ and the BEC Thomas–Fermi radius R , respectively. Note that $\Omega_c < \omega_r$ for repulsive interactions, while $\Omega_c > \omega_r$ for attractive interactions [16]. In a non-rotating BEC the presence of a vortex raises the energy of the system, indicating thermodynamic instability [48].

In experiments, vortices are formed only when the trap is rotated at a much higher frequency than Ω_c [3–5], demonstrating that the energetic criterion is a necessary, but not sufficient, condition for vortex nucleation. There must also be a dynamic route for vorticity to be introduced into the condensate, and hence (9.4) provides only a lower bound for the critical frequency.

The nucleation of vortices in rotating trapped BECs appears to be linked to instabilities of collective excitations. Numerical simulations based on the GPE have shown that once the amplitude of these excitations become sufficiently large, vortices are nucleated that subsequently penetrate the high-density bulk of the condensate [23, 27, 29, 49, 50].

One way to induce instability is to resonantly excite a surface mode by adding a rotating deformation to the trap potential. In the limit of small perturbations, this resonance occurs close to a rotation frequency $\Omega_r = \omega_\ell/\ell$, where ω_ℓ is the frequency of a surface mode with multipolarity ℓ . In the Thomas–Fermi limit, the surface modes satisfy $\omega_\ell = \sqrt{\ell}\omega_r$ [51], so $\Omega_r = \omega_r/\sqrt{\ell}$. For example, an elliptically-deformed trap, which excites the $\ell = 2$ quadrupole mode, would nucleate vortices when rotated at $\Omega_r \approx \omega_r/\sqrt{2}$. This value has been confirmed in both experiments [3–5] and numerical simulations [23, 27, 29, 49, 50]. Higher multipolarities were resonantly excited in the experiment of [6], finding vortex formation at frequencies close to the expected values, $\Omega = \omega_r/\sqrt{\ell}$, and lending further support to this picture.

A similar route to vortex nucleation is revealed by considering stationary states of the BEC in a rotating elliptical trap, which can be obtained in the Thomas–Fermi limit by solving hydrodynamic equations [52]. At low rotation rates only one solution is found; however at higher rotations ($\Omega > \omega_r/\sqrt{2}$) a bifurcation occurs and up to three solutions are present. Above the bifurcation point one or more of the solutions become dynamically unstable [53], leading to vortex formation [54]. Madison et al. [55] followed these stationary states experimentally by adiabatically introducing trap ellipticity and rotation, and observed vortex nucleation in the expected region.

Surface mode instabilities can also be induced at finite temperature by the presence of a rotating noncondensed “thermal” cloud. Such instabilities occur when the thermal cloud rotation rate satisfies $\Omega > \omega_\ell/\ell$ [56]. Since all modes can potentially be excited in this way, the criterion for instability and hence vortex nucleation becomes $\Omega_c > \min(\omega_\ell/\ell)$, analogous to the Landau criterion. Note that such a minimum exists at $\Omega_c > 0$ since the Thomas–Fermi result $\omega_\ell = \sqrt{\ell}\omega_r$ becomes less accurate for high ℓ [57]. This mechanism may have been important in the experiment of Haljan et al. [34], where a vortex lattice was formed by cooling a rotating thermal cloud to below T_c .

9.2.2 Nucleation by a Moving Object

Vortices can also be nucleated in BECs by a moving localized potential. This problem was originally studied using the GPE for 2D uniform condensate flow around a circular hard-walled potential [58, 59], with vortex–antivortex pairs being nucleated when the flow velocity exceeded a critical value.

In trapped BECs a similar situation can be realized using the optical dipole force from a laser, giving rise to a localized repulsive Gaussian potential. Under linear motion of such a potential, numerical simulations revealed vortex pair formation when the potential is moved at a velocity above a critical value [60].

The experiments of [61, 62] oscillated a repulsive laser beam in an elongated condensate. Although vortices were not observed directly, the measurement of condensate heating and drag above a critical velocity was consistent with the nucleation of vortices [63].

An alternative approach is to move the laser beam potential in a circular path around the trap center [64]. By “stirring” the condensate in this way one or more vortices can be created. This technique was used in the experiment of [6], where vortices were generated even at low stirring frequencies.

9.2.3 Other Mechanisms and Structures

A variety of other schemes for vortex creation have been suggested. One of the most important is that by Williams and Holland [65], who proposed a combination of rotation and coupling between two hyperfine levels to create a two-component condensate, one of which is in a vortex state. The non-vortex component can then either be retained or removed with a resonant laser pulse. This scheme was used by the first experiment to obtain vortices in BEC [1]. A related method, using topological phase imprinting, has been used to experimentally generate multiply-quantized vortices [66].

Apart from the vortex lines considered so far, vortex rings have also been the subject of interest. Rings are the decay product of dynamically unstable dark solitary waves in 3D geometries [7, 8, 67, 68]. Vortex rings also form in the quantum reflection of BECs from surface potentials [69], the unstable motion of BECs through an optical lattice [70], the dragging of a 3D object through a BEC [71], and the collapse of ultrasound bubbles in BECs [72]. The controlled generation of vortex rings [73] and multiple/bound vortex ring structures [74] have been analyzed theoretically.

A finite temperature state of a quasi-2D BEC, characterized by the thermal activation of vortex–antivortex pairs, has been simulated using classical field simulations [75]. This effect is thought to be linked to the Berezinskii–Kosterlitz–Thouless phase transition of 2D superfluids, recently observed experimentally in ultracold gases [76]. Similar simulations in a 3D system have also demonstrated the thermal creation of vortices [77, 78].

9.3 Dynamics of Vortices

The study of vortex dynamics has long been an important topic in both classical [79] and quantum [12] hydrodynamics. Helmholtz’s theorem for uniform, inviscid fluids, which is also applicable to quantized vortices in superfluids near zero temperature, states that the vortex will follow the motion of the background fluid. So, for example, in a superfluid with uniform flow velocity \mathbf{v}_s , a single straight vortex line will move with velocity \mathbf{v}_L , such that it is stationary in the frame of the superfluid.

Vortices similarly follow the “background flow” originating from circulating fluid around a vortex core. Hence vortex motion can be induced by the presence of other vortices, or by other parts of the same vortex line when it is curved. Most generally, the superfluid velocity \mathbf{v}_i due to vortices at a particular point \mathbf{r} is given by the *Biot–Savart* law [12], in analogy with the similar equation in electromagnetism,

$$\mathbf{v}_i = \frac{\Gamma}{4\pi} \int \frac{(\mathbf{s} - \mathbf{r}) \times d\mathbf{s}}{|\mathbf{s} - \mathbf{r}|^3}; \quad (9.5)$$

where $\mathbf{s}(\zeta, t)$ is a curve representing the vortex line where ζ denotes the arc length and Γ is the vortex circulation defined in Eq. (9.2). Equation (9.5) suffers from a divergence at $\mathbf{r} = \mathbf{s}$, so in calculations of vortex dynamics this must be treated carefully [80]. Equation (9.5) also assumes that the vortex core size is small compared to the distance between vortices. In particular, it breaks down when vortices cross during collisions, where reconnection events can occur. These reconnections can either be included “manually” [81], or by solving the full GPE [82]. The latter method also has the advantage of including sound emission due to vortex motion or reconnections [83, 84].

In a system with multiple vortices, motion of one vortex is induced by the circulating fluid flow around other vortices, and vice-versa [11]. This means that, for example, a pair of vortices of equal but opposite charge will move linearly and parallel to each other with a velocity inversely proportional to the distance between them. Two or more vortices of equal charge, meanwhile, will rotate around each other, giving rise to a rotating vortex lattice as will be discussed in Part VII. When a vortex line is curved, circulating fluid from one part of the line can induce motion in another. This effect can give rise to helical waves on the vortex, known as Kelvin modes [85]. It also has interesting consequences for a vortex ring, which will travel in a direction perpendicular to the plane of the ring, with a self-induced velocity that decreases with increasing radius. Classically, this is most familiar in the motion of smoke rings, though similar behavior has also been observed in superfluid helium [86].

This simple picture is complicated in the presence of density inhomogeneities or confining walls. In a harmonically-trapped BEC the density is a function of position, and therefore the energy, E , of a vortex will also depend on its position within the condensate. To simplify matters, let us consider a quasi-2D situation, where the condensate is pancake-shaped and the vortex line is straight. In this case, the energy of the vortex depends on its displacement \mathbf{r} from the condensate center [87], and a displaced vortex feels a force proportional to ∇E . This is equivalent to a Magnus force on the vortex [88–90] and to compensate the vortex moves in a direction perpendicular to the force, leading it to precess around the center of the condensate along a line of constant energy. This precession of a single vortex has been observed experimentally [2], with a frequency in agreement with theoretical predictions. In more 3D situations, such as spherical or cigar-shaped condensates, the vortex can bend [91–94] leading to more complicated motion [15]. Kelvin

modes [95, 96] and vortex ring dynamics [88] are also modified by the density inhomogeneity in the trap.

In the presence of a hard-wall potential, a new constraint is imposed such that the fluid velocity normal to the wall must be zero, $\mathbf{v}_s \cdot \hat{\mathbf{n}} = 0$. The resulting problem of vortex motion is usually solved mathematically [79] by invoking an “image vortex” on the other side of the wall (i.e. in the region where there is no fluid present), at a position such that its normal flow cancels that of the real vortex at the barrier. The motion of the real vortex is then simply equal to the induced velocity from the image vortex circulation.

9.4 Stability of Vortices

9.4.1 Thermal Instabilities

At finite temperatures the above discussion is modified by the thermal occupation of excited modes of the system, which gives rise to a noncondensed normal fluid in addition to the superfluid. A vortex core moving relative to the normal fluid scatters thermal excitations, and will therefore feel a frictional force leading to dissipation. This mutual friction force can be written as [11],

$$\mathbf{f}_D = -n_s \Gamma \{ \alpha \mathbf{s}' \times [\mathbf{s}' \times (\mathbf{v}_n - \mathbf{v}_L)] + \alpha' \mathbf{s}' \times (\mathbf{v}_n - \mathbf{v}_L) \}, \quad (9.6)$$

where n_s is the background superfluid density, \mathbf{s}' is the derivative of \mathbf{s} with respect to arc length ζ , α and α' are temperature dependent parameters, while \mathbf{v}_L and \mathbf{v}_n are the velocities of the vortex line and normal fluid respectively. The mutual friction therefore has two components perpendicular to the relative velocity $\mathbf{v}_n - \mathbf{v}_L$.

To consider an example discussed in the last section, an off-center vortex in a trapped BEC at zero temperature will precess in a way such that its energy remains constant. In the presence of a non-condensed component, however, dissipation will lead to a loss of energy. Since the vortex is topological it cannot simply vanish, so this lost energy is manifested as a radial drift of the vortex towards lower densities. In (9.6) the α term is responsible for this radial motion, while α' changes the precession frequency. The vortex disappears at the edge of the condensate, where it is thought to decay into elementary excitations [97]. Calculations based upon the stochastic GPE have shown that thermal fluctuations lead to an uncertainty in the position of the vortex, such that even a central vortex will experience thermal dissipation and have a finite lifetime [24]. This thermodynamic lifetime is predicted to be of the order of seconds [97], which is consistent with experiments [1, 3, 94].

9.4.2 Hydrodynamic Instabilities

Experiments indicate that the crystallization of vortex lattices is temperature-independent [5, 98]. Similarly, vortex tangles in turbulent states of superfluid

helium have been observed to decay at ultracold temperature, where thermal dissipation is virtually nonexistent [99]. These results highlight the occurrence of zero temperature dissipation mechanisms, as listed below.

9.4.2.1 Instability to Acceleration

The topology of a 2D homogeneous superfluid can be mapped on to a (2+1)D electrodynamic system, with vortices and phonons playing the role of charges and photons respectively [100]. Just as an accelerating electron radiates according to the Larmor acceleration squared law, a superfluid vortex is inherently unstable to acceleration and radiates sound waves.

Vortex acceleration can be induced by the presence of an inhomogeneous background density, such as in a trapped BEC. Sound emission from a vortex in a BEC can be probed by considering a trap of the form [45],

$$V_{\text{ext}} = V_0 \left[1 - \exp \left(-\frac{m\omega_d^2 r^2}{2V_0} \right) \right] + \frac{1}{2} m\omega_r^2 r^2. \quad (9.7)$$

This consists of a Gaussian dimple trap with depth V_0 and harmonic frequency component ω_d , embedded in an ambient harmonic trap of frequency ω_r . A 2D description is sufficient to describe this effect. This set-up can be realized with a quasi-2D BEC by focusing a far-off-resonant red-detuned laser beam in the center of a magnetic trap. The vortex is initially confined in the inner region, where it precesses due to the inhomogeneous density. Since sound excitations have an energy of the order of the chemical potential μ , the depth of the dimple relative to μ leads to two distinct regimes of vortex–sound interactions.

$$V_0 \gg \mu$$

The vortex effectively sees an infinite harmonic trap; it precesses and radiates sound but there is no net decay due to complete sound reabsorption. However, a collective mode of the background fluid is excited, inducing slight modulations in the vortex path (dotted line in Fig. 9.2).

$$V_0 < \mu$$

Sound waves are radiated by the precessing vortex. The ensuing decay causes the vortex to drift to lower densities, resulting in a spiral motion (solid line in Fig. 9.2), similar to the effect of thermal dissipation. The sound waves are emitted in a dipolar radiation pattern, perpendicularly to the instantaneous direction of motion (subplots in Fig. 9.2), with a typical amplitude of order $0.01n_0$ and wavelength $\lambda \sim 2\pi c/\omega_V$ [15], where c is the speed of sound and ω_V is the vortex precession frequency. The power radiated from a vortex can be expressed in the form [45, 101, 102],

$$P = \beta m N \left(\frac{a^2}{\omega_V} \right), \quad (9.8)$$

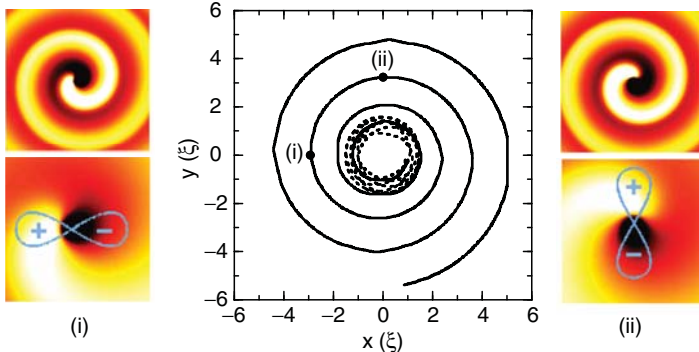


Fig. 9.2. Vortex path in the dimple trap geometry of (9.7) with $\omega_d = 0.28(c/\xi)$. Deep $V_0 = 10\mu$ dimple (dotted line): mean radius is constant, but modulated by the sound field. Shallow $V_0 = 0.6\mu$ dimple and homogeneous outer region $\omega_r = 0$ (dotted line): vortex spirals outwards. Outer plots: Sound excitations (with amplitude $\sim 0.01n_0$) radiated in the $V_0 = 0.6\mu$ system at different times. *Top:* Far-field distribution $[-90, 90]\xi \times [-90, 90]\xi$. *Bottom:* Near-field distribution $[-25, 25]\xi \times [-25, 25]\xi$, with an illustration of the dipolar radiation pattern. Copyright (2004) by the American Physical Society [45]

where a is the vortex acceleration, N is the total number of atoms, and β is a dimensionless coefficient. Using classical hydrodynamics [101] and by mapping the superfluid hydrodynamic equations onto Maxwell's electrodynamic equations [102], it has been predicted that $\beta = \pi^2/2$ under the assumptions of a homogeneous 2D fluid, a point vortex, and perfect circular motion. Full numerical simulations of the GPE based on a realistic experimental scenario have derived a coefficient of $\beta \sim 6.3 \pm 0.9$ (one standard deviation), with the variation due to a weak dependence on the geometry of the system [45].

When $\omega_r \neq 0$, the sound eventually reinteracts with the vortex, slowing but not preventing the vortex decay. By varying V_0 it is possible to control vortex decay, and in suitably engineered traps this decay mechanism is expected to dominate over thermal dissipation [45].

Vortex acceleration (and sound emission) can also be induced by the presence of other vortices. A co-rotating pair of two vortices of equal charge has been shown to decay continuously via quadrupolar sound emission, both analytically [103] and numerically [104]. Three-body vortex interactions in the form of a vortex–antivortex pair incident on a single vortex have also been simulated numerically, with the interaction inducing acceleration in the vortices with an associated emission of sound waves [104].

Simulations of vortex lattice formation in a rotating elliptical trap show that vortices are initially nucleated in a turbulent disordered state, before relaxing into an ordered lattice [50]. This relaxation process is associated with an exchange of energy from the sound field to the vortices due to these

vortex–sound interactions. This agrees with the experimental observation that vortex lattice formation is insensitive to temperature [5, 98].

9.4.2.2 Kelvin Wave Radiation and Vortex Reconnections

In 3D a Kelvin wave excitation will induce acceleration in the elements of the vortex line, and therefore local sound emission. Indeed, simulations of the GPE in 3D have shown that Kelvin waves excitations on a vortex ring lead to a decrease in the ring size, indicating the underlying radiation process [84]. Kelvin wave excitations can be generated from a vortex line reconnection [83, 84] and the interaction of a vortex with a rarefaction pulse [105].

Vortex lines which cross each other can undergo dislocations and reconnections [106], which induce a considerable burst of sound emission [83]. Although they have yet to be probed experimentally in BECs, vortex reconnections are hence thought to play a key role in the dissipation of vortex tangles in helium II at ultra-low temperatures [11].

9.5 Dipolar BECs

A BEC has recently been formed of chromium atoms [107], which feature a large dipole moment. This opens the door to studying of the effect of long-range dipolar interactions in BECs.

9.5.1 The Modified Gross–Pitaevskii Equation

The interaction potential $U_{dd}(\mathbf{r})$ between two dipoles separated by \mathbf{r} , and aligned by an external field along the unit vector $\hat{\mathbf{e}}$ is given by

$$U_{dd}(\mathbf{r}) = \frac{C_{dd}}{4\pi} \hat{e}_i \hat{e}_j \frac{(\delta_{ij} - 3\hat{r}_i \hat{r}_j)}{r^3}. \quad (9.9)$$

For low energy scattering of two atoms with dipoles induced by a static electric field $\mathbf{E} = E\hat{\mathbf{e}}$, the coupling constant $C_{dd} = E^2 \alpha^2 / \epsilon_0$ [108, 109], where α is the static dipole polarizability of the atoms and ϵ_0 is the permittivity of free space. Alternatively, if the atoms have permanent magnetic dipoles, d_m , aligned in an external magnetic field $\mathbf{B} = B\hat{\mathbf{e}}$, one has $C_{dd} = \mu_0 d_m^2$ [110], where μ_0 is the permeability of free space. Such dipolar interactions give rise to a mean-field potential

$$\Phi_{dd}(\mathbf{r}) = \int d^3 r U_{dd}(\mathbf{r} - \mathbf{r}') |\psi(\mathbf{r}')|^2, \quad (9.10)$$

which can be incorporated into the GPE to give,

$$i\hbar\psi_t = \left[-\frac{\hbar^2}{2m} \nabla^2 + g|\psi|^2 + \Phi_{dd} + V \right] \psi. \quad (9.11)$$

For an axially-symmetric quasi-2D geometry ($\omega_z \gg \omega_r$) rotating about the z -axis, the ground state wavefunction of a single vortex has been solved numerically [111]. Considering 10^5 chromium atoms and $\omega_r = 2\pi \times 100$ Hz, several solutions were obtained depending on the strength of the s -wave interactions and the alignment of the dipoles relative to the trap.

For the case of axially-polarized dipoles the most striking results arise for attractive s -wave interactions $g < 0$. Here the BEC density is axially symmetric and oscillates in the vicinity of the vortex core. Similar density oscillations have been observed in numerical studies of other non-local interaction potentials, employed to investigate the interparticle interactions in ${}^4\text{He}$ [112–115], with an interpretation that relates to the roton structure in a superfluid [115]. For the case of transversely-polarized dipoles, where the polarizing field is co-rotating with the BEC, and repulsive s -wave interactions ($g > 0$), the BEC becomes elongated along the axis of polarization [116] and as a consequence the vortex core is anisotropic.

9.5.2 Vortex Energy

Assuming a dipolar BEC in the TF limit (cf. Sect. 4 in Chap. 1), the energetic cost of a vortex, aligned along the axis of polarization (z -axis), has been derived using a variational ansatz for the vortex core [117], and thereby the critical rotation frequency Ω_c at which the presence of a vortex becomes energetically favorable has been calculated. For an oblate trap ($\omega_r < \omega_z$), dipolar interactions decrease Ω_c , while for prolate traps ($\omega_r > \omega_z$) the presence of dipolar interactions increases Ω_c . A formula resembling (9.4) for the critical frequency of a conventional BEC can be used to explain these results, with R being the modified TF radius of the dipolar BEC. Indeed, using the TF radius of a vortex-free dipolar BEC [118, 119] and the conventional s -wave healing length ξ , it was found that (9.4) closely matches the results from the energy cost calculation. Deviations become significant when the dipolar interactions dominate over s -wave interactions. In this regime the s -wave healing length ξ is no longer the relevant length scale of the system, and the equivalent dipolar length scale $\xi_d = C_{dd}m/(12\pi\hbar^2)$ will characterize the vortex core size.

For $g > 0$ and in the absence of dipolar interactions, the rotation frequency at which the vortex-free BEC becomes dynamically unstable, Ω_{dyn} , is always greater than the critical frequency for vortex stabilization Ω_c . However in the presence of dipolar interactions, Ω_{dyn} can become less than Ω_c , leading to an intriguing regime in which the dipolar BEC is dynamically unstable but vortices will not enter [117, 120]. As with attractive condensates [17], the angular momentum may then be manifested as center of mass oscillations.

9.6 Analogs of Gravitational Physics in BECs

There is growing interest in pursuing analogs of gravitational physics in condensed matter systems [121], such as BECs. The rationale behind such models

can be traced back to the work of Unruh [122, 123], who noted the analogy between sound propagation in an inhomogeneous background flow and field propagation in curved space–time. This link applies in the TF limit of BECs where the speed of sound is directly analogous to the speed of light in the corresponding gravitational system [124]. This has led to proposals for experiments to probe effects such as Hawking radiation [125, 126] and superradiance [127]. For Hawking radiation it is preferable to avoid the generation of vortices [121, 128], and as such will not be discussed here. However, the phenomena of superradiance in BECs, which can be considered as stimulated Hawking radiation, relies on the presence of a vortex [129–132], which is analogous to a rotating black hole.

Below we outline the derivation of how the propagation of sound in a BEC can be considered to be analogous to field propagation [121]. From the GPE it is possible to derive the continuity equation for an irrotational fluid flow with phase $S(\mathbf{r}, t)$ and density $n(\mathbf{r}, t)$, and a Hamilton–Jacobi equation whose gradient leads to the Euler equation. Linearizing these equations with respect to the background it is found that

$$\partial_t S' = -\frac{1}{m} \nabla S \cdot \nabla S' - gn' + \frac{\hbar^2}{4m\sqrt{n}} \left(\nabla^2 \frac{n'}{\sqrt{n}} - \frac{n'}{n} \nabla^2 \sqrt{n} \right), \quad (9.12)$$

$$\partial_t n' = -\frac{1}{m} \nabla \cdot (n \nabla S') - \frac{1}{m} \nabla \cdot (n' \nabla S), \quad (9.13)$$

where n' and S' are the perturbed values of the density n and phase S respectively. Neglecting the quantum pressure ∇^2 -terms, the above equations can be rewritten as a covariant differential equation describing the propagation of phase oscillations in a BEC. This is directly analogous to the propagation of a minimally coupled massless scalar field in an effective Lorentzian geometry which is determined by the background velocity, density and speed of sound in the BEC. Hence, the propagation of sound in a BEC can be used as an analogy for the propagation of electromagnetic fields in the corresponding space–time. Of course one has to be aware that this direct analogy is only valid in the TF regime, which breaks down on scales of the order of a healing length, i.e. the theory is only valid on large length scales, as is general relativity.

9.6.1 Superradiance

Superradiance in BECs relies on sound waves incident on a vortex structure and is characterized by the reflected sound energy exceeding the incident energy. This has been studied using (9.12) and (9.13) for monochromatic sound waves of frequency ω_s and angular wave number q_s incident upon a vortex [129] and a “draining vortex” (a vortex with outcoupling at its center) [130–132].

For the vortex case, a vortex velocity field $\mathbf{v}(r, \theta) = (\beta/r)\hat{\theta}$ and a density profile ansatz was assumed. Superradiance then occurs when $\beta q_s > A c_\infty$,

where A is related to the vortex density ansatz and c_∞ is the speed of sound at infinity [129]. Interestingly, this condition is frequency independent.

For the case of a draining vortex, an event horizon occurs at a distance a from the vortex core, where the fluid circulates at frequency Ω . Assuming a homogeneous density n and a velocity profile

$$\mathbf{v}(r, \theta) = \frac{1}{r} \left(-c\hat{\mathbf{r}} + \Omega a^2 \hat{\theta} \right),$$

where c is the homogeneous speed of sound, superradiance occurs when $0 < \omega_s < q_s \Omega$ [130–132].

The increase in energy of the outgoing sound is due to an extraction of energy from the vortex and as such it is expected to lead to slowing of the vortex rotation. However, such models do not include quantized vortex angular momentum, and as such it is expected that superradiance will be suppressed [132]. This raises tantalizing questions, such as whether superradiance can occur if vorticity is quantized, if such effects can be modeled with the GPE, and whether the study of quantum effects in condensate superradiance will shed light on quantum effects in general relativity.

References

1. M.R. Matthews, B.P. Anderson, P.C. Haljan, D.S. Hall, C.E. Wieman, E.A. Cornell, Phys. Rev. Lett. **83**, 2498 (1999)
2. B.P. Anderson, P.C. Haljan, C.E. Wieman, E.A. Cornell, Phys. Rev. Lett. **85**, 2857 (2000)
3. K.W. Madison, F. Chevy, W. Wohlleben, J. Dalibard, Phys. Rev. Lett. **84**, 806 (2000)
4. J.R. Abo-Shaeer, C. Raman, J.M. Vogels, W. Ketterle, Science **292**, 476 (2001)
5. E. Hodby, C. Hechenblaikner, S.A. Hopkins, O.M. Maragò, C.J. Foot, Phys. Rev. Lett. **88**, 010405 (2002)
6. C. Raman, J.R. Abo-Shaeer, J.M. Vogels, K. Xu, W. Ketterle, Phys. Rev. Lett. **87**, 210402 (2001)
7. B.P. Anderson, P.C. Haljan, C.A. Regal, D.L. Feder, L.A. Collins, C.W. Clark, E.A. Cornell, Phys. Rev. Lett. **86**, 2926 (2001)
8. Z. Dutton, M. Budde, C. Slowe, L.V. Hau, Science **293**, 663 (2001)
9. S. Inouye, S. Gupta, T. Rosenband, A.P. Chikkatur, A. Görlitz, T.L. Gustavson, A.E. Leanhardt, D.E. Pritchard, W. Ketterle, Phys. Rev. Lett. **87**, 080402 (2001)
10. M.W. Zwierlein, J.R. Abo-Shaeer, A. Schirotzek, C.H. Schunck, W. Ketterle, Nature **435**, 1047 (2005)
11. R.J. Donnelly, *Quantized vortices in Helium II* (Cambridge University Press, Cambridge, 1991)
12. C.F. Barenghi, R.J. Donnelly, W.F. Vinen (ed.), *Quantized Vortex Dynamics and Superfluid Turbulence* (Springer, Berlin Heidelberg New York, 2001)
13. D.R. Tilley, J. Tilley, *Superfluidity and Superconductivity* (IOP, Bristol, 1990)

14. F. Dalfovo, S. Giorgini, L.P. Pitaevskii, S. Stringari, Rev. Mod. Phys. **71**, 463 (1999)
15. A.L. Fetter, A.A. Svidzinsky, J. Phys.: Condens. Matter **13**, R135 (2001)
16. F. Dalfovo, S. Stringari, Phys. Rev. A **53**, 2477 (1996)
17. N.K. Wilkin, J.M.F. Gunn, R.A. Smith, Phys. Rev. Lett. **80**, 2265 (1998)
18. H. Saito, M. Ueda, Phys. Rev. A **69**, 013604 (2004)
19. E. Lundh, A. Collin, K.-A. Suominen, Phys. Rev. Lett. **92**, 070401 (2004)
20. G.M. Kavoulakis, A.D. Jackson, G. Baym, Phys. Rev. A **70**, 043603 (2004)
21. S.M.M. Virtanen, T.P. Simula, M.M. Salomaa, Phys. Rev. Lett. **86**, 2704 (2001)
22. C.W. Gardiner, J.R. Anglin, T.I.A. Fudge, J. Phys. B **35**, 1555 (2002)
23. A.A. Penckwitt, R.J. Ballagh, C.W. Gardiner, Phys. Rev. Lett. **89**, 260402 (2002)
24. R.A. Duine, B.W.A. Leurs, H.T.C. Stoof, Phys. Rev. A **69**, 053623 (2004)
25. M.J. Steel, M.K. Olsen, L.I. Plimak, P.D. Drummond, S.M. Tan, M.J. Collett, D.F. Walls, R. Graham, Phys. Rev. A **58**, 4824 (1998)
26. M.J. Davis, S.A. Morgan, K. Burnett, Phys. Rev. A **66**, 053618 (2002)
27. C. Lobo, A. Sinatra, Y. Castin, Phys. Rev. Lett. **92**, 020403 (2004)
28. T.P. Simula, P.B. Blakie, Phys. Rev. Lett. **96**, 020404 (2006)
29. M. Tsubota, K. Kasamatsu, M. Ueda, Phys. Rev. A **65**, 023603 (2002)
30. C.J. Pethick, H. Smith, *Bose–Einstein Condensation in Dilute Gases* (Cambridge, 2002)
31. A. Minguzzi, S. Succi, F. Toschi, M. P. Tosi, P. Vignolo, Phys. Rep. **395**, 223 (2004)
32. D.A. Butts, D.S. Rokshar, Nature **397**, 327 (1999)
33. E. Lundh, Phys. Rev. A **65**, 043604 (2002)
34. P.C. Haljan, I. Coddington, P. Engels, E.A. Cornell, Phys. Rev. Lett. **87**, 210403 (2001)
35. M. Möttönen, T. Mizushima, T. Isoshima, M.M. Salomaa, K. Machida, Phys. Rev. A **68**, 023611 (2003)
36. Y. Shin, M. Saba, A. Schirotzek, T.A. Pasquini, A.E. Leanhardt, D.E. Pritchard, W. Ketterle, Phys. Rev. Lett. **93**, 160406 (2004)
37. H. Pu, C.K. Law, J.H. Eberly, N.P. Bigelow, Phys. Rev. Lett. **59**, 1533 (1999)
38. T.P. Simula, S.M.M. Virtanen, M.M. Salomaa, Phys. Rev. A **65**, 033614 (2002)
39. C.A. Jones, P.H. Roberts, J. Phys. A **15**, 2599 (1982)
40. C.A. Jones, S.J. Puterman, P.H. Roberts, J. Phys. A **19**, 2991 (1986)
41. A.E. Leanhardt, Y. Shin, D. Kielpinski, D.E. Pritchard, W. Ketterle, Phys. Rev. Lett. **90**, 140403 (2003)
42. K. Kasamatsu, M. Tsubota, M. Ueda, Phys. Rev. Lett. **93**, 250406 (2004)
43. J. Ruostekoski and J.R. Anglin, Phys. Rev. Lett. **86**, 003934 (2001)
44. J. Ruostekoski, J.R. Anglin, Phys. Rev. Lett. **91**, 190402 (2003)
45. N.G. Parker, N.P. Proukakis, C.F. Barenghi, C.S. Adams, Phys. Rev. Lett. **92**, 160403 (2004)
46. P. Nozieres, D. Pines, *The Theory of Quantum Liquids* (Perseus, New York, 1999)
47. E. Lundh, C.J. Pethick, H. Smith, Phys. Rev. A **55**, 2126 (1997)
48. D.S. Rokhsar, Phys. Rev. Lett. **79**, 2164 (1997)
49. E. Lundh, J.P. Martikainen, K. A. Suominen, Phys. Rev. A **67**, 063604 (2003)
50. N.G. Parker, C.S. Adams, Phys. Rev. Lett. **95**, 145301 (2005); J. Phys. B **39**, 43 (2006)

51. S. Stringari, Phys. Rev. Lett. **77**, 2360 (1996)
52. A. Recati, F. Zambelli, S. Stringari, Phys. Rev. Lett. **86**, 377 (2001)
53. S. Sinha, Y. Castin, Phys. Rev. Lett. **87**, 190402 (2001)
54. N.G. Parker, R.M.W. van Bijnen, A.M. Martin, Phys. Rev. A **73**, 061603(R) (2006)
55. K.W. Madison, F. Chevy, V. Bretin, J. Dalibard, Phys. Rev. Lett. **86**, 4443 (2001)
56. J.E. Williams, E. Zaremba, B. Jackson, T. Nikuni, A. Griffin, Phys. Rev. Lett. **88**, 070401 (2002)
57. F. Dalfovo and S. Stringari, Phys. Rev. A **63**, 011601(R) (2001)
58. T. Frisch, Y. Pomeau, S. Rica, Phys. Rev. Lett. **69**, 1644 (1992)
59. T. Winiecki, J.F. McCann, C. S. Adams, Phys. Rev. Lett. **82**, 5186 (1999)
60. B. Jackson, J.F. McCann, C.S. Adams, Phys. Rev. Lett. **80**, 3903 (1998)
61. C. Raman, M. Köhl, R. Onofrio, D.S. Durfee, C.E. Kuklewicz, Z. Hadzibabic, W. Ketterle, Phys. Rev. Lett. **83**, 2502 (1999)
62. R. Onofrio, C. Raman, J.M. Vogels, J.R. Abo-Shaeer, A.P. Chikkatur, W. Ketterle, Phys. Rev. Lett. **85**, 2228 (2000)
63. B. Jackson, J.F. McCann, C.S. Adams, Phys. Rev. A **61**, 051603(R) (2000)
64. B.M. Caradoc-Davies, R.J. Ballagh, K. Burnett, Phys. Rev. Lett. **83**, 895 (1999)
65. J.E. Williams, M.J. Holland, Nature **401**, 568 (1999)
66. A.E. Leanhardt, A. Görlitz, A. Chikkatur, D. Kielpinski, Y. Shin, D.E. Pritchard, W. Ketterle, Phys. Rev. Lett. **89**, 190403 (2002)
67. N.S. Ginsberg, J. Brand, L.V. Hau, Phys. Rev. Lett. **94**, 040403 (2005)
68. S. Komineas, N. Papanicolaou, Phys. Rev. A **68**, 043617 (2003)
69. R.G. Scott, A.M. Martin, T.M. Fromhold, F.W. Sheard, Phys. Rev. Lett. **95**, 073201 (2005)
70. R.G. Scott, A.M. Martin, S. Bujkiewicz, T. M. Fromhold, N. Malossi, O. Morsch, M. Cristiani, E. Arimondo, Phys. Rev. A **69**, 033605 (2004)
71. B. Jackson, J.F. McCann, C.S. Adams, Phys. Rev. A **60**, 4882 (1999)
72. N.G. Berloff, C.F. Barenghi, Phys. Rev. Lett. **93**, 090401 (2004)
73. J. Ruostekoski, Z. Dutton, Phys. Rev. A **70**, 063626 (2005)
74. L.C. Crasovan, V.M. Pérez-García, I. Danaila, D. Mihalache, L. Torner, Phys. Rev. A **70**, 033605 (2004)
75. T.P. Simula, P.B. Blakie, Phys. Rev. Lett. **96**, 020404 (2006)
76. Z. Hadzibabic, P. Krüger, M. Cheneau, B. Battelier, J. Dalibard, Nature **441**, 1118 (2006)
77. M.J. Davis, S.A. Morgan, K. Burnett, Phys. Rev. Lett. **66**, 053618 (2002)
78. N.G. Berloff, B.V. Svistunov, Phys. Rev. A **66**, 013603 (2002)
79. H. Lamb, *Hydrodynamics* (Cambridge University Press, 1932)
80. M. Tsubota, T. Araki, S.K. Nemirovskii, Phys. Rev. B **62**, 11751 (2000)
81. K.W. Schwarz, Phys. Rev. B **31**, 5782 (1985)
82. J. Koplik, H. Levine, Phys. Rev. Lett. **71**, 1375 (1993)
83. M. Leadbeater, T. Winiecki, D.C. Samuels, C.F. Barenghi, C.S. Adams, Phys. Rev. Lett. **86**, 1410 (2001)
84. M. Leadbeater, D.C. Samuels, C.F. Barenghi, C.S. Adams, Phys. Rev. A **67**, 015601 (2003)
85. W. Thomson (Lord Kelvin), Philos. Mag. **10**, 155 (1880)
86. G.W. Rayfield, F. Reif, Phys. Rev. **136**, A1194 (1964)

87. A.A. Svidzinsky, A.L. Fetter, Phys. Rev. Lett. **84**, 5919 (2000)
88. B. Jackson, J.F. McCann, C.S. Adams, Phys. Rev. A **61**, 013604 (2000)
89. E. Lundh, P. Ao, Phys. Rev. A **61**, 063612 (2000)
90. S.A. McGee, M.J. Holland, Phys. Rev. A **63**, 043608 (2001)
91. J.J. García-Ripoll, V.M. Pérez-García, Phys. Rev. A **63**, 041603 (2001)
92. J.J. García-Ripoll, V.M. Pérez-García, Phys. Rev. A **64**, 053611 (2001)
93. A. Aftalion, T. Riviere, Phys. Rev. A **64**, 043611 (2001)
94. P. Rosenbusch, V. Bretin, J. Dalibard, Phys. Rev. Lett. **89**, 200403 (2002)
95. V. Bretin, P. Rosenbusch, F. Chevy, G.V. Shlyapnikov, J. Dalibard, Phys. Rev. Lett. **90**, 100403 (2003)
96. A.L. Fetter, Phys. Rev. A **69**, 043617 (2004)
97. P.O. Fedichev, G.V. Shlyapnikov, Phys. Rev. A **60**, R1779 (1999)
98. J.R. Abo-Shaeer, C. Raman, W. Ketterle, Phys. Rev. Lett. **88**, 070409 (2002)
99. S.I. Davis, P.C. Hendry, P.V.E. McClintock, Physica B **280**, 43 (2000)
100. D.P. Arovas, J.A. Freire, Phys. Rev. B **55**, 3104 (1997)
101. W.F. Vinen, Phys. Rev. B **61**, 1410 (2000)
102. E. Lundh, P. Ao, Phys. Rev. A **61**, 063612 (2000)
103. L.M. Pismen, *Vortices in Nonlinear Fields* (Clarendon, Oxford, 1999)
104. C.F. Barenghi, N.G. Parker, N.P. Proukakis, C.S. Adams, J. Low. Temp. Phys. **138**, 629 (2005)
105. N.G. Berloff, Phys. Rev. A **69**, 053601 (2004)
106. B.M. Caradoc-Davies, R.J. Ballagh, P.B. Blakie, Phys. Rev. A **62**, 011602 (2000)
107. A. Griesmaier, J. Werner, S. Hensler, J. Stuhler, T. Pfau, Phys. Rev. Lett. **94**, 160401 (2005)
108. M. Marinescu, L. You, Phys. Rev. Lett. **81**, 4596 (1998)
109. S. Yi, L. You, Phys. Rev. A **61**, 041604 (2000)
110. K. Góral, K. Rzażewski, T. Pfau, Phys. Rev. A **61**, 051601 (2000)
111. S. Yi, H. Pu, Phys. Rev. A **73**, 061602(R) (2006)
112. G. Ortiz, D.M. Ceperley, Phys. Rev. Lett. **75**, 4642 (1995)
113. M. Sadd, G.V. Chester, L. Reatto, Phys. Rev. Lett. **79**, 2490 (1997)
114. N. G. Berloff, P.H. Roberts, J. Phys. A **32**, 5611 (1999)
115. F. Dalfovo, Phys. Rev. B **46**, 5482 (1992)
116. J. Stuhler, A. Griesmaier, T. Koch, M. Fattori, T. Pfau, S. Giovanazzi, P. Pedri, L. Santos, Phys. Rev. Lett. **95**, 150406 (2005)
117. D.H.J. O’Dell, C. Eberlein, Phys. Rev. A **75**, 013604 (2007)
118. D.H.J. O’Dell, S. Giovanazzi, C. Eberlein, Phys. Rev. Lett. **92**, 250401 (2004)
119. C. Eberlein, S. Giovanazzi, D.H.J. O’Dell, Phys. Rev. A **71**, 033618 (2005)
120. R.M.W. van Bijnen, D.H.J. O’Dell, N.G. Parker, A.M. Martin, Phys. Rev. Lett. **98**, 150401 (2007)
121. C. Barceló, S. Liberati, M. Visser, Living Rev. Rel. **8**, 12 (2005)
122. W.G. Unruh, Phys. Rev. Lett. **46**, 1351 (1981)
123. W.G. Unruh, Phys. Rev. D **27**, 2827 (1995)
124. C. Barceló, S. Liberati, M. Visser, Class. Quant. Grav. **18**, 1137 (2001)
125. S.W. Hawking, Nature **248**, 30 (1974)
126. S.W. Hawking, Commun. Math. Phys. **43**, 199 (1975)
127. J.D. Bekenstein, M. Schiffer, Phys. Rev. **58**, 064014 (1998)
128. C. Barceló, S. Liberati, M. Visser, Phys. Rev. A **68**, 053613 (2003)
129. T.R. Slatyer, C.M. Savage, Class. Quant. Grav. **22**, 3833 (2005)
130. S. Basak, P. Majumdar, Class. Quant. Grav. **20**, 2929 (2000)
131. S. Basak, P. Majumdar, Class. Quant. Grav. **20**, 3907 (2000)
132. F. Federici, C. Cherubini, S. Succi, M.P. Tosi, Phys. Rev. A **73**, 033604 (2006)

Vortices in Bose–Einstein Condensates: Experiments

F. Chevy

10.1 Introduction: Vortices and Superfluidity

As discussed in the previous section, one of the most spectacular manifestation of superfluidity in Bose–Einstein condensates is the possibility of nucleating quantized vortices when the system is set into rotation. This property, first predicted by Feynman and Onsager [1, 2], has since been verified experimentally in superfluid ^4He and gaseous Bose–Einstein condensates. The observation of vortices has also been used to probe superfluidity in fermionic systems, where quantum ordering arises from Cooper pairing of two opposite spin particles [3]. Vortices and vortex lattices have been observed both in ultra-cold Fermi gases [4] and in liquid ^3He [5]. In this latter case, the coupling between the orbital and spin degrees of freedom leads to a new class of vortex-like excitations called skyrmions [6]. Finally, the formal identity between Coriolis and Lorentz forces permits to draw an interesting parallel between rotating systems and charged particles in magnetic fields where the flux quantization observed in superconductors is the complete analog of the circulation’s quantization in superfluids.

In this chapter, we will discuss experimental techniques used to generate and probe quantized vortices in bosonic systems, focusing mainly on the most recent advances in ultra-cold gaseous Bose–Einstein condensates. In the first part, we will concentrate on nucleation procedures and we will show that both quantum and hydrodynamical schemes were successfully used to generate vortices in gaseous Bose–Einstein condensates. We will then describe experimental tools used to probe the physical properties of these systems. In particular, we will address the interferometric characterization of the vortex phase, the measurement of the angular momentum of the cloud and the probing of the low energy excitation spectrum.

10.2 Nucleation of Vortices

By definition, the physics of superfluids lies at the frontier between quantum mechanics and classical hydrodynamics. This duality is made obvious by the different nucleation techniques that are used experimentally to generate quantized vortices in Bose–Einstein condensates. Indeed, although the most straightforward method to set a superfluid in rotation is the direct mechanical stirring of the system, it is also possible to act directly on the phase of the macroscopic wavefunction and phase imprint a 2π phase singularity characteristic of a single quantized vortex.

10.2.1 Vortices in Liquid Helium

Historically, the study of vortices in superfluids was initiated in the late 1950s by experiments on the rotational properties of superfluid liquid helium. In this system, the nucleation scheme is rather straightforward, since one simply has to set into rotation the vessel containing the liquid and wait for the nucleation of vortices. Their observation, however, is rather involved since in condensed matter systems, the size of the vortex core is of the order of the inter particle distance, i.e. a few Angströms. The first indirect evidence for the nucleation of quantum vortices was provided in [7]. In this experiment the authors transpose the historic Melde’s textbook experiment on the vibrating string [8] to the case of a wire immersed in a bucket of rotating helium. For a non-rotating non-viscous fluid (such as superfluid helium), the d’Alembert paradox states that no force is exerted by the liquid on the wire: in the absence of rotation, the resonance frequencies of the string are thus unaffected by the presence of the surrounding liquid. On the contrary, a rotating fluid acts on the string through a Magnus force which will shift the wire’s resonance frequencies, proportionally to the vorticity of the flow. Vinen successfully measured this shift [7], and showed unambiguously that it was quantized, thus proving the quantum nature of the rotating flow.

The direct observation of vortices was provided much later by the work of Packard [9] where electrons were trapped inside the vortex cores and were propelled towards a fluorescent screen by an external electric field parallel to the rotation axis. The impact points of the electrons thus marked the trace of the vortices’ positions, as shown in Fig. 10.1.

10.2.2 Phase Imprinting

The phase imprinting method involves shining the Bose–Einstein condensate with a far detuned laser that will act mainly on the phase profile of the wavefunction. Several schemes were proposed to nucleate a vortex using this technique, and the first observation of vortices in gaseous Bose–Einstein condensates was reported by the group of E.A. Cornell at Boulder [10] after a theoretical suggestion of Williams and Holland [11]. Williams and Holland’s

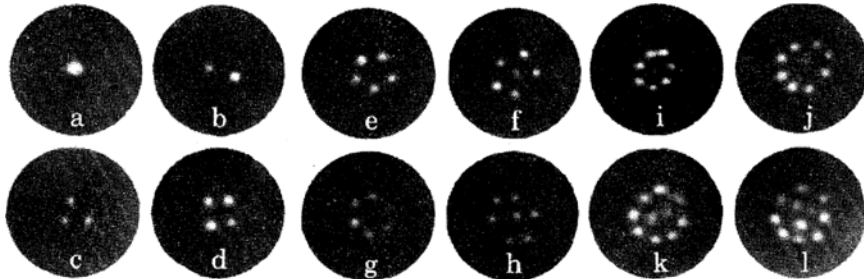


Fig. 10.1. Historical experiment of Packard adapted from [9]: each spot is the trace of a vortex made by electrons initially trapped in vortex cores and impacting a fluorescent screen placed above the rotating bucket. (a–l) corresponds to increasing rotation velocities of the bucket

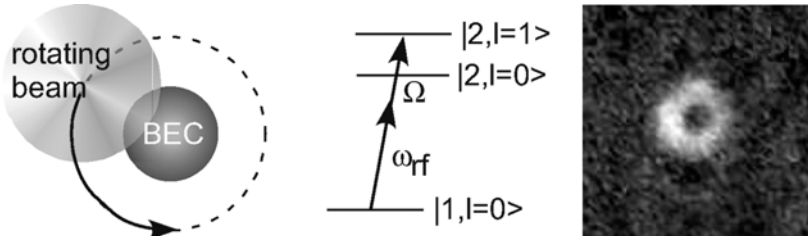


Fig. 10.2. Phase imprinting procedure. *Left:* Atoms are initially at rest in hyperfine state $|1\rangle$. The vortex state is formed using a combination of a rotating off centered laser beam and a radio-frequency coupling states $|1\rangle$ to a second hyperfine state $|2\rangle$. A vortex is formed when the sum of radiofrequency ω_{rf} and of the beam rotation frequency Ω is resonant with the transition frequency between the initial state and a vortex of state $|2\rangle$ atoms (center). The width of the laser beam is chosen small enough to affect only atoms at the edge of the cloud. *Right:* Density profile of state $|2\rangle$ atoms. The resulting final state is a baby-skyrmion, i.e. a vortex of particles in state $|2\rangle$, with a core filled with state $|1\rangle$ atoms at rest (data from [10])

scheme involves two internal atomic states labeled $|1\rangle$ and $|2\rangle$ (in practice the $|F = 1, m_F = -1\rangle$ and $|F = 2, m_F = +1\rangle$ hyperfine Zeeman sub-states of ground state rubidium). Starting with atoms in state $|1\rangle$, an off-resonance radio-frequency combined with a rotating far-detuned laser beam is used to drive resonantly atoms in $|1\rangle$ to state $|2\rangle$ rotating at the edge of the cloud (see Fig. 10.2). Note that in this scheme, the vortex formation is not a consequence of the mechanical force exerted by the laser beam: The sign of the vortex charge depends only on that of the radiofrequency detuning and both clockwise and anti-clockwise vortices can be nucleated with a beam rotating in a given direction. After the nucleation stage, the vortex of state $|2\rangle$ atoms is pinned by the presence the remaining state $|1\rangle$ atoms localized at the trap

center¹. This particular state, mixing phase and spin textures is known as a baby-skyrmion. Such states were also obtained at MIT using a different imprinting scheme using Berry's topological phases [12]. In this second experiment, the magnetic bias field used for trapping and hindering Majorana losses² is slowly varied to rotate the local direction of atomic spins. During this rotation, a position dependent quantum phase is accumulated by the atoms and may lead to the formation of phase defects in the wavefunction. For instance, when the final bias field is zero, skyrmions are nucleated [13], while when the field is inverted with respect to its initial direction, a one species vortex is nucleated. In this latter case, the charge of this vortex depends on the internal spin state of the atoms, and singly or doubly charged vortices are nucleated, as discussed below [12].

Finally, a very recent experiment [14] took advantage of the orbital angular momentum carried by Laguerre–Gauss beam to generate vortices. The electric field associated with a Laguerre–Gauss beam propagating along the z direction is characterized by a transverse profile of the form

$$E(\rho, \theta) = E_0 P_{n,q}(\rho) e^{iq\theta} e^{-\rho^2/w_0^2}, \quad (10.1)$$

where (ρ, θ) are the polar coordinates in the transverse (x, y) plane, $P_{n,q}$ is a Laguerre polynomial depending on the two integers n and q and w_0 is the waist of the beam.³ In particle terms, it can be shown that photons associated with a q Laguerre–Gauss beam carry an angular momentum $q\hbar$ along z . A cloud of ultra cold atoms is shined with two counter-propagating Laguerre–Gauss beams characterized respectively by $q = 0$ or $q = +1$. When the detuning between the two beams is well chosen, stimulated Raman scattering can be used to transfer a $q = +1$ photon carrying orbital angular momentum \hbar to the $q = 0$ beam with no angular momentum. In this scattering, the missing angular momentum is transferred to the atoms which are set into rotation.

10.2.3 Stirring

Gaseous Bose–Einstein condensates are usually confined in cylindrically symmetric magnetic traps resulting in an harmonic potential $V_{\text{MT}}(x, y, z)$ given by

$$V_{\text{MT}} = \frac{m}{2} (\omega_{\perp}^2 r_{\perp}^2 + \omega_z^2 z^2), \quad (10.2)$$

¹ The two states are chosen so that, even in absence of vortex, repulsive interactions between atoms lead to a phase separation of the two spin states, atoms $|1\rangle$ sitting at the center of the magnetic trap, and those in state $|2\rangle$ forming an outer shell.

² Majorana losses are due to non adiabatic spin flip in regions of weak or zero magnetic fields and are prevented by adding a bias field.

³ Note that $q \neq 0$ Laguerre–Gauss beams are the electromagnetic equivalent of matter-wave vortices.

with $r_{\perp}^2 = x^2 + y^2$. To set the cloud in rotation, it is necessary to break this symmetry by introducing a notch in the guise of an additional rotating harmonic potential

$$V_{\text{rot}}(X, Y) = \epsilon \frac{m\omega_{\perp}^2}{2} (X^2 - Y^2). \quad (10.3)$$

Here ϵ is a dimensionless parameter characterizing the transverse anisotropy of the trap (typically less than 10%), and X and Y are the coordinates in the frame rotating at an angular velocity Ω around the $z = Z$ axis of symmetry of the magnetic trap. In practice, the anisotropic potential is obtained by the addition of an external optical potential (see Fig. 10.3a for the ENS setup) or the modification of the magnetic field orbit in a TOP (Time Orbiting Trap) [15].

10.2.3.1 Dynamical Nucleation

The first vortices nucleated after stirring were obtained at ENS [16] in a Ioffe trap stirred by two rotating far detuned laser beams propagating along the symmetry axis of the cloud (Fig. 10.3a). The width of the laser beam is taken much larger than the transverse size, in order to impose a harmonic perturbation to the magnetic trapping potential. When the stirring frequency Ω is larger than $0.7\omega_{\perp}$, vortices, and vortex lattices are observed as clear

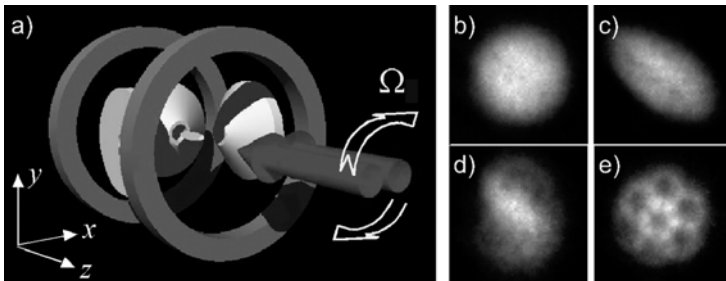


Fig. 10.3. (a) The ENS experimental setup: atoms are initially confined in a Ioffe–Pritchard magnetic trap cylindrically symmetric along the z axis. The cloud is set in rotation by two far-detuned rotating laser beams propagating along the symmetry axis of the magnetic trap. (b–e) Series of density profiles in the x – y plane taken by absorption imaging during vortex nucleation for a trap with $\omega_{\perp} = 2\pi \times 200$ Hz, $\omega_z = 2\pi \times 11.8$ Hz and $\Omega/\omega_{\perp} = 0.7$ (data from [19]). The separation between two pictures is about 150 ms. (b) Initial state of the cloud before the beginning of the stirring. (c) The rotating potential excites the quadrupole mode of the condensate as witnessed by the strong ellipticity of the cloud. (d) A dynamical instability of the strongly deformed profile leads to a turbulent phase during which vortices enter the cloud. (e) The cloud finally relaxes towards a new stationary state, here a lattice of seven vortices

depressions in the cloud density profile.⁴ This critical rotation frequency was surprisingly high, since the common view at the time was that the threshold for nucleation would be given by the comparison of the energies of the rotating and non rotating states, a scenario yielding a critical angular velocity of the order of $0.5\omega_{\perp}$ in the conditions of the experiment. This discrepancy was finally explained by a careful study of the mechanism of nucleation. It appeared that, before the emergence of the vortices, the cloud takes a very elliptical shape, as shown in Fig. 10.3.c. This observation suggests that the nucleation is triggered by a resonant excitation of the quadrupolar mode of the system. The frequency ω_{qp} of this mode can be calculated by the resolution of the superfluid hydrodynamics equations and is given by $\omega_{qp} = \sqrt{2}\omega_{\perp}$ [18]. Since the potential is modulated at 2Ω , the resonance condition reads $\Omega = \omega_{\perp}/\sqrt{2} \sim 0.7\omega_{\perp}$, in agreement with the experimental observations⁵ [19]. This scenario was confirmed by the linear stability analysis of the static density profile of a condensate induced by a superfluid irrotational flow [20]. It was demonstrated that beyond a critical frequency close to the quadrupole resonance condition, the rotationless flow was unstable and was entering a turbulent phase leading to the nucleation of vortices [21]. This stability phase diagram was tested experimentally [19] and a study performed at MIT showed later that it was possible to excite a large class of modes by using a strongly focused stirring beam, thus reducing dramatically the critical nucleation frequency [22].

10.2.3.2 Thermodynamical Nucleation

As shown in the previous section, the first stirring experiments demonstrated the dynamical nature of the nucleation mechanism, but raised a paradox, since it seemed to contradict thermodynamical arguments predicting a lower nucleation frequency. The reason for this discrepancy is that a static anisotropy of the magnetic trap dissipates very fast the angular momentum of the thermal component of the cloud [23]. In the experimental conditions of ENS experiment, this static anisotropy was only 0.5%, but led to a reduction by a factor about 20 of the angular momentum of the cloud with respect to its value for an isotropic trap. Consequently, the condensate is embedded in a non rotating thermal cloud and will not thermalize in the frame of the rotating potential. The thermodynamical nucleation of vortices could only be observed by the group of JILA after a careful compensation of the static anisotropy of the trap down to *one thousandth* [24]. This breakthrough opened the possibility of achieving very fast rotation by selectively evaporating particles with low angular momentum, simply by removing atoms at the center of the cloud

⁴ Note that in these experiments, atoms were not observed directly in the trap, but after a time of flight (see Fig. 10.4) and it can be demonstrated that the size of the vortex core is not significatively modified during the expansion [17].

⁵ The potential modulation frequency is not Ω , since the potential is unchanged after half a turn.

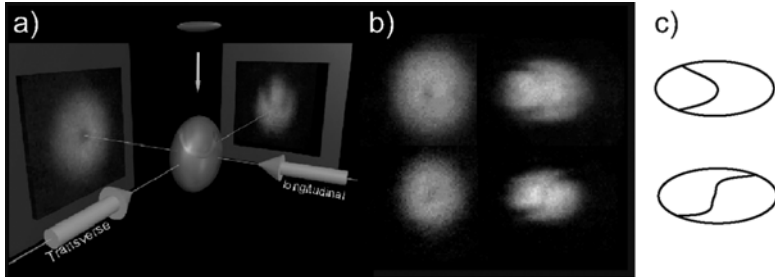


Fig. 10.4. Vortex line bending from [32]. (a) Experimental procedure. After a ballistic expansion of 25 ms during which repulsive interactions lead to an inversion of the ellipticity of the density profile, the condensate is imaged longitudinally and transversally with respect to its symmetry axis. (b) Longitudinal (left column) and transversal (right column) experimental density profiles. (c) Sketch of the transverse shape of the vortex line. The “U” and “S” shapes result from the inhomogeneity combined with the non-linearities due to the interatomic interactions

using a resonant laser pulse and letting the cloud rethermalize. This scheme permitted to reach effective rotation frequencies of $0.993\omega_{\perp}$, very close to the limit where the centrifugal force exactly compensates the transverse trapping. In this regime of very fast rotation, the condensate density is strongly reduced and new physical phenomena (in particular Lowest Landau Level or Laughlin states physics) are expected to take place as discussed in Part XI.

10.2.4 Rotationless nucleation

In the two classes of nucleation mechanisms presented above, the vortex nucleation is obtained using experimental setups whose main function is to impart angular momentum to the system. However, there are a few circumstances where vortices were observed without trying actively to set the condensate in rotation. Such surprising and slightly counterintuitive result was obtained for instance at MIT while moving an obstacle (in practice a repulsive laser beam) through the cloud to probe the superfluidity of the Bose–Einstein condensate. This experiment was first designed to probe Landau criterion for superfluidity in which energy transfer to the cloud is due to the emission of phonons by the moving object [25]. It was therefore expected that the laser should start heating the condensate for velocities larger than the sound velocity, in contradiction with actual experiments which demonstrated a lower threshold [26]. A later experiment showed that the onset of dissipation was actually due to vortex shedding in the wake of the laser beam [27], a phenomenon predicted in [28, 29] and akin to the (classical) von Karman vortex alleys drifting in the wake of bridge posts. Similarly, vortex rings were obtained as a result of the decay of a soliton [30] and the nucleation of thermally excited vortices was observed at the onset of superfluidity in a two dimensional ultra-cold Bose gas, in agreement with the Berezinsky–Kosterlitz–Thouless mechanism [31].

10.3 Experimental Characterization

10.3.1 Vortex Profile, Vortex Bending and Decay

In experiments being performed in cylindrically symmetric potentials, one would expect the vortex lines to be straight and aligned along the symmetry axis of the trap. However, the observation of the transverse profile of the cloud shows without ambiguity that the vortex line is bent [32]. At zero temperature, this surprising observation was explained by several theoretical studies showing that the inhomogeneity of the system was indeed leading to a symmetry breaking of the vortex profile characterized by an out of axis bending of its extremities [33, 34]. A simple physical interpretation of this effect highlights the intrinsic non-linearity of the Gross–Pitaevskii equation [34]. Let us consider a Bose–Einstein condensate rotating at a frequency Ω . For very elongated geometries, the cloud can be described as a stack of two dimensional slices characterized by different critical vortex nucleation frequencies $\Omega_c^{(2D)}(z)$. When approaching the border of the cloud, atom density decreases and so does $\Omega_c^{(2D)}$. At the very end of the cloud, we then have $\Omega < \Omega_c^{(2D)}$: the vortex is thus locally unstable at the edge of the condensate and drifts towards the border. Interestingly, since two counter propagating vortices tend to attract each other, the vortex line is expected to take a “U” shape, as seen in Fig. 10.4. However, for elongated traps, the two ends of the vortex are far away and the vortex interaction is rather weak. This implies that the bent ends can rotate almost freely around the symmetry axis of the system which explains the “S” shapes sometimes observed experimentally. These observations of the transverse vortex profiles provide a scenario for the vortex decay mechanism. Indeed, as time goes on, the bending of the vortex line becomes more and more pronounced and the distance d_z between the two ends decreases linearly with time (Fig. 10.5a). The thermal nature of the decay mechanisms is demonstrated by the evolution of \dot{d}_z with temperature (Fig. 10.5b) and suggests that the vortex lifetime is limited by friction with the thermal cloud.

10.3.2 Vortex Charge

The main characteristic of a vortex is its (topological) charge, that is to say the phase winding number of the wavefunction around the vortex core or, equivalently, its angular momentum per particle in units of \hbar . In this section, we present two complementary direct measurements of the vortex charge taking advantage of these dual interpretations. First using an interferometric scheme we demonstrate the phase defect at the vortex center. Second surface mode spectroscopy leads to a measurement of the angular momentum carried by the cloud. These two sets of experiments prove that vortices nucleated after stirring are all singly charged. This result is a consequence of the typical dynamical instability of multiply charged vortices, as demonstrated experimentally in the last section.

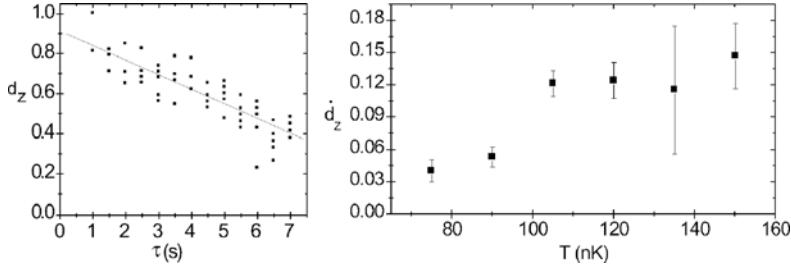


Fig. 10.5. Decay of a vortex in an elongated trap (data from [32]). *Left:* time evolution of the distance d_z along the symmetry axis of the two ends of the vortex, normalized to the total length of the cloud. The lifetime of the vortex d_z decreases linearly with time at a constant velocity \dot{d}_z . *Right:* temperature dependence of d_z . The decrease of the decay rate at low temperature emphasizes the role of the thermal cloud in angular momentum dissipation

10.3.2.1 Matter-Wave Interferometry

By analogy with optics, atom interferometry can be used to measure the telltale phase pattern of a vortex state [35–38]. Let us consider a Bose–Einstein condensate prepared in a coherent superposition of two wave packets separated by a distance d . At $t = 0$, the trap is turned off and the two clouds expand freely⁶ during a time of flight t (Fig. 10.6a). At a position M , the wavefunction after expansion is proportional to

$$\psi(M) \sim \int d^3M_1 \psi_1(M_1) e^{iS_{M_1 M}(t)/\hbar} + \int d^3M_2 \psi_2(M_2) e^{iS_{M_2 M}(t)/\hbar}, \quad (10.4)$$

where $S_{AB}(t) = mAB^2/2t$ is the classical action to go from A to B in a time t , and $\psi_{1,2}$ are the two initial wave packets. The long time of flight expansion (equivalent to the far field Fraunhofer diffraction limit in classical optics) of $\psi(M)$ yields

$$\psi(M) \sim \widehat{\psi}_1(md_1/\hbar t) e^{imd_1^2/2\hbar t} + \widehat{\psi}_2(md_2/\hbar t) e^{imd_2^2/2\hbar t}, \quad (10.5)$$

where d_i is the distance between M and the center of wave packet i and $\widehat{\psi}_i$ is the Fourier transform of ψ_i . This expression corresponds to the fact that, for long time of flight, the spatial density profile of a single wave packet is given by the in-trap momentum distribution. Since the momentum and position observables are conjugate, the phase patterns of ψ_i and $\widehat{\psi}_i$ are identical for charge q_i vortices, and we expect

⁶ The expansion of the cloud quickly converts mean-field energy into kinetic energy, and interactions between atoms are therefore important only briefly after turning off the trap. If the separation between the two wave packets is large enough, we can then consider single particle expansion only.

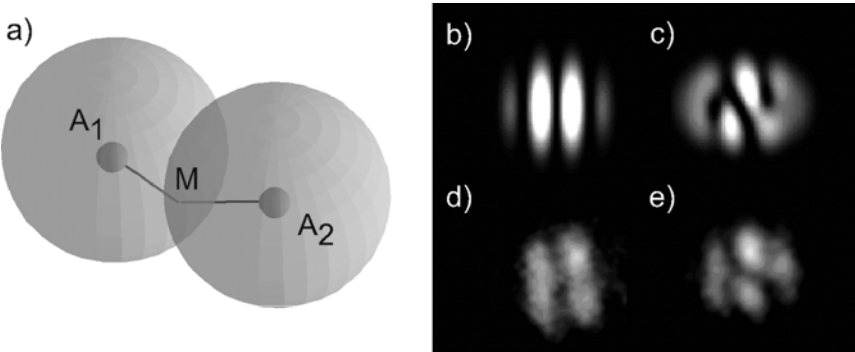


Fig. 10.6. Matter-wave interferometry. (a) Sketch of the experimental procedure. Two wave packets localized in A_1 and A_2 expand freely during a time of flight t . The probability of finding an atom in M present interference patterns characteristic of the phase of the wavefunction $\psi(M)$. When no vortex is present straight fringes are expected (b). When the initial wave packets both carry vortices, interference fringes merge at the vortex cores (c). (d) and (e) correspond to experimental results on a rubidium Bose–Einstein condensate after stirring slightly below (d) and slightly above (e) the critical velocity for vortex nucleation (data from [39])

$$\psi(M) \sim e^{iq_1\theta_1(M)} e^{imd_1^2/2\hbar t} + e^{iq_2\theta_2(M)} e^{imd_2^2/2\hbar t}, \quad (10.6)$$

where $\theta_i(M)$ is the polar angle of M with respect to the center A_i of the wave packet i . In the absence of a vortex ($q = 0$), the propagation and the relative dephasing of the two matter-waves leads to straight fringes with fringe spacing ht/md , as displayed in Fig. 10.6b,d. By contrast, the presence of a charge $q_1 = q_2 = q$ vortex in each wave packet provokes a merging of $q + 1$ fringes at each of the two vortex cores (Fig. 10.6c).

The results of such interference experiments are presented in reference [27] in the case of vortices nucleated in the wake of an obstacle and for vortices obtained after stirring [39]. Typical result for this latter case are presented in Fig. 10.6e. These pictures show nice agreement with the theoretical predictions and clearly demonstrate that single charge vortices were obtained in these experiments.

10.3.2.2 Surface Wave Spectroscopy

The study of low energy excitation modes provides a very powerful tool to characterize the properties of a physical system and can be used to measure directly the angular momentum of a Bose–Einstein condensate. Indeed, the presence of a vortex yields dramatic effects on the low energy spectrum by breaking the time reversal symmetry of the Bogoliubov–de Gennes equations describing the time evolution of weak perturbations (cf. Chap. 1, Sect. 4.2). The frequency of an excitation is then Doppler shifted by the condensate flow and depends on its direction of propagation with respect to that of the vortex.

In practice, this symmetry breaking leads to different frequencies for modes with opposite angular momenta m_z and $-m_z$, a phenomenon that was studied both theoretically [40, 41] and experimentally [42, 43] in the case of the so called scissors and quadrupolar modes. In geometric terms, the scissors mode corresponds to a tilting of the condensate with respect to its symmetry axis, and the quadrupolar mode is associated with an oscillation of the ellipticity in the (x, y) plan (see Fig. 10.7). These modes correspond respectively to symmetries $m_z = \pm 1$ and $m_z = \pm 2$ and are associated, respectively, with density perturbations of the form

$$\delta\rho_{\text{sc}} = \text{Re} \left(z(x \pm iy)e^{(-i\omega t)} \right), \quad (10.7)$$

$$\delta\rho_{\text{qp}} = \text{Re} \left((x \pm iy)^2 e^{(-i\omega t)} \right), \quad (10.8)$$

where the perturbation should only be applied where the perturbed density $\rho + \delta\rho$ is positive.

In the presence of a vortex, it was predicted using a sum rule approach that the two counter-propagating modes would undergo a frequency shift given by [40, 41]

$$\delta\omega_{\text{sc}} = \frac{2}{m} \frac{\langle \ell_z \rangle}{\langle r_{\perp}^2 \rangle}, \quad (10.9)$$

$$\delta\omega_{\text{qp}} = \frac{2}{m} \frac{\langle \ell_z \rangle}{\langle r_{\perp}^2 + 2z^2 \rangle}, \quad (10.10)$$

where ℓ_z is the angular momentum per particle in the z direction and $r_{\perp}^2 = x^2 + y^2$.

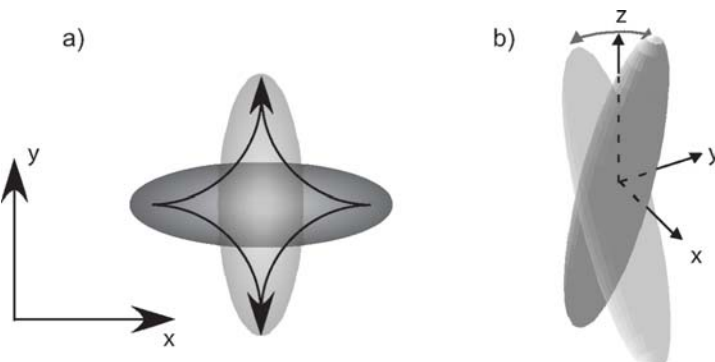


Fig. 10.7. Left: quadrupolar mode, associated with $m_z = \pm 2$. It corresponds to an oscillation of the ellipticity of the cloud in the transverse (x, y) plane. Right: scissors mode, associated with $m_z = \pm 1$, in which the condensate oscillate around the symmetry axis without deformation

If a non-rotating perturbation is used to excite the quadrupole or the dipole mode, both m_z and $-m_z$ will be excited with equal weights and, by analogy with the Foucault pendulum, the lift of the degeneracy between the two modes leads to a precession of the plane of oscillation at an angular velocity $(\omega_{m_z} - \omega_{-m_z})/m_z$. The experimental verifications of these predictions are presented in [42] for the quadrupole and [43] for the scissors. Experimental data extracted from [42] are presented in Fig. 10.8. They demonstrate that the axes of the quadrupole precess in the presence of a vortex. Using (10.10), the measurement of the precession rate (here $2\pi \times 66$ rad/ms) yields an angular momentum $\langle \ell_z/\hbar \rangle = 1.2(1)$, in fair agreement with the value $\langle \ell_z/\hbar \rangle = 1$ expected for a single unitary vortex.

10.3.2.3 Instability of Multiply Charged Vortices

When stirring is faster than the critical angular frequency either a multiply charged vortex or several singly charged vortices are nucleated. A very simple argument shows that the first possibility (nucleation of a single multiply charged vortex) is energetically unfavorable. Indeed, for an incompressible fluid contained in a cylindrical vessel of radius R and length L , the energy E_q of a single vortex with charge q is given by

$$E_q = \int d^3r \frac{\rho v^2}{2} = \rho L \frac{\hbar^2 q^2}{2m} \ln \left(\frac{R}{\xi} \right), \quad (10.11)$$

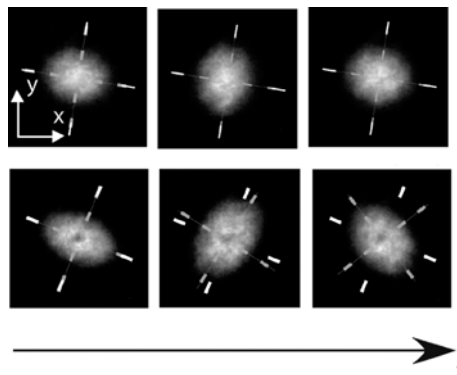


Fig. 10.8. Quadrupole oscillations of a rotating condensate (data from [42]). Series of transverse profiles after excitations of the quadrupolar mode of a non rotating (upper row) and rotating (lower row) condensate. For each series, two successive pictures are separated by half an oscillation period (2 ms). For a non rotating cloud, the principal axes of the profile are constant in time whereas they precess when a vortex is present. The measurement of the rate of precession (here $2\pi \times 66$ rad s $^{-1}$) gives access to the angular momentum of the cloud, here $1.2(1)\hbar$, in agreement with theoretical predictions

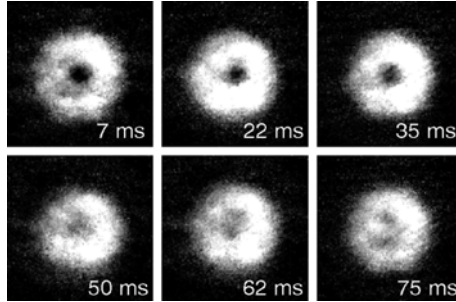


Fig. 10.9. Decay of a doubly charged vortex obtained after topological phase imprinting. Due to its instability, the vortex splits in a few tens of milliseconds into two singly charged vortices [47]. To improve the vortex contrast, a $30 \mu\text{m}$ thick slice is selectively observed by optical pumping to a second hyperfine state

where ρ is the density of the fluid and ξ is the healing length providing the ultra-violet cutoff of the integral. The energy of q vortices far away from each other is then simply $qE_1 < E_q$, since for any q , $q < q^2$, and we therefore expect multiply charged vortices to be unstable and decay into singly charged vortices. More refined analysis based on Bogoliubov equations confirms this analysis in the case of harmonic trapping and demonstrates that the excitation spectrum associated with a multiply quantized vortex confined in a harmonic⁷ trap may indeed possess imaginary eigenvalues signaling the presence of a dynamical instability [45, 46]. Experimentally, the observation of this instability was reported in [47]. In that work, a doubly quantized vortex was nucleated using topological phase imprinting and observed after a variable holding time τ . As shown in Fig. 10.9, the vortex splits into two vortices after 40 ms. This lifetime is very short compared to the one of a singly charged vortex which may live several seconds (see Fig. 10.5) and confirms the instability of a charge 2 vortex.

Let us note that the stability argument presented above is no longer valid in the case of spinor superfluid [6], such as ${}^3\text{He}$, and in this case stable multiply charged vortices were observed in [48].

10.3.3 Kelvin Modes of a Single Vortex Line

The excitation of a vortex line was first studied by Lord Kelvin in the framework of classical hydrodynamics [49]. This work was transposed to rotating Bose–Einstein condensates by Pitaevskii [50] who demonstrated that the dispersion relation of the Kelvin excitations (or kelvons) was given by

$$\omega_k = \frac{\hbar k^2}{2m} \ln(1/k\xi), \quad (10.12)$$

⁷ Note that this is not the case in a purely quartic trap, as predicted in [44].

where $\xi = (8\pi\rho a)^{-1}$ is the healing length (ρ is the density and a the scattering length). A striking property of these modes is that, contrarily to a usual string, kelvons can only possess a circular polarization, opposite to the rotation of the vortex. For a charge +1 vortex, they are therefore associated with $m_z = -1$ excitations. This peculiar behavior might be interpreted by noting that the vortex angular momentum along the symmetry axis of the trap is \hbar only if the vortex is centered on the trap. If the vortex is off-center, the angular momentum is reduced and vanishes when it reaches the edge of the cloud. Since the Kelvin mode corresponds to a snaking of the vortex line around the symmetry axis of the trap, it reduces the angular momentum of the system.

The Kelvin modes were observed in superfluid helium by trapping electrons in the vortex core and then exciting its motion by using a circularly polarized electromagnetic field. In a Bose–Einstein condensate, their excitation is more difficult. Indeed, it requires exciting the condensate on a length scale of the order of the vortex core, while usual excitations schemes involve a modification of the trapping potential and therefore act on a length scale of the order of the size of the cloud. Experimentally, the lowest frequency Kelvin mode, which corresponds to vortex precession around the symmetry axis of the cloud was observed and studied in [51]. Higher frequency Kelvin modes were observed using an indirect excitation from the quadrupolar mode via Beliaev coupling, a nonlinear process appearing when expanding the time dependent Gross–Pitaevskii equation beyond first order perturbation. Physically, it consists in the decay process $\gamma \rightarrow \gamma' + \gamma''$, where γ , γ' and γ'' are Bogoliubov excitations satisfying momentum and energy conservation. This process was first studied experimentally for the scissors mode in non rotating condensates [52] and was later transposed to the case of the quadrupolar mode of a rotating condensate [53]. According to the conservation of angular momentum, one quadrupolar $m_z = -2$ excitation can decay into two kelvons with $m_z = -1$, while $m_z = +2$ quadrupole cannot decay along this channel. The presence of a vortex thus increases the number of decay channels available to the $m_z = -2$ quadrupole mode and thus increases its damping rate. This prediction was verified by exciting selectively the $m_z = \pm 2$ by turning on again the rotating anisotropic potential used to nucleate the vortex, but with variable angular frequency Ω' and direction of rotations [53]. The response of the cloud to positive and negative rotations is displayed in Fig. 10.10. It clearly shows the resonance frequency shift of the two $m_z = \pm 2$ modes already discussed, but, additionally, it shows that the width of the $m_z = -2$ resonance is much larger than that of $m_z = +2$, indicating a smaller lifetime of $m_z = -2$ with respect to $m_z = +2$.

To confirm the origin of the decay increase, the BEC was imaged transversally to probe the transverse profile of the vortex line. When the $m_z = -2$ quadrupole is excited, fringes appear along the vortex line. They can be explained by noting that the velocity field associated with the propagation of kelvons along the vortex line creates a phase modulation of the condensate wavefunction. When the cloud expands during the time of flight expansion,

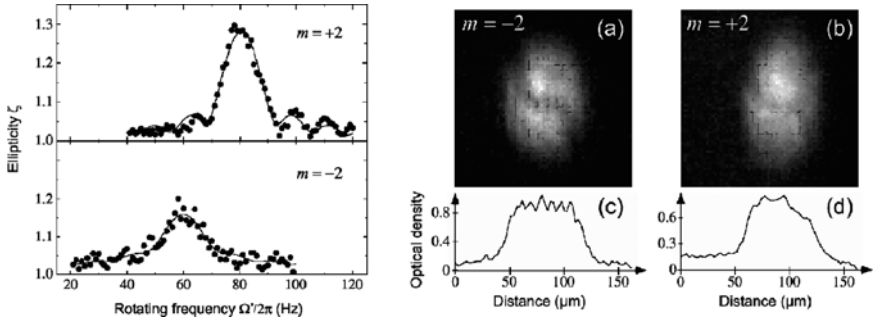


Fig. 10.10. Excitation of the Kelvin spectrum by Beliaev coupling to the quadrupolar mode [53]. *Left:* resonance peaks of the $m_z = \pm 2$ quadrupolar modes. The measured ellipticity ζ of the density profile is plotted versus the excitation frequency Ω . The transverse trapping frequency is $\omega_{\perp} = 2\pi \times 98$ Hz, yielding a quadrupole frequency $\omega_{qp} = 2\pi \times 70$ Hz for a non-rotating cloud. The presence of the vortex shifts the relative position of the two peaks proportionally to the angular momentum of the condensates and increases the width of the $m_z = -2$ due to the coupling to the Kelvin spectrum. *Right:* transverse imaging of the condensate after excitation of the rotating quadrupole. When $m_z = -2$ is resonantly excited, fringes appear along the vortex line, signaling the excitation of a Kelvin wave

matter-wave interferences convert these phase patterns into density modulations yielding the fringes observed in Fig. 10.10.

10.4 Conclusions

The observation of long lived quantized vortices is the most straightforward and “visual” demonstration of superfluidity in Bose–Einstein condensates. In this chapter, we restricted ourselves to situations where a single vortex was nucleated, but many spectacular effects are expected when the angular momentum is increased above the threshold for nucleation, such as the formation of Abrikosov lattices (cf. Part VII) or lattice melting and beyond mean-field effects when the trap rotation frequency is close the transverse trapping frequency. Beyond these fundamental aspects, topological properties of vortices may play a role in future quantum computers. Indeed, since by definition topological singularities are robust to any outer perturbation, they may be used as basic elements for a decoherence free quantum computer, a strategy known as topological quantum computing [54].

Acknowledgement. The author gratefully acknowledges support by the IFRAF institute and the ACI Nanosciences 2004 NR 2019. The author thanks J. Dalibard and J. McKeever for careful reading and insightful comments. Laboratoire Kastler Brossel is a research unit No. 8552 of CNRS, ENS, and Université Paris 6.

References

1. R.P. Feynman, in *Progress in Low Temperature Physics*, vol. 1, ed. by J. Gorter (North Holland, Amsterdam 1955).
2. L. Onsager, *Nuovo Cimento* **6**, 249 (1949)
3. P.G. de Gennes, *Superconductivity of metal and alloys*, Benjamin (1964)
4. M.W. Zwierlein, J.R. Abo-Shaeer, A. Schirotzek, C.H. Schunck, and W. Ketterle *Nature* **435**, 1047 (2005)
5. O.V. Lounasmaa, E. Thuneberg, *Proc. Natl. Acad. Sci. USA* **96**, 7760 (1999)
6. P.W. Anderson, G. Toulouse, *Phys. Rev. Lett.* **38**, 508 (1977)
7. W.F. Vinen, *Nature* **181**, 1524 (1958)
8. F. Melde, *Pogg. Ann.* **109**, 192 (1859)
9. E.J. Yarmchuck, M.J.V. Gordon, R.E. Packard, *Phys. Rev. Lett.* **43**, 214 (1979)
10. M.R. Matthews, B.P. Anderson, P.C. Haljan, D.S. Hall, C.E. Wieman, E.A. Cornell, *Phys. Rev. Lett.* **83**, 2498 (1999)
11. J.E. Williams, M.J. Holland, *Nature* **401**, 568 (1999)
12. A.E. Leanhardt, A. Görlitz, A.P. Chikkatur, D. Kielpinski, Y. Shin, D.E. Pritchard, W. Ketterle, *Phys. Rev. Lett.* **89**, 190403 (2002)
13. A.E. Leanhardt, Y. Shin, D. Kielpinski, D.E. Pritchard, W. Ketterle, *Phys. Rev. Lett.* **90**, 140403 (2003)
14. M.F. Andersen, C. Ryu, P. Cladé, V. Natarajan, A. Vaziri, K. Helmerson, W.D. Phillips, *Phys. Rev. Lett.* **97**, 170406 (2006)
15. O.M. Maragò, S.A. Hopkins, J. Arlt, E. Hodby, G. Hechenblaikner, C.J. Foot *Phys. Rev. Lett.* **84**, 2056 (2000)
16. K.W. Madison, F. Chevy, W. Wohlleben, J. Dalibard *Phys. Rev. Lett.* **84**, 806 (2000)
17. F. Dalfovo and M. Modugno, *Phys. Rev. A* **61**, 023605 (2000)
18. S. Stringari, *Phys. Rev. A* **58**, 2385 (1998)
19. K.W. Madison, F. Chevy, V. Bretin, J. Dalibard, *Phys. Rev. Lett.* **86**, 4443 (2001)
20. A. Recati, F. Zambelli, S. Stringari, *Phys. Rev. Lett.* **86**, 377 (2001)
21. S. Sinha, Y. Castin, *Phys. Rev. Lett.* **87**, 190402 (2001)
22. J.R. Abo-Shaeer, C. Raman, J.M. Vogels, W. Ketterle, *Science* **292**, 476 (2001)
23. D. Guéry-Odelin, *Phys. Rev. A* **62**, 033607 (2000)
24. P.C. Haljan, I. Coddington, P. Engels, E.A. Cornell, *Phys. Rev. Lett.* **87**, 210403 (2001)
25. I.M. Khalatnikov, *Introduction to the Theory of Superfluidity*, (Benjamin, New York 1965)
26. C. Raman, M. Köhl, R. Onofrio, D.S. Durfee, C.E. Kuklewicz, Z. Hadzibabic, W. Ketterle, *Phys. Rev. Lett.* **83**, 2502 (1999)
27. S. Inouye, S. Gupta, T. Rosenband, A.P. Chikkatur, A. Görlitz, T.L. Gustavson, A.E. Leanhardt, D.E. Pritchard, W. Ketterle, *Phys. Rev. Lett.* **87**, 080402 (2001)
28. T. Frisch, Y. Pomeau, S. Rica, *Phys. Rev. Lett.* **69**, 1644 (1992)
29. T. Winiecki, J.F. McCann, C.S. Adams, *Phys. Rev. Lett.* **82**, 5186 (1999)
30. B.P. Anderson, P.C. Haljan, C.A. Regal, D.L. Feder, L.A. Collins, C.W. Clark, E.A. Cornell, *Phys. Rev. Lett.* **86**, 2926 (2001)
31. Z. Hadzibabic, P. Krüger, M. Cheneau, B. Battelier, J. Dalibard, *Nature* **441**, 1118 (2006)

32. P. Rosenbusch, V. Bretin, J. Dalibard, Phys. Rev. Lett. **89**, 200403 (2002)
33. J.J. García-Ripoll, V.M. Pérez-García, Phys. Rev. A **63**, 041603 (2001)
34. M. Modugno, L. Pricoupenko, Y. Castin, Eur. Phys. J. D **22**, 235 (2003)
35. J. Tempere, J.T. Devreese, Solid State Commun. **108**, 993 (1998)
36. E.L. Bolda and D.F. Walls, Phys. Rev. Lett. **81**, 5477 (1998)
37. Y. Castin, R. Dum, Eur. Phys. J. D **7**, 399 (1999)
38. L. Dobrek, M. Gajda, M. Lewenstein, K. Sengstock, G. Birkl, W. Ertmer, Phys. Rev. A, **60**, R3381 (1999)
39. F. Chevy, K.W. Madison, V. Bretin, J. Dalibard, Phys. Rev. A **64**, 031601 (2001)
40. S. Stringari, Phys. Rev. Lett. **86**, 4725 (2001)
41. F. Zambelli, S. Stringari, Phys. Rev. Lett. **81**, 1754 (1998)
42. F. Chevy, K.W. Madison, J. Dalibard, Phys. Rev. Lett. **85**, 2223 (2000)
43. E. Hodby, S.A. Hopkins, G. Hechenblaikner, N.L. Smith, C.J. Foot, Phys. Rev. Lett. **91**, 090403 (2003)
44. E. Lundh, Phys. Rev. A **65**, 043604 (2002)
45. H. Pu, C.K. Law, J.H. Eberly, and N.P. Bigelow, Phys. Rev. A **59**, 1533 (1999)
46. M. Möttönen, T. Mizushima, T. Isoshima, M.M. Salomaa, and K. Machida, Phys. Rev. A **68**, 023611 (2003)
47. Y. Shin, M. Saba, M. Vengalattore, T.A. Pasquini, C. Sanner, A.E. Leanhardt, M. Prentiss, D.E. Pritchard, W. Ketterle, Phys. Rev. Lett. **93**, 160406 (2004)
48. R. Blaauwgeers, V.B. Eltsov, M. Krusius, J.J. Ruohio, R. Schanen, G.E. Volovik, Nature **404**, 471 (2000)
49. W. Thomson (Lord Kelvin), Philos. Mag. **10**, 155 (1880)
50. L.P. Pitaevskii, Sov. Phys. JETP **13**, 451 (1961)
51. B.P. Anderson, P.C. Haljan, C.E. Wieman, E.A. Cornell Phys. Rev. Lett. **85**, 2857 (2000)
52. E. Hodby, O.M. Maragò, G. Hechenblaikner, C.J. Foot, Phys. Rev. Lett. **86**, 2196 (2001)
53. V. Bretin, P. Rosenbusch, F. Chevy, G.V. Shlyapnikov, J. Dalibard, Phys. Rev. Lett. **90**, 100403 (2003)
54. M.H. Freedman, A. Kitaev, M.J. Larsen, Zhenghan Wang, Bull. Am. Math. Soc. **40**, 31 (2003)

Part VII

Vortex Lattices

Vortex Lattices in Bose–Einstein Condensates: Theory

M. Ueda and H. Saito

Some of the basic principles and recent developments of vortex lattices in a dilute Bose–Einstein condensate are reviewed. The topics covered include nucleation dynamics of scalar and spinor vortices, collective modes, and fast rotation.

11.1 Hydrodynamic Theory of Vortices

Classical and quantum vortices have many important features in common which can be described in hydrodynamics [1, 2]. Let $\rho(\mathbf{r}, t)$ and $\mathbf{v}(\mathbf{r}, t)$ be the mass density and the velocity field of the fluid at position \mathbf{r} and time t . The conservation of mass is guaranteed by the continuity equation

$$\frac{\partial \rho}{\partial t} + \nabla \cdot (\rho \mathbf{v}) = 0. \quad (11.1)$$

An ideal fluid is defined as one with no viscosity. Furthermore, if there is no thermal conduction, the fluid is adiabatic and the velocity changes according to the Euler equation

$$\frac{d\mathbf{v}}{dt} = \frac{\partial \mathbf{v}}{\partial t} + (\mathbf{v} \cdot \nabla) \mathbf{v} = -\frac{1}{\rho} \nabla p - \frac{1}{m} \nabla U, \quad (11.2)$$

where p is the pressure, m is the mass of the constituent particles of the fluid, and U is an external potential. An ideal fluid having neither viscosity nor thermal conduction is adiabatic and therefore the entropy is conserved. We then have $(1/\rho)\nabla p = \nabla w$, where w is the enthalpy, and (11.2) becomes

$$\frac{d\mathbf{v}}{dt} = \frac{\partial \mathbf{v}}{\partial t} + (\mathbf{v} \cdot \nabla) \mathbf{v} = -\nabla \left(w + \frac{U}{m} \right). \quad (11.3)$$

By using the identity

$$(\mathbf{v} \cdot \nabla) \mathbf{v} = \nabla \left(\frac{1}{2} \mathbf{v}^2 \right) - \mathbf{v} \times \operatorname{rot} \mathbf{v}, \quad (11.4)$$

we can obtain the fundamental equation for an ideal isentropic fluid:

$$\frac{\partial \mathbf{v}}{\partial t} - \mathbf{v} \times \boldsymbol{\omega} = -\nabla \left(\frac{1}{2} \mathbf{v}^2 + w + \frac{U}{m} \right). \quad (11.5)$$

Here

$$\boldsymbol{\omega} = \operatorname{rot} \mathbf{v} \quad (11.6)$$

is called vorticity. Since $\operatorname{div} \boldsymbol{\omega} = 0$, the vortex cannot appear or disappear in the liquid; it can only close upon itself or terminate on the boundary.

In the case of stationary flow, it is convenient to introduce a streamline which shows the direction of the mass flow. Putting $\partial \mathbf{v} / \partial t = 0$ in (11.5) and taking the inner product of the resulting equation with \mathbf{v} , we can find along the streamline that

$$\frac{1}{2} \mathbf{v}^2 + w + \frac{U}{m} = \text{constant}. \quad (11.7)$$

This is Bernoulli's equation.

The line integral of the velocity along closed contour C

$$\Gamma = \oint \mathbf{v} \, d\mathbf{r} \quad (11.8)$$

is called the circulation of the fluid. Stokes' theorem enables this integral to be converted into the surface integral over the area enclosed by contour C

$$\Gamma = \int_C \operatorname{rot} \mathbf{v} \, d\mathbf{S} = \int_C \boldsymbol{\omega} \, d\mathbf{S}. \quad (11.9)$$

Thus, the circulation gives the vorticity of the area enclosed by the contour. It follows from (11.3) that

$$\frac{d\Gamma}{dt} = \oint \frac{d\mathbf{v}}{dt} \, d\mathbf{r} + \oint \mathbf{v} \, d\mathbf{v} = - \oint \nabla \left(w + \frac{U}{m} \right) \, d\mathbf{r} + \frac{1}{2} \oint d(\mathbf{v}^2) = 0.$$

Thus, for isentropic flow, Γ is conserved as the contour moves with the liquid (Kelvin's theorem).

The fluid is said to be irrotational if the velocity field is expressed in terms of the gradient of a potential ϕ as

$$\mathbf{v} = \nabla \phi. \quad (11.10)$$

The fluid then has no vorticity as can be seen from (11.6). When the density of the fluid is constant, the fluid is said to be incompressible if the velocity field is divergence-free, i.e., $\operatorname{div} \mathbf{v} = 0$. More generally, the change in density caused by

an adiabatic change in pressure Δp is given by $\Delta\rho = (\partial\rho/\partial p)_S \Delta p = c^{-2} \Delta p$, where c is the sound velocity. On the other hand, from the Bernoulli equation, we have $\Delta p \sim \rho v^2$. Thus, the condition for the fluid being incompressible is given by

$$\frac{\Delta\rho}{\rho} \sim \left(\frac{v}{c}\right)^2 \ll 1. \quad (11.11)$$

That is, the fluid behaves as incompressible if its velocity is much lower than the velocity of sound. Condition (11.11) is usually well satisfied in superfluid helium, so that the system is always incompressible, while a gaseous BEC system can change from an incompressible to compressible regime as the frequency of rotation of the system is increased.

The conservation of circulation, together with the fact that a vortex does not appear or disappear in an ideal fluid, lends particular importance to the notion of vortices. In a classical fluid, however, it is often difficult to identify the precise location of a vortex because the circulation can take on any continuous value; it is usually identified as the local minimum of the pressure. In a superfluid, by contrast, the characteristics of vortices are well defined because they appear as phase singularities having topological quantum numbers, as shown in the next section.

Suppose now that the system is contained in a cylinder which rotates at angular frequency Ω about the symmetry axis. The kinetic energy of the fluid is given by

$$E = \int \frac{1}{2} \rho \mathbf{v}^2 d\mathbf{r}. \quad (11.12)$$

When the system possesses only one vortex at the center of the symmetry axis, (11.8) gives

$$v = \frac{\Gamma}{2\pi r}, \quad (11.13)$$

where r is the distance from the axis of the cylinder. Substituting this into (11.12) gives

$$E = \frac{\rho \Gamma^2 L}{4\pi} \ln \frac{R}{a}, \quad (11.14)$$

where a is the radius of the vortex core, R is the radius of the container, and L is the length of the vortex filament. The creation of a vortex thus costs energy. However, there is no energy minimum to create a classical vortex because Γ can take on any small value. The situation is different for quantum vortices in which Γ takes on quantized values.

The flow pattern becomes nonuniform in the presence of vortices. If the fluid rotates at angular frequency Ω , the average velocity of the fluid at position \mathbf{r} is given by $\bar{\mathbf{v}} = \Omega \times \mathbf{r}$. Decomposing \mathbf{v} into the sum of $\bar{\mathbf{v}}$ and the rest as $\mathbf{v} = \bar{\mathbf{v}} + \mathbf{v}_{\text{local}}$, we can rewrite (11.12) as

$$E = \frac{1}{2} I \Omega^2 + \boldsymbol{\Omega} \cdot \int \rho \mathbf{r} \times \mathbf{v}_{\text{local}} d\mathbf{r} + \frac{1}{2} \int \rho \mathbf{v}_{\text{local}}^2 d\mathbf{r}, \quad (11.15)$$

where $I = \int \rho r^2 dr$ is the classical moment of inertia. The angular momentum of the fluid is given by

$$\mathbf{L} = I\boldsymbol{\Omega} + \int \rho \mathbf{r} \times \mathbf{v}_{\text{local}} d\mathbf{r}. \quad (11.16)$$

When the container of the system rotates at frequency Ω_0 , the state of the system is determined by the requirement that

$$E - \boldsymbol{\Omega}_0 \cdot \mathbf{L} = \frac{1}{2} I(\boldsymbol{\Omega}^2 - 2\boldsymbol{\Omega} \cdot \boldsymbol{\Omega}_0) + (\boldsymbol{\Omega} - \boldsymbol{\Omega}_0) \cdot \int \rho \mathbf{r} \times \mathbf{v}_{\text{local}} d\mathbf{r} + \frac{1}{2} \int \rho \mathbf{v}_{\text{local}}^2 d\mathbf{r} \quad (11.17)$$

be minimal. To what extent the rotation of the system deviates from $\boldsymbol{\Omega}_0$ is determined from the last two terms of this equation, which, in turn, depend on the distribution of vortices, as will be discussed in Sect. 11.3.2.

Finally, we comment on the concept of boundary layers. The surface of a solid-state container has atomic-scale roughness which causes dissipation and viscosity η of the liquid. The boundary layer for an incompressible fluid obeys the Navier–Stokes equation which is (11.2) with the viscous term $(\eta/\rho)\nabla^2 \mathbf{v}$ added to its right-hand side. It is this boundary layer that is responsible for the exchange of momentum and angular momentum between the system and the container, and therefore the equilibrium thermodynamics should be defined in the frame of reference co-rotating with the container. To put it differently, the container plays the role of a heat bath. In the case of a gaseous BEC, the container comprises the electromagnetic potential and has no microscopic roughness. Therefore, the potential does not act as a heat bath, and the system can only be driven by the time-dependent potential that explicitly breaks the symmetry of the system.

11.2 Vortices in a Bose–Einstein Condensate

One of the hallmarks of superfluidity is the emergence of a phase which plays the role of a new thermodynamic variable. To show this, consider a situation in which a particle is removed at \mathbf{r}' from a system in state $|\Phi\rangle$ and added to the system at \mathbf{r} . The probability amplitude of the system to remain in the same quantum state after this process is given by the single-particle density matrix

$$\rho_1(\mathbf{r}, \mathbf{r}') = \langle \Phi | \hat{\psi}^\dagger(\mathbf{r}) \hat{\psi}(\mathbf{r}') | \Phi \rangle. \quad (11.18)$$

Under normal conditions, $\rho_1(\mathbf{r}, \mathbf{r}')$ decays exponentially with increasing $|\mathbf{r} - \mathbf{r}'|$. When the system undergoes BEC, de Broglie waves of individual bosons overlap, so that the particle at one location becomes indistinguishable from that at another. As a consequence, $\rho_1(\mathbf{r}, \mathbf{r}')$ remains nonvanishing over long distances $|\mathbf{r} - \mathbf{r}'|$. This implies the ability of a particle to travel a long distance without disturbing the state of the system. We can see here the crucial link between superfluidity and off-diagonal (i.e., $\mathbf{r} \neq \mathbf{r}'$) long-range order (ODLRO) [3].

For a uniform system at rest, it can be shown [4] that

$$\rho_1(\mathbf{r}, \mathbf{r}') \rightarrow \frac{n_0}{V} \quad \text{as } |\mathbf{r} - \mathbf{r}'| \rightarrow \infty, \quad (11.19)$$

where n_0 is the number of particles in the $\mathbf{k} = \mathbf{0}$ state. This result shows that the system exhibits ODLRO at the thermodynamic limit if and only if an extensive number of bosons (proportional to the volume) condense in the zero-momentum state. This demonstrates the equivalence between ODLRO and BEC.

The condition for BEC can also be stated as

$$\rho_1(\mathbf{r}, \mathbf{r}') \longrightarrow \psi^*(\mathbf{r})\psi(\mathbf{r}') \quad \text{as } |\mathbf{r} - \mathbf{r}'| \rightarrow \infty. \quad (11.20)$$

In this case, $\psi(\mathbf{r})$ becomes, to a very good approximation, an eigenfunction of single-particle density matrix $\rho_1(\mathbf{r}, \mathbf{r}')$ [4]:

$$\int d\mathbf{r} \rho_1(\mathbf{r}, \mathbf{r}') \psi(\mathbf{r}) \simeq n_M \psi(\mathbf{r}'), \quad n_M = \int d\mathbf{r} |\psi(\mathbf{r})|^2. \quad (11.21)$$

Here, $\psi(\mathbf{r})$ in (11.20) is often referred to as the condensate wavefunction or the order parameter, and n_M gives the number of condensed bosons. The ratio n_M/N is referred to as the condensate fraction. Comparing (11.20) with (11.19), we find that the condensate wavefunction is a thermodynamic quantity that emerges as a complex order parameter. It follows that the phase of the condensate wavefunction should behave as a new thermodynamic quantity.

Let us decompose the condensate wavefunction into the amplitude and the phase:

$$\psi(\mathbf{r}, t) = A(\mathbf{r}, t)e^{i\phi(\mathbf{r}, t)}. \quad (11.22)$$

Then the mass and current densities are given by

$$\rho(\mathbf{r}, t) = m|\psi|^2 = mA^2(\mathbf{r}, t), \quad (11.23)$$

$$\mathbf{j}(\mathbf{r}, t) = \frac{\hbar}{2i} (\psi^* \nabla \psi - \psi \nabla \psi^*) = \rho(\mathbf{r}, t) \frac{\hbar}{m} \nabla \phi(\mathbf{r}, t). \quad (11.24)$$

The ratio of the current density to the mass density defines the velocity field:

$$\mathbf{v}(\mathbf{r}, t) = \frac{\hbar}{m} \nabla \phi(\mathbf{r}, t). \quad (11.25)$$

Substituting this into (11.8) and assuming the single-valuedness of the condensate wavefunction, we obtain the celebrated quantization of circulation:

$$\Gamma = \frac{\hbar}{m} \oint \nabla \phi \cdot d\mathbf{r} = \kappa n \quad (n = 0, \pm 1, \pm 2, \dots), \quad (11.26)$$

where

$$\kappa = \frac{\hbar}{m} \quad (11.27)$$

is the quantum of circulation. It follows that the velocity field defined in (11.13) diverges at the origin. The wavefunction should therefore vanish at the center of the vortex core which is the branch point of the phase. Thus the quantized vortex features the phase singularity characterized by the topological quantum number n given in (11.26). Near the vortex core, the wavefunction is shown [5] to behave as

$$\psi \propto e^{in\theta} \left(\frac{r}{\xi}\right)^n, \quad (11.28)$$

where ξ is the healing length which characterizes the radius of the vortex core. It is worthwhile remarking that the velocity (11.13) with $\Gamma = h/m$ exceeds the sound velocity at $r \sim \xi$. This affords a good example of the fact that a superfluid is not destroyed if the velocity of the fluid exceeds the Landau critical velocity; only the superfluid density is being suppressed.

The energy per unit length of a singly quantized vortex ($n = 1$) reads

$$\epsilon = \frac{\rho_s \kappa^2}{4\pi} \ln \frac{R}{b}, \quad (11.29)$$

where a numerical analysis has shown $b \simeq 0.68\xi$ [5], and the angular momentum per unit length is given by

$$L \simeq 2\pi \int_0^R \rho_s v_s r^2 dr = \frac{1}{2} \rho_s \kappa R^2, \quad (11.30)$$

where ρ_s is the superfluid density. The free energy of the system at zero temperature is given by $F = \epsilon - L\Omega$, and the condition $F = 0$ gives the critical frequency for thermodynamic vortex nucleation as

$$\Omega_c \simeq \frac{\kappa}{2\pi R^2} \ln \frac{R}{b}. \quad (11.31)$$

An immediate consequence of the quantization of circulation is that a superfluid is not set into rotation if the rotation frequency of the container is below Ω_c , a phenomenon known as the Hess–Fairbank effect [6]. The process of nucleation for the case of a gaseous BEC system is different in that the trapping potential does not act as a heat bath (see the remark at the end of Sect. 11.1). In this case, the dynamic instability as well as the Landau (energetic) instability can trigger the nucleation process and determine the critical rotation frequency [7–9].

When the rotation frequency exceeds the critical frequency, vortices enter the system. For a uniform rotation, we have $\mathbf{v} = \boldsymbol{\Omega} \times \mathbf{r}$, so that the vorticity, or the circulation per unit area, is given by $\omega = |\text{rot } \mathbf{v}| = 2\Omega$. Since each vortex carries quantum of circulation κ , the number density of vortices for uniform rotation is given by

$$n_v = \frac{2\Omega}{\kappa}. \quad (11.32)$$

This relation is referred to as Feynman's rule [10].

The operator, $-i\partial/\partial\phi$, acting on the wavefunction has the same effect as multiplying the wavefunction by the number of particles, N . Conversely, operator $i\partial/\partial N$ can be identified as the phase of the wavefunction, ϕ . Then the Heisenberg equation of motion for ϕ gives

$$\hbar \frac{\partial \phi}{\partial t} = \frac{\partial H}{\partial N}. \quad (11.33)$$

Taking the expectation value of this equation gives

$$\hbar \frac{d\phi}{dt} = \frac{\partial E}{\partial N} = \mu. \quad (11.34)$$

Taking the gradient of (11.34), we find that

$$\frac{d\mathbf{v}}{dt} = \frac{1}{m} \nabla \mu. \quad (11.35)$$

This equation shows that the superfluid can be accelerated by a gradient of the chemical potential.

Let us take two different points 1 and 2 on closed contour C . Equation (11.26) implies that whenever a vortex comes in or out of C , the integral of $\nabla\phi$ along one segment between 1 and 2 differs from that along the other by $2\pi n$. The difference in chemical potential between points 1 and 2 is given from (11.34) as

$$\mu_1 - \mu_2 = \hbar \frac{d(\phi_1 - \phi_2)}{dt}. \quad (11.36)$$

Thus, the phase change, or phase slippage, generates a potential difference in a superfluid. This is in sharp contrast with an ideal classical fluid, in which vortices cannot move across a streamline because the chemical potential is constant along the streamline (Bernoulli's equation). Let dn/dt be the net number of vortices per unit time that cross segment 1-2 of C from one side to the other. Then

$$\mu_1 - \mu_2 = h \frac{dn}{dt}. \quad (11.37)$$

Let the distance between 1 and 2 be infinitesimal and call that segment dx , and let dy be an infinitesimal segment perpendicular to dx . Dividing (11.37) by dx , we obtain

$$\frac{d\mu}{dx} = h \frac{dn}{dxdy} \frac{dy}{dt}. \quad (11.38)$$

The left-hand side of this equation is equal to $m dv_x/dt$ (see (11.35)) and the right-hand side to $h(m\omega/h)(dy/dt)$, where $dn/dxdy = n_v$, $\omega = |\text{rot } \mathbf{v}| = 2\Omega = \kappa n_v$ is vorticity, and dy/dt is the drift velocity v_{drift} of the vortex. We thus obtain

$$\frac{d\mathbf{v}}{dt} = \mathbf{v}_{\text{drift}} \times \boldsymbol{\omega} + \nabla \mu, \quad (11.39)$$

where term $\nabla\mu$ is added to account for the pressure gradient. Equation (11.39) implies that, in the presence of the drift of vortices, the superfluid is accelerated in the direction perpendicular to both the direction of the drift velocity and that of the vorticity.

11.3 Collective Modes of Vortices

11.3.1 Vortex Filament

We will first consider a single straight vortex in the z direction. The fact that the vortex has an energy per unit length as in (11.29) suggests tension in the filament and hence an oscillatory mode. Since the vortex has a mass flow around it, the oscillatory mode forms a helix known as the Kelvin mode [2]. Due to the translational symmetry in the z direction, the normal mode constitutes the plane wave $\exp[i(kz - \omega t)]$ along the z direction and rotates on the perpendicular plane with the dispersion relation given by [11]

$$\omega = \pm \frac{\hbar k^2}{m} \ln(|k|\xi). \quad (11.40)$$

The corresponding formula in a harmonic potential in the Thomas–Fermi regime is derived in [12].

11.3.2 Vortex Lattice

When the frequency of rotation Ω_0 of the container is larger than Ω_c , vortices enter the system with the average density given by (11.32). In the equilibrium condition, vortices form a triangular lattice [13]. To find the frequency of rotation Ω of the system, we rewrite (11.17) as

$$E - \Omega_0 L = \frac{1}{2} I(\Omega^2 - 2\Omega\Omega_0) + \int d^2r n_v [E_v + L_v(\Omega - \Omega_0)], \quad (11.41)$$

where n_v denotes the local density of the vortices,

$$E_v = -\frac{\pi\hbar^2\rho}{2m^2} \ln \frac{\Omega}{\Omega_T} \quad (11.42)$$

is the energy per vortex, where $\Omega_T = \alpha\xi^{-2}$ with α being a constant depending on the geometry of the lattice and independent of Ω [13, 14], and

$$L_v = \frac{\pi^2\hbar^2\rho}{4\sqrt{3}m^2\Omega} \quad (11.43)$$

is the angular momentum per vortex. Minimizing (11.41) with respect to Ω , we find that [14]

$$\Omega = \Omega_0 - \frac{1}{I} \int d^2r n_v \left(L_v + \frac{E_v - \frac{\pi\hbar^2\rho}{2m^2}}{\Omega} \right). \quad (11.44)$$

Since the second term is of the order of \hbar/mR^2 , it can be neglected when the size of the system is much larger than the healing length of the vortex. In this case, $\Omega \simeq \Omega_0$ and the vortex lattice rotates with the container.

Expanding $E - \Omega_0 L$ around $\Omega = \Omega_0$ up to second order, we obtain

$$E - \Omega_0 L \simeq (E - \Omega_0 L)_{\Omega=\Omega_0} + \frac{I}{2}(\Omega - \Omega_0)^2 - \int d^2r \frac{\rho\hbar}{4m\Omega_0} (\Omega - \Omega_0)^2, \quad (11.45)$$

where the second term on the right-hand side is the kinetic energy for the uniform rotation of the fluid viewed from the rotating frame, and the last term can be interpreted as elastic energy E_{el} associated with a homogeneous displacement of the vortex lattice by the amount

$$\boldsymbol{\epsilon} = \frac{1}{2} \left(1 - \frac{\Omega}{\Omega_0} \right) \mathbf{r}. \quad (11.46)$$

For a triangular lattice, there is also the contribution from shear deformation, so the elastic energy can be written as

$$E_{\text{el}} = \int d^2r \left\{ 2C_1(\nabla \cdot \boldsymbol{\epsilon})^2 + C_2 \left[\left(\frac{\partial \epsilon_x}{\partial x} - \frac{\partial \epsilon_y}{\partial y} \right)^2 + \left(\frac{\partial \epsilon_x}{\partial y} + \frac{\partial \epsilon_y}{\partial x} \right)^2 \right] \right\}, \quad (11.47)$$

where C_1 is the compressive modulus and C_2 is the shear modulus with $C_2 = -C_1 = \hbar\rho\Omega_0/(8m)$ [13, 14]. Tkachenko [13] showed that the normal modes of an infinite triangular lattice involve an elliptical motion of the vortices around their equilibrium positions in a sense opposite to that of the uniform rotation. For $\Omega \ll ck$, the system is incompressible and the dispersion relation of the Tkachenko mode is given by [13]

$$\omega_T = \left(\frac{\hbar\Omega_0}{4m} \right)^{\frac{1}{2}} k, \quad (11.48)$$

while for $\Omega \gg ck$, the system becomes compressible and the dispersion relation becomes quadratic at the long-wavelength limit [15, 16] as

$$\omega_T = \sqrt{\frac{\hbar}{16m\Omega_0}} ck^2, \quad (11.49)$$

where c is the sound velocity, and furthermore in the quantum-Hall regime as

$$\omega_T = \frac{9}{4\pi^2\sqrt{10}} \frac{c^2 k^2}{\Omega_0}. \quad (11.50)$$

Apart from the Tkachenko mode, there is also the usual inertial mode whose dispersion relation is given by [15, 16]

$$\omega_I = \sqrt{4\Omega_0^2 + c^2 k^2}. \quad (11.51)$$

The Tkachenko mode was observed in liquid helium by Andereck and Glaberson [17] and in gaseous BEC by Coddington et al. [18]. The latter experiment was analyzed numerically by Mizushima et al. [19].

11.4 Dynamics of Vortex Nucleation

11.4.1 Scalar BEC

When the system is set into rotation, quantized vortices, which are nucleated outside of the condensate, penetrate into it. The dynamics of the vortex nucleation and formation of a vortex lattice can be described by a dissipative Gross–Pitaevskii (GP) equation [9, 20],

$$(i - \gamma)\hbar \frac{\partial \psi}{\partial t} = \left(-\frac{\hbar^2}{2m} \nabla^2 - \boldsymbol{\Omega} \cdot \mathbf{L} + V_{\text{trap}} \right) \psi + \frac{4\pi\hbar^2 a}{m} |\psi|^2 \psi - \tilde{\mu} \psi, \quad (11.52)$$

where γ is a phenomenological damping constant, $\mathbf{L} = -i\hbar\mathbf{r} \times \nabla$ is the angular momentum operator, V_{trap} is a harmonic trapping potential, and a is the s -wave scattering length. The last term on the right-hand side of (11.52) ensures conservation of the number of condensed atoms n_M , where

$$\tilde{\mu} = \frac{1}{n_M} \int d\mathbf{r} \left[\psi^* \left(-\frac{\hbar^2}{2m} \nabla^2 - \boldsymbol{\Omega} \cdot \mathbf{L} + V_{\text{trap}} \right) \psi + \frac{4\pi\hbar^2 a}{m} |\psi|^4 \right] \quad (11.53)$$

is the time-dependent chemical potential in the rotating frame. The physical origin of the dissipative term in (11.52) is inelastic collisions of the condensate with thermal and background atoms. The dissipative GP equation has been derived and applied to vortex lattice formation in [21].

Figure 11.1 shows examples of numerical simulations of (11.52) with $\gamma = 0.03$ [22]. As mentioned in Sect. 11.1, we must break the axisymmetry of the trap to drive the system into rotation. Here, we examine the displacement of a harmonic potential as

$$V_{\text{trap}} = \frac{1}{2} m \omega_{\perp}^2 [(x - \Delta)^2 + y^2] + \frac{1}{2} m \omega_z^2 z^2, \quad (11.54)$$

and $\boldsymbol{\Omega}$ is assumed to be parallel to the z direction. The potential (11.54) simulates a situation in which the trap center rotates on a circle of radius Δ . When the z dependence of ψ is frozen in a tight pancake-shaped trap, the dynamics of the system are confined to two dimensions (2D) with an effective interaction parameter given by $C = 4\sqrt{\pi\lambda n_M a}/a_{\text{ho}}$, and when the z dependence can be neglected in a long cigar-shaped trap, $C \simeq 8\pi a n_M/(2R_z)$, where $\lambda = \omega_z/\omega_{\perp}$, $a_{\text{ho}} = \sqrt{\hbar/(2m\omega_{\perp})}$, and R_z is the Thomas–Fermi radius in the z direction [9] (see also Chap. 1).

The dynamics shown in Fig. 11.1 tell us how vortex is nucleated and vortex lattice is formed. Topological defects first appear around the edge of BEC (the first row in Fig. 11.1b,c). These topological defects can be identified only in the phase profile, and hence they are called “ghost vortices” [20]. The density ripples are then excited on the surface (the second row), and some of them penetrate into the condensate as vortices (the third row), whereas the topological defects that cannot penetrate into the system remain hovering around

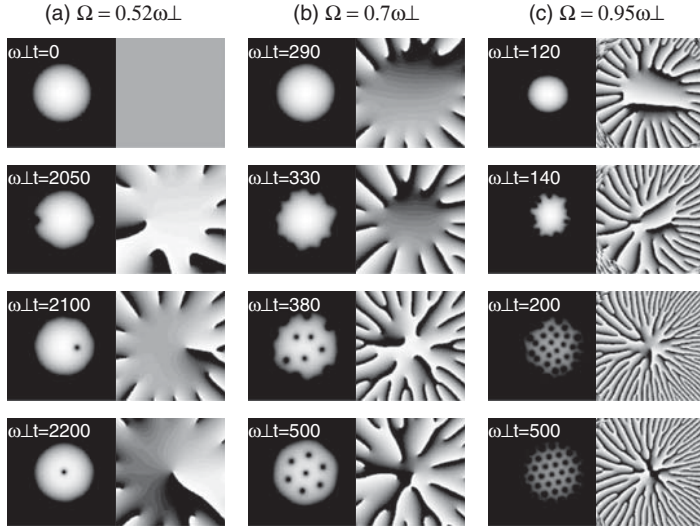


Fig. 11.1. Dynamics of vortex nucleation in the rotating frame of reference. The left (right) panels show the density (*phase*) profiles. The initial state is the ground state for $C = 500$ in an axisymmetric potential, as shown in the upper left panel ($\omega_\perp t = 0$). At $t = 0$, the trapping potential is displaced as in (11.54) with $\Delta = 0.3a_{ho}$, and rotated at frequency Ω . The size of the images is $20a_{ho} \times 20a_{ho}$ in (a) and (b), and $30a_{ho} \times 30a_{ho}$ in (c)

the condensate. The system eventually relaxes into either an axisymmetric single vortex state (the fourth row in Fig. 11.1a) or triangular (Abrikosov) lattices (the fourth row in Fig. 11.1b,c), depending on the rotation frequency of the trapping potential.

In most numerical studies of vortex nucleation, quadrupole distortion such as

$$V_{\text{trap}} = \frac{1}{2}m\omega_\perp^2[(1 + \epsilon_x)x^2 + (1 + \epsilon_y)y^2] + \frac{1}{2}m\omega_z^2z^2 \quad (11.55)$$

has been added to the trapping potential to drive the system into rotation, where ϵ_x and ϵ_y are small constants. A similar potential has also been used in École Normale Supérieure (ENS) experiments [23]. By exciting quadrupole modes, the potential (11.55) causes the condensate to undergo elliptic deformation with irrotational flow. Surface ripples are then excited, followed by vortex penetration into the condensate. The system maintains twofold symmetry in this process, reflecting the symmetry of the trapping potential (11.55), the minimum number of nucleated vortices being two. Vortex nucleation occurs most efficiently when the rotation frequency hits the resonant frequency of the quadrupole mode, which is $\omega_\perp/\sqrt{2}$ for the Thomas–Fermi limit. On the other hand, the trapping potential (11.54) breaks the twofold symmetry by

shifting from the trap center, and can therefore nucleate a single vortex as shown in Fig. 11.1(a).

A thermodynamic argument suggests that vortex nucleation occurs when the energy of the vortex state in the rotating frame, $E_v - \Omega L_v$, where L_v is the angular momentum of the vortex state, becomes smaller than that of nonvortex state E_{nv} , i.e., $\Omega > (E_v - E_{nv})/L_v$. In the case of Fig. 11.1, this frequency corresponds to $\Omega \simeq 0.31\omega_\perp$. In reality, however, vortices do not enter the condensate at this frequency. In fact, two instabilities play key roles in the nucleation of vortices: dynamical instability and energetic (Landau) instability. The dynamical instability arises from some excitation energies becoming complex due to nonlinearity. The imaginary part of the excitation energy causes exponential growth of the corresponding mode, leading to vortex nucleation. The dynamical instability for the trapping potential in (11.55) at the Thomas–Fermi limit has been studied in [7,8]. The energetic or Landau instability arises from the presence of negative excitation energies, and the system then becomes unstable against excitations by a negative-energy mode in the presence of dissipation. We should note that $\Omega > (E_v - E_{nv})/L_v$ is not a sufficient but necessary condition for the dynamical and energetic instabilities [24]. Both types of instabilities, which are involved in (11.52), are needed to account for the experimental results. If $\gamma = 0$ in (11.52), namely, if the energetic instability is excluded, vortices cannot be created, at least within the nucleation time observed in the experiments.

Vortex crystallization also needs some dissipation mechanism, since the free-vortex state (the third row in Fig. 11.1b,c) has greater entropy than the vortex lattice state (the bottom row). It has been reported [25, 26] that the vortex lattice can be formed by the GP equation without dissipative terms ($\gamma = 0$). However, in order to quantitatively reproduce the experimentally observed nucleation time of vortices and the relaxation time for vortex lattice formation, we must include some dissipative terms in the GP equation, as in (11.52).

When the interaction is changed from repulsive to attractive by using Feshbach resonance, for example, and when the attractive interaction dominates the quantum kinetic pressure, the system collapses. The collapse problem of a rotating BEC is interesting because of the topological constraint. The BEC atoms cannot enter the vortex core, and hence collapse must occur away from the vortices. An axisymmetric single-vortex state exhibits quadrupole instability when the attractive interaction exceeds the critical strength, and the system splits into two clusters, breaking the axisymmetry spontaneously [27]. The collapse dynamics of the vortex lattice are illustrated in Fig. 11.2. The atoms gather at places where the atomic density is high, and the vortex cores are expanded ($\omega_\perp t = 0.2$). Then local collapse occurs at vertices of the honeycomb lattice. After this local collapse, high-energy atoms are scattered out of the condensate as an atomic burst [28, 29]. Experimental observation of the interference between atomic bursts from the honeycomb lattice may clarify to what extent the burst is coherent.

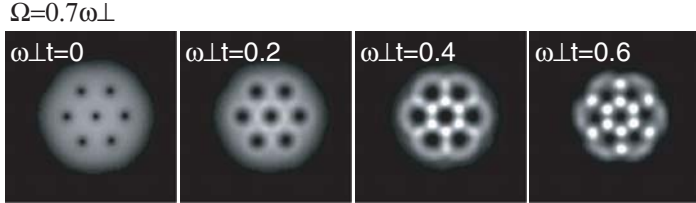


Fig. 11.2. Collapse of a vortex lattice with an attractive interaction. The initial state is prepared with $C = 500$ and $\Omega = 0.7\omega_{\perp}$ as in Fig. 11.1a, and at $t = 0$, the interaction is suddenly changed to $C = -200$. At $\omega_{\perp}t = 0.4$ and 0.6 , local collapses of the condensate are seen to occur at vertices of the honeycomb lattice

11.4.2 Spinor BEC

We next consider the formation dynamics of vortices in a spinor BEC (see also Part IX) which are quite different from those of a scalar BEC. The spinor BEC is described by a multi-component order parameter ψ_{α} , where α refers to the magnetic quantum number. For example, for the case of a spin-1 BEC, α takes on 1, 0, and -1 . The general form of a spin vortex is given by

$$\psi_{\alpha} = e^{i\chi_{\alpha}} e^{in_{\alpha}\theta} f_{\alpha}(r_{\perp}), \quad (11.56)$$

where χ_{α} is the global phase of each component, and $f_{\alpha}(r_{\perp})$ is a radial function with $r_{\perp} = (x^2 + y^2)^{1/2}$. Integers n_{α} are the topological charges that characterize a spin vortex. For example, in the case of the Mermin–Ho texture in a spin-1 BEC, the topological charges are given by $n_1 = 0$, $n_0 = 1$, and $n_{-1} = 2$.

For a spin-1 BEC, the interaction energy has the form

$$\int d\mathbf{r} \frac{2\pi\hbar^2}{m} (a_{\text{density}} D + a_{\text{spin}} \langle \mathbf{F} \rangle^2), \quad (11.57)$$

where $D = \sum_{\alpha} |\psi_{\alpha}|^2$ and $\langle \mathbf{F} \rangle = \sum_{\alpha,\beta} \psi_{\alpha}^* \mathbf{F}_{\alpha\beta} \psi_{\beta}$ with $\mathbf{F} = (F^x, F^y, F^z)$ being the vector representation of spin-1 matrices. For spin-1 ^{87}Rb and ^{23}Na atoms, the spin-independent scattering length, a_{density} , is positive and much larger in magnitude than the spin-dependent one, a_{spin} , and therefore total density D is determined mainly by the spin-independent energy. Consequently, the vortex core of the component of $n_{\alpha} \neq 0$ is occupied by the component of $n_{\alpha} = 0$, so that the total density D maintains the Thomas–Fermi profile. The spin vortices, in which one n_{α} is 0, are therefore called coreless spin vortices. When $n_1 = \pm 1$, $n_0 = 0$, and $n_{-1} = \mp 1$, the core is occupied by the $\alpha = 0$ component, which is called a polar-core vortex.

Vortices in a scalar BEC have circular flow of mass current (11.24). In a spinor BEC, the spin current can be defined by

$$\mathbf{J}_{\text{spin}}^j = \frac{\hbar}{2mi} \sum_{\alpha,\beta} \left[\psi_{\alpha}^* F_{\alpha\beta}^j \nabla \psi_{\beta} - \psi_{\beta} F_{\alpha\beta}^j \nabla \psi_{\alpha}^* \right], \quad (11.58)$$

where $j = x, y$, or z . The circulation of the spin current does not have to be quantized. For the Mermin–Ho texture, both mass and spin currents are nonzero, flowing around the core of the vortex. For the polar-core vortex given by

$$\psi_1 = e^{\pm i\theta + i\chi} f_1(r_\perp), \quad \psi_0 = f_0(r_\perp), \quad \psi_{-1} = e^{\mp i\theta - i\chi} f_1(r_\perp), \quad (11.59)$$

the mass current vanishes while the spin current is $\mathbf{J}_{\text{spin}}^x = \mathbf{J}_{\text{spin}}^y = \mathbf{0}$ and

$$\mathbf{J}_{\text{spin}}^z = \frac{2\hbar}{mr_\perp} f_1^2(r_\perp) \mathbf{e}_\theta, \quad (11.60)$$

where \mathbf{e}_θ is a unit vector in the azimuthal direction.

Let us consider a situation in which a spin-1 ^{87}Rb BEC is prepared in the $\alpha = 0$ state. Since the spin-dependent interaction of spin-1 ^{87}Rb is ferromagnetic ($a_{\text{spin}} < 0$), the system has a tendency to magnetize. However, uniform magnetization of the whole system in the same direction is prohibited because of the spin conservation – a fact markedly different from a solid-state ferromagnet. Consequently, spin textures develop in the course of spontaneous magnetization in such a manner that the total magnetization is conserved [30].

One of the spontaneously formed spin textures is the polar-core vortex [31]. This topological spin texture is energetically favorable within the constraint of spin conservation because the ferromagnetic energy costs only at the core of the spin vortex. Figure 11.3 illustrates spontaneous magnetization and

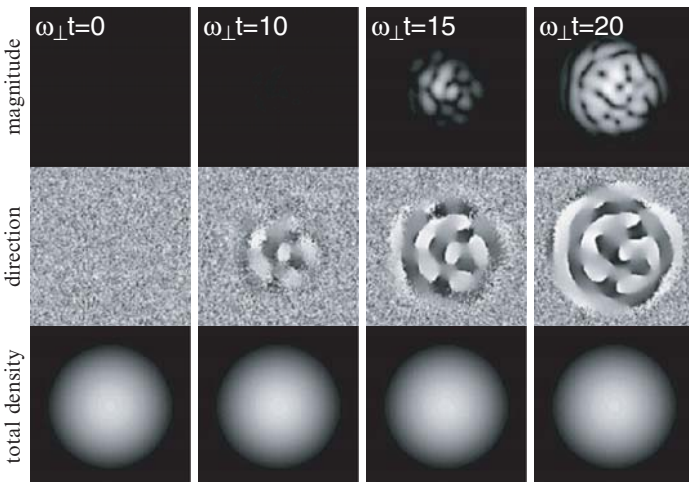


Fig. 11.3. Spontaneous magnetization of a spin-1 ^{87}Rb BEC. The *top* and *middle panels*, respectively, show the magnitude $(\langle F_x \rangle + \langle F_y \rangle)^{1/2}$ and direction $\tan^{-1}(\langle F_y \rangle / \langle F_x \rangle)$ of transverse magnetization, and the *bottom panels* show total density ρ . The dimensionless interaction parameters are chosen to be $C_{\text{density}} = 40,000$ and $C_{\text{spin}} = -185$. The size of the images is $50a_{\text{ho}} \times 50a_{\text{ho}}$.

topological-texture formation. The initial state is prepared in the ground state of the $\alpha = 0$ component and a small seed noise is added to the $\alpha = \pm 1$ components to trigger magnetization. A spin texture emerges first in the direction of magnetization ($\omega_{\perp}t = 10$) and then in its magnitude ($\omega_{\perp}t = 15$), and eventually a topological spin texture is spontaneously formed ($\omega_{\perp}t = 20$). The several holes in the magnetization at $\omega_{\perp}t = 20$ in Fig. 11.3 indicate the locations of polar-core vortices, around which the transverse spin vector rotates by 2π . The total density remains almost the same throughout the dynamics as shown in the bottom panels. Such topological texture formation in a spinor BEC has been observed experimentally [32].

Thus, in a spinor BEC, topological defects can be formed spontaneously in the quantum phase transition from a nonmagnetic to a magnetic state. This situation has a close similarity to the Kibble–Zurek mechanism [33, 34], which merits further study. We also note that the $\alpha = \pm 1$ components of the polar-core vortex (11.59) rotate in opposite directions, and hence a polar-core vortex lattice may be formed if an external potential can drive the $\alpha = \pm 1$ components in opposite directions.

11.5 Fast Rotating BEC

In exploring the physics of rotating BECs, it is useful to note a close analogy between a rotating BEC and a superconductor in a magnetic field. In fact, the system of neutral particles in a rotating frame of reference is equivalent to that of charged particles in a magnetic field through the correspondence:

$$\mathbf{p} - m\boldsymbol{\Omega} \times \mathbf{r} \iff \mathbf{p} - \frac{e}{2c}\mathbf{B} \times \mathbf{r}. \quad (11.61)$$

We can exploit this correspondence to establish several equivalent phenomena between the two systems. For example, the Hess–Fairbank effect in BECs corresponds to the Meissner effect in superconductors, and the critical frequency of rotation in BECs corresponds to the lower critical magnetic field in type-II superconductors. What happens to the BEC when Ω gets larger? In a type-II superconductor, the density of vortices increases with an external magnetic field and the system turns into the normal state when the vortex cores touch each other. The critical magnetic field at which the superconducting state becomes normal defines the upper critical magnetic field. In contrast, in BEC of neutral particles, the vortex core size and the vortex lattice spacing adjust to each other so that no overlap of vortices occurs at high rotation frequency [35]. Thus, there is no analog in BEC for the upper critical frequency beyond which the BEC becomes normal. Instead, in the limit of fast rotation, BEC is expected to become a strongly correlated system of vortex liquid.

Consider what happens if we increase the rotation frequency Ω to ω_{\perp} . Different phenomena can be expected, depending on the ratio ν of the number

of atoms N against the number of vortices. When $\nu > 1,000$, the behavior of the system can be described by the GP mean-field theory.

Suppose that the system is confined in a harmonic potential with radial trapping frequency ω_\perp . In a frame co-rotating with the container of the system, we have

$$E - \Omega L = \int d\mathbf{r} \left[\frac{1}{2m} |(\mathbf{p} - m\boldsymbol{\Omega} \times \mathbf{r})\psi|^2 + \frac{1}{2} m(\omega_\perp^2 - \Omega^2) \mathbf{r}^2 |\psi|^2 + \frac{g}{2} |\psi|^4 \right]. \quad (11.62)$$

It is clear from this expression that as Ω approaches ω_\perp , the condensate flattens out and becomes an effective two-dimensional system. When $1000 > \nu > 10$, the system enters the mean-field quantum Hall regime [36], in which the mean-field theory is still applicable but the state of the system can be well described in the lowest Landau level (LLL) approximation. It is also worthwhile noticing that when the mean-field interaction is much smaller than the single-particle energy-level spacing, the LLL approximation is justified no matter how small the rotation frequency is. In this case, the many-body wavefunction of the system can be expanded in terms of the states of the particles that rotate in the same sense as the rotation of the container. Let it be counterclockwise. Then the many-body wavefunction can, in general, be written as

$$\Psi(z_1, z_2, \dots, z_N) = f(z_1, z_2, \dots, z_N) \exp \left(-\frac{1}{2} \sum_{k=1}^N |z_k|^2 \right), \quad (11.63)$$

where $z_k = x_k + iy_k$ is the complex coordinate of the k th particle and f is a symmetric polynomial of z_1, z_2, \dots, z_N . When the interparticle interaction is attractive, we have [37]

$$f(z_1, z_2, \dots, z_N) \propto \left(\sum_{k=1}^N z_k \right)^L, \quad (11.64)$$

where $\hbar L$ is the total angular momentum of the system. On the other hand, when the interaction is repulsive and $0 \leq L \leq N$, we have [38, 39]

$$f(z_1, z_2, \dots, z_N) \propto \sum_{1 \leq i_1 < i_2 < \dots < i_L \leq N} z_{i_1} z_{i_2} \cdots z_{i_L}, \quad (11.65)$$

where the sum runs over all possible choices of L atoms out of the N atoms.

When $\nu < 10$, the vortex lattice melts and a strongly correlated system is expected to emerge. In particular, when $L = N(N - 1)$, we have [40–44]

$$f(z_1, z_2, \dots, z_N) \propto \prod_{i>j} (z_i - z_j)^2. \quad (11.66)$$

This state naturally circumvents the repulsive kinetic-energy cost at $z_i = z_j$ while maintaining the Bose statistics. It is nothing but the Laughlin state with filling fraction $\nu = 1/2$.

References

1. L.D. Landau and E.M. Lifshitz, *Fluid Mechanics*, 2nd edn (Butterworth-Heinemann, Oxford, 1997)
2. R.J. Donnelly, *Quantized Vortices in Helium II* (Cambridge Univ. Press, 1991)
3. C.N. Yang, Rev. Mod. Phys. **34**, 694 (1962)
4. O. Penrose, Phil. Mag. **42**, 1373 (1951); O. Penrose and L. Onsager, Phys. Rev. **104**, 576 (1956)
5. V.L. Ginzburg and L.P. Pitaevskii, Sov. Phys. JETP, **34**, 858 (1958)
6. G.B. Hess and W.M. Fairbank Phys. Rev. Lett. **19**, 216 (1967)
7. A. Recati, F. Zambelli, S. Stringari, Phys. Rev. Lett. **86**, 377 (2001)
8. S. Sinha, Y. Castin, Phys. Rev. Lett. **87**, 190402 (2001)
9. K. Kasamatsu, M. Tsubota, and M. Ueda, Phys. Rev. A **67**, 033610 (2003)
10. R.P. Feynman, Prog. in Low Temp. Phys. **1**, 17 (1955)
11. E.M. Lifshitz, L.P. Pitaevskii, *Statistical Physics Part 2*, 3rd edn (Butterworth-Heinemann, Oxford, 2000)
12. A.A. Svidzinsky and A.L. Fetter, Phys. Rev. A **62**, 063617 (2000)
13. V.K. Tkachenko, Sov. Phys. JETP **22**, 1282 (1966); *ibid.* **23**, 1049 (1966); *ibid.* **29**, 245 (1969)
14. G. Baym, E. Chandler, J. Low Temp. Phys. **50**, 57 (1983)
15. G. Baym, Phys. Rev. Lett. **91**, 110402 (2003)
16. M. Cozzini, L.P. Pitaevskii, and S. Stringari, Phys. Rev. Lett. **92**, 220401 (2004)
17. C.D. Andereck and W.I. Glaberson, J. Low Temp. Phys. **48**, 257 (1982)
18. I. Coddington, P. Engels, V. Schweikhard, and E.A. Cornell, Phys. Rev. Lett. **92**, 220401 (2004)
19. T. Mizushima, Y. Kawaguchi, K. Machida, T. Ohmi, T. Isoshima, and M.M. Salomaa, Phys. Rev. Lett. **92**, 060407 (2004)
20. M. Tsubota, K. Kasamatsu, and M. Ueda, Phys. Rev. A **65**, 023603 (2002)
21. A.A. Penckwitt, R.J. Ballagh, and C.W. Gardiner, Phys. Rev. Lett. **89**, 260402 (2002)
22. S. Choi, S.A. Morgan, and K. Burnett, Phys. Rev. A **57**, 4057 (1998)
23. K.W. Madison, F. Chevy, W. Wohlleben, and J. Dalibard Phys. Rev. Lett. **84**, 806 (2000)
24. T. Isoshima and K. Machida, Phys. Rev. A **60**, 3313 (1999)
25. C. Lobo, A. Sinatra, and Y. Castin, Phys. Rev. Lett. **92**, 020403 (2004)
26. N.G. Parker and C.S. Adams, Phys. Rev. Lett. **95**, 145301 (2005)
27. H. Saito and M. Ueda, Phys. Rev. Lett. **89**, 190402 (2002); Phys. Rev. A **69**, 013604 (2004)
28. E.A. Donley, N.R. Claussen, S.L. Cornish, J.L. Roberts, E.A. Cornell, and C.E. Wieman, Nature **412**, 295 (2001)
29. H. Saito and M. Ueda, Phys. Rev. Lett. **86**, 1406 (2001); Phys. Rev. A **65**, 033624 (2002)
30. H. Saito and M. Ueda, Phys. Rev. A **72**, 023610 (2005)
31. H. Saito, Y. Kawaguchi, and M. Ueda, Phys. Rev. Lett. **96**, 065302 (2006); Phys. Rev. A. **75**, 013621 (2007)
32. L.E. Sadler, J.M. Higbie, S.R. Leslie, M. Vengalattore, and D.M. Stamper-Kurn, Nature **443**, 312 (2006)
33. T.W.B. Kibble, J. Phys. A: Math. Gen. **9**, 1387 (1976)
34. W.H. Zurek, Nature (London) **317**, 505 (1985); W.H. Zurek, Phys. Rep. **276**, 177 (1996)

35. U. Fisher and G. Baym, Phys. Rev. Lett. **90**, 140402 (2003); G. Baym and C.J. Pethick, Phys. Rev. A **69**, 0437619 (2004)
36. T.-L. Ho, Phys. Rev. Lett. **87**, 060403 (2001)
37. N.K. Wilkin, J.M.F. Gunn, and R.A. Smith Phys. Rev. Lett. **80**, 2265 (1998)
38. G.F. Bertsch and T. Papenbrock Phys. Rev. Lett. **83**, 5412 (1999)
39. M. Ueda and T. Nakajima Phys. Rev. A **73**, 043603 (2006)
40. N.R. Cooper, N.K. Wilkin, and J.M.F. Gunn, Phys. Rev. Lett. **87**, 120405 (2001)
41. B. Paredes, P. Fedichev, J.I. Cirac, and P. Zoller, Phys. Rev. Lett. **87**, 010402 (2001)
42. J. Sinova, C.B. Hanna, A.H. MacDonald, Phys. Rev. Lett. **89**, 030403 (2002)
43. N. Regnault and Th. Jolicoeur, Phys. Rev. Lett. **91**, 030402 (2003)
44. T. Nakajima and M. Ueda, Phys. Rev. Lett. **91**, 140401 (2003)

Vortex Lattices in Bose–Einstein Condensates: Experiments

C. Raman

12.1 Overview

This chapter examines quantized vortex lattices from an experimental perspective. While vortices in dilute Bose gases have been the subject of a number of theoretical review papers [1–3] (see also Chaps. 9 and 11), here we wish to present a pedagogical overview from the experimental side. We will emphasize manipulating and observing the lattices, and what can be learned about their structure and dynamics¹. This chapter is not a comprehensive review of all experiments to date; rather, it is focused on the basic techniques and experiments. The reader will be familiar with some experimental methods from reading the chapter on individual vortex nucleation and formation. For completeness, we briefly review the method of creation and detection before discussing the specifics pertaining to the lattice structures.

Vortex lattices (as opposed to individual or a few vortices) are a natural point of study. It is relatively straightforward to mechanically add large quantities of angular momentum to a Bose–Einstein condensate, which then equilibrates to form an ordered lattice. Moreover, the state of rapid rotation is one of *bulk* vortex matter, possessing new properties and signatures. Under conditions of extremely rapid rotation (for harmonic traps this is where the normalized rotation rate $\tilde{\Omega} \equiv \Omega/\omega_{\text{trap}} \rightarrow 1$) the many body physics “reappears” from under the cloak of the usual mean-field description. That is, when the vortex and particle number become comparable, each must account for the other in determining the spatial structure, leading to highly correlated many-body wavefunctions similar to those encountered in quantum Hall physics [2, 5–7]. Thus far this regime has not been reached experimentally.

It is remarkable that an article summarizing experiments on vortex matter in BEC can even be written today. Until around the year 2000, no vortices had ever materialized in spite of many experimental efforts towards creating

¹ While we focus here on Bose gases, vortices have also recently been observed in Fermi gases, providing evidence for Fermi superfluidity [4].

them. The JILA group of Eric Cornell first succeeded at creating a vortex state through a phase imprinting method involving two internal hyperfine states. It was the Paris group of Jean Dalibard that eventually hit upon a simple formula for mechanical “stirring” which became widely adopted, both using optical potentials [8] as well as magnetic ones at JILA [9] and at Oxford in the group of Chris Foot [10]. Within a very short while it became possible to create large numbers of vortices $>\sim 150$ using this method, as the MIT group of Wolfgang Ketterle showed [11]. His group later also demonstrated that the nucleation of many vortices was quite insensitive to the details of the stirring method [12]. In light of this it is not so clear why the experimental study of vortices underwent such a phase transition around 2000. Earlier attempts at inducing rotation had failed, although they employed similar methods [13]. It is perhaps a feature of experimental science that the “phase space” of parameters within which one can observe a phenomenon often appears magnified once it has been first observed.

A typical experimental sequence (but by no means unique) involves first creating a Bose–Einstein condensate in a harmonic trap (usually a magnetic one, although nowadays optical as well) and setting it into rotation via a perturbing potential. After some time, typically 0.1–1 s, the perturbation is turned off, after which the rotating gas is allowed to equilibrate, i.e., to find the lowest energy configuration consistent with the total amount of angular momentum L . The experiment concludes by shutting off the trap, allowing the rotating gas to expand in order to magnify the vortex cores and to reduce the optical thickness of the cloud. Then the gas is imaged using near-resonant laser light, a standard technique. In most cases, the expanded gas containing vortices is simply a magnified version of the trapped one² [14, 16]. One can control L through the strength and frequency of the perturbation and the duration of its application. For very small L , one finds an irrotational flow, i.e. no vortices. As L increases, the vortices begin to appear. In the limit of large L , the vortex number observed after equilibration is in the range of a few hundred. We will focus entirely on this latter regime, where the system contains vortex matter in the bulk.

12.2 Experimental Observation

Figure 12.1 shows a typical experimental observation [12, 17]. These data, taken in Paris in 2000 and at MIT in 2001, provided the first signature

² The JILA group uses a different stirring method involving rotation of the thermal cloud followed by condensation into a rotating state. They observe the BEC with an anti-trapping expansion method somewhat more complex than simple shut-off. Their method allowed them to show that the three-dimensional character of the expansion affected the apparent size of the vortex cores, i.e., verified the prediction [14] that a simple magnification of all spatial features does not always apply [15].

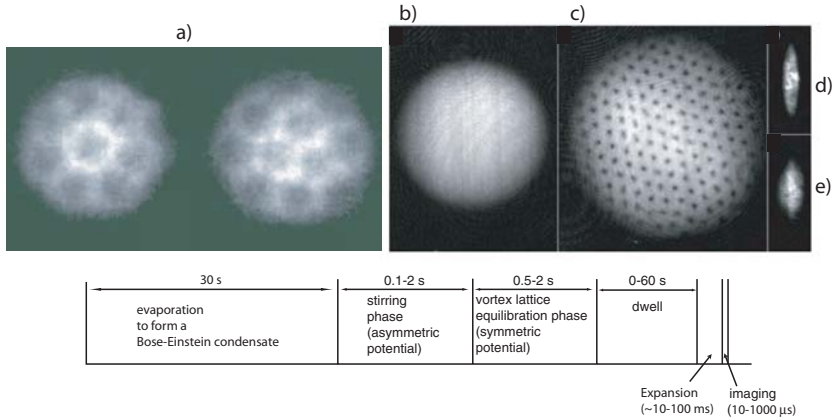


Fig. 12.1. First experimental observation of vortex lattices. Below the images we show a typical experimental sequence for creating and observing vortex lattices. (a) Arrays of up to 11 vortices observed in Paris in 2000 (data taken from [17]). In the second image the central three vortices are arranged in a triangle, a hint of the structure which should appear in the bulk. Absorption images are shown for (b) non-rotating and (c) rapidly rotating condensates from the MIT group (data taken from [12]). The latter image contains 160 vortices and clearly shows the Abrikosov lattice is regular up till the edges of the BEC. In (c) the centrifugal effect causes the BEC to expand faster in time-of-flight, resulting in a larger size. (d) in situ phase contrast images of a condensate at rest and (e) in rotation, observed perpendicular to the rotation axis. The aspect ratio is modified due to the centrifugal bulge

of vortex arrays. The Paris group showed that the structure of the array depended on the vortex number for small values, as seen in Fig. 12.1a. By contrast, the MIT experiments produced vortices in large numbers (Fig. 12.1c), where the Abrikosov, i.e., triangular, lattice structure became apparent.

These images are the primary source of experimental data. They are a two-dimensional map of the column density $\tilde{n}(\rho) = \int n(\rho, z) dz$, where z is the axis of imaging (in this case parallel to the rotation axis). The vortex lines, which lie parallel to z , appear simply as holes, i.e., regions depleted of atoms. Experimentally, the column density is derived from the raw transmission data for the laser beam that is recorded on the CCD camera, $T = I(\rho)/I_0(\rho) = e^{-\sigma \int n(\rho, z) dz}$. I and I_0 are the laser beam intensity profiles in the image plane $z = 0$, recorded in the presence and absence of atoms, respectively. The atomic absorption cross-section σ is known from basic spectroscopic data and the known laser detuning from resonance [18]. $\rho = (x, y)$ is the coordinate vector in the image plane. The expanded condensate is three-dimensional, and therefore in order to apply a two-dimensional theory to understand the images, the depth of focus must exceed the condensate size. For an optical resolution d , the depth of focus can be estimated from the confocal parameter $2 \times z_0$, where $z_0 = \pi d^2/\lambda$, where λ is the wavelength

of the light used. Typical numbers might be $d \sim 7 \mu\text{m}$, $\lambda \sim 0.8 \mu\text{m}$, yielding $2 \times z_0 \simeq 0.4 \text{ mm}$. Expanded condensates can have dimensions exceeding 1 mm. Therefore, clearer images are often obtained by “slicing” the condensate, i.e., selectively imaging a slice of 50–100 μm thickness near the center of the cloud using an optical pumping technique [19]. This method also avoids blurring of the vortex lines due to bending at the edges of the cloud.

Figure 12.1d,e show an alternate method of observing the rotation, namely, through *in situ* monitoring of the column density via phase-contrast imaging, a non-destructive technique. The imaging axis is perpendicular to the rotation z . Therefore, one observes the change in aspect ratio of the cloud due to the centrifugal distortion accompanied by rotation. Absorption imaging after time-of-flight is necessarily destructive, i.e., a single snapshot of the gas. Phase contrast images, however, only weakly perturb the condensate. Therefore, a succession of images can be used to monitor the dynamics of the vortices on a single run of the experiment. The individual vortices, with their core size of typically 0.3 μm , are too small to resolve optically. Therefore, only the macroscopic features of the rotation (for example the rotation rate vs. time) can be monitored using this method.

12.3 Spinning Condensates

One can spin up the condensate simply by adding a rotating asymmetry in the (x, y) plane to the otherwise cylindrically symmetric trapping potential. This process can be done either optically or magnetically. The magnetic approach is qualitatively similar to the optical one, and was used by the JILA group and the Oxford group [10]. In addition, there are variants on these methods used to create extremely rapid rotation very close to the trapping frequency pioneered by the JILA group [20]. For now, we will focus on the basic optical technique that creates a rotating asymmetry. In this approach, a far-detuned laser beam is focused near the condensate (see Fig. 12.2). This creates a potential maximum (minimum) at the focus for blue (red) detuning of the laser light from the atomic resonance. In the Paris experiments [8] the beam waist was 20 μm , whereas the Thomas–Fermi radius of the condensate was 2.6 μm . Moreover, a two-point pattern with separation 16 μm was generated by rapidly scanning the laser beam at a rate of 100 kHz, much faster than the radial oscillation frequency of $\omega_\perp \sim 200 \text{ Hz}$. The combined effect of the two beams is to create

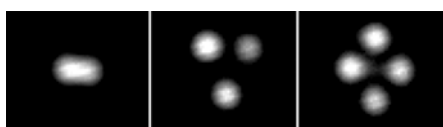


Fig. 12.2. Stirring of condensates using rotating optical potentials. Shown are typical laser beam profiles for 2, 3 and 4 point patterns, as discussed in the text

a potential energy that is (a) quadratic at the atoms' location and (b) asymmetric in the $x - y$ plane. This optical potential can be made to rotate in space at a slow frequency $\Omega \simeq 0.7\omega_{\perp}$ simply by slowly rotating the two-point pattern in the $x - y$ plane. In the reference frame co-rotating with the laser beams with coordinates (X, Y) , it appears simply as a static, quadrupolar deformation of the total potential

$$V_{\text{tot}}(\rho) = \frac{M}{2}\omega_{\perp}^2(\epsilon_x X^2 + \epsilon_y Y^2), \quad (12.1)$$

where $\epsilon_x \neq \epsilon_y$ and both are of the order of 1.0–1.1. In the laboratory frame the equipotential surface is an ellipsoid whose minor axis rotates about the z -direction at a rate Ω . Once the stirring is complete, the laser beams are turned off, whence the potential becomes symmetric (and static) once again:

$$V_{\text{tot}}(\rho) = \frac{M}{2}\omega_{\perp}^2(x^2 + y^2). \quad (12.2)$$

The MIT group used a similar method for stirring the condensate, but also created $l = 3$ and 4 point optical patterns, shown schematically in Fig. 12.2b,c. The goal was to investigate the role played by discrete surface modes possessing angular momentum $l\hbar$ that can “collapse” into vortices. The quadrupolar deformation above can drive the $l = 2$ surface mode [21–23]. The 3 and 4 point patterns were observed to enhance the vortex production in the vicinity of discrete resonances suggesting that higher order surface modes $l > 2$ were being excited.

Optical “stirring” experiments can also be done in the limit where the laser beam diameter is much smaller than the cloud [12]. In this case, the vortices are nucleated locally, near the boundary between the condensate and the stirrer. Theoretical studies of this process show that vortex-anti-vortex pairs are produced, which have no net angular momentum [24, 25]. Surprisingly, those experiments, which were performed at MIT, also created vortex lattices, i.e., rotating condensates. The explanation given was that when the laser beam moves in a circle, co-rotating vortices are favored, whereas counter-rotating vortices are expelled from the system. However, lattices were created even when the laser beam moved in a straight line through the cloud, which theoretically should not favor any rotation sense, but inevitably does due to minor misalignments and asymmetries. The conclusion of those experiments was that vortex lattices appear to be a rather ubiquitous feature of stirring experiments.

12.4 Lattice Basics

The vortex lattice is not stationary in the laboratory frame, but rotates at an angular frequency Ω , which in general can be different from the drive frequency Ω_{drive} . Typically, it is difficult to preserve the lattice in the presence

of even small amounts of asymmetry in the trapping potential, and a simple physical argument explains why. In a frame co-rotating with the lattice, a static asymmetry will appear as a counter-rotating perturbation, in effect, a “speed bump” for the vortices. This causes frictional damping of the atomic motion. In theory, a co-rotating perturbation at Ω should not damp the motion, since it appears as a static deformation in the moving frame. However, for rapidly rotating lattices this has been very difficult to observe. The likely explanation is that small residual asymmetries exist in the drive mechanism. Such asymmetries would naturally have temporal modulations at frequencies which are harmonics of Ω , leading to rapid spin-down. The JILA group of Eric Cornell recently has managed to pin vortices in a co-rotating potential by carefully managing the asymmetries [26].

In the absence of an externally applied asymmetry, the magnetic trap itself can have weak asymmetries due to imperfections in the coils used to create the trap. However, these can be minimized by carefully tuning the trap parameters. As a result, at very low temperatures where the thermal fraction is negligible, one can create vortex lattices that persist for many tens of seconds, and even higher. In this regime, the lattice rotates approximately as a rigid body, when the superfluid velocity field \mathbf{v}_s is coarse-grained over many vortices. We can apply the quantization condition for the circulation around a closed contour C

$$\oint_C \mathbf{v}_s \cdot d\mathbf{l} = N_v \frac{h}{M} = N_v \kappa, \quad (12.3)$$

assuming there are N_v singly quantized vortices within the domain bounded by C . $\kappa = h/M$ is the quantum of circulation, h the Planck constant, and M the atomic mass. If the vortices are uniformly distributed and their number is large, we may assume azimuthal symmetry of the velocity field provided that we average \mathbf{v}_s over regions of the size of the vortex core. In that case, we may use a circle of radius r for C , whence the circulation becomes $v_s \times 2\pi r$, where $v_s = |\mathbf{v}_s|$ and the flow is assumed to be purely azimuthally directed. Defining the two-dimensional vortex density $n_v = N_v/(\pi r^2)$ we find the velocity field is

$$v_s = \frac{n_v h}{2M} r, \quad (12.4)$$

which is that of a rigidly rotating body with angular frequency Ω defined through the relation:

$$n_v = \frac{2\Omega}{\kappa}. \quad (12.5)$$

The circulation per unit area, or vorticity, of the gas is

$$\bar{\omega} = \text{curl}(\mathbf{v}_s) = 2\Omega. \quad (12.6)$$

For a rotating gas in a harmonic potential in the rotating frame an additional, destabilizing centrifugal potential appears with “frequency” Ω . At $z = 0$ this can be written as

$$V_{\text{tot}} = \frac{1}{2}M\omega_{\perp}^2\rho^2 - \frac{1}{2}M\Omega^2\rho^2. \quad (12.7)$$

The net result is an effective harmonic radial trapping frequency of $\omega_{\perp,\text{eff}} = \sqrt{\omega_{\perp}^2 - \Omega^2}$. Thus, as the lattice rotation approaches the trap frequency the confinement strength diminishes. The Thomas–Fermi radius in the $x-y$ plane R_{TF} can be written as

$$R_{TF} = \sqrt{\frac{2\mu(\Omega)}{\omega_{\perp,\text{eff}}^2}}, \quad (12.8)$$

and increases without bound as $\omega_{\text{eff}} \rightarrow 0$. Simultaneously, through the reduced density (and therefore mean-field pressure), the axial Thomas–Fermi radius decreases, resulting in an oblate, rotating condensate. As $\tilde{\Omega} \rightarrow 1$, the vortex density approaches a constant $n_v \approx 2\omega_{\perp}/\kappa$, while the number of vortices increases with the system size. Eventually, one reaches a regime where the number of vortices and particles become comparable, and the entire edifice of mean-field theory begins to break down.

We will concern ourselves primarily with the regime of current experiments, i.e., where the three-dimensional gas progresses toward a rotating two-dimensional pancake. Experimentally, this corresponds to $\tilde{\Omega} \equiv \Omega/\omega_{\perp} \lesssim 0.99$, where mean-field theory is mostly applicable. One may deduce the rate of rotation from the in situ change of aspect ratio for a cloud confined in a cylindrically symmetric potential. In the Thomas–Fermi limit, the aspect ratio $\lambda = R_z/R_{\rho}$ of axial to radial Thomas–Fermi radii is simply equal to the frequency ratio $\lambda = \omega_{\rho}/\omega_z$. Since $\omega_{\rho} = \omega_{\perp,\text{eff}}$ we can directly calculate this as:

$$\lambda(\Omega) = \lambda_0 \sqrt{1 - \Omega^2/\omega_{\perp}^2}. \quad (12.9)$$

By measuring the aspect ratio λ with and without vortices, one can deduce the rate of rotation from the above formula. This method was shown to be accurate by comparing it to measurements of the frequency splitting between the $m = \pm 2$ surface modes [9] that directly yields Ω .

12.5 Lattice Dynamics

Assuming that three-dimensional vortex lines have entered the system, the first question one can ask is how do such ordered lattices appear? The MIT group varied the equilibration time and counted the number of vortices which were visible. Since visibility is reduced if the vortex lines are bent, this provides a measure of the degree of alignment of the vortices. The detection threshold was defined by a minimum column density. The result is shown in

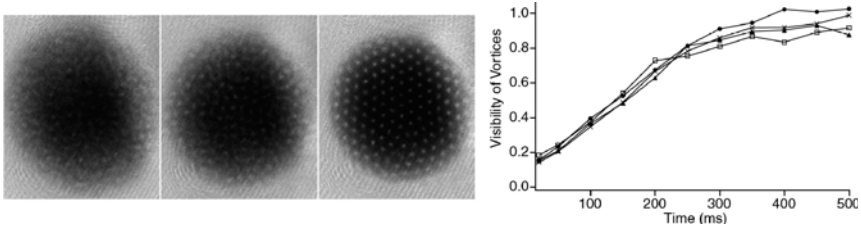


Fig. 12.3. Crystallization of a vortex lattice. Taken from [27]

Fig. 12.3. Immediately after stirring, the images appear mottled and blurry, due to the three-dimensional tangle of vortices. As time goes on, the lattice slowly materialized. The number of visible vortices normalized to the total number of vortices (the latter deduced from phase contrast measurements) is plotted for a range of temperatures below T_c , the transition temperature to a Bose–Einstein condensate. The conclusion they drew was that the formation of the lattice does not depend strongly on temperature, and could be, for example, due to the spontaneous reconnection of vortices [27].

After equilibration the vortex lattice in general need not be stationary, not even when viewed in a co-rotating frame. One expects a BEC with a single wavefunction to sustain density oscillations even in the zero temperature, collisionless limit [30]. However, the addition of vortices to the system creates additional degrees of freedom. For example, if one considers the vortices as three-dimensional lines, the transverse displacement of the line produces Kelvin modes of excitation. Due to the circulating fluid flow, these appear as helical waves that propagate along the vortex line, and an individual element of the vortex line moves in the opposite sense to the fluid circulation [31, 32]. The Paris group provided evidence for Kelvin mode-induced decay of ordinary hydrodynamic oscillations in a condensate containing a single vortex line [33]. The Oxford group observed the precession of an entire array of vortices [34].

Ordinarily, shear forces do not apply to a superfluid, since the flow is frictionless, but a superfluid filled with vortices has a finite shear modulus, as has been known from studies of liquid helium [35]. It can sustain transverse elastic modes. These Tkachenko waves, or spatio-temporal azimuthal oscillations of the vortex lattice about its equilibrium position, were observed by the JILA group in 2003 [28]. Since the positions of the vortices are not pinned by external potentials or impurities, they can oscillate about their mean position. This oscillation was excited in the following manner. A weak “blasting” laser pulse was used to remove atoms selectively from the center of the BEC, and the resulting radial motion of the atoms created azimuthal excitation of the lattice through the Coriolis forces. Fig. 12.4 shows an absorption image of the characteristic s-bend of the Tkachenko wave, as well as the amplitude of the wave vs. time after excitation. They measured a low frequency of 0.85 Hz, considerably smaller than the trap frequency $\nu_r = 8$ Hz, indicating the low

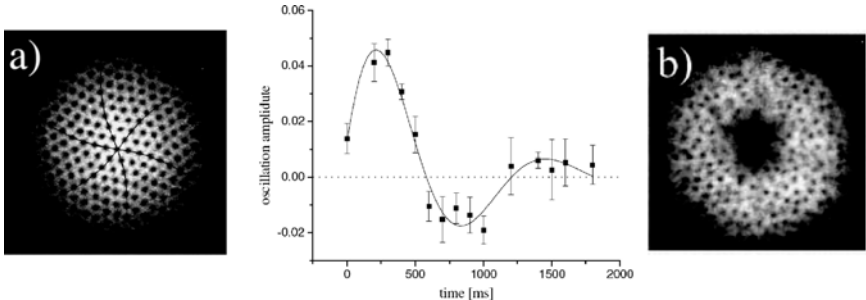


Fig. 12.4. (a) Tkachenko wave (left) creates an *s*-bend in the vortex lattice. Shown is the wave amplitude vs. time after excitation (taken from [28]). (b) The same method for exciting the Tkachenko wave could also be used to create a giant vortex (right). Taken from [29]

value of the shear modulus. For example, ordinary hydrodynamic oscillations of a BEC typically occur at frequencies larger than ν_r .

Atoms removed from the center have less angular momentum than the average, and thus removal of enough atoms will increase the rate of rotation of the remaining gas. This was used by the JILA group to achieve rotation rates above 95 % of the trap frequency. In the presence of an extremely weak laser pulse applied over a very long time up to 70 s, the lattice became unstable and disordered, eventually forming a “giant” vortex aggregate consisting of up to 60 quanta of circulation, as seen in Fig. 12.4. If the laser pulse was turned off, the aggregate eventually dissolved and the vortex lattice was restored. The aggregate behaved much as a single vortex, including precessing about the cloud center if it was displaced.

12.6 Seeing the Phase

Time-of-flight absorption imaging has proved instrumental for observing the density depletion at the vortex cores. However, about each vortex the macroscopic wavefunction undergoes a 2π phase winding which is not directly observed. In order to probe the phase, two experimental techniques have been developed. The Paris and MIT groups used interference between two condensates, while our group at Georgia Tech has used Bragg scattering of laser light. In the Paris experiment, a condensate containing vortices was split into two parts and made to interfere after time-of-flight expansion [36]. The presence of vortices caused the ordinarily straight interference fringes to exhibit dislocations (see Fig. 12.5). The figure shows a similar type of dislocation which was observed in the MIT experiments, where the interference was between a condensate containing a vortex and one free of vortices. Vortex/anti-vortex pairs were created by moving a laser beam through the cloud [37].

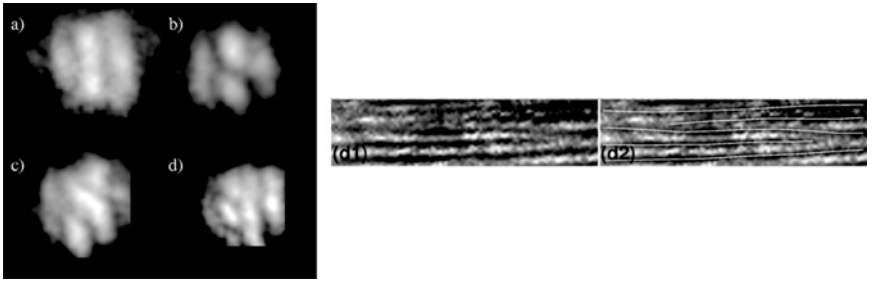


Fig. 12.5. A vortex appears as a dislocation in otherwise straight interference fringes. (a) zero, (b,c) one and (d) several vortices (taken from [36]). On the right are vortex/anti-vortex pairs (taken from [37])

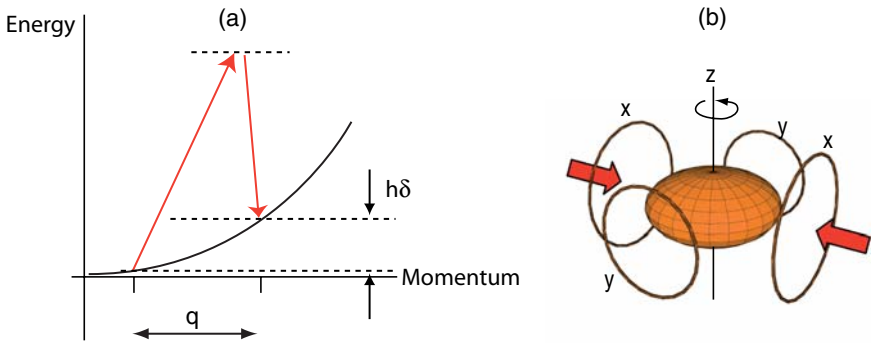


Fig. 12.6. Bragg scattering from vortices. (a) Energy-momentum relation for atoms in a BEC showing the momentum transfer q from the two-photon process. The Bragg resonance occurs at a frequency difference δ between the two laser beams that satisfies both energy and momentum conservation. (b) Diagram of experimental geometry. Vortices are created by rotating a BEC about the z -axis by phase control of the transverse fields produced in coil pairs x and y that control the TOP (time-orbiting potential) trap. The Bragg beam containing frequencies ω and $\omega + 2\pi\delta$ is applied along the x -direction and retroreflected. Taken from [38]

An alternate approach, Bragg scattering, was explored by our group at Georgia Tech [38]. Our focus was on observing the velocity field of the vortex lattice, which is the spatial gradient of the phase profile. Although our experiment was unable to resolve the phase singularity of individual vortices³ we could measure the coarse-grained velocity distribution in the following manner. Two photon scattering of laser light is sensitive to the phase of the atoms' wavefunction because of the Doppler effect. Our group employed two laser beams with frequencies ω and $\omega + 2\pi\delta$, as shown in Fig. 12.6b. An atom

³ This was not a fundamental limitation, but one of technical resolution due to additional complexities imposed by the Bragg technique. There are fundamental limitations to Bragg imaging as well, which are discussed in [39].

scatters a photon from one laser beam into another. The net result is to impart to it a momentum \mathbf{q} . For counter-propagating laser beams of wavelength λ , $q = |\mathbf{q}| = 2h/\lambda$ is twice the momentum of a single photon. The two photon process and the energy-momentum relation are shown schematically in Fig. 12.6a. For a condensate, q/M is typically much greater than the speed of sound, which characterizes the condensate expansion, and therefore, the diffracted cloud can be easily distinguished from the non-diffracted atoms. This is because the former have traveled an additional distance $\approx q/M \times t_{\text{tof}}$ during the time-of-flight t_{tof} after the trap has been shut off. The two clouds can then be separated in the images, as we show below. There is a resonance in the scattering of light when

$$\delta = \delta_{MF} + \frac{q^2}{2Mh} + \frac{\mathbf{q} \cdot \mathbf{v}}{h}, \quad (12.10)$$

which expresses the conservation of momentum and energy. In the above equation, the second term is the recoil energy, which must be provided by the energy difference between the two photons. For sodium atoms near the principal resonance, $q^2/2Mh = 100$ kHz. The third term is simply the Doppler shift, which makes the Bragg technique velocity sensitive. It is this term which is of primary importance, as the Bragg process selects a group of atoms with the same projection of velocity v_x along the direction of the momentum transfer $\mathbf{q} = q\hat{x}$. The term δ_{MF} contains the mean-field interaction shift of the zero-velocity resonance, and was about 1 kHz for our experiment [40, 41].

Figure 12.7 shows the result of the Georgia Tech experiment. We observed spatial structures in the diffracted atom cloud arising from the rotation. In Fig. 12.7a one can see the diffraction from an initially stationary condensate, and the diffracted atoms appear to the right and left of the stationary condensate. No particular structure is visible. However, in Fig. 12.7b, we initially prepared a vortex lattice, which caused the diffracted atoms to form a tilted, elongated spatial pattern. Moreover, when we reversed the direction of the applied rotation, the tilt angle with respect to the y -direction reversed as

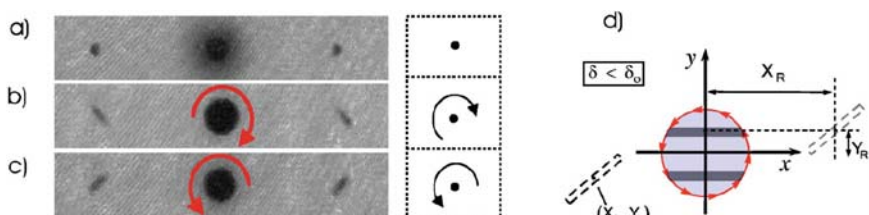


Fig. 12.7. Vortices probed by Bragg scattering. Outcoupled atoms (to the far right and left within each image) showed no particular structure for non-rotating clouds (a), whereas from vortices (b) and (c), the outcoupled atoms were tilted according to the direction of rotation. Each pair of Bragg frequencies is resonant with a thin strip of atoms parallel to the x -axis, as illustrated in (d). Taken from [38]

shown in Fig. 12.7c. By contrast, the time-of-flight absorption method discussed earlier does not provide any indication of the sense of rotation.

The results could be understood in terms of a rigid body picture of rotation combined with the spatial and velocity selectivity of the Bragg resonance. This resonance corresponds to a thin, horizontal band of atoms with $y > 0$ for atoms which are Bragg scattered to the right, and $y < 0$ for atoms scattered to the left (the dark shaded regions in Fig. 12.7d). Within those bands there is a detailed microscopic structure near the vortex cores which could not be resolved. As this band of atoms moves, the spread in velocities in the $x - y$ plane causes part of the band to move up while another part moves down. Thus it forms a tilted stripe in the images. Moreover, the tilt angle increases with time and could be used to independently measure the rate of rotation of the lattice.

12.7 The Rotating Speed Limit

As we saw earlier, for increasing rotation rates, the radial size of the gas increases without bound due to the centrifugal repulsion. At the same time, the two-dimensional vortex density approaches a constant $n_v \rightarrow 2\omega_{\perp}/\kappa$. Thus the particle to vortex number ratio (the so-called “filling factor”) $\nu = N/N_v$ becomes smaller. In this final section we explore this limit. There is a formal analogy between the rotating superfluid and a charged particle in a magnetic field [5]. In particular, the single particle excitations are Landau levels, and as the density of particles is lowered, eventually only a single Landau level is occupied. This LLL, or lowest Landau Level state is still amenable to a mean-field description, and is characterized by a chemical potential below the cyclotron energy $\mu < \hbar\omega_C = 2\hbar\Omega$. In addition, the gas becomes quasi-two dimensional when $\mu \lesssim \hbar\omega_z$, the axial oscillator energy. In this state, one still finds an ordered vortex lattice, but for very small ν below about 10 the lattice is predicted to melt due to quantum fluctuations. A variety of novel, strongly correlated phases are predicted bearing a similarity to the fractional quantum Hall effect [2].

For condensates containing 10^6 atoms and 100 vortices, $\nu \sim 10^4$, which indicates the level of difficulty in entering this regime. The JILA group has made the furthest progress in this regard, achieving an impressive $\tilde{\Omega} = 0.993$ with a filling factor in the range of 500 [20]. The gas entered the LLL state and was observed to have a dramatically reduced shear modulus, as measured by the reduced frequency of the Tkachenko mode. Increasing the rotation beyond what they have achieved becomes a practical matter of managing the instability. Due to the centrifugally weakened confinement, tiny asymmetries in the trap are likely to present an overwhelming perturbation. If one expresses the filling factor in terms of the rotation rate, one can show that $1 - \tilde{\Omega}^2$ becomes of order $1/N$ as ν approaches 1. However, one must have $1 - \tilde{\Omega}^2 > 0$ for stability of the gas. Therefore, it is also clear that the range of parameter

space where mean-field theory breaks down is exceedingly small except for very small condensates. These have the additional complication that small atom numbers are difficult to observe experimentally.

It is interesting to note that the stability requirement $\tilde{\Omega} < 1$ is strictly necessary only for harmonic confinement. The Paris group has demonstrated that it is possible to spin the gas at a rate equal to and even *above* the trapping frequency in the presence of an additional, quartic anharmonicity. Paradoxically, the extra confinement came from a repulsive laser beam superimposed on the harmonic magnetic trap [42]. However, the result was still a mean-field state, unlike that of the harmonic case when $\tilde{\Omega} \rightarrow 1$.

In a purely harmonic potential, if we take the non-interacting limit, the two-dimensional description of rotating bosons is equivalent to a harmonic oscillator, with energy eigenvalues

$$E_{n,m} = n\hbar(\omega_\perp + \Omega) + m\hbar(\omega_\perp - \Omega) + \hbar\omega_\perp, \quad (12.11)$$

where $n, m = 0, 1, 2, \dots$. The LLL regime corresponds to $n = 0$. As $\tilde{\Omega} \rightarrow 1$, the m level spacing $\hbar(\omega_\perp - \Omega)$ becomes much smaller than the n level spacing $\hbar(\omega_\perp + \Omega)$. When the number of m levels within one n level is of order N , there is a massive degeneracy, causing a breakdown in the mean-field description. If we set $N\hbar(\omega_\perp - \Omega) = \hbar(\omega_\perp + \Omega)$, we obtain

$$\frac{1}{N} \approx \frac{1}{4}(1 - \tilde{\Omega}^2) \quad (12.12)$$

as a rough estimate of the transition region. The presence of interactions in such a highly degenerate system generally leads to condensate fragmentation, as recently summarized by Mueller et al. [43]. The essence of this strongly correlated regime is that the particle and vortex densities are becoming comparable to one another, and in the presence of even weak interactions the mean-field state is no longer the lowest energy compared with a fragmented condensate.

12.8 Summary and Outlook

Unlike conventional superfluids, dilute Bose–Einstein condensates allow one to directly probe the superfluid order parameter through optical imaging. The ability to obtain real space images of the vortex lattice has allowed for the direct determination of its structure and dynamics, as we have illustrated. In this chapter we have largely focused on intrinsic properties of the lattices. Now researchers are beginning to manipulate the lattice state itself. The JILA group imposed an external *optical* lattice potential of variable symmetry to pin the vortex locations [26]. This brings hope for the possibility to engineer vortex arrays within “microtraps” where the atom number could be very small while the observed signatures could be quite large as they are the aggregate of many lattice sites. Similar to the method used to observe the Mott

superfluid-insulator transition [44], this might facilitate achieving the rapidly rotating regime described in the previous section. Another area which has been little explored is the role played by the atomic spin in the structure of the vortices as well as the overall lattice [45]. For instance a two-component spinor vortex lattice with rectangular structure has been predicted [46] and observed [47], while the corresponding three component structures have not yet been observed. Finally, while we have focused here on rotating systems, vortex/anti-vortex pairs have also been observed in the BKT (Berezinskii–Kosterlitz–Thouless) crossover in two dimensions [48]. While this chapter has provided an overview of the basic physics of vortex lattices it has necessarily been restricted. Many new findings are appearing in gaseous BECs that promise to penetrate the rich area of vortex physics using the full panoply of atomic techniques.

References

1. A.L. Fetter, A.A. Svidzinsky. J. Phys.-Cond. Matter **13**, R135–R194 (2001)
2. G. Baym, J. Low Temp. Phys. **V138**, 601–610 (2005)
3. P.G. Kevrekidis, R. Carretero-González, D.J. Frantzeskakis, I.G. Kevrekidis, Mod. Phys. Lett. B **18**, 1481–1505 (2004)
4. M.W. Zwierlein, J.R. Abo-Shaeer, A. Schirotzek, C.H. Schunck, W. Ketterle, *Nature* **435**, 1047–1051 (2005)
5. T.-L. Ho, Phys. Rev. Lett. **87**, 060403–4 (2001)
6. N.R. Cooper, N.K. Wilkin, J.M.F. Gunn, Phys. Rev. Lett. **87**, 120405 (2001)
7. J. Sinova, C.B. Hanna, A.H. MacDonald. Phys. Rev. Lett. **89**, 030403 (2002)
8. K.W. Madison, F. Chevy, W. Wohlleben, J. Dalibard, *Phys. Rev. Lett.* **84**, 806–809 (2000)
9. P.C. Haljan, I. Coddington, P. Engels, E.A. Cornell. *Phys. Rev. Lett.* **8721**, art. no.–210403 (2001)
10. E. Hodby, G. Hechenblaikner, S.A. Hopkins, O.M. Marago, C.J. Foot, *Phys. Rev. Lett.* **88**, 010405–4 (2002)
11. J.R. Abo-Shaeer, C. Raman, J.M. Vogels, W. Ketterle, *Science* **292**, 476–479 (2001)
12. C. Raman, J.R. Abo-Shaeer, J.M. Vogels, K. Xu, W. Ketterle. *Phys. Rev. Lett.* **87**, 210402 (2001)
13. M.R. Andrews, *Bose-Einstein Condensates and the Atom Laser*. Ph.d., Ph.D. thesis, Massachusetts Institute of Technology, 1998
14. E. Lundh, C.J. Pethick, H. Smith. *Phys. Rev. A* **58**, 4816 (1998)
15. I. Coddington, P.C. Haljan, P. Engels, V. Schweikhard, S. Tung, E.A. Cornell, *Phys. Rev. A* **70**, 063607–11 (2004)
16. Y. Castin, R. Dum. *Phys. Rev. Lett.* **77**, 5315–5319 (1996)
17. K.W. Madison, F. Chevy, W. Wohlleben, J. Dalibard. *J. Mod. Opt.* **47**, 2715 (2000)
18. H.J. Metcalf, P. van der Straten. *Laser Cooling and Trapping*, (Springer, New York, 1999)
19. M.R. Andrews, C.G. Townsend, H.-J. Miesner, D.S. Durfee, D.M. Kurn, W. Ketterle, *Science* **275**, 637–641 (1997)

20. V. Schweikhard, I. Coddington, P. Engels, V.P. Mogendorff, E.A. Cornell, Phys. Rev. Lett. **92**, 040404–4 (2004)
21. F. Dalfovo, S. Stringari. Phys. Rev. A **63**, 011601 (2001)
22. K.W. Madison, F. Chevy, V. Bretin, J. Dalibard, Phys. Rev. Lett. **86**, 4443 (2001)
23. S. Sinha, Y. Castin, Phys. Rev. Lett. **87**, 190402 (2001)
24. T. Frisch, Y. Pomeau, S. Rica, Phys. Rev. Lett. **69**, 1644 (1992)
25. B. Jackson, J.F. McCann, C.S. Adams, Phys. Rev. Lett. **80**, 3903 (1998)
26. S. Tung, V. Schweikhard, E.A. Cornell. Phys. Rev. Lett. **97**, 240402 (2006)
27. J.R. Abo-Shaeer, C. Raman, W. Ketterle. Phys. Rev. Lett. **88**, 070409 (2002)
28. I. Coddington, P. Engels, V. Schweikhard, E.A. Cornell. Phys. Rev. Lett. **91** (2003)
29. P. Engels, I. Coddington, P.C. Haljan, V. Schweikhard, E.A. Cornell, Phys. Rev. Lett. **90**, 170405 (2003)
30. C.J. Pethick, H. Smith, *Bose–Einstein Condensation in Dilute Gases*, (Cambridge University Press, Cambridge, 2002)
31. W. Thomson, Philos. Mag. **10**, 155 (1880)
32. D.R. Tilley, J. Tilley, *Superfluidity and Superconductivity*, (Wiley, New York, 1990)
33. V. Bretin, P. Rosenbusch, F. Chevy, G.V. Shlyapnikov, J. Dalibard, Phys. Rev. Lett. **90**, 100403 (2003)
34. N.L. Smith, W.H. Heathcote, J.M. Krueger, C.J. Foot, Phys. Rev. Lett. **93**, 080406 (2004)
35. E.B. Sonin, Rev. Mod. Phys. **59**, 87 (1987)
36. F. Chevy, K.W. Madison, V. Bretin, J. Dalibard. Phys. Rev. A **64** (2001)
37. S. Inouye, S. Gupta, T. Rosenband, A. P. Chikkatur, A. Grlitz, T.L. Gustavson, A.E. Leanhardt, D.E. Pritchard, W. Ketterle, Phys. Rev. Lett. **87**, 080402 (2001)
38. S.R. Muniz, D.S. Naik, C. Raman, Phys. Rev. A **73**, 041605 (2006)
39. S.R. Muniz, D.S. Naik, M. Bhattacharya, C. Raman. Math. Comput. Simul. **74**, 397 (2007)
40. P.B. Blakie, R.J. Ballagh, C.W. Gardiner. Phys. Rev. A **65**, 033602 (2002)
41. F. Zambelli, L. Pitaevskii, D.M. Stamper-Kurn, S. Stringari. Phys. Rev. A **61**, 063608 (2000)
42. V. Bretin, S. Stock, Y. Seurin, J. Dalibard, Phys. Rev. Lett. **92**, 050403–4 (2004)
43. E.J. Mueller, T.-L. Ho, Masahito Ueda, Gordon Baym. Phys. Rev. A **74**, 033612 (2006)
44. M. Greiner, O. Mandel, T. Esslinger, T.W. Hansch, I. Bloch. Nature **415**, 39–44 (2002)
45. E.J. Mueller. Phys. Rev. A **69**, 033606 (2004)
46. E.J. Mueller, T.-L. Ho, Phys. Rev. Lett. **88**, 180403 (2002)
47. V. Schweikhard, I. Coddington, P. Engels, S. Tung, E.A. Cornell. Phys. Rev. Lett. **93**, 210403 (2004)
48. Z. Hadzibabic, P. Kruger, M. Cheneau, B. Battelier, J. Dalibard, Nature **441**, 1118–1121 (2006)

Part VIII

Optical Lattices

Optical Lattices: Theory

A. Smerzi and A. Trombettoni

13.1 Introduction

This chapter presents an overview of the properties of a Bose–Einstein condensate (BEC) trapped in a periodic potential. This system has attracted a wide interest in the last years, and a few excellent reviews of the field have already appeared in the literature (see, for instance, [1–3] and references therein). For this reason, and because of the huge amount of published results, we do not pretend here to be comprehensive, but we will be content to provide a flavor of the richness of this subject, together with some useful references. On the other hand, there are good reasons for our effort. Probably, the most significant is that BEC in periodic potentials is a truly interdisciplinary problem, with obvious connections with electrons in crystal lattices, polarons and photons in optical fibers. Moreover, the BEC experimentalists have reached such a high level of accuracy to create in the lab, so to speak, paradigmatic Hamiltonians, which were first introduced as idealized theoretical models to study, among others, dynamical instabilities or quantum phase transitions.

The key feature of our problem is that the periodic potential naturally introduces a spatial *discreteness* in a nonlinear medium. The periodic potential is generally realized with two counter-propagating laser beams [4–12], so as to create an optical lattice (OL). As expected in the mean-field GPE limit, the BEC Bogoliubov excitation spectrum has a band structure, in analogy with the electronic Bloch bands [13–21]. When the power of the laser is much larger than the chemical potential, the lowest band dynamics maps on a discrete nonlinear Schrödinger (DNLS) equation [22]. This was an interesting remark especially because the DNLS was already widely investigated per se by the nonlinear physics community [23–25] which, indeed, was immediately attracted by the new possibilities offered by this system.

The BEC GPE dynamics in the array can be therefore studied in the framework of nonlinear lattice theory [22, 26–28]. The typical confining potential is given by the superposition of a harmonic trap and a periodic potential. For a 1D OL, the frequency at the bottom of the wells is typically of order of \sim kHz in

the OL direction, and the transverse confinement is provided by the magnetic potential (characterized by frequencies of order of 100 Hz). The axial dynamics of a Bose condensate induced by an external potential with cylindrical symmetry in the transverse directions can be studied introducing an effective 1D GPE equation [29]: for BECs in OLs, assuming that the Wannier wavefunctions (localized in each well) can be expressed in Thomas–Fermi approximation, it has been shown [30] that the main effect of the transverse confinement is to modify the degree of nonlinearity of the DNLS equation, giving rise to a generalized version of the DNLS equation. BECs in a periodic potential can allow for the observation of intrinsic localized modes (i.e., matter excitations localized on few lattice sites), as well as the study of solitons and breathers, possibly also with condensates having a repulsive interatomic interaction. We should also mention that the realization of two- and three-dimensional optical lattices [6, 31] opens the possibility to study discrete/nonlinear effects in higher spatial dimensions. A discussion of the derivation of the generalized DNLS equation is presented in Sect. 13.2.

In free space, the superflow of a uniform BEC is described by plane waves, which becomes energetically unstable in presence of defects when the BEC velocity is faster than sound, which is the Landau criterion for superfluidity. The propagation of sound in a harmonically trapped condensate without OL has been observed experimentally [32] and studied theoretically [33–36]. In the presence of a periodic potential, the condensate wavefunction can be expanded in Bloch waves, having amplitudes modulated with the periodicity of the OL, which can also become energetically unstable when the group velocity is larger than the sound velocity [17, 20, 37–40]. The energetic instability manifests itself with the emission of quasi-particles out of a condensate flowing against a small obstacle. This happens when the condensate velocity is larger than a critical value, which, in the limit of small obstacles is the sound velocity. The interplay between discreteness and nonlinearity is also crucial for the occurrence of modulational instabilities (MIs), well known in the theory of nonlinear media. MIs are dynamical instabilities characterized by an exponential growth of arbitrarily small fluctuations of a carrier wave, as a result of the interplay between dispersion and nonlinearity. The consequences of the modulational instability on the motion of BEC wave packets in OLs have been discussed in [41]. A different parametric instability, which will not be discussed here, can arise when modulating in time the height of the inter-well barriers or the strength of the interparticle interaction [42, 43]. In Sect. 13.3 we will discuss the excitation spectra of a BEC in a periodic potential, while in Sect. 13.4 we review the occurrence of a discrete modulational instability, comparing its effects with those of the Landau instability; a brief discussion of the the propagation of sound in the OL will be also presented. A discussion of the dynamics of BEC wave packets in OLs is given in Sect. 13.5.

The high laser power available nowadays allows for the investigation of low tunneling rates between adjacent wells of the periodic potential: in these regimes the quantum fluctuations play an important role, and, with a strength

of the optical potential V_0 large enough, it is expected a quantum transition from a superfluid phase to a Mott insulator phase. The model used to describe the quantum (beyond Gross–Pitaevskii) properties of ultracold atoms in deep optical lattices is the Bose–Hubbard Hamiltonian, which is nothing less than the quantized version of the DNLS Hamiltonian. The basic energy scales in the Bose–Hubbard model are the tunneling energy K (which decreases by increasing V_0) and the charging energy U_2 , due to the interaction among particles in the same well. Since the role of the quantum fluctuations depends on the ratio U_2/K , the OL provides an unique way to tune the effective interaction by varying the laser power V_0 . The phase structure is determined by the two competing terms of the Hamiltonian [44]: the interaction energy U_2 leads to localization of particles in the lattice (Mott phase), while the hopping term K favors superfluidity. The phase coherence of different condensates in the superfluid phase (and its disappearance in the Mott regime) in the array plays a crucial role in the dynamics, and can be experimentally studied observing the interference patterns created by the condensates after turning off the trapping potential. The observation of squeezed number states was reported in [45], while an experimental detection of the Mott-superfluid transition has been reported for 3D OLs in [31]. A systematic study of quantum phase transitions in low-dimensional (1D and 2D) OLs is presented in [46]. We also mention that by adding a disordered potential – created, e.g., by an optical speckle potential [47–49] or by superimposing laser with different periodicity [50, 51] – one expects, in presence of deep optical lattices and for large values of U_2/K , a Bose glass phase [44]. For space reasons, we will not discuss here the main properties of the Bose–Hubbard Hamiltonian and we refer the reader to the literature (see, e.g., [2] and references therein).

13.2 Discrete Equations for the Dynamics

The $T = 0$ dynamics of a BEC in an external potential $V(\mathbf{r})$ follows the GPE [52–55]

$$i\hbar\psi_t = -\frac{\hbar^2}{2m}\nabla^2\psi + [V + g|\psi|^2]\psi, \quad (13.1)$$

where $g = 4\pi\hbar^2a/m$, with a the s -wave scattering length and m the atomic mass. The condensate wave function is normalized to the total number of particles N . We write the external potential $V = V_{\text{MT}} + V_{\text{OL}}$ as the sum of the optical lattice potential V_{OL} , created by two or more counter-propagating laser beams, and the trap potential V_{MT} , whose form depends on the particular realization of the experiment. For a 1D OL, created by only two counter-propagating laser beams, it is $V_{\text{OL}}(\mathbf{r}) = V_L(y, z)\cos^2(2\pi x/\lambda)$, where $\lambda = \lambda_{\text{laser}}\sin(\theta/2)$, λ_{laser} being the wavelength of the lasers and θ the angle between the counter-propagating laser beams. The spacing in the lattice is $d = \lambda/2$ and $V_L(y, z)$ is determined by the transverse intensity profile of the

(nearly Gaussian) laser beams. E.g., in [4], $\lambda = 850 \text{ nm}$ and the $1/e^2$ radius of the transverse profile is $\approx 80 \mu\text{m}$, an order of magnitude larger than the transverse radius of the condensate, so that we can approximate the periodic potential by

$$V_{\text{OL}}(x) = V_0 \cos^2(k_x x), \quad (13.2)$$

where $k_x = 2\pi/\lambda$, V_0 is the trap depth at the center of the beam, and $V_0 = sE_R$ where $E_R = \hbar^2 k_x^2 / 2m$ is the recoil energy and s is the adimension-alized strength of V_0 measured in units of recoil energy. A 2D (3D) OL reads $V_{\text{OL}}(x, y) = V_0 [\cos^2(k_x x) + \cos^2(k_y y)]$ ($V_{\text{OL}}(\mathbf{r}) = V_0 [\cos^2(k_x x) + \cos^2(k_y y) + \cos^2(k_z z)]$). For the 1D periodic potential (13.2) it is useful to write $V(\mathbf{r}) = V_D(x) + V_L(\mathbf{r})$, where $V_D(x)$ is the x component of the potential $V_{\text{MT}} \equiv V_x(x) + V_y(y) + V_z(z)$. V_D has a simple physical meaning: $F = -(\partial V_D)/(\partial x)$ is the effective force acting on the center of mass of a condensate wave packet moving in the periodic potential.

When the laser power (i.e., V_0) is large enough, we can use a tight-binding approximation and decompose the condensate order parameter $\psi(\mathbf{r}, t)$ as a sum of wavefunctions $\Phi(\mathbf{r} - \mathbf{r}_j)$ localized in each well of the periodic potential:

$$\psi(\mathbf{r}, t) = \sum \psi_j(t) \Phi(\mathbf{r} - \mathbf{r}_j), \quad (13.3)$$

where we denote by j the different wells in the array and $\psi_j(t) = \sqrt{N_j(t)} e^{i\phi_j(t)}$ is the j th amplitude. Normalizing to 1 the Φ 's, it follows $\sum_j |\psi_j|^2 = N$.

By replacing ansatz (13.3) in (13.1), the GPE reduces to a DNLS equation [22]:

$$i\hbar \frac{\partial \psi_j}{\partial t} = -K (\psi_{j-1} + \psi_{j+1}) + \epsilon_j \psi_j + U_2 |\psi_j|^2 \psi_j, \quad (13.4)$$

where the tunneling rate is

$$K \simeq - \int d\mathbf{r} \left[\frac{\hbar^2}{2m} \nabla \Phi_j \nabla \Phi_{j+1} + \Phi_j V \Phi_{j+1} \right], \quad (13.5)$$

the on-site energies are

$$\epsilon_n = \int d\mathbf{r} \left[\frac{\hbar^2}{2m} (\nabla \Phi_n)^2 + V \Phi_n^2 \right],$$

and the nonlinear coefficient (which we will suppose equal in each site) is

$$U_2 = gN \int d\mathbf{r} \Phi_n^4. \quad (13.6)$$

Naturally, if one has a 2D (3D) OL, then the ansatz (13.3) would lead to a 2D (3D) DNLS equation. Equation (13.4) is the equation of motion $\dot{\psi}_j = \frac{\partial \mathcal{H}}{\partial(i\hbar\psi_j^*)}$, where \mathcal{H} is the Hamiltonian function

$$\mathcal{H} = -K \sum (\psi_j \psi_{j+1}^* + \psi_j^* \psi_{j+1}) + \sum \left(\epsilon_j |\psi_j|^2 + \frac{U_2}{2} |\psi_j|^4 \right). \quad (13.7)$$

Both the Hamiltonian \mathcal{H} and the normalization are conserved.

In the tight-binding ansatz (13.3) one includes only corrections from the first band, which is correct for large V_0 . For V_0 intermediate it is useful to introduce contributions from the higher bands, i.e., by considering the ansatz $\psi(\mathbf{r}, t) = \sum_{j,\gamma} \psi_{j,\gamma}(t) \Phi_\gamma(\mathbf{r} - \mathbf{r}_j)$, where γ labels the bands: a discussion of the resulting discrete vector equation is presented in [28]. We also notice that the DNLS equation for just two sites describes the dynamics of BEC in a double well, which reduces to the dynamics of a non-rigid pendulum [56–58]: the dynamical splitting of a BEC into two parts has been experimentally studied in [59, 60], while the direct observation of the atomic tunneling in a BEC double well has been reported in [61].

13.2.1 Effects of Transverse Confinement

The assumption (13.3) firstly relies on the fact that the inter-well barrier V_0 is much higher than the chemical potentials (e.g., in [9] for $V_0 \sim 5E_R$ it is $\mu \sim 0.1V_0$). A second important condition is that the energy of the system should be confined within the lowest band. Higher energy bands are not contained in the DNLS equation, and become important when the energy is of the order of $\hbar\omega$, where ω is the harmonic frequency of a single well of the lattice. The effective dimensionality of the BECs trapped in each well can also play a crucial role [30, 62], by modifying the degree of nonlinearity of the DNLS equation. In this prospect, the DNLS equation can be seen as a zero-order (perturbative) approximation of more complicated discrete, nonlinear equations.

The density profile of each condensate can strongly depend on the number of atoms present at a given instant in the same well. This introduce site- and time-dependent parameters in the DNLS (13.4), modifying, in particular, its effective degree of nonlinearity. The tight-binding approximation of nonlinear systems has to be generalized as [30]

$$\psi(\mathbf{r}, t) = \sum \psi_j(t) \Phi_j(\mathbf{r}; N_j(t)) \quad (13.8)$$

with $\Phi_j(\mathbf{r}; N_j(t))$ depending *implicitly* on time through $N_j(t) \equiv |\psi_j(t)|^2$. We stress here, and discuss again later, that the spatial wavefunctions Φ_j (which are considered sufficiently localized in each well) can also depend *explicitly* on time due to the excitation of internal modes. For typical experimental setups, however, we can consider the adiabatic limit in which the inter-well number/phase dynamics is much slower than the typical time associated with the excitations of such internal modes (and, of course, the cases where such modes are not already present in the initial configuration of the system). In this limit, which can be well satisfied in experiments, the spatial wavefunctions in (13.8) will adiabatically follow the tunneling dynamics and can be approximated with the *real* wavefunction $\Phi_j(\mathbf{r}; N_j(t))$. A discussion of the validity of the adiabatic approximation can be found in [30].

Replacing the nonlinear tight-binding approximation (13.8) in the GPE (13.1) and integrating out the spatial degrees of freedom one finds the following discrete nonlinear equation (DNL) [30]:

$$\begin{aligned} i\hbar \frac{\partial \psi_j}{\partial t} = & -\chi [\psi_j(\psi_{j+1}^* + \psi_{j-1}^*) + \text{c.c.}] \psi_j + \epsilon_j \psi_j + \mu_j^{\text{loc}} \psi_j \\ & - [K + \chi (|\psi_j|^2 + |\psi_{j+1}|^2)] \psi_{j+1} \\ & - [K + \chi (|\psi_j|^2 + |\psi_{j-1}|^2)] \psi_{j-1}. \end{aligned} \quad (13.9)$$

In (13.9), the “local” chemical potential is the sum of three contributions

$$\mu_j^{\text{loc}} = \int d\mathbf{r} \left[\frac{\hbar^2}{2m} (\nabla \Phi_j)^2 + V_L \Phi_j^2 + g |\psi_j|^2 \Phi_j^4 \right]. \quad (13.10)$$

μ_j^{loc} depends on the atom number N_j through the condensed wavefunction Φ_j . The tunneling rates $K_{j,j\pm 1}$ between the adjacent sites j and $j \pm 1$ also depend, in principle, on the respective populations: expanding the wavefunctions around an average number of atoms per site, N_0 , and keeping only the zeroth-order term $\Phi_j(N_j) \simeq \tilde{\Phi}_j(N_0)$ one finds $K_{j,j\pm 1} \approx K$, with K given by (13.5). The relative error committed in this approximation is on the order of 10^{-4} for typical experimental setups. The coefficient χ is given by

$$\chi = -g \int d\mathbf{r} \tilde{\Phi}_j^3 \tilde{\Phi}_{j\pm 1}. \quad (13.11)$$

The on-site energies arising from any external potential superimposed to the OL are $\epsilon_j = \int d\mathbf{r} V_D \Phi_j^2$: $\epsilon_j \propto j^2$ ($\epsilon_j \propto j$) when the driving field is harmonic (linear) – moreover ϵ_j does not depend on the on-site atomic populations. Numerical estimates show that spatial integrals involving next-nearest-neighbor condensates, as well as terms proportional to $\int d\mathbf{r} \Phi_j^2 \Phi_{j\pm 1}^2$, can be neglected, but not the terms proportional to χ . E.g., setting $\zeta = g \int d\mathbf{r} \tilde{\Phi}_j^2 \tilde{\Phi}_{j\pm 1}^2$ one has – for $V_0 \approx 20E_R$ and $N_0 \approx 10,000$ – $\chi N_0/K \sim 10^{-1}$ and $\zeta N_0/K \sim 10^{-4}$. In a double well potential, e.g., with height barrier $V_0 \approx 2\pi 500$ Hz and $N_0 \approx 3,000$, one has $\chi N_0/K \sim 1$, while $\zeta N_0/K \sim 10^{-3}$. For these reasons, one cannot neglect the χ terms in (13.9). Further studies of a BEC in a double well potential without neglecting terms proportional to $\int d\mathbf{r} \Phi_j^2 \Phi_{j\pm 1}^2$ are presented in [63, 64].

To make (13.9) useful, one has to guess the dependence of the localized wavefunction Φ_j on N_j . It turns out that a reasonable choice is given by supposing a Thomas–Fermi expression for the Φ_j ’s: to be more explicit, let us introduce the potential \tilde{V} at the bottom of wells, obtained expanding the potential V around the minima. At the lowest order $\tilde{V} \approx (m/2)(\tilde{\omega}_x^2 x^2 + \tilde{\omega}_y^2 y^2 + \tilde{\omega}_z^2 z^2)$. One has to compare the interaction energy with the frequencies $\tilde{\omega}_{x,y,z}$: we denote by $\mathcal{D} = 0, 1, 2, 3$ the *number* of spatial dimensions in which one can use the Thomas–Fermi approximation. E.g., $\mathcal{D} = 3$ means that we can approximate Φ_j with the Thomas–Fermi expression $\Phi_j(\mathbf{r}; N_j) \propto (\tilde{\mu}_j - \tilde{V}(\mathbf{r}))$ where $\tilde{\mu}_j$ is fixed by the normalization condition and depends on N_j – with

$\mathcal{D} = 2$, denoting by (let say) y and z the directions in which one can apply the Thomas–Fermi expression, one can factorize $\Phi_j = \phi_j(x)\phi_{\text{TF}}^{(j)}(y, z)$ with the Thomas–Fermi expression $\phi_{\text{TF}}^{(j)}(y, z; N_j) \propto (\tilde{\mu}_j - (m/2)(\tilde{\omega}_y^2 y^2 + \tilde{\omega}_z^2 z^2))$, $\tilde{\mu}_j$ yet being determined by the normalization of the Φ_j . Proceeding along this way, one gets [30]

$$\mu_j^{\text{loc}} = U_\alpha |\psi_j|^\alpha; \quad \alpha \equiv \frac{4}{2 + \mathcal{D}}. \quad (13.12)$$

The coefficient U_α is obtained from (13.10) and depends in general on the specific trap potential. An estimate for it in a particular setup is given below in (13.14). The DNLS (13.4) is recovered from the DNL (13.9) in the case $\mathcal{D} = 0$ (i.e., $\alpha = 2$) and neglecting terms proportional to χ . In conclusion, the main effect of the transverse confinement is to change the degree of nonlinearity and the generalized DNLS equation reads

$$i\hbar \frac{\partial \psi_j}{\partial t} = -K(\psi_{j-1} + \psi_{j+1}) + \epsilon_j \psi_j + U_\alpha |\psi_j|^\alpha \psi_j - \chi \mathcal{F}, \quad (13.13)$$

where $\mathcal{F} \equiv [\psi_j(\psi_{j+1}^* + \psi_{j-1}^*) + \text{c.c.}] \psi_j + (N_j + N_{j+1})] \psi_{j+1} + (N_j + N_{j-1})] \psi_{j-1}$.

To make the previous result more transparent, let us consider a harmonic trap potential $V_{\text{MT}} = (m/2)(\omega_x^2 x^2 + \omega_y^2 y^2 + \omega_z^2 z^2)$. When the Φ_j does not depend on N_j , one has $\mathcal{D} = 0$ and $\alpha = 2$, as in the standard DNLS equation. However, for deep 1D lattices, the effective frequencies in the x direction is given by $\tilde{\omega}_x = \sqrt{2V_0 k_x^2 / m}$ and is $\tilde{\omega}_x \sim 10 \text{ kHz}$ for $V_0 \sim 5E_R$, while $\omega_{x,y,z}/2\pi \sim 100 \text{ Hz}$, for ^{87}Rb . Then, for a number of particles $\sim 1000\text{--}10000$ one can use a Thomas–Fermi dependence on N_j for the wavefunctions in the y and z directions, but not in the x direction: with the previous notation, this means $\mathcal{D} = 2$ and $\alpha = 1$. This result can be simply obtained by factorizing the localized wavefunction Φ_j as a product of a Gaussian ϕ_j having width σ (in the x direction) and a Thomas–Fermi $\phi_{\text{TF}}^{(j)}$ (in the y and z coordinates): replacing in (13.1) and integrating out along the x direction, one obtains $\epsilon_j = \Omega j^2$, where $\Omega = \frac{m}{2} m \omega_x^2 (\frac{\lambda}{2})^2$, getting the DNL (13.9) with $\mathcal{D} = 2$ ($\alpha = 1$) and

$$U_1 = \sqrt{m \omega_r^2 g / \sqrt{2\pi} \pi \sigma}. \quad (13.14)$$

13.3 Excitation Spectra

In this section the Bloch and the Bogoliubov excitation spectra of the system in absence of any driving field ($V_L = 0$) are derived in the tight binding approximation. We also present a brief discussion of the comparison with numerical results for the excitation spectra of the continuous GPE [20].

13.3.1 Bloch Spectrum

The Bloch states $\Psi_p(\mathbf{r}) = e^{ipx/\hbar}\tilde{\Psi}_p(\mathbf{r})$, where $\tilde{\Psi}_p(\mathbf{r})$ is periodic in the x direction with period d , are exact stationary solutions of the Gross–Pitaevskii equation (13.1). The energy per particle $\varepsilon_\gamma(p)$ (Bloch energy) and the chemical potential $\mu_\gamma(p)$ of such solutions form a band structure, so that they can be labeled by the quasi-momentum p and the band index γ .

The generalized DNLS equation (13.13) describes only the lowest band of the spectrum. Exact solutions of the DNL equation are the “plane waves” $\psi_j = \psi_0 e^{i(kj - \mu t)/\hbar}$, where $p = \hbar k/d$ is the quasi-momentum. Note that the ψ_j are plane waves in the lattice, but do not correspond to plane waves in real space. Within the DNL equation framework, the energy per particle $\varepsilon(k)$ and chemical potential $\mu(k)$ corresponding to these solutions are found to be [20]

$$\varepsilon(k) = \varepsilon^{\text{loc}} - 2(K + 2 \chi N_0) \cos(k) = \varepsilon^{\text{loc}} - \frac{\hbar^2}{d^2 m_\varepsilon} \cos(k), \quad (13.15)$$

$$\mu(k) = \mu^{\text{loc}} - 2(K + 4 \chi N_0) \cos(k) = \mu^{\text{loc}} - \frac{\hbar^2}{d^2 m_\mu} \cos(k), \quad (13.16)$$

where $\varepsilon^{\text{loc}} = 2U_\alpha N_0^{\alpha/2}/(\alpha + 2)$ and $\mu^{\text{loc}} = \mu_j^{\text{loc}}|_{\psi_1=\psi_0} = \partial(N_0 \varepsilon^{\text{loc}})/\partial N_0$, with $N_0 = |\psi_0|^2$ the number of atoms per well. In the previous equations we have introduced the effective masses m_ε and m_μ , to emphasize the low momenta (long wavelength) quadratic behavior of the Bloch energy spectrum and of the chemical potential [21]. It turns out that several dynamical properties of the system can be intuitively understood in terms of such effective masses. This approach is quite common, for instance, in the theory of metals, where $m_\mu \equiv m_\varepsilon$. However in BEC, because of the nonlinearity of the Gross–Pitaevskii equation, the two relevant energies of the system, ε and μ , have the same $\cos(k)$ dependence on the quasi-momentum p , but different curvatures. Therefore, $m_\mu \neq m_\varepsilon$, with

$$\frac{1}{m_\varepsilon} \equiv \left. \frac{\partial^2 \varepsilon}{\partial p^2} \right|_0 = \frac{2d^2 (K + 2 \chi N_0)}{\hbar^2}, \quad \frac{1}{m_\mu} \equiv \left. \frac{\partial^2 \mu}{\partial p^2} \right|_0 = \frac{2d^2 (K + 4 \chi N_0)}{\hbar^2}. \quad (13.17)$$

It is possible to extend the definition of the effective masses to the full Brillouin zone, introducing the quasi-momentum dependent masses $m_\varepsilon(k) \equiv (\partial^2 \mu / \partial p^2)^{-1} = m_\varepsilon / \cos(k)$ and $m_\mu(k) \equiv (\partial^2 \mu / \partial p^2)^{-1} = m_\mu / \cos(k)$, where $m_\varepsilon \equiv m_\varepsilon(0)$ and $m_\mu \equiv m_\mu(0)$.

Similarly, one can introduce two different group velocities, defined as

$$v_\varepsilon \equiv \frac{\partial \varepsilon}{\partial p} = \frac{1}{m_\varepsilon} \frac{\hbar}{d} \sin(k), \quad v_\mu \equiv \frac{\partial \mu}{\partial p} = \frac{1}{m_\mu} \frac{\hbar}{d} \sin(k). \quad (13.18)$$

These two different group velocities are related by [20, 21] $v_\mu = v_\varepsilon + \frac{\partial v_\varepsilon}{\partial N_0} N_0$ with, given (13.17), $v_\mu > v_\varepsilon$. The current carried by a Bloch waves with quasi-momentum p is $\rho_0 v_\varepsilon(p)$, where ρ_0 is the average particle density; m_μ , on the

other hand, plays a crucial role in the Bogoliubov spectrum, which we will discuss below.

The concept of effective mass, defined as the inverse of the curvature of the corresponding spectrum (as that of *group velocity*, defined as the first derivative) can be extended to shallow OLs, where the nonlinear tight binding approximation breaks down. In this case, the quasi-momentum dependence of ε and μ will not be simply described by a cosine function, but will still remain periodic in the quasi-momentum p . In particular, the value k where $m_\varepsilon(p)$ changes sign (corresponding to $\partial^2\varepsilon/\partial p^2 = 0$) will be greater than $\pi/2$ and will in general not coincide with the momentum where m_μ changes sign (corresponding to $\partial^2\mu/\partial p^2 = 0$).

We remark that the Bloch states are not the only stationary solutions of the Gross–Pitaevskii equation. Because of nonlinearity, indeed, periodic solitonic solutions can also appear for a weak enough periodic potential, introducing new branches in the excitation spectra [65].

13.3.2 Bogoliubov Spectrum

In this subsection we study the Bogoliubov spectrum of elementary excitations. This describes the energy of small perturbations with quasi-momentum q on top of a macroscopically populated state with quasi-momentum p [stationary solution of (13.1)].

We consider first the case $\chi = 0$: in the homogeneous limit ($\epsilon_j = 0$), the stationary solutions of (13.13) are plane waves $\psi_j(t) = \psi_0 \exp[i(kj - \nu t)]$, with frequency ν given by $\hbar\nu = -2K \cos(k) + U|\psi_0|^\alpha$. The stability analysis of such states can be carried out by perturbing the carrier wave as $\psi_j(t) = (\psi_0 + u(t)e^{iqj} + v^*(t)e^{-iqj}) e^{i(kj - \nu t)}$. Retaining only terms proportional to u/ψ_0 and v/ψ_0 , one gets

$$i\hbar \frac{d}{dt} \begin{pmatrix} u \\ v \end{pmatrix} = \begin{pmatrix} \mathcal{A} & \mathcal{C} \\ -\mathcal{C}^* & -\mathcal{A} \end{pmatrix} \begin{pmatrix} u \\ v \end{pmatrix} = \hbar\omega_\pm \begin{pmatrix} u \\ v \end{pmatrix} \quad (13.19)$$

with $\mathcal{A} = 2K \cos(k) - 2K \cos(k+q) + (1/2)U\alpha|\psi_0|^\alpha$ and $\mathcal{C} = (1/2)U\alpha\psi_0^{*\alpha/2-1}\psi_0^{\alpha/2+1}$ [20]. From (13.19) it follows that the excitation spectrum (i.e., the Bogoliubov dispersion relation) for the DNLS with nonlinearity degree α is:

$$\omega_\pm/2K = \sin(k) \sin(q) \pm \sqrt{4 \cos^2(k) \sin^4\left(\frac{q}{2}\right) + \frac{\alpha U}{K} |\psi_0|^\alpha \cos(k) \sin^2\left(\frac{q}{2}\right)}. \quad (13.20)$$

The carrier wave becomes modulationally unstable when the eigenfrequency ω in (13.20) becomes imaginary: the condition for stability is

$$4K \cos^2(k) \sin^2\left(\frac{q}{2}\right) + \alpha U |\psi_0|^\alpha \cos(k) > 0. \quad (13.21)$$

When U is negative (positive), corresponding to negative (positive) scattering length, the plane waves with $\cos(k) < 0$ ($\cos(k) > 0$) are stable. When

the lhs side of (13.21) becomes negative, as a consequence of the fact that eigenfrequency ω in (13.20) becomes imaginary, there is an exponential growth of small perturbations of the carrier wave: we refer to this instability as the modulational instability.

In the general case $\chi \neq 0$ one can repeat the previous stability analysis getting [20]

$$\hbar\omega_{\pm} \approx \frac{\hbar^2 \sin(k) \sin(q)}{m_\mu d^2} \pm 2\sqrt{\frac{\hbar^4 \cos^2(k) \sin^4(q)}{m_\mu^2 d^4} + \frac{\hbar^2 N_0}{m_\varepsilon d^2} \frac{\partial \mu}{\partial N_0} \cos(k) \sin^2(q)} \quad (13.22)$$

with the chemical potential given by $\mu = \mu^{\text{loc}} - \frac{\hbar^2}{d^2 m_\mu} \cos(k)$ (see (13.16)), and $\mu^{\text{loc}} = U_\alpha |\psi_0|^\alpha$. For $\alpha = 2$ (i.e., $\mathcal{D} = 0$) and in the limit $\chi = 0$, we recover the well known results for the discrete nonlinear Schrödinger equation [66].

13.4 Landau and Dynamical Instabilities

From the relation (13.22), valid for the generalized DNLS (13.13) with $\chi \neq 0$, the small q (large wavelength) limit of the Bogoliubov dispersion relation becomes

$$\hbar\omega \approx \frac{\hbar}{dm_\mu} \sin(k) q + |q| \sqrt{\frac{1}{m_\varepsilon} \frac{\partial \mu}{\partial N_0} N_0 \cos(k)} \quad (13.23)$$

(we assume, for the moment, that $\frac{1}{m_\varepsilon} \frac{\partial \mu}{\partial N_0} N_0 \cos(k) > 0$). The linear behavior in q indicates that the system supports (low amplitude) sound waves, propagating on top of large amplitude traveling waves with velocity

$$v_{s,\pm} = \hbar \frac{\partial \omega}{\partial q} \Big|_{q \rightarrow 0^\pm} = \begin{cases} v_\mu + c, & (q \rightarrow 0^+) \\ v_\mu - c, & (q \rightarrow 0^-) \end{cases}, \quad (13.24)$$

where the “chemical potential group velocity” v_μ has been defined in (13.18), and the “relative sound velocity” c is defined as

$$c = \sqrt{\frac{1}{m_\varepsilon} \frac{\partial \mu}{\partial N_0} N_0 \cos(k)}. \quad (13.25)$$

The two velocities $v_{s,\pm}$ correspond, respectively, to a sound wave propagating in the same and in the opposite direction of the large amplitude traveling wave.

We remark that, contrary to the case of a Galilean invariant system ($s = 0$), the sound velocity depends on the quasi-momentum p . Moreover, v_s depends on the effective dimensionality of the condensates, since (cf.(13.12) and (13.16)) $\frac{\partial \mu}{\partial N_0} N_0 \sim \alpha U_\alpha N_0^{\alpha/2}$. In the limit $\alpha = 2$, $p \rightarrow 0$ and $m_\varepsilon, m_\mu \rightarrow m$ we get the sound velocity in the uniform case.

The system is energetically unstable if there exists an $\omega < 0$. In the limit $s = 0$, this corresponds to a group velocity larger than the sound velocity (Landau criterion for superfluidity). When the system has a discrete translational invariance ($s > 0$) the condition for this instability is obtained from the Bogoliubov excitation spectrum (13.22). Then, we have that the system is not superfluid when $\omega < 0$, corresponding to $v_\mu^2 > c^2$. This result should be compared with the well known Landau criterion for an homogeneous system ($s = 0$), stating that the superfluid is energetically unstable when $v^2 > c^2$, $v \equiv \frac{\partial \varepsilon}{\partial p} = \frac{\partial \mu}{\partial p}$ being the group velocity of the condensate, and $c = \sqrt{\frac{1}{m} \frac{\partial \mu}{\partial N_0}} N_0$ the sound velocity.

There is a further dynamical (modulational) instability mechanism associated with the appearance of an imaginary component in the Bogoliubov frequencies, which disappears in the absence of interatomic interactions, or in the translational invariant limit (if $a > 0$). The onset of this instability in the tight binding regime, coincides with the condition

$$c^2 < 0 \Rightarrow \cos(k) < 0 \Rightarrow |k| > \frac{\pi}{2}. \quad (13.26)$$

The dynamical instability drives an exponentially fast increase of the amplitude of the – initially small – fluctuations of the condensate (while the energetic instability should manifest itself in polynomial time [67]). Since the initial phases and amplitudes of the fluctuation modes are essentially random, their growth induce a strong dephasing of the condensate, and dissipates its translational kinetic energy (which is transformed in incoherent collective and single particles excitations). We remark here the different scaling of the energetic and dynamical instability with the interatomic interactions. Decreasing the scattering length, the sound velocity decreases, and smaller and smaller group velocities can break down the superfluidity of the system (when $a \rightarrow 0$, the sound velocity $c \rightarrow 0$: in the limit of vanishing interactions the condensate is energetically unstable for an arbitrary small group velocity). On the other hand, the dynamical modulational instability criterion does not depend on the scattering length. This apparent paradox is simply resolved noticing that the growth time of the unstable modes actually depends on interactions, and diverges when the scattering length vanishes ($\tau \rightarrow \infty$ when $a \rightarrow 0$). Therefore, a noninteracting condensate is always dynamically stable. There is a further point to remark: if we consider a condensate moving with an increasing velocity, the system always becomes first energetically unstable, then it hits the dynamical instability. As a matter of fact, however, in real experiments the energetic instability can grow quite slowly (and at zero temperature only in presence of impurities [17]), so that the dominant dephasing mechanism is given by the modulational instability.

13.5 Wave Packet Dynamics

In this Section we review the main properties to the wave packet dynamics of a BEC in an OL, summarizing here the results of a variational approach, previously considered in [22,30]. The approach uses a general variational wavefunction

$$\psi_j = \sqrt{\mathcal{K}(\sigma)} f \left(\frac{j - \xi}{\sigma} \right) e^{ip(j-\xi) + i\frac{\delta}{2}(j-\xi)^2} \quad (13.27)$$

where $\xi(t)$ and $\sigma(t)$ are, respectively, the center and the width of the wave packet, $p(t)$ and $\delta(t)$ their associated momenta and $\mathcal{K}(\sigma)$ a normalization factor (such that $\sum_j N_j = N$). f is a generic function, even in the variable $X = (j - \xi)/\sigma$. For simplicity, we will confine ourself to an exponential trial wavefunction $f(X) = e^{-X^2}$ for the standard DNLS equation (13.4), i.e., $\alpha = 2$ and $\chi = 0$. A discussion of the general case is reported in [41]. The wave packet dynamical evolution can be obtained by using the Euler–Lagrange equations for the Lagrangian $\mathcal{L} = \sum i\hbar \dot{\psi}_j \psi_j^* - \mathcal{H}$, with \mathcal{H} given by (13.7). In the following, we rescale the time as $t \rightarrow \hbar t/2K$, measuring the energies in units $2K$. We also set $\Lambda = U_2/2K$ and $E_j = \epsilon_j/2K$. The equations of motion for the variational parameters are [22]

$$\begin{aligned} \dot{p} &= -\frac{\partial \mathcal{V}}{\partial \xi}; \quad \dot{\xi} = \sin p \ e^{-\eta} \delta = \cos p \left(\frac{4}{\Gamma^2} - \delta^2 \right) e^{-\eta} + \frac{2\Lambda}{\sqrt{\pi \Gamma^3}} - 8 \frac{\partial \mathcal{V}}{\partial \Gamma}, \\ \dot{\Gamma} &= 2\Gamma \delta \cos p \ e^{-\eta}, \end{aligned} \quad (13.28)$$

where $\Gamma \equiv \sigma^2$, $\eta = 1/2\Gamma + \Gamma\delta^2/8$ and the effective potential \mathcal{V} is given by $\mathcal{V}(\Gamma, \xi) = \mathcal{K} \int_{-\infty}^{\infty} dn E_n \exp(-2(n - \xi)^2/\Gamma)$. The pairs ξ, p and $\frac{\Gamma}{8}, \delta$ are canonically conjugate dynamical variables with respect to the effective Hamiltonian

$$H = \frac{\Lambda}{2\sqrt{\pi \Gamma}} - \cos p \ e^{-\eta} + \mathcal{V}(\xi, \Gamma). \quad (13.29)$$

The effective mass $m^* \equiv m_\varepsilon = m_\mu$ (since $\chi = 0$) is given by $\frac{1}{m^*} \equiv \frac{\partial^2 H}{\partial p^2} = \cos p e^{-\eta}$: the quasi-momentum dependence of the effective mass allows a rich variety of dynamical regimes. Solitonic solutions with a positive nonlinear parameter $\Lambda > 0$, for instance, are allowed by a negative effective mass. A regime with a diverging effective mass $m^* \rightarrow \infty$ leads to a self-trapping of the wave packet, which has been recently experimentally observed [68].

In the homogeneous lattice, only the optical potential is present ($V_{\text{MT}} = V_D = 0$). Therefore the on-site energies E_n , as well as \mathcal{V} , are constant. The momentum is, of course, conserved and it is equal to the initial value: $p(t) = p(0) \equiv p_0$. We will discuss here only the case $\Lambda > 0$, in order to make contact with the experiments in which ^{87}Rb atoms with positive scattering length a are used; however, we observe that the equations of motion (13.28) are invariant with respect to the replacement $\Lambda \rightarrow -\Lambda$, $p_0 \rightarrow p_0 + \pi$ and $t \rightarrow -t$.

A detailed study of the variational equations of motion can be found in [69]. Here we quote only the main results and we discuss rather the physical implications and the comparison with a full numerical analysis. This comparison is surprisingly successful in describing even details of the quite complex dynamical and collisional behavior. Stability phase diagrams for such states are obtained by inspection of the profile dynamics equations [22]. The parameter Λ is the ratio between the nonlinear coefficient, induced by the interatomic interactions, and the coupling between condensates in neighbor wells: it is the only (geometry dependent) parameter which governs the dynamical regimes of the system. When Λ is small, the wave packet spreads out; in the opposite limit, the nonlinearity leads to a localization of the wave packet. When $\cos p_0 < 0$, an intermediate regime arises: in this case, the effective mass is negative and, for a suitable values of Λ , a balance can be reached between nonlinearity and diffusion. In terms of the variational parameters, this means that in the diffusive regime, $\Gamma \rightarrow \infty$ and (if $p_0 \neq 0$) $\xi \rightarrow \infty$, with an effective mass always finite. On the contrary, in the self-trapped regime, Γ remains finite and the center of mass ξ cannot go to ∞ ; furthermore, $1/m^* \rightarrow 0$, meaning that $\eta \rightarrow \infty$ and $\delta \rightarrow \infty$. Therefore, in this regime there is an energy transfer to the internal modes of oscillations, since δ is the momentum associated to the wave packet width: in the full numerical solution of (13.4), this corresponds to a breakdown of the wave packet. We note that a nonlinear self-trapping occurs also in a two-site model [57, 58, 70].

When $\cos p_0 > 0$, the solitonic regime is forbidden and we have only the diffusive and the self-trapped regimes. In order to show the transition between them, let us consider first the case $p_0 = 0$, in which the center of mass of the wave packet does not move ($\xi = 0$). Using as initial values $\delta_0 = 0$ and Γ_0 , the initial value of the Hamiltonian (13.29) is $H_0 = \Lambda/2\sqrt{\pi\Gamma_0} - e^{-1/2\Gamma_0}$. Since the Hamiltonian is a conserved quantity, it is $H_0 = \Lambda/2\sqrt{\pi\Gamma} - e^{-1/2\Gamma - \Gamma\delta^2/8}$. Therefore, $\frac{\Lambda}{2\sqrt{\pi\Gamma}} - H_0 > 0$: when $H_0 > 0$, Γ has to remain finite and, then, we have a self-trapped regime in which the wave packet remains localized and the nonlinearity forbids the diffusion. Vice versa, when $H_0 < 0$, $\Gamma \rightarrow \infty$ for $t \rightarrow \infty$: the wavefunction spreads out and we are in the diffusive regime. The transition occurs at $H_0 = 0$, with

$$\Lambda_c = 2\sqrt{\pi\Gamma_0}e^{-1/2\Gamma_0}. \quad (13.30)$$

In Figs. 13.1 and 13.2 we plot the density $|\psi_n|^2$ for different times with Λ in the diffusive region (Fig. 13.1) and in the self-trapped one (Fig. 13.2): the solid lines are the numerical solutions of (13.4), the dashed lines are the solutions of the variational equations (13.28). As we can see from Fig. 13.2, the numerical solution of (13.4) in the self-trapping region loses its Gaussian shape [68]. From numerical simulations is also seen that the occurrence of the transition between the diffusive and the self-trapped regimes does not depend on the chosen initial conditions: what changes is the critical value (13.30).

Also when $p_0 \neq 0$, in which the center of the wave packet moves on the lattice, there are two distinct regimes. $H_0 > 0$, i.e., $\Gamma(t) < \Gamma_{\max}$ corresponds

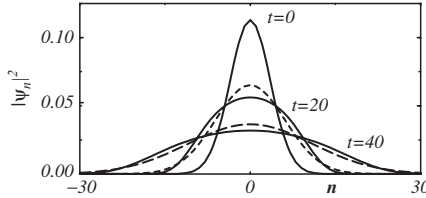


Fig. 13.1. Plot of the wavefunction density $\rho_n = |\psi_n|^2$ at times $t = 0, 20, 40$ with $\Lambda = 1$ in the diffusive regime. Numerical values: $p_0 = 0$, $\delta_0 = 0$, $\Gamma_0 = 50$. The critical value of Λ is in this case $\Lambda_c = 24.8$. *Solid lines*: solutions of (13.4) with 73 sites; *dashed lines*: solutions of variational (13.28)

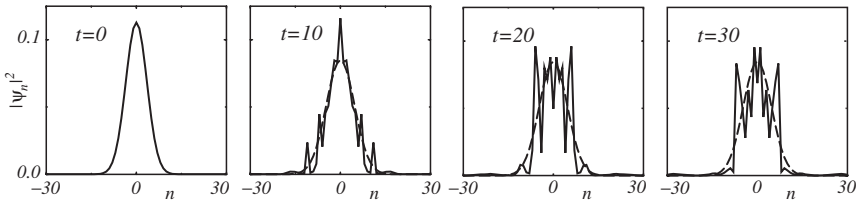


Fig. 13.2. Plot of the wavefunction density at times $t = 0, 10, 20, 30$ with $\Lambda = 100$ in the self-trapping region. The numerical values of the remaining parameters are as in Fig. 13.1

to the self-trapped regime in which the boson wave packet remains localized around few sites, while a diffusive regime occurs when $-\cos p_0 < H_0 \leq 0$. In this case $\Gamma(t \rightarrow \infty) \rightarrow \infty$ and $\dot{\xi} \approx -H_0/\tan p_0 = \text{const}$. The transition between the regimes occurs at $\Lambda_c = 2\sqrt{\pi\Gamma_0} \cos p_0 e^{-1/2\Gamma_0}$. With $\Lambda > \Lambda_c$, the ratio between the initial value of the width σ_0 and the limit width $\sigma_{\max}(t \rightarrow \infty)$ is given by

$$\sigma_0/\sigma_{\max} = (\Lambda - \Lambda_c)/\Lambda. \quad (13.31)$$

We checked the stability of the self-trapping transition also considering different initial forms of the wave packet. In Fig. 13.3 we consider a self-trapped state ($\Lambda > \Lambda_c$): the variational prediction is that $\dot{\xi} \rightarrow 0$ and that $\xi \rightarrow \text{const}$. As time progresses, the width increases (and it goes asymptotically to a constant value) and the momentum conjugate to the width goes to infinity. The full numerical solution cannot go to this state, because the transfer of energy to the internal state breaks down the wave packet: when the average position approaches to value predicted from the variational analysis (thick line), the wave packet deforms until it breaks. In the inset we compare the numerical and the variational average position, where this deformation determines a deviation between the two lines. We observe that, despite the fact that the variational analysis cannot exactly follow the full dynamics in the self-trapping, it can, however, predict the occurrence of the transition and give a fairly accurate estimate of the critical point.

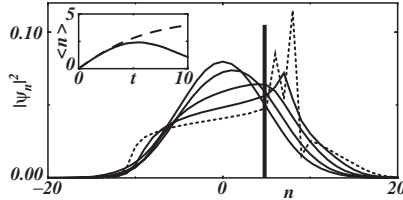


Fig. 13.3. Density profiles at times $t = 0, 1.25, 2.5, 3.75$ (solid lines) and at $t = 5$ (dotted) for $p_0 = \pi/4$, $\Gamma_0 = 100$ and $\Lambda = 50$ ($\Lambda_c = 24.8$). The thick line represents the asymptotic value predicted from the variational analysis. In the inset the variational (dashed line) and numerical (solid) average position vs. time are plotted

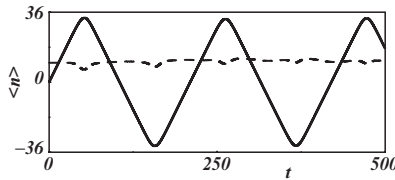


Fig. 13.4. Width (dotted line) and average position (solid line) calculated numerically for $\Lambda = \Lambda_{\text{sol}}$ and $p_0 = 3\pi/4$ in a finite array of 73 sites

For $\cos p_0 < 0$, soliton-like structures are present (cf. [23–25] for more references on discrete solitons and intrinsic localized excitations). When $\cos p < 0$ the self-trapping condition is given by $H_0 > |\cos p_0|$ and the critical value is

$$\Lambda_c = 2\sqrt{\pi\Gamma_0} |\cos p_0| (1 - e^{-1/2\Gamma_0}). \quad (13.32)$$

For $\Lambda < \Lambda_c$, $\Gamma \rightarrow \infty$, while for $\Lambda > \Lambda_c$, Γ remains finite. A soliton solution can be determined by imposing $\dot{\Gamma} = \dot{\delta} = 0$. One finds [22]

$$\Lambda_{\text{sol}} = 2\sqrt{\pi/\Gamma_0} |\cos p_0| e^{-1/2\Gamma_0}. \quad (13.33)$$

For $\Lambda = \Lambda_{\text{sol}}$ the center of the wave packet moves with a constant velocity $\dot{\xi}$ and its width remains essentially constant in time. We observe that for $\Gamma_0 > 1$, it is $\Lambda_c < \Lambda_{\text{sol}}$. In Fig. 13.4 we plot the average position and the width for $\Lambda = \Lambda_{\text{sol}}$. Since we are not using periodic boundary conditions, when the wave packet arrives to the end of the lattice, it hits a wall and upon rebounding, it regains its original shape. For $\Lambda_c < \Lambda < \Lambda_{\text{sol}}$, $\dot{\xi} \rightarrow \infty$ while $\Gamma(t)$ oscillates, corresponding to a breather solution. When $\Gamma_0 > 1$, the breather region extends until $\Lambda_{\text{breath}} > \Lambda_{\text{sol}}$ [69].

Before concluding, we discuss the relation between the present results and the modulational instability. As we discussed, if we consider a small perturbation on a plane wave $\psi_j \propto e^{ip_0 j}$, stability analysis shows that when $\cos p_0 < 0$ the eigenfrequencies of the linear modes become imaginary driving an exponential growth of small perturbations. When $\cos p_0 > 0$, the plane wave is

stable. In the present case, we are not considering a plane wave, but a localized wave function; therefore, we may expect to find the result previously stated by considering the case $\Gamma \gg 1$. In this case, when $\cos p_0 > 0$, $A_c \rightarrow \infty$ and the self-trapped region disappears: this corresponds to the result which there is no modulational instability for $\cos p_0 > 0$. To the contrary, when $\cos p_0 < 0$, then $A_c \rightarrow 0$ and always the system exhibits instability to small perturbation: this means that we have only self-trapping, as expected.

To conclude this section, we observe that the variational approach can be applied also in vertical arrays (i.e., when the gravity is acting) when Bloch oscillations occur. Similarly, Bloch oscillations are also possible in horizontal optical lattices realized by two counter-propagating laser beams with a frequency detuning varying linearly in time [8, 71]. The DNLS description of the dynamics is confined to the first band, and then a complete description of the Bloch oscillations in a tilted potential requires the study of the continuous GPE (see [37, 72–74] and references therein). A discussion on the Landau–Zener tunneling is presented in the following chapter. In a harmonic trap, one can induce and study dipole oscillations suddenly moving the magnetic potential: if the initial trap displacement is smaller than a critical value, it is possible to observe coherent Josephson-like oscillations [9]. When the initial displacement is larger than a critical value, the modulational instability [41] breaks down the dipole oscillations [75].

Acknowledgement. It is a pleasure to thank our colleagues and friends with whom we had pleasant brainstorms. Among the members of the BEC group in Trento, special thanks go to I. Carusotto, F. Dalfovo, S. Giorgini, C. Menotti, L.P. Pitaevskii and S. Stringari. Stimulating discussions with M. Albiez, T. Anker, J. Esteve, R. Gati, and M. Oberthaler are gratefully acknowledged. We also thank L.A. Collins, A.R. Bishop, P.G. Kevrekidis, D.J. Frantzeskakis, S.R. Shenoy, G. Giusiano, F.P. Mancini and P. Sodano and the members of the experimental group at LENS (Florence): F.S. Cataliotti, C. Fort, M. Inguscio, F. Minardi, G. Modugno and M. Modugno.

References

1. I. Bloch, J. Phys. B **38**, S629 (2005)
2. D. Jaksch, P. Zoller, Ann. Phys. (NY) **315**, 52 (2005)
3. O. Morsch, M.K. Oberthaler, Rev. Mod. Phys. **78**, 179 (2006)
4. B.P. Anderson, M.A. Kasevich, Science **282**, 1686 (1998)
5. K. Bongs, S. Burger, S. Dettmer, D. Hellweg, J. Arlt, W. Ertmer, K. Sengstock, Phys. Rev. A **63**, 31602 (2001)
6. M. Greiner, I. Bloch, O. Mandel, T.W. Haensch, T. Esslinger, Phys. Rev. Lett. **87**, 160405 (2001)
7. W.K. Hensinger, H. Haffer, A. Browaeys, N.R. Heckenberg, K. Helmerson, C. McKenzie, G.J. Milburn, W.D. Phillips, S.L. Rolston, H. Rubinsztein-Dunlop, B. Upcroft, Nature **412**, 52 (2001)
8. O. Morsch, J.H. Müller, M. Cristiani, D. Ciampini, E. Arimondo, Phys. Rev. Lett. **87**, 140402 (2001)

9. F.S. Cataliotti, S. Burger, C. Fort, P. Maddaloni, F. Minardi, A. Trombettoni, A. Smerzi, M. Inguscio, *Science* **293**, 843 (2001)
10. B. Eiermann, T. Anker, M. Albiez, M. Taglieber, P. Treutlein, K.P. Marzlin, M.K. Oberthaler, *Phys. Rev. Lett.* **92**, 230401 (2004)
11. T. Stoferle, H. Moritz, C. Schori, M. Kohl, T. Esslinger, *Phys. Rev. Lett.* **92**, 130403 (2004)
12. Z. Hadzibabic, S. Stock, B. Battelier, V. Bretin, J. Dalibard, *Phys. Rev. Lett.* **93**, 180403 (2004)
13. K. Berg-Sorensen, K. Molmer, *Phys. Rev. A* **58**, 1480 (1999)
14. J. Javanainen, *Phys. Rev. A* **60**, 4902 (1999)
15. D. Choi, Q. Niu, *Phys. Rev. Lett.* **82**, 2022 (1999)
16. M.L. Chiofalo, M.P. Tosi, *Phys. Lett. A* **268**, 406 (2000)
17. B. Wu, Q. Niu, *Phys. Rev. A* **64**, 061603(R) (2001)
18. B. Wu, R. Diener, Q. Niu, *Phys. Rev. A* **65**, 025601 (2002)
19. M. Machholm, C.J. Pethick, H. Smith, *Phys. Rev. A* **67**, 053613 (2003)
20. C. Menotti, A. Smerzi, A. Trombettoni, *New J. Phys.* **5**, 112 (2003)
21. M. Krämer, C. Menotti, L.P. Pitaevskii, S. Stringari, *Eur. Phys. J. D* **27**, 247 (2003)
22. A. Trombettoni, A. Smerzi, *Phys. Rev. Lett.* **86**, 2353 (2001)
23. D. Hennig, G.P. Tsironis, *Phys. Rep.* **307**, 333 (1999)
24. P.G. Kevrekidis, K.Ö Rasmussen, A.R. Bishop, *Int. J. Mod. Phys. B* **15**, 2833 (2001)
25. M.J. Ablowitz, B. Prinari, A.D. Trubatch, in *Discrete and Continuous Nonlinear Schrödinger Systems* (University Press, Cambridge, 2004)
26. F.Kh. Abdullaev, B.B. Baizakov, S.A. Darmanyan, V.V. Konotop, M. Salerno, *Phys. Rev. A* **64**, 43606 (2001)
27. V.V. Konotop, M. Salerno, *Phys. Rev. A* **65**, 021602 (2002)
28. G.L. Alfimov, P.G. Kevrekidis, V.V. Konotop, M. Salerno, *Phys. Rev. E* **66**, 046608 (2002)
29. L. Salasnich, A. Parola, L. Reatto, *Phys. Rev. A* **65**, 043614 (2002)
30. A. Smerzi, A. Trombettoni, *Phys. Rev. A* **68**, 023613 (2003)
31. M. Greiner, O. Mandel, T. Esslinger, T.W. Hansch, I. Bloch, *Nature* **415**, 39 (2002)
32. M.R. Andrews, D.M. Kurn, H.-J. Miesner, D.S. Durfee, C.G. Townsend, S. Inouye, W. Ketterle, *Phys. Rev. Lett.* **79**, 553 (1997)
33. E. Zaremba, *Phys. Rev. A* **57**, 518 (1998)
34. G.M. Kavoulakis, C.J. Pethick, *Phys. Rev. A* **58** 1563 (1998)
35. S. Stringari, *Phys. Rev. A* **58**, 2385 (1998)
36. B. Damski, *Phys. Rev. A* **69**, 043610 (2004)
37. B. Wu, Q. Niu, *New J. Phys.* **5**, 104 (2003)
38. E. Taylor, E. Zaremba, *Phys. Rev. A* **68**, 053611(2003)
39. D. Boers, C. Weiss, M. Holthaus, *Europhys. Lett.* **67**, 887 (2004)
40. M. Krämer, C. Menotti, M. Modugno, *J. Low Temp. Phys.* **138**, 729 (2005)
41. A. Smerzi, A. Trombettoni, P.G. Kevrekidis, A.R. Bishop, *Phys. Rev. Lett.* **89**, 170402 (2002)
42. Z. Rapti, P.G. Kevrekidis, A. Smerzi, A.R. Bishop, *J. Phys. B* **37**, S257 (2004)
43. M. Krämer, C. Tozzo, F. Dalfovo, *Phys. Rev. A* **71**, 061602 (2005)
44. M.P.A. Fisher, P.B. Weichman, G. Grinstein, D.S. Fisher, *Phys. Rev. B* **40**, 546 (1989)

45. C. Orzel, A.K. Tuchman, M.L. Fenselau, M. Yasuda, M.A. Kasevich, *Science* **291**, 2386 (2001)
46. M. Kohl, H. Moritz, T. Stoferle, C. Schori, T. Esslinger, *J. Low Temp. Phys.* **138** 635 (2005)
47. J.E. Lye, L. Fallani, M. Modugno, D.S. Wiersma, C. Fort, M. Inguscio, *Phys. Rev. Lett.* **95**, 070401 (2005)
48. D. Clément, A.F. Varón, M. Hugbart, J.A. Retter, P. Bouyer, L. Sanchez-Palencia, D.M. Gangardt, G.V. Shlyapnikov, A. Aspect, *Phys. Rev. Lett.* **95**, 170409 (2005)
49. T. Schulte, S. Drenkelforth, J. Kruse, W. Ertmer, J. Arlt, K. Sacha, J. Zakrzewski, M. Lewenstein, *Phys. Rev. Lett.* **95**, 170411 (2005)
50. R. Roth, K. Burnett, *Phys. Rev. A* **68**, 023604 (2003)
51. L. Fallani, J.E. Lye, V. Guarrera, C. Fort, M. Inguscio, *Phys. Rev. Lett.* **98**, 130404 (2007)
52. F. Dalfovo, S. Giorgini, L.P. Pitaevskii, S. Stringari, *Rev. Mod. Phys.* **71**, 463–512 (1999)
53. A.J. Leggett, *Rev. Mod. Phys.* **73**, 307 (2001)
54. C.J. Pethick, H. Smith, in *Bose-Einstein Condensation in Dilute Gases* (University Press, Cambridge, 2002)
55. L.P. Pitaevskii, S. Stringari, *Bose-Einstein Condensation* (Oxford University Press, Oxford, 2003)
56. G.J. Milburn, J. Corney, E.M. Wright, D.F. Walls, *Phys. Rev. A* **55**, 4318 (1997)
57. A. Smerzi, S. Fantoni, S. Giovanazzi, S.R. Shenoy, *Phys. Rev. Lett.* **79**, 4950 (1997)
58. S. Raghavan, A. Smerzi, S. Fantoni, S.R. Shenoy, *Phys. Rev. A* **59**, 620 (1999)
59. Y. Shin, M. Saba, T.A. Pasquini, W. Ketterle, D.E. Pritchard, A.E. Leanhardt, *Phys. Rev. Lett.* **92**, 050405 (2004)
60. T. Schumm, S. Hofferberth, L.M. Andersson, S. Wildermuth, S. Groth, I. Bar-Joseph, J. Schmiedmayer, P. Kruger, *Nature Phys.* **1**, 57 (2005)
61. M. Albiez, R. Gati, J. Folling, S. Hunsmann, M. Cristiani, M.K. Oberthaler, *Phys. Rev. Lett.* **95**, 010402 (2005)
62. P. Pedri, L.P. Pitaevskii, S. Stringari, C. Fort, S. Burger, F.S. Cataliotti, P. Maddaloni, F. Minardi, M. Inguscio, *Phys. Rev. Lett.* **87**, 220401 (2001)
63. D. Ananikian, T. Bergeman, *Phys. Rev. A* **73**, 013604 (2006)
64. E.W. Kirr, P.G. Kevrekidis, E. Shlizerman, M.I. Weinstein, *nlin.PS/0702038*
65. M. Machholm, A. Nicolin, C.J. Pethick, H. Smith, *Phys. Rev. A* **69**, 043604 (2004)
66. Yu.S. Kivshar, M. Peyrard, *Phys. Rev. A* **46**, 3198 (1992)
67. S. Ianeselli, C. Menotti, A. Smerzi, *J. Phys. B* **39**, S135 (2006)
68. T. Anker, M. Albiez, R. Gati, S. Hunsmann, B. Eiermann, A. Trombettoni, M.K. Oberthaler, *Phys. Rev. Lett.* **94**, 020403 (2005)
69. A. Trombettoni, A. Smerzi, *J. Phys. B* **34**, 4711 (2001)
70. E.A. Ostrovskaja, Yu.S. Kivshar, M. Lisak, B. Hall, F. Cattani, D. Anderson, *Phys. Rev. A* **61**, 031601 (2000)
71. L. Fallani, L. De Sarlo, J.E. Lye, M. Modugno, R. Saers, C. Fort, M. Inguscio, *Phys. Rev. Lett.* **93**, 140406 (2004)
72. M. Cristiani, O. Morsch, J.H. Müller, D. Ciampini, E. Arimondo, *Phys. Rev. A* **65**, 063612 (2002)

73. M. Jona-Lasinio, O. Morsch, M. Cristiani, N. Malossi, J.H. Müller, E. Courtade, M. Anderlini, E. Arimondo, Phys. Rev. Lett. **91**, 230406 (2003)
74. B.M. Breid, D. Witthaut, H.J. Korsch, New J. Phys. **8**, 110 (2006)
75. F.S. Cataliotti, L. Fallani, F. Ferlaino, C. Fort, P. Maddaloni, M. Inguscio, New J. Phys. **5**, 71 (2003)

Bose–Einstein Condensates in Optical Lattices: Experiments

O. Morsch

14.1 Introduction

In the early days of laser cooling, which together with magnetic trapping techniques led to the first observation of BEC in 1995, it was realized that the optical interference between the cooling beams could lead to a spatially periodic density modulation of the trapped atoms. This notion of a “three-dimensional egg-carton” for cold atoms quickly led to a number of experiments confirming the existence of such a light-bound crystal and exploring its properties [1–3]. It was found that, indeed, cold atoms could be trapped in such periodic structures, and it was possible to measure, for example, the quantized motion of the atoms inside the potential wells. While early experiments were carried out in the dissipative regime using near-resonant lattices in which the atoms were continuously cooled through the Sisyphus mechanism involving light scattering [4], more sophisticated experimental techniques later enabled studies on far-detuned lattices in which atoms evolved coherently.

Although optical lattices (OLs) attracted a lot of interest in the 1990s, the term “light-bound crystal” was something of a misnomer, as the vast majority of lattice sites was actually empty since typical atomic densities in MOTs and optical molasses were around two orders of magnitude lower than the density of lattice sites. Furthermore, in order to prepare atoms in the ground states of the wells it was necessary to use sophisticated techniques such as resolved-sideband Raman cooling. The advent of BEC solved both problems at once. Experimenters now had at their disposal dense samples of atoms at temperatures in the nano-Kelvin regime, which was an ideal starting point for loading the ground states of far-detuned OLs with unity or even larger filling. From the point of view of BEC experiments, on the other hand, adding OLs to the setup meant introducing periodicity and much smaller length scales into the problem, leading to a variety of new phenomena [5–11].

In this chapter we will discuss the technical requirements for working with BECs in OLs and discuss some of the experiments carried out so far, with particular emphasis on the rich physics resulting from the nonlinearity of the BEC.

14.1.1 Technical Considerations

Optical lattices are created by superposing two or more laser beams. The interaction between the resulting spatially varying laser intensity due to interference and an atomic transition through the ac-Stark shift results in a periodic potential landscape. For our purposes we will assume that the laser beams are far detuned from an atomic resonance so that photon scattering is negligible on the time scale of the experiment (usually on the order of milliseconds) and hence the lattice potential is conservative.

The simplest example of an OL is shown in Fig. 14.1a: Two linearly polarized, counter-propagating laser beams of wavevector $\pm\mathbf{k}_L$ and wavelength λ_L create an interference pattern with lattice constant $d = \lambda_L/2$ resulting in a potential of the form

$$V(x) = V_0 \cos^2(\pi x/d), \quad (14.1)$$

where the lattice depth

$$V_0 = \zeta \hbar \Gamma \frac{I_p}{I_0} \frac{\Gamma}{\Delta} \quad (14.2)$$

depends on the laser intensity I_p , the detuning Δ from the atomic resonance, the saturation intensity I_0 and linewidth Γ characterizing that resonance, and a dimensionless parameter ζ that depends on the level structure of the atom. This setup can easily be generalized by introducing an angle θ different from π between the two beams (Fig. 14.1b) such that the linear polarizations are perpendicular to the plane spanned by the two beams. The resulting OL has a lattice spacing $d(\theta) = d/\sin(\theta/2)$, and in practice lattice constants ranging from $\approx 0.4 \mu\text{m}$ to several μm have been realized using infrared laser beams. In the following, when referring to lattice spacings and lattice depths we will always cite d without the angle that was used to realize it, and the lattice

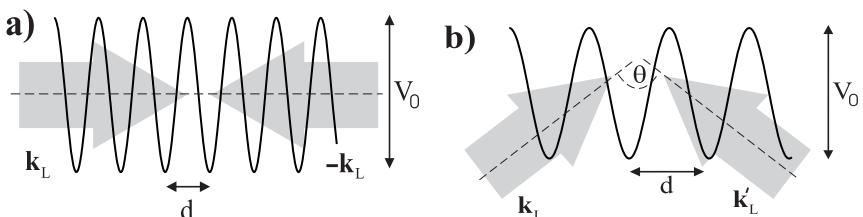


Fig. 14.1. A one-dimensional optical lattice created from counter-propagating laser beams (a) and with beams enclosing an angle θ (b). The parameters V_0 (lattice depth) and d (lattice spacing) are defined in the text. From [10]

depth will be expressed as $s = V_0/E_R$ in units of the corresponding lattice recoil energy

$$E_R = \frac{\hbar^2 \pi^2}{2md^2}, \quad (14.3)$$

where m is the mass of the atoms in the BEC. Where the mean-field interaction energy of the condensate (which depends on the condensate density n_0 and the scattering length a_s) plays a role, it will be expressed by the dimensionless parameter C defined as

$$C = \frac{gn_0}{8E_R} = \frac{n_0 a_s d^2}{\pi}. \quad (14.4)$$

It is clear from this expression that large values of the parameter C can be realized by choosing a large lattice constant.

In order to vary the lattice depth during an experiment, the beams are typically produced by sending laser light through acousto-optic modulators (AOMs). This is necessary in order to be able to load the BEC into the OL adiabatically by increasing the lattice depth from 0 to its final value. In the linear regime the minimum loading time can be estimated from the condition that there be no excitation of higher bands and is typically on the order of 10–100 μ s [12]. When the nonlinearity is not negligible, the adiabaticity criterion becomes more difficult to be predicted theoretically. In practice, loading times in the nonlinear regime can be on the order of tens of milliseconds [13–15].

The AOMs can also be used to move and accelerate the OL. If a small frequency difference $\Delta\nu$ is introduced between the two beams, the OL will move at a velocity $v_L = d\Delta\nu$, and if $\Delta\nu$ is linearly chirped, this results in an acceleration $a_L = d\frac{d\Delta\nu}{dt}$. While this acceleration can be used to apply a force on the atoms in the rest frame of the OL (and hence simulate the effect of an electric field on the electrons in a solid state crystal), a constant velocity enables loading into higher bands of the lattice [16].

All of the above can, obviously, be generalized to OLs in two and three dimensions. Although several approaches are possible, the simplest one is to use pairs of beams that create mutually orthogonal lattices. If a frequency difference on the order of several MHz is introduced between the beam pairs, their respective interference patterns will effectively be independent of one another and the potentials in the three spatial dimensions can simply be added. Otherwise, more complicated interference patterns are created that depend on the relative phases of the beams [17, 18], and by adding further beams and/or varying their directions and polarizations, one can realize complicated structures such as superlattices, quasi-periodic OLs, Kagomé lattices and disordered lattices [19–22].

14.1.2 Measurements, Observables and Calibration

When a BEC is loaded into an OL (typically from a magnetic or optical harmonic trap), one can think of the combined system as being similar to electrons

inside a crystal. While in the latter case information about the system is usually extracted in the form of transport measurements when an electric field is added, OLs offer a larger variety of diagnostic tools. The main reason for this is that, contrary to solid state systems, in OLs the periodic potential can be varied, modulated and even switched off completely. Therefore, just as in the case of a harmonic trap, it is possible to use time-of-flight (TOF) techniques to investigate the system. What one expects to see in such a scenario is most easily explained in the tight-binding limit. In this regime, the BEC in the lattice consists of wavefunctions localized at the lattice sites. When the lattice is switched off, these wavefunctions fall down under gravity and start to expand. In the far field, they all overlap and create an interference pattern similar to that of an N -slit interference experiment in optics (see Fig. 14.2). After a time t in TOF, the separation between the peaks in the interference pattern is $\Delta x = t \times 2v_R$, where the lattice recoil velocity $v_R = \pi\hbar/m d$. The relative intensities of the peaks depend on the depth of the lattice: The larger V_0 , the more peaks are visible because the wave packets in the lattice wells are narrower and lead to a wider Gaussian envelope of the interference pattern in the far field. This can be used in order to measure and hence calibrate the lattice depth: From the relative weight $P_{\pm 1}$ of the 0 and $\pm 2\hbar k_L$ ($k_L = \pi/d$) momentum peaks, the lattice depth can be calculated as $s = \frac{16}{[\ln(P_{\pm 1})]^2} P_{\pm 1}^{1/4}$ in the limit of deep lattices ($s > 5$) [23]. Other ways of measuring lattice depths include Landau-Zener tunneling measurements and Rabi oscillations at the band edge [10].

All of the above is true if the OL was stationary before it was switched off and if there are no nonlinear or quantum fluctuation effects. These effects, to be discussed later, can lead to a dephasing of the lattice wells and hence to reduction of the visibility of the interference pattern (loosely defined in analogy with spectroscopy). Hence, the visibility can be used as an observable of the system when dephasing plays a role. If the lattice was moving before the

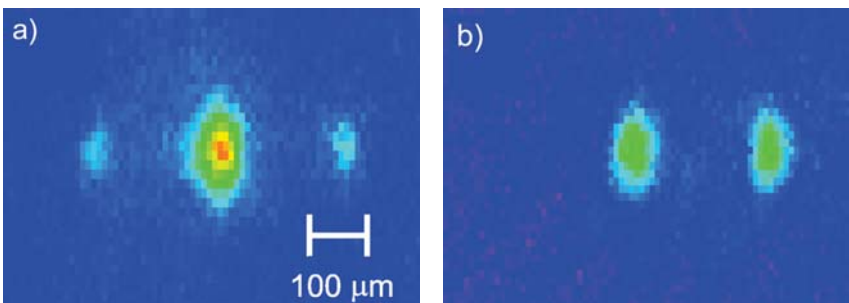


Fig. 14.2. Interference pattern of a Bose–Einstein condensate released from a one-dimensional optical lattice of depth $V_0 = 10 E_R$ after a time-of-flight of 20 ms. In (a), the lattice was at rest, whereas in (b) it had been accelerated to v_R

TOF, the relative phases between the wells also change, but in a deterministic way which leads to the weights of the interference peaks being modified. This allows one, for instance, to infer the group velocity of the BEC from a TOF measurement.

14.2 Linear and Nonlinear Dynamics

In this section we will review some of the experiments carried out with BECs in OLs. The control over the parameters of this system has enabled experiments in three different regimes:

- The *linear regime* reminiscent of the dynamics of electrons in solid state crystals
- The *weakly nonlinear regime* in which the linear BEC dynamics are modified but can still be qualitatively described by the linear approximation
- The *strongly nonlinear regime* characterized by the appearance of qualitatively new phenomena such as solitons and instabilities. In this regime, quantum effects can also become important, leading, e.g., to the Mott insulator transition

In the following we will discuss a selection of experiments carried out in these three regimes. For a more comprehensive picture, the reader is referred to specialized reviews [5–7, 10].

14.2.1 Bloch Oscillations

The formal resemblance between electrons in crystals and BECs in OLs inspired a number of experiments that probed their band structure and interband tunneling properties. Bloch oscillations, the most striking effect of the band structure of periodic potentials when a constant force is applied to the atoms, had already been observed in ultra-cold atoms before the advent of BEC [24, 25]. Bose–Einstein condensates, however, offered the possibility to investigate them more systematically and in different regimes. The first experiment along these lines was carried out in 1998 with a BEC of Rb atoms inside a vertical OL [26], sparking considerable interest both in the theoretical and experimental communities.

In order to observe Bloch oscillations in the linear regime using a BEC, it is necessary to reduce its density sufficiently so that the mean-field energy becomes negligible and hence the nonlinear parameter C is small (typically $C \ll 10^{-2}$ approximates the linear regime reasonably well). This can be achieved either by reducing the frequency of the harmonic trap and hence the density of the condensate before switching on the optical lattice, or else by releasing the condensate from the trap and allowing it to expand. Experiments in this regime were carried out by loading a BECs into a shallow ($V_0 \approx 2 E_R$) OL which was subsequently accelerated with acceleration a_L by

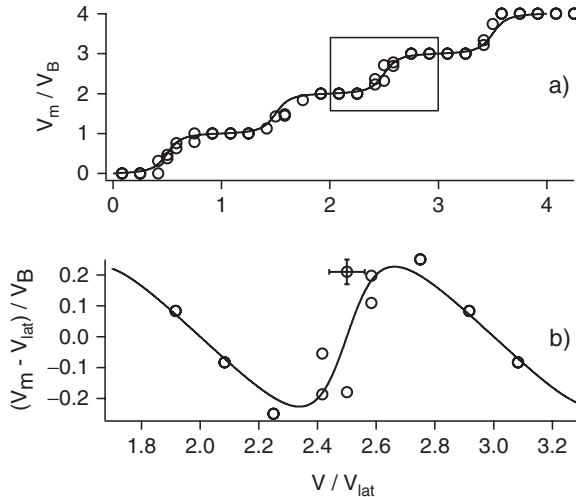


Fig. 14.3. Bloch oscillations (in velocity space) of a condensate in an optical lattice. In the laboratory frame of reference (a), these are visible as a stepwise increase of the mean condensate velocity v_m , whereas in the rest frame moving at the lattice velocity v_{lat} (b), the oscillations can be seen directly. Here $v_B = 2v_R$ is the Bloch velocity. From [23]

chirping the frequency difference between the lattice beams [23, 27]. After a variable acceleration time t_{acc} , the trap and lattice were switched off and a TOF measurement was made. From the resulting interference pattern, the condensate group velocity in the OLs rest frame could be calculated and plotted against the lattice velocity $v_{\text{lat}} = a_L t_{\text{acc}}$ (see Fig. 14.3), clearly showing the Bloch oscillations.

14.2.2 Landau–Zener Tunneling

While Bloch oscillations can be described by an adiabatic evolution of the BEC in the lowest lattice band for small a_L , the breakdown of this approximation for larger accelerations leads to Landau–Zener tunneling [25]. In this case, the condensate cannot adiabatically follow the variation of energy with quasimomentum in the lowest band. At the edge of the Brillouin zone ($q = 1$), there is a finite probability $r = \exp(-a_c/a_L)$ (where the critical acceleration $a_c \propto V_0^2$) for the condensate to tunnel into the first excited band. In the experiment by Anderson et al. [26], a vertically oriented lattice was used, with the Earth's acceleration g driving the atoms. The Landau–Zener tunneling events led to atomic “droplets” falling out of the lattice.

When the nonlinear term in the Gross–Pitaevskii equation is not negligible, the behavior of a BEC in an accelerated lattice deviates appreciably from the linear case $C \approx 0$ [5]. In particular, performing Landau–Zener tunneling

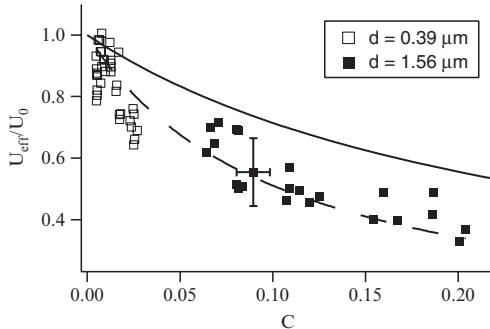


Fig. 14.4. Nonlinear Landau–Zener tunneling [27]. Shown here is the variation of the effective potential U_{eff} with the nonlinear parameter C . The square symbols are experimental data points and the solid and dashed lines are the theoretical prediction of [28] and a best fit with a re-scaled nonlinearity parameter, respectively

experiments as a function of the nonlinear parameter C (see Fig. 14.4), Morsch et al. found that the tunneling probability increased with increasing C [27]. This can be explained in the effective potential approximation introduced in [28] as a decrease in the effective potential $V_{\text{eff}} = V_0/(1+4C)$ and hence the band gap at the Brillouin zone edge, leading to increased tunneling. Intuitively, one can understand this as a “back-action” of the repulsive interactions of the condensate due to the density modulation produced by the OL potential.

If the same experiment is carried out in the opposite direction, i.e., starting out with the condensate in the first excited band, the effect of the nonlinear term is reversed. While in the linear case Landau–Zener tunneling from the lowest to the first excited energy band or vice versa occurs with the same probability, the mean-field interaction leads to an asymmetry in the tunneling. It was shown by Jona-Lasinio et al. [29] that in the nonlinear case one expects the tunneling probability from the first excited to the lowest band to be *reduced* rather than enhanced, as is the case for tunneling from the lowest to the first excited band. This asymmetry gets bigger as C increases and ultimately leads to a complete suppression of tunneling from the excited to the lowest energy band (see Fig. 14.5).

14.2.3 Josephson Effects

So far we have been dealing with BECs in shallow OLs for which the appropriate picture was that of delocalized Bloch waves. As the lattice depth is increased, the BEC wavefunction becomes increasingly localized in the individual lattice wells and the entire system can be viewed as an array of Josephson junctions. It is then useful to discretize the GPE and introduce a discrete nonlinear Schrödinger equation consisting of a set of coupled differential equations related to sets of neighboring lattice sites. One can further introduce “macroscopic” variables that describe the experimentally observable

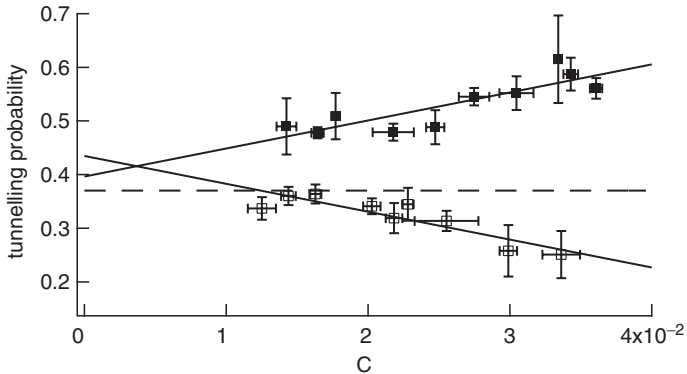


Fig. 14.5. Asymmetric Landau-Zener tunneling. When the nonlinearity is increased, the tunneling probability from the lowest to the first excited band increases (*solid squares*), whereas the probability for the inverse process decreases (*open squares*). *The solid lines* are linear fits to the data, and *the dashed line* indicates the linear Landau-Zener prediction based on the lattice parameters ($V_0 = 1.77 E_R$, $a_L = 33.9 \text{ ms}^{-2}$)

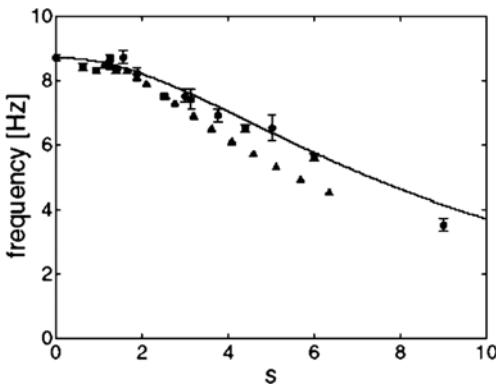


Fig. 14.6. Variation of the sloshing frequency of a condensate in the presence of an optical lattice of depth s . The circles are experimental data points from [30], whereas *the triangles* represent the theoretical prediction based on a Josephson model (discrete nonlinear Schrödinger equation). *The solid line* is a calculation based on an effective mass approach. Taken from [33]

envelope of the individual local BECs (which, in most experiments, cannot be resolved). Using this approach, Cataliotti et al. [30–32] observed the motion of this envelope when the harmonic trap superposed onto the optical lattice was suddenly displaced, leading to an overall sloshing motion of the envelope and, locally, to coherent tunneling between the lattice wells and an associated “Josephson current.” The dependence of the sloshing frequency on the lattice depth (see Fig. 14.6), which was varied between $s \approx 1$ and $s \approx 9$, indirectly

reflected the critical Josephson current I_c . Alternatively, it is possible to go back to a continuum description and explain the variation in sloshing frequency in terms of the effective mass. Using this approach, Kramer et al. [33] accurately reproduced the experimental data of [30] and thereby established a link between the effective mass regime and the Josephson-interpretation.

14.2.4 Instabilities

In our discussion of Bloch oscillations and Landau–Zener tunneling of BECs in OLs we dealt with dynamical phenomena that also occur in the linear regime and that are only slightly modified by the nonlinearity of the BEC. In other words, by rescaling some parameters of the problem in an appropriate way, we were able to describe the nonlinear dynamics using the linear approximation. From a theoretical point of view, this means that the solutions of the GPE are similar to those of the linear Schrödinger equation. We know, however, that in the nonlinear regime these solutions can exhibit energetic as well as dynamical instabilities.

In order to investigate instabilities experimentally, one first needs to find a measurable quantity that reflects this instability. For a Bose condensate in a lattice, the growth of an unstable mode will lead to a loss of phase coherence across the condensate which can be detected in a time-of-flight measurement. In [34], Cristiani et al. loaded a BEC into a lattice and subsequently accelerated the lattice up to a final velocity $v_{\text{final}} > v_R$, thus eventually crossing the edge of the Brillouin zone. The time-of-flight interference pattern was then characterized by its contrast (or visibility) as a function of the lattice acceleration. The latter determined the time the condensate spent in the quasimomentum region in which unstable modes are expected to be present. For small accelerations, beyond a critical quasimomentum the contrast of the interference pattern started to decrease, indicating the presence of unstable modes. In a similar experiment, Fallani et al. [35] loaded the condensate into a lattice moving at a finite velocity and hence at a finite quasimomentum q . After a waiting time ranging from a few milliseconds up to several seconds, the condensate was imaged after a time-of-flight and the number of atoms in the condensate fraction was determined. Again, it was found that beyond a critical quasimomentum $q_{\text{crit}} \approx 0.55$ the condensate started to be “destroyed,” i.e., atoms were lost from the condensed fraction (see Fig. 14.7). In contrast to [34], this experiment investigated a single value of q at a time rather than an integrated effect over a range of quasimomenta.

Both of the experiments described above can be interpreted in terms of a dynamical instability arising above a critical quasimomentum and growing with a characteristic rate, as predicted by several authors [36, 37]. A simple picture for the dynamical instability is that for a BEC with repulsive interactions, in the region of the Brillouin zone where the effective mass

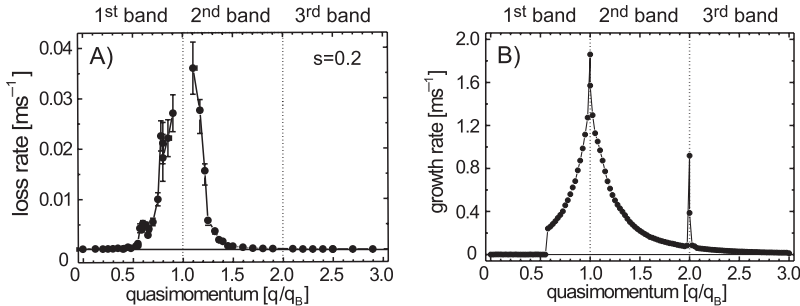


Fig. 14.7. Signatures of dynamical instability of a Bose condensate in an optical lattice. (a) shows the loss rates from a condensate held at a fixed quasimomentum q of a lattice with $s = 1.15$. In (b), the theoretically calculated growth rates for the dynamically most unstable mode are plotted as a function of q . Taken from [35]

$$m_{\text{eff}}(q_0) = \hbar^2 \left[\frac{\partial^2 E(q)}{\partial q^2} \Big|_{q_0} \right]^{-1}$$

is negative, the atoms effectively interact attractively. Thus, a small density fluctuation on the wavefunction is amplified and ultimately leads to an instability. Although [35] and [38] compare their results with numerical simulations, thorough and systematic measurements, e.g., of the growth rates of the unstable modes in different regions of parameter space (characterized by the lattice depth and the nonlinear parameter C) have yet to be done. An interesting prospect lies in the careful characterization of just *one* unstable mode such as the period-doubling mode theoretically discussed by [39]. The need for more careful (and more quantitative studies) is highlighted by the difficulty in interpreting the experimental results and determining the kind of instability involved. In an early experiment [40], the observed breakdown of superfluidity of the condensate was initially ascribed to an energetic (Landau) instability, i.e., to the lowering of the energy of the condensate through phonon emission. Although a theoretical analysis in this direction gave plausible results, a recent calculation [41] suggested, as pointed out earlier in [42], that the onset of instability occurs well beyond the critical velocity for an energetic instability but is, in fact, consistent with a dynamical instability [35].

14.2.5 Dispersion Management and Solitons

The quasimomentum-dependent effective mass of a BEC inside an OL can be used to explain Bloch oscillations as well as the origin of the dynamical instability. Furthermore, it can be used experimentally in order to control the dispersion of a wave packet inside an OL.

Quantum-mechanically, any wave packet with a finite width Δx will undergo dispersion in free space, i.e., it will expand with a velocity that is

inversely proportional to its original size. In the presence of a periodic potential dispersion still takes place, but now the effect of the periodicity of the potential acting on the matter-wave has to be taken into account through the effective mass m_{eff} . As the latter can be positive or negative, the resulting dispersion can be either normal (i.e., the wave packet expands) or anomalous (i.e., the wave packet contracts). Both regimes have been experimentally explored [43, 44] and it has been shown that an optical lattice can be used to effectively control the dispersion of a Bose–Einstein condensate. Such a dispersion management is analogous to similar schemes used in fiber optics.

The concept of effective mass can also be applied to collective excitations of the condensate [33] such as the dipole and quadrupole oscillation modes. The former corresponds to the condensate performing center-of-mass oscillations inside a harmonic trap, whereas the latter is a “breathing” oscillation. When a periodic potential is present, the frequencies of these modes are modified by a factor $\sqrt{m/m_{\text{eff}}}$ and, therefore, depend on the depth of the optical lattice. This dependence has been verified experimentally [45].

Finally, when the mean-field interaction in the condensate is appreciable, new phenomena appear. If the atom–atom interaction is repulsive, it is possible to choose a *negative* effective mass $m_{\text{eff}}(q_c)$ (through the corresponding quasimomentum q_c) such that the effective *attractive* interaction term in the Gross–Pitaevskii equation leads to the formation of stable bright solitons if the number of atoms is sufficiently small. These so-called gap solitons were recently observed [46].

14.3 Quantum Effects and the Mott Insulator Transition

The shallow-lattice phenomena discussed in the preceding sections could all be interpreted within the theoretical framework of the standard GPE (in the case of instabilities, this is true at least for the onset of the instability, if not for its subsequent growth) or its discretized form which is useful for deeper OLs ($V_0 > E_R$). When the lattice depth is increased further still, one enters an entirely new regime that requires a different theoretical treatment and leads to a qualitatively different physical picture.

In the limit of very deep OLs ($>10 E_R$), increasing the lattice depth and thus reducing the tunneling rate between adjacent wells can be viewed as a reduction of the number fluctuations at each lattice site. As it becomes less likely for the atoms to hop between wells, the number variance σ_n goes down. Quantum mechanically, this implies that the phase variance σ_ϕ , describing the spread in relative phases between the lattice wells, has to increase. This follows from an uncertainty principle involving the product $\sigma_n \sigma_\phi$, and its effects can be seen directly by looking at the interference pattern of a BEC released from an OL. In the first experiment performed by Orzel et al., the authors adiabatically loaded condensates of Rb atoms into a deep 1D lattice and characterized the quality of the interference pattern through the width

of the interference peaks in TOF [13]. As the ratio of the mean-field energy per particle to the tunneling energy decreased when the lattice depth was increased, the interference pattern was washed out. This alone only proves that phase coherence between adjacent wells was lost, but not *how* it was lost. In order to show that the loss of coherence was actually due to suppressed number fluctuations and hence the creation of number-squeezed states, the authors adiabatically lowered the lattice depth again and found that, indeed, phase coherence was restored. However, one has to keep in mind that in some cases interference patterns can appear when intuitively one would not expect to see them [47].

In a similar experiment, but using a 3D optical lattice, Greiner et al. [48] took this approach one step further and reached the Mott-insulator transition. In this quantum phase transition, the number fluctuations vanish and the system reaches a state in which all the lattice wells are occupied by a well-defined number of atoms. As in the experiment by Orzel et al., the tell-tale sign for the increasing phase fluctuations was the deterioration of the interference pattern. Again, this observation on its own did not unambiguously demonstrate the transition from the initial superfluid to a Mott insulator state [49]. A further piece of evidence in the experiment by Greiner et al. was the occurrence of a gap in the excitation spectrum of the Mott insulator (see Fig. 14.8). By applying a magnetic field gradient to the lattice (which amounts to “tilting” it),

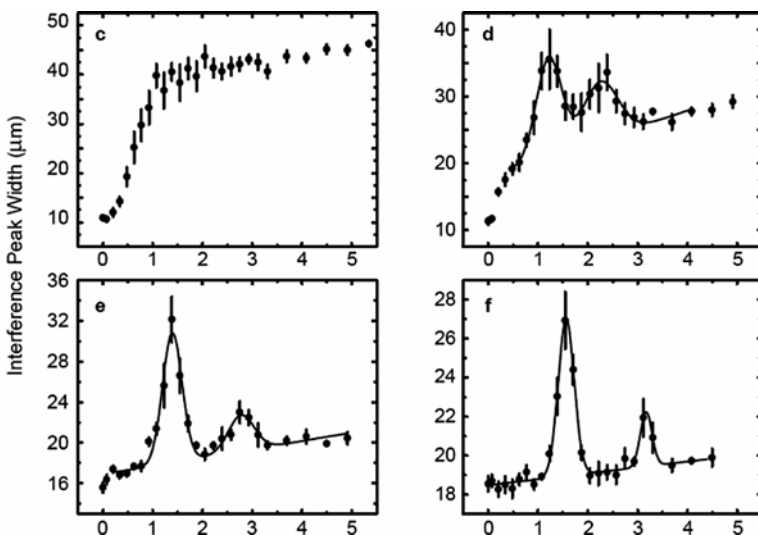


Fig. 14.8. The excitation spectrum of a superfluid (c) and a Mott insulator state (d)–(f) measured by applying an energy gradient between adjacent wells in the experiment of [48]. From (c) to (f), the lattice depth is increased, and the discrete excitation spectrum of the Mott insulator becomes visible. *The horizontal axes indicate the potential gradient expressed in kHz*

an energy difference between adjacent sites was created which allowed atoms to hop between the sites. Whereas in the superfluid regime (for small lattice depths) this hopping increases continuously with the energy difference between the sites, in the Mott insulator regime only well-defined energy differences are allowed, corresponding to the energy “penalty” for adding an atom to a lattice site already occupied by an atom (or several atoms). In their experiment, the authors also demonstrated that the Mott insulator transition is reversible by lowering the optical lattice depth. Similar results were obtained [50, 51] using lattices in one, two and three dimensions. More recently, the structure of the Mott insulator and the dynamics of the quantum phase transition were investigated further using noise-correlation techniques and microwave spectroscopy [52–54].

14.4 Mixtures, Molecules and Fermions in Lattices

The observation of BEC in dilute gases in 1995 was a major breakthrough in experimental atomic physics. More than 10 years on, research on BEC is still a thriving field, but more recently fermions have also caused a lot of excitement in the community. Obviously, in the case of fermions the principal interest lies in the fact that electrons in solid-state crystals are fermions. Ultra-cold, dilute clouds of fermionic atoms hence offer the enticing prospect of studying phenomena like the BCS-transition to superconductivity in a model system whose parameters can easily be controlled. Adding a periodic potential is, therefore, a natural further step in that direction. In one of the first experiments with fermions in an optical lattice [55], the fermionic character of ^{40}K was clearly seen by comparing sloshing oscillations between bosons and fermions in the superimposed magnetic trap whilst the lattice was present. Since the initial quasimomentum distribution of the fermions was much larger than that of the bosons due to the exclusion principle, the sloshing motion of the fermions was heavily damped in contrast to the undamped oscillations of the bosons.

More recently, experiments with fermions have been extended to studies of boson–fermion mixtures as well as molecules and weakly bound BCS pairs [56–60]. In a first experiment combining bosons and fermions in a lattice [61] the effect of a bosonic bath on fermions moving through an optical lattice was investigated. The results of these experiments show that, just as in condensed matter physics, interactions lead to a fermionic current that would be absent if the fermions moved on their own inside the periodic potential. Recently, the role of fermionic impurities on bosons in OLs was further investigated [62].

From a theoretical point of view, mixtures of bosonic and fermionic atoms in OLs produce extremely rich physics. Studying these mixtures in different regimes, [63] found several new quantum phases containing composite fermions (made up from a fermion and one or several bosons) which could be either delocalized superfluid or metallic phases or localized density wave or domain

insulator phases. Similar studies have been done by several other authors [64–66].

Another interesting aspect of a boson–fermion mixture is the possibility to create an array of dipolar molecules. It has been shown [67] that this can be achieved by first creating a combined Mott insulator state with one atom of both species per lattice site and then creating molecules by photoassociation. The dipolar molecules thus created could either be used as a resource for quantum computing or be transformed into a dipolar condensate by melting the Mott insulator phase.

14.5 Perspectives

Looking back at the short history of BECs in lattices, one notices that what originally started out as a curious addition to BEC research has grown up to be a thriving field of research in its own right, in many ways surpassing its parents. With the addition of fermions and molecules to this “quantum toolbox,” cold atoms in OLs have established themselves at the forefront of atomic physics research and are giving impulses to other fields. It is hard to predict where cold atoms in lattices will be in 10 years from now, but it is safe to assume that they will be on the scene for a while yet. Apart from being exciting in their own right, they are also increasingly being used as tools for realizing physical systems that otherwise are hard to implement. For instance, in a recent experiment using “stacks” of 2D condensates held in a 1D optical lattice, the Berezinskii–Kosterlitz–Thouless transition was observed [68, 69]. Using similar techniques, it might be possible to observe, e.g., the fractional quantum Hall effect with cold atoms. Quite generally, cold atoms in OLs are increasingly being used as “quantum simulators.” Owing to their flexibility, they can emulate a large variety of Hamiltonians that are difficult to realize in the solid state or to study numerically.

On a more practical level, BECs and fermions in OLs are also promising systems for atom interferometry and precision measurements [70, 71], e.g., for a determination of the Earth’s acceleration through the frequency of Bloch oscillations, as well as for the implementation of a quantum computer using neutral atoms [72, 73]. All in all, it is fair to say that cold atoms in lattices have come a long way since their first realization and have a promising future ahead.

References

1. P.S. Jessen, I.H. Deutsch, *Adv. Atom. Mol. Opt. Phys.* **37**, 95–138 (1996)
2. D.R. Meacher, *Contemp. Phys.* **39**(5), 329–350 (1998)
3. G. Grynberg, C. Robilliard, *Phys. Rep.* **355**, 335 (2001)
4. J. Dalibard, C. Cohen-Tannoudji, *J. Opt. Soc. Am. B* **6**, 2023 (1989)

5. O. Morsch, E. Arimondo, in *Dynamics and Thermodynamics of Systems with Long-Range Interactions*, ed. by T. Dauxois, S. Ruffo, E. Arimondo, M. Wilkens. Ultracold atoms and Bose-Einstein condensates in optical lattices (Springer, Berlin, 2002), pp. 312–331
6. I. Bloch, Phys. World **25**, (2004)
7. I. Bloch, J. Phys. B: At. Mol. Opt. Phys. **38**, S629 (2005)
8. I. Bloch, M. Greiner, Adv. Atom. Mol. Opt. Phys. **52**, 1 (2005)
9. I. Bloch, Nat. Phys. **1**, 23 (2005)
10. O. Morsch, M. Oberthaler, Rev. Mod. Phys. **78**, 179 (2006)
11. S.L. Rolston, Int. J. Mod. Phys. B **20**, 2755 (2006)
12. J.H. Denschlag, J.E. Simsarian, H. Häffner, C. McKenzie, A. Browaeys, D. Cho, K. Helmerson, S.L. Rolston, W.D. Phillips, J. Phys. B: At. Mol. Opt. Phys. **35**, 3095 (2002)
13. C. Orzel, A.K. Tuchman, M.L. Fenselau, M. Yasuda, M. Kasevich, Science **291**, 2386 (2001)
14. O. Morsch, J.H. Müller, D. Ciampini, M. Cristiani, P.B. Blakie, C.J. Williams, P.S. Julienne, E. Arimondo, Phys. Rev. A **67**, 31603 (2003)
15. T. Gericke, F. Gerbier, A. Widera, S. Fölling, O. Mandel, I. Bloch, J. Modern Opt. **54**, 735 (2007).
16. E. Peik, M. Ben Dahan, I. Bouchoule, Y. Castin, C. Salomon, Phys. Rev. A **55**, 2989 (1997)
17. M. Greiner, I. Bloch, O. Mandel, T.W. Hänsch, T. Esslinger, Appl. Phys. B **73**, 769 (2001)
18. M. Greiner, I. Bloch, O. Mandel, T.W. Hänsch, T. Esslinger, Phys. Rev. Lett. **87**, 160405 (2001)
19. L. Guidoni, C. Trich, P. Verkerk, G. Grynberg, Phys. Rev. Lett. **79**, 3363 (1997)
20. L. Santos, M.A. Baranov, J.I. Cirac, H.-U. Everts, H. Fehrmann, M. Lewenstein, Phys. Rev. Lett. **93**, 030601 (2004)
21. M. Weitz, G. Cennini, G. Ritt, C. Geckeler, Phys. Rev. A **70**, 043414 (2004)
22. T. Schulte, S. Drenkelforth, J. Kruse, W. Ertmer, J. Arlt, K. Sacha, J. Zakrzewski, M. Lewenstein, Phys. Rev. Lett. **95**, 170411 (2006)
23. M. Cristiani, O. Morsch, J.H. Müller, D. Ciampini, E. Arimondo, Phys. Rev. A **65**, 63612 (2002)
24. M. Ben Dahan, E. Peik, J. Reichel, Y. Castin, C. Salomon, Phys. Rev. Lett. **76**, 4508 (1996)
25. Q. Niu, X. G. Zhao, G.A. Georgakis, M.G. Raizen, Phys. Rev. Lett. **76**, 4504 (1996)
26. B.P. Anderson, M.A. Kasevich, Science **282**, 1686 (1998)
27. O. Morsch, J.H. Müller, M. Cristiani, D. Ciampini, E. Arimondo, Phys. Rev. Lett. **87**, 140402 (2001)
28. D.-I. Choi, Q. Niu, Phys. Rev. Lett. **82**, 2022 (1999)
29. M. Jona-Lasinio, O. Morsch, M. Cristiani, N. Malossi, J.H. Müller, E. Courtade, M. Anderlini, E. Arimondo, Phys. Rev. Lett. **91**, 230406 (2003)
30. F.S. Cataliotti, S. Burger, C. Fort, P. Maddaloni, F. Minardi, A. Trombettoni, A. Smerzi, M. Inguscio, Science **293**, 843 (2001)
31. F.S. Cataliotti, L. Fallani, F. Ferlaino, C. Fort, P. Maddaloni, M. Inguscio, J. Opt. B **5**, S17 (2003)
32. F.S. Cataliotti, L. Fallani, F. Ferlaino, C. Fort, P. Maddaloni, M. Inguscio, New J. Phys. **5**, 71 (2003)

33. M. Krämer, L. Pitaevskii, S. Stringari, Phys. Rev. Lett. **88**, 180404 (2002)
34. M. Cristiani, O. Morsch, N. Malossi, M. Jona-Lasinio, M. Anderlini, E. Courtade, E. Arimondo, Opt. Expr. **12**, 4 (2004)
35. L. Fallani, L. De Sarlo, J.E. Lye, M. Modugno, R. Saers, C. Fort, M. Inguscio, Phys. Rev. Lett. **93**, 140406 (2004)
36. B. Wu, Q. Niu, New J. Phys. **5**, 104 (2003)
37. M. Machholm, C.J. Pethick, H. Smith, Phys. Rev. A **67**, 053613 (2003)
38. L. De Sarlo, L. Fallani, J.E. Lye, M. Modugno, R. Sears, C. Fort, M. Inguscio, Phys. Rev. A **72**, 013603 (2005)
39. M. Machholm, A. Nicolin, C.J. Pethick, H. Smith, Phys. Rev. A **69**, 043604 (2004)
40. S. Burger, F.S. Cataliotti, C. Fort, F. Minardi, M. Inguscio, M.L. Chiofalo, M.P. Tosi, Phys. Rev. Lett. **86**, 4447 (2001)
41. M. Modugno, C. Tozzo, F. Dalfovo, (2004)
42. B. Wu, Q. Niu, S. Burger, F.S. Cataliotti, C. Fort, F. Minardi, M. Inguscio, M.L. Chiofalo, M.P. Tosi, Phys. Rev. Lett. **89**, 088901 (2002)
43. B. Eiermann, P. Treutlein, T. Anker, M. Albiez, M. Taglieber, K.-P. Marzlin, M.K. Oberthaler, Phys. Rev. Lett. **91**, 060402 (2003)
44. L. Fallani, F.S. Cataliotti, J. Catani, C. Fort, M. Modugno, M. Zawada, M. Inguscio, Phys. Rev. Lett. **91**, 240405 (2003)
45. C. Fort, F.S. Cataliotti, L. Fallani, F. Ferlaino, P. Maddaloni, M. Inguscio, Phys. Rev. Lett. **90**, 140405 (2003)
46. B. Eiermann, Th. Anker, M. Albiez, M. Taglieber, P. Treutlein, K.-P. Marzlin, M.K. Oberthaler, Phys. Rev. Lett. **92**, 230401 (2004)
47. Z. Hadzibabic, S. Stock, B. Battelier, V. Bretin, J. Dalibard, Phys. Rev. Lett. **93**, 180403 (2004)
48. M. Greiner, O. Mandel, T. Esslinger, T.W. Hänsch, I. Bloch, Nature (London) **415**, 39 (2002)
49. R. Roth, K. Burnett, Phys. Rev. A **67**, 031602 (2003)
50. M. Köhl, H. Moritz, T. Stöferle, C. Schori, T. Esslinger, J. Low Temp. Phys. **138**, 635 (2005)
51. T. Stöferle, H. Moritz, C. Schori, M. Köhl, T. Esslinger, Phys. Rev. Lett. **92**, 130403 (2004)
52. S. Fölling, F. Gerbier, A. Widera, O. Mandel, T. Gericke, I. Bloch, Nature (London) **434**, 481 (2005)
53. S. Fölling, A. Widera, T. Müller, F. Gerbier, I. Bloch, Phys. Rev. Lett. **97**, 060403 (2006)
54. G.K. Campbell, J. Mun, M. Boyd, P. Medley, A.E. Leanhardt, L.G. Marcassa, D.E. Pritchard, W. Ketterle, Science **313**, 649 (2006)
55. G. Modugno, F. Ferlaino, R. Heidemann, G. Roati, M. Inguscio, Phys. Rev. A **68**, 11601 (2003)
56. K. Günter, T. Stöferle, H. Moritz, M. Köhl, T. Esslinger, Phys. Rev. Lett. **96**, 180402 (2006)
57. C. Ospelkaus, S. Ospelkaus, L. Humbert, P. Ernst, K. Sengstock, K. Bongs, Phys. Rev. Lett. **97**, 120402 (2006)
58. K. Winkler, G. Thalhammer, F. Lang, R. Grimm, J. Hecker Denschlag, Nature (London) **441**, 853 (2006)
59. K. Günter, M. Köhl, T. Stöferle, H. Moritz, T. Esslinger, Phys. Rev. Lett. **96**, 030401 (2006)

60. J.K. Chin, D.E. Miller, Y. Liu, C. Stand, W. Setiawan, C. Sanner, K. Xu, W. Ketterle, *Nature (London)* **443**, 961 (2006)
61. H. Ott, E. de Mirandes, F. Ferlaino, G. Roati, G. Modugno, M. Inguscio, *Phys. Rev. Lett.* **92**, 160601 (2004)
62. S. Ospelkaus, C. Ospelkaus, O. Wille, M. Sacco, P. Ernst, K. Sengstock, K. Bongs, *Phys. Rev. Lett.* **96**, 180403 (2006)
63. M. Lewenstein, L. Santos, M.A. Baranov, H. Fehrmann, *Phys. Rev. Lett.* **92**, 050401 (2004)
64. A. Albus, F. Illuminati, J. Eisert, *Phys. Rev. A* **68**, 023606 (2003)
65. H. P. Büchler, G. Blatter, *Phys. Rev. Lett.* **91**, 130404 (2003)
66. R. Roth, K. Burnett, *Phys. Rev. A* **69**, 021601 (2004)
67. M.G. Moore, H.R. Sadeghpour, *Phys. Rev. A* **67**, 041603(R) (2003)
68. S. Stock, Z. Hadzibabic, B. Battelier, M. Cheneau, J. Dalibard, *Phys. Rev. Lett.* **95**, 190403 (2005)
69. Z. Hadzibabic, P. Krüger, M. Cheneau, B. Battelier, J. Dalibard, *Nature (London)* **441**, 1118 (2006)
70. H. Ott, E. de Mirandes, F. Ferlaino, G. Roati, G. Modugno, M. Inguscio, *Laser Phys.* **15**, 82 (2005)
71. G. Roati, E. de Mirandes, F. Ferlaino, H. Ott, G. Modugno, M. Inguscio, *Phys. Rev. Lett.* **92**, 230402 (2004)
72. O. Mandel, M. Greiner, A. Widera, T. Rom, T.W. Hänsch, I. Bloch, *Nature (London)* **425**, 937 (2003).
73. D. Jaksch, *Contemp. Phys.* **45**, 367 (2004)

Part IX

Multi-Component Bose–Einstein Condensates

Multi-Component Bose–Einstein Condensates: Theory

B. Malomed

This chapter presents an overview of models providing for theoretical description of basic one- and two-dimensional nonlinear patterns and their stability in mixtures of degenerate Bose and/or Fermi gases, in the mean-field approximation. The models are based on coupled Gross–Pitaevskii equations for bosonic gases, and mean-field-hydrodynamic equations for gases of fermions.

15.1 Introduction

Among various fascinating features demonstrated by BECs, much interest has been drawn to experiments performed in binary condensates composed of ^{87}Rb atoms in two different spin states. Binary condensates can be created by means of the *sympathetic-cooling* technique [1]. In addition to this most familiar type of the binary condensate, more sophisticated experimental techniques open a way to experiments with *heteronuclear* mixtures, such as ^{41}K – ^{85}Rb [2], ^{39}K – ^{85}Rb [3], and ^{85}Rb – ^{87}Rb [4]. Creation of degenerate fermion-boson mixtures, such as ^{40}K – ^{87}Rb [5], has been reported too. It is also possible to make binary degenerate fermion gases, including mixtures of two spin states of ^{40}K [6] and ^6Li atoms [7].

Actual experimental results reported thus far for binary BEC mixtures are limited. They include the demonstration of segregation between two species in immiscible BECs [8], and various vortex configurations in ^{87}Rb , with one spin-state species filling an empty core of a vortex created in the other species [9] (see Chap. 16). However, theoretical studies of the dynamics of binary BECs have advanced much farther. This chapter offers a brief review of basic theoretical models developed for binary BECs, and basic results obtained within the framework of these models, which are based on the mean-field approximation, i.e., rely on the Gross–Pitaevskii equations (GPEs). The results include segregation patterns in immiscible binary condensates in the form of *domain-walls* (DWs) and their generalizations in 2D geometries in the form of intersecting DWs (“crosses”) and “propellers” (rotating crosses), transition

to mixing in immiscible BECs induced by a resonant electromagnetic wave causing interconversion between two species representing different spin states, and various types of *symbiotic solitons*, which are only possible in binary systems including *symbiotic gap solitons* in self-repulsive condensates supported by periodic optical lattices (OLs). We also briefly considered the formation of DWs and transition to miscibility induced by the resonant electromagnetic wave in a binary degenerate fermion gas, described by means of the mean-field-hydrodynamic (MFHD) approximation. More sophisticated multi-component models, such as ones with nonpolynomial nonlinearity, and three-component systems of GPEs for spinor condensates, are included too.

15.2 Basic Models: Coupled Gross–Pitaevskii Equations

The starting point of the theoretical analysis is a system of coupled GPEs for wavefunctions $\phi(\mathbf{r}, t)$ and $\psi(\mathbf{r}, t)$ of two components of the condensate. In this article, one-dimensional (1D) and two-dimensional (2D) settings are reviewed for the above-mentioned practically significant case when the components represent two different spin states of the same atom, hence the corresponding atomic masses are equal. The normalized form of the coupled equations is

$$i\phi_t = -(1/2)\nabla^2\phi + (\Omega_1^2/2)r^2\phi + (g_{11}|\phi|^2 + g_{12}|\psi|^2)\phi - \kappa\psi, \quad (15.1)$$

$$\begin{aligned} i\psi_t = & -(1/2)\nabla^2\psi + (\Omega_2^2/2)r^2\psi + (g_{22}|\psi|^2 + g_{21}|\phi|^2)\psi \\ & - \kappa\phi + \Delta\mu \cdot \psi. \end{aligned} \quad (15.2)$$

Here $\Omega_{1,2}$ are trapping frequencies characterizing the strength of the parabolic potential, created by means of external magnetic and/or optical fields, which confines the condensate. Coefficients g_{11} , g_{22} and g_{12} , g_{21} account, respectively, for intra- and inter-species collisions between atoms; positive and negative values of g_{mn} correspond to repulsive and attractive interactions between atoms, respectively. The linear-mixing coefficient, $\kappa > 0$, accounts for the interconversion between the two spin states, which may be induced by a spin-flipping resonant electromagnetic wave [10]. In physical units, the frequency of the wave is in the GHz range.

Equations (15.1) and (15.2) also include an asymmetry between the components, accounted for by the chemical-potential difference, $\Delta\mu$, which may be induced by a spatially uniform dc magnetic field which couples to the atomic spin; various effects induced by the asymmetry were considered in [11]. This chapter concentrates on the fully symmetric model, with $\Delta\mu = 0$, $\Omega_1 = \Omega_2 \equiv \Omega$, and $g_{11} = g_{22} \equiv g_1$, $g_{12} = g_{21} \equiv g_2$, which casts (15.1) and (15.2) in a simplified form,

$$i\phi_t = -(1/2)\nabla^2\phi + (\Omega^2/2)r^2\phi + (g_1|\phi|^2 + g_2|\psi|^2)\phi - \kappa\psi, \quad (15.3)$$

$$i\psi_t = -(1/2)\nabla^2\psi + (\Omega^2/2)r^2\psi + (g_1|\psi|^2 + g_2|\phi|^2)\psi - \kappa\phi. \quad (15.4)$$

The coupled GPEs conserve the norm of the wavefunctions, which is proportional to the total number of atoms in the condensate,

$$N \equiv N_1 + N_2 = \int \left[|\phi(\mathbf{r})|^2 + |\psi(\mathbf{r})|^2 \right] d\mathbf{r}. \quad (15.5)$$

In the absence of linear interconversion ($\kappa = 0$), the norms of two species, N_1 and N_2 , are conserved separately. N may be scaled to be $N \equiv 1$, in which case the actual number of atoms, \mathcal{N} , is hidden in the definition of the nonlinear coefficients, g_1 and g_2 , in (15.3) and (15.4). In particular, if the lengths are measured in physical units (cf. Chap. 1), then, in the 1D case, $g_{1,2} = 4\pi a_{1,2} \mathcal{N}/S$, where a_1 and a_2 are scattering lengths characterizing the intra- and inter-species collisions, and S is an effective transverse area of the respective “cigar-shaped” (nearly-1D) trap. Similarly, $g_{1,2} = 4\pi a_{1,2} \mathcal{N}/a_\perp$ in the 2D case, when the condensate is trapped in a “pancake-shaped” configuration with transverse thickness a_\perp .

In the absence of trapping ($\Omega = 0$) and linear interconversion ($\kappa = 0$), the binary condensate is immiscible under the well-known condition,

$$\Delta \equiv (g_{12}g_{21} - g_{11}g_{22})/g_{11}^2 > 0 \quad (15.6)$$

[12], which has a simple meaning: the two species do not mix if their mutual repulsion is stronger than the repulsion between atoms belonging to the same species. In the mixture of two spin states in the ^{87}Rb condensate, the actual value of the immiscibility parameter is $\Delta \approx 9 \times 10^{-4}$ [1, 13]. In the mixed ^{23}Na condensate, it is larger, but still quite small too [14], $\Delta \approx 0.036$. The small values of Δ suggest that even weak linear coupling (mixing) induced by the interconversion between the species may induce a transition into a miscible state [11].

In addition to the norm, (15.3) and (15.4) conserve the energy,

$$E = \int \left[\frac{1}{2} \left(|\nabla \phi|^2 + |\nabla \psi|^2 \right) + (\Omega^2/2) r^2 (|\phi|^2 + |\psi|^2) \right. \\ \left. + \frac{1}{2} g_1 (|\phi|^4 + |\psi|^4) + g_2 |\phi|^2 |\psi|^2 - \kappa (\phi \psi^* + \phi^* \psi) \right] d\mathbf{r}, \quad (15.7)$$

where $*$ stands for complex conjugation. In the 2D case the total angular momentum $M = i \iint [(y\phi_x - x\phi_y) \phi^* + (y\psi_x - x\psi_y) \psi^*] dx dy$ is also conserved (note that, even in the absence of the linear mixing between the species, the energies and angular momenta are not conserved separately, unlike the norms).

Stationary solutions to (15.3) and (15.4) are looked for as $\phi = u(\mathbf{r})e^{-i\mu t}$ and $\psi = v(\mathbf{r})e^{-i\mu t}$, where μ is the chemical potential. Notice that the chemical potential should be equal between the components if $\kappa \neq 0$. In particular, stationary equations for real 1D functions are (the prime stands for d/dx)

$$\mu u = -(1/2)u'' + (\Omega^2/2)x^2 u + (g_1 u^2 + g_2 v^2) u - \kappa v, \quad (15.8)$$

$$\mu v = -(1/2)v'' + (\Omega^2/2)x^2 v + (g_1 v^2 + g_2 u^2) v - \kappa u. \quad (15.9)$$

In addition to the above-mentioned dynamical structures observed experimentally in the binary ^{87}Rb condensate, in the form of segregating immiscible spin states [8], and vortices in one component with cores filled by the other species [9], a number of more sophisticated patterns and dynamical effects have been predicted in theoretical works. Observation of new states in the experiment may be facilitated by the recently proposed method of Ramsey spectroscopy for the BEC [15]. The present review aims to present theoretical results concerning patterns that seem most fundamental. Left beyond the scope of this review are some specific effects induced by the linear coupling due to the interconversion between two spin states, such as Josephson- and Rabi-like oscillations between them [16], phase DWs (ones which do not separate the two species, but feature a changes of the phase shift between them by 2π [17]), “breathe-together” oscillation modes in the binary mixture [18], and nontopological vortex-like structures (in particular, necklace patterns featuring periodic separation of the two components along the azimuthal coordinate) [19]. Two-component vortices are not included either, as this topic was recently reviewed in [20].

15.3 Immiscible Species in One Dimension: Domain-walls and a Transition to Miscibility in Boson Gases

General consideration. As mentioned above, it is natural to expect that two immiscible species will try to separate by filling two spatially distinct domains, with a DW between them. On the other hand, both the pressure of the external trap, and linear interconversion between the species (if present in the model) try to mix them. In the absence of the latter factor, DW solutions of the coupled GPEs in one dimension were introduced in [21], and later in [22]. The solutions were constructed in [21] in an analytical form, based on the Thomas-Fermi (TF) limit (approximation which neglects the kinetic-energy terms, cf. Chap. 1), with $\kappa = 0$. It was concluded that, in the TF approximation, the ground state of the system, i.e., one minimizing energy (15.7), is represented by a configuration with one species occupying a central portion of the trap, separated by two DWs from side domains, which are occupied by the other species; however, the contribution from the kinetic energy favors a competing configuration, with a single DW formed in the center of trap, to separate two domains filled by the different species. Schematic examples of both configurations are displayed in Fig. 15.1.

Analytical approach. Both the separation of the two components and a transition to miscibility under the action of the linear interconversion between them can be readily understood in terms of an infinite system, with $\Omega = 0$ (while the numerical results displayed in this section below are borrowed from [11], the analytical findings reported in the present subsection are original).

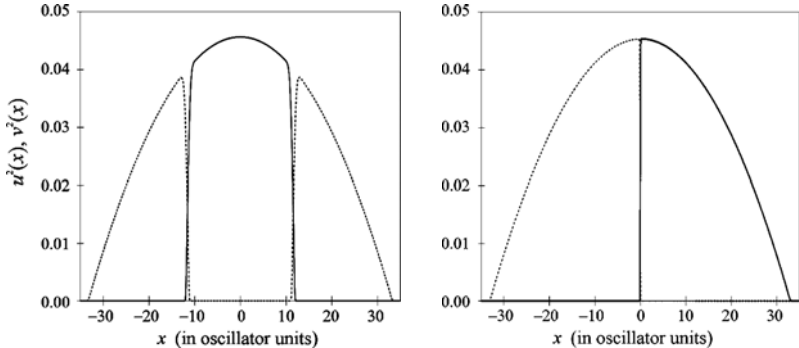


Fig. 15.1. Configurations formed in the 1D parabolic trap by two immiscible species containing equal numbers of atoms. In the *left* and *right* panels, the stationary density profiles of the two components, $u^2(x)$ and $v^2(x)$, feature two and one domain-walls, respectively

In this case, stationary equations (15.8) and (15.9) always have a solution corresponding to the spatially uniform mixed (symmetric) state,

$$u_0^2 = v_0^2 = (\mu + \kappa) / (g_1 + g_2) \quad (15.10)$$

(which assumes $\mu > -\kappa$). The *symmetry-breaking bifurcation*, alias onset of demixing, which gives rise to asymmetric spatially nonuniform (demixed) states, takes place when (15.8) and (15.9), with $\Omega = 0$, admit perturbed solutions,

$$\{u(x), v(x)\} = u_0 \pm u_1 \cos(qx), \quad (15.11)$$

with infinitesimal u_1 . The interpretation of expressions (15.11) as initiating segregation of the two components (*demixing*) is obvious, since maxima in the corresponding densities of the two components alternate. The linearization of (15.8) and (15.9) shows that solution (15.11) exists at $q^2 = 2[(g_2 - g_1)u_0^2 - \kappa]$. Because q^2 must be positive, the demixing (symmetry breaking) is *impossible* if the linear-mixing coefficient is large enough,

$$\kappa \geq \kappa_{\text{cr}} \equiv (g_2 - g_1)u_0^2, \quad (15.12)$$

$\kappa = \kappa_{\text{cr}}$ corresponding to $\mu = \mu_{\text{cr}} \equiv 2g_1u_0^2$.

Further analysis of the linearized (15.3) and (15.4) (with $\Omega = 0$) demonstrates that the symmetric uniform solution (15.10) is stable against small perturbations precisely under condition (15.12), while at $\kappa < \kappa_{\text{cr}}$ it is unstable against perturbations which break both the spatial uniformity of the solution and its symmetry with respect to u and v (in the case of $\kappa = 0$ and $g_2 > g_1$, the corresponding *modulational instability* is known in nonlinear fiber optics [23], where it generates domain-walls separating regions occupied by components u and v [24]).

An alternative physical interpretation of (15.12) is that the increase of the linear-mixing coefficient κ induces the *transition to miscibility* in the initially immiscible BEC, with $g_2 > g_1$ (see (15.6)), at value $\kappa = \kappa_{\text{cr}}$, which depends linearly on the condensate density, $n_0 = 2u_0^2$. In the presence of the harmonic trap ($\Omega > 0$), the transition to miscibility can be predicted by means of variational approximation (VA; a review of the method was given in [25]), which again yields the proportionality of κ_{cr} to $(g_2 - g_1)$, as in (15.12) [11].

The segregated (demixed) state, established as a result of the *symmetry-breaking bifurcation*, can be found in an approximate analytical form close to the bifurcation, i.e., at $0 < \delta\kappa \equiv \kappa_{\text{cr}} - \kappa \ll \kappa_{\text{cr}}$, by means of the perturbation theory. To this end, a stationary solution to (15.8) and (15.9) is looked for, beyond the linear approximation that was based on *ansatz* (15.11) with infinitesimal u_1 , as

$$\{u(x), v(x)\} = (u_0 + \delta u_0) \pm u_1 \cos(qx) + u_2 \cos(2qx), \quad (15.13)$$

where u_1 is small but finite, and, additionally, a shift $\delta\mu$ of the chemical potential against its value at the bifurcation point is assumed. Self-consistency implies the following ordering of the small quantities: $u_1^2 \sim u_2 \sim \delta u_0 \sim \delta\mu \sim \delta\kappa$, and, additionally, $q^2 \lesssim \delta\kappa$ (in fact, one has $q^2 < 2\delta\kappa$, see below). Then, the conservation of the number of atoms (i.e., the condition that the spatially-averaged density corresponding to (15.13), $\bar{n} \equiv \langle u^2(x) + v^2(x) \rangle \approx 2u_0^2 + u_1^2 + 4u_0\delta u_0$, remains equal to the density of the spatially uniform mixed state, $2u_0^2$), and expansion of (15.8) and (15.9) up to the third order in small amplitude u_1 (after the substitution of expression (15.13)), yields the following results:

$$u_1^2 = \frac{(g_1 + g_2)}{4(g_2 - g_1)(2g_1 + g_2)} (2\delta\kappa - q^2), \quad (15.14)$$

$$\delta u_0 = -\frac{u_1^2}{4u_0}, \quad u_2 = -\frac{(3g_1 - g_2)}{4(g_1 + g_2)} \frac{u_1^2}{u_0}, \quad \delta\mu = -(g_2 - g_1) u_1^2. \quad (15.15)$$

Note that the proportionality of the amplitude of the demixed state, u_1 , to the square root of *overcriticality* $\delta\kappa$ (when $q \rightarrow 0$), which follows from (15.14), is a typical feature of phase transitions of the second kind (in infinite systems) [26].

Equations (15.13)–(15.15) describe a family of the segregated (demixed) states, where squared wavenumber q^2 may take values $0 < q^2 < 2\delta\kappa$. The calculation of the average energy density, which is, according to (15.7), $\langle \mathcal{E} \rangle = \langle (g_1/2)(u^4 + v^4) + g_2 u^2 v^2 - 2\kappa u v \rangle$, yields the following result for the family of segregated states, at the first order in small $\delta\kappa$ (in this approximation $\langle \mathcal{E} \rangle$ does not depend on q^2):

$$\mathcal{E}_{\text{segr}}/u_0^4 \approx \mathcal{E}_{\text{cr}} + 2(g_2 - g_1)(1 - \kappa/\kappa_{\text{cr}}), \quad (15.16)$$

where $\mathcal{E}_{\text{cr}} \equiv 3g_1 - g_2$ corresponds to $\kappa = \kappa_{\text{cr}}$.

In the limit of $q = 0$, the binary BEC is described by x -independent solutions to (15.8) and (15.9) (with $\Omega = 0$, and $\kappa < \kappa_{\text{cr}}$, when breaking of

the symmetry is possible). There is an obvious symmetric state, with $u = v = u_0$, $\mu = (g_1 + g_2) u_0^2 - \kappa$, and a nontrivial *exact* solution, which breaks the symmetry between the species by making the ratio of their densities different from 1, but without introducing the segregation between them:

$$\{u^2, v^2\} = u_0^2 \left\{ 1 \pm \sqrt{1 - \kappa^2/\kappa_{\text{cr}}^2} \right\}, \quad (15.17)$$

the corresponding value of the chemical potential remaining $\mu \equiv \mu_{\text{cr}}$. The energy density corresponding to the symmetric and asymmetric solutions is, respectively,

$$\begin{aligned} \mathcal{E}_{\text{symm}}/u_0^4 &= g_1 + g_2 - 2(g_2 - g_1)\kappa^2/\kappa_{\text{cr}}^2, \\ \mathcal{E}_{\text{asymm}}/u_0^4 &= 2g_1 - (g_2 - g_1)\kappa^2/\kappa_{\text{cr}}^2. \end{aligned} \quad (15.18)$$

Comparison of expressions (15.16) and (15.18) for small $\delta\kappa \equiv \kappa_{\text{cr}} - \kappa$ demonstrates that $\mathcal{E}_{\text{segr}} - \mathcal{E}_{\text{cr}} \approx \mathcal{E}_{\text{asymm}} - \mathcal{E}_{\text{cr}} = (1/2)(\mathcal{E}_{\text{symm}} - \mathcal{E}_{\text{cr}})$, i.e., the symmetry breaking, at $\kappa < \kappa_{\text{cr}}$, through the spatial segregation between the species while keeping their average densities equal, or through making the ratio of the densities different from 1, but without introducing the segregation, are (in the first approximation) equivalent in terms of lowering the energy density, against the symmetric state.

Numerical results. As shown in [11], the predicted transition to the miscibility in the two-component segregated condensate trapped in the harmonic potential can be observed in numerical solutions of (15.8) and (15.9), with $\Omega > 0$ (asymmetric states with different numbers of atoms in the two species were looked for in [11] only in a case when the symmetry between (15.3) and (15.4) was broken by additional terms accounting for a difference in the chemical potentials between fields ϕ and ψ). Generic examples of the solutions are displayed in the left panel of Fig. 15.2. They clearly demonstrate that, while the species are strongly segregated at small values of κ , forming a sharp DW, the increase of κ pushes the density distributions of the two species toward each other, and, past a critical point, $\kappa = \kappa_{\text{cr}}$, the two distributions become identical.

The results are shown in the left panel of Fig. 15.2 for $g_1 = g_2/2 = 10$, $\Omega = 1$, and $N = 4$. The choice of $g_1 = g_2/2$ corresponds to strong immiscibility, with the purpose to demonstrate that, even in that case, the linear interconversion between the species may enforce the transition into a mixed state. The numerical analysis yields the corresponding critical value of the linear coupling, $\kappa_{\text{cr}} \approx 3.2$ (see right panel in Fig. 15.2). This value can be approximately predicted by (15.12), even though the equation was derived for uniform states in the infinite system (in the absence of the parabolic trap). Indeed, taking $u_0^2(x = 0) \approx 0.35$, as found at the central point of the trap, $x = 0$, in the symmetric state displayed in Fig. 15.2, (15.12) yields (for parameters corresponding to Fig. 15.2) $\kappa_{\text{cr}} \approx 3.5$, which is close to the above-mentioned numerically found value, $\kappa_{\text{cr}} = 3.2$.

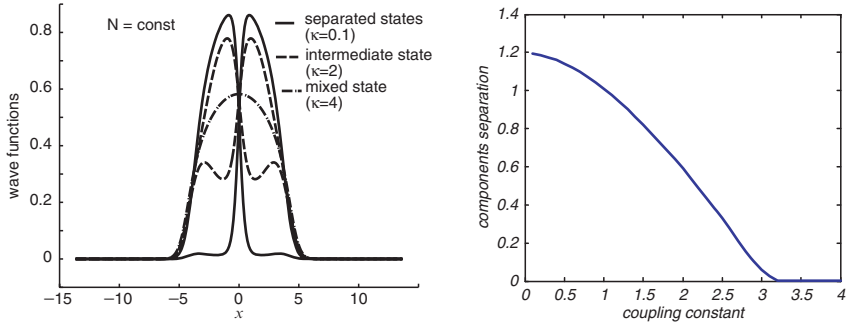


Fig. 15.2. *Left:* stationary states $u(x)$ and $v(x)$ of two species in the 1D boson mixture. One example corresponds to a strongly segregated state with weak linear coupling ($\kappa = 0.1$), and another one shows a completely mixed state for $\kappa = 4$, which somewhat exceeds the corresponding critical value, $\kappa_{\text{cr}} \approx 3.2$. An intermediate case is included too ($\kappa = 2$). Pairs of curves of the same type (*solid*, *dashed*, and *dashed-dotted*) depict the stationary wavefunctions of demixed (segregated) states pertaining to a given value of κ . The mixed state, with $u(x) \equiv v(x)$, is represented by a single *dashed-dotted* curve. *Right:* The order parameter (“components separation”), defined as per (15.19) (ξ_ϕ), vs. the linear-interconversion strength, κ . In the mixed phase ($\kappa > \kappa_{\text{cr}}$), $\xi_{\{\phi,\psi\}} \equiv 0$

For a quantitative description of the transition to miscibility, one can define the *order parameters*,

$$\begin{aligned} \xi_\phi &\equiv (N/2)^{-1} \int_{-\infty}^{+\infty} x |\phi(x)|^2 dx, \\ \xi_\psi &\equiv (N/2)^{-1} \int_{-\infty}^{+\infty} x |\psi(x)|^2 dx. \end{aligned} \quad (15.19)$$

As said above, we only consider the segregated states with equal numbers of atoms in the two species, hence one has $\xi_\phi + \xi_\psi = 0$. Then, the main characteristic of the phase transition (mixing–demixing) is the dependence of ξ_ϕ on the linear-interconversion rate κ , which is shown in the right panel of Fig. 15.2. In the mixed state, $\xi_\phi \equiv 0$.

As seen in the right panel of Fig. 15.2, the order parameter vanishes almost *linearly* with $\delta\kappa \equiv \kappa_{\text{cr}} - \kappa$, as one approaches the transition point, $\delta\kappa = 0$, while, in the standard theory of the second-order phase transitions in infinite media [26], the order parameter vanishes as $\sqrt{\delta\kappa}$. The difference is due to an effectively *finite size* of the BEC in the external trap.

Direct simulations of the stability of the mixed and segregated states within the framework of (15.3) and (15.4) (with $\Omega > 0$), reported in [11], confirm the expectation that the latter state, when it exists, is stable, while the mixed state is stable only when it is the single existing one, i.e., at $\kappa > \kappa_{\text{cr}}$. At $\kappa < \kappa_{\text{cr}}$, the unstable mixed state tends to develop the segregation.

15.4 Degenerate Binary Fermion Gases

A natural extension of the binary BEC is to develop a description of binary gases of fermion atoms in degenerate (quantum) states. A rigorous description of the dynamics of degenerate Fermi gases (DFGs) is based on the system of quantum-mechanical equations of motion for individual fermions (see, e.g., [27]), which is difficult to handle for many atoms. However, a simplified approach based on a mean-field-hydrodynamic (MFHD) equation for a single wavefunction, which is formally similar to the GPE, but features a different nonlinearity (see below), was elaborated for the description of DFGs in static [28] and dynamic [29] settings.

A system of coupled MFHD equations for a binary fermion gas was introduced in [30], where it was employed to predict the segregation in the binary DFG with repulsion between the species. In the recent work [31], the linear-interconversion terms were added to that system, which makes it possible to study the onset of miscibility (assuming the most experimentally relevant situation, with the two species representing two different spin states of the same fermion atom [6, 7]). The scaled 1D equations for the wavefunctions of the two fermion species are

$$i\phi_t = -\phi_{xx} + x^2\phi + \left(g_1|\phi|^{4/3} + g_2|\psi|^2\right)\phi - \kappa\psi, \quad (15.20)$$

$$i\psi_t = -\psi_{xx} + x^2\psi + \left(g_1|\psi|^{4/3} + g_2|\phi|^2\right)\psi - \kappa\phi, \quad (15.21)$$

supplemented by the normalization $\int[|\phi(x)|^2 + |\psi(x)|^2]dx = 2$. Here, the scaling is fixed by assuming $\Omega \equiv \sqrt{2}$, cf. (15.3) and (15.4), then the total number of atoms, N , is hidden in the parameter $g_1 \sim N^{2/3}$ accounting for the Fermi pressure, while the other coefficient, $g_2 \sim N$, accounts for the repulsion between the fermion species. As seen in (15.20) and (15.21), a characteristic feature of the MFHD approximation for the DFG is the power $4/3$ of the nonlinear self-repulsion terms.

Straightforward analysis of uniform mixed solutions, $u = v = u_0 e^{-i\mu t}$, to the counterparts of (15.20) and (15.21) for the infinite system (without the parabolic potential) yields a critical value of the linear-conversion rate at the point of the miscibility–immiscibility transition,

$$\kappa_{\text{cr}} = g_2 u_0^2 - (2/3)g_1 u_0^{4/3}, \quad (15.22)$$

(cf. (15.12)), the corresponding value of the chemical potential being $\mu_{\text{cr}} = (5g_1/3)u_0^{4/3}$. Formally negative values given by (15.22) at $g_2 < g_2^{\text{cr}} \equiv (2/3)g_1 u_0^{-2/3}$ imply that the binary DFG remains in the mixed state even with $\kappa = 0$.

Numerical solution of the stationary version of full (15.20) and (15.21), obtained with substitution $\{\phi, \psi\} = e^{-i\mu t} \{\Phi(x), \Psi(x)\}$, demonstrates a segregation pattern in the immiscible state of the binary fermion gas trapped in

the parabolic potential (see Fig. 15.3) which is drastically different from its counterpart in the boson gas, cf. left panel of Fig. 15.2. Indeed, in the fermion model the components do not form a DW, but, instead, arrange themselves into *antilocked* density waves, with maxima in one component coinciding with minima in the other. This pattern is characterized by its order parameter (cf. (15.19)),

$$\Xi \equiv \int_{-\infty}^{+\infty} x^2 [\Phi^2(x) - \Psi^2(x)] dx / \int_{-\infty}^{+\infty} x^2 [\Phi^2(x) + \Psi^2(x)] dx. \quad (15.23)$$

Another drastic difference from the segregation picture in the boson mixture is the spontaneous symmetry breaking of the number of atoms in the two species, N_1 and N_2 : while the states in the binary BEC reported in [11] have $N_1 = N_2$, the states found in [31], and shown in Fig. 15.4, are characterized by nonzero values of the additional *stoichiometric order parameter*, $\nu \equiv (N_1 - N_2) / (N_1 + N_2)$ (on the other hand, states with $\nu \neq 0$ may be possible in the binary boson gas too, as states of this type were not looked for in [11]). A transition to the mixed state with the increase of linear-mixing strength κ is characterized by respective dependences of both order parameters, Ξ and ν , on κ , as shown in Fig. 15.4.

Some of these numerical results can be explained by dint of a VA based on a simple Gaussian *ansatz*, $\{\Phi, \Psi\} = \{a, b\} e^{-x^2/2}$, with constant a and b [31]. In terms of this *ansatz*, the normalization condition fixes $a^2 + b^2 = 2/\sqrt{\pi}$, and the stoichiometric order parameter is $\nu = (\sqrt{\pi}/2)(a^2 - b^2)$. While this *ansatz* does not account for the formation of the modulated-density waves, it can explain the spontaneous breaking between the numbers of atoms in the two species. The most essential prediction of the VA is the critical value of the linear-interconversion rate at which the symmetry breaking sets in, $\kappa_{cr} \equiv g_2/\sqrt{2\pi} - 2g_1/(\sqrt{15}\pi^{1/3})$, cf. its counterpart (15.22) for the uniform states. This critical value vanishes at $g_2 = g_2^{cr} \equiv 2\sqrt{2/15}\pi^{1/6}g_1 \approx 0.884g_1$, implying that (as well as in the case of the uniform states, see above), at

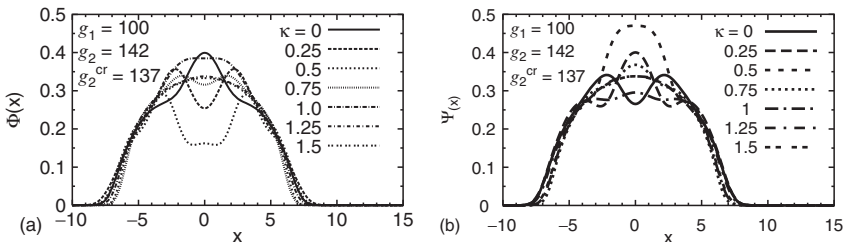


Fig. 15.3. A generic set of ground state wavefunctions of the binary degenerate fermion gas, $\Phi(x)$ and $\Psi(x)$, as obtained from the numerical solution of the stationary version of (15.20) and (15.21) for $g_1 = 100$ and $g_2 = 142$ and different values of κ

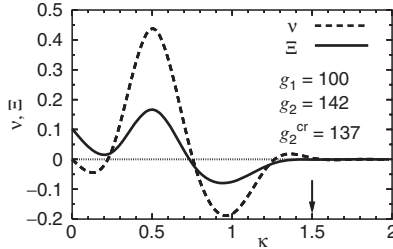


Fig. 15.4. Order parameters which characterize the spontaneously established inequality in numbers of atoms between the linearly coupled immiscible species in the fermion gas, ν , and anti-locking in the spatial density modulation of the species, Ξ (see (15.23)), as functions of κ . The arrow shows critical value κ_{cr} , at which complete mixing sets in. This example is borrowed from [31]; g_2^{cr} is the critical value of the interspecies repulsion, such that at $g_2 < g_2^{\text{cr}}$ the binary fermion gas falls into the mixed state even without the interconversion between the species, i.e., at $\kappa = 0$ (see text)

$g_2 < g_2^{\text{cr}}$, the binary DFG is in the mixed state even in the absence of the linear coupling [31].

15.5 Symbiotic Solitons in Binary BECs

It is well known that 1D configurations of BECs give rise to solitons of two distinct types: regular ones in self-attractive condensates (${}^7\text{Li}$), and gap solitons in self-repulsive condensates trapped in a periodic potential induced by optical lattices (OLs), see reviews of these topics in [32] (cf. Chap. 2) and [33] (cf. Chap. 6), respectively. In binary BECs, new types of solitons were predicted in the case when each species is self-repulsive, but the interspecies interaction is attractive, i.e., on the contrary to the case of repulsion between the components considered above, the respective system of GPEs (15.3) and (15.4) has $g_1 > 0$ and $g_2 < 0$. Solitons in this model, termed *symbiotic solitons*, may be stable against small perturbations, and withstand collisions between themselves [34].

An alternative setting is described by (15.3) and (15.4) with $g_1 < 0$ and $g_2 > 0$, corresponding to the mixture of two self-attractive condensates which repel each other. In an infinite system, each component would form its own soliton, and they would separate due to the mutual repulsion. However, in the presence of the external trap, the balance between the soliton repulsion and their trap confinement gives rise to a stable state with a finite separation between the solitons. This state may be interpreted as a two-component soliton with an *intrinsic* DW [35]. We also note in passing that depending on the relative signs of the intraspecies and interspecies interactions, one can also produce different species of solitary waves such as dark-antidark, dark-gray, bright-antidark or bright-gray ones [36].

An idea leading to a fermionic counterpart of symbiotic solitons was pursued in [37], where it was demonstrated that stable solitons may exist in a binary DFG if the two species of fermions attract each other, and the respective MFHD equations, (15.20) and (15.21), may be used, with $g_2 < 0$. In this connection, it is relevant to mention that stable 1D solitons and soliton trains were also predicted in a model of a Bose–Fermi mixture with repulsion between bosons and attraction between bosons and fermions [38].

Another variety of the symbiotic mechanism supporting solitons in binary condensates may be realized in a BEC mixture trapped in the periodic OL potential, in the case when the dominant interaction is the interspecies repulsion. As shown in [39], this mechanism gives rise to *symbiotic gap solitons*. In the 2D geometry, the corresponding system of coupled GPEs is (cf. (15.3) and (15.4), and note that this model does not include the linear coupling)

$$i\phi_t = -\nabla^2\phi - \varepsilon [\cos(2x) + \cos(2y)]\phi + (\rho|\phi|^2 + |\psi|^2)\phi, \quad (15.24)$$

$$i\psi_t = -\nabla^2\psi - \varepsilon [\cos(2x) + \cos(2y)]\psi + (\rho|\psi|^2 + |\phi|^2)\psi, \quad (15.25)$$

where the OL wavenumber is scaled to $k = 2$, ε measures the OL depth, and $\rho \geq 0$ is a relative strength of the intraspecies repulsion. Equations (15.24) and (15.25) are symmetric because ϕ and ψ represent two different states of the same atom. Since these equations do not include the linear interconversion, the two numbers of atoms, N_1 and N_2 , are conserved separately. Solitons are adequately characterized by the total and relative numbers of atoms, $N \equiv N_1 + N_2$ and $N_r \equiv N_1/N_2$.

The parabolic potential trap is not included in (15.24) and (15.25), as the periodic potential is sufficient to support gap solitons [33]. The most fundamental case is $\rho = 0$, when gap solitons are supported solely by the interspecies repulsion. In fact, the same model with $\rho = 0$ may also apply to a binary DFG with repulsion between the species, neglecting the “hydrodynamic” self-repulsion, cf. (15.20) and (15.21) (the latter assumption may be justified if the interspecies repulsion is strong enough in comparison to the Fermi pressure).

Obviously, the bandgap structures for wavefunctions, ϕ and ψ , generated by the linearized versions of (15.24) and (15.25), are identical. Accordingly, two-component solitons, $\{\phi, \psi\} = e^{-i\mu_{1,2}t} \{u(x, y), v(x, y)\}$, with real functions u and v , may be categorized as *intrigap* and *intergap* ones if the two chemical potentials, μ_1 and μ_2 , belong to the same or different bandgaps. We note that, for shallow OLs, the 2D spectrum of the linearized equations contains a single gap (on the contrary to the 1D spectrum, where the number of bandgaps is (formally) always infinite), hence only intragap solitons are possible in that case. A stronger 2D OL supports two bandgaps, opening the way to construct 2D intergap solitons.

As shown in [39], intragap solitons sitting in the first (lowest) bandgap, or the component of the intergap soliton belonging to the first bandgap, have a *tightly bound* structure, with a single maximum of density (as in ordinary

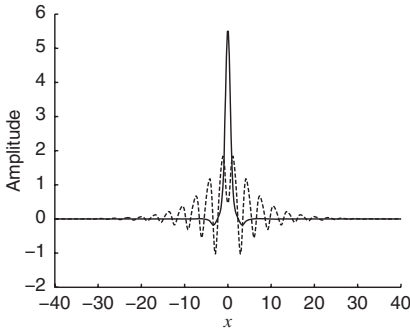


Fig. 15.5. An example of an intergap soliton, built as a bound state of tightly (solid) and loosely (dashed) bound components with equal norms ($N_r = 1$), for $\varepsilon = 4$ and $N = 70$. The corresponding chemical potentials, which fall in the first and second bandgaps, are $\mu_1 = -1.64$ and $\mu_2 = 3.3$, respectively. Shown are cross sections through $y = 0$ of the 2D stationary wavefunctions (“amplitudes”), $u(x, y)$ and $v(x, y)$

solitons). On the other hand, the solitons, or parts thereof, found in the second bandgap (if any) are *loosely bound*, featuring an undulate shape with many local maxima and zeros of the density, which is typical to gap solitons. The two components of an intergap soliton displayed in Fig. 15.5 present generic examples of both the tightly and loosely bound waveforms.

Numerical results demonstrate that, in shallow OLs, almost all the intragap solitons are stable; families of such solitons are displayed, in terms of the dependence of N on μ_1 and μ_2 , in panel (a) of Fig. 15.6. On the other hand, in a deep OL, where intergap solitons, as well as intragap ones sitting in the second bandgap, are possible, only relatively small portions of the soliton families are stable, see panel (b) in Fig. 15.6. A qualitatively similar picture is observed for the relative norm N_r [39]. As concerns unstable solitons, direct simulations demonstrate that, in most cases, they are completely destroyed by the instability.

In [39], symbiotic gap solitons were also investigated in the 1D version of the model. In that case, stability regions for the intragap solitons in the first bandgap and intergap solitons were accurately delineated, while all the intragap solitons in the second bandgap were found to be unstable (although their instability may be very weak in some cases). It has also been demonstrated that the addition of the intraspecies repulsion, i.e., $\rho > 0$ in (15.24) and (15.25), additionally stabilizes the solitons. In particular, intragap solitons in the second bandgap (in the 1D model) can be made completely stable in this way.

15.6 Domain-wall Crosses and “Propellers” in Two Dimensions

It is relevant to extend the concept of the DW to the 2D geometry [40]; this way, not only DWs cutting the condensate along a straight line were studied, but also circular DWs, which separate a less repulsive component in the middle of the trap and a more repulsive one forming an outer shell.

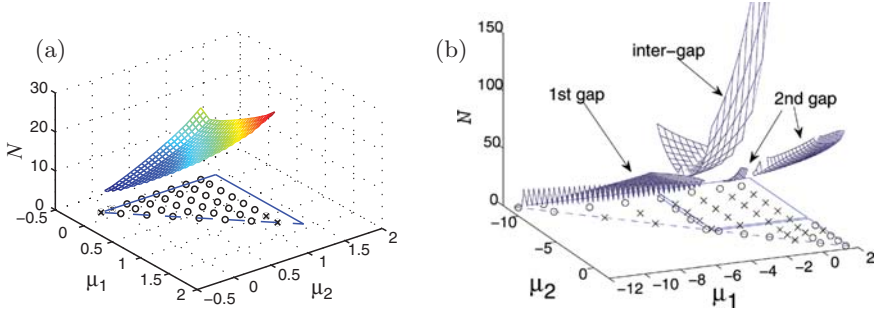


Fig. 15.6. (a) Existence and stability diagrams for intragap 2D solitons in the weak lattice potential, with $\varepsilon = 2$. The total norm of the soliton $N = N_1 + N_2$ is displayed vs. the chemical potentials of the two components, μ_1 and μ_2 . Solid lines in the (μ_1, μ_2) plane are the bandgap's borders, and the dashed diagonal is the symmetry axis, $\mu_1 = \mu_2$ (a mirror-image region on the other side of the diagonal is not shown). Stable and unstable solitons are designated, respectively, by circles (o) and crosses (x). (b) The same in a relatively strong lattice, with $\varepsilon = 10$. In this case, the linearization of the 2D Gross-Pitaevskii equation gives rise to two finite bandgaps, therefore the diagram includes the family of intergap solitons. “1st gap” and “2nd gap” refer to intragap solitons belonging to the respective gaps. Double solid lines separating the bandgaps in the (μ_1, μ_2) plane represent narrow Bloch bands between the gaps

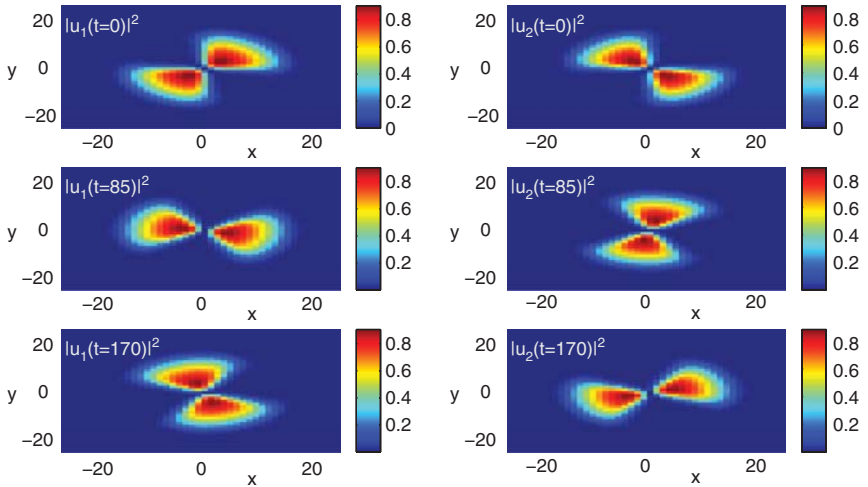


Fig. 15.7. A stable rotating cross (“propeller”) formed by two perpendicular domain-walls (with $N_1 = N_2$), for $g_{22}/g_{11} = 1.01$, $g_{12}/g_{11} = 1.52$, $\Omega = 0.1$, $\Omega_L = 0.012$. Snapshots of the density distributions in the two components are displayed at times $t = 0$, $t = T/6$ and $t = T/3$, where $T = 2\pi/\Omega_L \approx 500$ is the rotation period

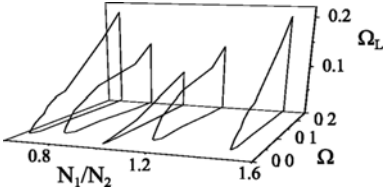


Fig. 15.8. The stability region for rotating domain-wall crosses. Note that the trap strength Ω and rotation frequency Ω_L required for the stable rotation take their minimum values in the symmetric case, $N_1/N_2 = 1$

It is also natural to consider a “cross” formed by the intersection of two rectilinear DWs, additionally assuming that the wavefunctions of the same species filling each pair of opposite quadrants have opposite signs (otherwise, the cross is subject to structural instability, as a small deformation may split it into a pair of quasi-parallel DWs). These 2D patterns were introduced and investigated in [41]. Also considered in that work was a situation when the trap containing the binary BEC rotates, at angular velocity Ω_L . In that case, (15.3) and (15.4) are replaced by the following scaled equations, written in the co-rotating reference frame:

$$i\phi_t = -(1/2)\nabla^2\phi - \Omega_L \hat{L}_z\phi + (\Omega^2/2)r^2\phi + (g_{11}|\phi|^2 + g_{12}|\psi|^2)\phi, \quad (15.26)$$

$$i\psi_t = -(1/2)\nabla^2\psi - \Omega_L \hat{L}_z\psi + (\Omega^2/2)r^2\psi + (g_{22}|\psi|^2 + g_{12}|\phi|^2)\psi, \quad (15.27)$$

where the angular-momentum operator is $\hat{L}_z = i(x\partial_y - y\partial_x)$, Ω_L is the rotation frequency, and the possibility of having unequal intraspecies scattering lengths in the two components, $g_{11} \neq g_{22}$, is restored. Because this system does not contain linear coupling, the two numbers of atoms, N_1 and N_2 , are conserved separately, as in (15.24) and (15.25). Accordingly, the DWs forming the cross intersect under angle $\pi N_2 / (N_1 + N_2)$, where $N_2 \leq N_1$ is assumed.

Investigation of the stability of nonrotating rectilinear DWs and crosses reported in [41] has demonstrated that the DW is stable only for $\Delta > 0.061$ (see (15.6)), which rules them out in the mixed-spin-state condensates of ^{87}Rb and ^{23}Na with smaller Δ as discussed above. On the other hand, the cross is stable for all positive values of Δ . Further, the cross readily remains stable in the co-rotating frame (thus becoming a “propeller”), as shown in Fig. 15.7.

The stability region for the “propellers” in parameter space $(N_1/N_2, \Omega, \Omega_L)$, which is shown in Fig. 15.8, was identified in [41] by means of systematic simulations. It was also found that all “higher-order” crosses, formed by the intersection of more than two DWs, are unstable. On the other hand, rotating straight DWs (single ones, which do not form crosses) may be stable in certain parameter regions.

15.7 More Complex Models

In addition to the theoretical models of BEC mixtures presented in some detail above, more sophisticated models were elaborated too. In particular,

while the cubic nonlinearity is fundamental to the GPE in three dimensions, the cubic terms in 1D systems of GPEs, such as (15.3) and (15.4), provide for the correct description only in the limit case of weak nonlinearity. In a more general case, when the effective 1D geometry is supported by tight confinement in the transverse plane, a consistent reduction of the underlying cubic 3D GPE to an effective 1D equation yields a *nonpolynomial Schrödinger equation* (NPSE), as first shown in [42]. Recently, a system of coupled NPSEs was derived for a binary BEC described by mean-field wavefunctions $\psi_k(x, t)$, $k = 1, 2$, in the nearly 1D trap [43]. It takes a tractable form in the case when the coefficients of the intra- and inter-species interactions in the original 3D equation are equal

$$i \frac{\partial \psi_k}{\partial t} = \left[-\frac{1}{2} \frac{\partial^2}{\partial x^2} + V(x) + \frac{g}{\bar{g}} (|\psi_1|^2 + |\psi_2|^2) + \frac{1}{2} \left(\frac{1}{\bar{g}} + \bar{g} \right) \right] \psi_k,$$

where $\bar{g} = \sqrt{1 + g(|\psi_1|^2 + |\psi_2|^2)}$, $V(x)$ is the 1D (axial) potential, and g the nonlinearity coefficient. This model allows to predict various dynamical effects, such as inelastic collisions of *scalar solitons*, i.e., ones in fields ψ_1 and ψ_2 [43].

In certain cases, *three-component* BEC models appear naturally, an important case being that of spinor condensates, formed by atoms with spin 1, hence the mean-field description is based on a set of three wavefunctions. In a normalized form, the respective system of coupled GPEs is

$$\begin{aligned} i\partial_t \phi_{\pm 1} &= -\partial_x^2 \phi_{\pm 1} - (\nu + a)(|\phi_{\pm 1}|^2 + 2|\phi_0|^2)\phi_{\pm 1} \\ &\quad - (\nu - a)|\phi_{\mp 1}|^2 \phi_{\pm 1} - 2a\phi_{\mp 1}^* \phi_0^2, \\ i\partial_t \phi_0 &= -\partial_x^2 \phi_0 - 2\nu|\phi_0|^2 \phi_0 \\ &\quad - (\nu + a)(|\phi_{+1}|^2 + |\phi_{-1}|^2)\phi_0 - 2a\phi_{+1}\phi_{-1}\phi_0^*, \end{aligned} \quad (15.28)$$

where the asterisk stands for the complex conjugate, the subscripts attached to the wavefunctions refer to the corresponding value of the z -component of the atomic spin, and coefficients ν and a are combinations of constants accounting for spin-independent and spin-exchange interactions between atoms [44]. Note that the equations include only cubic coupling terms. In the special case of $\nu = a = 1$, (15.28) are integrable by means of the inverse scattering transform [45].

Equation (15.28) may give rise to multi-component patterns, such as DWs. However, the corresponding states have not yet been investigated (in sufficient detail) in models of the spinor condensate, nor realized in the experiment.

15.8 Conclusions

Similar to the situation in other topics dealing with the nonlinear dynamics and patterns in BEC, theoretical studies of mixed condensates have advanced much farther than the corresponding experiments. Many results predicted in

theoretical works wait for realization in the laboratory. In fact, the predicted new effects do not require very exotic or extreme experimental conditions, therefore observation of these effects may be expected in near future.

As concerns further progress in theoretical studies, there remain quite a few unexplored possibilities that call for analysis, even in the simplest mean-field approximation. Among them are three-dimensional patterns, including those that may be supported by OLs (optical lattices). Recently, nontrivial localized states have been predicted in a system of coupled discrete 3D nonlinear Schrödinger equations, which may be regarded as corresponding to the limit case of a very deep OL. An interesting example is a stable complex consisting of two discrete localized vortices oriented perpendicular to each other [46], which may have its counterpart in the continuum. One can also imagine still more sophisticated objects, such as a pair of knotted vortex rings oriented along two mutually orthogonal planes, and various states resembling Skyrmions. In the 2D setting, an interesting issue may be a two-component state with *hidden vorticity*, i.e., a combination of vortices in the two components with opposite values of their vorticity. Recently, it was demonstrated that such objects have their stability regions in two-component models with cubic-quintic and saturable nonlinearities [47] (which is relevant for applications to nonlinear optics), as well as in a discrete version of the latter model [48]. A challenging issue is to find such stable vortex complexes, with the total vorticity equal to zero, in coupled GPEs in two dimensions.

References

1. C.J. Myatt, E.A. Burt, R.W. Ghrist, E.A. Cornell, C.E. Wieman, Phys. Rev. Lett. **78**, 586 (1997)
2. G. Modugno, M. Modugno, F. Riboli, G. Roati, M. Inguscio, Phys. Rev. Lett. **89**, 190404 (2002)
3. G.D. Telles, A.R.L. Caires, V.S. Bagnato, L.G. Marcassa, Phys. Rev. Lett. **92**, 133203 (2004)
4. S.B. Papp, C.E. Wieman, Phys. Rev. Lett. **97**, 180404 (2006)
5. M. Modugno, F. Ferlaino, F. Riboli, G. Roati, G. Modugno, M. Inguscio, Phys. Rev. A **68**, 043626 (2003); C. Ospelkaus, S. Ospelkaus, L. Humbert, P. Ernst, K. Sengstock, K. Bongs, Phys. Rev. Lett. **97**, 120402 (2006)
6. B. DeMarco, D.S. Jin, Science **285**, 1703 (1999)
7. K.M. O’Hara, S.L. Hemmer, M.E. Gehm, S.R. Granade, J.E. Thomas, Science **298**, 2179 (2002); K.E. Strecker, G.B. Partridge, R.G. Hulet, Phys. Rev. Lett. **91**, 080406 (2003); G.B. Partridge, W. Li, Y.A. Liao, R.G. Hulet, M. Haque, H.T.C. Stoof, Phys. Rev. Lett. **97**, 190407 (2006)
8. D.S. Hall, M.R. Matthews, J.R. Ensher, C.E. Wieman, E.A. Cornell, Phys. Rev. Lett. **81**, 1539 (1998)
9. B.P. Anderson, P.C. Haljan, C.E. Wieman, E.A. Cornell, Phys. Rev. Lett. **85**, 2857 (2000); V. Schweikhard, I. Coddington, P. Engels, S. Tung, E.A. Cornell, Phys. Rev. Lett. **93**, 210403 (2004)
10. R.J. Ballagh, K. Burnett, T.F. Scott, Phys. Rev. Lett. **78**, 1607 (1997)

11. M.I. Merhasin, B.A. Malomed, R. Driben, J. Phys. B **38**, 877 (2005)
12. V.P. Mineev, Zh. Eksp. Teor. Fiz. **67**, 263 (1974) [Sov. Phys. JETP **40**, 132 (1974)]
13. H. Pu, N.P. Bigelow, Phys. Rev. Lett. **80**, 1130 (1998); D.S. Hall, M.R. Matthews, J.R. Ensher, C.E. Wieman, E.A. Cornell, Phys. Rev. Lett. **81**, 1539 (1998)
14. D.M. Stamper-Kurn, M.R. Andrews, A.P. Chikkatur, S. Inouye, H.-J. Miesner, J. Stenger, W. Ketterle, Phys. Rev. Lett. **80**, 2027 (1998)
15. A. Kuklov, N. Prokof'ev, B. Svistunov, Phys. Rev. A **69**, 025601 (2004)
16. J. Williams, R. Walser, J. Cooper, E. Cornell, M. Holland, Phys. Rev. A **59**, R31 (1999); Phys. Rev. A **61**, 033612 (2000); P. Öhberg, S. Stenholm, Phys. Rev. A **59**, 3890 (1999); C. Lee, L. Shi, K. Gao, Phys. Rev. A **69**, 033611 (2004)
17. D.T. Son, M.A. Stephanov, Phys. Rev. A **65**, 063621 (2002)
18. S.D. Jenkins, T.A.B. Kennedy, Phys. Rev. A **68**, 053607 (2003)
19. Q.-H. Park, J.H. Eberly, Phys. Rev. A **70**, 021602(R) (2004)
20. K. Kasamatsu, M. Tsubota, M. Ueda, Int. J. Mod. Phys. B **19**, 1835 (2005)
21. M. Trippenbach, K. Góral, K. Rzażewski, B. Malomed, Y.B. Band, J. Phys. B **33**, 4017 (2000)
22. S. Coen, M. Haelterman, Phys. Rev. Lett. **87**, 140401 (2001)
23. M. Yu, C.J. McKinstrie, G.P. Agrawal, Phys. Rev. E **48**, 2178 (1993)
24. B.A. Malomed, Phys. Rev. E **50**, 1565 (1994)
25. B.A. Malomed, in *Progress in Optics*, vol. 43, ed. by E. Wolf (North-Holland, Amsterdam, 2002) pp. 71–193
26. L.D. Landau, E.M. Lifshitz, *Statistical Physics* (Butterworth-Heinemann, Oxford, 1980)
27. M. Salerno, Phys. Rev. A **72**, 063602 (2005)
28. A. Amoruso, I. Meccoli, A. Minguzzi, M.P. Tosi, Eur. Phys. J. D **8**, 361 (2000); R. Roth, H. Feldmeier, J. Phys. B **34**, 4629 (2001)
29. P. Capuzzi, A. Minguzzi, M.P. Tosi, Phys. Rev. A **67**, 053605 (2003); S.K. Adhikari, Phys. Rev. A **70**, 043617 (2004); Phys. Rev. A **72**, 053608 (2005); J. Phys. B **38**, 3607 (2005)
30. S.K. Adhikari, Phys. Rev. A **73**, 043619 (2006)
31. S.K. Adhikari, B.A. Malomed, Phys. Rev. A **74**, 053620 (2006)
32. K.E. Strecker, G.B. Partridge, A.G. Truscott, R.G. Hulet, New J. Phys. **5**, 73 (2003)
33. O. Morsch, M. Oberthaler, Rev. Mod. Phys. **78**, 179 (2006)
34. V.M. Pérez-García, J. Belmonte Beitia, Phys. Rev. A **72**, 033620 (2005)
35. P.G. Kevrekidis, H. Susanto, R. Carretero-González, B.A. Malomed, D.J. Frantzeskakis, Phys. Rev. E **72**, 066604 (2005)
36. P.G. Kevrekidis, H.E. Nistazakis, D.J. Frantzeskakis, B.A. Malomed, R. Carretero-González, Eur. Phys. J. D **28**, 181 (2004)
37. S.K. Adhikari, Eur. Phys. J. D **40**, 157 (2006)
38. T. Karpiuk, M. Brewczyk, S. Ospelkaus-Schwarzer, K. Bongs, M. Gajda, K. Rzażewski, Phys. Rev. Lett. **93**, 100401 (2004)
39. A. Gubeskys, B.A. Malomed, I.M. Merhasin, Phys. Rev. A **73**, 023607 (2006)
40. T.L. Ho, V.B. Shenoy, Phys. Rev. Lett. **77**, 3276 (1996); B.D. Esry, C.H. Greene, J.P. Burke Jr., J.L. Bohn, Phys. Rev. Lett. **78**, 3594 (1997); P. Öhberg, S. Stenholm, Phys. Rev. A **57**, 1272 (1998); B.D. Esry, C.H. Greene, Phys. Rev. A **59**, 1457 (1999); A.A. Svidzinsky, S.T. Chui, Phys. Rev. A **68**, 013612 (2003)

41. B.A. Malomed, H.E. Nistazakis, D.J. Frantzeskakis, P.G. Kevrekidis, Phys. Rev. A **70**, 043616 (2004); B.A. Malomed, H.E. Nistazakis, P.G. Kevrekidis, D.J. Frantzeskakis, Math. Comput. Simul. **69**, 400 (2005)
42. L. Salasnich, Laser Phys. **12**, 198 (2002); L. Salasnich, A. Parola, L. Reatto, Phys. Rev. A **65**, 043614 (2002); Phys. Rev. A **66**, 043603 (2002)
43. L. Salasnich, B.A. Malomed, Phys. Rev. A **74**, 053610 (2006); C.V. Ciobanu, S.-K. Yip, Tin-Lun Ho, Phys. Rev. A **61**, 033607 (2000)
44. T.L. Ho, Phys. Rev. Lett. **81**, 742 (1998)
45. J. Ieda, T. Miyakawa, M. Wadati, Phys. Rev. Lett. **93**, 194102 (2004)
46. P.G. Kevrekidis, B.A. Malomed, D.J. Frantzeskakis, R. Carretero-González, Phys. Rev. Lett. **93**, 080403 (2004); R. Carretero-González, P.G. Kevrekidis, B.A. Malomed, D.J. Frantzeskakis, Phys. Rev. Lett. **94**, 203901 (2005)
47. A.S. Desyatnikov, D. Mihalache, D. Mazilu, B.A. Malomed, C. Denz, F. Lederer, Phys. Rev. E **71**, 026615 (2005); A.S. Desyatnikov, D. Mihalache, D. Mazilu, B.A. Malomed, F. Lederer, Phys. Lett. A **364**, 231 (2007)
48. P.G. Kevrekidis, D.E. Pelinovsky, Proc. Roy. Soc. A **462**, 2671 (2006)

Multi-Component Condensates: Experiment

D.S. Hall

16.1 Introduction

The dawning recognition of the link between Bose–Einstein condensation (BEC) and superfluidity in ^4He led to the first theoretical contemplations of multi-component condensates in the mid-late 1950s [1]. The first candidate mixtures were of ^4He and ^6He , but the 0.8 s lifetime of the latter prevented any serious approach towards a true superfluid mixture, as had been recognized in experiments performed earlier that decade [2]. However, theoretical treatment of this mixture laid important groundwork for the later study of multi-component dilute-gas condensates [3]. The discovery of superfluidity in ^3He in the early 1970s presented a new possibility, in that the vector order parameter of the ^3He superfluid allows for *internal* degrees of freedom that manifest themselves in behavior such as domain-walls and spin textures [4]. Internal degrees of freedom were subsequently considered theoretically in a dilute Bose-condensed gas inhabiting two different hyperfine levels of spin-polarized hydrogen [5].

Multi-component condensates in dilute alkali gases were observed shortly after the achievement of Bose–Einstein condensation in 1995 [6–8]. The first of these experiments observed two coexisting condensates in two different hyperfine states of ^{87}Rb [9]. This experiment is the progenitor of a class of experiments on effective two-level condensates that are often coupled by resonant microwave or radiofrequency radiation. In the absence of this external coupling, spin-changing collisions lead to loss, not to interconversion between the species. Many of these experiments involve hyperfine states of magnetically-trapped ^{87}Rb , due to its unusually low hyperfine-changing collision rate. We will refer to these systems as the *pseudospin-1/2* (or simply *pseudospinor*) condensate systems, and they are the subject of Sect. 16.2.

The second main class of experiments (Sect. 16.3) follows in the footsteps of an early experiment in ^{23}Na [10], and consists of optically-trapped condensates that inhabit the various Zeeman levels of a single hyperfine level. In these *spinor* condensates the spin degree of freedom is liberated to some degree,

and spin-changing collisions lead to changing population among the magnetic sublevels. These experiments inherit some of the features of the superfluid ^3He systems, with behavior that includes spin dynamics and exotic topological defects.

As of this writing the only multiple condensate composed of different atoms has been achieved in a magnetic trap with ^{41}K and ^{87}Rb , where the potassium atoms were cooled sympathetically by the rubidium atoms [11]. The two condensates overlapped slightly in the magnetic trap, and the observed stability of the double condensate system, even in response to a dynamic perturbation in which one condensate periodically interacted with the other, indicated that the interspecies scattering length is positive [12]. The periodic interactions of the two condensates also caused rotational excitation of the condensates in the magnetic trap as one condensate slid past the other [12]. Experiments such as these are still in their infancy, but promise a rich variety of interesting terrain to explore.

The field has already expanded beyond what we can hope to cover in this limited space; no attempt is made, therefore, at completeness. In particular, we explore here neither the burgeoning fields of Bose–Fermi mixtures (e.g., [13] and Chap. 15) nor multi-component condensates in optical lattices (e.g., [14]).

In the remainder of this section we briefly consider imaging and trapping techniques that differ from their single-particle counterparts.

16.1.1 Imaging

Imaging techniques for multi-component condensates may be roughly divided into destructive (absorption) techniques, and nondestructive (phase contrast) techniques. In absorption imaging, the condensate scatters light out of a near-resonant beam on a cycling transition, casting a shadow that is imaged on a charge-coupled device (CCD) camera and subsequently processed to reveal the atomic density distribution. The process is destructive since the scattering process dramatically heats the sample. For multi-component condensates of different atomic species the frequency of the probe laser beam can generally be used to discriminate between the two species.

For systems involving different hyperfine levels, state-sensitive destructive imaging is slightly more complicated. For alkalis such as ^{87}Rb and ^{23}Na , the cycling transition is between the upper hyperfine level and the optically-excited states. With hyperfine intervals on the order of GHz, atoms in the upper hyperfine level are selectively imaged in the usual way. A brief pulse of “repump” light can take atoms from the lower hyperfine level to the upper hyperfine level, making it possible to image both states simultaneously with subsequently applied probe light. Atoms in the lower hyperfine level may be selectively imaged by preceding the repump pulse with a strong pulse of light, resonant with atoms in the upper hyperfine level, which serves to push them out of the field of view [15].

Laser detuning techniques are not quite as useful in discriminating between atoms in different Zeeman levels, since the level splittings are typically on the order of the laser linewidth. State-selective imaging in this case uses the fact that different Zeeman levels have different magnetic moments, and therefore separate spatially when briefly (\sim few ms) subjected to a magnetic field gradient (\sim few tens of G per cm). The different spin states therefore appear in different locations on the CCD. By making use of the quadratic Zeeman shift, atoms in different hyperfine levels can also be distinguished in this way.

In nondestructive (phase-contrast) imaging, an off-resonant probe beam is phase-shifted by the presence of the condensate; using a homodyne interference technique, the phase information is then converted to intensity information, from which the atomic density distributions can be extracted [16]. Atoms in different hyperfine levels can be distinguished nondestructively by tuning the probe laser between the two hyperfine levels and the optically excited state [17]. Atoms in the two hyperfine levels induce phase shifts of opposite sign, which leads to enhancement or diminution of the phase-contrast signal according to the local density. A phase-contrast technique has also been developed to distinguish between atoms in different Zeeman sublevels, as described in [18].

16.1.2 Trapping

The first Bose–Einstein condensates were created in magnetic traps, which confine weak-field seeking atoms in the minimum of an inhomogeneous magnetic field. The external potentials observed by the atoms depend on their magnetic moments through both the linear and quadratic Zeeman effects. In time-dependent field traps, such as the time-averaged orbiting potential (TOP) trap [19], other geometric forces can also be important [20, 21] and can be used to create differential potentials for states with similar magnetic moments.

Optical traps, on the other hand, use an induced *electric* dipole force, produced near the focus of an intense, far-detuned laser beam, to achieve confinement almost completely independent of the spin state of the atom [22]. It is, of course, this property that has permitted the proliferation of spinor condensate studies. The initial optical trapping experiments used condensates that were first produced in magnetic traps; it has since become common to create condensates in optical traps directly, as first achieved by the Georgia Tech group [23].

16.2 Pseudospinor Condensates

In this section we examine the physics of binary Bose–Einstein condensates, coupled by externally-applied radiofrequency and/or microwave fields. The name *pseudospinor* arises from the well-known equivalence of a two-level

system with a spin-1/2 system. An effective spin-1/2 system (with coupling) is succinctly pictured in terms of the Bloch sphere [24]. The two levels may be two different hyperfine, Zeeman, or even field-dressed sublevels of the same atom, provided they form a distinct doublet that can be appropriately coupled together. Our main focus will be on pseudospinor condensates realized in different hyperfine levels of ^{87}Rb . The road to this pseudospin doublet was paved by the observation, contrary to expectation, of a stable double condensate in the $|2, 2\rangle$ and $|1, -1\rangle$ hyperfine states of ^{87}Rb [9]. The coexisting condensates demonstrated that hyperfine-changing collisions were highly suppressed in ^{87}Rb , later understood theoretically as a result of the accidental near-equivalence of the singlet and triplet scattering lengths [25, 26]. This early experiment also demonstrated that the interspecies atomic interaction was repulsive, and the utility of sympathetic cooling – a process that would later be extended to producing condensates in different atomic species [12].

After the first experimental double-condensate production at JILA [9], binary condensate studies were quickly extended to the $|2, 1\rangle$ and $|1, -1\rangle$ hyperfine states (henceforth $|2\rangle$ and $|1\rangle$, respectively; see Fig. 16.1a). Both of these states experience nearly identical magnetic trapping potentials, since they have (to first order) the same magnetic moment and mass. The price paid for these advantages is the diminished magnetic trap lifetime of the $|2\rangle$ state due to two-body hyperfine-changing and spin-relaxing collisions. States $|1\rangle$ and $|2\rangle$ are separated by two units of angular momentum, and coupled with a two-photon radiofrequency and microwave transition via a virtual level close to the $|2, 0\rangle$ state. For intermediate-state detunings of ~ 1 MHz, the two-photon Rabi frequency is typically less than 1 kHz. Interconversion between the two states in the absence of the coupling drive is not observed; and thus the number of atoms in each state is conserved on a time-scale short compared to the inelastic losses. Any desired fraction of atoms can be converted from $|1\rangle$ to $|2\rangle$ with appropriate choice of the pulse length and overall strength of the coupling drive. Insofar as the pulse length is short compared to the timescale of atomic motion, the pulse may be considered to transfer atoms instantaneously from $|1\rangle$ to $|2\rangle$.

In a simple first experiment that demonstrates the main features of this pseudospinor system [15], the JILA group created a $|1\rangle$ condensate in equilibrium and transferred nearly 100% of it to the $|2\rangle$ state. Assuming both states experienced the same external potential, the principal effect of the transfer was to change the condensate scattering length instantaneously from its initial value (a_{11}) to a different value (a_{22}). The $|2\rangle$ condensate was therefore not in a stationary state, and it began to oscillate in a superposition of two $m = 0$ modes. From a hydrodynamic analysis of the measured axial and radial widths, the authors extracted the ratio of the two scattering lengths, $a_{11}/a_{22} = 1.062(12)$. In addition to establishing the properties of the binary condensate system, this experiment was among the first to demonstrate that fundamental atomic properties could be determined from an analysis of condensate dynamics.

16.2.1 Component Separation and Domain Formation

The time-evolution of a double condensate is governed by a pair of coupled GPEs,

$$i\hbar \frac{\partial \psi_i}{\partial t} = \left(-\frac{\hbar^2 \nabla^2}{2m} + V_{\text{ext}}^{(i)} + \frac{4\pi\hbar^2 a_{ii}}{m} |\psi_i|^2 + \frac{4\pi\hbar^2 a_{12}}{m} |\psi_j|^2 \right) \psi_i, \quad (16.1)$$

where i, j take on the values 1, 2 ($i \neq j$) and a_{12} being the interspecies scattering length. Neglecting kinetic energy, the double condensate system is stable against perturbations provided the relation $a_{12} < \sqrt{a_{11}a_{22}}$ holds; otherwise, it is unstable against component separation into domains populated mostly of either $|1\rangle$ or $|2\rangle$ [27–29] (see also Chap. 15).

The JILA group explored interactions between two condensates after transferring half of the atoms from $|1\rangle$ to $|2\rangle$ with nearly identical trapping potentials [30]. The condensates separated quickly ($\sim 1/2$ a radial period) into regions of mostly $|1\rangle$ or mostly $|2\rangle$ in an apparent “ball–shell” configuration, as viewed from the side (see Fig. 16.1b). The *total* density distribution remained largely unchanged. Since $a_{11} > a_{22}$, the $|1\rangle$ atoms experienced a positive “buoyancy” with respect to the $|2\rangle$ atoms, and the observed pattern of $|1\rangle$ atoms surrounding a $|2\rangle$ core minimized the total energy of the system. The observed approach to this equilibrium state was highly damped, with subsequent evolution consisting mainly of radial separation of the “ball” and “shell.”

In order to examine the boundary between the two condensates a vertical offset was introduced between the two trapping potentials, such that the $|1\rangle$ condensate had an equilibrium displacement $0.4\text{ }\mu\text{m}$ above the $|2\rangle$ condensate [20, 30]. The ensuing condensate behavior, now driven both by the mean-field and the trapping potential difference, involved dramatic rearrangement of the components and the appearance of transient interlacing spin domains that nevertheless preserved the *overall* density profile. Once again the motion was highly damped, and the condensates approached equilibrium with the $|1\rangle$ condensate above the $|2\rangle$ condensate and a significant overlap region at their common boundary. Experiments focusing on this boundary region are discussed in Sect. 16.2.2, below.

The strong damping observed in these first component separation experiments has resisted theoretical analysis. Recently the author’s laboratory has revisited these experiments, with attention paid to the cylindrical symmetry of the trapping potential ($\lesssim 0.5\%$) and coincidence of the external trapping potentials. We confirm most of the basic features observed by the JILA group, such as component separation and preservation of total density. We do not, however, observe the extreme damping that brings the condensates to equilibrium. Instead, we find an oscillatory behavior of the condensates that continues throughout the lifetime of the $|2\rangle$ condensate. Imaging the condensates from the top, i.e., along the symmetry axis of the trap, we also observe significantly more complex behavior than could be inferred from the side, with the

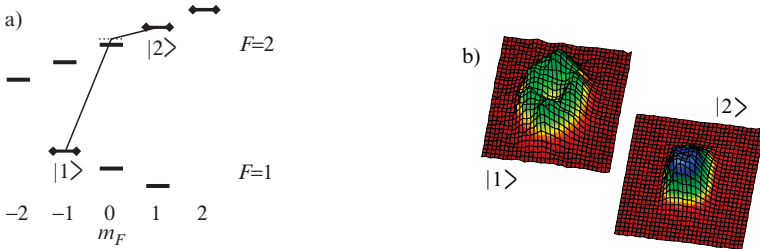


Fig. 16.1. (a) Hyperfine levels for ^{23}Na and ^{87}Rb . The magnetically trapped levels are indicated with diamonds, and the two-photon transition between states $|1\rangle$ and $|2\rangle$ is shown through a virtual state near the $|2, 0\rangle$ state, indicated by the dashed line. (b) Component separation and formation of a “ball” and “shell” density distribution in ^{87}Rb , after 30 ms evolution. Figure adapted from [30]

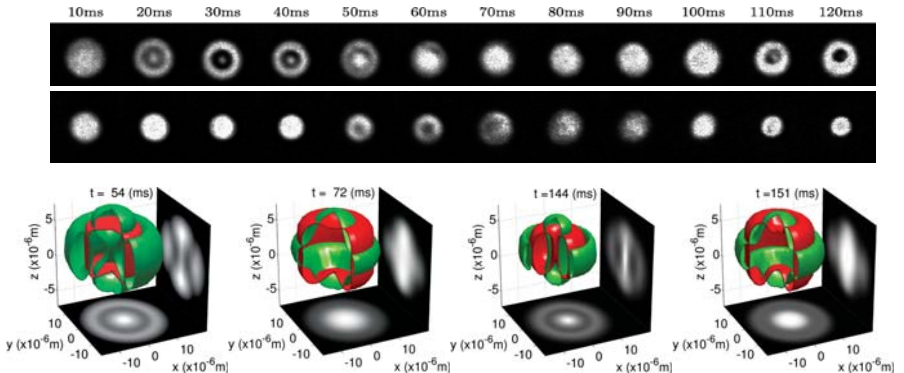


Fig. 16.2. Top: Time series evolution of the binary condensate. Bottom: Numerical results where each component is depicted by a contour slice at half of its corresponding maximal density (the $|1\rangle$ and $|2\rangle$ species are depicted, respectively, in green and red). The bottom (side) projection corresponds to the z - (x -) integrated density for the $|1\rangle$ component as it is observed in the laboratory experiments

emergence of transient ringlike density distributions that occur after the formation of the “ball” and “shell” (see Fig. 16.2). Numerical simulations of the separation process agree well with our data, suggesting a technical problem of some kind with the original JILA experiment.

In the two-component experiments, a_{12} is very nearly equal to its critical value $a_c = \sqrt{a_{11}a_{22}}$, meaning the stability of the system is sensitive to other effects, such as asymmetries in the trapping potential. It is therefore of some interest to explore regimes in which a_{12} and a_c differ more significantly. Such experiments may be possible near an interspecies Feshbach resonance. A complementary cousin of the ^{87}Rb pseudospinor condensate system described above exists between the $|F = 2, m_f = -1\rangle$ and $|F = 1, m_f = 1\rangle$

states, which also have nearly identical magnetic moments but cannot be trapped magnetically. Using an optical trap and a sequence of radiofrequency and Raman laser pulses, the Hamburg group has populated these two spin states and observed a narrow (1–2 mG) interspecies Feshbach resonance near 9.1 G through enhanced inelastic losses [31]. The resonance is predicted to change the magnitude of the interspecies scattering length a_{12} by a factor of about 3 [32], which may be enough to drive the binary condensate more deeply into the phase separation regime, i.e., $a_{12} > \sqrt{a_{11}a_{22}}$.

The pace of component separation can be greatly enhanced by the presence of a thermal cloud, as observed by McGuirk et al. [33]. Their experiment, essentially similar in outline to the JILA experiment described above [34], compared component separation in condensates with and without thermal clouds, and found that the condensate separated into spatial spin domains nearly six times faster in the presence of a thermal cloud than in its absence.

Component separation also becomes considerably richer if the initial condensate contains a vortex lattice, as described in [35]. In addition to effects due to the relative buoyancy of the two species, it is energetically favorable for a two-component condensate with repulsive interactions to form a set of interlacing square lattices [36, 37], with atoms from one component filling the cores of the other. In the experiment, a highly rotating condensate of $3.5\text{--}4 \times 10^6 |1\rangle$ atoms was confined in a weak magnetic trap. After application of a brief two-photon microwave coupling pulse that shifts 80–85% of the atoms to the $|2\rangle$ state, the two condensates negotiate a complicated evolution that involves elements of the usual (nonrotating) component separation dynamics as depicted in Fig. 16.3. Initially, the condensate exhibits a large number of vortex lines arranged in a hexagonal lattice, as shown in Fig. 16.3a, b. After this initial phase, the condensates went through a turbulent phase as they transitioned from the initial overlapping hexagonal lattice to a new interlaced square lattice. The observed square lattice was a lattice of skyrmions, in which the vortex cores of one species were filled by the fluid of the other, as the experimenters demonstrated using a second coupling pulse in a time-domain interferometric technique. The lattice was stable against perturbations and persisted for several seconds. Figure 16.3c depicts the two-color side-view images of the initial turbulent evolution. State $|1\rangle$ ($|2\rangle$) appears bright (dark) on gray background. The fine filament structures in (ii–v) are due to mutual filling of vortex cores.

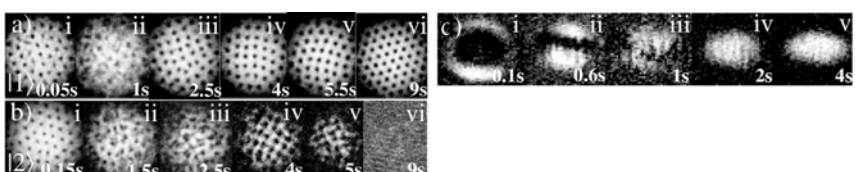


Fig. 16.3. Component separation in rotating condensates. See text for details. Figure adapted from [35]

The situation in ^{23}Na is not as favorable for studying condensates in two different hyperfine levels. Nevertheless, the MIT group created an optically confined binary condensate in the stretched $|2, -2\rangle$ and $|1, -1\rangle$ states by applying a pulse of microwave radiation to a single condensate in the lower hyperfine manifold [38]. The condensates rapidly separated into spin domains, even in the absence of magnetic field gradients, suggesting that the two components were immiscible. Other combinations of states in the two hyperfine manifolds perished within a few milliseconds.

Another binary condensate system was realized by the MIT group in a pair of optically-trapped levels, $|1, 0\rangle$ and $|1, 1\rangle$, in the $F = 1$ hyperfine manifold of ^{23}Na . Although this system is nominally a spinor condensate, at sufficiently high fields the spin dynamics are suppressed (see Sect. 16.3.2) and the system behaves much like the pseudospinor condensates described above. In its initial experiments in sodium, the MIT group reported observation of metastable domains in a superposition of $|1, 1\rangle$ and $|1, 0\rangle$ condensates, produced by a Landau-Zener sweep at an offset field of 15 G [39]. The spin domains consisted of interlaced regions of $|1\rangle$ and $|0\rangle$ condensate, each 10–50 μm in extent, appearing within 50 ms of the sweep and persisting for up to 20 s. The components separated quite cleanly since the component separation criterion $a_{01} > \sqrt{a_{00}a_{11}}$ was met. The interlaced arrangement was only metastable, however, since the global energy was minimized with only two regions, each with a single spin component.

16.2.2 Phase Coherence

We have heretofore discussed the double condensate system as being composed of two independent condensates, each described by its own order parameter with complex amplitude and phase. The phase of each condensate is not directly observable; in scalar or pseudospinor condensate systems, however, the relative phase between the two components can be measured using interferometric techniques that map phase variations into density variations. The classic example of the former is the celebrated MIT condensate interference experiment that demonstrated the first-order coherence of two spatially-separated condensates in the same spin state [40]. As the condensates were released from their confinement, they overlapped and created a beautiful set of interference fringes in the atomic density.

Condensates in two different spin states are distinguishable and do not interfere directly when they overlap. The influence of the relative phase can nevertheless be detected by (re-)introducing the electromagnetic coupling between the two states at a later time, as first explored at JILA [34]. Upon application of a second $\pi/2$ -pulse, the relative phase (transverse spin) of two partially-overlapping condensates was mapped into a longitudinal spin for detection. The resulting density profiles showed enhancement or diminution of the atomic density in the overlap region, depending on the relative phase of the coupling drive and the transverse spin as described above. By mapping

the peak density of the overlap region as a function of the delay between the two pulses, the difference frequency could be measured directly – the classic Ramsey experiment [41] – in the time domain. The experimenters discovered that the relative phase was not only observable but also fairly *reproducible* from shot-to-shot of the experiment, despite the rearrangement dynamics and strong damping that led to equilibrium [30].

The $|2, 2\rangle$ and $|2, 1\rangle$ states of ^{87}Rb have also been used to create a kind of Mach–Zehnder interferometer [42]. In this case, the magnetic moments of the two states differ by a factor of two; this leads to different confining frequencies and equilibrium locations for the two different species. A brief radiofrequency pulse populated several spin states from a single $|2, 2\rangle$ condensate [43,44]. Only the $|2, 2\rangle$ and $|2, 1\rangle$ states remained confined in the magnetic trap. The $|2, 1\rangle$ condensate underwent large-amplitude oscillations as a result of its initially large displacement from equilibrium, returning periodically to interact with the $|2, 2\rangle$ condensate. After a brief delay that permitted the condensates to separate in the trap, a second radiofrequency pulse was applied, creating two new superpositions of the two spin states, which then evolved in the trap for some additional time. Selective state imaging, after release and expansion, revealed striking interference fringes where the atoms from the two initial wave packets overlapped.

The relative phase of two *independently* produced condensates was explored in the author’s laboratory in an experiment [45] that explored the emergence of a spontaneous macroscopic spin [5] when the two condensates were brought together; this is the pseudospinor analogue of the MIT interference experiment [40]. The two condensates were produced simultaneously by evaporative cooling in the $|2, 2\rangle$ and $|1, -1\rangle$ states, just as in [9]. The $|1, -1\rangle$ atoms were then transferred to the $|2, 1\rangle$ state with a two-photon π -pulse. The trap was then turned off, after which the two condensates expanded into one another and overlapped. Insofar as the order parameter of each condensate is described by a density and phase, the system developed a macroscopic *transverse* spin (i.e., relative phase) where the two overlapped, much as a transverse spin existed in the overlap region in the JILA phase measurement experiment described above [34]. A $\pi/2$ -pulse, applied on the $|2, 2\rangle \rightleftharpoons |2, 1\rangle$ transition, then mapped this transverse spin into the longitudinal spin states. Exposure to a Stern–Gerlach magnetic field gradient separated the two spin states in space, revealing two sets of anticorrelated matter-wave fringes, corresponding to initially helical transverse spin structures in the originally overlapping condensates. Since the original condensates were produced independently, the relative phase (and thus the offset of the transverse spin structure) was random in each instantiation of the experiment.

16.2.3 Thermodynamics

The interplay between phase coherence and thermodynamics was explored in a key experiment by Lewandowski et al. [46]. Using finite-temperature samples

with condensates and thermal clouds prepared in dressed-state superpositions of $|1\rangle$ and $|2\rangle$, the authors observed the temperature of the system initially decrease as the thermal cloud decohered. To understand this effect, consider a combined condensate and thermal cloud in a superposition of states $|1\rangle$ and $|2\rangle$. As the normal cloud decoheres, the thermal atoms become distinguishable and have to be counted as two different species. The number of $|1\rangle$ atoms in the thermal component is therefore smaller than it needs to be to support its corresponding condensate at the temperature of the sample. The condensate responds by supplying atoms to the thermal component in order to restore thermal equilibrium. Since there are now more atoms in the normal component, and essentially the same total thermal energy, the temperature of the sample decreases. This is a delightful example of how a multi-component condensate can illuminate the connection between coherence and thermodynamics. Similar experiments have now been conducted in spinor condensates, as discussed in Sect. 16.3.4.

16.2.4 Wavefunction Engineering

Pseudospinor condensates, as prototypical two-level systems, offer unique opportunities to engineer wavefunctions with specific amplitudes and phases. The process involves transferring atoms from one state to the other state in the presence of a modulating potential. The amplitude and phase of the condensate atoms arriving in the second state depend deterministically on the details of the modulation and the applied two-photon coupling. For additional details on this technique the reader is directed to [47] and [48].

As a specific example, we consider the production of a vortex state [17], following an idea of Williams and Holland [47]. A similar method has also been used to create filled solitons, as described in [49], and generalizations of the method have been proposed to create, *inter alia*, vortices with higher circulation and quadrupole excitations [47]. The experiment [17] began with a single $|2\rangle$ condensate confined in a weak spherical trap. The condensate was then illuminated by the edge of a weak Gaussian laser beam, detuned slightly to the blue of the $F = 2 \rightarrow F' = 3$ transition frequency. The laser beam rotated around the edge of the condensate, introducing a maximum modulation of the trapping potential (due to the AC Stark effect) at the edge of the condensate. The microwave coupling was then introduced, transferring up to 50% of the condensate atoms from state $|2\rangle$ to state $|1\rangle$ in a ring at the edge of the $|2\rangle$ condensate (see left panel in Fig. 16.4). Crucially, the phase of the modulating potential at an azimuthal position ϕ was simply ϕ , and thus the transfer wrote the 2π phase wrap directly into the transferred atoms. The end result is a rotating $|1\rangle$ condensate surrounding a nonrotating $|2\rangle$ core. The 2π phase wrap was verified interferometrically by applying a $\pi/2$ -pulse of the two-photon microwave coupling. The effect of this pulse is to map the 2π variation of the relative phase in the region of condensate overlap into an intensity variation, as shown in the right panel of Fig. 16.4.

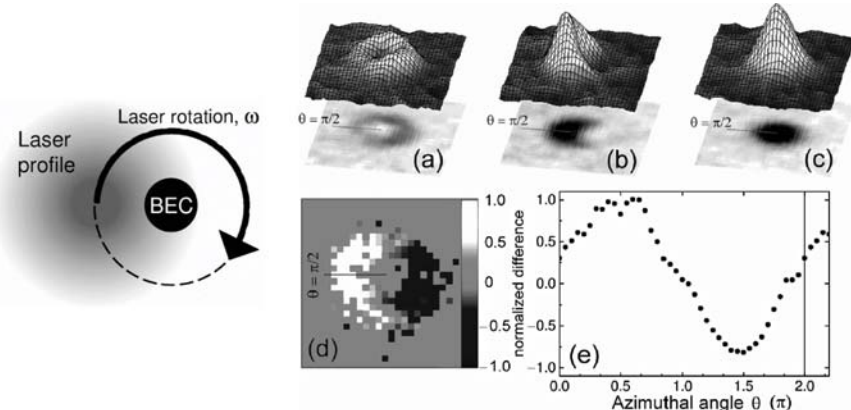


Fig. 16.4. Creation of a vortex by wavefunction engineering. *Left:* modulation scheme. *Right:* interferometric detection of the vortex state. Figure adapted from [17]

The two components can be exchanged with a π -pulse, such that the $|2\rangle$ atoms are rotating and the $|1\rangle$ atoms form the nonrotating core. Such vortices are unstable due to the positive buoyancy of the $|1\rangle$ atoms [17]. The atoms in the core can also be removed by applying resonant light, leaving a pure rotating $|1\rangle$ or $|2\rangle$ condensate; this has been a useful starting point for experiments involving single vortices with unfilled cores [50]. Other experiments explored the precession of vortex cores in the presence and absence of filling, observing that bare-core precession is modestly faster than filled-core precession [51].

16.2.5 Spin Textures

Spin textures are regions in which the (pseudo-)spin orientation varies continuously over some region of space. We have already examined examples involving coreless vortices [17, 35] in pseudospin-1/2 condensates in ^{87}Rb (see also transient coreless vortex production in [52]). A related experiment by the JILA group created an interesting “soliton-train” spin texture by exposing the condensate to a coupling, for which the Rabi frequency varied across the extent of the condensate due to the uncompensated gravitational potential of the magnetically-insensitive intermediate state [53]. The result was a helical winding in the relative phase of the order parameter. For long exposures to the coupling the energy cost of maintaining smaller and smaller spin domains forced the condensate to evolve in a manner such that the effect of the drive was to *unwind* the relative phase, and the condensate returned to a situation close to its initial condition.

16.3 Spinor Condensates

In the second part of this chapter we consider true spinor condensates, i.e., condensates for which lossless spin-changing collisions significantly influence the dynamics. Since much of this work is more recent and correspondingly less familiar, we shall spend some additional time developing the mean-field theory of the interacting spinor Bose–Einstein condensate for the common cases of ^{23}Na and ^{87}Rb . These two atoms are the most-studied as of this writing; both have nuclear spin $I = 3/2$ and therefore have two hyperfine levels labeled by angular momentum $F = 1$ and $F = 2$.

16.3.1 Basic Magnetic Properties

The mean-field theory (and GPE) has proven highly successful in predicting the behavior of scalar condensates. It is therefore sensible to seek a similar theoretical paradigm within which to treat spinor condensates. An effective mean-field Hamiltonian, including its magnetic response, may be derived from its second-quantized form. The effective mean-field Hamiltonian is written

$$\hat{H} = \hat{T} + V_{\text{ext}}(\mathbf{r}) + \hat{H}_Z + \hat{H}_S,$$

where $\hat{T} = -\hbar^2 \nabla^2 / 2m$ is the kinetic energy and $V_{\text{ext}}(\mathbf{r})$ an external potential arising from, e.g., an optical trap. We shall henceforth neglect the kinetic energy term (Thomas–Fermi approximation). The terms \hat{H}_Z and \hat{H}_S represent the magnetic (Zeeman) and spin-dependent interaction terms, respectively; these two terms are discussed below.

Most analysis to date makes use of the so-called single-mode approximation (SMA), in which the spatial and spin degrees of freedom are separated. In this approximation, the spinor condensate order parameter is written

$$\psi(\mathbf{r}, t) = \sqrt{n(\mathbf{r})} \zeta(t) \exp(-i\mu t/\hbar),$$

where n is the atomic density, $\zeta(t)$ is a normalized spinor of $2F+1$ components for hyperfine manifold F , and μ is the chemical potential. The SMA makes it possible to express the Hamiltonian in terms of expectation values of the spin $\langle \mathbf{F} \rangle = \zeta_a^\dagger \mathbf{F}_{ab} \zeta_b$ (repeated indices summed) and density $\langle n \rangle = \int n^2 d^3r$.

The magnetic (Zeeman) term \hat{H}_Z arises from the interaction of the effective magnetic moment of an atom with an externally-applied magnetic field B . For $I = 3/2$ alkali atoms, the magnetic term for weak fields is approximated by expanding the Breit–Rabi [41] equation to first order and discarding terms proportional to the nuclear magnetic moment. The result is $\hat{H}_Z^{\{(1),(2)\}} = \mp p \langle F_z \rangle \mp q \langle 4 - F_z^2 \rangle$, where $p = \mu_B B / 2$ characterizes the linear Zeeman effect with Bohr magneton μ_B , $q = p^2 / \hbar \omega_{\text{hfs}}$ characterizes the quadratic Zeeman effect, and the upper (lower) sign corresponds to $F = 1$ ($F = 2$).

The mean-field term \hat{H}_S accounts for interactions between atoms in the condensate. It arises from projecting the pair of (symmetrized) atomic spin

states into states of total angular momentum \mathcal{F} , which for bosons in hyperfine level F is the set of even values between 0 and $2F$. After a few quantum-mechanical manipulations, one finds $\hat{H}_S^{(1)} = (c_0^{(1)}\langle n \rangle + c_2^{(1)}\langle n \rangle \langle \mathbf{F} \rangle^2)/2$ for $F = 1$, and $\hat{H}_S^{(2)} = (c_0^{(2)}\langle n \rangle + c_2^{(2)}\langle n \rangle \langle \mathbf{F} \rangle^2 + c_4^{(2)}\langle n \rangle |S_0|^2)/2$ for $F = 2$, where in the latter case $S_0 = \zeta_0^2/2 - \zeta_{+1}\zeta_{-1} + \zeta_{+2}\zeta_{-2}$ is the spin singlet amplitude. The coupling coefficients are linear combinations of the s -wave scattering lengths $a_{\mathcal{F}}$:

$$\begin{aligned} c_0^{(1)} &= \frac{4\pi\hbar^2}{m} \left(\frac{a_0+2a_2}{3} \right), \quad c_2^{(1)} = \frac{4\pi\hbar^2}{m} \left(\frac{a_2-a_0}{3} \right), \\ c_0^{(2)} &= \frac{4\pi\hbar^2}{m} \left(\frac{3a_4+4a_2}{7} \right), \quad c_2^{(2)} = \frac{4\pi\hbar^2}{m} \left(\frac{a_4-a_2}{7} \right), \quad c_4^{(2)} = \frac{4\pi\hbar^2}{m} \frac{4}{5} \left(\frac{3a_4-10a_2+7a_0}{7} \right). \end{aligned} \quad (16.2)$$

The Hamiltonian terms for $F = 1$ and $F = 2$ can now be expressed:

$$\hat{H}^{(F=\{1,2\})} = V_{\text{ext}}(\mathbf{r}) \mp (p\langle F_z \rangle \mp q\langle 4 - F_z^2 \rangle) + \hat{H}_S^{\{(1),(2)\}}. \quad (16.3)$$

Similar expressions can be obtained for higher spin. These expressions are valid under the same conditions as the SMA approximation, i.e., the condensate spatial extent is much larger than the spin healing length $\xi_s = 2\pi\hbar/\sqrt{2m|c_2|n}$.

The *global* ground state minimizes the total energy, independent of constraints on total magnetization and angular momentum; it is therefore in the lower hyperfine level, and depends on the relative strengths of the spin-dependent magnetic ($\propto p$) and interaction energies ($\propto c \equiv c_2\langle n \rangle$). In the *magnetic* regime, for which $c < p$, the global ground state is simply the $|1,1\rangle$ state. In the *interaction* regime, spin-dependent interactions determine the ground-state structure [54–57]. For $F = 1$, the spin dependence is entirely contained in $c_2^{(1)}$; if positive (negative), the ground state will be the state that minimizes (maximizes) $\langle \mathbf{F} \rangle^2$, and is named *polar* or *antiferromagnetic (ferromagnetic)*. For $F = 2$ the situation is more complicated, with the appearance of a *cyclic* phase in addition to analogues of the $F = 1$ polar and ferromagnetic phases [58].

If inelastic processes occur for sufficiently long times, then the total number and total magnetization are conserved by the Hamiltonian equations (16.3). The character of the ground state in a uniform field thus depends on the interplay of the Hamiltonian terms proportional to q and c and *not* on the term proportional to p , since spin-dependent interactions (such as $|0\rangle + |0\rangle \rightleftharpoons |+1\rangle + |-1\rangle$) conserve the total magnetization and, therefore, the total linear Zeeman energy [10, 59, 60]. A spatial dependence on the p term can be introduced, however, with the application of a magnetic field gradient; the ground-state structures are fully parameterized in terms of the strength of p , q , and c [10].

We next consider experimental work by the MIT group in the $F = 1$ manifold of ^{23}Na , in which an initial spin population with total spin 0 in an optical trap was permitted to relax to its ground-state over several seconds at various values of p (due to applied field gradients) and q [10]. The experiments determined that the ground state is polar by observing the near-complete

miscibility of $|1, \pm 1\rangle$ states at small values of p and q . In contrast, the $|1, 0\rangle$ and $|1, \pm 1\rangle$ states were found to be immiscible, and underwent component separation at higher fields (see Sect. 16.2.1). By analyzing the overlap of the miscible $|\pm 1\rangle$ states the value of $c_2^{(1)}$ was extracted, and therefore the difference between the scattering lengths a_2 and a_0 .

The unusually small hyperfine-changing collision rate in ^{87}Rb allows study of both the $F = 2$ and $F = 1$ manifolds. The $F = 2$ manifold was first examined by the Hamburg group, which measured the time evolution of various initial spin compositions at a field of a few hundred mG. Different initial spin compositions evolved on different timescales, allowing different collision processes to be identified. Spin dynamics (discussed in greater detail in Sect. 16.3.2) dominated the shortest timescales; over 40 ms, an initially-prepared $|2, 0\rangle$ sample, for example, relaxed to a nearly equal distribution of states across the entire manifold. The polar nature of the ground state was determined by the stability of an equal superposition of $|2, 2\rangle$ and $|2, -2\rangle$ states against spin dynamics, as well as by their observed miscibility. The slow evolution of a cyclic initial state, consisting of a superposition of $|2, 2\rangle$, $|2, 0\rangle$, and $|2, -2\rangle$ states, suggested that the ground state structure is quite close to the cyclic state, as predicted theoretically [58]. Relatively long-lived superpositions, such as the polar mixture described above, were susceptible to hyperfine-changing collisions at intermediate timescales, and this allowed the group to determine a two-body loss rate due to these collisions. Over the longest timescales the condensates decayed via three-body recombination; this was probed by observing loss from pure $|2, 2\rangle$ condensates, can participate neither in spin dynamics nor hyperfine-changing collisions.

Studies of the lower hyperfine manifold ($F = 1$) in ^{87}Rb revealed much slower spin dynamics, on a time scale of seconds rather than milliseconds. The Hamburg group provided the first evidence that the ground state is ferromagnetic, observing the spin-mixing of an equal superposition of $|1, \pm 1\rangle$ states [59]. The Georgia Tech group also found a ferromagnetic ground state by examining the results of spin-mixing as a function of magnetic field with a small field gradient [60].

16.3.2 Spin Dynamics

The first spin dynamics experiments observed overdamped oscillations [59–61] with quantum-correlated fluctuations in the populations $\rho_{\pm 1}$ [60] and a strong suppression of the spin dynamics as an increasing function of the applied magnetic field [61]. The theory of spin dynamics advanced considerably in response to this work, and we now review it briefly, specializing momentarily to the simplest $F = 1$ case. We write a set of three coupled spinor equations for a normalized spinor $\zeta = (\zeta_+, \zeta_0, \zeta_-)$ based on the purely spin-dependent parts of the Hamiltonian (16.3):

$$i\hbar\dot{\zeta}_{\pm} = (\mp p - 3q)\zeta_{\pm} + c \left[(|\zeta_{\pm}|^2 + |\zeta_0|^2 - |\zeta_{\mp}|^2) \zeta_{\pm} + \zeta_0^2 \zeta_{\mp}^* \right], \quad (16.4)$$

$$i\hbar\dot{\zeta}_0 = -4q\zeta_0 + c \left[(|\zeta_+|^2 + |\zeta_-|^2) \zeta_0 + 2\zeta_+ \zeta_- \zeta_0^* \right], \quad (16.5)$$

where c is defined in the previous section. The transformation $\zeta_{\pm} \rightarrow \zeta_{\pm} \exp(\mp ipt/\hbar)$ and $\zeta_0 \rightarrow \zeta_0$ eliminates the Larmor precession due to the linear Zeeman energy, and therefore the terms proportional to p in (16.3). Writing $\zeta = (\sqrt{\rho_+}e^{i\phi_+}, \sqrt{\rho_0}e^{i\phi_0}, \sqrt{\rho_-}e^{i\phi_-})$, the GP equations (16.4) and (16.5) reduce to a pair of dynamical equations for the population of the $|1, 0\rangle$ state ρ_0 and the relative phase $\theta = \phi_+ + \phi_- - 2\phi_0$:

$$\dot{\rho}_0 = \frac{2c}{\hbar} \sqrt{(1 - \rho_0)^2 - M^2} \sin \theta, \quad (16.6)$$

$$\dot{\theta} = -\frac{2q}{\hbar} + \frac{2c}{\hbar}(1 - 2\rho_0) + \frac{2c}{\hbar} \frac{(1 - \rho_0)(1 - 2\rho_0) - M^2}{\sqrt{(1 - \rho_0)^2 - M^2}} \cos \theta, \quad (16.7)$$

where $M = \rho_+ - \rho_-$, the total magnetization, is a constant of the motion.

Several experiments have explored the validity of (16.6) and (16.7) in regimes where either the c or q terms dominated the spin dynamics. In the mean-field regime ($c \gg q$), the Georgia Tech group [62] used a sequence of rf and microwave pulses to generate particular initial condensate superpositions that underwent a series of spin oscillations before damping away due to the breakdown of the SMA. By measuring the frequency of the oscillations in ρ_0 and the overall atomic density, the experimenters were able to measure $c_2^{(1)}$ directly, which is equivalent to measuring the scattering length difference $a_2 - a_0$. In the quadratic Zeeman regime ($q \gg c$), the authors observed small-amplitude ($\sim 1/q$), rapid ($\Omega = 2q$) oscillations, as shown in Fig. 16.5a.

Having established the existence of these two regimes, the experimenters then used short ($\sim 20\text{ }\mu\text{s}$) 600 mG magnetic field pulses to control directly the dynamics of a spinor condensate evolving in the mean-field regime. During the pulse, the energy of the ζ_0 spinor component was reduced with respect to the $\zeta_{\pm 1}$ components, introducing a phase shift $\Delta\theta = \int q(t) dt$ that dramatically influenced the ensuing population oscillations. With particular choices of pulse length and populations, the experimenters could even bring the oscillations to a complete halt and restore them at a later time with a second magnetic field pulse. From amplitude measurements as a function of the delay time between a pair of pulses, the authors extracted a spinor decoherence time of 3 s for the $F = 1$ level of ^{87}Rb .

An experiment by the Hamburg group explored the interplay between the mean-field term and the quadratic Zeeman term in the form of a striking enhancement of the spin dynamics where these two energies were roughly comparable to one another [63]. In this experiment, conducted in the $F = 2$ level of ^{87}Rb , the spin dynamics was discovered to be enhanced at a field at which the magnetic energy and the mean-field energy were nearly comparable. To see this, the authors argued that a spin-2 system that begins in $|2, 0\rangle$ can be treated as an effective spin-1 system, where the dominant dynamics involve the usual exchange reaction $|2, 1\rangle + |2, -1\rangle \rightleftharpoons |2, 0\rangle + |2, 0\rangle$. In

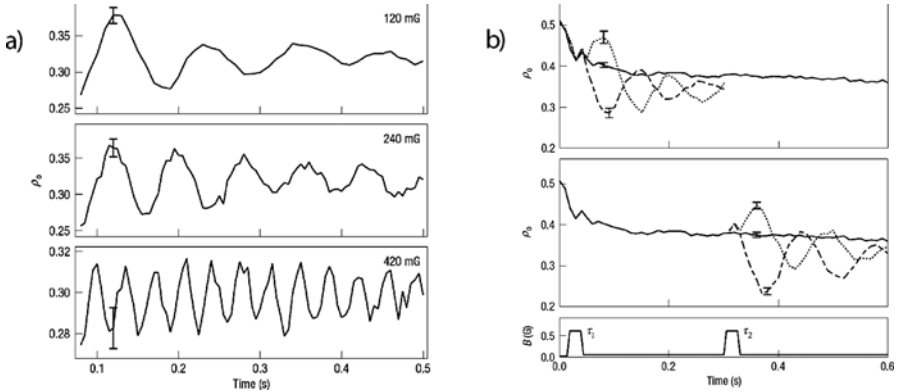


Fig. 16.5. (a) Population of $|0\rangle$ as a function of time for three magnetic fields. For low fields (*top panel*) the interaction energy dominates and leads to damped spin oscillations. At higher fields, the quadratic Zeeman energy dominates, leading to more rapid spin oscillations (*bottom panel*). (b) The spin dynamics can be controlled by applying brief pulses that take the system from the mean-field regime (15 mG) to the quadratic Zeeman regime (600 mG), as described in the text. The *top panel* shows three curves, corresponding to different pulse lengths; the *solid curve* shows that the spin oscillations can be completely terminated. The oscillations can be restarted with a second pulse at a later time (*bottom panel*). Figure adapted from [62]

particular, the dynamical equations (16.6) and (16.7) apply *mutatis mutandis*. For large fields, the quadratic Zeeman term dominates, and $\dot{\theta} \approx 2q/\hbar$ (the sign changes for terms proportional to q in the $F = 2$ manifold); the phase therefore increases roughly linearly, leading to oscillations of the population ρ_0 , according to the sign of $\sin \theta$ in (16.7). The amplitude of these oscillations is small, and the frequency comparatively large, as was observed in other experiments in both the $F = 2$ [61] and $F = 1$ [62] manifolds. For weak (but nonvanishing) fields, on the other hand, the mean-field term is significant, and counteracts the quadratic Zeeman term as the population ρ_0 grows large enough, causing θ to decrease. The population ρ_0 then decreases, at which point θ increases once again. Under these conditions θ oscillates about zero, and the population ρ_0 undergoes small-amplitude oscillations. At intermediate fields, where $c \approx q$, the phase θ changes quite slowly and can lead to much larger population oscillations, as observed experimentally [63].

The authors of [63] also pointed out that the direction of the initial spin mixing from the rotated spinor is determined by the phase introduced by the quadratic Zeeman effect. This can be seen by examining the evolution of the relative phase θ , which, in the quadratic Zeeman regime, initially decreases from its initial value $\theta = 0$ at the end of the $\pi/2$ -pulse: $\dot{\theta} \equiv -2q/\hbar$. Since $\dot{\rho}$ is proportional to $c \sin \theta$, with $c < 0$, the authors note that the population ρ_0 should initially increase, just as they observed experimentally. This was taken as further evidence of the coherence of the spin dynamics.

16.3.3 Symmetry Breaking and Domain Formation

A complementary view of the interplay between the c and q terms in the Hamiltonian (16.3) is found in the recent work of Sadler et al. [64]. The relatively large (2×10^6) condensates were confined in a highly anisotropic optical potential such that the SMA was valid only along the imaging axis; individual spin domains could therefore form along the other two orthogonal axes. The experiments began with a pure $|0\rangle$ condensate of ^{87}Rb , which was rapidly taken from a field of 2 G (i.e., $q \gg c$) to a final field of 50 mG ($q \ll c$). After a variable hold time, the magnetization was measured using a nondestructive phase-contrast imaging technique [18]. The transverse magnetization was extracted from the phase and amplitude of the Larmor precession on a pixel-by-pixel basis, with the applied field perpendicular to the imaging axis; the longitudinal magnetization was observed by adiabatically rotating the magnetization so that it pointed along the imaging axis. Analysis of the nondestructive images revealed the formation of $|\pm 1\rangle$ spin domains as a result of spontaneous symmetry breaking in the condensate. Domain formation was further accelerated by the immiscibility of the $|\pm 1\rangle$ spin states for $c < 0$ [10], leading to characteristic features such as domain walls and topological defects such as spin vortices. In particular, the group observed “polar-core” spin vortices, consisting of a superposition of oppositely-rotating vortices in the $|\pm 1\rangle$ spin states with a nonrotating filled core of $|0\rangle$ atoms.

16.3.4 Thermodynamics

The separation in timescales observed between spin dynamics and thermalization makes possible a number of interesting experiments that explore coherence and decoherence in spinor Bose condensates, especially when thermalization occurs much more rapidly than the spin dynamics, as is true for $F = 1$ condensates in ^{87}Rb . One particularly beautiful experiment [65] began with a semicondensed mixture of $|1\rangle$ and $| - 1\rangle$ atoms; spin-mixing in the condensate then drove the reaction $|1\rangle + | - 1\rangle \rightarrow |0\rangle + |0\rangle$. The $|0\rangle$ atoms quickly thermalized and joined a growing $|0\rangle$ thermal cloud, since a $|0\rangle$ condensate could not initially be supported at the temperature of the sample. The overall temperature of the system therefore decreased slightly as the (fixed) thermal energy was divided among a growing number of thermal atoms. Once the critical number of atoms in the $|0\rangle$ state was reached, however, further spin-mixing began to populate the $|0\rangle$ component at *constant* temperature. The authors point out that this process is nearly orthogonal to the usual process of condensate creation, in which the temperature (and number) are reduced by evaporation.

A similar experiment exploited spin-mixing behavior to generate different magnetizations of the condensate and thermal components from an initial mixture of $|1\rangle$ and $|0\rangle$ atoms [66]. The spin-dynamics initially drove the reaction $|0\rangle + |0\rangle \rightarrow |1\rangle + | - 1\rangle$, further populating the $|1\rangle$ condensate and initially

building up a $| -1 \rangle$ thermal cloud, since a $| -1 \rangle$ condensate could not be supported at the sample temperature, as discussed above. The system reached equilibrium with equally-populated, saturated thermal clouds; of the atoms that left the $| 0 \rangle$ condensate, half joined the $| 1 \rangle$ condensate but the other half was distributed among thermal atoms in the $| 1 \rangle$ and $| -1 \rangle$ states. The equilibrium thermal cloud is unmagnetized, but the magnetization of the condensate is increased by this process.

16.4 Future Prospects/Conclusions

A decade of research on multi-component condensates has revealed many interesting and new phenomena. With the assistance of theory, some of the ground states of simple pseudospinor and spinor systems have been realized, and elementary component separation behavior studied in a variety of different contexts. The time-evolution of the relative phase in a binary condensate has been observed, and coherent control of the system demonstrated in a process of state engineering. Similarly, the role of the magnetic field in spin oscillations has been elucidated and used as a control mechanism.

In such a rapidly growing field even the best predictions of future prospects are likely to be rapidly overtaken by experimental progress. It is nevertheless striking that one of the most elementary properties of multi-component condensates remains largely unexplored, viz., the experimental study of elementary excitations. Other interesting and fundamental studies include the determination of the ground state of a spinor condensate in the absence of a magnetic field (interaction regime) and further work on spin textures and topological defects. The recent achievement of Bose–Einstein condensation in chromium [67] offers a more expansive ground state ($J = 3$) with a large ($6 \mu_B$) magnetic moment that should emphasize dipole-dipole interactions. Finally, other combinations of condensates are being considered, some of which may realize tunable interspecies interactions (via Feshbach resonances) and the study of interatomic interactions. These possibilities, and doubtless others, will provide experimenters with much to do in the years to come.

References

1. I.M. Khalatnikov, Sov. Phys. JETP **5**, 542 (1957)
2. L. Guttman, J.R. Arnold, Phys. Rev. **92**, 547 (1953)
3. W.B. Colson, A.L. Fetter, J. Low Temp. Phys. **33**, 231 (1978)
4. D. Vollhardt, P. Wölfle, *The Superfluid Phases of Helium 3* (Taylor and Francis, New York, 1990)
5. E.D. Siggia, A.E. Ruckenstein, Phys. Rev. Lett. **44**, 1423 (1980)
6. M.H. Anderson, J.R. Ensher, M.R. Matthews, C.E. Wieman, E.A. Cornell, Science **269**, 198 (1995)

7. K.B. Davis, M.-O. Mewes, M.R. Andrews, N.J. van Druten, D.S. Durfee, D.M. Kurn, W. Ketterle, Phys. Rev. Lett. **75**, 3969 (1995)
8. C.C. Bradley, C.A. Sackett, J.J. Tollett, R.G. Hulet, Phys. Rev. Lett. **75**, 1687 (*ibid.* **79**, 1170 (1997))
9. C.J. Myatt, E.A. Burt, R.W. Ghrist, E.A. Cornell, C.E. Wieman, Phys. Rev. Lett. **78**, 586 (1997)
10. J. Stenger, S. Inouye, D.M. Stamper-Kurn, H.-J. Miesner, A.P. Chikkatur, W. Ketterle, Nature **396**, 345 (1998)
11. G. Modugno, G. Ferrari, G. Roati, R.J. Brecha, A. Simoni, M. Inguscio, Science **294**, 1320 (2001)
12. G. Modugno, M. Modugno, F. Riboli, G. Roati, M. Inguscio, Phys. Rev. Lett. **89**, 190404 (2002)
13. Z. Hadzibabic, C.A. Stan, K. Dieckmann, S. Gupta, M.W. Zwierlein, A. Görlitz, W. Ketterle, Phys. Rev. Lett. **88**, 160401 (2002)
14. A. Widera, O. Mandel, M. Greiner, S. Kreim, T.W. Hänsch, I. Bloch, Phys. Rev. Lett. **92**, 160406 (2004)
15. M.R. Matthews, D.S. Hall, D.S. Jin, J.R. Ensher, C.E. Wieman, E.A. Cornell, F. Dalfovo, C. Minniti, S. Stringari, Phys. Rev. Lett. **81**, 243 (1998)
16. M.R. Andrews, M.-O. Mewes, N.J. van Druten, D.S. Durfee, D.M. Kurn, W. Ketterle, Science **273**, 84 (1996)
17. M.R. Matthews, B.P. Anderson, P.C. Haljan, D.S. Hall, C.E. Wieman, E.A. Cornell, Phys. Rev. Lett. **83**, 2498 (1999)
18. J.M. Higbie, L.E. Sadler, S. Inouye, A.P. Chikkatur, S.R. Leslie, K.L. Moore, V. Savalli, D.M. Stamper-Kurn, Phys. Rev. Lett. **95**, 050401 (2005)
19. W. Petrich, M.H. Anderson, J.R. Ensher, E.A. Cornell, Phys. Rev. Lett. **74**, 3352 (1995)
20. D.S. Hall, J.R. Ensher, D.S. Jin, M.R. Matthews, C.E. Wieman, E.A. Cornell, Proc. SPIE **3270**, 98 (1998)
21. J.H. Müller, O. Morsch, D. Ciampini, M. Anderlini, R. Mannella, E. Arimondo, Phys. Rev. Lett. **85**, 4454 (2000)
22. D.M. Stamper-Kurn, M.R. Andrews, A.P. Chikkatur, S. Inouye, H.-J. Miesner, J. Stenger, W. Ketterle, Phys. Rev. Lett. **80**, 2027 (1998)
23. M.D. Barrett, J.A. Sauer, M.S. Chapman, Phys. Rev. Lett. **87**, 010404 (2001)
24. L. Allen, J.H. Eberly, *Optical Resonance and Two-Level Atoms.* (Dover, New York, 1987)
25. P.S. Julienne, F.H. Mies, E. Tiesinga, C.J. Williams, Phys. Rev. Lett. **78**, 1880 (1997)
26. J.P. Burke, J.L. Bohn, B.D. Esry, C.H. Greene, Phys. Rev. A **55**, R2511 (1997)
27. B.D. Esry, C.H. Greene, J.P. Burke Jr., J.L. Bohn, Phys. Rev. Lett. **78**, 3594 (1997)
28. P. Ao, S.T. Chu, Phys. Rev. A **58**, 4836 (1998)
29. E. Timmermans, Phys. Rev. Lett. **81**, 5718 (1998)
30. D.S. Hall, M.R. Matthews, J.R. Ensher, C.E. Wieman, E.A. Cornell, Phys. Rev. Lett. **81**, 1539 (1998)
31. M. Erhard, H. Schmaljohann, J. Kronjäger, K. Bongs, K. Sengstock, Phys. Rev. A **69**, 032705 (2004)
32. E.G.M. van Kempen, S.J.J.M.F. Kokkelmans, D.J. Heinzen, B.J. Verhaar, Phys. Rev. Lett. **88**, 093201 (2002)
33. J.M. McGuirk, D.M. Harber, H.J. Lewandowski, E.A. Cornell, Phys. Rev. Lett. **91**, 150402 (2003)

34. D.S. Hall, M.R. Matthews, C.E. Wieman, E.A. Cornell, Phys. Rev. Lett. **81**, 1543 (1998)
35. V. Schweikhard, I. Coddington, P. Engels, S. Tung, E.A. Cornell, Phys. Rev. Lett. **93**, 210403 (2004)
36. E.J. Mueller, T.-L. Ho, Phys. Rev. Lett. **88**, 180403 (2002)
37. K. Kasamatsu, M. Tsubota, M. Ueda, Phys. Rev. A **71**, 043611 (2005)
38. A. Görlitz, T.L. Gustavson, A.E. Leanhardt, R. Löw, A.P. Chikkatur, S. Gupta, S. Inouye, D.E. Pritchard, W. Ketterle, Phys. Rev. Lett. **90**, 090401 (2003)
39. H.-J. Miesner, D.M. Stamper-Kurn, J. Stenger, S. Inouye, A.P. Chikkatur, W. Ketterle, Phys. Rev. Lett. **82**, 2228 (1999)
40. M.R. Andrews, C.G. Townsend, H.-J. Miesner, D.S. Durfee, D.M. Kurn, W. Ketterle, Science **275**, 637 (1997)
41. N.F. Ramsey, *Molecular Beams* (Oxford University Press, London, 1956)
42. C. Fort, P. Maddaloni, F. Minardi, M. Modugno, M. Inguscio, Opt. Lett. **26**, 1039 (2001)
43. J.L. Martin, C.R. McKenzie, N.R. Thomas, J.C. Sharpe, D.M. Warrington, P.J. Manson, W.J. Sandle, A.C. Wilson, J. Phys. B **32**, 3065 (1999)
44. P. Maddaloni, M. Modugno, C. Fort, F. Minardi, M. Inguscio, Phys. Rev. Lett. **85**, 2413 (2000)
45. M.H. Wheeler, K.M. Mertes, J.D. Erwin, D.S. Hall, Phys. Rev. Lett. **93**, 170402 (2004)
46. H.J. Lewandowski, J.M. McGuirk, D.M. Harber, E.A. Cornell, Phys. Rev. Lett. **91**, 240404 (2003)
47. J.E. Williams, M.J. Holland, Nature **401**, 568 (1999)
48. P.C. Haljan, *Vortices in a Bose-Einstein Condensate*. PhD thesis, University Of Colorado, Boulder, 2003
49. B.P. Anderson, P.C. Haljan, C.A. Regal, D.L. Feder, L.A. Collins, C.W. Clark, E.A. Cornell, Phys. Rev. Lett. **86**, 2926 (2001)
50. P.C. Haljan, B.P. Anderson, I. Coddington, E.A. Cornell, Phys. Rev. Lett. **86**, 2922 (2001)
51. B.P. Anderson, P.C. Haljan, C.E. Wieman, E.A. Cornell, Phys. Rev. Lett. **85**, 2857 (2000)
52. A.E. Leanhardt, Y. Shin, D. Kielpinski, D.E. Pritchard, W. Ketterle, Phys. Rev. Lett. **90**, 140403 (2003)
53. M.R. Matthews, B.P. Anderson, P.C. Haljan, D.S. Hall, M.J. Holland, J.E. Williams, C.E. Wieman, E.A. Cornell, Phys. Rev. Lett. **83**, 3358 (1999)
54. T.-L. Ho, Phys. Rev. Lett. **81**, 742 (1998)
55. C.K. Law, H. Pu, N.P. Bigelow, Phys. Rev. Lett. **81**, 5257 (1998)
56. T. Ohmi, K. Machida, J. Phys. Soc. Jpn. **67**, 1822 (1998)
57. M. Koashi, M. Ueda, Phys. Rev. Lett. **84**, 1066 (2000)
58. C.V. Ciobanu, S.-K. Yip, T.-L. Ho, Phys. Rev. A **61**, 033607 (2000)
59. H. Schmaljohann, M. Erhard, J. Kronjäger, M. Kottke, S. van Staa, L. Cacciapuoti, J.J. Arlt, K. Bongs, K. Sengstock, Phys. Rev. Lett. **92**, 040402 (2004)
60. M.-S. Chang, C.D. Hamley, M.D. Barrett, J.A. Sauer, K.M. Fortier, W. Zhang, L. You, M.S. Chapman, Phys. Rev. Lett. **92**, 140403 (2004)
61. T. Kuwamoto, K. Araki, T. Eno, T. Hirano, Phys. Rev. A **69**, 063604 (2004)
62. M.-S. Chang, Q. Qin, W. Zhang, L. You, M.S. Chapman, Nature Physics **1**, 111 (2005)

63. J. Kronjäger, C. Becker, P. Navez, K. Bongs, K. Sengstock, Phys. Rev. Lett. **97**, 110404 (2006)
64. L.E. Sadler, J.M. Higbie, S.R. Leslie, M. Vengalattore, D.M. Stamper-Kurn, Nature **443**, 312 (2006)
65. M. Erhard, H. Schmaljohann, J. Kronjäger, K. Bongs, K. Sengstock, Phys. Rev. A **70**, 031602 (2004)
66. H. Schmaljohann, M. Erhard, J. Kronjäger, K. Sengstock, K. Bongs, Appl. Phys. B **79**, 1001 (2004)
67. A. Griesmaier, J. Werner, S. Hensler, J. Stuhler, T. Pfau, Phys. Rev. Lett. **94**, 160401 (2005)

Part X

Manipulations of Coherent Matter-Waves

Manipulations of Coherent Matter-Waves

P.G. Kevrekidis, D.J. Frantzeskakis, and R. Carretero-González

17.1 Introduction

Since the experimental realization of atomic Bose–Einstein condensates (BECs) [1], this field has experienced an enormous increase of interest. Indeed, the perspectives are very promising and range from coherent matter-wave optics to precision measurements and quantum information processing. Nowadays there exists an unprecedented control over the external magnetic, electric, or optical fields that are used to confine or alter the properties of the BECs, while matter-wave devices, such as the atom chips [2], have been developed as well. These advances, along with the formal similarities between nonlinear and matter-wave optics [3] indicate that coherent matter-waves, such as matter-wave solitons and vortices, may in principle be controlled similarly to their optical siblings in optical fibers, waveguides, photonic crystals, and so on [4].

In that respect, it is not surprising that there exist many recent works devoted to the manipulation of solitons and matter-waves. In this chapter we try to summarize these efforts, taking into regard that “manipulation” may refer to two possibilities, namely engineering either the “environment” of the matter-wave, or the matter-wave itself; both tasks are achieved by appropriately engineered external potentials. We will mainly focus on the *guidance and driving* of the matter-waves and briefly discuss – for the sake of completeness – the change of their “internal” properties and dynamics; the latter possibility was already covered, to some extent, in previous chapters (see, e.g., the discussions concerning the use of the Feshbach resonance to engineer the properties of the condensates in Chap. 2).

Our principal aim is to examine the design and use of appropriate external potentials that are able to pin and can be adiabatically translated to drag the matter-wave. We consider different types of potentials, including harmonic traps, optical lattices, barriers (and impurities), as well as combinations thereof, with appropriate, experimentally relevant, time-dependencies.

The chapter is organized as follows. We will start our presentation from the manipulation of solitons, where we will demonstrate that one may use their particle-like nature emanating from their robustness under perturbations (such as the above mentioned time-dependent potentials) to guide and drive them almost at will. We will then consider the manipulation of vortices and vortex lattices. Finally, we will briefly discuss how to engineer the matter-waves' internal dynamics upon employing external potentials that directly control the interactions and collisional dynamics of the atoms; a prominent example is the use of temporally- or spatially-dependent external fields in the vicinity of a Feshbach resonance.

17.2 General Aspects of Guidance and Driving of Matter-Waves

17.2.1 Matter-Wave Solitons in the Mean-Field Picture

We first consider the case of a quasi one-dimensional (1D) BEC confined in a trap with frequencies ω_x and $\omega_r \gg \omega_x$. Then, for sufficiently low temperatures, this quasi-1D BEC can be described by an effective 1D Gross–Pitaevskii (GP) equation [see, e.g., (1.12) of Chap. 1] of the following dimensionless form:

$$i\partial_t\psi(x, t) = \left(-\frac{1}{2}\partial_x^2 + V_{\text{ext}}(x; t) + s|\psi(x, t)|^2 \right) \psi(x, t). \quad (17.1)$$

In (17.1), the BEC density $|\psi|^2$ is rescaled by the peak density n_0 , the variables x and t are respectively measured in units of $a_r/\sqrt{2n_0|a|}$ and $(2n_0|a|\omega_r)^{-1}$ (with a being the scattering length and $a_r \equiv \sqrt{\hbar/m\omega_r}$ being the transverse harmonic oscillator length), while the energy is measured in units of the chemical potential of the system, $\mu = g_{1\text{D}}n_0$, where $g_{1\text{D}} \equiv 2\hbar\omega_r a$ is the effective 1D coupling constant. Finally, the coefficient of the nonlinear term is $s = \pm 1$ corresponding, respectively, to repulsive ($a > 0$) or attractive ($a < 0$) interatomic interactions.

In the absence of any external potential, the GP (17.1) is the completely integrable nonlinear Schrödinger (NLS) equation. In the case of attractive interatomic interactions ($s = -1$), the NLS equation possesses *bright* soliton solutions of the following form [5] (see also Chaps. 1 and 2),

$$\psi(x, t) = \eta \operatorname{sech}[\eta(x - vt)] \exp[i(kx - \omega t)], \quad (17.2)$$

where η is the amplitude and inverse spatial width of the soliton, k is the soliton wavenumber, $\omega = (1/2)(k^2 - \eta^2)$ is the soliton frequency, and, finally, $v \equiv \partial\omega/\partial k = k$ is the soliton velocity. Note that stationary bright solitons correspond to $k = 0$. On the other hand, in the case of repulsive interatomic

interactions ($s = +1$), (17.1) admits *dark* soliton solutions of the form [6] (see also Chap. 1 and Part III),

$$\psi(x, t) = (a \tanh z + iv) \exp(-i\mu_0 t), \quad (17.3)$$

where $\mu_0 \equiv u_0^2$ is the dimensionless chemical potential, $a = u_0 \cos(\varphi)$ and $v = u_0 \sin(\varphi)$ are the depth and velocity of the dark soliton respectively (φ is the phase shift across the dark soliton, with $|\varphi| < \pi/2$), and $z \equiv a(x - vt)$. Note that $\varphi = 0$ corresponds to a quiescent *black* soliton, i.e., $u = u_0 \tanh(u_0 x) \exp(-i\mu_0 t)$. Finally, as was highlighted in Part IV, if the external potential V_{ext} is an optical lattice, the appearance of a band structure in the spectrum allows for the formation of bright or dark *lattice solitons* for either attractive or repulsive interactions.

Importantly, as is known from the extensive study of the NLS equation, the above mentioned soliton solutions are robust under perturbations. This may also be the case where the external potential V_{ext} is also incorporated in (17.1): if V_{ext} can be considered as a small perturbation (e.g., if it is weak, varies slowly on the solitons' scale, etc), one may use, e.g., the perturbation theory for solitons [7] to investigate the soliton dynamics. To the leading-order of this approach, the soliton behaves like a *quasi-particle* moving in an effective potential, say V_{eff} , directly connected to the original external potential V_{ext} . This type of behavior was already discussed in previous chapters (see, e.g., Chaps. 2–5). Here, adopting the particle-like picture of matter-wave solitons, we aim to employ appropriately crafted external potentials, leading to such effective potentials V_{eff} , that will be able to guide and drive the matter-wave solitons. Below, we will assume that V_{ext} takes a rather general form, consisting of a harmonic trap, and/or an optical lattice, and/or a barrier potential (or a localized impurity).

17.2.2 Time-Dependent External Potentials

Time-dependent harmonic traps are often used (in both theory and experiment) as a means to manipulate the dynamical properties of matter-waves, and/or induce the generation of coherent nonlinear structures. For example, as was predicted theoretically in [8] and verified experimentally in [9], the displacement of the harmonic trap from one location to another, in the presence of an optical lattice, may lead to the onset of modulational instability (see, e.g., the recent review [10]) in a chain of weakly coupled BECs, which, in turn, undergoes a superfluid-insulator transition. In another context [11], setting the BEC into motion by displacing the harmonic trap, was crucial for the potential creation of solitons and vortices by Bragg reflection of the moving BEC in an optical lattice. Similarly, the displacement of the harmonic trap, but in the presence of a localized impurity rather than an optical lattice, may induce the formation of dark solitons [12]. Moreover, setting into motion a repulsive BEC trapped in optical lattices, was crucial for the experimental generation of gap matter-wave solitons [13] (cf. Part IV). Apart from

displacements, harmonic traps may be periodically modulated as in the very recent experiment of [14]; there, and in accordance to an earlier theoretical prediction [15], a time-periodic manipulation of the transverse confinement of the condensate induced longitudinal oscillations and the formation of Faraday patterns. Finally, time-dependent barrier (and impurity) potentials, in the form of off-resonant laser beams (as discussed above), were also of paramount importance for fundamental experiments. In that respect, one should mention a series of seminal experiments, such as the observation of interference of two freely expanding BECs after the switch-off of a “laser sheet” [16], or the stirring of the condensates by means of time-dependent laser beams, to create vortices [17] and vortex lattices [18].

To illustrate some case examples of guidance/manipulation, we return to (17.1) and assume the following form of $V_{\text{ext}}(x; t)$

$$V_{\text{ext}}(x; t) = \frac{1}{2} \Omega^2 x^2 + V_{\text{OL}}^{(0)} \cos^2[k(x - x_o(t)) + \phi] + V_{\text{B}}^{(0)} f(x - x_i(t)), \quad (17.4)$$

where the three contributions correspond, respectively, to a harmonic (e.g., magnetic) trap, V_{HT} , an optical lattice potential, V_{OL} , centered at x_o and a barrier (or impurity) potential, V_{B} centered at x_i . The harmonic potential is characterized by its strength $\Omega = (2n_0|a|)^{-1}(\omega_x/\omega_r)$ and may, in general, be a function of time. On the other hand, the periodic optical lattice potential is characterized by its strength $V_{\text{OL}}^{(0)}$, wavenumber k , constant phase ϕ , and a time-varying position $x_o(t)$ (cf. Chap. Part VIII). Finally, the barrier potential, assumed to be generated by a laser beam, has strength $V_{\text{B}}^{(0)}$, and is located at the time varying position $x_i(t)$. As far as the shape of the barrier is concerned, we assume the most natural beam shape, namely the Gaussian profile

$$V_{\text{B}}(x, t) = V_{\text{B}}^{(0)} \exp[-(x - x_i(t))^2/\sigma^2], \quad (17.5)$$

where σ is the width; note that in the limit $\sigma \rightarrow 0$ the barrier profile becomes a strongly localized (in fact, δ -like) impurity; in such a case, we will denote the barrier potential by V_{Imp} . The sign of the optical lattice and the barrier strengths depend on the detuning of the optical field with respect to the resonant frequency of the atoms. The case $V_{\{\text{OL,B}\}}^0 > 0$ ($V_{\{\text{OL,B}\}}^0 < 0$) corresponds to a blue- (red-) detuned laser beam, repelling (attracting) the atoms in the condensate.

The guidance and driving of matter-waves can be achieved by an external potential that must (a) effectively attract the structure to the desired pinning position, and (b) translate the pinning position with sufficient adiabaticity so that the wave can follow. We will show that an impurity or an optical lattice potential can perform these operations. The adiabatic translation of these potentials will be achieved by the following path for their centers,

$$\{x_i(t), x_o(t)\} = \eta_i + \frac{1}{2}(\eta_f - \eta_i) \left[1 + \tanh\left(\frac{t - t_0}{\tau}\right) \right], \quad (17.6)$$

where η_i and η_f denote the initial and final locations, t_0 relates to the switching time for the translation and τ measures the degree of adiabaticity of the process.

17.3 Matter-Waves and Localized Impurities

17.3.1 Bright Matter-Wave Solitons

The interaction of waves with impurities has attracted much attention in the theory of nonlinear waves [7] and solid state physics [19, 20]. In these contexts, a quite relevant study is the interaction of a bright soliton with impurities [21] (see also recent work in [22] and references therein). Here, we reexamine this problem in the context of BECs, where a harmonic trapping potential is also incorporated in the NLS equation. In particular, in this subsection, assuming that the optical lattice is absent ($V_{OL}^{(0)} = 0$), we will describe the pinning and dragging of a quasi-1D bright matter-wave soliton by a strongly localized (delta) impurity, V_{Imp} .

As noted above, for $V_{ext} = 0$, the GP (17.1) possesses a stationary bright soliton solution [see (17.2) with $k = 0$]. The existence, stability and dynamics of these bright solitons in the presence of the external potential can be analyzed using perturbation techniques [7, 23] or the Lyapunov–Schmidt theory [24]. In fact, the combined effects of the harmonic trap and a delta impurity, namely $V_{Imp}(x) = V_{Imp}^{(0)} \delta(x)$, yield an effective force on the bright soliton [25],

$$F_{\text{eff}} = F_{\text{HT}} + F_{\text{Imp}} = -2\Omega^2\eta\zeta - 2\eta^3V_{\text{Imp}}^{(0)} \tanh(\eta(x_i - \zeta)) \operatorname{sech}^2(\eta(x_i - \zeta)), \quad (17.7)$$

where the first (second) term corresponds to the harmonic trapping (localized impurity) potential. This effective force induces a Newton-type dynamics for the center ζ of the bright soliton:

$$\frac{d^2\zeta(t)/dt^2}{dt^2} = F_{\text{eff}} = F_{\text{HT}} + F_{\text{Imp}}.$$

It is important to note that the effective force exerted by the harmonic trap always points towards the center of the trap while the direction of force induced by the impurity depends on the sign of $V_{\text{Imp}}^{(0)}$. Thus, by appropriately choosing $V_{\text{Imp}}^{(0)}$ it is possible to find non-trivial positions of the bright soliton where the two effective forces balance. Specifically, (17.7) has, generically, one or three zeros. Upon closer inspection, there is always a stable fixed point close to the origin (bright soliton at the bottom of the harmonic trap) while the other two fixed points emanate from a pair of saddle-node bifurcations at finite (positive and negative, respectively) values of $V_{\text{Imp}}^{(0)}$ (see Fig. 17.1).

These results illustrate the possibility of pinning bright solitons at desired locations, using an appropriate localized impurity created by a sharply focused

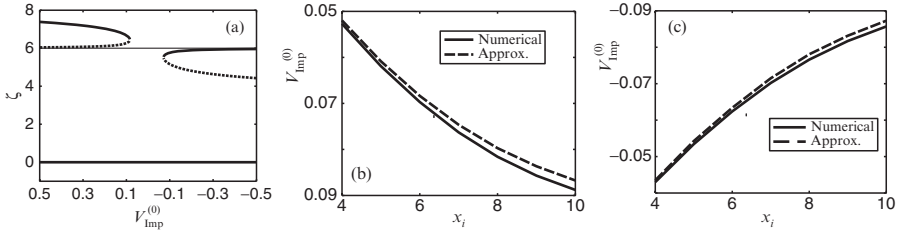


Fig. 17.1. (a) Stationary locations of a bright soliton vs. the strength of a localized impurity placed at $x_i = 6$. Stable/unstable fixed points are depicted with solid/dashed lines. (b) and (c): Critical values of $V_{\text{Imp}}^{(0)}$ for the disappearance of the two non-trivial steady states in the saddle-node bifurcation vs. x_i . Reproduced from [25] with permission

laser beam. Moreover, it is possible to drag bright solitons in a controllable way by means of an adiabatically moving impurity. An important result in that connection is that the beam's intensity must exceed a critical value in order to pin (and potentially carry) the soliton [25]. In Fig. 17.1, panels (b) and (c), we depict this critical value vs. the position of the focused impurity from the full numerics on the GP equation (solid lines) and the quasi-particle approximation (dashed lines).

Dynamical trapping of a bright matter-wave soliton may also be achieved by means of a barrier (or an impurity) potential with a rapidly oscillating position. In such a case, as discussed in Chap. 2 (see also [26] for more details) the soliton's motion takes place in an effective double-well potential.

17.3.2 Dark Matter-Wave Solitons

The interaction of a NLS dark soliton with a strongly localized (delta-like) impurity was first considered in [27] and in the BEC context in [28]. More recently, a variety of relevant problems, namely the interaction of a dark soliton with potential steps and barriers [29, 30], or with a finite size obstacle [30, 31] were also analyzed. Here, we will focus on the possibility of pinning and dragging dark matter-wave solitons by localized impurities. This case can be treated using perturbation theory for dark solitons [32]. We consider again an external potential comprised of a harmonic trap plus a delta-impurity potential, of the form $V_{\text{Imp}}(x) = V_{\text{Imp}}^{(0)} \delta(x)$. First, one needs to compute the perturbation induced by the presence of the impurity on the background field (i.e., the Thomas–Fermi cloud) and, in turn, use this modified background to compute the effect on the dark soliton dynamics [28]. This last step is achieved by the adiabatic perturbation theory developed in [32] resulting in a Newton-type equation for the center ζ of the dark soliton, i.e.,

$$\frac{d^2\zeta(t)/dt^2}{dt^2} = -dV_{\text{eff}}(\zeta)/d\zeta;$$

here, the effective potential is given by

$$V_{\text{eff}}(\zeta) = V_{\text{HT}}^{\text{eff}}(\zeta) + V_{\text{Imp}}^{\text{eff}}(\zeta) = \frac{1}{2}V_{\text{HT}}(\zeta) + \frac{1}{4}V_{\text{Imp}}^{(0)} \operatorname{sech}^2(\zeta). \quad (17.8)$$

The main result from this analysis is that while a positive (i.e., repulsive, $V_{\text{Imp}}^{(0)} > 0$) impurity, has the net effect of repelling the dark soliton centered at the bottom of the harmonic trap, for a negative (i.e., attractive, $V_{\text{Imp}}^{(0)} < 0$) impurity the bottom of the magnetic trap is a stable fixed point for the dark soliton. The tiny “dimple” induced by the attractive impurity might be used to capture and drag a dark soliton initially placed at the bottom of the harmonic trap. Indeed, if a sufficiently strong impurity is moved with sufficient adiabaticity [τ sufficiently large in (17.6)], it can drag a dark soliton [28]. This dragging can be successfully carried up to a certain distance where the “pull” exerted by the magnetic trap is strong enough to take the dark soliton off the impurity, that in turn performs the well-known [28, 33–35] harmonic oscillations inside the parabolic trap.

Another interesting type of dark soliton manipulation employing potential barriers was suggested in [36]. In that work, it was shown that a parametric driving potential, consisting of a pair of two periodically-modulated Gaussian barriers, oscillating in antiphase at a frequency close to the soliton frequency, pumps energy into the dark soliton. This energy pumping may compensate the inhomogeneity-induced emission of radiation of the dark solitons (see [37] and [35] for a numerical and an analytical study respectively), as well as the damping due to the presence of the thermal cloud [38].

17.3.3 Matter-Waves in Optical Lattices and Subject to Localized Impurities

In the general theme of wave scattering by localized impurities, a problem that has attracted attention is the existence and stability of the so-called defect (or impurity) modes, namely spatially localized oscillatory states at the impurity sites. This problem is of particular interest as it is directly related to self-trapping and energy localization in nonlinear inhomogeneous (and even disordered) systems [39]. In the BEC context, defect modes were recently analyzed in [40] for a BEC confined in an optical lattice and subject to an additional localized (defect) potential that is driven across the condensate.

In the same context, a relevant problem is the interaction of a lattice matter-wave soliton with a localized impurity [41, 42]. The main goal of [41] was to show that smooth modulations of the optical lattice may be used to manipulate matter-wave solitons, which may accelerate, decelerate, oscillate or be reflected, depending on the type of the modulation. On the other hand, in [42], the manipulation of the lattice soliton was based on its interaction with a defect (which was in fact a barrier potential). In particular, the abrupt transition from complete transmission to complete reflection of the soliton for

a critical height of the defect suggests the possibility for a “quantum switch”; in addition, the trapping of the soliton in (and its release on demand from) a defect-induced effective potential well, suggests the possibility for a “quantum memory”.

17.4 Driving Matter-Waves by Optical Lattices

17.4.1 Bright Matter-Wave Solitons

Let us now consider the manipulation of bright solitons by time-dependent optical lattices (see Chap. 1 for a brief discussion and Part VIII for more details). Consider a bright soliton trapped by the standard parabolic potential and an optical lattice as in (17.4) (with $V_B^{(0)} = 0$) with a phase $\phi = -\pi/2$, so that the optical lattice potential initially (at $t = 0$) reads $V_{OL}(x) = V_{OL}^{(0)} \sin^2(kx)$. Adopting again the quasi-particle picture of solitons and applying standard perturbation techniques [7, 23] it is possible to obtain an effective Newton-type equation of motion for the center of the bright soliton with an effective potential [43]:

$$V_{\text{eff}}(\zeta) = \eta\Omega^2\zeta^2 - \pi V_{OL}^{(0)} k \operatorname{csch}(k\pi/\eta) \cos(2k\zeta), \quad (17.9)$$

where ζ and η are the position and amplitude of the bright soliton. Note that this effective potential might have a single extremum at $\zeta = 0$ or multiple ones. The stability of the soliton resting at a stationary position can also be analyzed in terms of the effective potential (17.9): the soliton is stable if its position corresponds to an effective potential minimum. This result can be rigorously derived using the theory developed in [44] and reformulated in [45] (see also [46, 47]). Notice that the minima of the effective potential (17.9) *differ* from the minima of the external potential $V(x)$ which traps the atoms. Once a stable fixed point of the potential in (17.9) has been found, it is in principle possible to adiabatically displace [i.e., this is successful for sufficiently large τ in (17.6)] the optical lattice as per (17.4) and drag the bright soliton [43] to such a desired location. An example of this technique is depicted in the left panel of Fig. 17.2.

In the absence of the optical lattice, the bright soliton in the parabolic trap, when displaced from the center, performs harmonic oscillations with the frequency Ω , as a consequence of the Ehrenfest theorem (alias the Khon theorem [48], which states that the motion of the center of mass of a cloud of particles trapped in a parabolic potential decouples from the internal excitations). The presence of the optical lattice alters the soliton dynamics and suggests the possibility of capturing a freely oscillating bright soliton by switching-on an

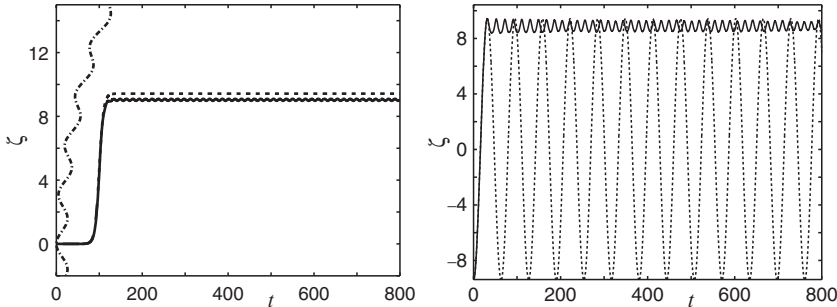


Fig. 17.2. Manipulation of a bright soliton by an optical lattice. *Left:* Transferring a bright soliton by adiabatically translating the optical lattice along the path depicted by the *dashed line*. The center of the bright soliton is depicted by the *solid line* while the *dash-dotted line* represents the combination of the harmonic and optical lattice potential at the end of the transfer. *Right:* Snaring an originally moving bright soliton (the *solid line* depicts its trajectory) by switching-on an optical lattice – see (17.10) (*solid line*). Without switching the optical lattice on, the soliton would perform harmonic oscillations (shown by the *dashed line*) in the parabolic trap. Reproduced from [43] with permission

initially static optical lattice, e.g., assuming a time-dependent optical lattice of the form,

$$V_{\text{OL}}(x; t) = \frac{1}{2} V_{\text{OL}}^{(0)} \left[1 + \tanh \left(\frac{t - t_0}{\tau} \right) \right] \sin^2(kx), \quad (17.10)$$

where t_0 and τ are constants controlling, respectively, the switch-on time and duration of the process; the latter, needs to be performed with a sufficiently strong optical lattice and an appropriately chosen position of the optical lattice so that when the soliton reaches its maximum oscillating amplitude (and zero velocity) the optical lattice is suddenly switched on with an effective potential minimum at the soliton location. This scenario is depicted on the right panel of Fig. 17.2.

17.4.2 Dark Matter-Wave Solitons

Dark matter-wave solitons may also be manipulated by means of time-dependent optical lattices. We will investigate this possibility upon considering the dynamics of dark solitons under the presence of the parabolic trap and the optical lattice (we again assume that $V_B^{(0)} = 0$). A long-period optical lattice (with respect to the healing length [1]) can be efficiently treated as a slowly-varying perturbation (and can be again treated within the realm of perturbation theory for dark solitons [32]); a short-period optical lattice, on the other hand, can be averaged out under a multiple-scale approach. Both of the above, as well as the more interesting case where the optical lattice

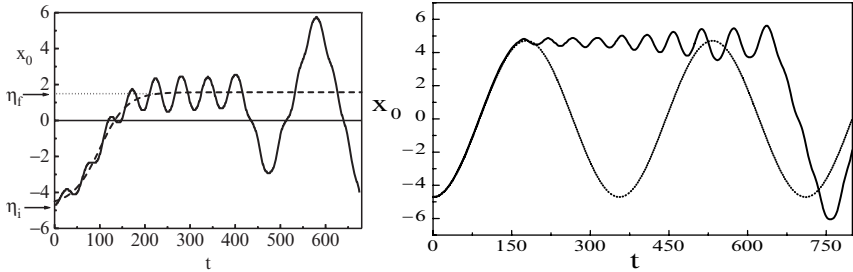


Fig. 17.3. Manipulation of a dark soliton by an optical lattice. *Left:* Typical targeted transfer of a dark soliton from its initial position, $\eta_i = -3\pi/2$, to the final one, $\eta_f = \pi/2$. The soliton delivered by the optical lattice to the pre-selected destination stays there, performing small oscillations, during the time interval $200 < t < 400$; later, it escapes due to radiation loss. *Right:* Snaring a moving dark soliton (*solid line*), initially placed at $x_0(0) = -3\pi/2$, by a potential well belonging to the time-modulated optical lattice (similar to the right panel in Fig. 17.2). The *dashed line* represents the original motion without switching the optical lattice on. After getting trapped, the dark soliton performs small-amplitude oscillations in the lattice well and later escapes due to radiation loss. Reproduced from [49] and [50] with permission

and the healing length are comparable, were treated in [49]. In the intermediate regime of $\lambda \sim \xi$, it is possible to drag the dark soliton using the optical lattice [50]. In fact, similarly to the case of bright solitons discussed in the previous section, it is possible either to drag a dark soliton by an adiabatically moving optical lattice (see left panel of Fig. 17.3), or to snare an oscillating dark soliton by the sudden switching on of the optical lattice; this should be done at the precise moment when the soliton reaches the turning point of its oscillation (see right panel of Fig. 17.3). It is important to note that in both cases, the dark soliton always eventually escapes due to radiation losses [49, 51]. A physical interpretation for this phenomenon is that a dark soliton becomes shallower due to emission of radiation and thus gains kinetic energy. Thus, after the dark soliton has gained enough speed, it escapes its local trough and performs large-amplitude oscillations.

17.4.3 Matter-Wave Solitons in Optical Superlattices

Matter-wave solitons may be manipulated also by means of “optical superlattices”, composed by two sublattices, using four laser beams with different wavenumbers and amplitudes [52]. An optical superlattice may be described as

$$V_{OL}(x) = V_1(x) + V_2(x) = V_1^{(0)} \cos(\kappa_1 x) + V_2^{(0)} \cos(\kappa_2 x), \quad (17.11)$$

where κ_1 and $\kappa_2 > \kappa_1$ are, respectively, the primary and secondary lattice wavenumbers, and $V_1^{(0)}$ and $V_2^{(0)}$ are the associated sublattice amplitudes.

A superlattice provides an additional length scale, which, together with the experimental tunability of its parameters, enhances the flexibility and hence controllability of the manipulation.

Earlier work on matter-wave solitons in optical superlattices includes studies on dark [53] and gap [54] solitons, while in a more recent work [55], all possible cases, namely the kinematics, stability, and dynamics of bright solitons (for attractive interactions) as well as dark and gap solitons (for repulsive interactions) were considered. In [53] it was shown that the interactions between dark solitons can be effectively controlled in optical superlattices, while in [54] it was shown that the effective matter-wave dispersion at the edges of the minigaps of the superlattice Bloch wave spectrum can be controlled by the relative depths of the superlattice wells; therefore, it is possible to control both the peak density and the spatial width of the emerging gap solitons. Finally, in [55], it was suggested that “dynamical superlattices”, in which specific lattice parameters are time-dependent similarly to the ones of a regular optical lattice (see Sects. 17.4.1 and 17.4.2), can be used to guide, deposit, and manipulate bright, dark, or gap matter-wave solitons.

17.5 Manipulations of Vortices

In this section, we will discuss manipulations of vortices, which are supported by higher-dimensional BECs [56, 57]. In particular, first we will consider a 2D setting, which is described by an effective 2D GP equation [the 2D analogue of (17.1), along with the 2D generalizations of the external potential contributions in (17.4)], in which vortices are not subject to 3D instabilities (e.g., corrugation of the vortex axis [56]), as the transverse dimension is effectively suppressed. In this context, we will briefly describe the interaction of vortices with impurities and optical lattices, and discuss possibilities for their manipulation. We will also discuss a number of other possible applications, some of which have already been reported in experiments.

17.5.1 Manipulating Vortices by Localized Impurities

Let us first consider the possibility of dragging the vortices by localized impurities. In the absence of the harmonic trap, vortex solutions exist for all impurity’s parameter values and the solution is stable for repulsive impurities (i.e., $V_{\text{Imp}}^{(0)} > 0$). In the presence of both the harmonic trap and the impurity, the pinning force exerted by the impurity has to be stronger than the vortex precession force induced by the harmonic trap [58–61] in order to pin the vortex at an off-center position; furthermore, as shown in [62], one needs a relatively deep impurity in order to avoid emission of sound waves.

One can also adiabatically displace the impurity in order to drag the vortex to a pre-specified location. Obviously, manipulation needs to be restricted to positions where the above-mentioned pinning exists. Figure 17.4a summarizes

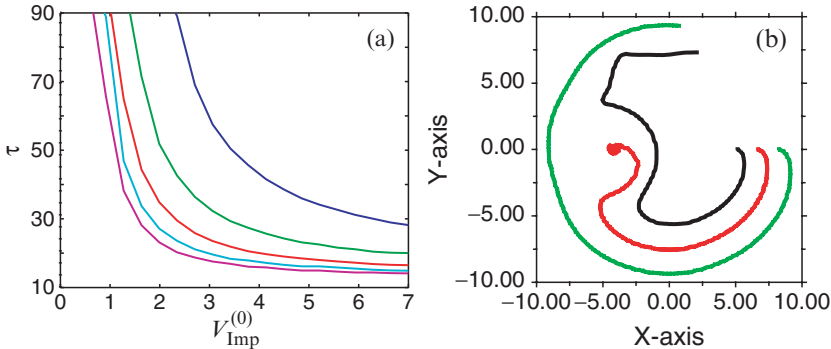


Fig. 17.4. (a) Regions (above the curves) of impurity strength $V_{\text{Imp}}^{(0)}$ vs. adiabaticity τ for successful dragging of vortices from the harmonic trap center to a position half the distance across the Thomas–Fermi radius. The different curves, corresponding to impurity widths $\sigma = 0.6, 0.8, 1.0, 1.2, 1.4$ from *top to bottom*. (b) Vortex (of unit charge) captured by a standing laser impurity. Shown are three vortex orbits starting at different distance from the harmonic trap center. The inner (outer) curve depicts the case where the radius of precession of the vortex was too small (large) to be captured by the standing laser centered at $(x_i, y_i) = (-5, 0)$. The middle curve depicts a successful capture of the vortex

results for the successful dragging across the condensate of a vortex initially placed at the center of the harmonic trap. Successful dragging was defined when the vortex was safely moved half of the Thomas–Fermi radius. The figure shows the threshold curves for successful dragging as a function of the impurity strength $V_{\text{Imp}}^{(0)}$ and adiabaticity parameter τ [see (17.6)] for different impurity widths σ [cf.(17.5)]. Naturally, for a sufficiently strong impurity and for sufficient adiabaticity it is possible to safely drag the vortex to any desired location.

Another interesting question concerns the possibility of capturing a precessing vortex by means of the impurity. Figure 17.4b shows a proof-of-principle example of this: start with a vortex pinned by an impurity at $r = r_0$, and a second impurity on the opposite side of the trap with a separate radius, $r = r_1$. The pinning impurity is then adiabatically switched-off to release the vortex allowing it to precess around the trap. If the second impurity is located at r_1 appropriately smaller than r_0 , the vortex can be pulled from its precession and captured by the impurity (middle curve in figure); otherwise the procedure fails.

17.5.2 Vortices in Optical Lattices and Vortex Lattices

Vortices in BECs confined in optical lattices and harmonic traps have been considered in various works, including vortex stability and dynamics [63, 64].

In the absence of the harmonic trap, “gap vortices” existing in the gaps of the matter-wave band-gap spectrum due to Bragg scattering were reported [65] (see also Part IV), and methods for their generation and detection were proposed [66]. Moreover, purely 3D *discrete* vortices were found to be supported by the discrete NLS equation [67], which models BECs trapped in strong optical lattices (see Part VIII).

A type of vortex manipulation occurring in this setting is the “pinning” of a vortex in the optical lattice. In particular, as shown in [63], depending on the phase of the optical lattice (in the presence of the harmonic trap), it is possible to trap the vortex at the center of the trap, or to expel it; in the latter case, the vortex moves along an unwinding spiral due to the vortex precession inside the magnetic trap (cf. [58–60]). An interesting extension of the pinning of vortices by an optical lattice is the case when a vortex lattice (cf. Part VII) is illuminated by an optical lattice. For example, it is possible to induce a transition from the triangular Abrikosov vortex lattice to a square lattice forced by the optical lattice as the strength of the latter is increased [68,69]. In a very recent relevant experiment [70], it was observed that vortices are pinned to columnar pinning sites created by a co-rotating optical lattice superimposed on a rotating condensate. Similar types of vortex manipulation include the use of large-amplitude quadrupolar shape oscillations of the condensate to induce structural phase transitions (e.g., from triangular to orthorhombic) or generation of interesting patterns (such as vortex sheets) [71], the blasting of some atoms (by external lasers) to induce Tkachenko oscillations [72], and more recently, the observation of interlaced square vortex lattices in rotating spinor BECs due to interaction between spinor states [73].

17.5.3 Vortex and Dark Soliton Nucleation Induced by Moving Impurities

Up to this point we have focused on static and *slowly* moving impurities through the condensate. If, on the other extreme, an impurity is moved with *large* speeds through the condensate, it is known to nucleate dark solitons in 1D [74] and vortices in higher dimensions [75]. These nonlinear waves can be thought of as a type of nonlinear Cerenkov radiation that is emitted, when the motion of the impurity is supercritical with respect to the local speed of sound of the BEC. Recently, a combined experimental and theoretical study of the Cerenkov emission of phonons by a laser obstacle was reported [76], and in a different study [77], it has been shown that for large obstacles the Cerenkov cone transforms into a spatial shock wave consisting of a chain of dark solitons.

An interesting variant of this problem arises in the case of *multi-component* BECs (see Part IX), which can support rich families of solutions such as combination of dark and bright solitons in the different species [78]. Then, each component has, in general, a different speed of sound (see, e.g., [79]). Therefore, as highlighted in the recent work [80] where the case of a binary BEC

with miscible components was considered, three different regimes exist for the velocity of the impurity (i) Both components are subcritical and no coherent structure is emitted. (ii) Both components are supercritical and coherent structures are nucleated in both; the structures have the form of coupled gray solitons in 1D, or vortex-lump type structures (also discussed in [79]). (iii) An intermediate regime where only one component is supercritical; this gives rise to dark-antidark solitons (i.e., bright solitons on a finite background) in 1D, and vortex-lump dipoles (obtained in stationary form in [81]) in 2D.

17.6 Manipulations of the *s*-Wave Scattering Length

Recently, much effort has been invested on the manipulations of matter-waves by appropriate “adjustments” of the *s*-wave scattering length a . The latter controls the coupling constant g [i.e., the coefficient of the nonlinear term of the GP equation – see, e.g., (1.3) of Chap. 1], leading to many interesting possibilities for “nonlinearity management” of BECs. A well-known way to change and control the scattering length is to tune an external field in the vicinity of a Feshbach resonance; this external field may be a magnetic [82], an optical [83] or a dc-electric one [84]. In low-dimensional settings, one can also tune the effective scattering length by changing the BEC’s transversal confinement [85].

Temporal variations of the scattering were crucial to many important experimental discoveries, including the formation of bright matter-wave solitons [86], the formation of molecular condensates [87] and probing the BEC–BCS crossover [88]. Additionally, theoretical studies have predicted that a time-dependent modulation of the scattering length can be used to stabilize attractive condensates in two [89] and three [90] dimensions (in the latter case, the Feshbach resonance based technique is combined with a quasi-1D optical lattice), to create robust matter-wave solitons [91], periodic waves [92], or shock waves [93].

On the other hand, the possibility of varying the scattering length *locally* (i.e., spatially) has also been recently proposed, and emerges as an interesting new direction for the manipulation of coherent matter-waves. Such spatial dependence of a , which can be implemented upon utilizing a spatially inhomogeneous external magnetic field in the vicinity of a Feshbach resonance [94] renders the collisional dynamics inhomogeneous across the BEC. These, so-called, “collisionally inhomogeneous” BECs [94] have recently attracted much attention, as they are relevant to many interesting studies and applications: These include adiabatic compression of matter-waves [94,95], atomic soliton emission and atom lasers [96], enhancement of transmittivity of matter-waves through barriers [97,98], dynamical trapping of matter-wave solitons [97], dynamics of matter-waves in the presence of periodic or random spatial variations of the scattering length [99], stable condensates exhibiting both attractive and repulsive interatomic interactions [100], and so on.

Moreover, relevant studies in a quasi-2D setting were reported in [101], while more rigorous results concerning the existence and the stability of solutions of the relevant GP equations also appeared in [102].

Conclusions

The topic of matter-wave manipulation has proved to be of great importance in the physics of BECs, as the relevant research has revealed many fundamental properties of matter-waves. Moreover, and perhaps more importantly, it has provided many ideas that can potentially be used in a variety of applications. In fact, the various possible manipulations of matter-waves pave the way of controlling macroscopic quantum states that could potentially be used for matter-wave optics applications (similar to the ones in nonlinear optics), for precision measurements and relevant devices in atomic physics, as well as for storage and processing of quantum information.

References

1. F. Dalfovo, S. Giorgini, L.P. Pitaevskii, S. Stringari, Rev. Mod. Phys. **71**, 463 (1999)
2. R. Folman, P. Krueger, J. Schmiedmayer, J. Denschlag, C. Henkel, Adv. Atom. Mol. Opt. Phys. **48**, 263 (2002)
3. S.L. Rolston W.D. Phillips, Nature **416**, 219 (2002)
4. Yu.S. Kivshar, G.P. Agrawal, *Optical Solitons: From Fibers to Photonic Crystals* (Academic Press, New York, 2003)
5. V.E. Zakharov, A.B. Shabat, Sov. Phys. JETP **34**, 62 (1971)
6. V.E. Zakharov, A.B. Shabat, Sov. Phys. JETP **37**, 823 (1973)
7. Yu.S. Kivshar, B.A. Malomed, Rev. Mod. Phys. **61**, 763 (1989)
8. A. Smerzi, A. Trombettoni, P.G. Kevrekidis, A.R. Bishop, Phys. Rev. Lett. **89**, 170402 (2002)
9. F.S. Cataliotti, L. Fallani, F. Ferlaino, C. Fort, P. Maddaloni, M. Inguscio, New J. Phys. **5**, 71 (2003)
10. P.G. Kevrekidis, D.J. Frantzeskakis, Mod. Phys. Lett. B **18**, 173 (2004)
11. R.G. Scott, A.M. Martin, T.M. Fromhold, S. Buikiewicz, F.W. Sheard, M. Leadbeater, Phys. Rev. Lett. **90**, 110404 (2003)
12. G. Theocharis, P.G. Kevrekidis, H.E. Nistazakis, D.J. Frantzeskakis, A.R. Bishop, Phys. Lett. A **337**, 441 (2005)
13. B. Eiermann, Th. Anker, M. Albiez, M. Taglieber, P. Treutlein, K.P. Marzlin, M.K. Oberthaler, Phys. Rev. Lett. **92**, 230401 (2004)
14. P. Engels, C. Atherton, M.A. Hoefer, Phys. Rev. Lett. **98**, 095301 (2007)
15. K. Staliunas, S. Longhi, G.J. de Valcárcel, Phys. Rev. Lett. **89**, 210406 (2002); Phys. Rev. A **70**, 011601 (2004)
16. M.R. Andrews, C.G. Townsend, H.J. Miesner, D.S. Durfee, D.M. Kurn, W. Ketterle, Science **275**, 637 (1997)

17. K.W. Madison, F. Chevy, W. Wohlleben, J. Dalibard, Phys. Rev. Lett. **84**, 806 (1999); S. Inouye, S. Gupta, T. Rosenband, A.P. Chikkatur, A. Görlitz, T.L. Gustavson, A.E. Leanhardt, D.E. Pritchard, W. Ketterle, Phys. Rev. Lett. **87**, 080402 (2001)
18. J.R. Abo-Shaeer, C. Raman, J.M. Vogels, W. Ketterle, Science **292**, 476 (2001); P. Engels, I. Coddington, P.C. Haljan, E.A. Cornell, Phys. Rev. Lett. **89**, 100403 (2002)
19. A.A. Maradudin, *Theoretical and Experimental Aspects of the Effects of Point Defects and Disorder on the Vibrations of Crystal* (Academic Press, New York, 1966)
20. I.M. Lifshitz, A.M. Kosevich, Rep. Prog. Phys. **29**, 217 (1966)
21. A.M. Kosevich, Physica D **41**, 253 (1990)
22. R.H. Goodman, P.J. Holmes, M.I. Weinstein, Physica D **192**, 215 (2004)
23. R. Scharf, A.R. Bishop, Phys. Rev. E **47**, 1375 (1993)
24. T. Kapitula, Physica D **156**, 186 (2001)
25. G. Herring, P.G. Kevrekidis, R. Carretero-González, B.A. Malomed, D.J. Frantzeskakis, A.R. Bishop, Phys. Lett. A **345**, 144 (2005)
26. F.Kh. Abdullaev, J. Garnier, Phys. Rev. A **75**, 033603 (2007)
27. V.V. Konotop, V.M. Pérez-García, Y.-F. Tang, L. Vázquez, Phys. Lett. A **236**, 314 (1997)
28. D.J. Frantzeskakis, G. Theocharis, F.K. Diakonos, P. Schmelcher, Yu.S. Kivshar, Phys. Rev. A **66**, 053608 (2002)
29. N.G. Parker, N.P. Proukakis, M. Leadbeater, C.S. Adams, J. Phys. B **36**, 2891 (2003)
30. N.P. Proukakis, N.G. Parker, D.J. Frantzeskakis, C.S. Adams, J. Opt. B **6**, S380 (2004)
31. N. Bilas, N. Pavloff, Phys. Rev. A **72**, 033618 (2005)
32. Yu.S. Kivshar, X. Yang, Phys. Rev. E **49**, 1657 (1994)
33. Th. Busch, J.R. Anglin, Phys. Rev. Lett. **84**, 2298 (2000)
34. V.V. Konotop, L. Pitaevskii, Phys. Rev. Lett. **93**, 240403 (2004)
35. D.E. Pelinovsky, D.J. Frantzeskakis, P.G. Kevrekidis, Phys. Rev. E **72**, 016615 (2005)
36. N.P. Proukakis, N.G. Parker, C.F. Barenghi, C.S. Adams, Phys. Rev. Lett. **93**, 130408 (2003)
37. N.G. Parker, N.P. Proukakis, M. Leadbeater, C.S. Adams, Phys. Rev. Lett. **90**, 220401 (2003)
38. P.O. Fedichev, A.E. Muryshev, G.V. Shlyapnikov, Phys. Rev. A **60**, 3220 (1999)
39. S.A. Gredeskul, Yu.S. Kivshar, Phys. Rep. **216**, 1 (1992)
40. V.A. Brazhnyi, V.V. Konotop, V.M. Pérez-García, Phys. Rev. A **74**, 023614 (2006); Phys. Rev. Lett. **96**, 060403 (2006)
41. V.A. Brazhnyi, V.V. Konotop, V. Kuzmiak, Phys. Rev. A **70**, 043604 (2004)
42. V. Ahufinger, A. Mebrahtu, R. Corbalán, A. Sanpera, New J. Phys. **9**, 4 (2007)
43. P.G. Kevrekidis, D.J. Frantzeskakis, R. Carretero-González, B.A. Malomed, G. Herring, A.R. Bishop, Phys. Rev. A, **71**, 023614 (2005)
44. M. Grillakis, J. Shatah, W. Strauss, J. Funct. Anal. **74**, 160 (1987); *ibid.* **94**, 308 (1990)
45. T. Kapitula, P.G. Kevrekidis, B. Sandstede, Physica D, **195**, 263 (2004)
46. D.E. Pelinovsky, Proc. Roy. Soc. A **461**, 783 (2005)

47. Y.-J. Oh, Comm. Math. Phys. **121**, 11 (1989); J. Diff. Eq. **81**, 255 (1989)
48. W. Kohn, Phys. Rev. **123**, 1242 (1961)
49. G. Theocharis, D.J. Frantzeskakis, R. Carretero-González, P.G. Kevrekidis, B.A. Malomed, Math. Comput. Simulat. **69**, 537 (2005)
50. G. Theocharis, D.J. Frantzeskakis, R. Carretero-González, P.G. Kevrekidis, B.A. Malomed, Phys. Rev. E **71**, 017602 (2005)
51. N.G. Parker, N.P. Proukakis, C.F. Barenghi, C.S. Adams, J. Phys. B **37**, S175 (2004)
52. S. Peil, J.V. Porto, B.L. Tolra, J.M. Obrecht, B.E. King, M. Subbotin, S.L. Rolston, W.D. Phillips, Phys. Rev. A **67**, 051603(R) (2003)
53. P.J.Y. Louis, E.A. Ostrovskaya, Yu.S. Kivshar, J. Opt. B **6**, S309 (2004)
54. P.J.Y. Louis, E.A. Ostrovskaya, Yu.S. Kivshar, Phys. Rev. A **71**, 023612 (2005)
55. M.A. Porter, P.G. Kevrekidis, R. Carretero-González, D.J. Frantzeskakis, Phys. Lett. A, **352**, 210 (2006)
56. A.L. Fetter, A.A. Svidzinsky, J. Phys.: Cond. Matt. **13**, R135 (2001)
57. P.G. Kevrekidis, R. Carretero-González, D.J. Frantzeskakis, I.G. Kevrekidis, Mod. Phys. Lett. B **18**, 1481 (2004)
58. B.P. Anderson, P.C. Haljan, C.E. Wieman, E.A. Cornell, Phys. Rev. Lett. **85**, 2857 (2000)
59. A.A. Svidzinsky, A.L. Fetter, Phys. Rev. Lett. **84**, 5919 (2000)
60. S.A. McGee, M.J. Holland, Phys. Rev. A **63**, 043608 (2001)
61. Yu.S. Kivshar, J. Christou, V. Tikhonenko, B. Luther-Davis, L.M. Pismen, Opt. Commun. **152**, 198 (1998)
62. N.G. Parker, N.P. Proukakis, C.F. Barenghi, C.S. Adams, Phys. Rev. Lett. **92**, 160403 (2004)
63. P.G. Kevrekidis, R. Carretero-González, G. Theocharis, D.J. Frantzeskakis, B.A. Malomed, J. Phys. B: At. Mol. Phys. **36**, 3467 (2003)
64. A.B. Bhattacherjee, O. Morsch, E. Arimondo, J. Phys. B: At. Mol. Phys. **37**, 2355 (2004)
65. E.A. Ostrovskaya, Yu.S. Kivshar, Phys. Rev. Lett. **93**, 160405 (2004)
66. E.A. Ostrovskaya, T.J. Alexander, Yu.S. Kivshar, Phys. Rev. A **74**, 023605 (2006)
67. P.G. Kevrekidis, B.A. Malomed, D.J. Frantzeskakis, R. Carretero-González, Phys. Rev. Lett. **93**, 080403 (2004); R. Carretero-González, P.G. Kevrekidis, B.A. Malomed, D.J. Frantzeskakis, Phys. Rev. Lett. **94**, 203901 (2005); T.J. Alexander, E.A. Ostrovskaya, A.A. Sukhorukov, Yu.S. Kivshar, Phys. Rev. A **72**, 043603 (2005)
68. J.W. Reijnders, R.A. Duine, Phys. Rev. Lett. **93**, 060401 (2004)
69. H. Pu, L.O. Baksmaty, S. Yi, N.P. Bigelow, Phys. Rev. Lett. **94**, 190401 (2005)
70. S. Tung, V. Schweikhard, E.A. Cornell, Phys. Rev. Lett. **97**, 240402 (2006)
71. P. Engels, I. Coddington, P.C. Haljan, E.A. Cornell, Phys. Rev. Lett. **89**, 100403 (2002)
72. I. Coddington, P. Engels, V. Schweikhard, E.A. Cornell, Phys. Rev. Lett. **91**, 100402 (2003)
73. V. Schweikhard, I. Coddington, P. Engels, S. Tung, E.A. Cornell, Phys. Rev. Lett. **93**, 210403 (2004)
74. V. Hakim, Phys. Rev. E **55**, 2835 (1997); A. Radouani, Phys. Rev. A **70**, 013602 (2004); R. Carretero-González, P.G. Kevrekidis, D.J. Frantzeskakis, B.A. Malomed, A.R. Bishop, Math. Comput. Simulat. **74**, 361 (2007)

75. T. Frisch, Y. Pomeau, S. Rica, Phys. Rev. Lett. **69**, 1644 (1992); B. Jackson, J.F. McCann, C.S. Adams, Phys. Rev. Lett. **80**, 3903 (1998); T. Winiecki, J.F. McCann, C.S. Adams, Phys. Rev. Lett. **82**, 5186 (1999)
76. I. Carusotto, S.X. Hu, L.A. Collins, A. Smerzi, Phys. Rev. Lett. **97**, 260403 (2006)
77. G.A. El, A. Gammal, A.M. Kamchatnov, Phys. Rev. Lett. **97**, 180405 (2006)
78. P.G. Kevrekidis, G. Theocharis, D.J. Frantzeskakis, B.A. Malomed, R. Carretero-González, Eur. Phys. J. D: At. Mol. Opt. Phys. **28** 181 (2004)
79. N.G. Berloff, cond-mat/0412743
80. H. Susanto, P.G. Kevrekidis, R. Carretero-González, B.A. Malomed, D.J. Frantzeskakis, A.R. Bishop, Phys. Rev. A **75**, 055601 (2007)
81. K. Kasamatsu, M. Tsubota, M. Ueda, Phys. Rev. Lett. **93**, 250406 (2004)
82. S. Inouye, M.R. Andrews, J. Stenger, H.J. Miesner, D.M. Stamper-Kurn, W. Ketterle, Nature **392**, 151 (1998); J.L. Roberts, N.R. Claussen, J.P. Burke, Jr., C.H. Greene, E.A. Cornell, C.E. Wieman, Phys. Rev. Lett. **81**, 5109 (1998)
83. M. Theis, G. Thalhammer, K. Winkler, M. Hellwig, G. Ruff, R. Grimm, J.H. Denschlag, Phys. Rev. Lett. **93**, 123001 (2004)
84. L. You, M. Marinescu, Phys. Rev. Lett. **81**, 4596 (1998)
85. M. Olshanii, Phys. Rev. Lett. **81**, 938 (1998); T. Bergeman, M.G. Moore, M. Olshanii, Phys. Rev. Lett. **91**, 163201 (2003)
86. K.E. Strecker, G.B. Partridge, A.G. Truscott, R.G. Hulet, Nature **417** 150 (2002); L. Khaykovich, F. Schreck, G. Ferrari, T. Bourdel, J. Cubizolles, L.D. Carr, Y. Castin, C. Salomon, Science, **296** 1290 (2002); S.L. Cornish, S.T. Thompson, C.E. Wieman, Phys. Rev. Lett. **96**, 170401 (2006)
87. J. Herbig, T. Kraemer, M. Mark, T. Weber, C. Chin, H.C. Nagerl, R. Grimm, Science **301**, 1510 (2003); C.A. Regal, C. Ticknor, J.L. Bohn, D.S. Jin, Nature **424**, 47 (2003); M. Greiner, C.A. Regal, D.S. Jin, Nature **426**, 537 (2003)
88. M. Bartenstein, A. Altmeyer, S. Riedl, S. Jochim, C. Chin, J. Hecker Denschlang, R. Grimm, Phys. Rev. Lett. **92**, 203201 (2004); T. Bourdel, L. Khaykovich, J. Cubizolles, J. Zhang, F. Chevy, M. Teichmann, L. Tarruell, S.J.J.M.F. Kokkelmans, C. Salomon, Phys. Rev. Lett. **93**, 050401 (2004)
89. F.Kh. Abdullaev, J.G. Caputo, R.A. Kraenkel, B.A. Malomed, Phys. Rev. A **67**, 013605 (2003); H. Saito, M. Ueda, Phys. Rev. Lett. **90**, 040403 (2003); G.D. Montesinos, V.M. Pérez-García, P.J. Torres, Physica D **191**, 193 (2004)
90. M. Matuszewski, E. Infeld, B.A. Malomed, M. Trippenbach, Phys. Rev. Lett. **95**, 050403 (2005); M. Trippenbach, M. Matuszewski, B.A. Malomed, Europhys. Lett. **70**, 8 (2005)
91. P.G. Kevrekidis, G. Theocharis, D.J. Frantzeskakis, B.A. Malomed, Phys. Rev. Lett. **90**, 230401 (2003); D.E. Pelinovsky, P.G. Kevrekidis, D.J. Frantzeskakis, Phys. Rev. Lett. **91**, 240201 (2003); Z.X. Liang, Z.D. Zhang, W.M. Liu, Phys. Rev. Lett. **94**, 050402 (2005)
92. F.Kh. Abdullaev, A.M. Kamchatnov, V.V. Konotop, V.A. Brazhnyi, Phys. Rev. Lett. **90**, 230402 (2003)
93. V.M. Pérez-García, V.V. Konotop, V.A. Brazhnyi, Phys. Rev. Lett. **92**, 220403 (2004)
94. G. Theocharis, P. Schmelcher, P.G. Kevrekidis, D.J. Frantzeskakis, Phys. Rev. A **72**, 033614 (2005)
95. F.Kh. Abdullaev, M. Salerno, J. Phys. B **36**, 2851 (2003)

96. M.I. Rodas-Verde, H. Michinel, V.M. Pérez-García, Phys. Rev. Lett. **95**, 153903 (2005); A.V. Carpenter, H. Michinel, M.I. Rodas-Verde, V.M. Pérez-García, Phys. Rev. A **74**, 013619 (2006)
97. G. Theocharis, P. Schmelcher, P.G. Kevrekidis, D.J. Frantzeskakis, Phys. Rev. A **74**, 053614 (2006)
98. F.Kh. Abdullaev, J. Garnier, Phys. Rev. A **74**, 013604 (2006)
99. F.Kh. Abdullaev, J. Garnier, Phys. Rev. A **72**, 061605(R) (2005)
100. G. Dong, B. Hu, W. Lu, Phys. Rev. A **74**, 063601 (2006)
101. H. Sakaguchi, B.A. Malomed, Phys. Rev. E **73**, 026601 (2006)
102. G. Fibich, Y. Sivan, M.I. Weinstein, Physica D **217**, 2006; Y. Sivan, G. Fibich, M.I. Weinstein, Phys. Rev. Lett. **97**, 193902 (2006)

Part XI

Beyond Gross–Pitaevskii Mean Field Theory

Beyond Gross–Pitaevskii Mean-Field Theory

N.P. Proukakis

18.1 Introduction

A large number of effects related to the phenomenon of Bose–Einstein Condensation (BEC) can be understood in terms of lowest order mean-field theory, whereby the entire system is assumed to be condensed, with thermal and quantum fluctuations completely ignored [1]. Such a treatment leads to the Gross–Pitaevskii Equation (GPE) [2] used extensively throughout this book. Although this theory works remarkably well for a broad range of experimental parameters, a more complete treatment is required for understanding various experiments, including experiments with solitons and vortices. Such treatments should include the dynamical coupling of the condensate to the thermal cloud, the effect of dimensionality, the role of quantum fluctuations, and should also describe the critical regime, including the process of condensate formation.

The aim of this chapter is to give a brief but insightful overview of various recent theories, which extend beyond the GPE (some of which have already been briefly mentioned in earlier chapters). As the author has been heavily involved in the development and implementation of such theories, the presentation will follow a somewhat personal perspective, following a logical progression from simple to more complex approaches, rather than a historical account. To keep the discussion brief, only the main notions and conclusions will be presented. While numerous appropriate key references are given, it is unfortunately not possible to mention all works that have contributed to the vast and growing field of finite temperature theories, and the author apologizes in advance for any such potential omissions.

This chapter generalizes the presentation of Chap. 1, by explicitly maintaining fluctuations around the condensate order parameter. While the theoretical arguments outlined here are generic, the emphasis is on approaches suitable for describing *single weakly-interacting atomic* Bose gases in *harmonic* traps. Interesting effects arising when condensates are trapped in double-well potentials and optical lattices (see Parts IV and VIII), as well as the cases of

spinor condensates (see Part IX), and atomic-molecular coupling, along with the modified or alternative theories needed to describe them, will not be covered here.

18.2 Microscopic Derivation of the Gross–Pitaevskii Equation

For a sufficiently dilute ultracold atomic gas, where only binary interactions are relevant, the Hamiltonian of the system takes the form

$$\hat{H} = \int d\mathbf{r} \hat{\Psi}^\dagger(\mathbf{r}, t) \hat{H}_0 \hat{\Psi}(\mathbf{r}, t) + \frac{1}{2} \int d\mathbf{r} d\mathbf{r}' \hat{\Psi}^\dagger(\mathbf{r}, t) \hat{\Psi}^\dagger(\mathbf{r}', t) V(\mathbf{r} - \mathbf{r}') \hat{\Psi}(\mathbf{r}', t) \hat{\Psi}(\mathbf{r}, t) \quad (18.1)$$

where $\hat{\Psi}^{(\dagger)}(\mathbf{r}, t)$ are the Bose field annihilation (creation) operators, $V(\mathbf{r} - \mathbf{r}')$ is the two-body interatomic potential, and $\hat{H}_0 = -(\hbar^2/2m)\nabla^2 + V_{\text{ext}}(\mathbf{r}, t)$ is the ‘single-particle’ operator in an external potential $V_{\text{ext}}(\mathbf{r}, t)$. In the usual discussion of BEC, the Bose field operator is typically split into two parts [3]

$$\hat{\Psi}^{(\dagger)}(\mathbf{r}, t) = \Psi^{(*)}(\mathbf{r}, t) \hat{\zeta}^{(\dagger)}(\mathbf{r}, t) + \hat{\psi}'^{(\dagger)}(\mathbf{r}, t), \quad (18.2)$$

respectively corresponding to the condensate, and non-condensate contributions. Here $\Psi^{(*)}$ is the complex ‘classical’ amplitude of the condensate, while the operator $\hat{\zeta}^{(\dagger)}$ is related to the annihilation (creation) of a particle from the condensate and accounts for fluctuations in the condensate phase. Initially, we restrict ourselves to relatively large 3D systems, sufficiently far from the regime of critical fluctuations, where we can, to good approximation, ignore the effect of the condensate operator $\hat{\zeta}^{(\dagger)}$. This approximation relies on the notion of spontaneous breaking of the $U(1)$ symmetry, and leads to the appearance of a condensate mean-field, $\Psi(\mathbf{r}, t)$, often termed the ‘condensate wavefunction’, with all related fluctuations contained in the ‘non-condensate’ operator $\hat{\psi}'(\mathbf{r}, t)$. We will return to the role and physical interpretation of $\hat{\zeta}^{(\dagger)}(\mathbf{r}, t)$ at appropriate points in this chapter.

Symmetry-Breaking Picture: We expand the Bose field operator in terms of a complete basis set $\{\phi_i(\mathbf{r})\}$ via $\hat{\Psi}^{(\dagger)}(\mathbf{r}, t) = \sum_i \hat{a}_i^{(\dagger)}(t) \phi_i^{(*)}(\mathbf{r})$, where brackets distinguish between creation and annihilation operators. We assume that each single-particle mode occupied by the condensate can be expressed in terms of a mean-field amplitude $z_i^{(*)} = \langle \hat{a}_i^{(\dagger)} \rangle$, and a fluctuation operator $\hat{c}_i^{(\dagger)} = \hat{a}_i^{(\dagger)} - \langle \hat{a}_i^{(\dagger)} \rangle$, obeying $\langle \hat{c}_i^{(\dagger)} \rangle = 0$, where $\langle \dots \rangle$ denotes averaging over all states. The *exact* equation of motion for the condensate mean-field amplitude of a general state n thus becomes [4, 5]

$$i\hbar \frac{dz_n}{dt} = \hbar\omega_n z_n + \sum_{ijk} \langle ni | \hat{V} | jk \rangle \left[z_i^* z_j z_k + 2 \langle \hat{c}_i^\dagger \hat{c}_j \rangle z_k + z_i^* \langle \hat{c}_j \hat{c}_k \rangle + \langle \hat{c}_i^\dagger \hat{c}_j \hat{c}_k \rangle \right], \quad (18.3)$$

where $\langle ni|\hat{V}|jk\rangle = (1/2)\{(ni|\hat{V}|jk) + (ni|\hat{V}|kj)\}$ is the interaction matrix element with $(ni|\hat{V}|jk) = \int \int d\mathbf{r} d\mathbf{r}' \psi_n^*(\mathbf{r})\psi_i^*(\mathbf{r}')V(\mathbf{r} - \mathbf{r}')\psi_j(\mathbf{r}')\psi_k(\mathbf{r})$, and $\hbar\omega_n = \langle n|\hat{H}_0|n\rangle$. The first three terms in the sum of (18.3) depend on the condensate mean-field, with the second term additionally depending on the non-condensate density, $\langle \hat{c}_i^\dagger \hat{c}_j \rangle$, and the third term on the average of two annihilation operators, $\langle \hat{c}_j \hat{c}_k \rangle$, termed the ‘anomalous average’. Importantly, however, (3) contains an additional term due to correlations of *three* fluctuation operators which does *not* depend directly on the condensate mean-field. Although such ‘triplet’ terms $\langle \hat{c}_i^\dagger \hat{c}_j \hat{c}_k \rangle$ were ignored in the majority of early treatments (see, e.g. [6–8] and references therein), it is *precisely* these contributions, which enable the transfer of atoms and energy between the condensate and the thermal cloud in kinetic theories [4, 5, 9–13].

Introduction of an Effective Interaction: The usual ‘naive’ justification for the Gross–Pitaevskii Equation, is to ignore *all* non-condensate fluctuations, while simultaneously approximating the interatomic potential by a delta function, via $V(\mathbf{r} - \mathbf{r}') = g\delta(\mathbf{r} - \mathbf{r}')$, where g a suitable effective interaction strength. While instructive, this is misleading, because $V(\mathbf{r} - \mathbf{r}')$ corresponds to the *actual* interatomic potential, whereas g is the interaction strength for a complete effective binary *s*-wave scattering contact interaction in vacuum [14], which generally proceeds via *virtual intermediate* excited states, which may be occupied. This ‘renormalization’ of the coupling constant was first discussed for the homogeneous Bose gas by Beliaev [15] and generalized to finite temperatures by Popov [16]; this problem was recently discussed by various approaches by Stoof et al. [17, 18], Proukakis et al. [19–21], Shi and Griffin [22] and Morgan [23]. We follow the notation of Proukakis et al. [5] and investigate the condensate evolution at zero temperature, where there is a negligible non-condensate population, such that $\langle \hat{c}_i^\dagger \hat{c}_j \rangle \approx \langle \hat{c}_i^\dagger \hat{c}_j \hat{c}_k \rangle \approx 0$. Apart from pure mean-field effects, $z_i^* z_j z_k$, the equation for the mean amplitude z_n still contains a contribution from the anomalous average. The latter can be separated via $\langle \hat{c}_j \hat{c}_k \rangle = \langle \hat{c}_j \hat{c}_k \rangle_0 + \delta\langle \hat{c}_j \hat{c}_k \rangle$ into a slowly-varying contribution over low-lying states, $\langle \hat{c}_j \hat{c}_k \rangle_0$, and a contribution over high-lying states, $\delta\langle \hat{c}_j \hat{c}_k \rangle$, which varies *within* a collisional timescale. By using the corresponding equation of motion for $\delta\langle \hat{c}_j \hat{c}_k \rangle$ to adiabatically eliminate this quantity from the zero-temperature limit of (18.3), the latter takes the form [4, 19]

$$i\hbar \frac{dz_n}{dt} = \hbar\omega_n z_n + \sum_{ijk} \langle ni|\hat{T}^{2B}|jk\rangle z_i^* [z_j z_k + \langle \hat{c}_j \hat{c}_k \rangle_0], \quad (18.4)$$

where \hat{T}^{2B} represents an effective two-body interaction term obeying a Lippmann–Schwinger relation [4] expressing the complete repeated scattering amplitude for two particles in an empty trap. This procedure corresponds to a diagrammatic resummation of a selected class of diagrams [4, 17, 22]. This effective interaction is strictly only valid when used to describe the coupling between low momentum states [4, 13, 23, 24], and cannot be used as a real

potential acting between the atoms. Ignoring all energy and momentum dependence, this ‘renormalized’ interaction can now be approximated by an effective contact (pseudo)potential $\hat{T}^{2B}(\mathbf{r}, \mathbf{r}') = g\delta(\mathbf{r} - \mathbf{r}')$, where $g = 4\pi\hbar^2 a/m$, and a is the s -wave scattering length [14, 25]. The implicit assumption of a constant, momentum-independent, scattering amplitude must be used cautiously, and is valid only up to some maximum momentum $k_{\max} \propto 1/a$ [16]. The anomalous contribution $\langle \hat{c}_j \hat{c}_k \rangle_0$ accounts for many-body effects which are typically neglected in dilute weakly-interacting gases (see Sect. 18.3). Re-expressing the mean-value equation in terms of the condensate mean-field $\Psi(\mathbf{r}, t)$, we obtain the Gross–Pitaevskii Equation at $T = 0$,

$$i\hbar \frac{\partial}{\partial t} \Psi(\mathbf{r}, t) = \left[\hat{H}_0 + g |\Psi(\mathbf{r}, t)|^2 \right] \Psi(\mathbf{r}, t) = \hat{H}_{GP} \Psi(\mathbf{r}, t), \quad (18.5)$$

Number-Conserving Treatment: The above treatment assumes the existence of a mean-field, and thus relies on spontaneous symmetry breaking. While convenient, this notion is somewhat ill-defined for a finite trapped gas with a fixed atom number N , since the condensate mean-field corresponds to the ensemble average over number states $|N\rangle$, with $\langle N|\hat{\Psi}(\mathbf{r}, t)|N\rangle = \Psi(\mathbf{r}, t)\langle N|N-1\rangle = 0$. The usual justification is that for a system with a large number of particles, $N \pm 1 \approx N$ with accuracy $(1/N)$, essentially assuming that the condensate operators commute [26]. Such arguments are valid in the grand canonical ensemble, where the atom number is not fixed, and one minimizes the shifted Hamiltonian $(\hat{H} - \mu \hat{N})$, where μ is the chemical potential and \hat{N} is the number operator. Also, no difficulties arise if, by analogy to laser theory, we treat the condensate as a coherent state $|\alpha\rangle$, i.e. a superposition of number states for which $\langle \alpha|\alpha\rangle \neq 0$ by construction.

Gardiner argued that the apparent non-conservation of particle numbers arises from an inappropriate definition of the quasi-particle operators. This led to the development of a $U(1)$ -symmetry-preserving approach, relying on the separation of the ‘particle’ and ‘phonon’ concepts [27]. Following Gardiner’s notation, $\hat{\Psi}(\mathbf{r}) = \hat{A}[\xi(\mathbf{r}) + (1/\sqrt{N})\hat{\chi}(\mathbf{r})]$ where $\xi(\mathbf{r})$ is the condensate wavefunction obeying the usual GPE, $\hat{\chi}(\mathbf{r})$ is a phonon field operator, and \hat{A} is a generalized annihilation operator ensuring total particle number conservation. This approach sets the correct basis for further treatment [28], with an equivalent approach formulated by Castin and Dum [29] and extended to finite temperatures by Morgan [23].

The remaining sections generalize the above treatment to finite temperatures. Crudely speaking, one can divide such generalized treatments into those that rely on a suitably truncated hierarchy of coupled equations of motion for generalized mean-fields (Sects. 18.3 and 18.4), and those in which the lowest modes of the system, which include both condensate and quasi-particles, are described in a unified manner by appropriate probability distribution functions (Sect. 18.5), giving rise to various stochastic approaches (Sect. 18.6). Section 18.7 briefly discusses the importance of fluctuations in the phase of the condensate, relevant in low dimensional systems.

18.3 Generalized Mean-Fields: Static Thermal Cloud

From (3), it is clear that the condensate mean-field $\Psi(\mathbf{r}, t)$ is coupled to ‘higher order’ mean-fields (normal and anomalous averages). Their corresponding equations of motion are, in turn, coupled to yet higher order correlations of the non-condensate operators, and so forth. A closed set of equations requires a consistent set of decoupling approximations, thereby uniquely defining a set of generalized mean-fields which should accurately determine the static and dynamic properties of the system [30]. Equations of this form are well-known in the literature and can be derived by variational [17, 31], or diagrammatic [22] methods. A description in terms of the three lowest order averages $\langle \hat{\Psi} \rangle$, $\langle \hat{\psi}'^\dagger \hat{\psi}' \rangle$ and $\langle \hat{\psi}' \hat{\psi}' \rangle$ is known as the Hartree–Fock–Bogoliubov (HFB) theory (see below) [32].

Mean-Field Approximation: To first approximation, one can ignore *particle exchange* between condensate and thermal cloud (i.e. the triplets), and allow only *mean-field coupling* between them. Such a theory arises upon reducing the Hamiltonian of (18.1) to quadratic form via the ‘mean-field’ approximations [4, 8, 23] $\hat{\psi}'^\dagger \hat{\psi}' \hat{\psi}' \approx 2\langle \hat{\psi}'^\dagger \hat{\psi}' \rangle \hat{\psi}' + \hat{\psi}'^\dagger \langle \hat{\psi}' \hat{\psi}' \rangle$ and $\hat{\psi}'^\dagger \hat{\psi}'^\dagger \hat{\psi}' \hat{\psi}' \approx 4\langle \hat{\psi}'^\dagger \hat{\psi}' \rangle \hat{\psi}'^\dagger \hat{\psi}' + \langle \hat{\psi}'^\dagger \hat{\psi}'^\dagger \rangle \hat{\psi}' \hat{\psi}' + \langle \hat{\psi}' \hat{\psi}' \rangle \hat{\psi}'^\dagger \hat{\psi}'^\dagger - 2\langle \hat{\psi}'^\dagger \hat{\psi}' \rangle \langle \hat{\psi}'^\dagger \hat{\psi}' \rangle - \langle \hat{\psi}' \hat{\psi}' \rangle \langle \hat{\psi}'^\dagger \hat{\psi}'^\dagger \rangle$ the latter justified from Wick’s theorem [14]. This leads to an effective quadratic Hamiltonian in which single-particle energies are shifted by the added mean-field potentials. Such a Hamiltonian can be diagonalized by the Bogoliubov transformation $\psi'(\mathbf{r}) = \sum_i \phi_i(\mathbf{r}) \hat{c}_i = \sum_j [u_j(\mathbf{r}) \hat{\beta}_j - v_j^*(\mathbf{r}) \hat{\beta}_j^\dagger]$, mapping single-particle non-condensate operators \hat{c}_i into mixtures of ‘quasi-particle’ operators $\hat{\beta}_j$ and $\hat{\beta}_j^\dagger$. This leads to a generalized GPE

$$i\hbar \frac{\partial}{\partial t} \Psi(\mathbf{r}, t) = \left[\hat{H}_0 + g \left[|\Psi(\mathbf{r}, t)|^2 + 2n'(\mathbf{r}, t) \right] \right] \Psi(\mathbf{r}, t) + \tilde{m}_0(\mathbf{r}, t) \Psi^*(\mathbf{r}, t), \quad (18.6)$$

which, compared to the GPE of (18.5) contains additional contributions from the *mean-field coupling* of the condensate Ψ to the non-condensate n' (with the factor of two arising due to direct and exchange contributions [14]) and the anomalous average \tilde{m}_0 . The above equation is coupled to finite temperature ‘Bogoliubov-de Gennes’ equations for the excitation amplitudes $u_j(\mathbf{r})$, $v_j(\mathbf{r})$. Such a closed set of equations (see Eqs. (18.7)–(18.8)) is known as the HFB theory [8, 14, 31, 32].

Many-Body Effects: We argued that the two-body effective interaction, \hat{T}^{2B} , arises via adiabatic elimination of rapidly-varying anomalous averages. Such an effective interaction describes the collisional amplitude in vacuum, whereas in trapped gases collisions take place within a medium of other condensed and excited particles. This leads to important modifications in the description of atom-atom interactions [17, 19, 20, 22] which can again be incorporated into a more general effective interaction, the many-body T-matrix, \hat{T}^{MB} . This can be approximated (in the zero-energy, zero-momentum limit)

by a contact potential with a position-dependent amplitude $g_{\text{eff}}(\mathbf{r}) = g[1 + \tilde{m}_0(\mathbf{r})/\psi^2(\mathbf{r})]$ [21, 24, 34]; here $\tilde{m}_0(\mathbf{r})$ denotes the ‘regularized’ position representation of the anomalous average over low-lying states (see below). Since $\tilde{m}_0(\mathbf{r})$ is of the same order of magnitude as the non-condensate density $n'(\mathbf{r})$, its effect should, in general, not be ignored [33].

HFB and Related Approaches: To first approximation, the non-condensate component is treated as static, yielding the static HFB equations, which, written in a slightly more general notation to facilitate subsequent discussion, take the form

$$\left[\hat{H}_0 - \mu + g_{\text{con}}(\mathbf{r})|\psi(\mathbf{r})|^2 + 2g_{\text{exc}}(\mathbf{r})n'(\mathbf{r}) \right] \psi(\mathbf{r}) = 0, \quad (18.7)$$

$$\begin{pmatrix} \hat{L} & \hat{M} \\ -\hat{M}^* & -\hat{L}^* \end{pmatrix} \begin{pmatrix} u_j \\ v_j \end{pmatrix} = \hbar\omega_j \begin{pmatrix} u_j \\ v_j \end{pmatrix}, \quad (18.8)$$

where $\hat{L}(\mathbf{r}) = \hat{H}_0 - \mu + 2g_{\text{con}}(\mathbf{r})|\psi(\mathbf{r})|^2 + 2g_{\text{exc}}(\mathbf{r})n'(\mathbf{r})$ and $\hat{M} = g_{\text{con}}(\mathbf{r})\psi^2(\mathbf{r})$.

This general form distinguishes between the effective interaction for a collision between two condensate atoms, $g_{\text{con}}(\mathbf{r})$, from the corresponding one for collisions involving a condensate and a non-condensate atom, $g_{\text{exc}}(\mathbf{r})$. Solving Eqs. (18.7)–(18.8) yields the ‘Bogoliubov functions’ $u_j(\mathbf{r})$ and $v_j(\mathbf{r})$, in terms of which we can directly obtain the time-independent normal $n'(\mathbf{r}) = \sum_j (|u_j(\mathbf{r})|^2 + |v_j(\mathbf{r})|^2)N_{\text{BE}}(\varepsilon_j) + |v_j(\mathbf{r})|^2$ and anomalous $\tilde{m}_0(\mathbf{r}) = \sum_j u_j(\mathbf{r})v_j^*(\mathbf{r})[2N_{\text{BE}}(\varepsilon_j) + 1] - \tilde{m}_{\text{UV}}(\mathbf{r})$ averages. Here $N_{\text{BE}}(\varepsilon_j) = [\exp(\beta\hbar\omega_j) - 1]^{-1}$ is the Bose–Einstein distribution with $\beta = 1/k_B T$. The term $\tilde{m}_{\text{UV}}(\mathbf{r})$ is required to ensure the regularization of the anomalous average by subtracting off the ultraviolet divergences arising in the homogeneous limit due to the use of a momentum-independent contact interaction.

The standard HFB limit is based on $g_{\text{con}}(\mathbf{r}) = g_{\text{exc}}(\mathbf{r}) = g$ everywhere *except* in (18.7) where $g_{\text{exc}}(\mathbf{r}) = g$ still, but $g_{\text{con}}(\mathbf{r}) = g_{\text{eff}}(\mathbf{r})$. This inconsistent treatment of effective interactions leads to the appearance of a gap in the homogeneous single-particle excitation spectrum at zero momentum, in direct contrast to the Goldstone theorem which guarantees a gapless spectrum in the presence of $U(1)$ symmetry-breaking [35], and the Hugenholtz–Pines theorem [36]. As a result, the full HFB theory should not be used to calculate excitation frequencies. One common way to overcome this problem, is to completely ignore the *additional* influence of the medium on collisions of trapped atoms, i.e. to set $\tilde{m}_0(\mathbf{r}) = 0$ [8, 22]. This led to the first quantitative predictions of excitation frequencies of trapped Bose gases at low temperatures [37], in agreement with experiments. The reduced gapless theory with $\tilde{m}_0(\mathbf{r}) = 0$ is often termed ‘HFB-Popov’ approximation (but see [33].)

In order to obtain a consistent theory for excitation frequencies, but additionally include the modification imposed by the medium on the collisional properties (i.e. $\tilde{m}_0(\mathbf{r} \neq 0)$), one may use the above generalized form of the

theory, with the effective interaction $g_{\text{con}}(\mathbf{r}) = g_{\text{eff}}(\mathbf{r})$ for the scattering of two atoms in the condensate, and the mean-field coupling between the condensate and non-condensate, $g_{\text{exc}}(\mathbf{r})$, approximated either by g , or by $g_{\text{eff}}(\mathbf{r})$ consistently throughout Eqs. (18.7)–(18.8). These correspond to different approximate treatments of the relative momenta of colliding atoms, and give rise to two different generalized ‘gapless’ theories, GHFB1 and GHFB2 [21, 24] (see also [38]). These theories have been applied to excitation frequencies, vortices and the study of coherence of 2D condensates [34, 39]. Alternative approaches to the HFB gap problem appear in [33, 40].

18.4 Generalized Mean-Fields: Dynamic Thermal Cloud

So far, the non-condensate has been treated as static. Such approaches cannot account for common dissipative process in the condensate, e.g. *Landau* damping (coalescence of two excitations into a single one of higher energy) and *Beliaev* damping (breaking up of an excitation into two excitations of lower energies), which require a coupled dynamical description of both condensate and non-condensate [1]. A complete theoretical picture must also describe collisions between condensate and non-condensate atoms, as well as between two non-condensate atoms.

18.4.1 Time-Dependent Hartree–Fock–Bogoliubov

This section outlines the work of the author [4] as finalized in [9]. The exact equation of motion for the non-condensate $\langle \hat{c}_i^\dagger \hat{c}_j \rangle$ depends on averages of up to four fluctuation operators $\hat{c}_i = \hat{a}_i - z_i$. Using second order perturbation theory, and considering for simplicity a single condensate mean-field amplitude, z_0 , coupled to numerous excited levels of populations n_i , one obtains coupled equations governing their evolution. The equation for dn_i/dt includes, among other terms, the following contribution accounting for collisions between two non-condensate atoms

$$\left(\frac{4\pi}{\hbar^2} \right) \sum_{rms} |T_{rmsi}^{2B}|^2 [(n_i + 1)(n_m + 1)n_r n_s - n_i n_m (n_r + 1)(n_s + 1)] \delta(\omega_{rmsi}) \quad (18.9)$$

where $\omega_{rmsi} = (\omega_r + \omega_s - \omega_m - \omega_i)$. We also obtain the following *additional* contribution to the thermal cloud dynamics dn_i/dt due to the presence of a condensate

$$\left(\frac{4\pi}{\hbar^2} \right) |z_0|^2 \sum_{rs} |T_{rs0i}^{2B}|^2 [(n_i + 1)n_r n_s - n_i (n_r + 1)(n_s + 1)] \delta(\omega_{rs0i}). \quad (18.10)$$

This term is proportional to $|z_0|^2$ and describes the change in the non-condensate population of level i induced by the transfer of a single atom to, or from the condensate (level 0). One must also consider the corresponding change in the condensate population associated with such processes. Adiabatic elimination of the triplet correlation $\langle \hat{c}_i^\dagger \hat{c}_j \hat{c}_k \rangle$ in (18.3) leads to [4]

$$\begin{aligned} i\hbar \frac{dz_0}{dt} &= \hbar\omega_0 z_0 + \left(T_{0000}^{2B} |z_0|^2 + 2 \sum_i T_{0ii0}^{2B} n_i \right) z_0 \\ &\quad + i \left(\frac{2\pi}{\hbar} \right) z_0 \sum_{irs} |T_{rs0i}^{2B}|^2 [(n_i + 1)n_r n_s - n_i(n_r + 1)(n_s + 1)] \delta(\omega_{rs0i}), \end{aligned} \quad (18.11)$$

which clearly contains both energy shifts due to mean-fields and damping. The equations given above contain the essential *key elements* for a consistent kinetic theory for a partially-Bose-condensed gas. These reveal that while the scattering of a particle into an excited state i is ‘bosonically enhanced’ by the factor $(n_i + 1)$, the corresponding scattering into the condensate does not feature spontaneous growth (i.e. one simply obtains $|z_0|^2$ and z_0 in Eqs. (18.10) and (18.11) respectively).

The discussion thus far relied on a perturbative expansion beyond a single-particle basis of *bare* (undressed) particles, and has led to dressing of the energies from the mean-fields of the condensate, $|z_0|^2$, and the non-condensate, n_i . Such basis choice is, however, not very suitable for typical systems containing a condensate spanning numerous trap eigenstates. While one could transform the above equations to a quasi-particle basis, this leads to rather involved expressions [41,42]. An alternative, but *equivalent*, approach is to *first* incorporate all relevant HFB mean-field effects into the basis, i.e. shift from bare single-particle energies $\hbar\omega_n = \langle n | \hat{H}_0 | n \rangle$ to dressed quasi-particle energies $\hbar\omega_n^{\text{HFB}} = \langle n | \hat{H}_{\text{HFB}} | n \rangle$ where \hat{H}_{HFB} is the reduced quadratic Hamiltonian with mean-field effects included [14], and *subsequently* perform second order perturbation theory beyond this dressed basis. In this case, the perturbative terms arise from the difference between the *exact* expressions of products of fluctuation operators, and their corresponding HFB mean-field decompositions. For example, one part of the perturbative Hamiltonian arises from the ‘beyond-mean-field’ quantity $\langle \hat{\psi}'^\dagger \hat{\psi}'^\dagger \hat{\psi}' \hat{\psi}' \rangle - (2\langle \hat{\psi}'^\dagger \hat{\psi}' \rangle^2 + \langle \hat{\psi}'^\dagger \hat{\psi}'^\dagger \rangle \langle \hat{\psi}' \hat{\psi}' \rangle)$ as suggested by Morgan [23] and Zaremba, Nikuni and Griffin [43]. Explicitly performing this (see [9] for details) yields a set of coupled time-dependent non-Markovian equations for the mean-field amplitudes z , $\langle \hat{c}^\dagger \hat{c} \rangle$ and $\langle \hat{c} \hat{c} \rangle$, corresponding to Ψ , n' and \tilde{m}_0 . These equations describe all atomic collisions, including not only collisions within the condensate, but also particle exchange between condensate and non-condensate and collisions of two thermal atoms. This theory was first derived by Walser et al. [12,44], using slightly different, but entirely equivalent, arguments (based on separation of timescales for the evolution of the relevant physical parameters), and subsequently obtained by

the author [9]. The reader is referred to [9, 12, 44] for details, implementation, and relation to other treatments.

The perturbation theory presented here can also be derived, perhaps somewhat more systematically, from the method of non-commutative cumulants, in which the cumulants capture the essential correlations in the system by subtracting factorizable contributions from the correlation functions, as mentioned above, with such an approach already successfully implemented in diverse contexts [45].

Gapless Second-Order Perturbation Theory: To monitor situations close to equilibrium, Giorgini [6], and Rusch and Burnett [46] performed a linear response treatment around static values of the HFB parameters z , $\langle \hat{c}^\dagger \hat{c} \rangle$, and $\langle \hat{c} \hat{c} \rangle$. This was discussed in detail in a series of papers by Morgan [23], who additionally reconciled the rigorous introduction of an effective interaction with the number-conserving formalism. Morgan’s approach, based on a perturbative treatment beyond the HFB basis, accounts for the indirect excitation of the condensate via excitation of the thermal cloud, as needed to interpret the excitation frequencies and damping rates at JILA [47] (see also [48, 49]). The resulting form of the Bogoliubov-de Gennes equations for the excitations are similar to those of Eqs. (18.7)–(18.8), but with additional, or modified terms to ensure orthogonality between condensate and non-condensate and number conservation. Such a theory consistently includes damping effects, population changes due to quasi-particle collisions and finite size effects.

18.4.2 Theory of Zaremba–Nikuni–Griffin

Parallel to the above developments, Zaremba, Nikuni and Griffin (ZNG) presented the first computationally implementable generalized mean-field theory describing the coupled evolution of condensate and thermal cloud [43]. The starting point is the same as the time-dependent HFB approach. While the subsequent treatment ignores the anomalous average (i.e. many-body effects included in [9, 12]), this theory made a significant contribution by implementing local energy and momentum conservation [30]. The resulting kinetic equations are valid in both mean-field and hydrodynamic regimes. In this theory, the condensate evolves according to

$$i\hbar \frac{\partial}{\partial t} \Psi(\mathbf{r}, t) = \left[\hat{H}_0 + g \left[|\Psi(\mathbf{r}, t)|^2 + 2n'(\mathbf{r}, t) \right] - iR(\mathbf{r}, t) \right] \Psi(\mathbf{r}, t) \quad (18.12)$$

with the coupled non-condensate density $n'(\mathbf{r}, t)$ described in terms of a Wigner phase-space representation $f(\mathbf{r}, \mathbf{p}, t)$ via $n'(\mathbf{r}, t) = \int d\mathbf{p}/(2\pi\hbar)^3 f(\mathbf{r}, \mathbf{p}, t)$, with f obeying a generalized ‘Quantum Boltzmann’ kinetic equation [50]

$$\frac{\partial}{\partial t} f(\mathbf{r}, \mathbf{p}, t) + \frac{\mathbf{p}}{m} \cdot \nabla f(\mathbf{r}, \mathbf{p}, t) - \nabla V_{\text{eff}}(\mathbf{r}, t) \cdot \nabla_p f(\mathbf{r}, \mathbf{p}, t) = C_{12}[f] + C_{22}[f] \quad (18.13)$$

with an effective mean-field potential $V_{\text{eff}}(\mathbf{r}, t) = V_{\text{ext}}(\mathbf{r}, t) + 2g[|\Psi(\mathbf{r}, t)|^2 + n'(\mathbf{r}, t)]$. This equation contains two collisional terms: C_{22} describing collisions between *non-condensate* atoms, and C_{12} describing the *transfer of an atom* from the non-condensate into the condensate, and its inverse process. These are given by

$$\begin{aligned} C_{22}[f] &= \frac{4\pi}{\hbar} g^2 \int \frac{d\mathbf{p}_2}{(2\pi\hbar)^3} \int \frac{d\mathbf{p}_3}{(2\pi\hbar)^3} \int \frac{d\mathbf{p}_4}{(2\pi\hbar)^3} (2\pi\hbar)^3 \delta(\mathbf{p} + \mathbf{p}_2 - \mathbf{p}_3 - \mathbf{p}_4) \\ &\quad \delta(\varepsilon + \varepsilon_2 - \varepsilon_3 - \varepsilon_4) [(1+f)(1+f_2)f_3f_4 - ff_2(1+f_3)(1+f_4)] \end{aligned} \quad (18.14)$$

$$\begin{aligned} C_{12}[f] &= \frac{4\pi}{\hbar} g^2 |\Psi|^2 \int \frac{d\mathbf{p}_2}{(2\pi\hbar)^3} \int \frac{d\mathbf{p}_3}{(2\pi\hbar)^3} \int \frac{d\mathbf{p}_4}{(2\pi\hbar)^3} (2\pi\hbar)^3 \delta(m\mathbf{v}_c + \mathbf{p}_2 - \mathbf{p}_3 - \mathbf{p}_4) \\ &\quad \delta(\varepsilon_c + \varepsilon_2 - \varepsilon_3 - \varepsilon_4) (2\pi\hbar)^3 [\delta(\mathbf{p} - \mathbf{p}_2) - \delta(\mathbf{p} - \mathbf{p}_3) - \delta(\mathbf{p} - \mathbf{p}_4)] \\ &\quad \times [(1+f_2)f_3f_4 - f_2(1+f_3)(1+f_4)], \end{aligned} \quad (18.15)$$

where $f_i = f(\mathbf{r}_i, \mathbf{p}_i, t)$, $\varepsilon_i = p_i^2/2m + V_{\text{eff}}(\mathbf{r})$, and $\varepsilon_c = \mu_c + mv_c^2/2$ is the local condensate energy. The condensate growth term, $-iR(\mathbf{r}, t)$ in (18.12) arises from ‘triplet’ correlations and is defined by $R(\mathbf{r}, t) = \hbar/2|\Psi|^2 \int d\mathbf{p}/(2\pi\hbar)^3 C_{12}[f]$.

The original numerical implementation of this theory [11] successfully addressed the issue of condensate formation by relying on the ergodic approximation [50], which assumes that equilibration is rapid for atoms with similar energies, thus enabling the phase-space variable $f_i = f(\mathbf{r}_i, \mathbf{p}_i, t)$ to be expressed only in terms of an energy variable $E(\mathbf{r}_i, \mathbf{p}_i, t)$. These calculations were subsequently generalized [49, 51] to strongly non-equilibrium regimes by representing the phase-space density by a collection of N discrete ‘test particles’, with collisions between them handled via an appropriate Monte Carlo sampling scheme. Despite ignoring many-body effects, this theory yields remarkable agreement with various experiments, e.g. scissor’s mode, quadrupole excitations and transverse breathing modes of elongated condensates [51]. Hydrodynamic collective modes and vortex nucleation at finite temperatures were also discussed [52, 53]. The ZNG theory also explained the observed dark soliton decay in the Hannover experiment [54], and ascertained the required conditions for the observation of dark soliton oscillations in elongated harmonically-confined BECs [55]. The ZNG theory arises as a limiting case of the approaches of Stoof and Gardiner, Zoller and co-workers discussed next.

Damping of excitations was also addressed by a different approach by Fedichev, Shlyapnikov and collaborators who studied stability of vortices and dark solitons by considering the scattering of excitations from such macroscopically excited states [57], with this formalism applied to bright solitons by Sinha et al. [58].

18.5 Kinetic Theories based on Probability Distribution Functions

All the above theories have the common feature of treating the condensate as a separate entity from the thermal cloud, with the former typically identified as the mean value of the Bose field operator $\langle \hat{\Psi}(\mathbf{r}, t) \rangle$. Such perturbative theories cannot predict phenomena in the critical regime, e.g. onset of condensation, or the shift in the critical temperature T_c . An alternative ‘class’ of approaches was thus developed, in which one treats the low-lying part of the spectrum, including *both* the condensate and the low-lying excitations as one entity, with the remaining high-lying modes treated separately, by means of a Quantum Boltzmann Equation.

18.5.1 Stoof’s Non-Equilibrium Theory

Stoof developed a unified finite temperature quantum kinetic theory by investigating the evolution of the entire system by means of a Wigner probability distribution $P[\phi^*, \phi; t]$ [18,56]. At time t , this distribution gives the probability of the system to be in a coherent state $|\phi(\mathbf{r}); t\rangle = \exp\{\int d\mathbf{r} \phi(\mathbf{r}) \hat{\Psi}^\dagger(\mathbf{r}, t)\}|0\rangle$, where $|0\rangle$ is the vacuum state. Using suitably normalized coherent states, $P[\phi^*, \phi; t] = Tr [\hat{\rho}(t_0)|\phi; t\rangle\langle\phi; t|]$, where $\hat{\rho}(t_0)$ the initial density matrix of the system prior to the onset of condensation, the determination of the probability function reduces to the calculation of a functional integral containing the probabilities $|\langle\phi; t|\phi_0; t_0\rangle|^2$. This can be evaluated as a ‘path integral’ over all field evolutions from t to t_0 and back to t , leading to the Keldysh non-equilibrium formalism. Such an approach, enables a systematic consideration of the fluctuations around the mean-field, with all correlation functions obtained from moments of the distribution $P[\phi^*, \phi; t]$. The derivation of this theory is given in [56], with a brief insightful account presented in Refs. [59–61]. By working with a quantized quadratic effective action, in which interactions are ‘renormalized’ to the many-body T-matrix, one obtains a Fokker–Planck equation for the full probability distribution function $P[\phi^*, \phi; t]$. One then ‘decouples’ condensate and non-condensate modes, via the substitution $P[\phi^*, \phi; t] = P_0[\Phi^*, \Phi; t] P_1[\phi'^*, \phi'; t]$. This gives rise to a coupled set of equations: firstly, a Fokker–Planck equation for the temporal evolution of the probability distribution of the condensate wavefunction in the presence of a thermal cloud [56]

$$\begin{aligned} i\hbar \frac{\partial}{\partial t} P_0 &= - \int d\mathbf{r} \frac{\delta}{\delta \Phi(\mathbf{r})} \left[\hat{H}_0 - \mu(t) - iR(\mathbf{r}, t) + g |\Phi(\mathbf{r})|^2 \right] \Phi(\mathbf{r}) P_0 \\ &\quad + \int d\mathbf{r} \frac{\delta}{\delta \Phi^*(\mathbf{r})} \left[\hat{H}_0 - \mu(t) + iR(\mathbf{r}, t) + g |\Phi(\mathbf{r})|^2 \right] \Phi^*(\mathbf{r}) P_0 \\ &\quad - \frac{1}{2} \int d\mathbf{r} \frac{\delta^2}{\delta \Phi(\mathbf{r}) \delta \Phi^*(\mathbf{r})} \Phi^*(\mathbf{r}) \hbar \Sigma^K(\mathbf{r}, t) P_0 [\Phi^*, \Phi; t]. \end{aligned} \quad (18.16)$$

Here $iR(\mathbf{r}, t)$ corresponds to particle exchange between the condensate and non-condensate, while the Keldysh self-energy $\Sigma^K(\mathbf{r}, t)$ (see (18.19)) expresses thermal fluctuations due to incoherent collisions between condensate and non-condensate atoms. The above equation contains both ‘streaming’ and ‘diffusion’ terms; the absence of third-order derivatives (present in [62, 63]), arises from the consistent elimination of selected terms in the effective action, required to avoid double-counting in the many-body approximation. The non-condensate dynamics is parametrized by introducing a Wigner distribution via $N(\mathbf{r}, \mathbf{p}, t) + 1/2 = \int d\mathbf{r}' e^{-i\mathbf{p} \cdot \mathbf{r}'} \langle \phi'(\mathbf{r} + \mathbf{r}'/2) \phi'^*(\mathbf{r} - \mathbf{r}'/2) \rangle(t)$ with $N(\mathbf{r}, \mathbf{p}, t)$ obeying a Quantum Boltzmann Equation. The formulation of this theory ensures that the fluctuation-dissipation theorem relating $R(\mathbf{r}, t)$ and $\Sigma^K(\mathbf{r}, t)$ is satisfied at equilibrium, thus guaranteeing that the condensate relaxes to the correct equilibrium distribution. Although qualitative predictions regarding condensate formation can be made, the solution of this reduced Fokker–Planck equation under general conditions is complicated, because terms appearing within this equation depend implicitly on $\Phi^{(*)}$ via their dependence on energy. One therefore typically resorts to approximate solutions, by means of the stochastic GPE discussed in Sect. 18.6. Related non-equilibrium quantum field theoretic approaches have been recently discussed in [64].

18.5.2 The Gardiner–Zoller Quantum Kinetic Master Equation

In a series of papers [65], Gardiner, Zoller and co-workers used techniques from quantum optics to derive a quantum kinetic master equation for the condensate, coupled to a time-dependent thermal cloud. This treatment is based on splitting the physical system into two ‘energy bands’, each of which has its own evolution, but with the two bands additionally exchanging both particles and energy: (i) The ‘Condensate Band’, R_C , is a band of low-lying states which typically include the condensate, and those low-lying non-condensate modes that are heavily affected by the presence of the condensate. It is formulated within the Bogoliubov number-conserving approximation, with the basis expansion performed in terms of many-body eigenfunctions. This band is fully described by the total number of atoms and the quantum state of the quasi-particles within R_C . While the atoms are conserved, the quasi-particles are mixtures of phonon states, and their number may change by the absorption, or creation, of a quasi-particle in a single collisional process. (ii) The ‘Non-Condensate’ Band, R_{NC} : Atoms with energies higher than some appropriate cut-off energy, E_R , are described in terms of a wavelet expansion, with particles binned into discrete shells in phase space, on the basis of their position and momentum. This is often treated as being in thermal equilibrium, with a local particle phase-space density $f(\mathbf{r}_i, \mathbf{p}_i, t)$, temperature T , and chemical potential μ . The master equation for the condensate band, including both condensate and quasi-particles, is thus obtained [65], following the standard methodology of quantum optics [66]. A simplified version gives rise to a rate equation for the mean number, N_c , of atoms

in the condensate [28] $dN_c/dt = 2W^+(N_c)[(1 - \exp(-\beta\Delta\mu))N_c + 1]$, where $W^+(N_c) \approx [4m(akT)^2/\pi\hbar^3] e^{2\beta\mu}$ denotes a growth rate depending on the system scattering length a , temperature T , and chemical potentials of the condensate and non-condensate, with $\Delta\mu$ the difference in chemical potential between the two subsystems. This approach led to the first quantitative predictions of condensate growth [28], and to good agreement with experiments [67, 68]. Subsequent improved work also took into account the evolution of occupations of lower trap levels via the ergodic quantum Boltzmann equation.

18.6 Stochastic Approaches to Condensate Dynamics

18.6.1 Classical Field Methods

Although the preceding discussion indicates severe limitations to the validity of the GPE at finite temperatures, remarkably the GPE *can* actually be used to model the evolution of *any* system described by the Hamiltonian of Eq. (1) *provided that* such a system primarily behaves in a classical manner. Such classical evolution was first studied in the context of condensation by Kagan, Svistunov and Shlyapnikov [69]. This approximation was also used to study an ideal superfluid approaching equilibrium in [70], with a qualitative 2D study of evaporative cooling performed in [71], and large scale homogeneous simulations performed in [72]. The use of the GPE to study a weakly-interacting trapped gas stems from the realization that when all relevant modes of the system are highly occupied ($n_k \gg 1$), the classical fluctuations of this field are much larger than quantum fluctuations. Such modes can then be fairly accurately represented by a coherent wavefunction, in analogy to the classical description of highly-occupied laser modes.

The Projected Gross–Pitaevskii Equation: A classical description can only work for modes up to a certain energy cut-off, since the condition of high occupation will break down for high-lying modes. Such a cut-off can be implemented through the use of a projector, \hat{P} , onto highly-populated modes, giving rise to

$$i\hbar \frac{\partial}{\partial t} \Psi(\mathbf{r}, t) = \hat{H}_0 \Psi(\mathbf{r}, t) + g \hat{P} \left\{ |\Psi(\mathbf{r}, t)|^2 \Psi(\mathbf{r}, t) \right\} + f(\hat{\eta}). \quad (18.17)$$

The term $f(\hat{\eta})$ appearing above is a rather complicated function of the ‘fluctuation operator’ $\hat{\eta} = (\hat{1} - \hat{P})\hat{\Psi}(\mathbf{r})$ [13, 73], describing the coupling of the classical region to a heat bath, whose modes are not highly populated and are orthogonal to the condensate. Ignoring $f(\hat{\eta})$ leads to the ‘Projected Gross–Pitaevskii Equation’ (PGPE) introduced by Davis, Morgan and Burnett [73]. This is similar to the usual GPE, (18.5), apart from the presence of the projection operator, \hat{P} , which ensures that all computed quantities remain within the classical region. The projector used in this theory is diagonal in

the single-particle basis of the Hamiltonian and is defined by $\hat{P}\{F(\mathbf{r}, t)\} = \sum_{n \in C} \phi_n(\mathbf{r}) \int d^3\mathbf{r} \phi_n^*(\mathbf{r}') F(\mathbf{r}', t)$ where $\phi_n(\mathbf{r})$ denotes the n^{th} eigenfunction, with n restricted within the coherent (classical) region C . Although the PGPE contains no damping terms, since the quantity $f(\hat{\eta})$ has been dropped, the presence of elastic collisions ensures that a highly non-equilibrium initial configuration relaxes to an equilibrium distribution of given energy, without being particularly sensitive to the initial conditions. Such a distribution can be assigned a temperature, upon noting that the mean occupation will actually be given by the classical limit $n(\varepsilon_i) = [\beta(\varepsilon_i - \mu)]^{-1}$ of the Bose–Einstein distribution. Importantly, the field $\Psi(\mathbf{r}, t)$ obtained from the PGPE represents the quantum field of *many* low-lying modes, rather than a *single* condensate mode. This theory has been used to investigate the evolution of vorticity in homogeneous systems and generalized to trapped systems to discuss the process of evaporative cooling, the shift in the critical temperature T_c and the study of spontaneous vortex-antivortex pair production in quasi-2D gases [74]. Since the PGPE is non-perturbative, it can be applied even at the critical region. Related classical field approaches studying the equilibration of randomized initial conditions of specified energy by means of the GPE appear in [75].

The Truncated Wigner Approximation: The idea of evolving randomized initial conditions via a classical field equation, such as the GPE, can be rigorously justified by consideration of the Wigner quasi-distribution function. In general, the equation of motion for the Wigner distribution of a gas of ultracold atoms contains both first and third order derivatives with respect to the atomic field, and the Truncated Wigner Approximation (TWA) amounts to ignoring the latter higher-order derivatives. This is justified provided that the number of particles in the system is much larger than the number of accessible modes, such that all modes have an occupation larger than unity. Thus, the main idea behind this approach is to create a set of random classical fields which accurately sample the Wigner distribution function of the density operator of the system, and evolve these via the Gross–Pitaevskii equation. Despite the deterministic nature of this equation, effects of quantum noise are actually maintained in an approximate manner in the initial state, in the form of mode amplitude fluctuations [62], which should be appropriately sampled. The first numerical implementation of the TWA was performed in Ref. [63], with appropriate sampling techniques analyzed in Refs. [76]. The TWA was recently used to study colliding condensates [62], condensate reflection from a steep barrier, three-body recombination processes, and collapsing condensates [77]. Polkovnikov performed a systematic perturbation theory in quantum fluctuations around the classical system evolution, obtaining the GPE to lowest order and the TWA to next order [78].

In addition to the (truncated) Wigner representation, a quantum system described by a master, or Fokker–Planck, equation, can also be studied within the context of the positive-P representation [66], which gives exact results

provided that the ensemble averages converge, thus restricting both system size and evolution timescales. The evaporative cooling dynamics were studied by Drummond and Corney [79], with significant progress made recently [80]. This discussion omits various related techniques, e.g. Monte-Carlo methods.

In our treatment so far, the system relaxes to some equilibrium state, due to noise implemented in the initial conditions only. However, the only way to guarantee that the system will relax to the correct equilibrium is to allow the condensate to be coupled to a thermal cloud, which provides in an intuitive manner the necessary irreversibility. One possibility to extend beyond the PGPE or the TWA is to treat the high energy modes as a thermal reservoir, as discussed below.

18.6.2 The Stochastic Gross–Pitaevskii Equation

The Fokker–Planck equation derived by Stoof [56], (18.16), can be mapped directly onto a Langevin equation [66] for the order parameter of the system $\Phi(\mathbf{r}, t)$, with multiplicative noise [61]. This problem can be simplified considerably by assuming that the thermal cloud is sufficiently close to equilibrium, that it can be described by a Bose distribution with a chemical potential μ and temperature T . In this regime, the thermal cloud acts as a heat bath to the condensate, and the Langevin equation for the condensate takes the form [81]

$$i\hbar \frac{\partial}{\partial t} \Phi(\mathbf{r}, t) = \left[\left(\hat{H}_{GP} - \mu \right) - iR(\mathbf{r}, t) \right] \Phi(\mathbf{r}, t) + \eta(\mathbf{r}, t) \quad (18.18)$$

where $\hat{H}_{GP} = \hat{H}_0 + g|\Phi(\mathbf{r}, t)|^2$ is the usual ‘Gross–Pitaevskii’ Hamiltonian. This Stochastic GPE (SGPE) describes both mean-field effects of the condensate and low-lying excited states, *and* fluctuations about the mean-field, thus providing valuable information on both diagonal and off-diagonal elements of the one-particle density matrix. In the ‘classical’ approximation, where $N(\varepsilon_i) = [\beta(\varepsilon_i - \mu)]^{-1}$, the dissipative term obeys $iR(\mathbf{r}, t) = -(\beta/4)\hbar\Sigma^K(\mathbf{r}, t)\hat{H}_{GP}$. The contribution $\eta(\mathbf{r}, t)$ denotes a ‘noise term’, with Gaussian correlations $\langle \eta^*(\mathbf{r}, t)\eta(\mathbf{r}', t') \rangle = i(\hbar^2/2)\Sigma^K(\mathbf{r}, t)\delta(t-t')\delta(\mathbf{r}-\mathbf{r}')$. The equivalence between (18.18) and (18.16) comes about because averaging the product $\Phi^*(\mathbf{r}, t)\Phi(\mathbf{r}, t)$ over the different realizations of the noise $\eta(\mathbf{r}, t)$ is *by construction* equivalent to averaging over the Wigner distribution $P[\Phi^*, \Phi; t]$. The Keldysh self-energy $\Sigma^K(\mathbf{r}, t)$ describing the strength of the thermal fluctuations due to incoherent collisions between condensate and non-condensate atoms is given by

$$\begin{aligned} \Sigma^K(\mathbf{r}, t) = & -i \left(\frac{4\pi}{\hbar} \right) g^2 \int \frac{d\mathbf{p}_2}{(2\pi\hbar)^3} \int \frac{d\mathbf{p}_3}{(2\pi\hbar)^3} \int \frac{d\mathbf{p}_4}{(2\pi\hbar)^3} (2\pi\hbar)^3 \delta(\mathbf{p}_2 - \mathbf{p}_3 - \mathbf{p}_4) \\ & \delta(\varepsilon_c + \varepsilon_2 - \varepsilon_3 - \varepsilon_4) \times [(1+N_2)N_3N_4 + N_2(1+N_3)(1+N_4)] \end{aligned} \quad (18.19)$$

where $N_i = N(\varepsilon_i)$ the Bose distribution for the eliminated part of the gas, with energy $\varepsilon_i = (\mathbf{p}_i^2 + V_{\text{ext}}(\mathbf{r}) + 2g|\Phi|^2)$, and ε_c corresponds to the average local chemical potential. A simplified form of this SGPE, assuming time-independent occupation numbers in the non-condensate, and thus a time-independent self-energy $\Sigma^K(\mathbf{r})$ has been used to study [81] the reversible condensate formation observed experimentally when cycling through the phase transition [82], quasi-condensate growth on an atom chip, fluctuations of one-dimensional Bose gases, and the growth of coherence of an atom laser [83]. This theory is also amenable to variational calculations, and such a technique has been used to discuss collisional frequencies and damping rates of collective excitations, growth-collapse cycles in attractive condensates [61], and finite temperature dynamics of a single vortex [84].

Additionally ignoring the ‘noise term’ η in (18.18), in the ‘classical’ approximation discussed here, the condensate evolution can be cast in the form

$$i\hbar \frac{\partial}{\partial t} \Phi(\mathbf{r}, t) = (1 - i\gamma) \left(\hat{H}_{GP} - \mu \right) \Phi(\mathbf{r}, t), \quad (18.20)$$

with a temperature- and position-dependent damping rate $\gamma = i(\beta/4)\hbar\Sigma^K(\mathbf{r})$. Phenomenological damping of this form was originally proposed by Pitaevskii [85], and first implemented to trapped Bose gases with a constant, position-independent rate γ by Choi et al. [86]. A related phenomenologically-damped equation with the factor $(1 - i\gamma)$ appearing on the *left* hand side of the equation has been used in diverse studies, including vortex lattice growth and dark soliton decay [87].

A similar SGPE has been recently derived by Gardiner et al. [88] in terms of the Wigner function representation. This combines the ideas of the quantum kinetic theory of Gardiner, Zoller and co-workers [65] with those of the finite temperature GPE [13]. The system is formally split into low- and high-lying modes by means of the projectors \hat{P} and $(1 - \hat{P})$, with the high-lying modes treated as a heat bath. This leads to a master equation for the interaction of a condensate with a fixed bath of non-condensed atoms, which can be mapped onto a Fokker–Planck equation. Subtle differences arise between the approaches of Stoof and Gardiner, in the effective interactions (many-body vs. two-body), the elimination of high energy modes, and the introduction and type of noise terms. When projection operators and noise contributions are ignored, this equation leads precisely to (18.20), which has been used to study rotating condensates and vortex lattice formation [89].

18.7 The Role of System Dimensionality

In a homogeneous system, BEC arises only in 3D (or 2D at $T = 0$). Recent experimental progress has enabled the achievement of weakly-interacting quasi-2D (quasi-1D) geometries, in which motion in the transverse direction(s) is ‘frozen out’ by tight harmonic confinement, whose typical level spacing

$\hbar\omega_\perp$ exceeds both thermal and interaction energies. Although condensation is approximately regained in such reduced dimensionality systems at sufficiently low temperatures, a partially-condensed system, in general, suffers from phase fluctuations which limit the coherence to a region smaller than the ‘condensate’ spatial extent, as experimentally observed [90]; the system is then said to contain a ‘quasi-condensate’ [16]. While the stochastic theories presented earlier can be used to describe such systems [83], any attempt to perform a mean-field analysis of this regime requires consideration of the ‘condensate operator’ $\hat{\zeta}$ of (18.2) [91]. In general, the Bose field operator should be expressed as $\hat{\Psi}(\mathbf{r}) = \sqrt{n_0(\mathbf{r})}e^{i\hat{\chi}(\mathbf{r})} + \hat{\psi}'(\mathbf{r})$ [92], where, n_0 is the quasi-condensate density, and $\hat{\chi}(\mathbf{r})$ an operator accounting for phase fluctuations. Clearly n_0 must vanish in the thermodynamic limit in 1D and 2D ($T \neq 0$) and yield the condensate density in 3D, which occurs when the condensate density is identified as $\text{Lim}\{n_0\exp\{-(1/2)[\hat{\chi}(\mathbf{r}) - \hat{\chi}(\mathbf{r}')]\^2\}\}$ when $(\mathbf{r} - \mathbf{r}') \rightarrow \infty$. This approach provides *ab initio* predictions for the equilibrium properties of *weakly-interacting* trapped gases in *all* dimensions, in agreement with the stochastic GPE [83].

As soon as phase fluctuations come into play, the GPE fails to predict the behavior of the condensate, or its excitations. Therefore, all predictions of the 1D or 2D GPE presented in this book are necessarily only valid in appropriately elongated geometries which are, however, *sufficiently far* both from the regime of quasi-1D (quasi-2D) behavior and from T_c . Finally, we note that the very rich 1D and 2D strongly-interacting regimes can also not be described by the GPE. As a result, one should generally use the Gross–Pitaevskii Equation with caution when describing the dynamics of macroscopic excitations (solitons, vortices), for systems of low dimensionality at nonzero temperatures.

Acknowledgement. Over the past few years I have had the pleasure of numerous extended discussions and collaborations with Keith Burnett and Henk Stoof. I would also like to thank David Hutchinson and Brian Jackson for detailed comments on this manuscript, and Usama Al Khawaja, Rob Ballagh, Matt Davis, Reinholt Walser, and Eugene Zaremba for interesting discussions.

References

1. C.J. Pethick, H. Smith, *Bose–Einstein Condensation in Dilute Gases* (Cambridge University Press, Cambridge 2004); L.P. Pitaevskii, S. Stringari, *Bose–Einstein Condensation* (Clarendon, Oxford 2003) F. Dalfovo, S. Giorgini, L.P. Pitaevskii, S. Stringari, Rev. Mod. Phys. **71**, 463 (1999) A.J. Leggett, Rev. Mod. Phys. **73**, 307 (2001)
2. E.P. Gross, J. Math. Phys. **74**, 195 (1963); L.P. Pitaevskii, Sov. Phys. JETP **13**, 451 (1961)
3. A.L. Fetter, Ann. Phys. **70**, 67 (1972)
4. N.P. Proukakis, DPhil Thesis, University of Oxford (1997)
5. N.P. Proukakis, K. Burnett, J. Res. Natl. Inst. Stand. Technol. **101**, 457 (1996)

6. S. Giorgini, Phys. Rev. A **57**, 2949 (1998); *ibid.* **61**, 033601 (2000)
7. E. Zaremba, A. Griffin, T. Nikuni, Phys. Rev. A **57**, 4695 (1998)
8. A. Griffin, Phys. Rev. B **53**, 9341 (1996)
9. N.P. Proukakis, J. Phys. B **34**, 4737 (2001)
10. T. Nikuni, E. Zaremba, A. Griffin, Phys. Rev. Lett. **83**, 10 (1999)
11. M.J. Bijlsma, E. Zaremba, H.T.C. Stoof, Phys. Rev. A **62**, 063609 (2000)
12. R. Walser, J. Williams, J. Cooper, M. Holland, Phys. Rev. A **59**, 3878 (1999)
13. M.J. Davis, R.J. Ballagh, K. Burnett, J. Phys. B **34**, 4487 (2001)
14. A.L. Fetter, J.D. Walecka, *Quantum theory of many-particle systems* (McGraw Hill, New York, 1971); J.-P. Blaizot, G. Ripka, *Quantum Theory of Finite Systems* (MIT Press, Cambridge MA, 1986)
15. S.T. Beliaev, Sov. Phys. JETP **34**, 289 (1958); *ibid.* **34** 299 (1058)
16. V.N. Popov, Sov. Phys. JETP **20**, 1185 (1965). V.N. Popov, *Functional Integrals and Collective Excitations* (Cambridge University Press, 1987)
17. M. Bijlsma, H.T.C. Stoof, Phys. Rev. A **55**, 498 (1997); H.T.C. Stoof, M. Bijlsma, M. Houbiers, J. Res. Natl. Inst. Stand. Technol. **101**, 443 (1996)
18. H.T.C. Stoof, Phys. Rev. Lett. **78**, 768 (1997)
19. N.P. Proukakis, K. Burnett, H.T.C. Stoof, Phys. Rev. A **57**, 1230 (1998)
20. N.P. Proukakis, K. Burnett, Philos. Trans. R. Soc. A **355**, 2235 (1997)
21. N.P. Proukakis, S.A. Morgan, S. Choi, K. Burnett, Phys. Rev. A **58**, 2435 (1998)
22. H. Shi, A. Griffin, Phys. Rep. **304**, 1 (1998)
23. S.A. Morgan, J. Phys. B **33**, 3847 (2000); Phys. Rev. A **69**, 023609 (2004); *ibid.* **72**, 043609 (2005)
24. K. Burnett, Proc. Int. School of Physics - Enrico Fermi, ed. M. Inguscio, S. Stringari, C. Wieman (IOS Press, Amsterdam, 1999)
25. K. Huang, C.N. Yang, Phys. Rev. **105**, 767 (1957); *ibid.* **106**, 1135 (1957)
26. N.N. Bogoliubov, J. Phys. USSR **11**, 23 (1957)
27. C.W. Gardiner, Phys. Rev. A **56**, 1414 (1997); M. Girardeau, A. Arnowitt, Phys. Rev. **113**, 755 (1959); M. Girardeau, Phys. Rev. A **58**, 775 (1998)
28. C.W. Gardiner, P. Zoller, R.J. Ballagh, M.J. Davis, Phys. Rev. Lett. **79**, 1793 (1997)
29. Y. Castin, R. Dum, Phys. Rev. A **57**, 3008 (1998)
30. T.R. Kirkpatrick, J.R. Dorfman, Phys. Rev. A **28**, 2576 (1983); J. Low Temp. Phys. **58**, 301 (1985); *ibid.* **58**, 399 (1985); U. Eckern, *ibid.* **54**, 333 (1984)
31. D.A.W. Hutchinson, K. Burnett, R.J. Dodd, S.A. Morgan, M. Rusch, E. Zaremba, N.P. Proukakis, M. Edwards, C.W. Clark, J. Phys. B **33**, 3825 (2000)
32. D.A. Huse, E.D. Siggia, J. Low Temp. Phys. **46**, 137 (1982); P. Dörre, H. Haug, D.B. Tran Thoai, *ibid.* **35**, 465 (1979); D.H. Kobe, Ann. Phys. **45**, 15 (1968); V.V. Goldman, I.F. Silvera, A.J. Leggett, Phys. Rev. B **24**, 2870 (1981)
33. V.I. Yukalov, H. Kleinert, Phys. Rev. A **73**, 063612 (2006)
34. D.A.W. Hutchinson, R.J. Dodd, K. Burnett, Phys. Rev. Lett. **81**, 2198 (1998)
35. J. Goldstone, Nuovo Cimento **19**, 154 (1961)
36. N.M. Hugenholtz, D. Pines, Phys. Rev. **116**, 489 (1959); P.C. Hohenberg, P.C. Martin, Ann Phys. **34**, 291 (1965); L.P. Kadanoff, G. Baym, *Quantum Statistical Mechanics* (New York: Benjamin, 1962)
37. D.A.W. Hutchinson, E. Zaremba, A. Griffin, Phys. Rev. Lett. **78**, 1842 (1997)
38. M. Olshanii, L. Pricoupenko, Phys. Rev. Lett. **88**, 010402 (2002)

39. S.M.M. Virtanen, T.P. Simula, M.M. Salomaa, J. Phys: Condens. Matter **13**, L819 (2001); C. Gies and D.A.W. Hutchinson, Phys. Rev. A **70**, 043606 (2004); C. Gies, M.D. Lee, D.A.W. Hutchinson, J. Phys B **38**, 1797 (2005)
40. P. Tommasini, E.J.V. de Passos, M.O.C. Pires, A.F.R. de Toledo Piza, J. Phys: Condens. Matter **17**, 3165 (2005); T. Kita, J. Phys. Soc. Jpn. **75**, 044603 (2006)
41. J. Wachter, Master's Thesis, University of Boulder, Colorado (2000)
42. M. Imamovic-Tomasovic, A. Griffin, J. Low Temp. Phys. **122**, 617 (2001)
43. E. Zaremba, T. Nikuni, A. Griffin, J. Low Temp. Phys. **116**, 277 (1999)
44. J.R. Walser, J. Cooper, M. Holland, Phys. Rev. A **63**, 013607 (2000); S.G. Bhongale, R. Walser, M.J. Holland, cond-mat/0203415 (2002); R. Walser, Opt. Commun. **243**, 107 (2004); J. Wachter, R. Walser, J. Cooper, M. Holland, Phys. Rev. A **64**, 053612 (2001)
45. T. Köhler, K. Burnett, Phys. Rev. A **65**, 033601 (2002); T. Köhler, T. Gasenzer, K. Burnett, Phys. Rev. A **67**, 013601 (2003); T. Köhler, Phys. Rev. Lett. **89**, 210404 (2002)
46. M. Rusch, K. Burnett, Phys. Rev. A **59**, 3851 (1999)
47. D.S. Jin, M.R. Matthews, J.R. Ensher, C.E. Wieman, E.A. Cornell, Phys. Rev. Lett. **78**, 764 (1997); S.A. Morgan, M. Rusch, D.A.W. Hutchinson, K. Burnett, Phys. Rev. Lett. **91**, 250403 (2001)
48. M. Bijlsma, H.T.C Stoof, Phys. Rev. A **60**, 3973 (1999); U. Al Khawaja, H.T.C. Stoof, Phys. Rev. A **62**, 053602 (2000).
49. B. Jackson, E. Zaremba, Phys. Rev. Lett. **88**, 180402 (2002)
50. D.W. Snoke, J.P. Wolfe, Phys. Rev. B **39**, 4030 (1989) M. Holland, J. Williams, J. Cooper, Phys. Rev. A **55**, 3670 (1997) D.V. Semikoz, I.I. Tkachev, Phys. Rev. Lett. **74**, 3093 (1995) O.J. Luiten, M.W. Reynolds, J.T.M. Walraven, Phys. Rev. A **53**, 381 (1996)
51. B. Jackson, E. Zaremba, Phys. Rev. Lett. **87**, 100404 (2001); *ibid.* **89**, 150402 (2002); Phys. Rev. A **66**, 033606 (2002); New. J. Phys. **5**, 88 (2003)
52. T. Nikuni, A Griffin, Phys. Rev. A **69**, 023604 (2004); *ibid.* **63**, 033608 (2001)
53. J.E. Williams, E. Zaremba, B. Jackson, T. Nikuni, A. Griffin, Phys. Rev. Lett. **88**, 070401 (2002)
54. S. Burger, K. Bongs, S. Dettmer, W. Ertmer, K. Sengstock, A. Sanpera, G.V. Shlyapnikov, M. Lewenstein, Phys. Rev. Lett. **83**, 5198 (1999)
55. B. Jackson, N.P. Proukakis, C.F. Barenghi, Phys. Rev. A **75**, 051601(R)(2007)
56. H.T.C. Stoof, J. Low Temp. Phys. **114**, 11 (1999)
57. P.O. Fedichev, G.V. Shlyapnikov, J.T.M. Walraven, Phys. Rev. Lett. **80**, 2269 (1998); P.O. Fedichev and G.V. Shlyapnikov, Phys. Rev. A **58**, 3146 (1998); P.O. Fedichev and G.V. Shlyapnikov, Phys. Rev. A **60**, R1779 (1999); P.O. Fedichev, A.E. Muryshev, G.V. Shlyapnikov, Phys. Rev. A **60**, 3220 (1999)
58. S. Sinha, A. Cherny, D. Kovrizhin, J. Brand, Phys. Rev. Lett. **96**, 030406 (2006)
59. H.T.C. Stoof, Dynamics: Models and Kinetic Methods for Non-Equilibrium Many-Body Systems, J. Karkheck (ed.) (Kluwer Academic Publishers, 1999)
60. H.T.C. Stoof, in *Coherent Atomic Matter Waves*, Proceedings of the Les Houches Summer School Session 72, 1999, ed. R. Kaiser et al. (Springer, Berlin 2001).
61. R.A. Duine, H.T.C. Stoof, Phys. Rev. A **65**, 013603 (2001)

62. A.A. Norrie, R.J. Ballagh, C.W. Gardiner, Phys. Rev. A **73**, 043618 (2006)
63. M.J. Steel, M.K. Olsen, L.I. Plimak, P.D. Drummond, S.M. Tan, M.J. Collett, D.F. Walls, R. Graham, Phys. Rev. A **58**, 4824 (1998)
64. D.G. Barci, E.S. Fraga, R.O. Ramos, Phys. Rev. Lett. **85**, 479 (2000); D.G. Barci, E.S. Fraga, M. Gleiser, R.O. Ramos, Phys. A **317**, 535 (2003); A.M. Rey, B.L. Hu, E. Calzetta, A. Roura, C.W. Clark, Phys. Rev. A **69**, 033610 (2004); A.M. Rey, B.L. Hu, E. Calzetta, C.W. Clark, Phys. Rev. A **72**, 023604 (2005); T. Gasenzer, J. Berges, M.G. Schmidt, M. Seco, Phys. Rev. A **72**, 063604 (2005); K. Temme and T. Gasenzer, Phys. Rev. A **74**, 053603 (2006)
65. C.W. Gardiner, P. Zoller, Phys. Rev. A **55**, 2902 (1997); D. Jaksch, C.W. Gardiner, P. Zoller, Phys. Rev. A **56**, 575 (1997); C.W. Gardiner, P. Zoller, Phys. Rev. A **58**, 536 (1998); D. Jaksch, C.W. Gardiner, K.M. Gheri, P. Zoller, Phys. Rev. A **61**, 033601 (2000); M.D. Lee, C.W. Gardiner, Phys. Rev. A **62**, 033606 (2000); M.J. Davis, C.W. Gardiner, R.J. Ballagh, Phys. Rev. A **62**, 063608 (1997)
66. See, e.g., C.W. Gardiner, P. Zoller, *Handbook of Stochastic Methods*, 3rd ed. (Springer, Berlin, 2004)
67. C.W. Gardiner, M.D. Lee, R.J. Ballagh, M.J. Davis, P. Zoller, Phys. Rev. Lett. **81**, 5266 (1998)
68. H.J. Miesner, D.M. Stamper-Kurn, M.R. Andrews, D.S. Durfee, S. Inouye, W. Ketterle, Science **279**, 1005 (1998)
69. B.V. Svistunov, J. Mosc. Phys. Soc. **1**, 373 (1991); Yu. Kagan, B.V. Svistunov, G. Shlyapnikov, Sov. Phys. JETP **75**, 387 (1992); Yu. Kagan, B.V. Svistunov, Sov. Phys. JETP **78**, 187 (1994); Yu. Kagan, B.V. Svistunov, Phys. Rev. Lett. **79**, 3331 (1997) Sov. Phys. JETP **75**, 387 (1992)
70. K. Damle, S.N. Majumdar, S. Sachdev, Phys. Rev. A **54**, 5037 (1996)
71. R.J. Marshall, G.H.C. New, K. Burnett, S. Choi, Phys. Rev. A **59**, 2085 (1999)
72. N.G. Berloff, B.V. Svistunov, Phys. Rev. A **66**, 013603 (2002)
73. M.J. Davis, S.A. Morgan, K. Burnett, Phys. Rev. Lett. **87**, 160402 (2001)
74. M.J. Davis, S.A. Morgan, K. Burnett, Phys. Rev. A **66**, 053618 (2001); P.B. Blakie, M.J. Davis, Phys. Rev. A **72**, 063608 (2005); M.J. Davis P.B. Blakie, Phys. Rev. Lett. **96**, 060404 (2006); T.P. Simula P.B. Blakie, Phys. Rev. Lett. **96**, 020404 (2006)
75. K. Goral, M. Gajda, K. Rzazewski, Phys. Rev. A **66**, 051602 (2002); H. Schmidt, K. Goral, F. Floegel, M. Gajda, K. Rzazewski, J. Opt. B **5**, S96 (2003); M. Leadbeater, T. Winiecki, C.S. Adams, J. Phys. B **36**, L143 (2003)
76. A. Sinatra, C. Lobo, Y. Castin, Phys. Rev. Lett. **87**, 210404 (2001); A. Sinatra, C. Lobo, and Y. Castin, J. Phys. B **35**, 3599 (2002)
77. R.G. Scott, D.A.W. Hutchinson, C.W. Gardiner, Phys. Rev. A **74**, 053605 (2006); A.A. Norrie, R.J. Ballagh, C.W. Gardiner, A.S. Bradley, Phys. Rev. A **73**, 043618 (2006); S. Wüster, B.J. Dabrowska-Wüster, A.S. Bradley, M.J. Davis, P.B. Blakie, J.J. Hope, and C.M. Savage, Phys. Rev. A **75**, 043611 (2007)
78. A. Polkovnikov, Phys. Rev. A **68**, 033609 (2003); *ibid.* **68**, 053604 (2003)
79. P.D. Drummond, J.F. Corney, Phys. Rev. A **60**, R2661 (1999)
80. P. Deuar, P.D. Drummond, Phys. Rev. Lett. **98**, 120402 (2007)
P.D. Drummond, P. Deuar, J. Opt. B **5**, S281 (2003)

81. H.T.C. Stoof, M.J. Bijlsma, *J. Low Temp. Phys.* **124**, 431 (2001)
82. D.M. Stamper-Kurn, H.-J. Miesner, A.P. Chikatur, S. Inouye, W. Ketterle, *Phys. Rev. Lett.* **81**, 2194 (1998)
83. N.P. Proukakis, J. Schmiedmayer, H.T.C. Stoof, *Phys. Rev. A* **73**, 053603 (2006); N.P. Proukakis, *Phys. Rev. A* **74**, 053617 (2006); *Las. Phys.* **13**, 527 (2003)
84. R.A Duine, B.W.A. Leurs, and H.T.C. Stoof, *Phys. Rev. A* **69**, 053623 (2004)
85. L.P. Pitaevskii, *Sov. Phys. JETP* **35**, 282 (1959)
86. S. Choi, S.A. Morgan, K. Burnett, *Phys. Rev. A* **57**, 4057 (1998)
87. M. Tsubota, K. Kasamatsu, M. Ueda, *Phys. Rev. A* **65**, 023603 (2002); M. Tsubota, K. Kasamatsu, M. Ueda, *Phys. Rev. A* **67**, 033610 (2003)
N.P. Proukakis, N.G. Parker, C.F. Barenghi, C.S. Adams, *Phys. Rev. Lett.* **93**, 130408 (2004)
88. C.W. Gardiner, J.R. Anglin, T.I.A. Fudge, *J. Phys. B* **35**, 1555 (2002); C.W. Gardiner, M.J. Davis, *J. Phys. B* **36**, 4731 (2003); A.S. Bradley, P.B. Blakie, C.W. Gardiner, *J. Phys. B* **38**, 4259 (2005)
89. A.A. Penckwitt, R.J. Ballagh, C.W. Gardiner, *Phys. Rev. Lett.* **89**, 260402 (2002)
90. See, e.g., S. Richard, F. Gerbier, J.H. Thywissen, M. Hugbart, P. Bouyer, A. Aspect, *Phys. Rev. Lett.* **91**, 010405 (2003); Z. Hadzibabic, P. Krüger, M. Cheneau, B. Battelier, J.B. Dalibard, *Nature* **441**, 1118 (2006) and references therein
91. D.S. Petrov, G.V. Shlyapnikov, J.T.M. Walraven, *Phys. Rev. Lett.* **85**, 3745 (2000); D.S. Petrov, G.V. Shlyapnikov, J.T.M. Walraven, *Phys. Rev. Lett.* **87**, 050404 (2001); D.L. Luxat and A. Griffin, *Phys. Rev. A* **67**, 043603 (2003); C. Mora, Y. Castin, *Phys. Rev. A* **67**, 053615 (2003)
92. J.O. Andersen, U. Al Khawaja, H.T.C. Stoof, *Phys. Rev. Lett.* **88**, 070407 (2002); U. Al Khawaja, J.O. Andersen, N.P. Proukakis, H.T.C. Stoof, *Phys. Rev. A* **66**, 013615 (2002); U. Al Khawaja, J.O. Andersen, N.P. Proukakis, H.T.C. Stoof, *Phys. Rev. A* **66**, 059902(E) (2002); U. Al Khawaja, N.P. Proukakis, J.O. Andersen, M.W.J. Romans, H.T.C. Stoof, *Phys. Rev. A* **68**, 043603 (2003); N.P. Proukakis, *Phys. Rev. A* **73**, 023605 (2006)

Part XII

Asymptotic Reductions of the Gross–Pitaevskii Equation

Asymptotic Reductions of the Gross–Pitaevskii Equation

D.E. Pelinovsky

Various analytical techniques are reviewed in the context of asymptotic reductions of the Gross–Pitaevskii (GP) equation, which is the nonlinear Schrödinger (NLS) equation with an external potential. When the external potential is periodic, the GP equation can be reduced to the coupled-mode (Dirac) system, the continuous NLS equation and the discrete NLS equation by using formal multi-scale expansion methods and their rigorous mathematical analogues. When the external potential is decaying at infinity, finite-dimensional reductions of the GP equation can be derived for modeling of dynamics of localized modes. When the external potential is confining, the GP equation can be recovered from the multi-particle linear Schrödinger equation.

19.1 Introduction

The main part of this book is devoted to characterization of various properties of localized and periodic modes trapped by external potentials in the physics of Bose–Einstein condensation. Localized and periodic modes are modeled typically by the dimensionless Gross–Pitaevskii (GP) equation

$$iu_t = -\Delta u + V(x)u + \sigma|u|^2u, \quad x \in \mathbf{R}^N, \quad t \geq 0, \quad u \in \mathbf{C}, \quad (19.1)$$

where $\Delta = \partial_{x_1}^2 + \cdots + \partial_{x_N}^2$, $\sigma = \pm 1$, and $V(x)$ is an external potential. Many theoretical results described in other chapters of this book are of numerical nature. For instance, various software packages are employed to run the time evolution problem (19.1) or fixed-point iterations of the stationary problem

$$\omega\phi = -\Delta\phi + V(x)\phi + \sigma\phi^3, \quad x \in \mathbf{R}^N, \quad \phi \in \mathbf{R}, \quad \omega \in \mathbf{R}. \quad (19.2)$$

Other theoretical results are based on robust computational methods beyond the numerical simulations such as variational approximations, energy estimations, and asymptotic multi-scale expansions. This chapter is intended to link some of these methods with modern mathematical analysis of the GP

equation. The presentation will remain on the “physical” level with sparse technical details, but links to rigorous mathematical techniques with relevant references, if available, will be made. It should be pointed out that the system of amplitude equations derived with few lines of formal computations can sometimes be proved by careful functional analysis over a hundred of journal pages.

A natural question that would arise is: *Why would we care about asymptotic reductions of the GP equation (19.1)?* The answer follows from understanding that the GP equation (19.1) is a space-inhomogeneous infinite-dimensional dynamical system, which is often unsuitable for direct analysis. On the other hand, some reductions of the GP equation are derived in the form of space-homogeneous differential or difference equations or in terms of finite-dimensional dynamical systems, which may possess exact or approximate solutions. For instance, existence of gap solitons (decaying solutions in periodic potentials) was proved in the stationary problem (19.2) from the elliptic theory [1], bifurcation methods [2, 3] and the variational theory [4] but the localized solutions are not available in a closed analytic form. On the other hand, approximations of the gap solitons in the closed analytic form can be obtained from the asymptotic reductions of the stationary equation (19.2) to the coupled-mode system [5] or to the continuous NLS equation [6].

The main part of this chapter consists of three sections; each section is devoted to a different class of the potential function $V(x)$. I shall start with a class of periodic potentials and describe simplifications of the GP equation to one of the three models: the coupled-mode system of Dirac equations, the continuous nonlinear Schrödinger (NLS) equation and its discrete counterpart, the discrete NLS equation. I will then consider the class of decaying potentials and describe the finite-dimensional models for localized modes of the GP equation. Finally, I will review other results relevant for the class of confining potentials.

Most results discussed in this chapter are based on consideration of the one-dimensional problem ($N = 1$), while open questions are mentioned about extensions of these results to multi-dimensional problems ($N \geq 2$). The main focus of this chapter is at the approximations of the localized modes of the stationary equation (19.2), while fewer details will be given on the derivation of the time-evolution versions of the reduced systems from the time-dependent GP equation (19.1).

19.2 Class of Periodic Potentials

We shall assume here that $V(x + d) = V(x)$ is a bounded periodic potential with the smallest irreducible period d . Depending on the strength of the potential amplitude $V_\infty = \|V\|_{L^\infty}$, one can develop three different reductions of the time-dependent GP equation (19.1) and the stationary problem (19.2). The crucial information for derivation of these reductions comes from the

spectrum of the linear operator $L = -\Delta + V(x)$ in the space of infinitely smooth, compactly supported functions. It is well-known that the spectrum of L denoted by $\sigma(L)$ is purely continuous, consisting of a sequence of spectral bands located on a subset of the real axis. For one-dimensional potentials ($N = 1$), the spectral bands do not overlap and may allow for existence of non-empty gaps between two adjacent bands. In general, the one-dimensional Hill's equation

$$L\psi(x) = -\psi''(x) + V(x)\psi(x) = \omega\psi(x) \quad (19.3)$$

has bounded solutions $\psi(x)$ called the Bloch functions if and only if ω is in the union of spectral bands

$$\sigma(L) = [\omega_0, \omega_1] \cup [\omega_2, \omega_3] \cup [\omega_4, \omega_5] \cup \dots,$$

where $\omega_{2m-2} < \omega_{2m-1} \leq \omega_{2m}$, $m \in \mathbf{N}$ and $\omega_m \rightarrow \infty$ as $m \rightarrow \infty$. For a fixed ω in the interior point of the n th spectral band of $\sigma(L)$, both fundamental solutions of the Hill's equation (19.3) are quasi-periodic in x and have the representation

$$\psi = u_{n,k}^{\pm}(x)e^{\pm ikx},$$

where k is the quasi-momentum defined in the fundamental interval $k \in [-\frac{\pi}{d}, \frac{\pi}{d}]$, and

$$u_{n,k}^{\pm}(x+d) = u_{n,k}^{\pm}(x)$$

are bounded periodic functions satisfying the relations $u_{n,k}^{-}(x) = \bar{u}_{n,k}^{+}(x)$. Let us represent the n th spectral band of $\sigma(L)$ by the dispersion relation $\omega = \omega_{n,k}$. Then $\omega_{n,k}$ can be extended into an even periodic function of $k \in \mathbf{R}$ with period $2\pi/d$, according to the Fourier series

$$\omega_{n,k} = \sum_{l \in \mathbf{Z}} \hat{\omega}_{n,l} e^{ikld},$$

where the real Fourier coefficients $\hat{\omega}_{n,l}$ satisfy the relations $\hat{\omega}_{n,l} = \hat{\omega}_{n,-l}$.

For a fixed $\omega \in \mathbf{R} \setminus \sigma(L)$, the two fundamental solutions of the Hill's equation (19.3) grow exponentially either in x or $-x$ and have the representation $\psi = \phi_{\pm}(x)e^{\pm \kappa x}$, where $\phi_{\pm}(x) = \phi_{\pm}(x+d)$ and κ depends on $\omega \in \mathbf{R} \setminus \sigma(L)$. When $\omega = \omega_0$ represents a particular end-point of a spectral band of $\sigma(L)$, one of the solutions $\psi = \psi_0(x)$ is either d -periodic (corresponding to $k = 0$) or d -antiperiodic (corresponding to $k = \pi/d$) and the other fundamental solution ψ grows linearly in x .

It has been shown numerically in [5, 6] that localized solutions of the nonlinear problem (19.2) (so-called gap solitons) exist in any finite gap of the spectrum $\sigma(L)$ and in the semi-infinite gap in the focusing case $\sigma = -1$. A rigorous theorem on existence of gap solitons was proved in [4]. Analytical approximations of the gap solitons with the coupled-mode theory and the discrete NLS equation were considered in [5], while those with the continuous NLS equation were described in [6]. We shall focus on these three approximations in the remainder of this section.

19.2.1 Small Strength: Coupled-Mode Equations

Coupled-mode equations have been exploited traditionally in the context of nonlinear optics [7] and photonic crystals [8]. Extensions of the standard one-dimensional coupled-mode equations to the higher-dimensional couplings between advective and dispersive terms were recently modeled in [9]. The role of the coupled-mode equations is fundamental: they provide normal forms for Bragg resonances of periodic or anti-periodic Bloch waves in a nonlinear system with a *small* periodic potential $V(x)$, when $V_\infty = \|V\|_{L^\infty}$ is a small parameter. We shall review the derivation of the coupled-mode equations by working with the Lyapunov–Schmidt reduction technique, similar to the analysis of [10]. In particular, we shall consider the stationary problem (19.2) in one dimension $N = 1$ and apply either periodic or anti-periodic boundary conditions to the solution $\phi(x)$. Let $V(x)$ and $\phi(x)$ be expanded into the Fourier series

$$V(x) = \sum_{m \in \mathbf{Z}} v_{2m} e^{(2\pi i mx)/d}, \quad \phi(x) = \sum_{m \in \mathbf{Z}'} \phi_m e^{(\pi i mx)/d}, \quad (19.4)$$

where \mathbf{Z}' contains all even numbers for periodic $\phi(x)$ and all odd numbers for anti-periodic $\phi(x)$ and $\phi_{-m} = \bar{\phi}_m$ for real-valued $\phi(x)$. After substitution of (19.4) into (19.2), the differential equation (19.2) with $N = 1$ becomes the lattice problem:

$$\left(\omega - \frac{\pi^2 m^2}{d^2} \right) \phi_m = \sum_{m_1 \in \mathbf{Z}'} v_{m-m_1} \phi_{m_1} + \sigma \sum_{m_1 \in \mathbf{Z}'} \sum_{m_2 \in \mathbf{Z}'} \phi_{m_1} \phi_{m_2} \phi_{m-m_1-m_2}, \quad (19.5)$$

where $m \in \mathbf{Z}'$ and the convolution sums are closed both in periodic and anti-periodic cases since $V(x)\phi(x)$ and $\phi^3(x)$ are periodic or anti-periodic if $\phi(x)$ is periodic or anti-periodic, respectively. The left-hand-side of the nonlinear lattice equation (19.5) is represented by an infinite-dimensional matrix operator which is singular if and only if $\omega = \omega_n$, where $\omega_n = (\frac{\pi n}{d})^2$ for some $n \in \mathbf{N}$. If $\omega \neq \omega_n$, the matrix operator is invertible and the zero solution $\phi_m = 0, \forall m \in \mathbf{Z}'$ is uniquely continued in the nonlinear lattice equation (19.5) according to the Implicit Function Theorem. No bifurcations of non-linear periodic or anti-periodic solutions are possible for $\omega \neq \omega_n$. However, if $\omega = \omega_n$, some eigenvectors (one for $n = 0$ or two for $n \neq 0$) belong to the kernel of the singular matrix operator, and the non-zero solutions may bifurcate due to the presence of the right-hand-side terms of the lattice equation (19.5). The method of Lyapunov–Schmidt reductions provide the decomposition of the infinite-dimensional vector $\phi = (\dots, \phi_{-2}, \phi_{-1}, \phi_0, \phi_1, \phi_2, \dots)^T$ into the finite-dimensional and infinite-dimensional parts along the kernel and its complement, the construction of the mapping of the infinite-dimensional part in coordinates of the finite-dimensional part by using the Implicit Function Theorem, and finally the projections of the full system (19.5) to the reduced

bifurcation equations [11]. Using this method for $n \neq 0$, we represent the vector ϕ and the parameter ω in the form

$$\phi = a\mathbf{e}_n + b\mathbf{e}_{-n} + \varphi, \quad \omega = \left(\frac{\pi n}{d}\right)^2 + \Omega,$$

where $\mathbf{e}_{\pm n}$ are unit eigenvectors in the space of infinite-dimensional vectors, $(a, b) \in \mathbf{C}^2$ are coordinates of the kernel of the matrix operator, φ belongs to the orthogonal complement of the kernel, and Ω is a parameter. Due to the requirement that $\phi(x)$ is real-valued, we note the symmetry constraint $b = \bar{a}$. By the Implicit Function Theorem in the space $l_s^2(\mathbf{Z})$ with the norm

$$\|\phi\|_{l_s^2}^2 = \sum_{m \in \mathbf{Z}} (1 + m^2)^s |\phi_m|^2 < \infty$$

for $s > \frac{1}{2}$, a smooth mapping $\varphi = \varphi(a, b; \Omega, \mathbf{v})$ exists in a local neighborhood of $(a, b) = (0, 0)$ for small values of Ω and $\|\mathbf{v}\|_{L^1}$ [11]. As a result, the bifurcation equations for $(a, b) \in \mathbf{C}^2$ becomes closed. The truncated equations at the leading order take the explicit form:

$$\Omega a = v_0 a + v_{2n} b + \sigma(|a|^2 + 2|b|^2)a, \quad \Omega b = v_{-2n} a + v_0 b + \sigma(2|a|^2 + |b|^2)b, \quad (19.6)$$

where the truncation error is of the order of $O(\|\mathbf{v}\|_{L^1}^2, (|a| + |b|)^5)$. Since $v_{-2n} = \bar{v}_{2n}$, the symmetry constraint $b = \bar{a}$ is satisfied and one equation (19.6) is redundant.

It is a subject of ongoing studies to derive a full time-dependent version of the coupled-mode equations (19.6) which would be valid in the energy space $(a, b) \in H^1(\mathbf{R}, \mathbf{C}^2)$ on the infinite line $x \in \mathbf{R}$. The formal derivation is based on the asymptotic multi-scale expansions [8], which result in the coupled-mode system

$$\begin{aligned} i(\partial_t + \partial_x) a &= v_0 a + v_{2n} b + \sigma(|a|^2 + 2|b|^2)a, \\ i(\partial_t - \partial_x) b &= v_{-2n} a + v_0 b + \sigma(2|a|^2 + |b|^2)b, \end{aligned} \quad (19.7)$$

where (x, t) are rescaled space-time variables. The presence of exact localized solutions in the coupled-mode equations (19.7) makes this reduced model particularly useful for analysis of existence, stability and time evolution of gap solitons [12]. Other rigorous methods for justification of the coupled-mode equations (19.7) can be found in [13, 14], where localized modes are controlled up to a finite-time interval and up to a small error (which may not be localized in space).

Coupled-mode equations are formally extended in the space of two and three dimensions [8], e.g., for four counter-propagating waves in the GP equation with $N = 2$. The system of four coupled-mode equations may possess a gap in the continuous spectrum [8], where stationary two-dimensional gap solitons may reside. However, since no gaps may exist in a two-dimensional periodic potential $V(x_1, x_2)$ in the limit of small strength $V_\infty = \|V\|_{L^\infty}$ [15],

these gap solitons cannot be fully localized in the original GP equation (19.1). Therefore, the breakup in convergence of iterations is expected when the methods of Lyapunov–Schmidt reductions are applied to the higher-dimensional GP equation (19.1) with $N \geq 2$.

19.2.2 Moderate Strength: Continuous NLS Equations

The envelope approximation for modulated nonlinear dispersive waves was used to simplify problems of nonlinear optics, plasma physics, and water-waves since the works of Leontovich in 1930s and Talanov in 1960s [16]. In the simplest situation, this approximation results in a reduction of the second-order time-evolution partial differential equations (PDEs), such as the Maxwell equations, into the first-order time-evolution PDE represented by the nonlinear Schrödinger (NLS) equation. The NLS equation is different from the GP equation (19.1) in that the potential term $V(x)$ is absent. In the context of the *finite* periodic potentials, the NLS equation was derived formally in [6] near the band edges of the spectral bands but earlier works on the use of the NLS approximation in the same context have been known for quite some time, e.g. in [17]. We shall justify the NLS approximation for the stationary problem (19.2) in one dimension $N = 1$ by using elements of the Floquet theory and dynamical systems, similar to [18]. The two Floquet multipliers of the Hill's equation (19.3) associated with the periodic potential $V(x)$ belong to the unit circle when ω is in the interior point of $\sigma(L)$, collide at $+1$ or -1 when ω is at the band edge of $\sigma(L)$ and split along positive or negative real axis outside and inside the unit circle when ω is in the point of a spectral gap. We shall consider a transformation of the stationary problem (19.2) when ω is close to a particular band edge ω_0 . For instance, let $\omega = \omega_0 + \epsilon^2 \Omega$, where ϵ is a small parameter to measure the deviation $|\omega - \omega_0|$. Let us introduce two functions $\psi_0(x)$ and $\psi_1(x)$ from the solutions of the ODEs:

$$-\psi_0'' + V(x)\psi_0 = \omega_0\psi_0, \quad -\psi_1'' + V(x)\psi_1 = \omega_0\psi_1 + 2\psi_0'. \quad (19.8)$$

These functions are either periodic or anti-periodic on $x \in [0, d]$, depending on the band edge ω_0 . The second eigenfunction $\psi_1(x)$ called the generalized Bloch function solves the inhomogeneous Hill's equation.

Let us represent the solution $\phi(x)$ of the stationary problem (19.2) in the form

$$\phi(x) = \epsilon [a(x)\psi_0(x) + b(x)\psi_1(x)]$$

subject to the constraint $a'\psi_0 + b'\psi_1 = b\psi_0$. Another constraint on the normal coordinates (a, b) follows from the ODE (19.2):

$$a'\psi_0' + b'(\psi_1' + \psi_0) = b\psi_0' - \epsilon^2 \Omega(a\psi_0 + b\psi_1) + \epsilon^2 \sigma(a\psi_0 + b\psi_1)^3. \quad (19.9)$$

The determinant of the coefficient matrix in the left-hand-side of the system (19.9) is

$$D(x) = \psi_0(x)\psi'_1(x) - \psi'_0(x)\psi_1(x) + \psi_0^2(x).$$

It is easy to check by direct differentiation that the determinant is x -independent, such that $D(x) = D_0$. We will assume here that $D_0 \neq 0$ and show later that this condition gives a sufficient condition for existence of the gap on one side of the point $\omega = \omega_0$. By diagonalizing the system (19.9) and rescaling the variables $X = \epsilon x$, $a = A(X)$ and $b = \epsilon B(X)$, we rewrite the system (19.9) in an equivalent form:

$$\begin{aligned}\dot{A} &= B + \frac{\epsilon}{D_0} [\sigma\psi_1(A\psi_0 + \epsilon B\psi_1)^3 - \Omega\psi_1(A\psi_0 + \epsilon B\psi_1)], \\ \dot{B} &= -\frac{1}{D_0} [\sigma\psi_0(A\psi_0 + \epsilon B\psi_1)^3 - \Omega\psi_0(A\psi_0 + \epsilon B\psi_1)],\end{aligned}\quad (19.10)$$

where the dots (\dot{A}, \dot{B}) denote derivatives in $X = \epsilon x$, while the functions ψ_0 and ψ_1 depend on $x = X/\epsilon$. Therefore, a regular averaging method is applied to decompose (A, B) into the mean-field and varying parts, so that the varying part is defined uniquely in terms of the mean-field part [19]. Furthermore, the ODE system (19.10) is associated with the Jordan block for a double zero eigenvalue, which is brought into a normal form by a standard normal form transformation [18]. By using these two rigorous techniques, the truncated normal form at the leading order is written as follows:

$$D_0 \ddot{A} - \Omega A(\psi_0, \psi_0)_{[0,d]} + \sigma A^3(\psi_0^2, \psi_0^2)_{[0,d]} = 0, \quad (19.11)$$

where

$$(u, v)_{[0,d]} = \frac{1}{d} \int_0^d u(x)v(x)dx$$

is the averaging operator. Depending on the signs between D_0 , Ω and σ , the averaged second-order ODE (19.11) may have a homoclinic orbit expressed in terms of the hyperbolic sech-function. According to the asymptotic procedure above, the sech-soliton of the reduced problem (19.11) resembles the gap soliton of the stationary problem (19.2) near the band edge $\omega = \omega_0$.

In order to relate the quantity D_0 to the linear spectrum of $L = -\partial_x^2 + V(x)$, we shall consider the Bloch function

$$\psi = u_{n,k}^{\pm}(x)e^{\pm ikx}$$

of the spectral band $\omega = \omega_{n,k}$ near the band edge $\omega = \omega_0$. At $\omega = \omega_0$, the quasi-momentum is $k = 0$ if $\psi_0(x)$ is a periodic Bloch function and $k = \pi/d$ if $\psi_0(x)$ is an anti-periodic function. Therefore, by abusing slightly notations we can represent the solution of the Hill's equation (19.3) for $\omega = \omega_{n,k} \equiv \omega_k$ in the form $\psi \equiv \phi_k(x)e^{ikx}$, where k is now near zero if ω_k is near ω_0 and $\phi_k(x)$ is

either periodic or anti-periodic function, which satisfies the generalized Hill's equation

$$-\phi_k'' + V(x)\phi_k = \omega_k\phi_k + 2ik\phi_k' - k^2\phi_k. \quad (19.12)$$

Because of analyticity of $\phi_k(x)$ and ω_k with respect to k (see [20]), one can expand

$$\omega_k = \omega_0 + \frac{1}{2}\omega_k''k^2 + O(k^3)$$

and

$$\phi_k = \psi_0(x) + ik\psi_1(x) + k^2\psi_2(x) + O(k^3)$$

and derive the inhomogeneous problem for ψ_2 :

$$-\psi_2'' + V(x)\psi_2 = \omega_0\psi_2 + \frac{1}{2}\omega_k''\psi_0 - 2\psi_1' - \psi_0. \quad (19.13)$$

The function $\psi_2(x)$ is periodic or anti-periodic if and only if the right-hand-side of the ODE (19.13) is orthogonal to $\psi_0(x)$ on $x \in [0, d]$. This condition results in the constraint

$$\frac{1}{2}\omega_k''(\psi_0, \psi_0)_{[0,d]} = (\psi_0, \psi_0)_{[0,d]} + 2(\psi_0, \psi_1')_{[0,d]} = (1, D)_{[0,d]} = D_0.$$

With this relation, the stationary equation (19.11) can be rewritten in the form

$$\frac{1}{2}\omega_k''\ddot{A} - \Omega A + \sigma\chi A^3 = 0, \quad \chi = \frac{(\psi_0^2, \psi_0^2)_{[0,d]}}{(\psi_0, \psi_0)_{[0,d]}} > 0. \quad (19.14)$$

If $\omega_k'' \neq 0$, the gap exists on the other side of the point $\omega = \omega_0$ relative to the band $\omega = \omega_k$ and the gap solitons bifurcate as solutions of the truncated problem (19.14) under the conditions that ω_k'' , Ω and σ are of the same signs.

Localized modes of the stationary problem (19.2) associated with the periodic potential $V(x)$ have their linear counterparts, called *defect modes*, which are bound states of the linear Schrödinger operator with a sum of periodic and small decaying potentials. For instance, one can look for localized solutions of the linear problem

$$-\phi'' + V(x)\phi + \epsilon W(x)\phi = \omega\phi, \quad (19.15)$$

where $V(x)$ is a bounded periodic potential, ω is in the gap of the spectrum $L = -\partial_x^2 + V(x)$, $W(x)$ is a bounded exponentially decaying potential, and ϵ is small parameter. The first rigorous works on analysis of isolated eigenvalues in the linear Schrödinger problem (19.15) are dated back to 1980s [21], while recent activities on this subject are motivated by studies of defect modes in nonlinear photonic lattices [22, 23].

The problem of bifurcations of isolated eigenvalues of the spectral problem (19.15) can be effectively solved with the Evans function method. The Evans function was successfully used in a similar context of the edge bifurcation from

the continuous spectrum [24]. Let $L = -\partial_x^2 + V(x)$, $\omega \notin \sigma(L)$, and consider two particular solutions $\phi_{1,2}(x)$ of the linear problem (19.15), so that $\phi_1(x)$ converges to the Bloch functions $\phi_+(x)e^{\kappa x}$ as $x \rightarrow -\infty$ and $\phi_2(x)$ converges to the Bloch function $\phi_-(x)e^{-\kappa x}$ as $x \rightarrow +\infty$, respectively. Such solutions are well-defined for $\operatorname{Re} \kappa > 0$ by the ODE theory [25]. The parameter $\operatorname{Re} \kappa > 0$ is called the Lyapunov exponent and it depends on ω , such that $\operatorname{Re} \kappa \rightarrow 0$ as $\omega \rightarrow \omega_0$, where ω_0 is a particular band edge of the spectrum of $\sigma(L)$.

Let the spectral band $\omega = \omega_{n,k} \equiv \omega_k$ be represented by

$$\omega_k = \omega_0 + \frac{1}{2}\omega''_k k^2 + O(k^3)$$

on one side of the point $\omega = \omega_0$, where k is near zero and $\omega''_k \neq 0$. By abusing notations again we can consider κ to be a small real parameter on the other side of the point $\omega = \omega_0$. The inverse dependence of $\kappa(\omega)$ for $\omega \notin \sigma(L)$ is defined by the expansion

$$\omega = \omega_0 - \frac{1}{2}\omega''_k \kappa^2 + O(\kappa^3).$$

The Evans function $E(\kappa, \epsilon)$ is the 2×2 Wronskian determinant of the 2 -vector extensions of the two fundamental solutions $\phi_1(x)$ and $\phi_2(x)$. When $E(\kappa_*, \epsilon_*) = 0$ for some $\kappa_* \in \mathbf{C}$ with $\operatorname{Re} \kappa > 0$ and $\epsilon_* \in \mathbf{R}$, the two solutions become linearly dependent. They span an exponentially decaying solution $\phi(x)$ of the spectral problem (19.15) on $x \in \mathbf{R}$ for the corresponding value ω_* which is found from the dependence $\omega_* = \omega(\kappa_*)$. It is proved in standard analysis [25] that $E(\kappa, \epsilon)$ is analytic with respect to κ and ϵ for $\operatorname{Re} \kappa > 0$ and $\epsilon \in \mathbf{R}$ and it can be analytically extended in κ near $\kappa = 0$.

Since $\phi_+(x)$ and $\phi_-(x)$ are linearly dependent at $\kappa = 0$ and $\epsilon = 0$, then $E(0, 0) = 0$. If $\partial_\kappa E(0, 0) \neq 0$, the zero $\kappa = 0$ is continued into a simple zero $\kappa = \kappa_*$ of $E(\kappa, \epsilon)$ near $\kappa = 0$ and $\epsilon = 0$ by using the Implicit Function Theorem and the expansion

$$E(\kappa, \epsilon) = \kappa \partial_\kappa E(0, 0) + \epsilon \partial_\epsilon E(0, 0) + O(\kappa^2, \epsilon \kappa, \epsilon^2).$$

If $\operatorname{Re} \kappa_* > 0$, the zero of $E(\kappa, \epsilon)$ corresponds to the eigenvalue of (19.15) with an exponentially decaying eigenfunction $\phi(x)$. First derivatives of $E(\kappa, \epsilon)$ are computed explicitly at $(\kappa, \epsilon) = (0, 0)$. Since

$$E(\kappa, 0) = \begin{vmatrix} \phi_+(x) & \phi_-(x) \\ \phi'_+(x) + \kappa \phi_+(x) & \phi'_-(x) - \kappa \phi_-(x) \end{vmatrix} = \phi_+ \phi'_- - \phi_- \phi'_+ - 2\kappa \phi_+ \phi_-$$

and $\phi_\pm(x) = \psi_0(x) \pm \kappa \psi_1(x) + O(\kappa^2)$, then

$$\partial_\kappa E(0, 0) = 2\psi_1 \psi'_0 - 2\psi_0 \psi'_1 - 2\psi_0^2 = -2D_0 = -\omega''_k(\psi_0, \psi_0)_{[0,d]}.$$

On the other hand,

$$\partial_\epsilon E(\kappa, 0) = (\phi'_2 \partial_\epsilon \phi_1 - \phi_2 \partial_\epsilon \phi'_1) - (\phi_2 \partial_\epsilon \phi'_1 - \phi_1 \partial_\epsilon \phi'_2) = - \int_{-\infty}^{\infty} W(x) \phi_1 \phi_2 dx,$$

where $\phi_1(x)$ and $\phi_2(x)$ are the two fundamental solutions of the ODE (19.15) so that $\phi_{1,2} \rightarrow \psi_0(x)$ as $\epsilon \rightarrow 0$ and $\kappa = 0$. Therefore,

$$\partial_\epsilon E(0, 0) = -(\psi_0, W(x)\psi_0)_{\mathbf{R}}.$$

The root of $E(\kappa, \epsilon)$ near $(\kappa, \epsilon) = (0, 0)$ bifurcates in the domain $\kappa > 0$ if the matrix element $(\psi_0, \epsilon W(x)\psi_0)_{\mathbf{R}}$ has the opposite sign to the sign of ω''_k . The leading-order approximation for the root follows from the expansions above:

$$\omega = \omega_0 - \frac{\epsilon^2}{2\omega''_k} \left| \frac{(\psi_0, W(x)\psi_0)_{[0,d]}}{(\psi_0, \psi_0)_{[0,d]}} \right|^2 + \mathcal{O}(\epsilon^3). \quad (19.16)$$

The same formula was derived in [22] with a decomposition technique when a localized solution $\phi(x)$ is represented in terms of the complete set of Bloch functions over the spectrum $\sigma(L)$ and the asymptotic analysis of integrals with pole singularities is performed in the limit $\epsilon \rightarrow 0$ and $\omega \rightarrow \omega_0$. The asymptotic analysis is based on a rigorous technique, when the integral is decomposed into a rank-one singular and infinite-dimensional non-singular parts and the non-singular part is estimated in terms of the single component of the singular part of the integral [26]. This technique is similar to the method of Lyapunov–Schmidt reductions for integral equations.

The time-dependent version of the stationary equation (19.14) is the NLS equation

$$iA_t = \frac{1}{2}\omega''_k A_{XX} + \sigma\chi|A|^2A. \quad (19.17)$$

Rigorous justification of the NLS equation (19.17) was reported in [27] from the Maxwell equations with nonlocal terms and in [28] from a lattice system that models the Fermi–Pasta–Ulam problem. These results are valid in the space of continuous functions on a finite time interval, where the spatial decay rate of the error terms can not be controlled.

Formal extensions of the NLS equation (19.17) in two and three dimensions can be developed when the dispersion surface $\omega = \omega_{\mathbf{k}}$ of the multi-dimensional periodic potential $V(\mathbf{x})$ admits extremal points $\omega = \omega_0$ where $\nabla_{\mathbf{k}}\omega_{\mathbf{k}} = \mathbf{0}$ and the Hessian matrix of $\omega_{\mathbf{k}}$ is sign-definite. A spectral gap exists on the other side of the extremal point $\omega = \omega_0$ relative to the band $\omega = \omega_{\mathbf{k}}$. Bifurcations of the multi-dimensional gap solitons near the band edge $\omega = \omega_0$ can be described by the multi-dimensional NLS equation, e.g. for $N = 2$:

$$iA_t = \frac{1}{2} (\omega''_{k_1} A_{X_1 X_1} + \omega''_{k_2} A_{X_2 X_2}) + \sigma\chi|A|^2A, \quad (19.18)$$

where (X_1, X_2) are appropriate coordinates which diagonalize the Hessian matrix of $\omega_{\mathbf{k}}$. Since ω''_{k_1} and ω''_{k_2} are of the same sign near the band edge,

bifurcation of two-dimensional NLS solitons occurs when the NLS equation (19.18) is of the focusing type. However, such solutions are unstable and the critical blow-up occurs in the time-evolution of the two-dimensional NLS equation (19.18) in finite time [16]. On the other hand, no finite-time blow up occurs in the defocusing GP equation (19.1) with $\sigma = +1$, so that the correspondence between the GP equation and the NLS equation is lost for $N \geq 2$.

19.2.3 Large Strength: Discrete NLS Equations

Discrete NLS equations were used for modeling of various physical problems involving arrays of coupled oscillators [29]. Similar to this traditional application of the lattice equations, periodic continuous problems with *large* spacing between wells of the periodic potential $V(x)$ or *large* strength $V_\infty = \|V\|_{L^\infty}$ can also be reduced to the discrete problems in a so-called tight-binding approximation [5]. The Wannier function decomposition method was shown in [30] to be relevant for the derivation of the discrete NLS equation from the continuous GP equation (19.1).

We shall describe the Wannier function decomposition based on the analysis of [20]. Let us consider the stationary problem (19.2) in one dimension $N = 1$ and recall the construction of the Bloch functions $\psi = u_{n,k}^\pm(x)e^{\pm ikx}$ and the spectral band $\omega = \omega_{n,k}$ of the operator $L = -\partial_x^2 + V(x)$. By definition, the Wannier function $a_n(x)$ for the n th spectral band $\omega = \omega_{n,k}$ is constructed from the Bloch function

$$\psi_{n,k} \equiv u_{n,k}^+(x)e^{ikx}$$

by

$$a_n(x) = \left(\frac{d}{2\pi} \right)^{1/2} \int_{-\pi/d}^{\pi/d} \psi_{n,k}(x) dk. \quad (19.19)$$

It is proved in [20] for a class of symmetric potentials $V(-x) = V(x)$ that there exists only one Wannier function $a_n(x)$ for each $n \geq 0$, so that $a_n(x)$ is a real function, $a_n(x)$ is either even or odd about $x = 0$, and $a_n(x)$ decays exponentially as $|x| \rightarrow \infty$. Because of the decay, the set of Wannier functions $\{a_{n,l}(x)\}_{n \geq 0, l \in \mathbf{Z}}$ with $a_{n,l}(x) \equiv a_n(x - ld)$ provide a nice basis for decomposition of any function in $L^2(\mathbf{R})$ provided that the set is complete. Completeness of the set of Wannier functions follows from the Shannon's Sampling Theorem which relates the Fourier transform of a discrete unbounded sequence of functions and the Fourier transform of a continuous, compactly supported function. Indeed, since

$$\sum_{l \in \mathbf{Z}} e^{ild(k' - k)} = \frac{2\pi}{d} \delta(k' - k), \quad \forall k, k' \in \left[-\frac{\pi}{d}, \frac{\pi}{d} \right],$$

where $\delta(k)$ is the Dirac delta function, one can find a pair of Fourier transforms between the Wannier functions $a_{n,l}(x)$ and the Bloch functions $\psi_{n,k}(x)$:

$$a_{n,l}(x) = \left(\frac{d}{2\pi}\right)^{1/2} \int_{-\pi/d}^{\pi/d} \psi_{n,k}(x) e^{-ikld} dk, \quad \psi_{n,k}(x) = \left(\frac{d}{2\pi}\right)^{1/2} \sum_{l \in \mathbf{Z}} a_{n,l}(x) e^{ikld}.$$

Let us normalize the Bloch functions by the Dirac's orthogonality relations

$$(\psi_{n',k'}, \psi_{n,k})_{\mathbf{R}} = \int_{\mathbf{R}} \psi_{n',k'}(x) \bar{\psi}_{n,k}(x) dx = \delta_{n',n} \delta(k' - k),$$

where $\delta_{n',n}$ is the Kronecker delta symbol. It follows by direct computation that the set of Wannier functions

$$\{a_{n,l}(x)\}_{n \geq 0, l \in \mathbf{Z}}$$

satisfies the orthogonality relations

$$(a_{n',l'}, a_{n,l})_{\mathbf{R}} = \delta_{n',n} \delta_{l',l}.$$

Any function in $L^2(\mathbf{R})$ can be uniquely represented in terms of the set of Wannier functions

$$\{a_{n,l}(x)\}_{n \geq 0, l \in \mathbf{Z}}.$$

For instance, a solution $\phi(x)$ of the stationary problem (19.2) can be represented by

$$\phi(x) = \sum_{n \geq 0} \sum_{l \in \mathbf{Z}} c_l a_{n,l}(x),$$

where

$$\{c_{n,l}\}_{n \geq 0, l \in \mathbf{Z}}$$

is the set of projection coefficients. Using this representation, we reduce the stationary problem (19.2) to the nonlinear lattice problem

$$\omega c_{n,l} = \sum_{l_1 \in \mathbf{Z}} c_{n,l_1} \hat{\omega}_{n,l-l_1} + \sigma \sum_{(n_1, n_2, n_3) \geq 0} \sum_{(l_1, l_2, l_3) \in \mathbf{Z}^3} W_{l_1, l_2, l_3, l}^{n_1, n_2, n_3, n} c_{n_1, l_1} c_{n_2, l_2} c_{n_3, l_3}, \quad (19.20)$$

where

$$W_{l_1, l_2, l_3, l}^{n_1, n_2, n_3, n} = (a_{n_1, l_1} a_{n_2, l_2}, a_{n_3, l_3} a_{n, l})_{\mathbf{R}}$$

are matrix elements of the projections and $\hat{\omega}_{n,l}$ are Fourier coefficients for the spectral band

$$\omega_{n,k} = \sum_{l \in \mathbf{Z}} \hat{\omega}_{n,l} e^{ikld}.$$

In the limit of large $V_\infty = \|V\|_{L^\infty}$, the coefficients $\hat{\omega}_{n,l}$ are large at $l = 0$ and negligibly small at $l \neq 0$. Similarly, the matrix elements $W_{l_1, l_2, l_3, l}^{n_1, n_2, n_3, n}$ are large at $l_1 = l_2 = l_3 = l$ and $n_1 = n_2 = n_3 = n$ and negligibly small at

$|l_j - l| \neq 0$ and $|n_j - n| \neq 0$, $\forall j = 1, 2, 3$. Using these properties and the renormalization $\omega = \hat{\omega}_{n,0} + \Omega$, the truncated system of ODEs (19.20) at the leading order can be written as the tridiagonal system

$$\Omega c_{n,l} = \hat{\omega}_{n,1} (c_{n,l+1} + c_{n,l-1}) + \sigma W_{l,l,l,l}^{n,n,n,n} |c_{n,l}|^2 c_{n,l}. \quad (19.21)$$

By rescaling of Ω and $c_{n,l}$, the coefficients of the tridiagonal system (19.21) can be normalized to ± 1 . The tridiagonal system (19.21) is formally extended to the time-evolution system called the discrete NLS equation

$$i\dot{\psi}_l = \epsilon (\psi_{l+1} + \psi_{l-1}) + \sigma |\psi_l|^2 \psi_l, \quad (19.22)$$

where

$$\psi_l(t) = c_{n,l} e^{-i\Omega t} / \sqrt{W_{l,l,l,l}^{n,n,n,n}}$$

and $\epsilon = \hat{\omega}_{n,1}$. No works on rigorous justification of the discrete NLS equation (19.22) from the time-dependent GP equation (19.1) have been reported so far. A straightforward formal method was proposed in [31], where the periodic potential of a large strength V_∞ was approximated by a sequence of Dirac delta functions

$$V(x) = -V_\infty \sum_{l \in \mathbf{Z}} \delta(x - ld).$$

The individual delta-function potential $V(x) = -V_\infty \delta(x)$ admits the ground state

$$\phi_0(x) = e^{-\frac{1}{2} V_\infty |x|}$$

for the lowest eigenvalue $\omega_0 = -\frac{1}{4} V_\infty^2$. The direct decomposition of the solution of the GP equation (19.1) is based on the representation

$$\psi(x, t) = \sum_{l \in \mathbf{Z}} c_l(t) \phi_0(x - ld).$$

Although the basis functions $\{\phi_0(x - ld)\}_{l \in \mathbf{Z}}$ are not orthogonal to each other, the inner product of

$$(\phi_0(x - ld), \phi_0(x - l'd))_{\mathbf{R}}$$

is $2/V_\infty$ for $l' = l$ and exponentially small in terms of $1/V_\infty$ for $l' \neq l$, e.g.

$$(\phi_0(x - ld), \phi_0(x - (l \pm 1)d))_{\mathbf{R}} = \frac{2 + dV_\infty}{V_\infty} e^{-\frac{1}{2} V_\infty d}.$$

By substituting the decomposition for $\psi(x, t)$ into the GP equation (19.1) and by using the projection algorithm, one can find the leading-order amplitude equations for $c_l(t)$:

$$i\dot{c}_l + \frac{1}{4} V_\infty^2 c_l = -\frac{1}{4} V_\infty^2 \left(1 + \frac{1}{2} dV_\infty\right) e^{-\frac{1}{2} V_\infty d} (c_{l+1} + c_{l-1}) + \frac{1}{2} \sigma |c_l|^2 c_l. \quad (19.23)$$

Under the transformation

$$c_l(t) = \sqrt{2}\psi_l(t)e^{\frac{i}{4}V_\infty^2 t},$$

the system (19.23) becomes the discrete NLS equation (19.22) with

$$\epsilon = -\frac{1}{4}V_\infty^2 \left(1 + \frac{1}{2}dV_\infty^d\right) e^{-\frac{1}{2}V_\infty d}.$$

The discrete NLS equation (19.21) has an exponentially small coupling term ϵ in terms of $1/V_\infty$. The limit of zero coupling term ($\epsilon = 0$) is referred to as the *anti-continuum limit*. It has been used successfully in the proof of existence [32] and stability [33] of discrete solitons in one spatial dimension. Extensions of this method have been reported in the context of two-dimensional [34, 35] and three-dimensional [36] vortices. Since localized modes of the discrete NLS equation and the eigenvalues of the relevant linearizations are known at $\epsilon = 0$, the method of Lyapunov–Schmidt reductions can be used to derive the conditions when these localized modes and their corresponding eigenvalues can be continued in $\epsilon \neq 0$. Power series expansions in ϵ are constructed and studied in the technical implementation of the algorithm. It is however clear that the second-order terms $O(\epsilon^2)$ of the Lyapunov–Schmidt reductions in [33–36] are comparable with the terms proportional to $\hat{\omega}_{n,2}$, which are truncated beyond the tridiagonal system (19.21). Therefore, some discrepancies may occur between the predictions of the continuous GP equation (19.1) and those of the discrete NLS equation (19.22).

The situation becomes worse in the space of higher dimensions. By using the same technique, the discrete NLS equation (19.22) with $N = 1$ is extended to the two-dimensional lattice with $N = 2$ in the form

$$i\dot{\psi}_{l,m} = \epsilon (\psi_{l+1,m} + \psi_{l-1,m} + \psi_{l,m+1} + \psi_{l,m-1}) + \sigma |\psi_{l,m}|^2 \psi_{l,m}, \quad (19.24)$$

where the spectral band $\omega_{\mathbf{k}}$ is assumed to be isotropic so that the Fourier coefficients for $\omega_{n,\mathbf{k}}$ satisfy the conditions $\hat{\omega}_{n,1,0} = \hat{\omega}_{n,-1,0} = \hat{\omega}_{n,0,1} = \hat{\omega}_{n,0,-1}$. The two-dimensional discrete NLS equation (19.24) takes into account the horizontal and vertical couplings between adjacent sites. The next-order term contributing to the discrete NLS equation on a square lattice is the diagonal coupling term which is proportional to the coefficients

$$\hat{\omega}_{n,1,1} = \hat{\omega}_{n,1,-1} = \hat{\omega}_{n,-1,1} = \hat{\omega}_{n,-1,-1}.$$

If $\hat{\omega}_{n,1,0} \sim e^{-V_\infty d}$ for large V_∞ , then

$$\hat{\omega}_{n,1,1} \sim e^{-\sqrt{2}V_\infty d},$$

i.e. $\hat{\omega}_{n,1,1}$ is much larger than

$$\hat{\omega}_{n,1,0}^2, \hat{\omega}_{n,2,0} \sim e^{-2V_\infty d}.$$

If the Lyapunov–Schmidt reductions would depend crucially on the results of the second-order computations, the predictions without the account of the diagonal couplings between two-dimensional lattice sites could be incorrect.

19.3 Class of Decaying Potentials

We shall assume here that $V(x)$ is a decaying potential at infinity, which is given by a continuously differentiable function on $x \in \mathbf{R}^N$. If the potential $V(x)$ is absent, the stationary problem (19.2) admits a solution $\phi_0(x)$ decaying to zero as $|x| \rightarrow \infty$ in the focusing case with $\sigma = -1$ and $\omega < 0$. In the space of one dimension $N = 1$, this solution is nothing but the sech-soliton $\phi_0 = \sqrt{2|\omega|} \operatorname{sech}(\sqrt{|\omega|}|x - s|)$, where $s \in \mathbf{R}$ is an arbitrary translation parameter. We shall ask if the solution $\phi_0(x)$ persists in the full stationary problem (19.2) with a given potential $V(x)$. To answer this question, let us assume the existence of the localized solution of the stationary problem (19.2) with $\omega \notin \sigma(L)$ which is given by a continuously differentiable function $\phi(x)$ on $x \in \mathbf{R}^N$. We multiply the stationary problem (19.2) by $\partial_{x_j} \phi(x)$, $j = 1, \dots, N$ and integrate over $x \in \mathbf{R}^N$. Since $\phi(x)$ decays to zero at infinity with an exponential rate for $\omega \notin \sigma(L)$, contributions from $(N - 1)$ -dimensional integrals vanish at infinity. As a result, the following integrals must be identically zero

$$\int_{\mathbf{R}^N} \phi^2(x) \partial_{x_j} V(x) dx = 0, \quad j = 1, \dots, N. \quad (19.25)$$

Of course, these conditions give simply constraints on the profile of the classical solution $\phi(x)$ of the stationary problem (19.2), which *has been assumed* to exist. However, in two special cases, one can use the leading-order approximation $\phi(x) = \phi_0(x - s)$ with $s \in \mathbf{R}^N$ obtained for $V(x) = 0$ in the integral (19.25) and interpret the corresponding conditions as the persistence equations for continuation of $\phi_0(x - s)$ into a full solution $\phi(x)$ of the stationary problem (19.2) with $V(x) \neq 0$.

The special cases when the integrals (19.25) are small occur for *small* or *wide* potentials $V(x)$ relative to the amplitude or width of the stationary solution $\phi_0(x)$. In the first case, one can use the representation $V = \epsilon W(x)$, such that the conditions (19.25) have the magnitude of $O(\epsilon)$ [37]. In the second case, one can use the representation $V = W(\epsilon x)$, such that the same conditions occur also at $O(\epsilon)$ [38]. In either case, the rigorous technique for finding of the necessary condition for persistence of stationary solutions is based on the method of Lyapunov–Schmidt reductions [37, 38]. Moreover, the same technique can be extended to derive the sufficient condition for persistence, to study stability of the persistent configurations and to approximate the time-evolution dynamics of localized modes in the external potential $V(x)$ with the Newton’s equation of motion

$$m_0 \ddot{s} = -\nabla U(s), \quad (19.26)$$

where m_0 is an effective mass, s is the position of the localized mode on $x \in \mathbf{R}^N$, and $U(s)$ is an effective potential given by

$$U(s) = \frac{\int_{\mathbf{R}^N} V(x) \phi_0^2(x - s) dx}{\int_{\mathbf{R}^N} \phi_0^2(x) dx}. \quad (19.27)$$

Due to the Galilean translation of solutions of the GP equation

$$u(x, t) \mapsto e^{\frac{i}{2}v \cdot x - \frac{i}{4}|v|^2 t} u(x - vt, t),$$

the constant m_0 is found to be $m_0 = 1/2$ independently of N [38]. In the space of one dimension $N = 1$, it follows from the Newton's equation of motion (19.26) that the localized mode $\phi_0(x - s)$ persists at the particular value $s = s_0$ with $U'(s_0) = 0$ if $U''(s_0) \neq 0$, it is stable if $U''(s_0) > 0$ and unstable if $U''(s_0) < 0$ and the long-term dynamics of localized mode is described by the long-term oscillations in the case $U''(s_0) > 0$. If there are several points s_0 with $U'(s_0) = 0$, the Newton's equation of motion (19.26) provides global information on stability of each equilibrium configuration and local dynamics in a neighborhood of the equilibria. In the space of two and three dimensions $N \geq 2$, the Newton's equation of motion (19.26) is not applicable for predictions of dynamics of localized modes due to spectral instabilities of solitons $\phi_0(x)$ of the multi-dimensional focusing NLS equation (19.1) with $V(x) = 0$ and $\sigma = -1$.

The formal derivation of the Newton's equation of motion (19.26) for dynamics of a localized mode in an external potential $V(x)$ was developed first in [39, 40] by using asymptotic multi-scale expansions. This formal technique is recovered from the Ehrenfest's theorem

$$\frac{d}{dt} \int_{\mathbf{R}^N} \frac{i}{2} (\bar{u} \nabla u - u \nabla \bar{u}) dx = \int_{\mathbf{R}^N} |u|^2 \nabla V(x) dx \quad (19.28)$$

for any continuously differentiable solution $u(x, t)$ of the GP equation (19.1). The slow dynamics of a localized mode is supported by the smallness of the right-hand-side of (19.28), which occurs generally if $\nabla V(x)$ is small (either $V = \epsilon W(x)$ or $V = W(\epsilon x)$ with a small parameter ϵ). In this case, the leading-order solution $u(x, t)$ is an orbit of the moving soliton

$$u = e^{\frac{i}{2}v \cdot x - i\theta} \phi_0(x - s)$$

with $\dot{s} = v$ and $\dot{\theta} = \omega + \frac{|v|^2}{4}$, where all parameters (s, v, θ, ω) are (slow) functions of time t . (If $V = W(\epsilon x)$, one can shift parameters of $\phi_0(x)$ to remove $W(0)$ from the leading-order solution.) The balance equation (19.28) reduces in this leading-order approximation to the Newton's equation of motion (19.26).

Although the decomposition of the asymptotic multi-scale expansion method may seem rough and inaccurate, it has been rigorously proved in the case $V = W(\epsilon x)$ by two methods. The weak variational formalism was employed in [41] to prove convergence of the GP equation in the semi-classical limit to the set of Newton's equations of motion for a superposition of localized modes. The skew-orthogonal projection method, Lyapunov–Schmidt decompositions, and lower-upper bound estimates on the energy functional were developed in [38] for dynamics of a single localized mode. The same authors

also extended their method to the case of confining potentials in [42] and derived the same Newton's equation of motion (19.26).

The other case $V = \epsilon W(x)$ with decaying $W(x)$ is even easier since the technique of [38] would work without any modifications. For instance, the sufficient condition of persistence of localized solutions, i.e. $U'(s_0) = 0$ and $U''(s_0) \neq 0$, follows from a classical application of Lyapunov–Schmidt reductions to the elliptic problem (19.2) with a perturbation term in $H^2(\mathbf{R})$ [37]. This method was recently applied to the case of dark solitons which are localized solutions with non-zero boundary conditions existing in the defocusing case $\sigma = 1$ and $\omega > 0$. Recent work [43] contains a rigorous proof of persistence and stability of dark solitons in small decaying potentials $V = \epsilon W(x)$ and numerical evidences that the Newton's law of motion modified by the radiative terms is relevant for slow dynamics of dark solitons. Following discussions in [44], we mention that the Ehrenfest's theorem (19.28) is not relevant for the derivation of the Newton's equation of motion for dark solitons as it gives a wrong value of the mass constant m_0 .

A very similar technique can be developed to deal with localized modes of the GP equation when the decaying potential $V(x)$ is represented by a superposition of K identical single-well potentials $W(x)$ located on an equal *large* distance s far from each other:

$$V(x) = \sum_{k=1}^K W(x - (k-1)s). \quad (19.29)$$

The localized modes of the stationary problem (19.2) with the potential $V(x)$ in the form (19.29) persist and evolve according to an effective interaction potential. This theory of interaction of localized modes distant from each other was elaborated long ago by using formal methods in [40] and it was rigorously verified recently by using geometric constructions in [45].

In order to place this theory on mathematical footing, let us assume that the operator $L = -\partial_x^2 + W(x)$ associated with each potential well $W(x)$ has a number of isolated eigenvalues and the corresponding bound states. By using the classical Lyapunov–Schmidt reductions [11], each bound state for a simple isolated eigenvalue is uniquely continued into a nonlinear localized mode of the nonlinear problem (19.2) with $V = W(x)$. The ground state for the smallest eigenvalue is typically of the highest interest due to its stability with respect to time evolution in the nonlinear GP equation (19.1).

We now consider the stationary problem (19.2) with the potential $V(x)$ in the form (19.29) in the limit of large s . First, let us neglect the nonlinear terms and consider the splitting of eigenvalues of the linear operator $L = -\partial_x^2 + V(x)$. When $s = \infty$, the smallest eigenvalue of L has multiplicity K . However, the multiplicity of the eigenvalue of L is broken when $s \neq \infty$. Detailed computations for the case $K = 3$ were performed in [46] where a general geometric method of [45] for construction of multi-pulse solutions was employed to the analysis of splitting of eigenvalues of L . As a result of

the reductive procedure, the bifurcating eigenvalues with the corresponding eigenfunctions are computed in the form

$$\lambda = \lambda_0 \pm 2\sqrt{2}\psi_0\left(\frac{s}{2}\right)\psi'_0\left(\frac{s}{2}\right) : \quad \psi_{\pm} = \frac{1}{2} \left(\pm \psi_0(x) + \sqrt{2}\psi_0(x-s) \pm \psi_0(x-2s) \right),$$

while the persistent eigenvalue with the corresponding eigenfunction is

$$\lambda = \lambda_0 : \quad \tilde{\psi}_0 = \frac{1}{\sqrt{2}} (\psi_0(x) - \psi_0(x-2s)),$$

where λ_0 and $\psi_0(x)$ are the smallest eigenvalue and the corresponding ground state of the linear operator $L = -\partial_x^2 + W(x)$. Using projections to the three eigenstates for sufficiently large s and employing the method of Lyapunov–Schmidt reductions in the nonlinear stationary problem (19.2), the authors of [46] found a system of nonlinear equations for projections and classified all coupled localized modes that exist in the three-well potential, including their spectral stability and predicted time evolution. A similar method was employed in [47] to consider continuations of eigenvalues of the linear problem associated with a confining potential due to the perturbation of a small periodic potential.

19.4 Class of Confining Potentials

We shall assume here that $V(x)$ is a confining potential in the sense that $\inf_{|x| \geq R} V(x) \rightarrow \infty$ as $R \rightarrow \infty$. Since most experimental settings are based on the so-called harmonic traps, a typical approximation of the general confining potentials is a quadratic function

$$V(x) = \frac{1}{2} \sum_{j=1}^N \omega_j^2 x_j^2$$

with parameters $(\omega_1, \dots, \omega_N)$. The Schrödinger operator $L = -\nabla^2 + V(x)$ associated with the quadratic function $V(x)$ possesses an exact set of eigenvalues and bound states written in terms of the Gauss–Hermite polynomials.

Gauss–Hermite polynomials can be used for decomposition of the solution of the time-dependent GP equation (19.1) with the quadratic potential function $V(x)$ and reduction of the time-evolution PDE problem to the equivalent lattice problem. This approach was used in [48], where the lattice problem was truncated in the Galerkin approximation at the two dominant modes. The two-mode approximation was shown to represent adequately all main dynamical phenomena associated with existence, stability and evolution of localized modes in the confining potentials.

In all asymptotic reductions of this chapter up to this point, we have taken the GP equation (19.1) and its stationary counterpart (19.2) as starting equations of analysis and performed some actions to simplify them to other reduced

equations. On the other hand, the GP equation (19.1) is itself a reduction of the primary equations of physics, which are based on the multi-particle wavefunction formalism in the system of interacting bosons. One can ask therefore if the GP equation (19.1) can be derived rigorously from equations of multi-particle quantum mechanics.

These questions were answered for the stationary problem (19.2) with $N = 3$ in [49]. Extensions of this work for $N = 1, 2$ and for other physical settings are given in the stream of subsequent publications reviewed in [50]. The authors of [49] considered the Hamiltonian operator of n identical bosons

$$H = \sum_{j=1}^n [-\nabla_i^2 + V(x_i)] + \sum_{i < j} v(|x_i - x_j|), \quad (19.30)$$

where $V(x)$ is the confining potential, $v(|x|)$ is an interaction potential and $x_j \in \mathbf{R}^3$ for all $j = 1, \dots, n$. The ground state of the Hamiltonian operator H is a totally symmetric square integrable wavefunction denoted by $\Psi(x_1, x_2, \dots, x_n)$. It exists for the eigenvalue (energy level) $E_{\text{QM}}(n, a)$, where a is the scattering length defined by the formula

$$a = \lim_{r \rightarrow \infty} (r - u(r)/u'(r))$$

from the solution $u(r)$ of the boundary-value problem

$$-u''(r) + \frac{1}{2}v(r)u(r) = 0$$

with $u(0) = 0$.

The main results of [49] (and equivalent theorems in [50]) are proved in the limit of many particles $n \rightarrow \infty$ and zero scattering length $a \rightarrow 0$, such that na is fixed. In particular, it is proved that

$$\forall a_1 > 0 : \lim_{n \rightarrow \infty} \frac{1}{n} E_{\text{QM}} \left(n, \frac{a_1}{n} \right) = E_{\text{GP}}(1, a_1), \quad (19.31)$$

where $E_{\text{GP}}(n, a)$ is the energy of a solution of the stationary problem (19.2) defined by

$$E_{\text{GP}}(n, a) = \int_{\mathbf{R}^3} (|\nabla \phi|^2 + V(x)|\phi|^2 + 4\pi a|\phi|^4) dx, \quad (19.32)$$

subject to the normalization condition

$$\int_{\mathbf{R}^N} |\phi|^2 dx = n.$$

The ground state solution $\phi(x)$ is defined by the minimal value of E_{GP} subject to the fixed L^2 -norm. Not only the energy level E_{QM} of the multi-particle Hamiltonian H in (19.30) converges to the energy level E_{GP} of the ground

state solution of the stationary problem (19.2) but also the solutions converge weakly in $L^2(\mathbf{R}^{3n})$, i.e.

$$\forall a_1 > 0, a = \frac{a_1}{n} : \quad \lim_{n \rightarrow \infty} \int_{\mathbf{R}^{3n-3}} |\Psi(x, x_2, \dots, x_n)|^2 dx_2 \dots dx_n = \phi^2(x), \quad (19.33)$$

in the sense that the integral of the difference between the left-hand-side and right-hand-side terms of the equality (19.33) on $x \in \mathbf{R}^3$ converges to zero as $n \rightarrow \infty$.

The results of [49, 50] are only proved for stationary solutions of the GP equation (and only for the ground state solutions). The time-dependent GP equation (19.1) was considered recently in [51] within a similar asymptotic limit $n \rightarrow \infty$ under the constraint that $n^\epsilon a$ is fixed with $0 < \epsilon < 3/5$. It is proved that the limit points of the k -particle density matrices of the multi-particle wavefunction $\Psi(x, x_2, \dots, x_n, t)$ solve asymptotically the GP equation and the associated hierarchy of evolution equations. Thus, only proved rigorously in 2006, the Gross–Pitaevskii model has been widely used in atomic physics since the pioneer works of Gross and Pitaevskii in 1960s.

Conclusions

I have described reductions of the stationary and time-dependent GP equations used for analysis of existence, stability and dynamics of localized modes in external potentials. Depending on the properties of the potential $V(x)$, the spatially inhomogeneous GP equation (19.1) reduces either to the homogeneous PDEs such as the coupled-mode system or the continuous NLS equation or to differential-difference equations such as the discrete NLS equation or to finite-dimensional models such as the Newton's equations of motion or the ODE system for truncated Gauss–Hermite polynomials.

The limited space of the chapter does not allow me to consider other asymptotic reductions relevant for physics of Bose–Einstein condensation, such as reductions of the time-periodic GP equation relevant for the Feshbach resonance management of the Bose–Einstein condensates (see, e.g., [52]). I conclude by saying that ways of rigorous analysis remain opened for further work in the context of the Gross–Pitaevskii equation. Some of the open problems have been mentioned explicitly in this chapter. Some other problems will show up themselves to young researchers who will take the risk to get involved into challenging topics of the modern mathematical physics.

Acknowledgement. This article was written under the financial support of the Humboldt Research Fellowship. The author thanks P. Kevrekidis for continuing collaborations and enthusiasm in solving mathematical problems arising in physics of Bose–Einstein condensates.

References

1. S. Alama, Y.Y. Li, J. Diff. Eqs. **96**, 89–115 (1992)
2. H.P. Heinz, T. Kupper, C.A. Stuart, J. Diff. Eqs. **100**, 341–354 (1992)
3. T. Kupper, C.A. Stuart, Nonlinear Anal. **18**, 893–903 (1992)
4. A. Pankov, Milan J. Math. **73**, 259–287 (2005)
5. N.K. Efremidis, D.N. Christodoulides, Phys. Rev. A **67**, 063608 (2003)
6. D.E. Pelinovsky, A.A. Sukhorukov, Yu.S. Kivshar, Phys. Rev. E **70**, 036618 (2004)
7. C.M. de Sterke, J.E. Sipe, Prog. Opt. **33**, 203 (1994)
8. D. Agueev, D. Pelinovsky, SIAM J. Appl. Math. **65**, 1101–1129 (2005)
9. T. Dohnal, A.B. Aceves, Stud. Appl. Math. **115**, 209–232 (2005)
10. A. Georgieva, T. Kriecherbauer, S. Venakides, SIAM J. Appl. Math. **60**, 272–294 (1999)
11. M. Golubitsky, D.G. Schaeffer, *Singularities and Groups in Bifurcation Theory*, vol. 1, (Springer, Berlin Heidelberg New York, 1985)
12. M. Chugunova, D. Pelinovsky, SIAM J. Appl. Dyn. Syst. **5**, 66–83 (2006)
13. R.H. Goodman, M.I. Weinstein, P.J. Holmes, J. Nonlinear. Sci. **11**, 123–168 (2001)
14. G. Schneider, H. Uecker, Asymp. Anal. **28**, 163–180 (2001)
15. P. Kuchment, in *Mathematical Modeling in Optical Sciences* (SIAM, Philadelphia, 1999)
16. C. Sulem, P. Sulem, *The Nonlinear Schrödinger Equation, Self-Focusing and Wave Collapse* (Springer, Berlin Heidelberg New York, 1999)
17. T. Iizuka, J. Phys. Soc. Jpn. **63**, 4343–4349 (1994)
18. G. Iooss, M. Adelmeyer, *Topics in Bifurcation Theory and Applications* (World Scientific, Singapore, 1998)
19. A.I. Neishtadt, J. Appl. Math. Mech. **48**, 133–139 (1985)
20. W. Kohn, Phys. Rev. **115**, 809–821 (1959)
21. S. Alama, P.A. Deift, R. Hempel, Comm. Math. Phys. **121**, 291–321 (1989)
22. F. Fedele, J. Yang, Z. Chen, Stud. Appl. Math. **115**, 279–301 (2005)
23. J. Yang, Z. Chen, Phys. Rev. E **73**, 026609 (2006)
24. T. Kapitula, B. Sandstede, Discr. Cont. Dyn. Syst. B **10**, 857–869 (2004)
25. E.A. Coddington, N. Levinson, *Theory of Ordinary Differential Equations* (McGraw-Hill, New York, 1955)
26. D.E. Pelinovsky, C. Sulem, Theor. Mat. Phys. **122**, 98–106 (2000)
27. G. Schneider, H. Uecker, Z. angew. Math. Phys. **54**, 677–712 (2003)
28. J. Giannoulis, A. Mielke, Nonlinearity **17**, 551–565 (2004)
29. P.G. Kevrekidis, K.O. Rasmussen, A.R. Bishop, Int. J. Mod. Phys. **15**, 2833–2900 (2001)
30. G.L. Alfimov, P.G. Kevrekidis, V.V. Konotop, M. Salerno, Phys. Rev. E **66**, 046608 (2002)
31. A.A. Sukhorukov, Yu.S. Kivshar, Phys. Rev. E **65**, 036609-14 (2002)
32. R.S. MacKay, S. Aubry, Nonlinearity **7**, 1623–1643 (1994)
33. D.E. Pelinovsky, P.G. Kevrekidis, D.J. Frantzeskakis, Physica D **212**, 1–19 (2005)
34. P.G. Kevrekidis, D.E. Pelinovsky, Proc. Royal Soc. A **462**, 2671–2694 (2006)
35. D.E. Pelinovsky, P.G. Kevrekidis, D.J. Frantzeskakis, Physica D **212**, 20–53 (2005)

36. M. Lukas, D.E. Pelinovsky, P.G. Kevrekidis, nlin.PS/0610070
37. T. Kapitula, Physica D **156**, 186–200 (2001)
38. J. Fröhlich, S. Gustafson, B.L.G. Jonsson, I.M. Sigal, Comm. Math. Phys. **250**, 613–642 (2004)
39. F. Abdullaev, *Theory of Solitons in Inhomogeneous Media* (Wiley , Chichester, 1994)
40. K.A. Gorshkov, L.A. Ostrovsky, Physica D **3**, 428–438 (1981)
41. J.C. Bronski, R.L. Jerrard, Math. Res. Lett. **7**, 329–342 (2000)
42. B.L.G. Jonsson, J. Fröhlich, S. Gustafson, I.M. Sigal, Ann. Henri Poincare **7**, 621–660 (2006)
43. D.E. Pelinovsky, P. Kevrekidis, cond-mat/0610881
44. V.A. Brazhnyi, V.V. Konotop, Phys. Rev. A **68**, 043613 (2003)
45. B. Sandstede, Trans. Am. Math. Soc. **350**, 429–472 (1998)
46. T. Kapitula, P. Kevrekidis, Z. Chen, SIAM J. Appl. Dyn. Syst. **5**, 598–633 (2006)
47. T. Kapitula, P. Kevrekidis, Chaos **15**, 037114-13 (2005)
48. T. Kapitula, P. Kevrekidis, Nonlinearity **18**, 2491–2512 (2005)
49. E.H. Lieb, R. Seiringer, J. Yngvason, Phys. Rev. A **61**, 043602 (2000)
50. E.H. Lieb, R. Seiringer, J.P. Solovej, J. Yngvason, *The Mathematics of the Bose Gas and its Condensation*, in Oberwolfach Seminars, vol 34 (Birkhäuser, Basel, 2005)
51. A. Elgart, L. Erdös, B. Schlein, H.T. Yau, Arch. Ration. Mech. Anal. **179**, 265–283 (2006)
52. D.E. Pelinovsky, P.G. Kevrekidis, D.J. Frantzeskakis, V. Zharnitsky, Phys. Rev. E **70**, 047604 (2004)

Index

A

Abrikosov lattice, *see* vortex lattice,
Abrikosov
Anti-vortex, *see* vortex, pair
Atom laser
pulsed, **146**

B

Bloch
bands, 247
functions, 11, 103, 379, 382, 383,
385–387
oscillations, 262, **271**, 276, 280
spectrum, **254**, 341
waves, **102**, 104, 119, 248, 254, 273,
380
waves, nonlinear, 99, **104**, 121, 123,
126

Bogoliubov

Bogoliubov-de Gennes equation, 13,
134, 174, 200, 203, 357, 361
excitations, 105, 115, 204
spectrum, 247, **255**, 257

Bose-Einstein condensate

dipolar, 26, 40, 143, 183, 184, 280
homogeneous, 16, 68, 77, 80, 141,
181, 186, 355, 396
inhomogeneous, 39, 74, 344
molecular, 6, 49, **279**, 344
rotating, 175, 177, 195, 198, 203,
220, 225, 232, 235, 238, 240, 313,
343, 368
spinor, 51, 124, 168, 223, 302, **309**,
314, **318**, 320, 343, 354

Bright soliton, **14**, **27**, 109, 143, 335,
338

gap, *see* gap soliton

multi-dimensional, *see* multi-dimensional solitons
ring, **149**, 151
Townes, 39, 143, 151
train, 14, 36, 41, **54**, 58, **113**, 146,
149, 298, 317

C

Chemical potential, 9, 11, 16, 50, 67,
72, 89, 93, 102, 106, 109, 125,
137, 181, 217, 220, 251, 254, 289,
318, 332, 356, 367
Collapse, 12, 25, 28, 39, 41, 45, 49, 56,
107, 112, 143, 222
Coupled-Mode, **380**

D

Dark soliton, **14**, **68**, 87, 89, 134, 158,
336, 339
ring, **137**
spherical shell, **137**
train, **80**, 162, 164, 167
Density engineering, **79**, 87, 158, 159,
166, 316
Discrete nonlinear Schrödinger equation, *see* nonlinear Schrödinger equation, discrete
Dissipation, **77**, 92, 137, 174, 180, 181,
197, 214, 222
DNLS, *see* nonlinear Schrödinger equation, discrete

Domain-wall, 287, **290**, 299, 307, **311**, 323
 cross, 287, **299**
 propeller, 287, **299**

F

Fermion, 7, 41, 48, 173, 191, 287, 295, 298
 in lattices, **279**
 Feshbach resonance, 4, **5**, 26, 28, 36, 38, **46**, 48, 56, 72, **80**, 146, 222, 312, 344, 396

G

Gap
 multi-component states, **124**
 soliton, 99, 104, **109**, 277, 288, 297, 341, 378, 381
 vortex, **121**, 123, 343
 GPE, *see* Gross–Pitaevskii Equation
 Gross–Pitaevskii Equation
 coupled, **288**, 295, 298, 301, 302, 311
 derivation, **4**, **354**
 generalized, 357
 modified, 146, **183**
 multi-dimensional, 377
 one-dimensional, **8**, 10, 27, 50, 67, 102, 332
 stochastic, 114, 174, 180, 364, **365**, **367**, 369
 three-dimensional, 5, **8**, 66, 101, 184, 220, 249, 356
 two-dimensional, **8**, 39, 103, 139
 Ground state, *see* State, ground

H

Hartree-Fock-Bogoliubov, 146, 148, 357, **359**
 Healing length, 8, 14, 55, 57, 66, 86–88, 126, 139, 142, 159, 162, 164, 175, 176, 184, 203, 204, 216, 218, 319, 340
 Heat bath, *see* thermal, bath
 Helium, *see* liquid Helium
 Hydrodynamic
 equations, 70, 177, 182, 196, 287, 295

instability, **180**, 236
 theory, 142, **211**, 288

I

Immiscibility
 transition to immiscibility, 288, **290**, 292
 Impurities
 localized, 26, 75, 79, 177, 236, 331, 334–337, 341, 343
 Instability
 dynamical, 13, 99, 105, 114, 136, 143, 176, 195, 198, 203, **256**, 257, 275
 hydrodynamical, *see* hydrodynamic instability
 Landau, 216, 222, **256**, 276
 modulational, 14, 41, 57, 99, 105, 114, 147, 248, 256, 257, 291, 333
 snaking, 134, 136, **163**, 275
 symmetry breaking, 110
 thermal, **180**
 thermodynamic, 69, 174, 176

Interactions

interatomic, 4, **5**, **49**, 125, 332, 344
 interatomic, attractive, 5, 25, 38, 45, 144, 184, 332
 interatomic, repulsive, 5, 25, 66, 86, 95, 99, 143, 174, 184, 333
 soliton-impurity, 26, 75, **335**, **336**, 337
 soliton-soliton, 41, 54, 70, **148**, 166
 vortex-impurity, **341**

Interferometry

matter-wave, 89, 93, **199**

J

Josephson
 effect, 117, **273**
 oscillations, 262, 290

K

Kelvin mode, *see* wave, Kelvin
 Kinetic Theory
 Gardiner–Zoller, 362, **364**
 Stoof, 355, 362, **363**

L

Landau-Zener tunneling, 112, 262, 270, **272**

Liquid Helium, 3, 173–175, 179, 181, 192, 204, 213, 219, 236, 307

M

Management

dispersion/diffraction, 99, **106**, 109, **276**

nonlinearity, *see* Feshbach resonance

Matter-wave

guidance/manipulation, 101, **331**, **332**, 333, 334, 341

interferometry, *see* interferometry

Mean-field Theory

beyond mean-field Theory, 149, 249, **353**

Miscibility, *see* immiscibility

Mott insulator, 242, 249, 271, **277**

Multi-component condensates

multi-component solitons, 126, 133, 142, 288, **297**, 317

multi-component vortices, 290, 313, 323

Multi-dimensional solitons, **38**, **133**, 143, 152, **157**

N

NLS, *see* nonlinear Schrödinger equation

Nonlinear Schrödinger Equation

discrete, **10**, 118, 247, **249**, 250, 252, 253, 256, 273, 303, 343, 377, 379, 387

nonpolynomial, 28, 288, 302

polynomial, 10, 72

quintic, 10, 38, 39, 72, 75, 303

saturable, 303

Nonlinearity

higher order, *see also* nonlinear Schrödinger equation (quintic, polynomial), 46, **56**, 75

O

Optical

lattice, 6, 7, 10, 36, 88, **99**, 152, **247**, **267**, 297, 333, 334, 337–339, 342

nonlinear lattice, 37, 120

superlattice, 8, 269, **340**

trapping, 50

P

Perturbation Theory

adiabatic, 30, 32, 336

Phase

coherence, 146, 249, 275, 278, **314**

engineering, 14, 87, 89, 158, 316

imprinting, **79**, 87, 89, 91, 93, 116, 121, 176, 178, **192**, 203, 230

Potential

Confining, **394**

confining, *see also* magnetic

decaying, 378, 384, **391**

effective, 26, 32, 35, 37, 126, 258, 273, 333, 337, 338

external, 4, **6**, 70, 143, 211, 249, 309, 333, 354, 377

harmonic, *see* magnetic

interatomic, 46, 354, 355

linear, 8, 29, **34**

localized, *see* impurities

magnetic, 7, 8, 26, 66, 86, 174, 194, 220, 235, 288, 334, 394

optical lattice, *see* optical lattice

Periodic, **378**

periodic, *see also* optical lattice

quadratic, *see* magnetic

random, 27, 36, 38

time-varying, 8, 27, 34, 78, 177, 182, 249, 269, 333

R

Radiation effects, 30, **33**, 35, 37, 181, 337, 340

S

Scattering length

space-varying, 27, 30, 36, 344

time-varying, *see also* Feshbach resonance, 27, 30, 38, 39

Shock wave, *see* wave, shock

Skyrmion, 133, 143, 157, 176, 191, 194, 303, 313

Soliton

bright, *see* bright soliton

dark, *see* dark soliton

gap, *see* gap soliton

- Spectroscopy
 surface wave, 198, **200**
- Spin
 dynamics, **320**
 textures, *see also* skyrmion, 143, 194, 224, **317**
- Spinor condensates, *see* Bose–Einstein condensates, spinor
- State
 Bloch, *see* Bloch
 excited, 50, 105, 121, 125, 126, 151, 180, 308, 355, 360, 362, 367
 ground, 9, **11**, 13, 28, 40, 48, 52, 66, 67, 73, 77, 102, 113, 117, 125, 137, 139, 158, 160, 184, 225, 267, 290, 319, 389, 393, 395
- Superfluidity, 5, 162, 165, 173, 180, **191**, 197, 213, 214, 236, 257, 276, 365
 helium, *see* liquid Helium
 turbulence, 142
- Superradiance, **185**
- Surface mode, *see* wave, surface
- Symbiotic solitons, 288, **297**
- Symmetry breaking, 133, 151, 195, 198, 201, 214, 220, 291, 293, 296, 323, 354, 356–358
- T**
- Thermal
 bath, **148**, 214, 365, 367
 cloud, 58, 65, 92, 115, 117, 148, 177, 196, 198, 230, 313, 316, 323, 337, 353, 355, **357**, **359**, 361, 363, 364, 367
- Thermodynamic instability, *see* instability, thermodynamic
- Thermodynamics, 196, 214, 216, 222, **315**, **323**, 369
- Tkachenko mode, 218, 219, 236, 240, 343
- V**
- Vortex, **14**, **175**, **214**
 bending, 179, 198, **198**, 232, 235
 charge, 16, 122, 123, 150, **173**, 175, 193, **198**, **202**, 223, 316
 decay, 176, 182, **198**
 discrete, 343
- dynamics, **178**, 232
 energy, **184**, 218
 filament, 85, 123, 135, 176, 178, 179, 203, 213, **218**, 231, 235, 313
 gap, *see* gap, vortex
 higher order, *see* vortex, multiply-charged
 lattice, *see* vortex lattice
 line, *see* vortex filament
 manipulation, 332, **341**, 343
 molecules, 176
 multi-component, *see* multi-component, vortices
 multiply-charged, 137, 175, 176, 178, 198, **202**, 316
 necklace, 138, 290
 nucleation, 176, **176**, 177, **177**, 192, **192**, 194, **195–197**, 216, **220**, 233, 343, 362
 pair, 52, 133, 134, 173, 176–178, 182, 233, 237, 366
 profile, 16, 175, **198**
 ring, 85, 133, 139, 140, **141**, 157, 159, **163**, 168, 173, 176, 178
 spin, *see* multi-component, vortices
 stack, 124, 198
 svortex, 133, 140
 texture, 143
- Vortex lattice, 14, 173, 177, 179, 180, 182, 195, **211**, **218**, **229**, 230, 233, 235, 313, 332, 334, 342, 368
- Abrikosov, 175, 205, 221, 231, 343
- W**
- Wave
 Bloch, *see* Bloch, waves
 Kelvin, 142, 179, 183, **203**, 204, 218, 236
 matter, *see* matter-wave
 packet, 37, 50, 79, 106, 109, 118, 199, 200, 248, 250, 258–260, 276, 315
 shock, 159, 162, 164, 343, 344
 sound, **71**, 76, 80, 162, 181, 185, 256, 341
 surface, *see also* spectroscopy, 177, 200, 220, 221, 233, 235
 Tkachenko, *see* Tkachenko mode
- Winding number, *see* vortex charge

Springer Series on
ATOMIC, OPTICAL, AND PLASMA PHYSICS

Editors-in-Chief:

Professor G.W.F. Drake

Department of Physics, University of Windsor
401 Sunset, Windsor, Ontario N9B 3P4, Canada

Professor G. Ecker

Ruhr-Universität Bochum, Fakultät für Physik und Astronomie
Lehrstuhl Theoretische Physik I
Universitätsstrasse 150, 44801 Bochum, Germany

Professor H. Kleinpoppen

Fritz-Haber-Institut
Max-Planck-Gesellschaft
Faradayweg 4–6, 14195 Berlin, Germany

Editorial Board:

Professor W.E. Baylis

Department of Physics, University of Windsor
401 Sunset, Windsor, Ontario N9B 3P4, Canada

Professor U. Becker

Fritz-Haber-Institut
Max-Planck-Gesellschaft
Faradayweg 4–6, 14195 Berlin, Germany

Professor P.G. Burke

Brook House, Norley Lane
Crowton, Northwich CW8 2RR, UK

Professor R.N. Compton

School of Mathematics and Physics
David Bates Building
Queen's University
Belfast BT7 1NN, UK

Professor M.R. Flannery

School of Physics
Georgia Institute of Technology
Atlanta, GA 30332-0430, USA

Professor C.J. Joachain

Faculté des Sciences
Université Libre Bruxelles
Bvd du Triomphe, 1050 Bruxelles, Belgium

Professor B.R. Judd

Department of Physics
The Johns Hopkins University
Baltimore, MD 21218, USA

Professor K.P. Kirby

Harvard-Smithsonian Center for Astrophysics
60 Garden Street, Cambridge, MA 02138, USA

Professor P. Lambropoulos, Ph.D.

Max-Planck-Institut für Quantenoptik
85748 Garching, Germany, and
Foundation for Research
and Technology – Hellas (F.O.R.T.H.),
Institute of Electronic Structure
and Laser (IESL),
University of Crete, PO Box 1527
Heraklion, Crete 71110, Greece

Professor G. Leuchs

Friedrich-Alexander-Universität
Erlangen-Nürnberg
Lehrstuhl für Optik, Physikalisches Institut
Staudtstrasse 7/B2, 91058 Erlangen, Germany

Professor P. Meystre

Optical Sciences Center
The University of Arizona
Tucson, AZ 85721, USA

Springer Series on
ATOMIC, OPTICAL, AND PLASMA PHYSICS

- 10 **Film Deposition by Plasma Techniques**
By M. Konuma
- 11 **Resonance Phenomena in Electron–Atom Collisions**
By V.I. Lengyel, V.T. Navrotksy, and E.P. Sabad
- 12 **Atomic Spectra and Radiative Transitions**
2nd Edition
By I.I. Sobel'man
- 13 **Multiphoton Processes in Atoms**
2nd Edition
By N.B. Delone and V.P. Krainov
- 14 **Atoms in Plasmas**
By V.S. Lisitsa
- 15 **Excitation of Atoms and Broadening of Spectral Lines**
2nd Edition, By I.I. Sobel'man, L. Vainshtein, and E. Yukov
- 16 **Reference Data on Multicharged Ions**
By V.G. Pal'chikov and V.P. Shevelko
- 17 **Lectures on Non-linear Plasma Kinetics**
By V.N. Tsytovich
- 18 **Atoms and Their Spectroscopic Properties**
By V.P. Shevelko
- 19 **X-Ray Radiation of Highly Charged Ions**
By H.F. Beyer, H.-J. Kluge, and V.P. Shevelko
- 20 **Electron Emission in Heavy Ion–Atom Collision**
By N. Stolterfoht, R.D. DuBois, and R.D. Rivarola
- 21 **Molecules and Their Spectroscopic Properties**
By S.V. Khristenko, A.I. Maslov, and V.P. Shevelko
- 22 **Physics of Highly Excited Atoms and Ions**
By V.S. Lebedev and I.L. Beigman
- 23 **Atomic Multielectron Processes**
By V.P. Shevelko and H. Tawara
- 24 **Guided-Wave-Produced Plasmas**
By Yu.M. Aliev, H. Schlüter, and A. Shivarova
- 25 **Quantum Statistics of Nonideal Plasmas**
By D. Kremp, M. Schlanges, and W.-D. Kraeft
- 26 **Atomic Physics with Heavy Ions**
By H.F. Beyer and V.P. Shevelko
- 27 **Quantum Squeezing**
By P.D. Drumond and Z. Ficek
- 28 **Atom, Molecule, and Cluster Beams I**
Basic Theory, Production and Detection of Thermal Energy Beams
By H. Pauly
- 29 **Polarization, Alignment and Orientation in Atomic Collisions**
By N. Andersen and K. Bartschat
- 30 **Physics of Solid-State Laser Physics**
By R.C. Powell
(Published in the former Series on Atomic, Molecular, and Optical Physics)
- 31 **Plasma Kinetics in Atmospheric Gases**
By M. Capitelli, C.M. Ferreira, B.F. Gordiets, A.I. Osipov
- 32 **Atom, Molecule, and Cluster Beams II**
Cluster Beams, Fast and Slow Beams, Accessory Equipment and Applications
By H. Pauly
- 33 **Atom Optics**
By P. Meystre
- 34 **Laser Physics at Relativistic Intensities**
By A.V. Borovsky, A.L. Galkin, O.B. Shiryaev, T. Auguste
- 35 **Many-Particle Quantum Dynamics in Atomic and Molecular Fragmentation**
Editors: J. Ullrich and V.P. Shevelko